学位論文

Search for Gluinos using Final States with One Isolated Lepton in the LHC-ATLAS Experiment

(LHC-ATLAS 実験における 1 レプトン終状態を用いたグルイーノ探索)

平成 29 年 7 月博士 (理学) 申請

東京大学大学院理学系研究科
物理学専攻

陳　詩遠

Search for Gluinos using Final States with One Isolated Lepton in the LHC-ATLAS Experiment

Ph. D dissertation

Shion Chen

Department of Physics,
School of Science,
The University of Tokyo
7-3-1, Hongo, Bunkyo-ku, 113-0033, Tokyo, Japan

July 2017

Abstract

Despite the enormous success of the Standard Model in particle physics, there are still a number of problems left to be solved such as the fine tuning problem of the higgs mass, or the unaccounted presence of dark matter and so on. It is then strongly motivated to extend the Standard Model, and the Minimal Super-symmetric Standard Model (MSSM) has been one of the most appealing candidates, where a boson-fermion symmetry (super-symmetry; SUSY) is introduced. Experimental searches of SUSY particles predicted by MSSM has been widely performed over the decade in collider experiments. Though no evidence has been claimed so far, searches in the Large Hadron Collider (LHC) are anticipated with the unprecedented high center-of-mass energy and increased data statistics, allowing one to probe heavier SUSY particles. Gluino is one of the SUSY particles of which search is increasingly motivated after the discovery of higgs boson with its mass of 125 GeV.

This thesis presents the updated search for gluinos via proton-proton collisions with the center-of-mass energy of $\sqrt{s} = 13$ TeV at LHC, by focusing on the final state with exactly one lepton. With respect to the past searches, the sensitivity to heavier gluino is drastically gained using the improved analysis technique and updated data statistics (36.1 fb^{-1} of integrated luminosity) collected in the ATLAS detector.
No significant data excess is found in the unblinded dataset, and the exclusion limits are set on all the targeted gluino decay scenarios. As a general conclusion, it is confirmed that up to 1.7 TeV $\sim$ 2.0 TeV in gluino mass and up to $\sim$ 1 TeV in the lightest neutralino mass is excluded for typical mass spectra, while the limit extends up to 1.5 TeV $\sim$ 1.9 TeV in gluino mass for the case of the dark matter oriented mass spectra.

Contents

Chapter 1

Introduction

This section provides the backgrounds necessary to motivate and understand the context of rest of the thesis. Starting with an brief theoretical overview of the Standard Model (SM) in the particle physics (widely referred from [1] and [2]) which is current our best validated knowledge about the universe, following by a review of the remained problems of SM to be solved. The concept of super-symmetry (SUSY) is then introduced as a candidate for the solution. A particular emphasis is placed on the Minimal Super-Symmetric Standard Model (MSSM), outlining the phenomenology and the experimental constraints given up to today. The goal of the study is finally set in the bottom in the chapter. Targeted experimental signature and the searching strategy are widely discussed.

1.1 The Standard Model of Elementary Particles

The particle content of the SM is shown in Table 1.1 and Table 1.2. There are three types of particles: fermions with the spin of 1/2 that consist matters: gauge bosons with the spin of 1 mediating the interaction acting between particles: and the spin-0 Higgs boson feeding their masses through the Brout-Englert-Higgs (or BEH) mechanism [3] [4].

The three types of gauge bosons; gluon (g); weak bosons ($W^{\pm}, Z$) and photon (γ) respectively characterize strong interaction, weak interaction and electromagnetic interaction. Fermions have two families; quarks which sense all the three gauge interactions; leptons which couple only via weak and electromagnetic interaction. Both families have up- and down-type. There are also two more duplications of them ("2nd / 3rd generation") with exactly the same properties except the masses. Each fermions furthermore have the charge conjugated partner called anti-fermions.

1.1.1 The Gauge Principle and Particle Interaction

A successful theory for elementary particles must be quantum and relativistic. The theory of SM is constructed in a relativistic framework of field theory, fully exploiting the virtue that time (t) and position ($\boldsymbol{x}$) are treated equivalently in that both are coordinates rather than observables. It is characterized by a Lorentz-invariant Lagrangian in which particles are described by a function in

Table 1.1: Fermion contents in the SM. The quantum numbers Q, T, T^3 and Y are respectively electric charge, weak iso-spin number, the third component of weak iso-spin and weak hyper charge. N_C represents the number of color states. The subscripts L, R indicate the chirality (left- or right-handed respectively), and the pharentheses denote the $SU(2)_L$ doublet.

	Generation			Q	T	T^3	Y	N_C
	1st	2nd	3rd					
Quarks	$\begin{pmatrix} u \\ d \end{pmatrix}_{\mathrm{L}}$	$\begin{pmatrix} c \\ s \end{pmatrix}_{\mathrm{L}}$	$\begin{pmatrix} t \\ b \end{pmatrix}_{\mathrm{L}}$	$\begin{pmatrix} 2/3 \\ -1/3 \end{pmatrix}$	1/2	$\begin{pmatrix} 1/2 \\ -1/2 \end{pmatrix}$	1/3	3
	u_{R}	c_{R}	t_{R}	2/3	0	0	4/3	3
	d_{R}	s_{R}	b_{R}	−1/3	0	0	−2/3	3
Leptons	$\begin{pmatrix} \nu_e \\ e^- \end{pmatrix}_{\mathrm{L}}$	$\begin{pmatrix} \nu_\mu \\ \mu^- \end{pmatrix}_{\mathrm{L}}$	$\begin{pmatrix} \nu_\tau \\ \tau^- \end{pmatrix}_{\mathrm{L}}$	$\begin{pmatrix} 0 \\ -1 \end{pmatrix}$	1/2	$\begin{pmatrix} 1/2 \\ -1/2 \end{pmatrix}$	−1	0
	e_{R}	μ_{R}	τ_{R}	−1	0	0	−2	0

Table 1.2: Gauge bosons and higgs in the SM. The notation for the quantum numbers are the same with Table 1.1.

		Q	T	T^3	Y	N_C
gluon	g	0	0	0	0	8
weak bosons	$W^\pm$	±1	1	±1	0	0
	Z	0	0	0	0	0
photon	γ	0	0	0	0	0
higgs	h	0	1/2	-1/2	1	0

terms of x^μ ("fields") following the Lorentz transformation law of corresponding spin expression. The free Lagrangian for a fermion are given by:

$$\mathcal{L} = i\bar{\psi}\gamma^\mu\partial_\mu\psi - m\bar{\psi}\psi + \text{h.c.} \tag{1.1}$$

where ψ is a spinor field with the mass of m, and γ^μ is the 4-dimensional gamma matrices. The first term corresponds to the kinetic terms and the second is to the mass term of the fermion.

Interaction between particles are ruled by a local symmetries referred as "gauge symmetry". The interaction terms are obtained by imposing on the free Lagrangian an invariant nature against the gauge transformation. In case of electromagnetic interaction, for instance, the gauge transformation is given by:

$$\psi \to e^{i\theta(x)Q}\psi = e^{i\theta(x)q}\psi \tag{1.2}$$

where Q is the generator of the $U(1)$ transformation, q is charge that the fermion f has, and $\theta(x)$ is an arbitrary time-space dependent phase. The free Lagrangian in Eq. (1.5) is not invariant under this transformation, however can be fix by a small hack in the differential in the free Lagrangian (∂_μ) such as:

$$\partial_\mu \to D_\mu := \partial_\mu - ieA_\mu(x) \tag{1.3}$$

where e is the elementary charge and $A(x)$ is a vector field transformed by the gauge transformation:

$$A_\mu \to A_\mu + \frac{1}{e}\partial_\mu \theta(x). \tag{1.4}$$

The interaction term then emerges as the extra terms in the Lagrangian:

$$\mathcal{L}_{\text{int.}} = e\bar{\psi}\gamma^\mu \psi A_\mu. \tag{1.5}$$

From the consistency with classical Maxwell equation, this describes the electromagnetic force acting on the fermion, and A_μ corresponds to the electromagnetic potential in the classical electromagnetism or the particle field for photon.

1.1.2 Perturbation and Renormalization

The effect of interaction is often characterized via transition amplitude from an initial state (i) to a final state (f):

$$\langle f| \, e^{-i\mathcal{H}_{\text{int.}} t} \, |i\rangle \,, \tag{1.6}$$

where $\mathcal{H}_{\text{int.}}$ is the interaction Hamiltonian obtained by a Legendre transformation of interaction Lagrangian. The amplitude is often a basic building block of phenomenological predictions such as interaction cross-section or decay branch, however it is in most of the cases not analytically calculable. It is therefore done through a perturbation expansion in terms of the coupling constant of the interaction, for which $\alpha := e^2/4\pi$ is conventionally used for electromagnetic interaction.

The small coupling constant of electromagnetic interaction ($\alpha \sim 1/137$) may sound to guarantee a good convergence behavior of the expansion in which the impact from the truncated orders in the series is small enough. It is however found that the higher-order contribution immediately leads to divergence quite everywhere in cross-section calculation (infrared / ultraviolet divergences), causing the theory unpredictable. This problem was solved by a procedure called "renormalization" where theory parameters (i.e. the masses and coupling constants) are redefined to absorb the infinities, maintaining a finite cross-section calculation. Historically, this formulation firstly succeeded in QED, and then understood by that the gauge symmetry played an important role in calcelling the divergence [5] [6]. From this moment, gauge symmetry started establishing the status as a guidance principle in constructing theories, beyond merely a prescription. It is also shown with considerable generality that well-behaving theory ("renormalizable theory") must respect gauge symmetry [7].

The consequence of renormalization also provided a critical insight that the magnitude of theory parameters effectively vary depending on the energy scale with which the interaction happen. The evolution is characterized by the renormalization group equation (RGE), for example, as for the coupling constant (α):

$$\frac{1}{\alpha(Q)^2} - \frac{1}{\alpha(Q_0)^2} = -\frac{\beta(\alpha)}{2\pi}\log\left(\frac{Q}{Q_0}\right), \tag{1.7}$$

where Q is the scale defined by the typical momentum transfer of the interaction process, and $\beta(\alpha)$ is the beta function, proportional to α^2 at 1-loop level. This evolution is known as the "running" effect, which is an useful proxy for exploring the behavior of theory over the scale.

1.1.3 QED, QCD, and the Electroweak Theory

The Lagrangian for Quantum Electromagnetic Theory (QED) is given by adding the kinetic terms of photon ($-\frac{1}{4}F_{\mu\nu}F^{\mu\nu}$) to one obtained in Sec. 1.1.1:

$$\mathcal{L} = -\frac{1}{4}F_{\mu\nu}F^{\mu\nu} + i\bar{\psi}\gamma^{\mu}\partial_{\mu}\psi - m\bar{\psi}\psi \; + \text{h.c.} \tag{1.8}$$

with $F_{\mu\nu}$ being the field strength:

$$F_{\mu\nu} := \partial_{\mu}A_{\nu} - \partial_{\nu}A_{\mu}. \tag{1.9}$$

Similar to what is done in QED with the gauge group of $U(1)$, the Lagrangian for strong and weak interaction can be generated by considering gauge groups of $SU(2)_L$ and $SU(3)$:

$$\psi \to e^{i\theta_a(x)\lambda^a}, \psi \qquad a = 1, 2, \ldots (N^2-1) \qquad\qquad (\text{for } SU(N))$$

with λ^a being the generators of the gauge group. The choice of the gauge groups are motivated by:

- ($SU(2)$ for weak interaction) the observation of approximate iso-spin symmetry in theories of nucleus decay,
- ($SU(3)$ for strong interaction) the factor of 3 enhancement in cross-section of the Drell-Yan process for quark-antiquark production with respect to muon pair production: $\sigma(ee \to q\bar{q})/\sigma(ee \to \mu\mu) = 3N_q$ where N_q is number quark species.

Strong Interaction

The Lagrangian for strong interaction is:

$$\begin{aligned} \mathcal{L}_{\text{QCD}} &= -\frac{1}{4}\hat{\boldsymbol{G}}_{\mu\nu}\hat{\boldsymbol{G}}^{\mu\nu} + \; \bar{q}(i\gamma^{\mu}D_{\mu} - m)q + \text{h.c.}, \\ D_{\mu} &:= \partial_{\mu} + ig_s\sum_{a=1}^{8} G_{\mu}^{a}\frac{\lambda_a}{2} \\ \hat{\boldsymbol{G}}_{\mu\nu} &:= \partial_{\mu}\boldsymbol{G}_{\nu} - \partial_{\nu}\boldsymbol{G}_{\mu} - g_s\,\boldsymbol{G}_{\mu}\times\boldsymbol{G}_{\nu}, \\ \boldsymbol{G}_{\mu} &:= \{G_{\mu}^{a}; a = 1, 2, \ldots, 8\} \end{aligned} \tag{1.10}$$

where G_{μ}^{a} and q represent the fields for gluons and quarks respectively. g_s is related to the strong coupling constant α_s by $\alpha_s = g_s^2/4\pi$. The charge of strong interaction is called "color", and the theoretical framework is referred to Quantum Chromo Dynamics (QCD). Quarks are in the triplet and gluons are in the octet expression with 3 and 8 degenerated states respectively. In addition, due to the non-Abelian nature of $SU(3)$, gluon has self-interaction with coupling to itself. One distinct consequence of this is the negative running coupling:

$$\alpha_s(Q) = \frac{4\pi\alpha_s(\mu_R)}{4\pi + \beta_0\alpha_s(\mu_R)\log\left(Q^2/\Lambda_{\text{QCD}}^2\right)} \tag{1.11}$$

where $\beta = 11 - 2n_f/3$ (n_f is number of quarks with the mass above Q), μ_R the renormalization scale (a reference scale of renormalization, different from the physical energy scale Q), and $\Lambda_{\rm QCD}$ the QCD cut-off scale at ~ 200 MeV. The indication of $\beta < 0$ is decreasing coupling constant with increased energy scale Q. Despite of the generally larger coupling than that of electromagnetic interaction, in the energy scale interested in LHC ($Q > 100$ GeV), α_s typically about 0.1, which is small enough to recover the perturbative picture ("asymptotic freedom"). On the other hand, the coupling becomes increasingly strong as approaching to $\Lambda_{\rm QCD}$, leading to an immediate catastrophe of the perturbation picture. As a result of this strong coupling, colored particles are forced to combine each other to form a color singlet state ("confinement"),

Electro-weak interaction

Weak interaction is described by a larger gauge group $SU(2)_L \times U(1)_Y$, in a manner where weak and electromagnetic interaction reside altogether [8] [9] [10]. The basic idea is that they share the common origin at high energy scale and branch into separate interactions at some point through a spontaneous symmetry breaking $SU(2)_L \times U(1)_Y \to U(1)_Q$. The regime of unified interaction is commonly referred as electroweak (EW) interaction.

The gauge transformation distinguishes chirality of fermions, in that $SU(2)_L$ selectively acts to the left-handed component, accounting for the observed parity violating nature of weak interaction [11] [12]:

$$\psi_{\rm L} \to e^{i\theta T_3 + i\Theta Y}\psi_{\rm L} \tag{1.12}$$

$$\psi_{\rm R} \to e^{i\Theta Y}\psi_{\rm R}. \tag{1.13}$$

The Lagrangian arrives at:

$$\begin{aligned}
\mathcal{L}_{\rm EW} &= -\frac{1}{4}\hat{\boldsymbol{W}}_{\mu\nu}\hat{\boldsymbol{W}}^{\mu\nu} - \frac{1}{4}B_{\mu\nu}B^{\mu\nu} + \ \bar{\psi}(i\gamma^{\mu}D_{\mu} - m)\psi + \text{h.c.}, \\
D_{\mu} &:= \partial_{\mu} + ig\sum_{a=1}^{3} W_{\mu}^{a}\tau_a + ig^{'}\frac{Y}{2}B_{\mu} \\
\hat{\boldsymbol{W}}_{\mu\nu} &= \partial_{\mu}\boldsymbol{W}_{\nu} - \partial_{\nu}\boldsymbol{W}_{\mu} - g\boldsymbol{W}_{\mu} \times \boldsymbol{W}_{\nu} \\
\boldsymbol{W}_{\mu} &:= \{W_{\mu}^{a}; a = 1, 2, 3\} \\
B_{\mu\nu} &= \partial_{\mu}B_{\nu} - \partial_{\nu}B_{\mu}
\end{aligned} \tag{1.14}$$

where W_{μ}^{a} and B_mu are the fields of EW gauge bosons, and $g, g^{'}$ are the coupling respectively for $SU(2)_L$ and $U(1)_Y$. $\boldsymbol{\tau}(= \boldsymbol{\sigma}/2)$ are generators of $SU(2)$.

The Lagrangian can be also re-written by introducing weak currents J_μ:

$$\begin{aligned}
\mathcal{L}_{\mathrm{EW}} &= -\frac{1}{4}\sum_{a=1}^{3} W^a_{\mu\nu}W^{a\mu\nu} - \frac{1}{4}B_{\mu\nu}B^{\mu\nu} \\
&\quad - \frac{g}{2}(J^+_\mu W^{-\mu} + J^-_\mu W^{+\mu}) - gJ^3_\mu W^{3\mu} - \frac{g^{'}}{2}J^Y_\mu B^\mu + \text{h.c.} \\
J^\pm_\mu &:= \frac{1}{\sqrt{2}}(W^1_\mu \mp iW^2_\mu) \\
J^a_\mu &:= \bar{\psi}_L\gamma^\mu\tau_q W^a_\mu\psi_L \ \ (a = 1, 2, 3) \\
J^Y_\mu &:= Y\bar{\psi}_L\gamma^\mu\psi_L.
\end{aligned} \tag{1.15}$$

$J^\pm_\mu$ represent currents changing T_3, while J^0_μ and J^Y_μ neutral current conserving either T_3 and Y.

The EW symmetry breaking is expressed by mixing the fields (W^3_μ, B_μ) into (Z_μ, A_μ):

$$\begin{pmatrix} Z_\mu \\ A_\mu \end{pmatrix} := \begin{pmatrix} \cos\theta_W & -\sin\theta_W \\ \sin\theta_W & \cos\theta_W \end{pmatrix} \begin{pmatrix} W^3_\mu \\ B_\mu \end{pmatrix} \tag{1.16}$$

with a mixing angle (Weinberg angle θ_W) of:

$$\tan\theta_W := \frac{g^{'}}{g}. \tag{1.17}$$

The current terms in the Lagrangian Eq. (1.15) then becomes:

$$\begin{aligned}
&- \frac{g}{2}(J^+_\mu W^{-\mu} + J^-_\mu W^{+\mu}) \\
&+ \frac{g}{\cos\theta_W}\left(-\cos^2\theta_W J^3_\mu + \frac{\sin^2\theta_W}{2}J^Y_\mu\right) Z^\mu \\
&- g\sin\theta_W\left(J^3_\mu + \frac{1}{2}J^Y_\mu\right) A^\mu
\end{aligned} \tag{1.18}$$

By choosing $Y := 2(Q - T^3)$, A_μ becomes associated with the gauge field of electromagnetic interaction, and the electric charge is found to be related to the weak coupling constant by the Weinberg angle: $e = g\sin\theta_W$.

1.1.4 Electroweak Symmetry Breaking and the Higgs boson

One outstanding problem in the EW Lagrangian is the prohibition of mass terms, for both gauge bosons and fermions, since they explicitly violates the gauge invariance. The BEH mechanism [3] [4] is then employed to solve the problem, where assuming a $SU(2)$ doublet ϕ $(Y = -1, T = 1/2)$ with scalar fields $\phi = (\phi_1, \phi_2) = (\phi^+, \phi^0)$, and a potential $V(\phi)$ added in the Lagrangian:

$$\begin{aligned}
\mathcal{L}_{\mathrm{Higgs}} &:= (D_\mu\phi)^\dagger(D^\mu\phi) - V(\phi) \\
V(\phi) &:= \mu^2\phi^\dagger\phi + \lambda(\phi^\dagger\phi)^2.
\end{aligned} \tag{1.19}$$

While the minimum of the potential is always found in $\phi = (0, 0)$ in the $\phi_1 - \phi_2$ plane when $\mu^2 > 0$, negative μ^2 leads to non-trivial minima in $v := |\phi|^2 = -\mu^2/2\lambda$. This causes a shift of the vacuum expectation value : $\langle 0|\,\phi\,|0\rangle = 0 \to v$ (spontaneous symmetry breaking).

Redefining the field ϕ by the variation around the new vaccum $(0,v)$ $h(x)$:

$$\phi = \begin{pmatrix} 0 \\ v + h(x) \end{pmatrix} \tag{1.20}$$

and applying the $\partial_\mu \to D_\mu$ prescription to Eq. (1.19), one finds the mass terms for W, Z as:

$$\begin{aligned} m_W &= gv/2 \\ m_Z &= \sqrt{g^2 + g'^2}\, v/2, \end{aligned}$$

where the mass for W and Z is successfully provided.

The mass for scalar field h is also found to be:

$$m_h = \sqrt{-2\mu^2}.$$

thus h can be also regarded is physical mode, referred as higgs particle.

The fermion masses are fed by adding following Gauge invariant terms to Lagrangian:

$$\begin{aligned} \mathcal{L}_{\text{Yukawa}} := &- \bar{\psi}_{i,L} y_{\text{u}}^{ij} \phi \psi_{j,R} - \bar{\psi}_{i,R} y_{\text{u}}^{ij} \phi^\dagger \psi_{j,L} \\ &- \bar{\psi}_{i,L} y_{\text{d}}^{ij} \phi^c \psi_{j,R} - \bar{\psi}_{i,R} y_{\text{d}}^{ij} \phi^{c\dagger} \psi_{j,L} \\ &- \bar{\psi}_{i,L} y_{e}^{ij} \phi \psi_{j,R} - \bar{\psi}_{i,R} y_{e}^{ij} \phi^\dagger \psi_{j,L} \end{aligned} \tag{1.21}$$

where $i, j = 1, 2, 3$ index the generations of fermions. y_{u}^{ij}, y_{d}^{ij}, and y_{e}^{ij} are the components of Yukawa matrices respectively for up-, down-type quarks and down-type leptons. The Yukawa matrices are 3×3 matrices spanning over the family space, in which Yukawa couplings for each fermion are accommodated. The off-diagonal components are also responsible for the mixing between generations, which are set all zero for down-type leptons, while they are non-zero in case of quarks characterized by the CKM matrix [13].

Inserting Eq. (1.20), $\mathcal{L}_{\text{Yukawa}}$ is finally reduced to:

$$\begin{aligned} \mathcal{L}_{\text{Yukawa}} &= \sum_f y_f v \bar{\psi}\psi + y_f \bar{\psi}\psi h \\ &= \sum_f m_f \bar{\psi}\psi + y_f \bar{\psi}\psi h, \end{aligned} \tag{1.22}$$

where f is the index of fermions, with y_f (ϕ_f) being the mass eigenvalues (eigenstates) of the Yukawa matrices.

Higgs boson was discovered in LHC in 2012 [14] [15], bringing the last piece of the Standard Model in human knowledge. Measurements on its properties including the mass, spin [16] [17] and couplings [18] [19] are underway, which is all consistent with the SM so far. Figure 1.1 shows the coupling measurement by ATLAS and CMS in LHC Run1. Further Precision measurement is planned in the later stages in LHC as well as the future linear collider projects such as ILC (International Linear Collider).

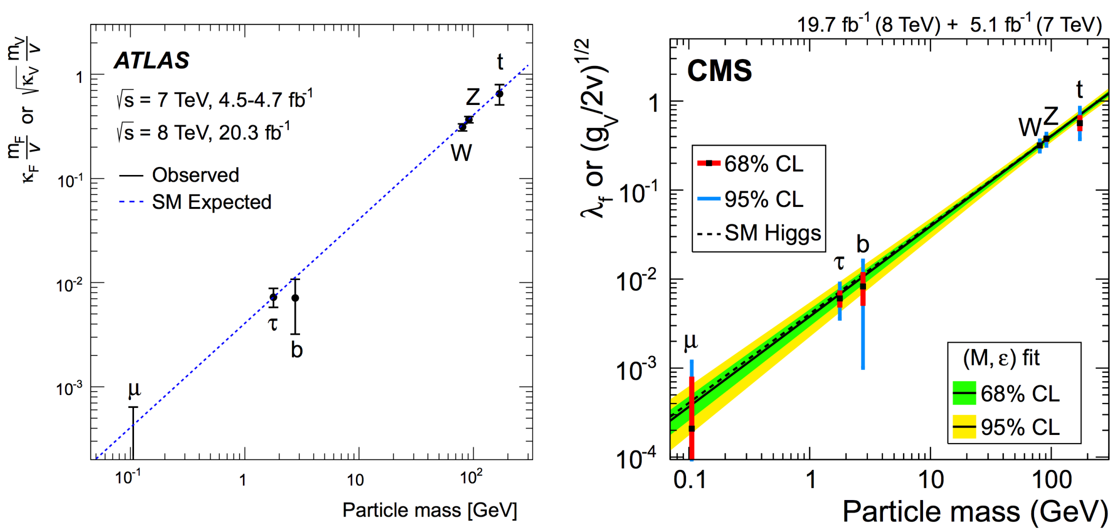

(a) (b)

Figure 1.1: Higgs coupling measurement in LHC Run1 carried out by (a) ATLAS [18] and (b) CMS [19].

1.2 Remained Problems for the Standard Model and the SUSY Solution

There is couple of homework from the SM, from critical issues to desirable extensions towards the ultimate theory. In this section, a focus on problems in which SUSY is particularly motivated as the solution.

1.2.1 The Fine-tuning Problem in Higgs Mass

Though divergences appearing in higher-order calculations in SM are universaly cured in renormalization by the cenceling with the counter terms, it has been pointed that the magnitude of the cancelling terms are unnaturally large in case of the radiation correction on the higgs mass [20] [21] [22] [23]. For instance, the loop correction given by a top-quark loop before renormalization is:

$$\Delta m_h^2 = -\frac{3|\lambda|^2}{8\pi^2}\Lambda^2 + O\left(\log \Lambda\right), \tag{1.23}$$

which is related by the renormalized mass ($m_{h,\mathrm{obs.}}$) and the bare mass ($m_{h,\mathrm{bare}}$) with:

$$m_{h,\mathrm{obs.}}^2 = m_{h,\mathrm{bare}}^2 + \Delta m_h^2. \tag{1.24}$$

The magnitude of the correction term Δm_h^2 can be order of $10^{38}(\mathrm{GeV})^2$ assuming SM is valid upto the Planck scale: $\Lambda \sim 10^{19}(\mathrm{GeV})^2$, while the observed mass is 125 GeV. Naively thinking this implies that the bare mass $m_{h,\mathrm{bare}}$ and the correction Δm_h has to cancel in a precision of 10^{-17} ("fine tuning problem" or "naturalness problem"). It is highly unnatural for a theory to contain such extraordinary scale hierarchy in it, therefore it is preferred to conceive the underlying mechanism behind it.

The simplest solution is to add a partner particle yielding the opposite contribution to cancel it. In SUSY, this is done by introducing scalar-top (bosonic partner of top-quark "stop") with the mass of m_S and the same couplings as tops. The quadratic terms cancel out as:

$$\begin{aligned} \tilde{\Delta} m_h^2 &= 2 \times \frac{3|\lambda|^2}{16\pi^2}\Lambda^2 + O\left(\log \Lambda\right) \\ \Delta m_{h,\mathrm{stop}}^2 &= \Delta m_h^2 + \tilde{\Delta} m_h^2 = O\left(\log \Lambda\right) \end{aligned} \tag{1.25}$$

where the 10^{-34} order of fine-tuning is no longer needed.

1.2.2 Grand Unification

It is the ultimate desire for physicists to explain all phenomena in the universe by a single principle. While in the SM, the EW symmetry breaking $SU(2)_L \times U(1) \to SU\!\!\!/(2) \times U(1)_Q$ implies a common origin of electromagnetic and weak interaction, this encourages physicists to conceive another unification together with strong interaction at a higher scale (Grand Unification Theory; GUT).

Running coupling constants are useful proxies to analyze the possibility of such unification. The evolution of coupling constants along scale is given by the RGE:

$$\frac{1}{\alpha_i(Q)^2} - \frac{1}{\alpha_i(Q_0)^2} = -\frac{\beta_i}{2\pi} \log\left(\frac{Q}{Q_0}\right), \tag{1.26}$$

with the indices $i = 1, 2, 3$ denote strong, weak and electro-magnetic interaction respectively. β_i are the beta functions. In the SM at 1-loop level, these are:

$$\begin{pmatrix} b_1 \\ b_2 \\ b_3 \end{pmatrix} = \begin{pmatrix} 1/10 \\ -43/6 \\ -11 \end{pmatrix} + n_{\text{gen}} \begin{pmatrix} 4/3 \\ 4/3 \\ 4/3 \end{pmatrix}, \tag{1.27}$$

where n_{gen} is the number of generation of fermions, which is equal to 3 for $Q > m_t$. One naively expects a convergence of the three couplings at a certain scale (μ_{GUT}) in case of the grand unification. Unfortunately, this does not happen in the SM, as illustrated in Figure 1.2 (a). However, it can be relatively easily realized in the SUSY regime, where more fermion particles can participate in the game changing the slope of the running. For instance, the beta function for MSSM is:

$$\begin{pmatrix} b_1 \\ b_2 \\ b_3 \end{pmatrix} = \begin{pmatrix} 3/5 \\ 1 \\ -3 \end{pmatrix}, \tag{1.28}$$

and the coupling unification is achieved at $\mu_{\text{GUT}} \sim 10^{16}$ GeV, as shown in Figure 1.2 (b). This is superizing given that the convergence can be easily violated with even a little different particle content, and this is one of the reasons that SUSY is particularly special among the BSM frameworks.

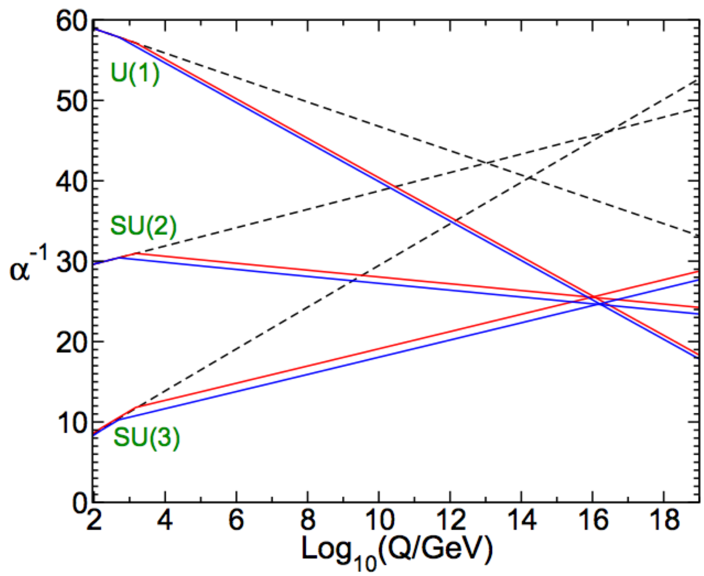

Figure 1.2: Two-loop renormalization group evolution of the inverse gauge coupling $1/\alpha_i$ in case of SM (dashed lines), and a scenario in MSSM (solid lines) where the masses of SUSY partners are set between 500 GeV and 1.5 TeV [24].

1.2.3 Dark Matter

Historically, the argument of dark matter (DM) originated from observations on velocity of galaxy rotation, implying excessive masses in galaxy center beyond the expectation from spectroscopy [25] [26]. The non-baryonic dark matter hypothesis has been strongly supported by the a number of observatory facts that comes up later including gravitational lensing effect. Currently the most commonly considered framework of dark matter is the Λ-CDM model (Cold Dark Matter) in which DM is assumed to:

- sense very weak interaction except gravitation (Weakly Interacting Massive Particles; WIMPs) [1]
- be non-relativistic, given that DM is relatively spatially localized such as in galaxy center.

The density abundance is dedicatedly measured via cosmic microwave background (CMB) by WMAP [28] and Planck [29] under the Λ-CDM regime:

$$\Omega_{\mathrm{CDM}}h^2 = \begin{cases} 0.1138 \pm 0.0045 & \text{(WMAP)} \\ 0.1186 \pm 0.0020 & \text{(Planck, TT+lowP+lensing)}, \end{cases} \tag{1.29}$$

While the SM has no candidates for DM, SUSY provides several attractive candidates when assuming the R-parity conservation (Sec 1.3.2) in which the lightest SUSY particle (LSP) becomes stable. It is worth noting that the LSP mass will be constrained by an upper bound about 3 TeV, when trying to explain the whole abandunce by SUSY. Though SUSY can be at any scale from theotical point of view, this is a strong motivation to believe in TeV-SUSY.

1.3 Super-Symmetry and the MSSM

Minimal Super-Symmetric Standard Model (MSSM) is a SUSY framework where minimum matter contents and degrees of freedom are newly introduced with respect to the SM such as:

- Only one set of SUSY partners is employed ($\mathcal{N}_{\mathrm{SUSY}} = 1$),
- SUSY partners of SM fermions have the spin of 0, while the partners for boson in SM (gauge boson and higgs) are spin-1/2
- Use only two higgs doublets to construct the higgs sector. [2]

Though it is called "minimal", MSSM is a framework general enough to expressing the typical natures of SUSY at phenomenology level, therefore this thesis will confine the scope within MSSM. An overview on MSSM is given in the rest of the section, widely based on the reference [24].

1.3.1 Particle Contents in MSSM

The particle contents are summarized in Table 1.3. Note that scalar-fermions (sfermions) have two modes indexed by L, R indicating that they are the SUSY partners of left-handed or right-handed

[1] This almost requires electrically neutral, but completely forbidden [27].

[2] Introducing multiple VEV is the simplest solution against the quantum anomalies that newly arise when extending to SUSY.

Table 1.3: Matter content of MSSM. The left column defines the naming convention for SUSY particles. $n[SU(3)_C](n[SU(2)_L])$ represents the degree of freedom of the $SU(3)_C(SU(2)_L)$ multiplet that the field(s) belongs to. All of them belongs to the single of $U(1)_Y$, thus the $U(1)$ charge Y is shown instead. There are also two set of replications for the 2nd and 3rd generation of (s)quarks/(s)leptons, which are not shown here.

Super-multiplet		SM sect.	SUSY partner	$n[SU(3)_C]$	$n[SU(2)_L]$	Y
gluon/gluino	G	g	$\tilde{g}$	8	1	0
EW gauge boson /	W	$W^{\pm}, W^0$	$\tilde{W}^{\pm}, \tilde{W}^0$	1	3	0
EW gaugino	B	B^0	$\tilde{B}^0$	1	1	0
lepton / slepton	L	$(\nu_e, e)_{\mathrm{L}}$	$(\tilde{\nu}_e, \tilde{e})_L$	1	2	-1
	E	$\tilde{e}_{\mathrm{R}}$	e_{R}	1	1	-2
quark / sqaurk	Q	$(u_{\mathrm{L}}, d_{\mathrm{L}})$	$\left(\tilde{u}_{\mathrm{L}}, \tilde{d}_{\mathrm{L}}\right)$	3	2	1/3
	U	u_{R}	$\tilde{u}_{\mathrm{R}}$	3	1	4/3
	D	d_{R}	$\tilde{d}_{\mathrm{R}}$	3	1	-2/3
Higgs boson /	H_{u}	$(H_{\mathrm{u}}^+, H_{\mathrm{u}}^0)$	$(\tilde{H}_{\mathrm{u}}^+, \tilde{H}_{\mathrm{u}}^0)$	1	2	1
higgsino	H_{d}	$(H_{\mathrm{d}}^0, H_{\mathrm{d}}^-)$	$(\tilde{H}_{\mathrm{d}}^0, \tilde{H}_{\mathrm{d}}^-)$	1	2	-1

SM fermions respectively. On the other hand, gauginos are all Majorana, in order to match the degree of freedom with either the patner gauge bosons and higgs bosons.

MSSM higgs sector has two higgs doublets ($\boldsymbol{H}_{\mathrm{u}} := (H_{\mathrm{u}}^+, H_{\mathrm{u}}^0)$, $\boldsymbol{H}_{\mathrm{d}} := (H_{\mathrm{d}}^-, H_{\mathrm{d}}^0)$) with their own vacuum expectation values (VEV):

$$v_{\mathrm{u}} := \left\langle H_{\mathrm{u}}^0 \right\rangle, \quad v_{\mathrm{d}} := \left\langle H_{\mathrm{d}}^0 \right\rangle,$$

where each provides the masses for up- or down-type fermions respectively. Their splitting is commonly parametrized using a mixing angle β as:

$$\tan\beta := v_{\mathrm{u}}/v_{\mathrm{d}}. \tag{1.30}$$

The consistency with SM is ensured by relating the VEVs as:

$$v_{\mathrm{SM}}^2 = v_{\mathrm{u}}^2 + v_{\mathrm{d}}^2. \tag{1.31}$$

Note that if gravity is quantized in the picture of QFT, there should be also the corresponding gauge boson "graviton" and its SUSY partner "gravitino" along a natural extension. In some SUSY scenarios, gravitino do act a important role such as in GMSB (Gauge Mediated SUSY Breaking), however we do not assume them in the study of this thesis.

1.3.2 The MSSM Lagrangian

Construction of a super-symmetric Lagrangian is commonly done by the method of super-potential or super-space. Though the procedure is skipped here, it may worth noting that it is not as a simple extension from SM Lagrangian as just adding terms accounting for the extra particle contents.

The outcome MSSM Lagrangian can be divided into two parts:

$$\mathcal{L}^{\mathrm{MSSM}} = \mathcal{L}^{\mathrm{MSSM}}_{\mathrm{SUSY}} + \mathcal{L}^{\mathrm{MSSM}}_{\mathrm{soft}}. \tag{1.32}$$

$\mathcal{L}^{\mathrm{MSSM}}_{\mathrm{SUSY}}$ is the SUSY invariant part of the Lagrangian which is given by:

$$\begin{aligned}
\mathcal{L}^{\mathrm{MSSM}}_{\mathrm{SUSY}} = & \frac{1}{4}F_{a\mu\nu}F^{a\mu\nu} + D^{\mu}\phi^{*}D_{\mu}\phi + \psi^{\dagger}\bar{\sigma}^{\mu}D_{\mu}\psi + i\lambda^{\dagger a}\bar{\sigma}D_{\mu}\lambda_a && \text{(Kinetic terms)}\\
& - \frac{1}{2}W^{ij}\psi_i\psi_j + h.c. && \text{(Yukawa interaction terms)}\\
& - \sqrt{2}g(\phi^{*}T^{a}\psi)\lambda_a + h.c. && \text{(Gaugino interaction terms)}\\
& - \sum_i \left|\frac{\delta W}{\delta\phi_i}\right|^2 + \frac{1}{2}(g_a\phi^{*}T^{a}\phi)^2 && \text{(Residual terms from the aux. fields)}
\end{aligned} \tag{1.33}$$

where ψ is SMS fermions are ϕ is the corresponding spin-0 SUSY partners, while λ are gauginos. W_{ij} is the second derivative of super-potential W, with W being defined by:

$$\begin{aligned}
W_{ij} &:= \frac{\delta^2 W}{\delta\phi_i\delta\phi_j},\\
W &:= U\boldsymbol{y}_{\mathrm{u}}QH_{\mathrm{u}} - D\boldsymbol{y}_{\mathrm{d}}QH_{\mathrm{d}} - E\boldsymbol{y}_{e}LH_{\mathrm{d}} + \mu H_{\mathrm{d}}H_{\mathrm{u}}.
\end{aligned} \tag{1.34}$$

$\boldsymbol{y}_{\mathrm{u}}$, $\boldsymbol{y}_{\mathrm{d}}$ and $\boldsymbol{y}_{e}$ are the same Yukawa matrices in Eq. (1.21). Note that no theory parameters are newly introduced compared with SM in $\mathcal{L}^{\mathrm{MSSM}}_{\mathrm{SUSY}}$. The soft SUSY breaking term $\mathcal{L}^{\mathrm{MSSM}}_{\mathrm{soft}}$ is SUSY variant part of the Lagrangian. Further caveats are provided as below:

SUSY breaking While an exact super-symmetry requires the SUSY partners being in the identical masses with respect to the SM particles, it is not the case at least in the energy scale of current our universe since no SUSY particles have been discovered so far. Therefore, a realistic SUSY model as an effective theory at the EW scale, must contain a scheme of SUSY breaking in its Lagrangian ($\mathcal{L}^{\mathrm{MSSM}}_{\mathrm{soft}}$). On the other hand, we don't want to ruin the desired features in SUSY at the cost of it, particularly as the solution of the higgs mass fine-tuning problem (Sec. 1.2.1). Therefore, it is common to restrict the SUSY breaking in a form of "soft breaking" where the cancelation of the quadratic divergence in the higgs mass loop correction Eq. (1.25) is maintained.

The most general form of the soft breaking terms is given by:

$$\begin{aligned}
\mathcal{L}_{\text{soft}}^{\text{MSSM}} &= \frac{1}{2}\left(M_3\,\tilde{g}\tilde{g} + M_2\tilde{W}\tilde{W} + M_1\tilde{B}\tilde{B} + \text{c.c.}\right) && \text{(gaugino mass terms)} && (1.35)\\
&- Q^\dagger\,\boldsymbol{m}_Q^2\,Q - L^\dagger\,\boldsymbol{m}_L^2\,L - U\,\boldsymbol{m}_U^2\,U^\dagger - D\,\boldsymbol{m}_D^2\,D^\dagger - E\,\boldsymbol{m}_E^2\,E^\dagger && \text{(sfermion mass terms)} && (1.36)\\
&- (U\boldsymbol{a}_{\text{u}}QH_{\text{u}} - D\boldsymbol{a}_{\text{d}}QH_{\text{d}} - E\boldsymbol{a}_eLH_{\text{d}} + \text{c.c.}) && \text{(trilinear coupling)} && (1.37)\\
&- m_{H_{\text{u}}}^2H_{\text{u}}^\dagger H_{\text{u}} - m_{H_{\text{d}}}^2H_{\text{d}}^\dagger H_{\text{d}} - (bH_{\text{u}}H_{\text{d}} + \text{c.c.}) && \text{(Higgs potential)} && (1.38)
\end{aligned}$$

The notation of the particle fields ($\tilde{g}$,$\tilde{W}$,$\tilde{B}$) and super-multiplet (Q,L,U,D,E,H_{u},H_{d}) follow the definition in Table 1.3. The first line Eq. (1.35) show the mass terms for gauginos, with M_1, M_2 and M_3 are respectively bino, wino and gluino mass. Eq. (1.37) and (1.36) are the Yukawa terms for SUSY particles where the former are the standard sfermion mass terms, and latter the trilinear terms describing the Yukawa interaction coupling left-handed and right-handed sfermions, emerged as the cross terms of super-multiplet. The mass matrices ($\boldsymbol{m}_Q$, $\boldsymbol{m}_L$, $\boldsymbol{m}_U$, $\boldsymbol{m}_D$, $\boldsymbol{m}_E$), and the A terms ($\boldsymbol{a}_{\text{u}}$, $\boldsymbol{a}_{\text{d}}$ and $\boldsymbol{a}_e$) are 3×3 matrices spanned in family space, equivalent to the CKM matrix in the SM sector multiplied by sparticles masses. The last terms are the MSSM higgs potential, controlling the EW symmetry breaking.

Though not specifically targeted in the thesis, there are a number of models in the market offering explicit mechanisms of the soft SUSY breaking. The most minimal models are known as GMSB (Gauge-Mediated SUSY Breaking [30]), AMSB (Anomaly-Mediated SUSY Breaking [31] [32]) or mSUGRA (minimal SUper Gravity [33]).

R-parity A quantum number R associated with the number of "SUSY partner" (analogous to the lepton number or baryon number etc.) can be defined by the spin, baryon number and lepton number as:

$$R := (-1)^{3(B-L)+2S}. \tag{1.39}$$

The corresponding symmetry is referred to R-parity, which conservation law will prohibit single production of SUSY particles, as well as SM particles annihilating into a resonance of a SUSY particle. This leads a set of spectacular phenomenological advantages:

- The lightest SUSY particles (LSP) become the DM candidates if they are electric neutral, in particular the lightest neutralino is the most commonly assumed.
- Proton decays via diagrams in Figure 1.3 are prohibited, naturally reconciling with the constraints set by experiments [34].

In the framework of MSSM, the R-parity conservation (RPC) is explicitly assumed, which is equivalent to discard following terms in the most general soft breaking Lagrangian:

$$\begin{aligned}
W_{\Delta L=1} &= \frac{1}{2}\lambda^{ijk}L_iL_j\bar{e}_{\text{k}} + \lambda'^{\,ijk}L_iQ_j\bar{d}_k + \mu'^{\,i}L_iH_{\text{u}}\\
W_{\Delta B=1} &= \frac{1}{2}\lambda''^{\,ijk}\bar{u}_i\bar{d}_j\bar{d}_k.
\end{aligned} \tag{1.40}$$

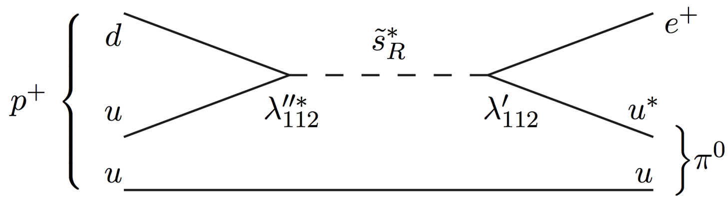

Figure 1.3: An example process of a proton decay triggered by intermediate SUSY particles (scalar-strenge quark here). λ''_{112} and λ'_{112} are couplings for corresponding interaction vertices which violate R-parity.

1.3.3 Mass spectra in MSSM

The masses of SUSY particles are derived by specifying the coefficient associated with mass terms (e.g. m in $m\phi\phi$), after a full expansion of the Lagrangian in Eq. (1.32). This is effectively done by extracting relevant terms and performing the diagonalization on the mass matrices, accounting for the mixing between eigenstates of interactions.

Squarks and sleptons Sfermion masses are fed solely from the soft Lagrangian. Generally, they are allowed to mix between different generations via the off-diagonal components either in the mass matrices or the A terms. These are however known to lead to a significant rate of flavor changing natural current which are experimentally highly disfavored thus usually set to zero:

$$\begin{aligned} &\boldsymbol{m}_Q^2 = m_Q^2\,\mathbf{1}, \quad \boldsymbol{m}_L^2 = m_L^2\,\mathbf{1}, \quad \boldsymbol{m}_{\bar{u}}^2 = m_{\bar{u}}^2\,\mathbf{1}, \quad \boldsymbol{m}_{\bar{d}}^2 = m_{\bar{d}}^2\,\mathbf{1}, \quad \boldsymbol{m}_{\bar{e}}^2 = m_{\bar{e}}^2\,\mathbf{1}, \\ &\boldsymbol{a}_{\mathrm{u}} = A_{\mathrm{u}}\,\mathbf{1}, \quad \boldsymbol{a}_{\mathrm{d}} = A_{\mathrm{d}}\,\mathbf{1}, \quad \boldsymbol{a}_e = A_e\,\mathbf{1} \end{aligned} \tag{1.41}$$

In addition, it is also allowed to mix left-handed sfermion and right-handed sfermion since they share the same gauge quantum numbers. Ignoring the off-diagonal components of the Yukawa matrix, the mass matrix for sfermion $\tilde{f}$ reduces to:

$$\begin{aligned} &\begin{pmatrix} m_{\tilde{f}_{\mathrm{L}}}^2 + m_Z^2\,(T_{3,f} - Q_f \sin\theta_W{}^2)\cos 2\beta + m_f^2 & v_f(A_f - \mu y_f) \\ v_f(A_f - \mu y_f) & m_{\tilde{f}_{\mathrm{R}}}^2 + m_Z^2\, Q_f \sin\theta_W{}^2 \cos 2\beta + m_f^2 \end{pmatrix}, \\ &v_f = \begin{cases} v_{\mathrm{u}} & (\tilde{f} = \tilde{u}, \tilde{c}, \tilde{t}) \\ v_{\mathrm{d}} & (\tilde{f} = \tilde{d}, \tilde{s}, \tilde{b}) \end{cases} \end{aligned} \tag{1.42}$$

where $T_{3,f}$ and Q_f are the iso-spin and electric charge of $\tilde{f}$. As the magnitude off-diagonal component scales with the Yukawa coupling, the effect of the mixing can be only sizable in case of third generation sfermions (stop, sbottom and stau). This is why the third generation sfermions are particularly phenomenologically important, since the masses of lighter eigenstates can be significantly lowered, enhancing the chance of being within experimental reach.

Gauginos The mass terms of EW gauginos and higgsinos are sourced by $\mathcal{L}_{\mathrm{SUSY}}^{\mathrm{MSSM}}$. The eigenstate of charged EW gauginos (charginos; $\tilde{W}^{\pm}, \tilde{H}_{\mathrm{u}}^{+}, \tilde{H}_{\mathrm{d}}^{-}$) in the same signs will mix each other. The mass matrices are common and described as:

$$\begin{pmatrix} M_2 & \sqrt{2}m_W \sin\beta \\ \sqrt{2}m_W \sin\beta & \mu \end{pmatrix}.$$

The diagonalized mass eigenstates are then:

$$m^2_{\tilde{\chi}^\pm_{1,2}} = \frac{1}{2}\left[(M_2^2 + \mu^2 + 2m_W^2) \mp \sqrt{(M_2^2 + \mu^2 + 2m_W^2)^2 - 4(\mu M_2 - m_W^2 \sin 2\beta)^2}\right]. \tag{1.43}$$

The mass matrix for neutral EW gauginos (neutralinos; $\tilde{B}, \tilde{W}^0, \tilde{H}^0_{\mathrm{u}}, \tilde{H}^0_{\mathrm{d}}$) are given as:

$$\begin{pmatrix} M_1 & 0 & -\cos\beta\sin\theta_W m_Z & \sin\beta\sin\theta_W m_Z \\ 0 & M_2 & \cos\beta\cos\theta_W m_Z & -\sin\beta\cos\theta_W m_Z \\ -\cos\beta\sin\theta_W m_Z & \cos\beta\cos\theta_W m_Z & 0 & -\mu \\ \sin\beta\sin\theta_W m_Z & -\sin\beta\cos\theta_W m_Z & -\mu & 0 \end{pmatrix}.$$

The eigenfunction is quartic and the solutions are:

$$\begin{aligned} m_1 &= M_1 + \frac{m_Z^2 \sin^2\theta_W}{M_1^2 - \mu^2}(M_1 + \mu + \sin 2\beta) \\ m_2 &= M_2 + \frac{m_Z^2 \cos^2\theta_W}{M_2^2 - \mu^2}(M_2 + \mu + \sin 2\beta) \\ m_3 &= \mu + \frac{m_Z^2(1 + \sin 2\beta)}{2(\mu - M_1)(\mu - M_2)}(\mu - \cos\theta_W M_1 - \sin\theta_W M_2) \\ m_4 &= \mu + \frac{m_Z^2(1 - \sin 2\beta)}{2(\mu + M_1)(\mu + M_2)}(\mu + \cos\theta_W M_1 + \sin\theta_W M_2) \end{aligned} \tag{1.44}$$

The conventional notation for neutralino masses $m_{\tilde{\chi}^0_{1-4}}$ are defined by sorting these eigenvalues as $m_{\tilde{\chi}^0_1} < m_{\tilde{\chi}^0_2} < m_{\tilde{\chi}^0_3} < m_{\tilde{\chi}^0_4}$.

Finally, gluinos are color-octet fermions and do not mixed to any other sfermions.

The MSSM Higgs sector Due to the two higgs doublets with 4 real and 4 imaginary parts, there are in total five degree of freedoms as physical particles after the gauge fixing. The MSSM higgs potential is given by:

$$\begin{aligned} V = &\left(|\mu|^2 + m^2_{H_{\mathrm{u}}}\right)\left(|H^0_{\mathrm{u}}|^2 + |H^+_{\mathrm{u}}|^2\right) \\ &+ \left(|\mu|^2 + m^2_{H_{\mathrm{d}}}\right)\left(|H^0_{\mathrm{d}}|^2 + |H^-_{\mathrm{d}}|^2\right) \\ &+ \left[b(H^+_{\mathrm{u}}H^-_{\mathrm{d}} - H^0_{\mathrm{u}}H^0_{\mathrm{d}}) + \mathrm{c.c.}\right] \\ &+ \frac{1}{8}\left(g^2 + g'^2\right)\left(|H^0_{\mathrm{u}}|^2 + |H^+_{\mathrm{u}}|^2 - |H^0_{\mathrm{d}}|^2 - |H^-_{\mathrm{d}}|^2\right)^2 \\ &+ \frac{1}{2}|H^+_{\mathrm{u}}H^{0*}_{\mathrm{u}} + H^+_{\mathrm{d}}H^{-*}_{\mathrm{d}}|. \end{aligned} \tag{1.45}$$

Similarly to the case in SM, implementing the spontaneous symmetry breaking by plugging $H_{\rm u,d} \to v_{\rm u,d} + \eta_{\rm u,d}$ into Eq. (1.45), and requiring $dV/dv_{\rm u} = dV/dv_{\rm d} = 0$, one arrives:

$$\sin 2\beta = \frac{2b}{m_{H_{\rm u}}^2 + m_{H_{\rm d}}^2 + 2|\mu|^2} \tag{1.46}$$

$$\frac{1}{2}m_Z^2 = -|\mu|^2 + \frac{m_{H_{\rm u}}^2 - m_{H_{\rm d}}^2 \tan^2\beta}{\tan^2\beta - 1} \tag{1.47}$$

The higgs masses are found by the masses terms with inserting Eq. (1.46)-(1.47) back to Eq. (1.45):

$$\begin{aligned} m_A^2 &= 2|\mu|^2 + m_{H_{\rm u}}^2 + m_{H_{\rm d}}^2, \\ m_{H^\pm}^2 &= m_{A^0}^2 + m_W^2 \\ m_{h,H}^2 &= \frac{1}{2}\left(m_{A^0}^2 + m_Z^2 \mp \sqrt{(m_{A^0}^2 + m_Z^2)^2 - 4m_Z^2 m_{A^0}^2 \cos^2 2\beta}\right), \end{aligned} \tag{1.48}$$

where $H^\pm$ is the charged, A the CP-odd higgs respectively. H and h are the mass eigenstates of CP-even neutral higgs, where the lighter one h is often associated with the SM higgs. Given that no observation of H has been claimed upto 400 GeV $-$ 1 TeV, it is generally preferred to have large mass splitting between h and H, which implies a large $\tan\beta$.

1.3.4 Running masses and GUT

Though the SUSY masses are mostly free parameters in MSSM, an useful insight can be obtained from an quick analysis under the GUT regime in which the coupling constants are unify at the GUT scale: $\mu_{\rm GUT} \sim 10^{16-17}$ GeV.

In the SUSY context, the mass unification is often in addition considered, typically under the regime where:

- all sfermions masses converge to $m_{1/2}$
- all gaugino masses converge to m_0
- all higgs boson (H_u, H_d) masses converge to $(\mu^2 + m_0^2)^{1/2}$.

This configuration is particular advantageous in that it naturally causes EW symmetry breaking at the EW scale, and adopted in many minimal models including SUGRA and so on.

Starting with gaugino masses, using the general condition satisfied in the 1-loop renormalization:

$$\frac{d(M_i/\alpha_i)}{d\mu} = 0, \quad (i = 1, 2, 3),$$

it turns that (M_i/α_i) is constant in arbitrary scales. Therefore, one obtains:

$$\frac{M_i}{\alpha_i}|_{\mu=\mu_{\rm EW}} = \frac{M_i}{\alpha_i}|_{\mu=\mu_{\rm GUT}} = \frac{m_{1/2}}{\alpha_{\rm GUT}}, \tag{1.49}$$

resulting in an univeral ratio in gaugino masses valid in any scale:

$$M_1 : M_2 : M_3 \sim 6 : 2 : 1. \tag{1.50}$$

This is the reason this mass hierarchy between gluino, wino and bino are especially motivated and commonly assumed in SUSY phenomenology, though it is true that the assumption of mass unification may be too strong.

As for sfermions, the running masses also provide some idea about the mass spectra at the EW scale. The running masses are calculated unambiguously using the renormalization group equations:

$$\begin{aligned}
m^2_{\tilde{d}_\mathrm{L}} &= m_0^2 + K_3 + K_2 + \frac{1}{36} K_1 + \Delta_{\tilde{d}_\mathrm{L}} \\
m^2_{\tilde{u}_\mathrm{L}} &= m_0^2 + K_3 + K_2 + \frac{1}{36} K_1 + \Delta_{\tilde{u}_\mathrm{L}} \\
m^2_{\tilde{d}_\mathrm{R}} &= m_0^2 + K_3 + \frac{1}{9} K_1 + \Delta_{\tilde{d}_\mathrm{R}} \\
m^2_{\tilde{u}_\mathrm{R}} &= m_0^2 + K_3 + \frac{4}{9} K_1 + \Delta_{\tilde{u}_\mathrm{R}} \\
m^2_{\tilde{e}_\mathrm{L}} &= m_0^2 + K_2 + \frac{1}{4} K_1 + \Delta_{\tilde{e}_\mathrm{L}} \\
m^2_{\tilde{\nu}_\mathrm{L}} &= m_0^2 + K_2 + \frac{1}{4} K_1 + \Delta_{\tilde{\nu}_\mathrm{L}} \\
m^2_{\tilde{e}_\mathrm{R}} &= m_0^2 + K_1 + \Delta_{\tilde{e}_\mathrm{R}}
\end{aligned} \tag{1.51}$$

where K_1, K_2 and K_3 respectively denotes the contribution from the interaction of $U(1)_Y$, $SU(2)_L$ and $SU(3)_C$, which are approximately:

$$K_1 \sim 0.15\, m^2_{1/2}, \;\; K_1 \sim 0.5\, m^2_{1/2}, \;\; K_3 \sim 6\, m^2_{1/2}, \tag{1.52}$$

and the correction factors $\Delta_{\tilde{f}}$ are given by:

$$\begin{aligned}
\Delta_{\tilde{f}_\mathrm{L}} &= (T_3 - Q \sin^2\theta_W)\, m_Z^2 \cos 2\beta + m_f^2 \\
\Delta_{\tilde{f}_\mathrm{R}} &= Q \sin^2\theta_W\, m_Z^2 \cos 2\beta + m_f^2.
\end{aligned} \tag{1.53}$$

Since the effect of running masses are always larger for squarks than sleptons due to the $SU(3)_C$ interaction, it generally implies lighter masses for sleptons. The typical running mass spectra is shown in Figure 1.4.

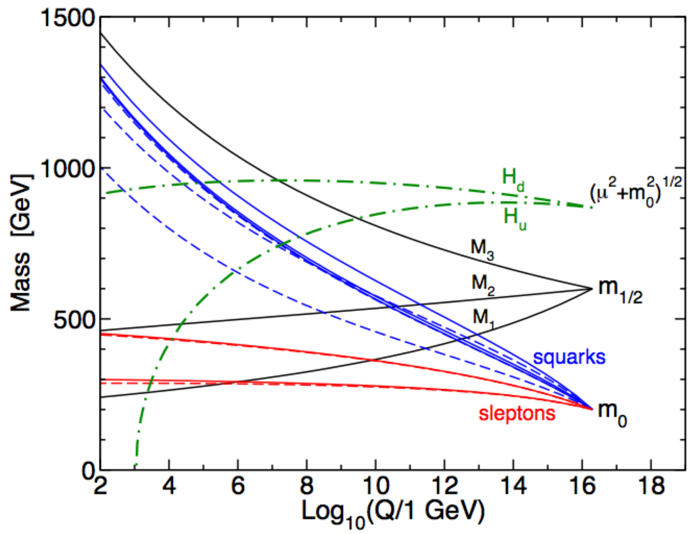

Figure 1.4: Evolution of scalar and gaugino mass parameters in the MSSM with mSUGRA boundary conditions [24]. The parameters are $m_0 = 200$ GeV, $m_{1/2} = 600$ GeV, $A^0 = -600$ GeV, $\tan\beta = 10$ and sign(μ)> 0.

1.4 Experimental Constraints on SUSY so far

1.4.1 Constraints from Observed Standard Model Higgs Mass

It is a striking fact that in MSSM the mass of 125 GeV higgs (h) is bounded by:

$$m_h < m_Z \cos 2\beta < m_Z = 91.2 \text{ GeV}, \tag{1.54}$$

according to Eq. (1.48). Therefore, a sizable radiation correction is needed to achieve 125 GeV. The 1-loop correction is dominantly given by the remnant of cancellation of top and stop loop in Eq. (1.25):

$$\Delta m_h^2 := \frac{3}{4}\frac{m_t^4}{v_{\text{SM}}^2}\left[\log\frac{m_{\tilde{t}}^2}{m_t^2} + \frac{X_t^2}{m_{\tilde{t}}^2}\left(1 - \frac{X_t^2}{12 m_{\tilde{t}}^2}\right)\right], \tag{1.55}$$

which has to accord with

$$\sqrt{(125 \text{ GeV})^2 - m_Z^2} \sim 85 \text{ GeV}. \tag{1.56}$$

This is a tremendously powerful constraint that forces either of following two ambivalent choices:

1. without assuming anything on stop mixing (e.g. X_t is free) and $O(10$ TeV$)$ of stop mass, with relatively large fine tuning ($\Delta_{m_h} > 1000$), as shown in Figure 1.5.

2. maximal stop mixing ($X_t \sim \sqrt{6} m_{\tilde{t}}$), and 500 GeV $-$ 1 TeV of stop mass, with mild fine tuning ($\Delta_{m_h} \sim 100$).

The consequent implication from the former choice is that all the squrks and sleptons are heavy, and only gauginos could be explored in LHC, while the latter leads to light stop (or sbottom)

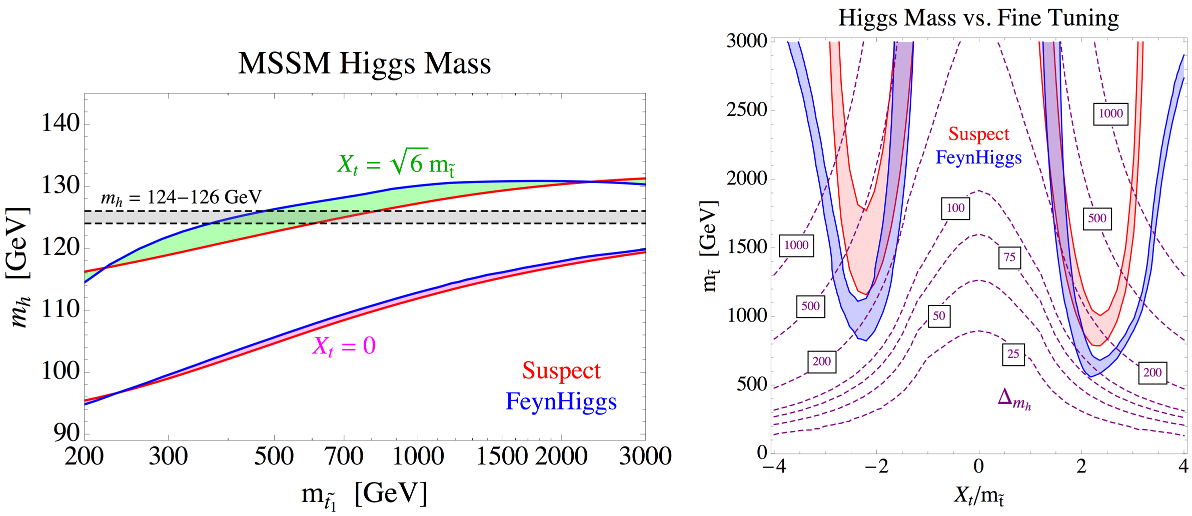

(a) (b)

Figure 1.5: Relation of mass of SM-like higgs and stop mass in MSSM [35]. (a) The SM-like higgs mass as a function of lightest stop mass ($m_{\tilde{t}}$), with the no ($X_t = 0$) or maximal stop mixing ($X_t \sim \sqrt{6} m_{\tilde{t}}$). Red/blue solid lines correspond the computation using Suspect/FeynHiggs. (b) A 2D-constraint on the stop mass and stop mixing $X_t/m_{\tilde{t}}$ by observed SM-like higgs mass, with $m_{\tilde{Q}} = m_{u_3} = m_{\tilde{t}}$ and $\tan\beta = 20$. The dashed contour shows the gauge of fine tuning Δ_{m_h} defined by Eq. (1.57).

accessible by the LHC energy while the others are not necessarily so.

The higgs mass fine tuning argument in MSSM is rather subtle, since the observed m_h is no longer as straightforwardly associated with its own mass parameter H_{u} as in the case in SM (Sec. 1.2.1), but also involved by the other MSSM parameters as seen in Eq. (1.48). The magnitude of fine tuning is usually quoted by the linear response of any arbitrary MSSM parameters p_i:

$$\Delta_{m_h} := \max_i \left| \frac{\partial \log[m_h^2(\text{1-loop})]}{\partial \log p_i} \right| . \tag{1.57}$$

In scenario 1. above, the resultant fine tuning is typically $1/\Delta_{m_h} \sim O(10^{-3})$, while $\sim 1\%$ is achievable in the scnerio 2 in the most optimistic case with ~ 500 GeV stop.
As a level of $\sim O(10^{-3})$ of the fine tuning is not as fatal as that in the SM (10^{-34}), in the thesis, we pursue the former scenario, and probing gluinos in the experiment assuming all the squarks are all decoupled.

1.4.2 Constraint from Dark Mater Relic Density

The main stream of current DM theory is based on the "cold matter" regime in which DM used to be in a thermal equilibrium at the beginning of the universe, and cooled down according to the cosmic expansion later on, and being decoupled at a certain scale, fixing the abundance upto now. The relics is strongly related by the annihilation cross-section, which can be calculated within the MSSM framework.

Phenomenologically there are a couple of major classes of DM scenarios depending on the component of LSP. The case of pure bino-LSP can be almost immediately excluded, in a limit where all the squarks are decoupled, since it has to then rely on the annihilation channel via sleptons [36], where $m_{\tilde{\ell}} < 110$ GeV is needed to achieve the observed relic abundance (Eq. (1.29)) which is actually already excluded by LEP2.

On the other hand, the annihilation cross-section tends to be too large in case of pure-wino or pure-higgsino LSP, where roughly ~ 3 TeV of wino mass or ~ 1 TeV of higgsino mass is needed to match with the observed relic Eq. (1.29), which is unfortunately beyond the LHC reach.

What if the mixed case? It is particular interesting to consider doping a bit of wino or higgsino component into bino-dominated LSP, where moderated annihilation cross-section and experimental accessible LSP mass can be achieved simultaneously. This type of LSP is called "well-tempered" neutralino LSP [36], typically predicting a moderately small mass splitting between the next-to-the-lightest SUSY particle (NLSP) and the LSP with $20 - 50$ GeV [37] [38].

Note that a number of caveat remarks are to be added on the discussion:

- The observed relics is always based on Λ-CDM within the cold DM regime. The constraint on SUSY could therefore drastically different if DM is "warm" produced non-thermally.

- The DM annihilation cross-section calculation so far is dominantly done at the lowest-order (LO) in the perturbation. The contribution of higher order terms will generally increase annihilation cross-section.

- Non-perturbative effects (continuous interaction) in a collision of non-relativistic particles often lead to a sizable increase in annihilation cross-section ("Sommerfeld enhancement").

- Is is a bit awkward though, it is possible for other new physics to supply the DM relics when SUSY is not capable of explaining the entire relic.

Given these too many uncertainties, it is sensible to regard the relic constraint as soft constraint. However, generally it is more fatal to have excessive relics than the opposite case, here we promise to respect the observed relic more as upper bound.

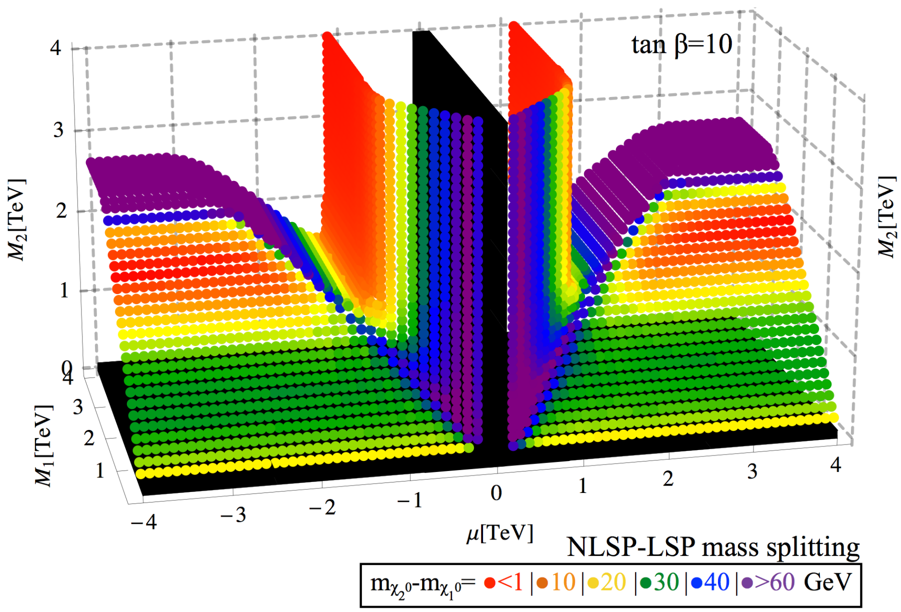

Figure 1.6: Mass spliting between NLSP (next-to-the-lightest SUSY particle) and LSP, as function of M_1, M_2 and μ when assigning the DM relic constraint [38]. The effect of Sommerfeld enhancement is taken into the calculation. Within the reach by the LHC energy ($\min(M_1, M_2) < 1$ TeV), the resultant NLSP-LSP mass splitting is about 20 GeV $\sim$ 30 GeV. Black points correspond to parameter space excluded by LEP.

1.4.3 Constraint from Direct Search at Collider Experiments

The direct search of SUSY had been widely performed in collider experiments including LEP, Tevatron and LHC covering over a number of signatures and scenarios. Unfortuanately no evidence has been claimed, it is interpreted into constraints either on specific full models (mainly SUGRA-type models, GMSB and cMSSM), or on particular production and decay chains ("simplified model" as discussed in Sec 1.5.2). This sub-section overviews the status of constraints placed on simplified models.

Gluinos The best job is done by hadron collider experiments due to its outstandingly high production cross-section. It is particularly the case in LHC Run2, dominating the sensitivity in most of the scenarios in terms of the mass spectra and gluino decays.

The exclusion limits on the most typical gluino decays set by ATLAS and CMS are shown in Figure 1.7, namely (a) the direct decay where gluino directly fall into LSP with emitting two quarks, or (b) the 1-step decay via NLSP chargino. Upto ~ 2 TeV in gluino mass is excluded for case with large mass splitting between gluino and LSP, and $1.2 \sim$ TeV for the most pessimistic case where gluino and LSP are highly compressed. Note that the listed limits are all up-to-date published results as of July 2017. While most of them is with full 2016 dataset (integrated luminosity of $\mathcal{L} \sim 36$ fb^{-1}), the ATLAS 1-lepton analysis (ATLAS-CONF-2016-054) is with smaller dataset ($\mathcal{L} = 14.8$ fb^{-1}). **This study is meant for the update of it with the up-to-date dataset ($\mathcal{L} = 36.1$ fb^{-1}) as well as the improved analysis method**.

Gluino decaying with top quarks addresses particular importance since it can be enhanced by the light stop which is motivated by naturalness. They are exclusively searched with dedicated signal regions, and the resultant limit in given in Figure 1.8. **This type of models are also the scope of the thesis, for which an improved result will be provided with respect to the existing ones.**

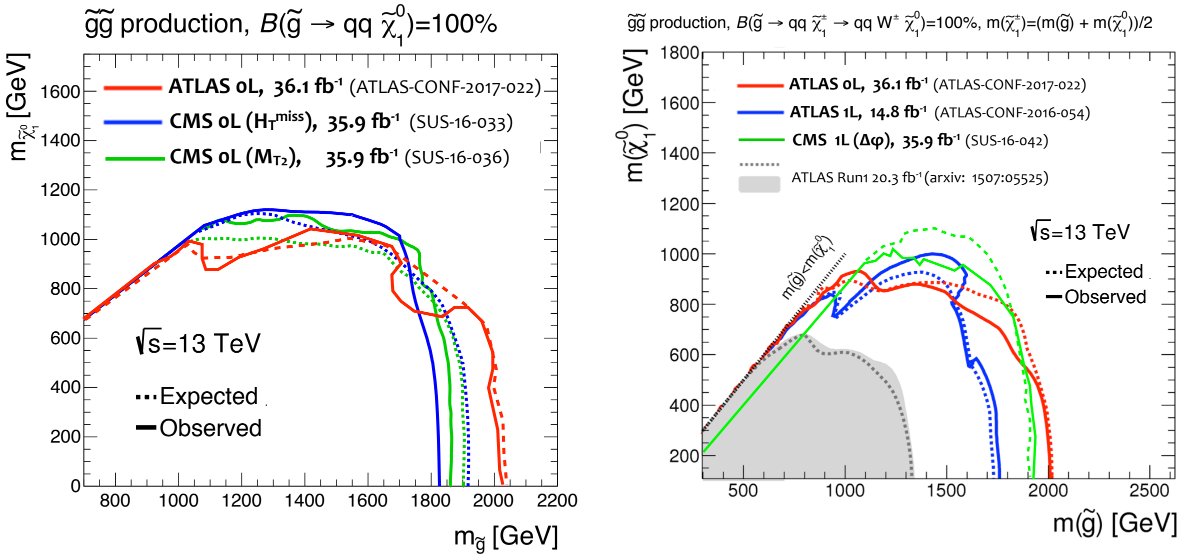

(a) (b)

Figure 1.7: Up-to-date constraints set by ATLAS and CMS on (a) direct gluino decay: $\tilde{g} \to q\bar{q}\tilde{\chi}_1^0$, and (b) the 1-step chargino-mediated gluino decay: $\tilde{g} \to q\bar{q}\tilde{\chi}_1^{\pm}$ with the mass being in the middle between gluino and the LSP. The article numbers for corresponding references are labeled on the plots. "0L" and "1L" respectively denote searches with 0-lepton and 1-lepton final state.

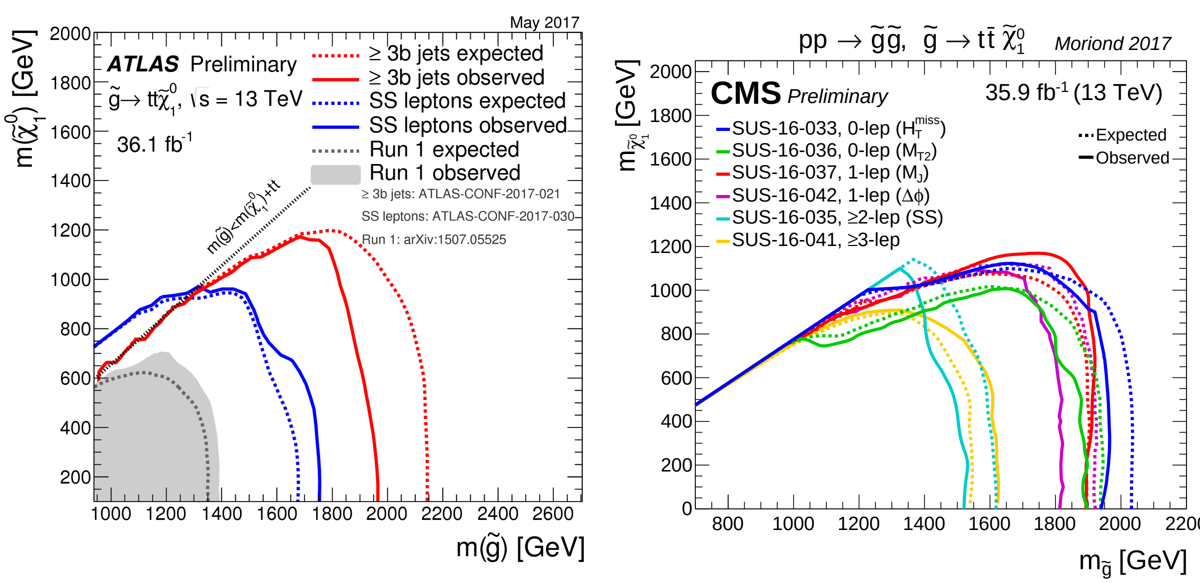

(a) (b)

Figure 1.8: Up-to-date constraints on pair produced gluinos directly decaying with top quarks ($\tilde{g} \to t\bar{t}\tilde{\chi}_1^0$) set by (a) ATLAS and (b) CMS. The summary plots are referred from [39] (ATLAS) and [40] (CMS).

Squarks A class of analyses are dedicated for direct stop production with numerious stop decay scenarios and mass configuratons. The strongest limits are provided by LHC, and upto about 400 GeV $\sim$ 1 TeV in stop mass is generally excluded. Figure 1.9 presents the example limits on the direct stop decay scenario: $\tilde{t} \to t\tilde{\chi}_1^0$ provided by ATLAS and CMS.

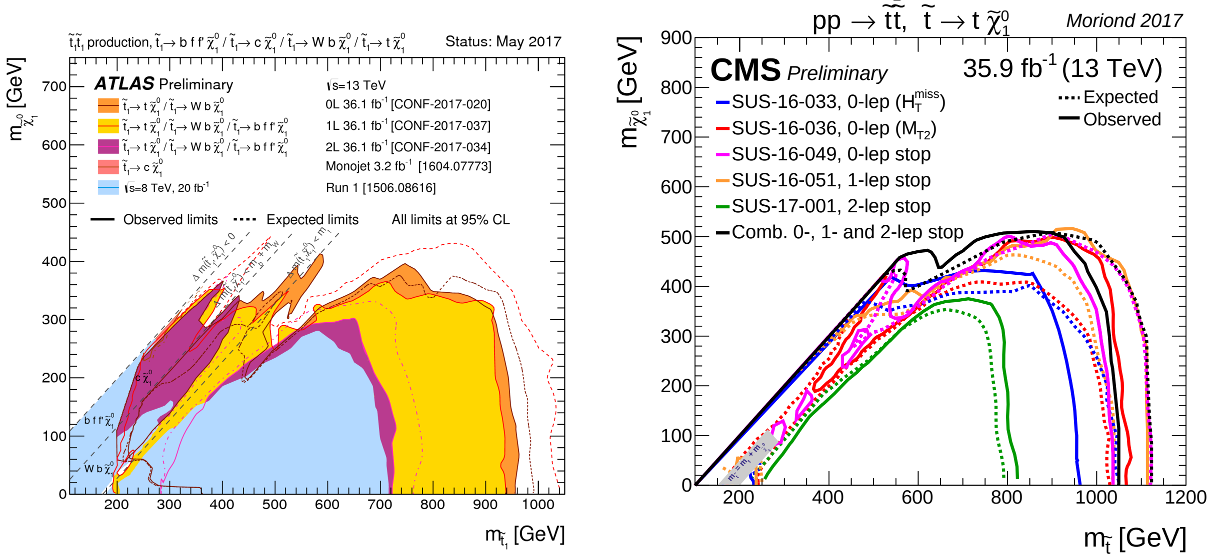

(a) (b)

Figure 1.9: Up-to-date constraints on stop pair production with direct decay $\tilde{t} \to t\tilde{\chi}_1^0$ set by (a) ATLAS and (b) CMS. The summary plots are referred from [39] (ATLAS) and [40] (CMS).

Electroweak Gauginos A number of searches for direct EW gaugino prodicution have been performed in LEP, Tevatron and LHC, and LHC provides the majority of current storngest limits. The targeted signature is mostly pair produced NLSPs ($\tilde{\chi}_1^{\pm}$ or $\tilde{\chi}_2^0$) decaying to LSP, where decoupled squarks are often assumed. [3]

Bino-LSP/wino-NLSP is the most commonly assumed configuration since it is easily explored; the signal typically leaves multiple leptons and large missing E_T in the final states. The exclusion limits set by ATLAS and CMS are shonw in Figure 1.10. About upto 500 GeV of NLSP mass is excluded for cases with large NLSP-LSP mass splitting, and 150 − 250 GeV for small splitting.

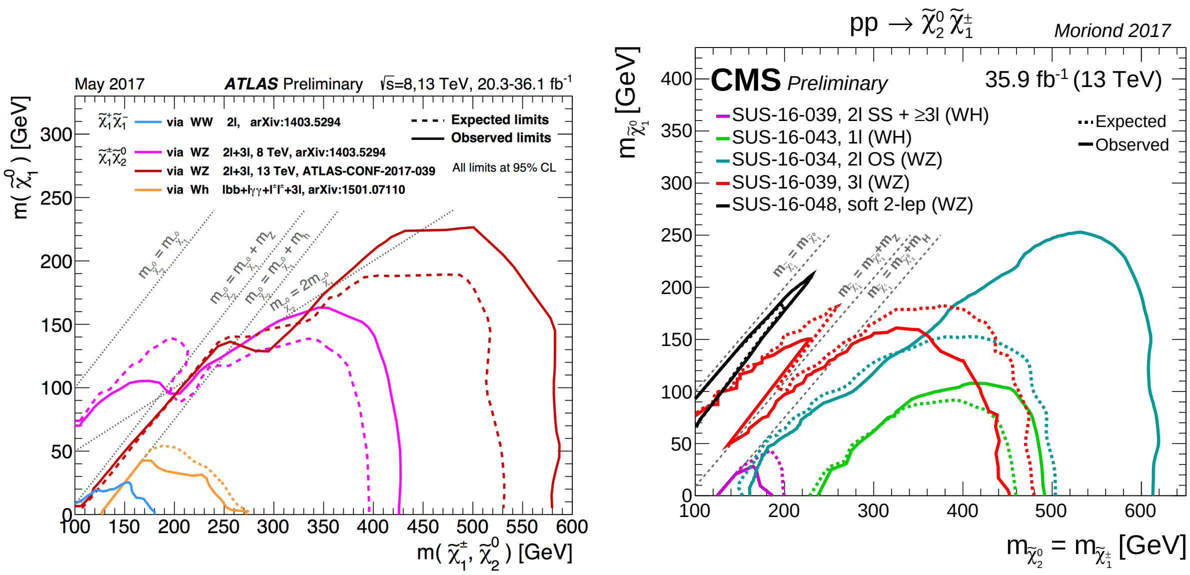

(a) (b)

Figure 1.10: Up-to-date constraints on direct EW gaugino production with decays via $W/Z/h$ set by (a) ATLAS [41] and (b) CMS [42]. The summary plots are referred from [39] (ATLAS) and [40] (CMS).

The wino-LSP scenario is explored using a strikingly different approach. Since the mass splitting between NLSP wino-chargino and the wino-LSP is extremely compressed (150 $\sim$ 160 MeV), wino-chargino retains O(ns) of moderately long lifetime, resulting in a characterstic disappearing track signature where a traveling chargino track stops halfway in the tracker due to the decay into a soft pion. The results from ATLAS (Run2) and CMS (Run1) are given in Figure 1.11. The exlusion runs upto 300 − 500 GeV in wino mass at the lifetime (or the NLSP-LSP mass splitting) predicted by MSSM.

Although motivated by in light of naturalness, almost no constraint is set for direct higgsino production so far by LHC, due to the marginal production cross-section ($\sim 1/4$ of that of the wino production) as well as the experimentally challenging small NLSP-LSP splitting generally predicted in case of higgsino LSP.

[3]Under the decoupled squark scenario, bino production is strongly suppressed.

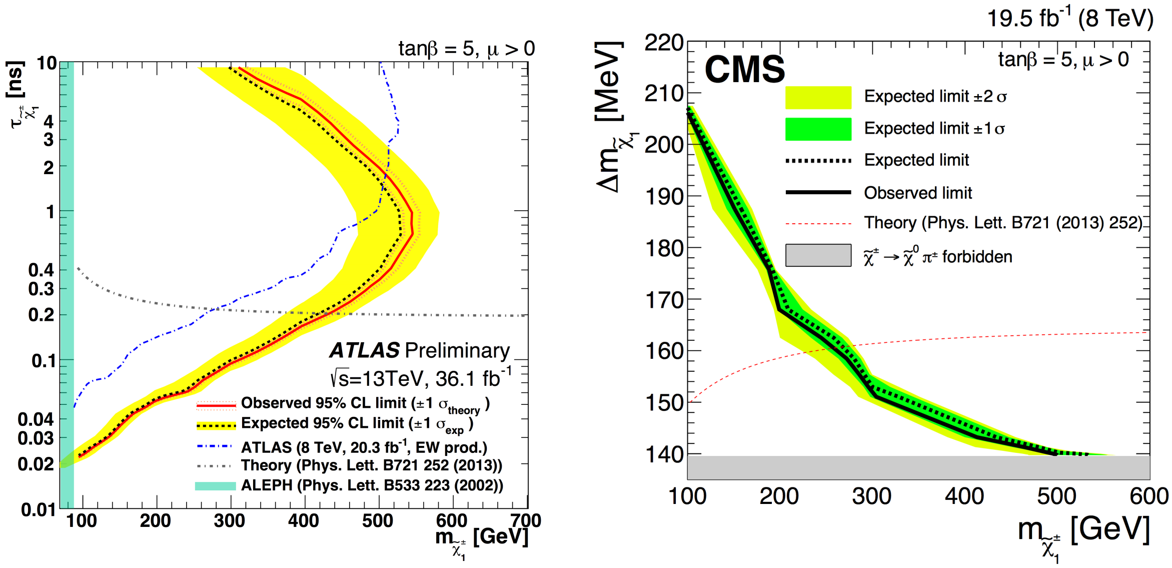

(a) (b)

Figure 1.11: Constraints on the wino-LSP scenario set by (a) ATLAS [43] and (b) CMS [44].

the strongest limit on direct higgsino production is still held by LEP2. The limit is shown in Figure 1.12, where upto $\sim$ 90 GeV of LSP mass is excluded.

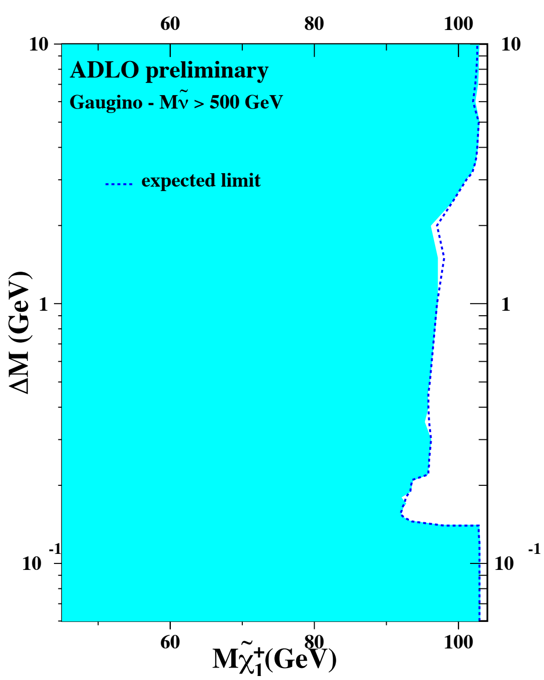

Figure 1.12: Exclusion limit on direct production of higgsino pairs set by LEP2. Combined result from all the four experiments is shown [45].

1.5 Targeted SUSY Scenario and the Search Strategy in this work

1.5.1 Targeted SUSY Scenario

To summarize the discussion above, thesis focuses on the MSSM scenarios where:

- Squarks are all heavy (> 3 TeV).
- Allow the higgs mass fine tuning at order of 10^{-3}.
- LSP is neutralino.
- Loosely respect the observed DM relic (Eq. (1.29)).

The targeted experimental signature is the pair production of gluinos (Figure 1.13) with the mass of 800 GeV − 2 TeV. Although the seach is inclusively carried out with no particular assumption on the mass spectra, a special attention will be made for the case of $\Delta m(\tilde{\chi}_1^{\pm}/\tilde{\chi}_2^0, \tilde{\chi}_1^0) =$ 20 GeV $\sim$ 30 GeV motivated by the well-tempered neutralino DM scenario.

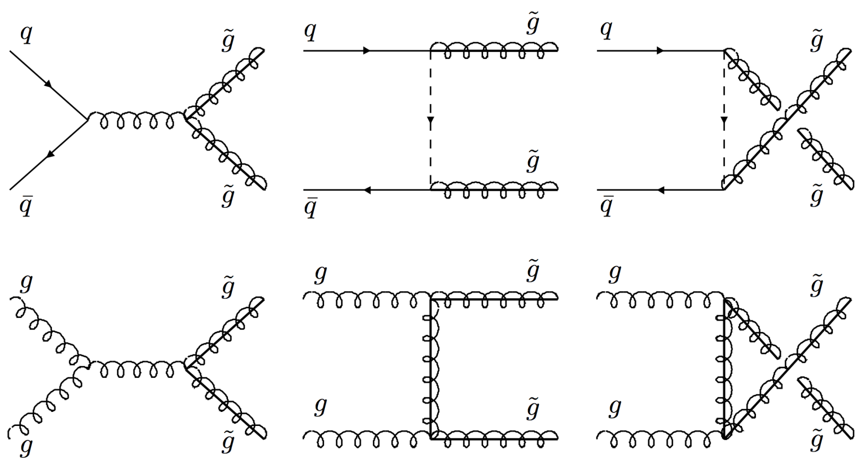

Figure 1.13: Feynmann diagrams for tree-level gluino pair production in LHC [46].

1.5.2 The Strategy of Decay Chain Based Search

Though minimality is still respected in principle, it would be more sensible to extend the scope of the search to a more general direction with respect to past analyses, given that the most straightforward scenarios has already been largely excluded by LHC so far. Ideally, we prefer to consider as general as possible e.g. MSSM, but constraining the full parameter spaces is not realistic (e.g. > 100 parameters for the most general MSSM). However, it is also true that most of the MSSM parameters only affect the spins or decay branchings of SUSY particles, rather than kinematics i.e. they do not change the signal acceptance. On the other hands, kinematics of SUSY signatures are dominantly determined by SUSY mass spectra. Therefore, we only have to care about the mass dependence, once a full decay chain is specified. In other words, setting the cross-section upper limit on each decay chain and mass spectra is no less general than considering the full parameter space of the MSSM.
[4]

Placing upper limits on particular decay chain $A \to B$ is essentially equivalent to setting exclusion limit on following model called "simplified model" where:

- $\mathrm{Br}(A \to B)$ is 100%.
- Parameters other than SUSY masses are fixed to an arbitrary configuration. For instance, in LHC analysis, the EW gaugino mixing is usually set so that NLSP and LSP become wino- and bino-dominant.

Though interpretation has already been widely employed based on the simplified model in LHC searches, the critical problem is that the coverage of decay chains and mass spectra is far from complete, for instance, in case of gluino, only a few decays are considered. In this thesis, all the viable gluino decay chains will be considered, and setting the limit on each of them with full coverage of mass assumption on gluino and EW gauginos. In the following sub-section, the target decay chains are explicitly specified.

1.5.3 Targeted Gluino Decay Chains

Under the decoupled squarks scenario, gluino always decays 3-body; 2 SM quarks and a EW gaugino via heavy virtual squarks:

$$\tilde{g} \to \begin{cases} (u\bar{d}, c\bar{s}, t\bar{b}) \times (\tilde{\chi}^{-}_{1,2}) \\ (d\bar{u}, s\bar{c}, b\bar{t}) \times (\tilde{\chi}^{+}_{1,2}) \\ (u\bar{u}, d\bar{d}, s\bar{s}, c\bar{c}, b\bar{b}, t\bar{t}) \times (\tilde{\chi}^{0}_{1-4}). \end{cases}$$

Including the subsequent EW gaugino decays, it leads to an enormous number of final states. However kinematically some the them are approximately equivalent which can be merged or trimmed. For instance, since the acceptance is mearly invariant between light quark flavors (u, d, s, c), they are merged into a single simplified model where gluino has equal decay branches into u, d, s, c.

[4] This is the same to admit our search has no sensitivity in determining the model parameters other than masses.

In addition, the four higgsino (or two wino) states can be regarded as a single state since their masses are highly compressed each other [5] leading the same kinematics. The mass spectra can be eventually reduced into either the three scenario schematized in Figure 1.14, involving three types of gluino decays:

- "direct" decay in which gluino directly de-excites into LSP,
- "1-step" decay with one intermediate EW gaugino state,
- "2-step" decay in which gluino decays via two resolved intermediate EW gauginos mass states.

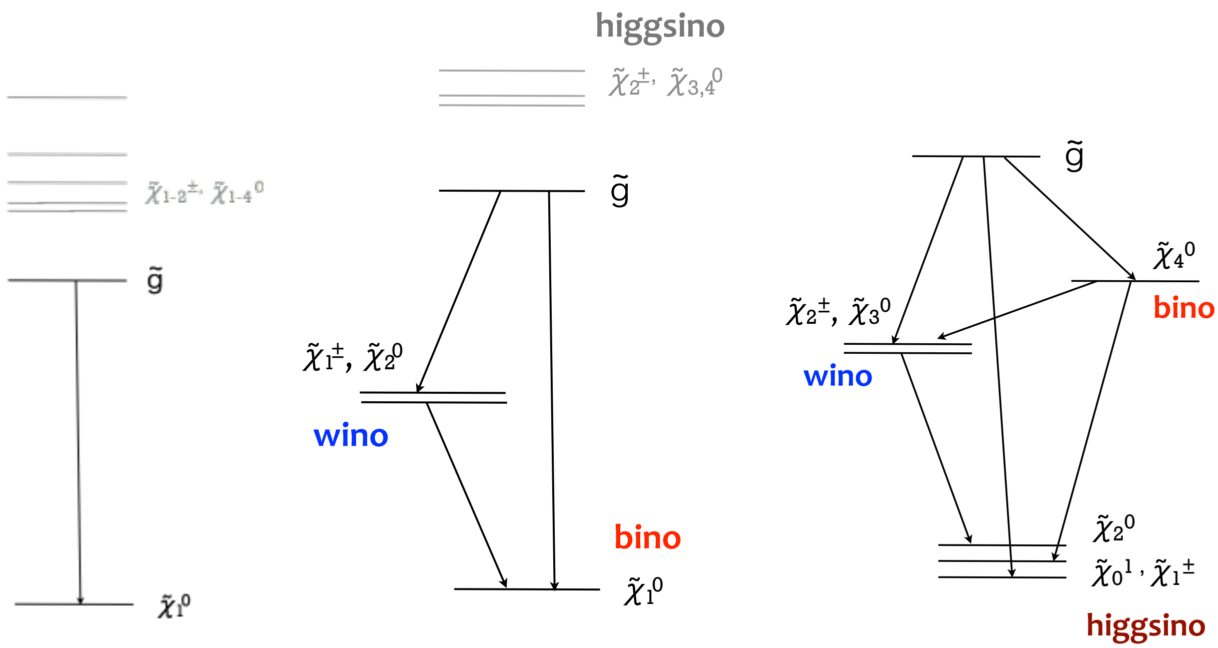

(a) (b) (c)

Figure 1.14: Illustration of possible gluino decay paths under various scenario of the mass spectra. (a) All the EW gauginos are heavier than gluino except the LSP (gluino decay: direct). (b) One of the EW gauginos (bino, wino, higgsino) is heavier than gluino while the other EW gauginos are lighter (gluino decay: direct or 1-step). (c) All the EW gauginos are below gluino mass (gluino decay: direct or 1-step or 2-step).

As for the scenario (c) in Figure 1.14, a numerous MSSM parameters scans demonstrate that the probability of 2-step decays are generally much lower than that of direct or 1-step decays, except for some of the cases where each of the intermediate masses are aligned with relatively equal distance. Therefore, in the analysis, we confine our scope within the direct and 1-step decays.

For subsequent EW gaugino decays, charginos are always assumed to emit on-shell or off-shell W-boson, while there are two options for neutralino decays i.e. via Z or h. The decays into slepton

[5]The splitting will be rarely greater than 50 GeV even when all M_1, M_2 and μ are at the same mass leading to the maximum mixing.

is ignored here, majorly for convenience sake of restricting the number of final states, however with a few justifications; under the regime of sfermion mass unification (Sec. 1.3.4), slepton masses are in the same order of squark masses which are assumed to be decoupled here ; when respecting the observed DM relic abundance, the mass splitting between NLSP and LSP becomes generally small (typically < 50 GeV). Decays via sleptons then requires slepton masses to be just within the small gap between the NLSP and LSP, which is however very unnatural.

With all the consideration, the targeted gluino decay chains are reduced into Table 1.4 with corresponding Feymann diagrams shown in Figure 1.15.

Table 1.4: Summary of targeted gluino decay chains. The number in the pharenthese indicates the numbers of chains in the categoty.

Direct decay (3)	$\tilde{g} \to (q\bar{q}, q\bar{q}, q\bar{q})\tilde{\chi}_1^0$
1-step decay (8)	$\tilde{g} \to (q\bar{q}', t\bar{b}(b\bar{t}))\ \tilde{\chi}_1^{\mp}, \quad \tilde{\chi}_1^{-} \to W^{\mp}\tilde{\chi}_1^0$
	$\tilde{g} \to (q\bar{q}, b\bar{b}, t\bar{t})\ \tilde{\chi}_2^0, \quad \tilde{\chi}_2^0 \to Z\tilde{\chi}_1^0)$
	$\tilde{g} \to (q\bar{q}, b\bar{b}, t\bar{t})\ \tilde{\chi}_2^0, \quad \tilde{\chi}_2^0 \to h\tilde{\chi}_1^0)$

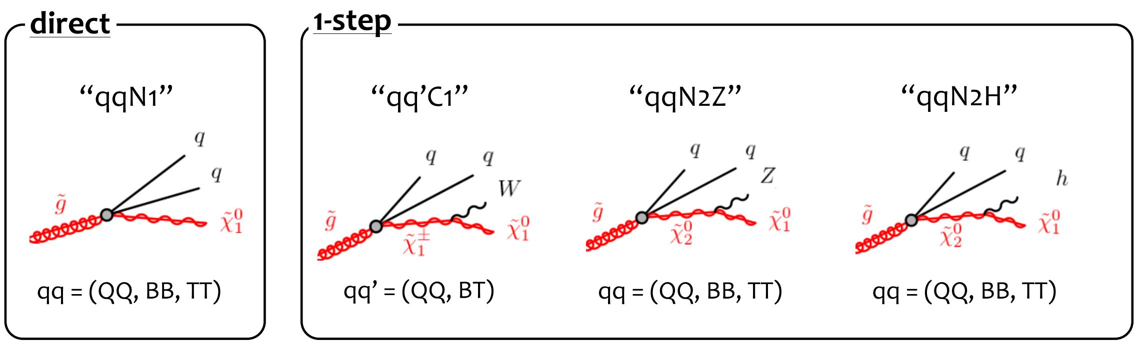

Figure 1.15: Target gluino decay chains.

The full decay chains of pair produced gluinos become increasingly complicated: 11 symmetric decays (two gluinos experience the same decay chains), 55 symmetric decays (two gluinos experience different decay chains). In total, 66 decay chains are identified as the candidate for the targets.

1.5.4 Target Signal Models for 1-lepton Final State

In LHC, analyses are conventionally divided based on number of hard leptons in the final state, since either signal kinematics and the background strategy are drastically different. In gluino decays, when ignoring the decays into sleptons, leptons are always generated via decays of W/Z/H bosons. Therefore, giving their small leptonical branching ratio, 0-lepton or 1-lepton final state are the most promising channels for inclusive search, while 2/3-leptons final states are more specialized in specific types of scenarios such as long-chain multi-step gluino decays involving a large number of W/Z/H bosons.

This thesis focuses on the final state with exactly one lepton. After excluding the decay chains with marginal branching ratio into final state with exactly 1-lepton, 45 decay chains are selected as the benchmark models for the thesis. The full list are shown in Table 1.5 - Table 1.7, with the naming convention for each decay chain defined as:

$$\begin{aligned} \text{Model name} &:= [aaXX][bbYY] \\ aa, bb &= \text{“QQ”},\text{“BB”},\text{“TT”},\text{“BT”} \\ XX, YY &= \text{“N1”},\text{“C1”},\text{“N2Z”},\text{“N2H”} \end{aligned} \tag{1.58}$$

where each sub-block ($[aaXX]$,$[bbYY]$) denotes the full chain of one gluino decay, corresponding to either of the topology shown in Figure 1.15.

Since the signal regions will be segmented based on the numberof b-tagged jets, the benchmark models are further categorized (BV/BT/3B) based on the number of expected b-quarks in the final state. The reference models for each b-categories are respectively chosen as **QQC1QQC1**,**QQC1BTC1** and **TTN1TTN1** for BV, BT and 3B (Figure 1.16), which will be used as the reference in designing signal regions and other various studies. The Feynman deagrams for the reference models are illustrated in Figure 1.16.

Note that simplified models with asymmetric gluino decays are not realistic due to the assumption of 100% branching ratio, since there is always branching to symmetric decays when asymmetric decays happen. However, this is in fact a more user friendly presentation since it provides the upper limit on the acceptance for each decay chain so that the compatibility between observation and models can be easily tested using it, which is not the case in case of an interpretation with a realistic models where many sorts of decays are mixed.

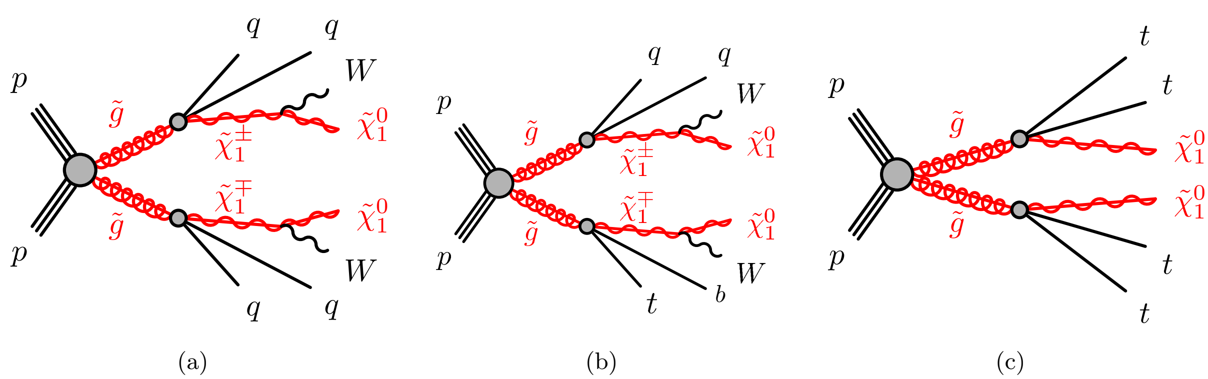

Figure 1.16: Feymann diagrams for the reference models (a) **QQC1QQC1** (b) **QQC1BTC1** (c) **TTN1TTN1**.

Table 1.5: Target models with no b-jets at tree level (BV models). The average jet multiplicity (n_J) and b-jet multiplicity (n_B) are calculated based on number of quarks and b-quarks appearing in the final state. The PDG values [47] are referred for branching ratio of top, W/Z/h bosons. "✓″ specifies the models with the final result derived using the samples with the fast detector simulation (ATLFast 2 [48]), while the others are with emulated truth samples.

1-step decay	n_J	n_B	Br(1L)/Br(0L)	Br(1L)/Br(2L)	det sim.?
QQN1QQC1	5.5	0.0	0.33	-	
QQC1QQC1	7.0	0.0	0.67	6	✓
QQC1QQN2Z	7.3	0.3	0.35	3.86	✓

Table 1.6: Target models with 1 or 2 b-jets at tree level (BT models). Definition of $n_{\mathrm{B,J}}$, branching and "✓″ are the same as Table 1.5.

Direct decay	n_J	n_B	Br(1L)/Br(0L)	Br(1L)/Br(2L)	det sim.?
QQN1TTN1	7.0	2.0	0.67	6	
1-step decay	n_J	n_B	Br(1L)/Br(0L)	Br(1L)/Br(2L)	det sim.?
QQC1QQN2H	7.4	1.1	0.46	7.07	✓
QQN1BTC1	7.0	2.0	0.67	6	
QQN1TTN2Z	8.8	2.3	0.68	3.30	
QQC1BTC1	8.5	2.0	1.0	3	✓
QQC1BBN2Z	7.3	2.3	0.35	3.86	
QQC1TTN2Z	10.3	2.3	1.02	2.34	
QQN2ZTTN2Z	10.7	2.6	0.7	2.31	
BBN1QQC1	5.5	2.0	0.33	-	
BTC1QQN2Z	8.8	2.3	0.68	3.30	
TTN1QQC1	8.5	2.0	1.0	3	
TTN1QQN2Z	8.8	2.3	0.68	3.30	

Table 1.7: Target models with 3 or more b-jets at tree level (3B models). Definition of $n_{\mathrm{B,J}}$, branching and "✓" are the same as Table 1.5 and 1.6.

Direct decay	n_{J}	n_{B}	Br(1L)/Br(0L)	Br(1L)/Br(2L)	det sim.?
BBN1TTN1	7.0	4.0	0.67	6	
TTN1TTN1	10	3.9	1.33	2	✓
1-step decay	n_{J}	n_{B}	Br(1L)/Br(0L)	Br(1L)/Br(2L)	det sim.?
QQN1TTN2H	8.9	3.1	0.79	3.64	
QQC1BBN2H	7.4	3.1	0.46	7.07	
QQC1TTN2H	10.4	3.1	1.12	2.34	
QQN2ZTTN2H	10.8	3.4	0.8	2.56	
QQN2HTTN2H	10.8	4.3	0.91	2.70	
BBN1BTC1	7.0	4.0	0.67	6	
BBN1TTN2Z	8.8	4.3	0.68	3.30	
BBN1TTN2H	8.9	5.1	0.79	3.64	
BBN2ZTTN2Z	10.7	4.6	0.7	2.31	
BBN2ZTTN2H	10.8	5.4	0.8	2.56	
BBN2HTTN2H	10.8	6.3	0.91	2.70	
BTC1QQN2H	8.9	3.1	0.79	3.64	
BTC1BTC1	10	4.0	1.33	2	
BTC1BBN2Z	8.8	4.3	0.68	3.30	
BTC1BBN2H	8.9	5.1	0.79	3.64	
BTC1TTN2Z	11.8	4.3	1.35	1.75	
BTC1TTN2H	11.9	5.1	1.46	1.70	
TTN1QQN2H	8.9	3.1	0.79	3.64	
TTN1BTC1	10	4.0	1.33	2	
TTN1BBN2Z	8.8	4.3	0.68	3.30	
TTN1BBN2H	8.9	5.1	0.79	3.64	
TTN1TTN2Z	11.8	4.2	1.35	1.75	
TTN1TTN2H	11.9	5.1	1.46	1.70	
TTN2ZQQN2H	10.8	3.4	0.8	2.56	
TTN2ZBBN2H	10.8	5.4	0.8	2.56	
TTN2ZTTN2Z	13.7	4.5	1.36	1.55	
TTN2ZTTN2H	13.8	5.4	1.47	1.53	
TTN2HTTN2H	13.8	6.2	1.58	1.49	

1.6 Structure of the thesis

This dissertation is organized as follows:

- Chapter 2 overviews the experiment apparatus used in the study; the LHC and the ATLAS detector.
- Chapter 3 describes the off-line algorithms utilized for reconstruction and identification of particles and hadronic jets.
- Chapter 4 describes the setup of the MC simulation employed in the analysis.
- Chapter 5 describes the pre-selection and designed signal regions.
- Chapter 6 includes comprehensive discussion on the background estimation method and its validation.
- Chapter 7 overviews the evaluated systematic uncertainties associated with background estimation and signal modeling.
- Chapter 8 summerizes the results and resultant limits.
- Chapter 9 discusses the impact of the obtained result.
- Chapter 10 close the thesis with concluding remarks.

Chapter 2

Experiment Apparatus: The ATLAS Detector at the LHC

2.1 The Large Hadron Collider

The Large Hadron Collider (LHC) [49] is a 27 km long circular proton accelerator embedded underground of the Geneva area. It is designed to collide protons at a center-of-mass energy of $\sqrt{s} = 14$ TeV, at the four detector cites (ATLAS [50], CMS [51], ALICE [52] and LHCb [53]) built on the accelerator ring. ATLAS and CMS are general purpose detectors designed to study a vast range of physics programs, while LHCb and ALICE are specialized in studying b-hadrons and heavy-ion collisions respectively.

The operation started in 2010, offering proton-proton (pp) collisions at a center-of-mass energies of 7 TeV and 8 TeV with 4.7fb^{-1} and 20.3fb^{-1} of integrated luminosity until 2012 (Run1). The center-of-mass energies has been almost doubled to 13 TeV in the runs starting from 2015 (Run2). The LHC has also delivered lead-ion (Pb-Pb) collisions with a center-of-mass energy of $\sqrt{s_{NN}} = 2.76$ TeV and proton-lead (p-Pb) collisions with $\sqrt{s_{NN}} = 5.02$ TeV.

The acceleration of protons with various steps: Protons are firstly seeded from hydrogen gas, by blowing the electrons off the hydrogen atoms using electric field. They are injected in the linear accelerator LINAC2 accelerated upto 50 MeV, and sent to the Proton Synchrotron Booster (PSB) with being accelerated up to an energy of 1.4 GeV. The subsequent accelerator is the Proton Synchrotron (PS) elevating the energy of the protons to 25 GeV, and injecting them into the Super Proton Synchrotron (SPS). After being accelerated to 450 GeV in SPS, the protons finally enter the two LHC pipes running the beam oppositely each other. The whole acceleration chain is illustrated in Figure 2.1.

The LHC accelrator consists of octant-shaped 2.45 km arcs with 1232 superconducting magnets located at the curves, providing 8.33T of magnetic field to bend the proton trajectory. In total, 39 bunch-trains can be filled simultaneously at the design condition, and 2808 bunches per beam are brought to collision in the LHC. Each bunch contains about 10^{11} protons. The beam bunches are collided with a crossing angle of 285 mrad. The peak luminosity amounts upto

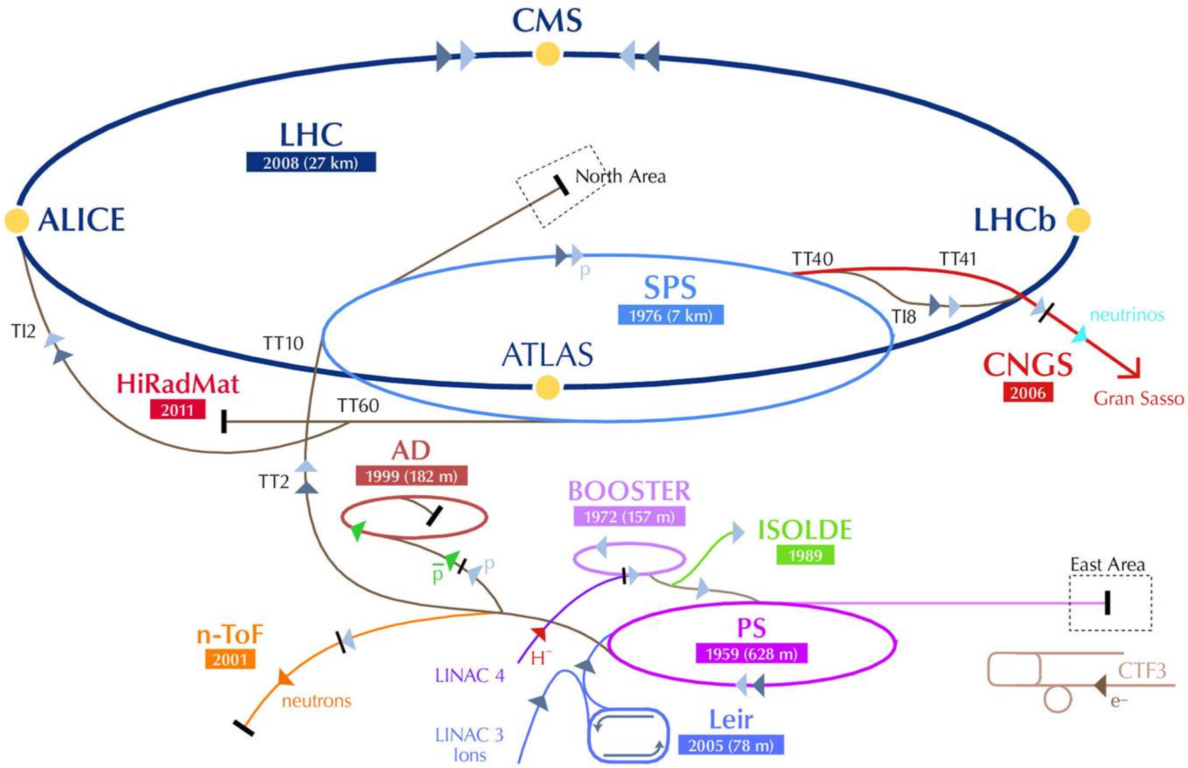

Figure 2.1: The LHC and associated booster accelerator system. [54]

$L = 0.7 - 1.4 \times 10^{34}\text{cm}^2\text{s}^{-1}$ in the 2015-2016 runs, as shown in Figure 2.2 (a).

Due to the high frequency of collisions and the dense proton bunches, multiple proton collisions can take place within the same bunch crossing, referred as "pile-up". The average pile-up μ, defined as the mean number of interactions per bunch crossing, has been evolved according to the peak luminosity increase. The μ profile in Run2 is shown in Figure 2.2 (b) where $\mu = 20 \sim 40$ is typically achieved.

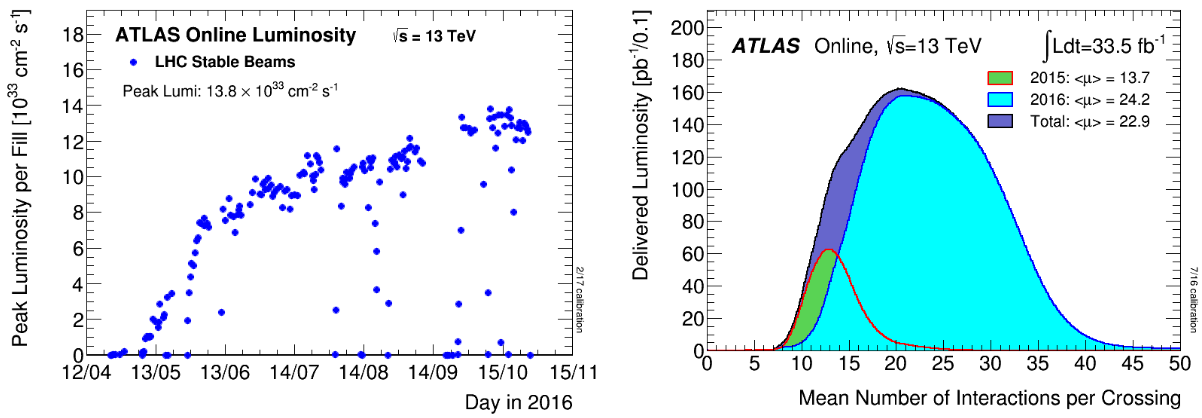

(a) (b)

Figure 2.2: (a) Peak luminosity evolution in 2016 runs [55], and (b) the pile-up profile obtained in 2015-2016 runs [56].

2.2 The ATLAS Detector

2.2.1 Overview

ATLAS (A Toroidal LHC ApparatuS) is a general purpose detector, aiming to a wide range of physics programs from precision measurements to the energy frontier experiments, through a dedicated measurement of particles produced in the *pp* collisions. The detector extends over 44m in width and 25m in height weighing 7000 tons in total, covering the interaction point (IP) by a cylindrical barrel and two end-caps, achieving a nearly full solid angle coverage. The cut-away image is shown in Figure 2.3.

The purposes of the detector are mainly two-fold:

- identification of particle species,
- determination of particle's energy and momentum,

with two complementary concepts of measurement:

- fast measurement to provide triggers
- precision measurement for physics analyses

To satisfy these functionalities at the same time, following sub-detectors are arranged in a designed order from the inner to the outer with respect to the IP.

- Inner detector (and magnets) to identify and measure electrically charged particles, as well as to define the primary vertices.
  Charged particle can easily interact with materials by ionizing the molecules inside. The path of flight can be "imaged" as a track, by recording the position of ionization. In ATLAS, a

complex of discrete layers of silicon sensors and a continuously volumed gas chambers are placed in the innermost part. The momentum can be measured by applying a magnetic field, and quantifying the curvature of the bent trajectory.

- Calorimeters to measure the energy of electron, photon and hadrons.
  Electrons and photons traveling inside materials above certain energy [1] lose their energy through electromagnetic showering; photons create e^+e^- pairs and electrons spew bremsstrahlung photons; the daughter electrons and photons are multiplicated by the recursive splitting; ending up in a particle shower. Most of the energy are absorbed after traversing about 20 radiation lengths (X_0) of material. Hadrons (mostly pions) also cause similar cascade reactions. The shower branch evolves by interacting with nucleus in the material via strong interaction, meanwhile produced π_0s promptly decay into two photons which shower electromagnetically. The resultant shower is a combination of a long hadronic shower and small local EM clusters in it. Electromagnetic and hadronic calorimeters are set as the outer layers of the trackers.

- Muon spectrometer (and the magnet) to measure the muons penetrating the detector.
  Among all the particles that interact with material, muons are only exception that do not seriously deposit the energy in the calorimeter. This is due to the fact that muons are the leptons happening to have the mass realizing the minimum EM interaction with material (Minimum Ionizing Particle; MIP), and the corresponding critical energy for EM showering is usually at several TeV level. This is actually a lovely coincident for human being (or poor particle physicists), since they can be easily identified i.e. particles punching through the calorimeter are automatically muons. The muon spectrometer located the outermost serves for identifying such muons as well as measuring the tracks together with the information from the inner tracker.

- Given the total momentum conservation in the transverse direction in each collision, the presence of non-interacting particles such as neutrinos and hypothetical new particles can be indirectly detected through the transeverse momentum imbalance; This is referred to missing E_{T} ($E_{\mathrm{T}}^{\mathrm{miss}}$), [2] defined by the negative of the vectoral sum of transverse momentum of all detected particles.

In the following sections, each of the sub-detector system is overviewed, comprehensively based on references [50] and [57].

2.2.2 Coordinate System

For referencing the position of the detector as well as the orientation of particles, a right-handed Cartesian coordinate system is defined where the interaction point is the origin; the x-axis pointing to the center of the LHC ring; the y-axis and z-axis are accordingly the direction of sky or the beam direction respectively. Polar angle θ and azimuthal angle ϕ are defined by the cylindrical

[1] Referred to the critical energy. ~ 800 MeV for typical material.

[2] The "E_{T}" in the name is due to a historical reason; it used to be calculated only using calorimeter deposits, which is now actually outdated

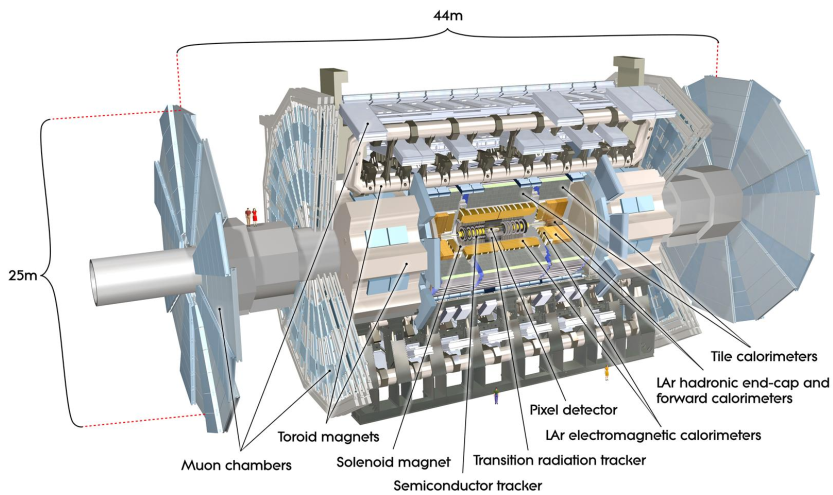

Figure 2.3: Full-body view of the ATLAS detector [58]. The geometry is completely forward-back symmeric.

representation (θ, ϕ, z): θ ranges from 0 to π with respect to the z-axis, and ϕ runs from $-\pi$ to π from the x-axis. The two end-caps in the ATLAS detector are referred as "A-side" and "C-side", [3] corresponding to the position of positive and negative coordinate in the z-axis.

It is the unfortunate fate for hadron colliders that particles generated by collisions are usually highly boosted along z-axis, since the energy of the initial interacting partons inside the hardons are asymmetric. From this point of view, a set of variables with Lorentz-invariant nature are introduced for describing the momentum or position for such particles. In particular, it is useful to define the transverse component of variables, such as transverse momentum $p_{\mathrm{T}} := p \sin\theta$ or transverse energy $E := E \sin\theta$. The advantage over the use of p or E is obvious that they do express the intrinsic hardness of the particles in the center-of-mass frame of the reaction, and also that the vectoral sum of all particles conserves before and after the collision.

Similarly, pseudo-rapidity η is defined below, serving as the coordinate of polar angle:

$$\eta := -\ln\left(\tan\frac{\theta}{2}\right). \tag{2.1}$$

It has two practical advantages over θ; the difference in pseudo-rapidity between particles $\Delta\eta$ are invariant against the boost towards z-direction. [4] ; η has an effectively wider dynamic range upto a very forward region thanks to the finer measure, where θ suffers from the degeneracy in $\cos\theta \sim 1$, thus more convenient in expressing the orientation of forward particles.

Angular distance between two particles are commonly expressed by R, defined as:

$$\Delta R := \sqrt{(\Delta\eta)^2 + (\Delta\phi)^2}. \tag{2.2}$$

[3] Reportedly named after the direction towards (Geneva) Airport and the Charie's Pub in St. Genis-Pouilly from the ATLAS respectively.

[4] This is true when the particles are massless, which is approximately valid given that the boos along z-axis is sourced by the momentum of order of the beam energy.

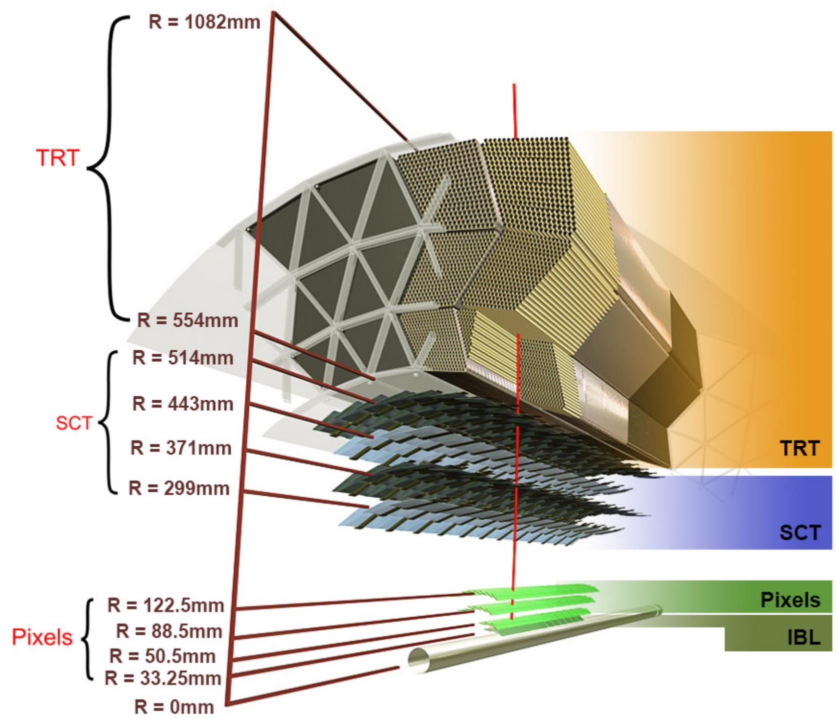

Figure 2.4: Cross-section of the ATLAS inner detectors [50].

2.2.3 Inner Detectors

The inner detector (ID) is placed the inner-most of the ATLAS detector, designed to measure the tracks of charged particles, as well as precisely determining the position of vertices of the hardest scattering in interest. It consists of a silicon tracker (the pixel detector and the semiconductor tracker ;SCT) at the inner radii, and the Transition Radiation Tracker (TRT) for continuous tracking at the outer radii. The detector arrangement is illustrated in Figure 2.4 and Figure 2.5. The outer radius is surrounded by the central solenoid, providing a magnetic field of 2T along the z-axis, to bend the tracks traveling inside the ID volume. As a general requirement, ID has to contain material as less as possible, to avoid disturbing the measurement downstream by the energy loss. Figure 2.6 shows the total material profile of the ID as function of $|\eta|$. The material volume is suppressed below 2.5 radiation length and 1 nucleus interaction length, which is low enough compared with energy dropped in the calorimeter.

The silicon trackers: Pixel and SCT The detection principle of silicon detector is based on the electron-hole pair creation induced by a traverse of a charged particle. Those electron-hole pairs are then inhaled by the bias voltage applied on the sensor, and transferred into an electric signal. The choice of silicon is largely due to its radiation hardness sufficient to endure the enormously high radiation around the IP. On the other hand, the performance (e.g. noise level, gain) is relatively sensitive to temperature, therefore they are kept in low temperature ($-5 \sim 0\,^{\circ}$C) during the operation.

The pixel detector is the unit of layers of pixelated silicon sensors located closest to the IP of all the detector component. Oxygen enriched n-in-n silicon semiconductor is used for the sensors.

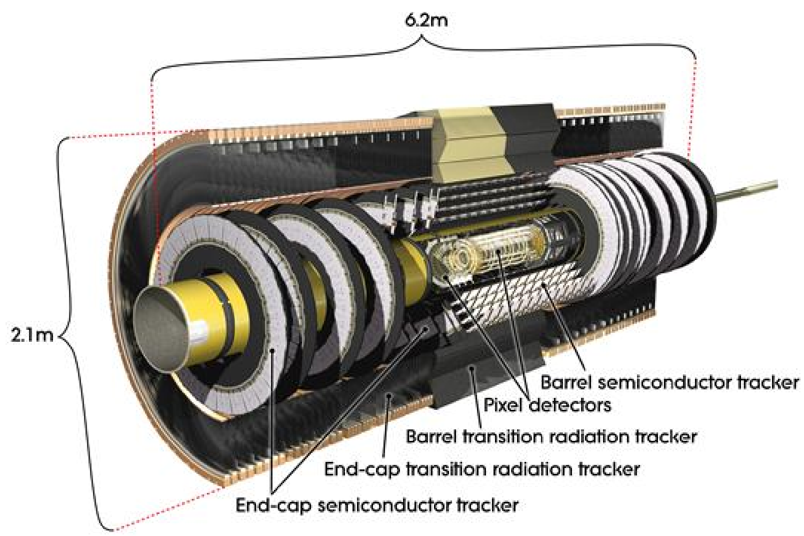

Figure 2.5: Cut-away view of the ATLAS inner-detector [50].

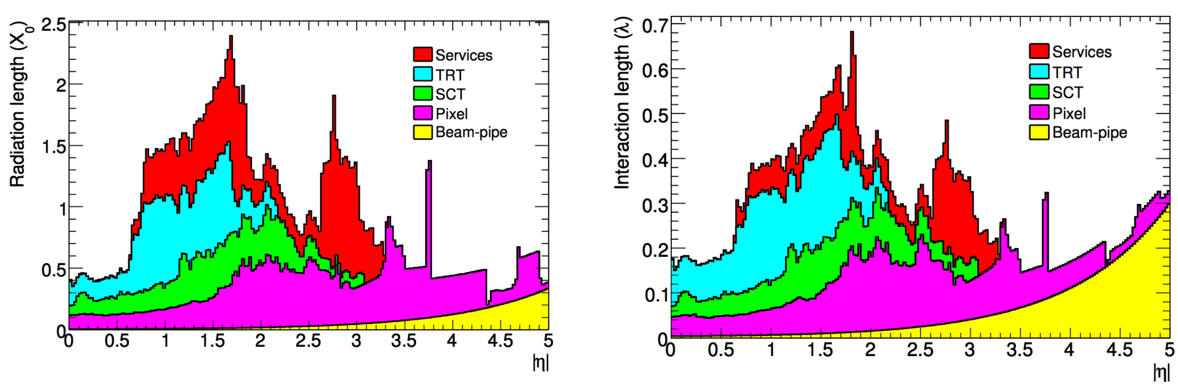

(a) (b)

Figure 2.6: Simulated material profile of whole ID in unit of (a) electro-magnetic radiation length and (b) nucleus interaction length [50]. The peak in $|\eta| \sim 1.5$ corresponds to the barrel-end-cap transition area through which service cables travel.

Four cylindrical layers are placed in the barrel at the radial distance of 31 mm $\sim$ 122.5 mm with respect to the IP, and 3 disk layers cover each side of the end-cap, providing an acceptance of $|\eta| < 2.5$. The innermost layer in the barrel provides the highest precision referred as the "insertable b-layer" (IBL) installed during the long shutdown between Run1 and Run2. The pixels are in the 50×250 μm granularity in the IBL, and 50×400 μm in the other layers. The resolution is purely determined by the pixel size. A spatial resolution of 4 μm and 115 μm is achieved along the radial and beam z-direction respectively, by combining the hit information from the four layers.

The SCT is located outside of the pixel detector. The sensors are made by single-sided p-on-n silicon semiconductors. The strips of barrel SCT aligning along the z-axis with 80 μm pitch, giving a precision position in the $r-\phi$ plane. A slight angle stereo (40 mrad) alternated by layers is applied to the arrangement, providing decent z-position determination in addition. The barrel region is surrounded by four layers, while nine discs are placed in each end-cap. The intrinsic resolution is 17 μm(580 μm) in $r - \phi(z)$ direction respectively. The strips in the end-cap SCT are aligned in a mesh in terms of $x - y$, capable of 3D position determination together with the z-coordinate of the disks.

Trasition radiation tracker TRT is a gaseous detector designed for tracking particles as well as identifying the species using the characteristic transition radiation. The detector is filled with 4mm-diameter straw tubes in which xenon-based active gas is confined. Ionized secondary electrons are collected by the 30 μm-diameter gold-plated tungsten-Rhenium anode wire in the center of each straws. 73 layers of aligned straw tubes are arranged in the barrel, and 160 layers in the end-cap sectors. The tube length is 144 cm (37 cm) in the barrel (end-cap) region. The barrel tubes are arranged in parallel along the beam pipe, with 7 mm of interval between layers. The intrinsic position resolution per straw is about 130 μm. A traverse of charged particle fires 36 straws on average.

Transition material is inserted between the straws. 19 μm-diameter polypropylene fibers are used in barrel, and 15 μm-thick polypropylene radiator foils isolated by a polypropylene net are set for the end-caps. Transition radiation can address unique sensitivity in particle identification, particularly to e/π separation, since the intensity is sensitive to incident particle's velocity (proportional to $\gamma = E/m$) rather than the energy or momentum. Given that the signal of transition radiation typically yield more amplitude than the nominal gas ionization, two different thresholds are set in the TRT ; the lower threshold to collect the signal of ionization caused by a particle traverse; the high threshold defining the signal of transition radiation. The high threshold is carefully designed so that only electrons in the typical range of energy (0.5 GeV $-$ 150 GeV) can fire while pions are inert to it.

Figure 2.7 shows the γ-dependence of high threshold rate, demonstrating a good separation of particles in the electron-like momentum and pion-like momentum.

Combined Tracking Performance The combined tracking performance has been validated via the measurement of cosmic muons [58]. The resolution for a single muon track is obtained as

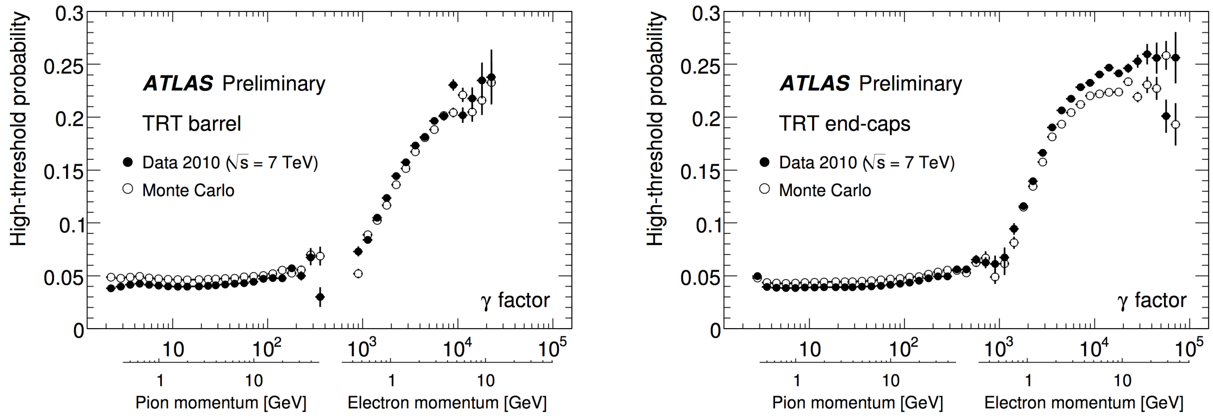

Figure 2.7: TRT high threshold rate as function of Lorentz factor ($\gamma = E/m$) of incident particles [59]. The γ scale of typical pions and electrons are labeled aside. The left (right) plot corresponds to the rate in barrel (end-caps) respectively.

function of muon transverse momentum:

$$\frac{\sigma_{p_\mathrm{T}}}{p_\mathrm{T}} = 1.6\% \oplus \frac{0.053\%}{\mathrm{GeV}} \times p_\mathrm{T}. \tag{2.3}$$

2.2.4 Calorimetery

The ATLAS calorimetery located outside the ID is composed of the electromagnetic calorimeter (EM calorimeter), the hadronic calorimeter (HC), and the forward calorimeter. The whole view is given by Figure 2.9. The calorimeters employ two detector thechnologies:

- Liquid-Argon sampling calorimeter (LAr) with alternately sandwiching the lead absorber layers and the sensor layer filled with liquid-argon.
- "Tile calorimeter" consisting of the sensor layers with scintillator tiles and steel absorber.

The detector technology and the spatial segmentation in each pseudo-rapidity coverage are summarized in Table 2.8. Thanks to the fast response of the readout, calorimeter can provide the function of trigger, based on the fast processing of particle identification and the energy measurement using the information of individual showers, as detailed in Sec. 2.2.7.

EM CALORIMETER	**Barrel**	**End-cap**	
Coverage	$\|\eta\| < 1.475$	$1.375 < \|\eta\| < 3.2$	
Longitudinal segmentation	3 samplings	3 samplings	$1.5 < \|\eta\| < 2.5$
		2 samplings	$1.375 < \|\eta\| < 1.5$
			$2.5 < \|\eta\| < 3.2$
Granularity ($\Delta\eta \times \Delta\phi$)			
Sampling 1	0.003×0.1	0.025×0.1	$1.375 < \|\eta\| < 1.5$
		0.003×0.1	$1.5 < \|\eta\| < 1.8$
		0.004×0.1	$1.8 < \|\eta\| < 2.0$
		0.006×0.1	$2.0 < \|\eta\| < 2.5$
		0.1×0.1	$2.5 < \|\eta\| < 3.2$
Sampling 2	0.025×0.025	0.025×0.025	$1.375 < \|\eta\| < 2.5$
		0.1×0.1	$2.5 < \|\eta\| < 3.2$
Sampling 3	0.05×0.025	0.05×0.025	$1.5 < \|\eta\| < 2.5$
PRESAMPLER	**Barrel**	**End-cap**	
Coverage	$\|\eta\| < 1.52$	$1.5 < \|\eta\| < 1.8$	
Longitudinal segmentation	1 sampling	1 sampling	
Granularity ($\Delta\eta \times \Delta\phi$)	0.025×0.1	0.025×0.1	
HADRONIC TILE	**Barrel**	**Extended barrel**	
Coverage	$\|\eta\| < 1.0$	$0.8 < \|\eta\| < 1.7$	
Longitudinal segmentation	3 samplings	3 samplings	
Granularity ($\Delta\eta \times \Delta\phi$)			
Samplings 1 and 2	0.1×0.1	0.1×0.1	
Sampling 3	0.2×0.1	0.2×0.1	
HADRONIC LAr		**End-cap**	
Coverage		$1.5 < \|\eta\| < 3.2$	
Longitudinal segmentation		4 samplings	
Granularity ($\Delta\eta \times \Delta\phi$)		0.1×0.1	$1.5 < \|\eta\| < 2.5$
		0.2×0.2	$2.5 < \|\eta\| < 3.2$
FORWARD CALORIMETER		**Forward**	
Coverage		$3.1 < \|\eta\| < 4.9$	
Longitudinal segmentation		3 samplings	
Granularity ($\Delta\eta \times \Delta\phi$)		$\sim 0.2 \times 0.2$	

Figure 2.8: Summary of partition and geometry of the ATLAS calorimetery [57].

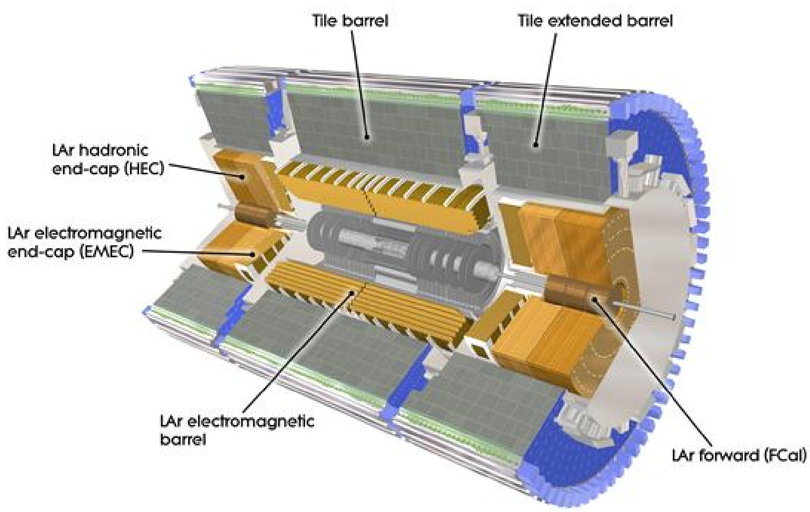

Figure 2.9: Cut-away view of the ATLAS calorimetery [50].

Electromagnetic calorimeter The basic unit of LAr calorimeter consists of a gap filled with liquid argon (gap width: 1.1-2.2mm) generating the ionized electrons, a copper-kapton electrodes to collect the ionized charge, and a steel-claded lead absorber layer to develop the EM shower (layer width: 1.13-1.53mm). A bias voltage of 2000V between the electrodes and the absorbers is applied, achieving the drift time of 450ns. The readout signal is amplified by a pre-amplifier, and shaped into a 13 ns widthsignal pulse by a bi-polar shaper managing the 25 ns width bunch crossings. The detector is maintained at a constant temperature of $88K$ by cryostats surrounding the barrel EM calorimeter.

The geometry and cell segmentation varies between barrel and end-cap depending on the desired function. Figure 2.10 illustrates the segmentation in the barrel ECM. 3 sampling blocks are placed along shower with different $\eta \times \phi$ segmentation. The first sampling layer has the finest $\eta \times \phi$ granularity (0.0031×0.098) identifying the precise angular position of the incident particle. The second sampling addresses the largest volume ($16X_0$) containing the most of shower in which the energy is mainly measured. The third sampling layer is intended to measure the tail of EM showers, providing information about the longitudinal profile together with the other layers. The layer units are arranged in an accordion geometry, which is the characteristic to the barrel ECM, designed to be fully hermitic in terms of angular acceptance. In order to compensate the upstream energy loss, a presampling layer is additionally placed in front of the first layer of the EM calorimeter for both barrel and the end-caps. The total thickness amounts to $> 22X_0$ in the barrel and $> 24X_0$ in the end-cap, which can fully accommodate the EM showers of photons or electrons in an energy of upto a few TeV. The transition region between the barrel and end-caps ($1.37 < |\eta| < 1.52$) is dedicated to detector services and therefore not fully instrumented.

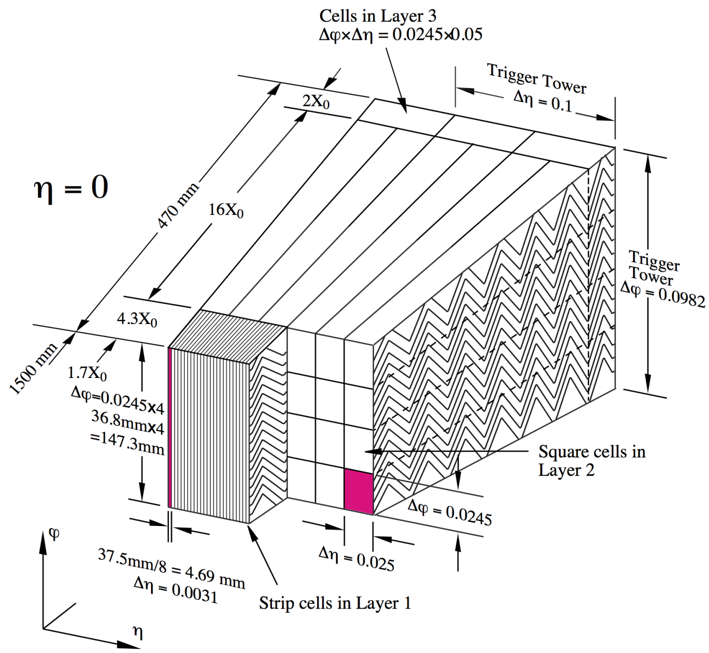

Figure 2.10: Geometry of barrel LAr sampling layers. Position resolution is addressed by the innermost sampling layer by the highest $\eta \times \phi$ granularity of 0.0031×0.098, and the energy measurement is mainly provided by the second layer with the largest volume. The third layer standing behind in the plot is the tail catcher providing information of the shower profile. [57].

The designed resolution is given in Eq. 2.6 [60]:

$$\frac{\sigma_E}{E} = \frac{10\%}{\sqrt{E}} \oplus \frac{17\%}{E} \oplus 0.7\%. \tag{2.4}$$

The energy resolution for the off-line objects can be further improved through the dedicated calibration exploiting the full detail of the shower and information from the other detector.

Hadronic Calorimeter The ATLAS hadronic calorimeter consists of the barrel Tile HC ($|\eta| < 1.7$) and end-cap LAr HC. Barrel Tile HC is segmented into three sections, the central barrel section ($|\eta| < 1.0$) and the two extended barrel sections ($1.0 < |\eta| < 1.7$), using different channel dimensions. There are three sampling layers along the shower development with the thickness of 1.5λ, 4.1λ and 1.8λ for barrel, and 1.5λ, 2.6λ and 3.3λ for extended barrel respectively. Figure 2.11 (a) schematizes one module in the Tile HC. Generated scintillation photons are read out by the photo-multiplier tubes equipped at the ends of the module via wavelength shifting fibers. The end-cap HC is the sampling calorimeter with liquid-argon sensor layers and copper absorber. The choice of material is dominantly based on the durability against the extremely high radiation flux in the forward region.

The intrinsic resolution of barrel Tile HC and end-cap LAr HC for an individual hadron jet is given by Eq. 2.6 [61]:

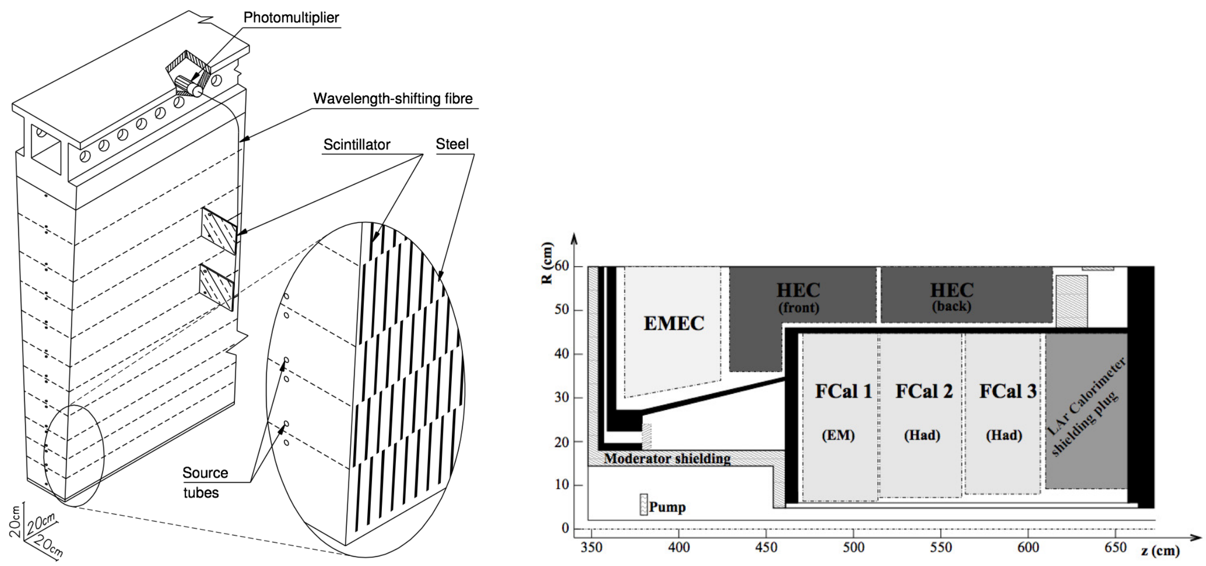

(a) (b)

Figure 2.11: (a) Illustration of a Tile HC module. (b) Alignment of each detectors in an end-cap; end-cap LAr EM calorimeter (EMEC); end-cap LAr Hadronic calorimeter (HEC); and the Forward calorimeter (FCal)) [50].

$$\frac{\sigma_E}{E} = \frac{50\%}{\sqrt{E}} \oplus 3\%, \qquad \text{(Tile HC)} \tag{2.5}$$

$$\frac{\sigma_E}{E} = \frac{100\%}{\sqrt{E}} \oplus 10\%, \quad \text{(End-Cap LAr HC)} \tag{2.6}$$

Forward Calorimeter A set of LAr calorimeter layers are arranged in a very forward region close to the beam axis covering $3.1 < |\eta| < 4.9$, designed to capture the full content of jets or particles from hard scattering particles from extremely boosted center-of-mass. The location with respect to the adjacent calorimeter systems are illustrated as Figure 2.11 (b). Forward calorimeter is made by three sampling layers in which both functions of EM calorimeter and hadronic calorimeter are integrated; The first layer is with copper absorber working as EM calorimeter, and the later two layers are with tungsten functioning as EM calorimeter. The overlap region with respect to the end-cap HC is deliberated to realize smooth transition.

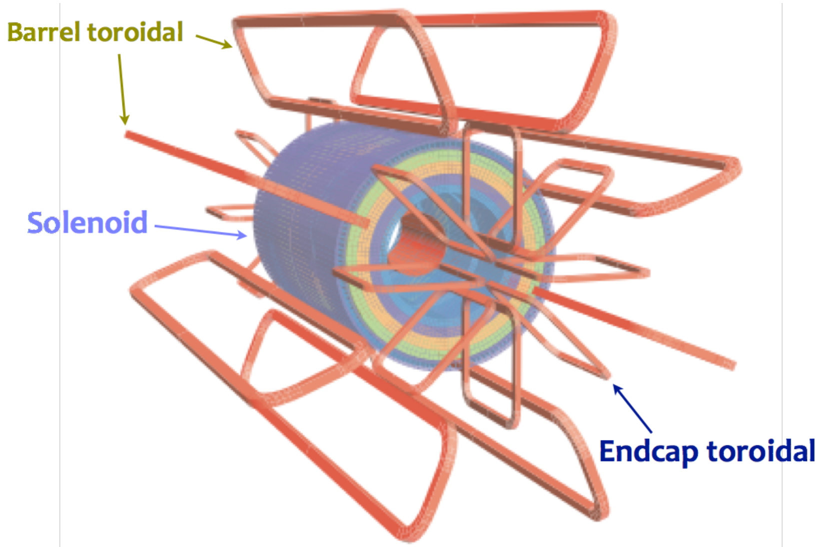

Figure 2.12: Schematic of the ATLAS magnet system with one central solenoid and 3 toroidals (barrel+2 end-caps) [50].

2.2.5 Muon Spectrometer

Muon spectrometers are located outermost in the ATLAS, consisting of four sub-detectors; Monitored Drift Tube (MDT); Cathode Strip Chamber (CSC); Resistive Plate Chamber (RPC); and the Thin-Gap Chamber (TGC). The former two are dedicated to precision measurement of muon tracks and the latter two are to triggering. The spectrometer covers the pseudo-rapidity range $|\eta| < 2.7$ and allows identification of muons with momenta above 3 GeV and precise determination of p_{T} up to about 1 TeV with 10% momentum resolution.

The magnetic field for tracking is sourced by the three pieces of toroidal superconducting magnets i.e. two end-cap toroids and a barrel toroid embedded in the space inside the muon spectrometers. $3.9T$ and $4.1T$ B-field is provided in the barrel and end-cap region respectively. The internal volume of toroidal coils are vacant ("air-core"), in order to reduce the material with which muons experience the multiple scattering. The integrated B-filed profile at the position of MDT is shown in Figure 2.13, while the global schematic of the magnet system is given in Figure 2.12.

Monitor Drift Tubes (MDT) MDT is a gaseous drift chamber filled with the basic detection elements of 30 mm-diameter aluminum tubes that are covered by a 400 μm-thick wall. Drifting electrons are absorbed by a 50 μm-diameter tungsten-Rhenium wire in the center of a tube with a bias voltage of 3080 V is applied, and read out by a low-impedance current sensitive preamplifier. The gas mixture is with Ar (93%) and CO_2 (7%), maintaining the maximum drift time of 700 ns. The position resolution by a single wire is about 80 μm. There are three layers of MDT chambers located both in barrel and end-cap, covering a pseudo-rapidity range of $|\eta| < 2.0$. The limitation in the η-coverage is determined by its maximum durable rate ($150 cm^{-1}s^{-1}$). CSC takes over the role in such forward region.

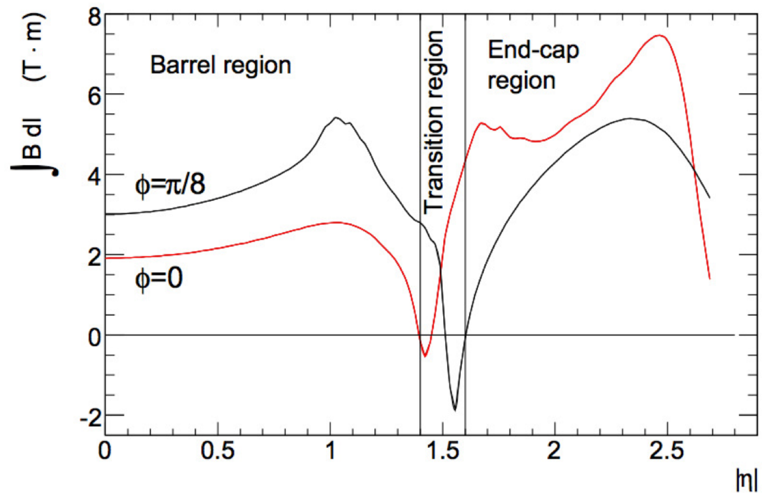

Figure 2.13: Simulated magnetic field integral provided by a single troid octant, from the innermost MDT layer to the outermost. [50].

Cathode Strip Chamber (CSC) The CSCs are multi-wire proportional chambers covering the forward region ($|\eta| > 2.0$) in the end-caps, providing 2D position of incident particles. It is operated with a gas mixture of Ar (80%) and CO2 (20%) and with a bias voltage of 1900 V applied. The cells are symmetric in terms of the pitch of readout cathodes and the anode-cathode spacing, which is equally set to 2.54 mm. Since the spatial resolution of the CSCs is sensitive to the inclination of tracks and the Lorentz angle, the chamber is fixed at tilted posture so that tracks originating from the IP become approximately orthogonal to the chamber surface.

Resistiv Plate Chamber (RPC) The RPCs are digital gaseous detectors specialized in fast timing response for triggering. They are mechanically mounted on the surface in the barrel MDT, covering the pseudo-rapidity range of $|\eta| > 1.05$. The elementary detection unit is a gas gap filled with non-flammable gas mixture (94.7% $C_2H_2F_4$, 5% Iso-C_4H_10, 0.3% SF_6). An uniform high electric field ($\sim$ 4900 V/mm) is applied so that the ionized electrons amplitude by themselves via the avalanches. Signals are read out by a metal strip attached on both ends of the gaps, arranged with a pitch of 30 mm $\sim$ 39.5 mm. The typical spatial and timing resolution achieved by a RPC chamber are 1 cm and 2 ns respectively.

Thin-Gap Chamber (TGC) The TGCs are a special type of multi-wire proportional chambers characterized by the notably small distance between the anode wires and the read out cathode strips (1.4mm). A quick drain of secondary electrons is achieved by the quenching gas mixture of CO_2 (55%) and n-pentan (45%), yielding the timing response of 5 ns. TGCs also contribute to the momentum determination by supplementing the measurement in ϕ by MDT. Three modules are placed per end-cap, covering $1.05 < |\eta| < 2.7$ by the innermost one and $1.05 < |\eta| < 2.4$ by the two behind. Trigger is generated using tracks in $1.05 < |\eta| < 2.4$, while all tracks are subjected to the momentum measurement.

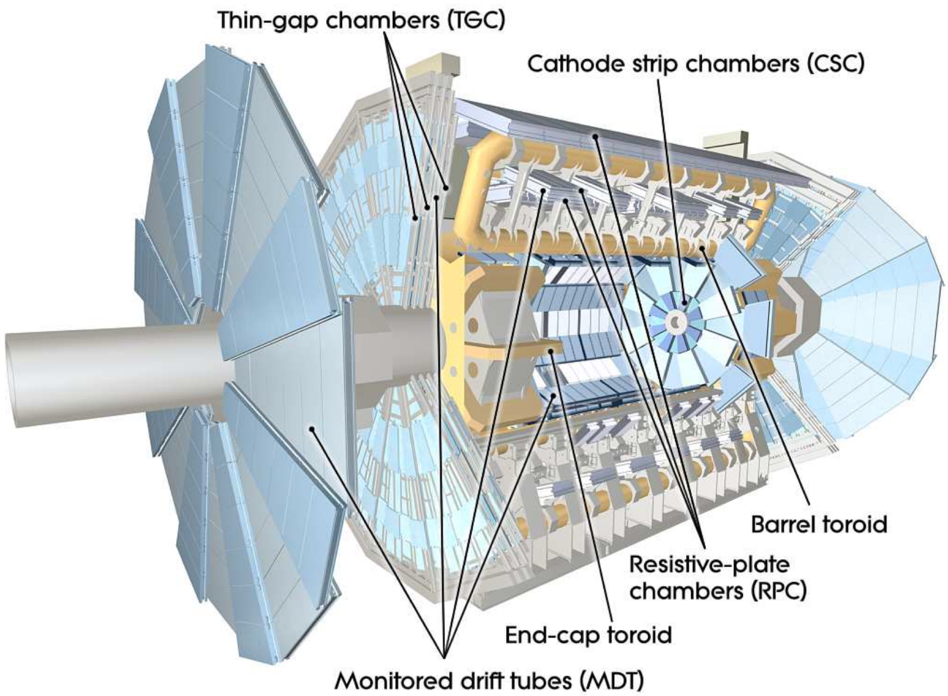

Figure 2.14: Global view of the ATLAS muon spectrometers [50].

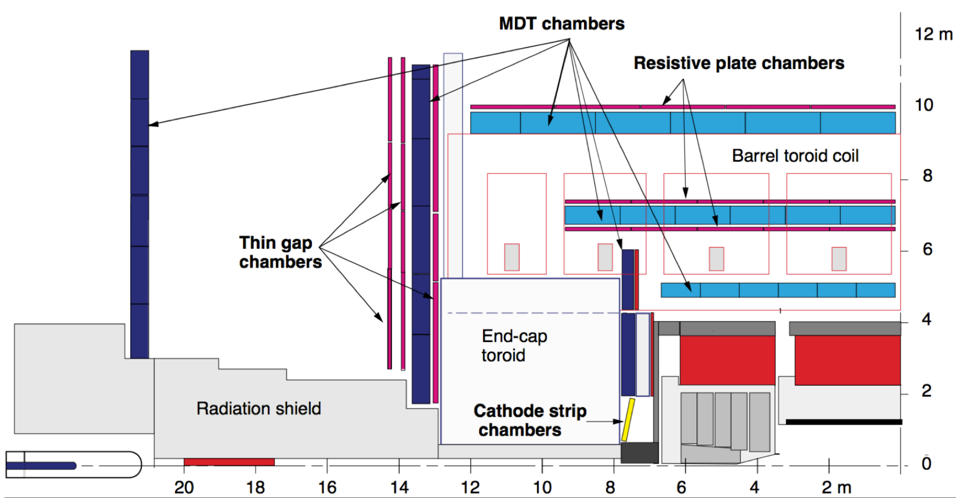

Figure 2.15: Cross-section of the ATLAS Muon spectrometer [58].

2.2.6 Luminosity Detectors

Luminosity determination is particular important since it provides the reference of normalizing simulated dataset which enables the comparison to data. The instantaneous luminosity is calculated by the formula below:

$$\mathcal{L} = \frac{\mu n_b f_b}{\sigma}, \tag{2.7}$$

where n_b is the number of colliding bunches and f_b the frequency of the beam circulation. σ is total fiducial cross-section of pp-interaction including both elastic and inelastic scattering, and μ is the average number of such interaction per bunch crossing. While σ is provided by a dedicated calibration (van der Meer scan [62]) measuring the lateral beam profile using overlapping two beams, μ is obtained directly by exploiting the rate information from luminosity detectors located in the very forward region nearby the beam pipe. Dedicated calibration and luminosity determination algorithm studied in [63]. Two luminosity detectors mainly contribute to the luminosity measurement:

LUCID (LUminosity measurements using Cherenkov Integrating Detector)
LUCIDs are located at the both ends of the ATLAS detector at a distance of 17m from the IP, covering the pseudo-rapidity range of $5.6 < |\eta| < 6.0$. The LUCID detector consists of 16 aluminum tubes filled with C_4F_{10} gas filled inside, designed to count the Cherenkov photons kicked out by charged particles flying along the beam axis which are mainly generated by proton-proton inelastic scattering in the IP.

ALFA (Absolute Luminosity For ATLAS)
ALFA is located beyond the ATLAS envelope at $z = \pm 240$ m, sandwiching the beam pipe from top and bottom. The detectors are composed of 8 scintillating fibers, designed to measure the elastic scattering component of the pp-interaction.

2.2.7 Trigger and Data Acquisition System

While ATLAS enjoys incredibly high collision rate of about 100 MHz (40 MHz beam bunch crossing together with pile-up), these data cannot entirely read out due to the limitation from data transmission as well as the computation resource. Luckily or unluckily, most of them are junk QCD reactions resulting in cheap low p_{T} jets, the rate can be drastically suppressed by requiring hard jets, leptons or $E_{\mathrm{T}}^{\mathrm{miss}}$ in the events.

The ATLAS Trigger and Data Acquisition System (TDAQ) [64] is the data acquisition system handling the trigger and readout. The schematic of the readout streams are shown in Figure 2.16. It consists of a two-staged trigger pipeline served by the hardware-based Level-1 Trigger (L1) and the software-based High-Level Trigger (HLT). The idea is to reject the major trivial QCD events in L1, based on a fast particle reconstruction with coarse resolution, and perform further filtering in HLT using more sophisticated reconstruction and energy measurent benefited by the timing latency that L1 earns. The benchmark of rate suppression is 100 kHz at the end of L1 and down to 1 kHz after the HLT on average.

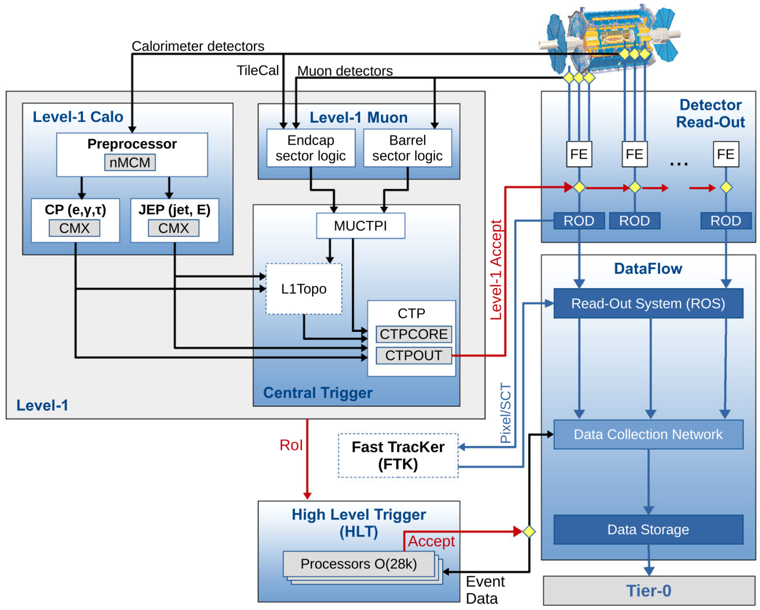

Figure 2.16: The logic of ATLAS trigger system [64]. Trigger detectors have separated readout line for trigger, sending input information for trigger decision to CTP. The CTP reconstructs L1 objects and issue a global accept signal relieving the buffered data, once the trigger criteria are satisfied. The (η, ϕ) position of identified trigger object is sent to downstream HLT, in which offline-like software-based triggers run to filter events further. L1 topological trigger (L1 Toplo) and Fast Tracker (FTK) have been in commissioning since 2015.

The L1 consists of two independent sub-trigger systems; L1Calo identifying the EM or hadronic clusters in calorimeter and reconstruct primitive jets, electrons, photons and taus (L1 objects) with calibrated energy in EM scale; L1Muon identifying and measuring the tracks in the muon spectrometer designed to accept events with muons. The object reconstruction is based on the coarsely segmented blocks of combined detector channel called "trigger tower" with $\eta \times \phi$ granularity of 0.1×0.1. $E_{\mathrm{T}}^{\mathrm{miss}}$ is also calculated at the L1 stage by the vectoral sum of the calorimeter deposits, referred as L1XE. Trigger accept is issued by the Central Trigger Processors (CTP) when the L1 objects meet certain criteria in terms of p_{T} threshold and number of objects.

In the HLT, offline-like algorithms are employed to refine the energy of L1 objects, or recover the mis-identified objects (low-p_{T} muons most typically) by scanning over whole detector. This is performed by a set of custom farmwares with a processing time of 0.2s on an average. The event triggered by the HLT is subsequently sent to event storage infrastructures outside the ATLAS. Figure 2.17 illustrates the rate of HLT acceptance in 2016 operation. The performance of triggers relevant to the analysis is dedicatedly overviewed in Sec. 5.1.

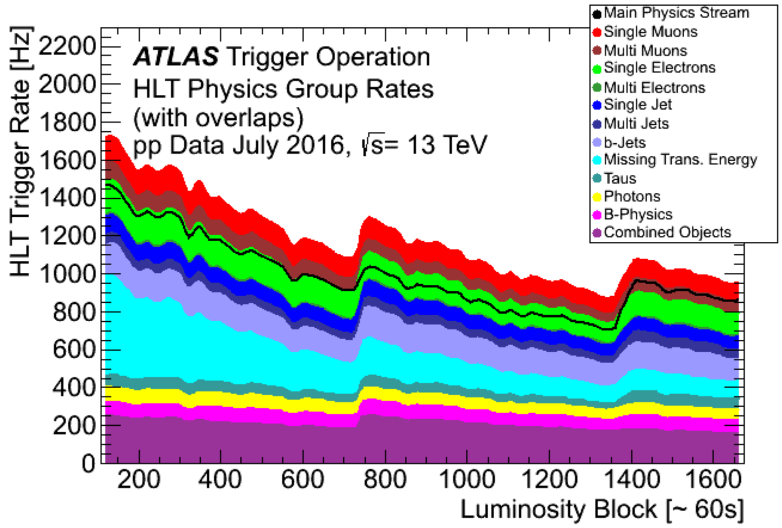

Figure 2.17: Rate of HLT streams for physics analyses during the 2016 data-taking [65]. Horizontal axis is in unit of lumi-clock, the smallest unit of data-taking in the same configuration.

2.3 Recorded Data by ATLAS

The *pp*-collision data analyzed in this study has been collected by ATLAS during 2015 and 2016. Quality requirements are applied for the recorded data base on each lumi-block which is the smallest unit of data-taking defined as a period in the same run configuration and conditions of beam and detector. Rejected data is typically at the periods with more than a certain of fraction of modules in the sub-detectors being disabled or in a wrong operation configuration (e.g. voltage or temperature etc.). After the quality requirement, the total integrated luminosity available for the analysis is 36.1 fb^{-1} with the measurement error of 3.2%.

Chapter 3

Object Reconstruction and Identification

The raw detector-level information of particles is translated into physics quantities through the sequence of particle reconstruction, identification and calibration. Though this is partially done at the trigger level, the recorded events are further elaborated by the sophisticated off-line algorithms, enjoying the detail of full event information and absence of critical timing latency. These off-line reconstructed particles refer to "object". In this analysis, electrons, muons, jets and missing transverse energy (MET) are used. Figure 3.1 schematizes the workflow of these objects being formed from detector information to analysis level objects via low-level objects. This section will overview the definition of each object and involved steps, namely reconstruction, identification, calibration etc.

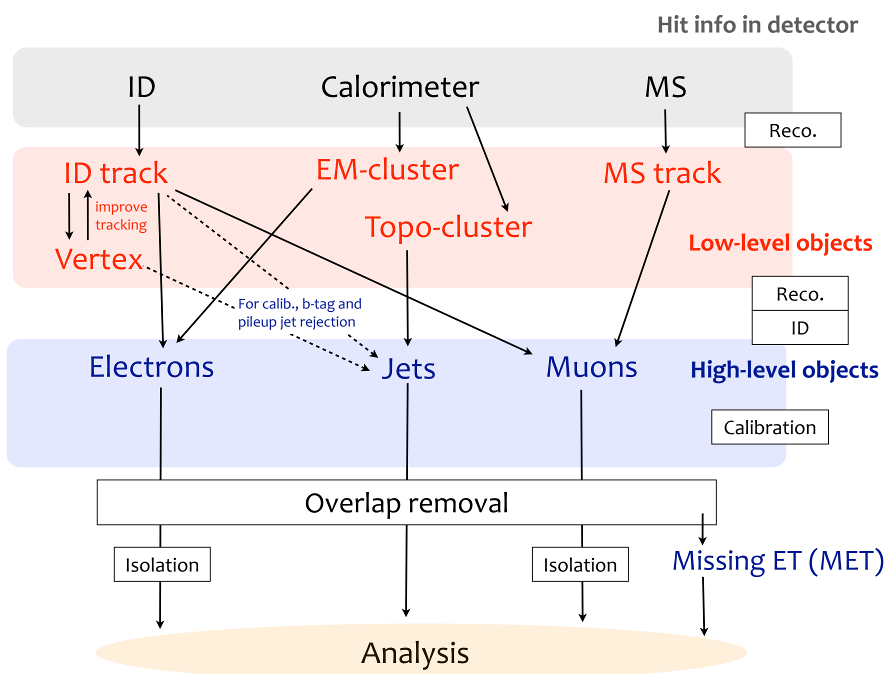

Figure 3.1: Schematic flow of analysis-level object formation from detector-level hit infomation. Black squares symbolize the procedures that dedicated off-line algorithms are working on.

3.1 Tracks

Charged tracks are the fundamental units seeding almost in all the off-line particle reconstruction. Standard tracks used in ATLAS refers to ID tracks, reconstructed by the hits create in the inner detector (ID). The MS tracks for muon identification are separately reconstructed, which is described in Sec. 3.5.1. The reconstruction algorithm mainly consists of the 4 steps as following. More detail can be found in [66].

- Based on the 3-dimensional position information and the readout charge associated to each hit in the silicon detectors, spatial charge profile is constructed event-by-event. Hits from the same particle traverse are merged, using a combination of a pattern recognition technique called connected component analysis (CCA) [67], and a neural network classifier [68]. Seed tracks are then reconstructed from three aligned clusters.
- The seed tracks are extrapolated outward, and the association with the TRT hits are tested using the Kalman fitter characterized by five tracking parameters, with a pion track hypothesis assuming the MIP energy loss in the ID material.
- If the first pattern recognition fit fails, a second fit is attempted based on an electron hypothesis with a modified algorithm that allows energy loss at each hit surface, recovering electrons with significant energy loss due to bremsstrahlung.
- Successful tracks from the Kalman Filter are rerun using the ATLAS Global χ^2 Track Fitter [69]. A pion or an electron hypothesis is used, depending on which was used successfully in the previous step.

A refined algorithm (Tracking In Dense Environment; TIDE) is used from Run2 [66], to cope with denser particle environment due to the increased pile-up and collision energy. The performance is shown red lines in Figure 3.2. Typically over 95% of efficiency is maintained.

3.2 Primary Vertices

The positions of pp-collisions are identified using the reconstructed ID tracks. These vertices refers to "primary vertices" (PV) [1] and are important for providing reference origin point of retracking and objects calibrations. PVs are reconstructed using the Iterative Vertex Finding algorithm [70] [71], identifying the peak in the z distribution of extrapolated tracks. The position of identified PVs are further elaborated using the adaptive vertex fitting algorithm [72]. The ID tracks are then re-fit taking advantage of these reconstructed PVs. The retracking procedure in principle lasts until all the tracks are associated to either of the PVs. PVs with less than two associated tracks are discard.

Though $10-30$ PVs are reconstructed per bunch crossing, usually there is only one PV causing meaningful scattering reaction that fires the trigger. This PV is referred as the "hard-scatter" vertex identified as the PV with the highest sum of associated track p_{T} ($\sum p_{\mathrm{T}}$), and the position

[1] The "primary" is meant to distinguish with vertices generated by the late decaying particles known as "secondary-vertices".

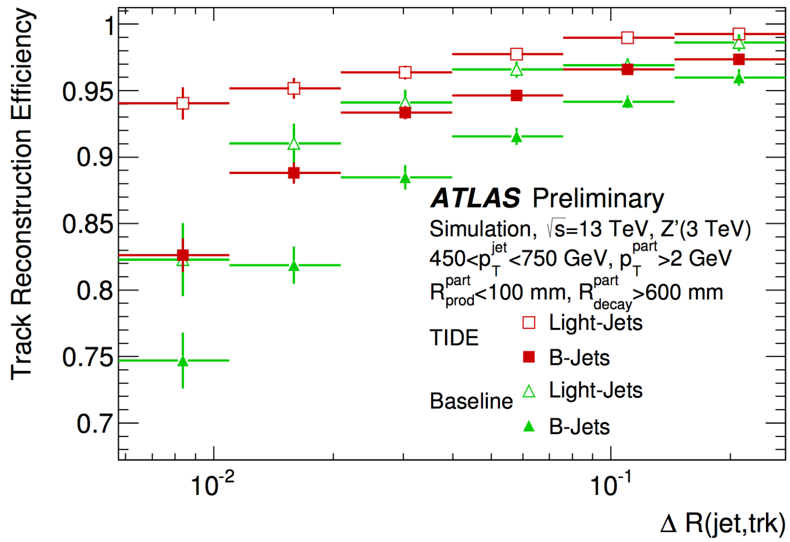

Figure 3.2: Reconstruction efficiency of tracks in jets as function of anglular distance with respect to barycenter of the jet [66]. Red points corresponds to the tracking algorithm used from Run2.

is used as the origin for object calibration.

3.3 Topo-clusters

Topo-cluster (or TC) is the basic unit of energy measurement in calorimeter and used as the input for jet clustering (Sec. 3.6.1) as well as in computing the isolation variables (Sec. 3.8). It is formed by three-dimensionally grouping the cells with significant energy deposit. The clustering algorithm proceed as follow [73]:

- Find cells with energy deposit exceeding 4σ from the expected noise level. These cells are identified as seed cells.
- Neighboring cells touching the boundary of seed cells with energy deposit exceeding 2σ from the expected noise level are added to the cluster and become the seed cells for the next iteration.
- Iterate the previous step until the cluster stops growing.
- Split the cluster if there are two or more local maxima with $E_{\text{cell}} > 500$ MeV.

EM-scaled energy is assigned for TCs.

3.4 Electron

3.4.1 Reconstruction

The electron reconstruction algorithm proceeds as following, widely referred from [74]:

- **Reconstruction of a EM cluster from energy deposit in the EM calorimeter.**
  This is done by the sliding window algorithm. Cells in the all four layers in the EM calorimeter are grouped into $\eta \times \phi$ towers of 0.025×0.025, and a window defined by the 3×5 units of towers are slided over the detector. A local maximum in the window energy above 2.5 GeV is identified as the cluster. About 95% (99%) of clustering efficiency are maintained with electrons in $E_{\mathrm{T}} = 7$ GeV (> 15 GeV).

- **Track-Cluster matching and refitting.**
  The EM cluster is matched with a ID track reconstructed based on the electron hypothesis (see Sec. 3.1) in the angular distance $\Delta R = \sqrt{(\Delta\eta)^2 + (\Delta\phi)^2}$. Closest track in ΔR with respect to the EW cluster is chosen if multiple tracks satisfy the matching criteria. The matched track enjoys further correction by a re-tracking using the Gaussian Sum Fitter (GSF) [75] algorithm in which Bremstralung is dedicated modeled.

- **Energy determination.**
  The information from track momentum and calibrated EM cluster energy are combined using a multivariate algorithm [76], achieving the best available energy resolution.

The reconstruction efficiency is measured by $Z \to ee$ events. Figure 3.3 presents the result together with the prediction by MC. Over $96\% - 98\%$ of efficiency is achieved for $E_{\mathrm{T}} > 20$ GeV.

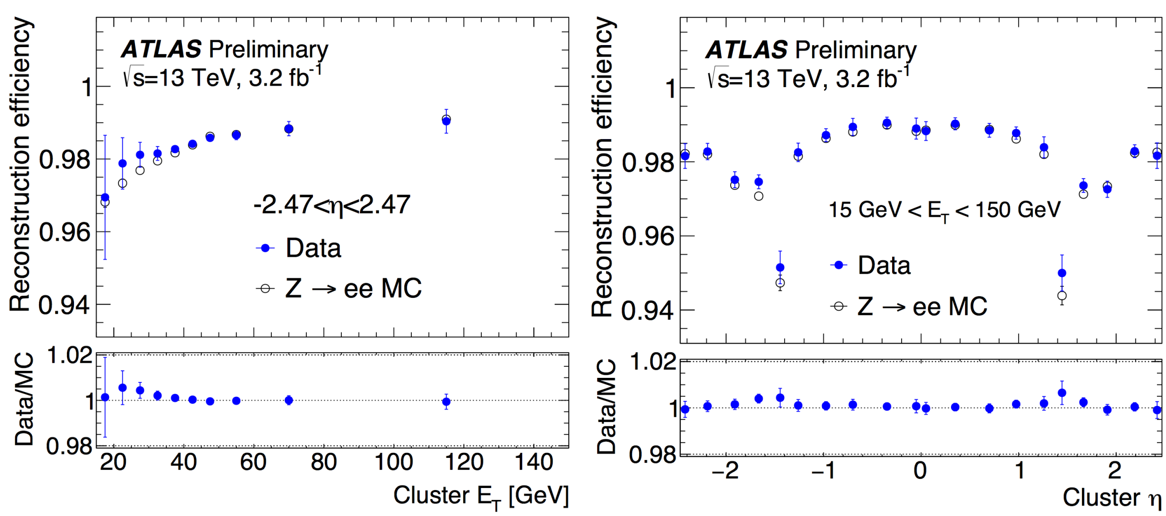

Figure 3.3: Reconstruction efficiency simulated (grey) or measured (blue) using $Z \to ee$ events [74] as function of (a) E_{T}, and (b) pseudo-rapidity of reconstructed EM clusters.

3.4.2 Identification

Reconstructed electrons are dominated by fakes from pions in the jets, particularly when they are low-E_{T}. Therefore, a powerful identification algorithm is employed in the subsequent identification, using a multi-dimensional likelihood exploiting all the relevant detector information. The number of input variables amounts up to 17, including the longitudinal and transverse EM shower profile and the number of high-threshold hits in TRT etc. The full list of input variables is found in [74]. The discriminant is given by a form of likelihood ratio, which is known to generally provide the best separation [77]. The signal and background PDF is modeled using the simulated events of $Z \to ee$ and di-jet respectively. Figure 3.4 shows the efficiency of electron identification. Multiple working points are available with different cut value in the likelihood ratio. In the analysis, two working points"Loose" and "Tight" are used, which corresponds about 90% and 70% of efficiencies at $E_{\mathrm{T}} = 30$ GeV.

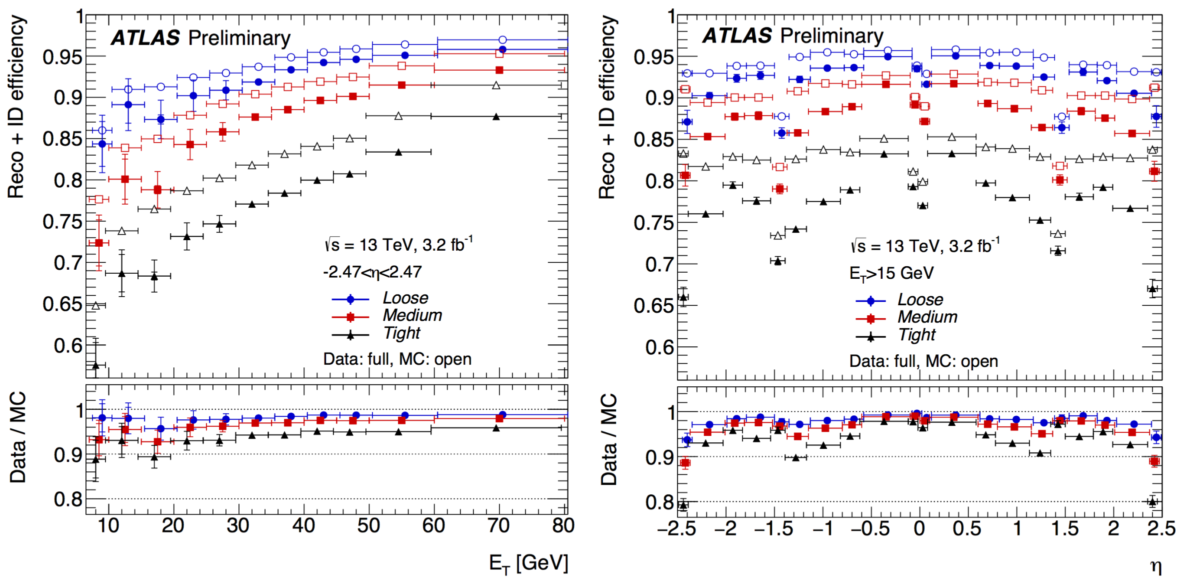

Figure 3.4: Electron identification efficiency as function of (a) E_{T}, or (b) pseudo-rapidity of reconstructed electron candidates [74]. $Z \to ee$ events are used for both MC and data.

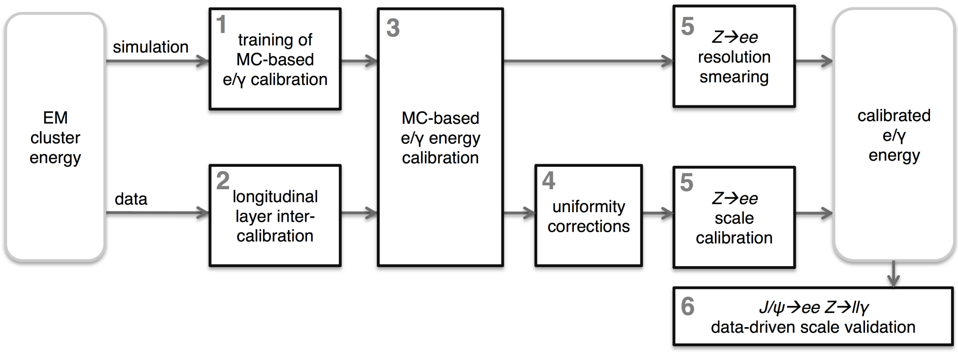

Figure 3.5: Flow chart of electron calibration applied respectively MC and data [76].

3.4.3 Calibration

The electron calibration consists of several different procedures, differently applied to simulation and data. The flow of steps is illustrated in Figure 3.5.

A MC-based calibration using BDT

Though the energy of cell deposit in EM calorimeter and electron cluster is already calibrated in EM scale, it still suffers from residual due to the energy loss in the material upstream of the calorimeter, energy leakage out of the either the reconstructed clusters or EM calorimeter and so on. A multi-variate algorithm (BDT regression) is employed, to estimate the true energy from the various input including the raw energy of reconstructed electron, as well as other angular position, shower profile and hit information from other auxiliary detectors such hadronic calorimeter. The full detail can be found in [76] [78].

Longitudinal calorimeter layer inter-calibration

The scales along longitudinal layers is equalized in data with respect to simulation, prior to the determination of the overall energy scale, in order to ensure the correct extrapolation of the response in the full p_{T} range. This is only applied in data.

Non-uniformity correction in ϕ

A set of corrections are applied to data, to account for various on-line instrumental effects not included in simulation such as non-optimal high voltage regions, geometric effects such as the inter-module widening or biases in the LAr calorimeter electronic calibration.

Residual scale calibration on data / Resolution correction on simulated electrons.

The residual mis-calibration in data is corrected by shifting the energy scale so that it agrees with the expectation from simulation. This is done by comparing the mass of Z-peak in $Z \to ee$ events.

It is found that the resolution in data is slightly worse than that in simulation using the same event sample. The corrections are derived and applied to simulation to match the data.

Numerous minor corrections follow additionally, which is detailed in [76]. The calibration is widely validated using data events of $J/\psi \to ee$ and $Z \to ee$.

3.5 Muon

3.5.1 Reconstruction

Muon tracks are reconstructed independently from ID, referred as MS-tracks. The tracking begins with finding the hits inside each MDT/CSC chamber and forming small track segments per chamber. A Hough transform is employed to convert the bending detector plane geometry into flat plane. A straight-line fit are then performed on the flattened plane for the track segments. The hits in RPC and TGC are used to determine the coordinate orthogonal to the MDT/CSC detector plane. The search algorithm employ a loosened requirement on the compatibility of the track and the hits, to account for the muon energy loess by interaction with material.

The trajectory and momentum of muons are decided by a synergy between the reconstructed MS track and the measurement by the other detectors. There are four different schemes of combination [79]:

Combined muons: A MS track is matched to a reconstructed track in the ID, and the measurements of the momenta are combined.

Segment-tagged muons: A fragmet of MS track is matched with an ID track, with the momentum taken from the ID track.

Standalone muons: MS tracks found outside the ID acceptance ($2.5 < |\eta| < 2.7$), with the momentum quoted from the MS track.

Calorimeter-tagged muons: A special type of reconstruction dedicated to muons traveling to the inactive crack of the MDT at $|\eta| < 0.1$. The ID tracks with $p_{\mathrm{T}} > 15$ GeV associated calorimeter deposit consistent with a minimum ionizing particle are tagged, with the momentum of ID track.

In this analysis, the combined muons is always in defining muons, while the segment-tagged muons are used for correcting the MET calculation as described in Sec. 3.9.

3.5.2 Identification

Additional identification requirements are imposed to purify the sample of reconstruction muons. Cuts on following three variables are applied:

$\sigma(q/p)$: Fitting error of a tracking parameter q/p associated with the quality of measurement.

ρ': p_{T} difference between ID and MS track normalized by the p_{T} of the combined track.

χ^2: A generic measure of fit quality defined as normalized χ^2 of the combined track fit.

The `Medium` working point defined in [80] is used throughout the analysis, where only $\sigma(q/p) < 7$ is required. Figure 3.6 summarizes the performance of reconstruction and ID for muons.

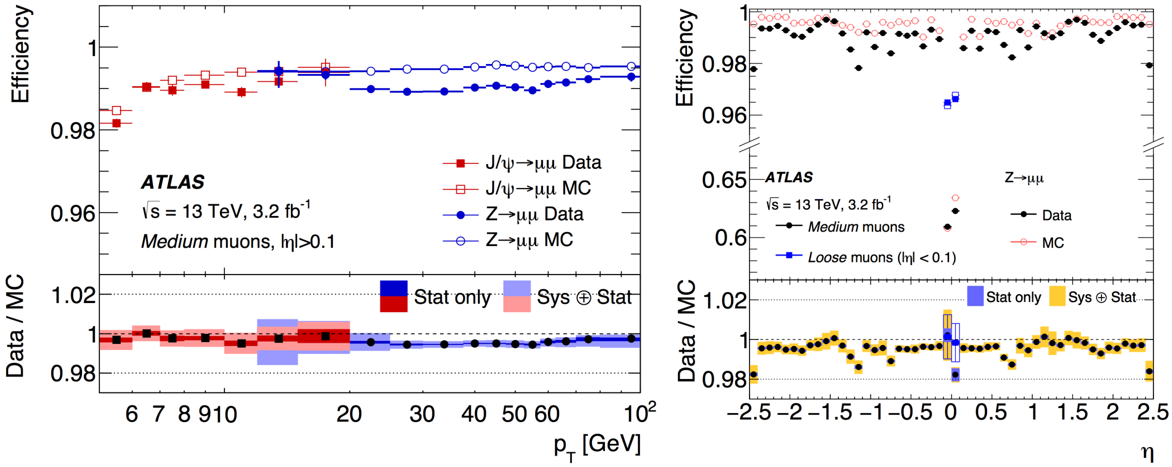

(a) p_{T} **(b)** η

Figure 3.6: Simulated / measured efficiency for reconstruction and identification of muons, using $J/\phi\mu\mu$ and $Z \to \mu\mu$ events [80].

3.5.3 Calibration

As the momentum of a muon track is already well-representing the particle-level momentum of muon, the scale calibration only subjects to a series of minor corrections, accounting for the imperfect knowledge of the magnetic field integral inside the detector, and the energy loss of muons traverse through the calorimeter or other materials between the interaction point and the MS.

The momentum correction is performed on each muon based on the formula below [79]:

$$p_{\mathrm{T}}^{\mathrm{Cor.}} = \frac{s_0 + p_{\mathrm{T}}^{\mathrm{MC}}(1+s_1)}{1 + \Delta r_0 g_0 + \Delta r_1 p_{\mathrm{T}}^{\mathrm{MC}} g_1 + \Delta r_2 \left(p_{\mathrm{T}}^{\mathrm{MC}}\right)^2 g_2} \tag{3.1}$$

where $p_{\mathrm{T}}^{\mathrm{MC}}$ and $p_{\mathrm{T}}^{\mathrm{Cor.}}$ represent respectively the momentum before and after the correction, and $g_m(m = 0, 1, 2)$ are random numbers generated by an uniform PDF ranging from 0 to 1. The numerator corresponds to the scale correction, and the denominator is responsible for the correction of resolution modeling by MC. The parameterization of denominator is based on the fact that muon resolution obeys a p_{T} dependence of:

$$\frac{\sigma(p_{\mathrm{T}})}{p_{\mathrm{T}}} = \frac{a}{p_{\mathrm{T}}} \oplus b \oplus c \cdot p_{\mathrm{T}}. \tag{3.2}$$

The coefficients s_i, Δr_i are determined bin-by-bin in (η, ϕ), by applying a template fit on $J/\phi \to \mu\mu$ and $Z \to \mu\mu$ events.

3.6 Jet

3.6.1 Jet Clustering

Jet reconstruction starts employs the AntiKt algorithm [81] using the topo-clusters (TCs) calibrated with EM scale as input. The basic step of the algorithm is to merge the proximate two TCs based on a distance measure defined by:

$$d_{i,j} = \min(p_{T,i}^{-2}, p_{T,j}^{-2})\frac{\Delta R_{i,j}^2}{r^2} \tag{3.3}$$

where i and j denote the index of topo-clusters, and $\Delta R_{i,j}^2$ is the angular distance between the them. r is the cone parameter dictating the typical size of resultant jets, which is set to $r = 0.4$ in the analysis. The two TCs with smallest $d_{i,j}$ are merged in each step, and the iteration continues until it becomes:

$$\min_{i,j}\left[d_{i,j}\right] > \min_{i}\left[p_{T,i}^{-2}\right]. \tag{3.4}$$

The anti-k_{T}jet clustering is characterized by the negative power index on the p_{T} in the metric $d_{i,j}$, where soft clusters are always added to hard components instead of merging together with other soft clusters. This results in a well boundary behavior of jets, giving an insensitive nature to soft components on which perturbative QCD does not provide robust prediction. This collinear- and infrared-safety is an extremely welcomed feature since it provides well-defined observables allowing one to straightforwardly compare the theory and data, benefiting either the theoretical description and the jet calibration in experiment.

3.6.2 Energy Calibration

As the energy of TC is calibrated in the EM scale, clustered jet needs extra calibration to account for the hadronic interaction activity. Particle-level jets in simulated events (referred as "truth jets") are used for the reference of the truth energy. They are reconstructed using the anti-kt algorithm with $R = 0.4$ using stable, final-state particles as input. The input particles are required to have a lifetime of $c\tau > 10m$. Muons, neutrinos, and particles from pile-up activity are excluded. Truth jets with $p_{\mathrm{T}} > 7$ GeV and $|\eta| < 4.5$ are used for the calibration. In simulated events, corresponding reconstructed calorimeter jets can be found by geometrically matching in terms of the $\Delta R := \sqrt{(\Delta\eta)^2 + (\Delta\phi)^2}$

A dedicated calibration procedure detailed in [82] is employed to restore the energy to that of truth jets reconstructed at the particle-level energy scale. It mainly proceeds as following stages:

Origin correction

The angular coordinates assigned to each topo-cluster is based on the origin defined by the designed IP position with which the actual hard-scatter vertex is displaced in z-axis direction. The jet orientation is recalculated based on the refined origin defined by the position of the reconstructed vertex that the jet is associated with [83].

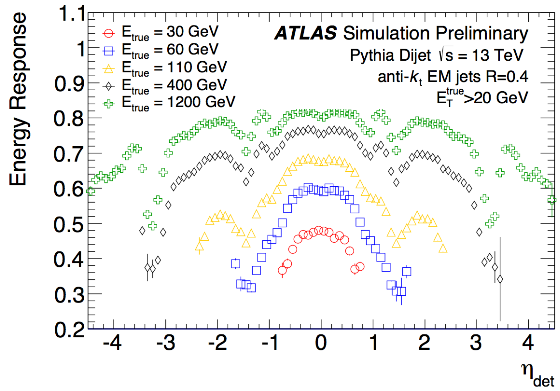

(a)

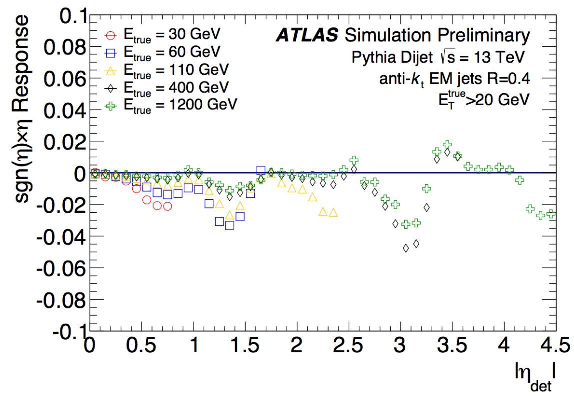

(b)

Figure 3.7: (a) Energy response and (b) η reconstruction bias defined in Eq. 3.6 before the MC-based calibration. [82]

Pileup subtraction

The contribution of particles from pile-up jets either in the same bunch crossing ("in-time pile-up") or those nearby ("out-of-time pile-up") is removed using the technique of an area-based p_{T} density subtraction [84] applied at the per-event level, followed by a residual correction derived from the simulation. The correction is characterized as:

$$p_{\mathrm{T}}^{\mathrm{corr.}} = p_{\mathrm{T}}^{\mathrm{reco.}} - \rho \times A - \alpha \times (N_{PV} - 1) - \beta \times \mu, \tag{3.5}$$

where $p_{\mathrm{T}}^{\mathrm{reco.}}$ and $p_{\mathrm{T}}^{\mathrm{corr.}}$ are the transverse momentum before and after the correction respectively. A is the jet area which roughly corresponds to the area jet energy distributes in $\eta - \phi$ plane calculated using the ghost-association [85]. ρ is the average p_{T} density from the contribution of pile. The idea is to treat the pile-up as an uniform noise level over the detector, and the contribution is proportional to the area the jet is overlaying to it. The residual impact of pile-up is found to be linear in terms of the number of reconstructed primary vertices (N_{PV}) and the average number of interactions per bunch crossings (μ) independent of one another. The linear coefficients α and β are determined using the simulation as function of p_{T} and η of the jet.

MC-based calibration

The main energy calibration is provided by comparing the energy of reconstructed jets to the corresponding truth jets in the simulated di-jet events from Pythia. The energy response R and η response R_η defined by

$$R = \left\langle \frac{p_{\mathrm{T}}^{\mathrm{reco.}}}{p_{\mathrm{T}}^{\mathrm{truth}}} \right\rangle, \quad R_\eta = \left\langle \frac{\eta^{\mathrm{reco.}}}{\eta^{\mathrm{truth}}} \right\rangle, \tag{3.6}$$

are calculated in various p_{T} and η bins. The obtained response is used for the scale that brings the energy of reconstructed jets to the particle-level energy scale. The conversion from the EM scale to the hadronic scale essentially happen in this stage.

Global Sequential Calibration

While only the information on topo-clusters are used for the jet energy determination so far, further improvements are achieved by applying corrections exploiting the global detector information from calorimeter, muon detector, and reconstructed tracks from inner detector.

The procedure involves 5 independent stages, referred as the Global Sequential Calibration (GSC) [86], killing residual dependence of jet energy scale on the number of associated tracks or the spatial energy profile of the jet and etc. using the simulation.

The most important function of GSC is adding robustness against varying jet flavors, in particular between quark-initiated jets and gluon-initiated, in jet energy measurement.

Residual in-situ calibration

A residual calibration is derived using in-situ measurements applied only to data, accounting for the differences in the jet response between data and MC simulation. The differences is quantified using data events of $\gamma+$jet and $Z \to \mu\mu+$jet, by balancing the p_{T} of a jet against the well-measured counterpart objects as reference.

3.6.3 B-tagging

Hadron jets originating from b-quarks can be exclusively identified by taking advantage of the long lifetime ($c\tau \sim 450\,\mu$m) of b-hadrons, creating distinct secondary decay vertices. Four independent sub-algorithms (IP2D, IP3D, SV, JetFitter) exist addressing unique b-finding power. Their outcomes are combined by inputting them into a BDT classifier (MV2), which output is used as the final discriminant. Each sub-algorithm works as following (widely referred from [87] [88] [89]):

Impact parameter based algorithm: IP2D and IP3D IP2D and IP3D are the likelihood based classifiers using the impact parameter information of tracks associated to the jets. The track level likelihood is defined in terms of the transverse impact parameter d_0 and its significance $\sigma(d_0)$ (and longitudinal impact parameter z for the case of IP3D), and modeled using MC respectively for the tracks in the b-jet and light-flavor jet. The jet-level likelihood is calculated by taking the product over all the associated tracks to the jet. The IP2D (IP3D) is then defined by the likelihood ratio between the b-jet and light-flavor jet hypothesis.

Secondary vertex finding algorithm: SV The SV algorithm [90] explores secondary vertex finding algorithm in an explicit manner. After a set of qualification requirements on tracks in the jet, all the seed tracks are paired testing the consistency with the two-track vertex hypotheses. Found vertices consistent with the decays of other long-lived particles (such as K_s or Λ), photon conversions or hadronic interaction with a material are rejected. As further requirements, the sum of the two impact parameter significances of the two tracks is required greater than 2, and vertices with the invariant masses exceeding 6 GeV are removed given the masses of the b- or c-hadrons. Vertex with the highest invariant mass is chosen if multiple candidates are found.

Decay chain multi-vertex algorithm: JetFitter `JetFitter` [91] is a kinematic fitting algorithm, exploiting the topological structure of weak b- and c-hadron decays inside the jet and

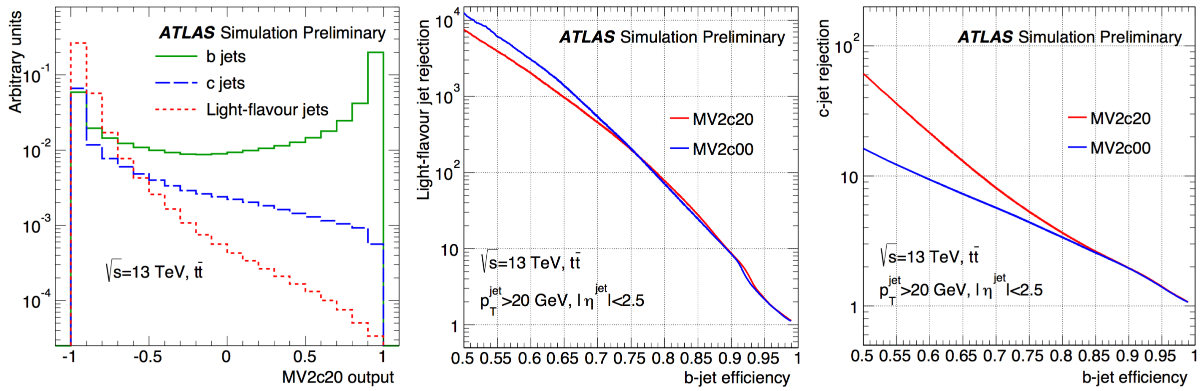

Figure 3.8: Left plot presents the output BDT distribution for signal (b-quark jets) and backgrounds (light flavor and c-quark jets). The score of MV2c20 is shown in which c-jets rejection is reinforced. The middle and right plot respectively show the signal efficiency vs light flavor jet rejection, and vs c-jet rejection. [87]

attempt to reconstruct the full b-hadron decay chain. Using the Kalman fitter, it finds a common line to which the PV and the bottom and charm vertices belong, approximating the b-hadron flight path, as well as their positions. The notable advantage of this approach is that the vertices of b- and c-hadron can be reconstructed, even when only a single track is attached to any of them.

Combinating algorithm: MV2 A Boosted Decision Tree (BDT) is used to combine the output from the four algorithms. The input variables includes the likelihood values from IP2D and IP3D, properties of reconstructed secondary vertex (mass, position etc.) and the associated tracks providing by SV, and the information of fitted vertices including subsequent decays of b-hadrons from JetFitter. The full list can be found in [87].

The output distribution and the performance is shown in Figure 3.8. Although the input information between the algorithms is highly correlated, the combined performance shows drastic improvement over those of either single algorithm.

Multiple working points are defined to provide different relative discrimination power against light-flavor jets and c-jets. For example, MV2c10 (MV2c20) are designed to address more rejection power towards c-jets, trained using the background sample with light-flavor jets admixtured with c-jets by 10% (20%). The MV2c10 working point is used in the analysis.

3.6.4 Pile-up Jet Tagging and Rejection

Significant fraction of reconstructed jets are originated from pile-up, particularly when they are low-p_{T}. In order to suppress the contamination, a pile-up jet rejection is applied using the Jet Vertex Tagger (JVT) discriminant [92] exploiting the vertex information.

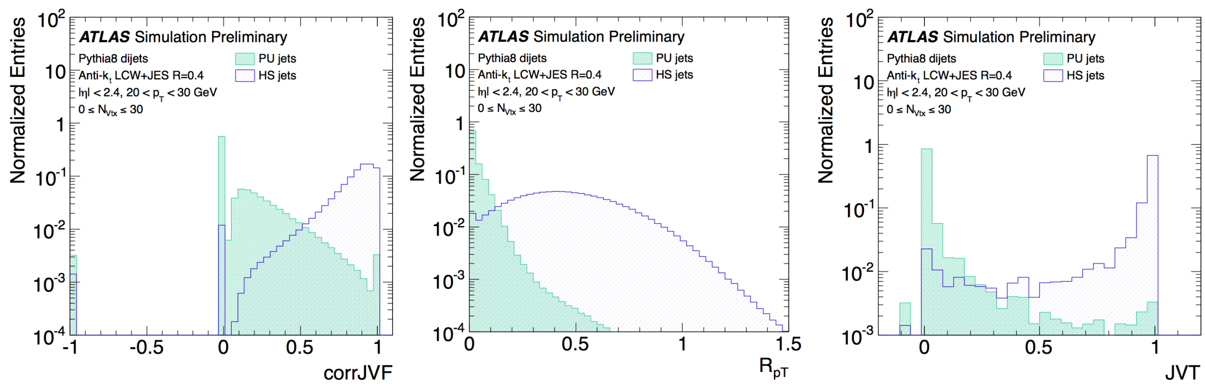

Figure 3.9: Left two plot display the distribution of input variables for JVT; corrJVF and R_ϕ. corrJVF$= -1$ represents the jets with no associated tracks. The right plot is resultant output likelihood score, JVT [92].

JVT is based on a 2D-likelihood function in terms of the corrected Jet Vertex Fraction (corr. JVT) and R_{p_T}:

$$\mathrm{corrJVF} := \frac{\sum_k p_\mathrm{T}^{\mathrm{trk}_k}(\mathrm{PV}_0)}{\sum_l p_\mathrm{T}^{\mathrm{trk}_l}(\mathrm{PV}_0) + \sum p_\mathrm{T}(\mathrm{PU})/(\kappa \cdot n_\mathrm{trk}^\mathrm{PU})}, \qquad \sum p_\mathrm{T}(\mathrm{PU}) := \sum_{n\geq 1}\sum_k p_\mathrm{T}^{\mathrm{trk}_k}(\mathrm{PV}_n)$$
$$R_{p_\mathrm{T}} := \frac{\sum_k p_\mathrm{T}^{\mathrm{trk}_k}(\mathrm{PV}_0)}{p_\mathrm{T}^\mathrm{jet}}, \tag{3.7}$$

where PV_0 denotes the hard-scatter vertex and $\mathrm{PV}_j (j \geq 1)$ the other primary vertices presumably dut to the in-time pile-up interaction. JVF (Jet Vertex Fraction) was a variable originally used for the pile-up suppression in Run1 [93] defined by the fraction of charged tracks associated to the hard-scatter vertex:

$$\mathrm{JVF} := \frac{\sum_k p_\mathrm{T}^{\mathrm{trk}_k}(\mathrm{PV}_0)}{\sum_l p_\mathrm{T}^{\mathrm{trk}_l}(\mathrm{PV}_0) + \sum p_\mathrm{T}(\mathrm{PU})}. \tag{3.8}$$

While the performance of JVF is sensitive to the pileup since $\sum p_\mathrm{T}(\mathrm{PU})$ scales linearly according to number of pileup, $\sum p_\mathrm{T}(\mathrm{PU})$ is divided by the number of PU tracks $n_\mathrm{trk}^\mathrm{PU}$ in the corrJVF to kill the linear dependency, together with the scale factor $\kappa = 0.01$ conserving the absolute normalization of the PU term. R_{p_T} is the charged energy fraction in the jet, design to address to the jets with small number of tracks leading to low corrJVF value. A 2D-likelihood profile in terms those two variables is respectively modeled for hard-scatter jets and pile-up jets, and the JVT is defined as likelihood ratio.

Figure 3.9 shows the typical separation. The JVT selection JVT> 0.57 is applied for jets with 20 GeV $< p_\mathrm{T} <$ 60 GeV and $|\eta| < 2.4$, in which the pile-up jets dominantly populates.

3.7 Overlap Removal between Reconstructed Objects

Electrons, muons and jets are reconstructed in parallel, allowing the ambiguity that an identical particle is reconstructed or identified as multiple types of particles simultaneously. For instance, electrons are typically reconstructed either as electrons and jets. This is designed to provide flexibility in the object definition to satisfy various needs by analyses.

A sequence of "overlap-removal" procedure is applied to resolve the ambiguity and avoid the double-counting, based on the angular distance $\Delta R = \sqrt{\eta^2 + \phi^2}$ between them. The algorithm begins with the electron-jet overlap removal. Any light-flavor jet [2] reconstructed within $\Delta R < 0.2$ with respect to identified electrons is rejected. The electron is otherwise removed if the overlapping jet is b-tagged jet, to avoid rejecting b-jets due to the non-prompt lepton nearby caused by the decays of b-hadrons. Next, to remove bremsstrahlung from muons followed by a photon conversion into electron pairs, electrons lying within $\Delta R < 0.01$ of a preselected muon are discarded.

Subsequently, the contamination of muons from heavy-flavored hadron decays is suppressed by removing muons that lie within $\Delta R < \min(0.04 + (10\ \text{GeV})/p_{\text{T}}, 0.4)$ of any remaining jet, or within $\Delta R < 0.2$ of a b-tagged jet or a jet containing more than three tracks with $p_{\text{T}} > 500$ MeV. In the former case, the p_{T}-decreasing angular separation mitigates the rejection of energetic muons close to jets in boosted event topologies. Finally, jets reconstructed within $\Delta R < 0.2$ of remaining electrons or muons are excluded.

The identification of hadronically decaying taus and photons are not exploited in the analysis, since they are not explicitly used as objects in event selections. Instead, those with sufficiently high transverse momentum pass the jet reconstruction as well as the JVT requirement, thus treated as jets in the analysis.

[2] defined as reconstructed jets with b-tagging score MV2c10< 0.1758 which corresponds to 85% efficiency for real b-jets.

3.8 Fake Leptons and the Isolation Requirement

Light flavor leptons (electrons or muons) produced in LHC subject to two types; "prompt leptons" directly originated from the hard scattering via decays of real and virtual gauge bosons; "non-prompt leptons" generated via decays of heavy flavor hadrons (contains b or c quarks) and tau leptons, or pair creation of photons (mostly stemming from π_0 in jets). The leptons interested in the new physics or EW physics always refer to the prompt leptons, while non-prompt leptons are trivial and disturbing, degrading the use of leptons in the analysis. There are also a type of reconstructed leptons by wrongly identified pions from jets. In the thesis, these unwilling kinds of leptons (non-prompt leptons and pions) are simply referred as "fake lepton", and suppressed by employing the extra requirement described as follows.

Impact parameter requirement Non-prompt leptons are generated in relatively displaced position with respect to the primary vertex. Therefore, the information of transverse impact parameters address a nice discriminating power. The selection used in the analysis is as Table 3.1. While the d_0 and $|z_0 \sin\theta|$ of prompt-leptons populate close to 0, those for non-prompt leptons result in wide distributions, leading many of them to be rejected.

Table 3.1: Impact parameter requirements used in the analysis. d_0 and (z_0) is the transverse (longitudinal) impact parameter. σ_{d_0} is the defined by the error matrix of the track fit.

	Electron	Muon
$\lvert d_0/\sigma_{d_0}\rvert$	< 5	< 3
$\lvert z_0 \sin\theta\rvert$	< 0.5 mm	< 0.3 mm

Isolation While the path of flight of prompt-leptons rarely overlap with other particles, fake leptons generally fly closely by jets for their origin. Relatively higher jet activity around fake leptons is expected, therefore the isolation requirement with respect to proximate cluster or tracks provide significant rejecting power of fake leptons. Two isolation variables are defined:

Calorimeter isolation ($E_{\mathrm{T}}^{\mathrm{cone}\ 0.2}$): Sum of transverse energies by the calibrated topo-clusters with $\Delta R < 0.2$ with respect to the lepton. An E_{T}, η dependent pileup correction is applied. For electron, the energy leakage due to the bremstralung is compensated.

Track isolation ($p_{\mathrm{T}}^{\mathrm{cone}\ 0.2}$): Sum of transverse momentum of tracks within the angular distance of $R = \min(0.2, 10\ \mathrm{GeV}/p_{\mathrm{T}})$ with respect to the lepton. The variable cone size is intended to loosen the isolation cut for high-p_{T} leptons, based on the fact that most of fake leptons are below 20 GeV.

The isolation requirement is done by applying a cut in a 2D-plane of $E_{\mathrm{T}}^{\mathrm{cone}\ 0.2}$ and $p_{\mathrm{T}}^{\mathrm{cone}\ 0.2}$. In the analysis, the `GradientLoose` working point is chosen, in which a p_{T}-dependent cut is applied designed to recover the efficiency in high-p_{T}. Figure 3.10 shows the isolation efficiency respectively for electrons and muons.

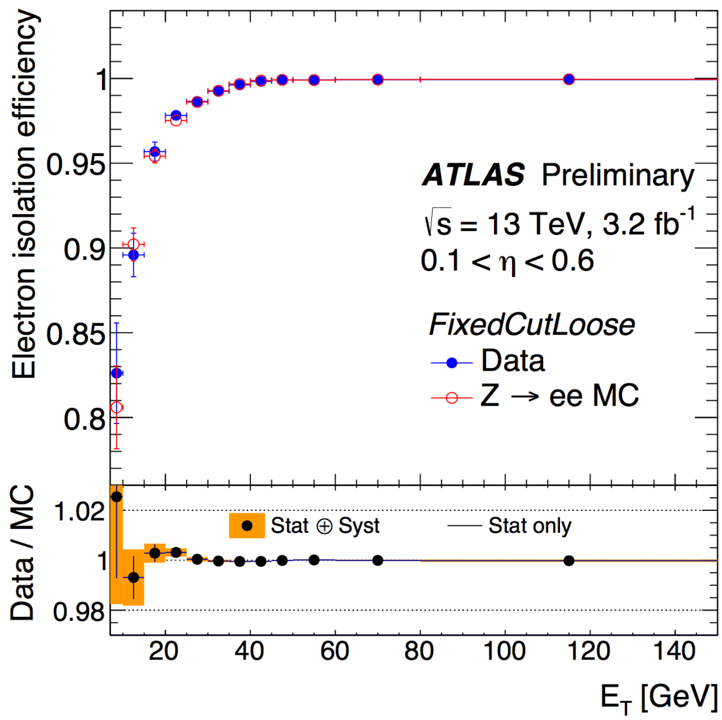

(a)

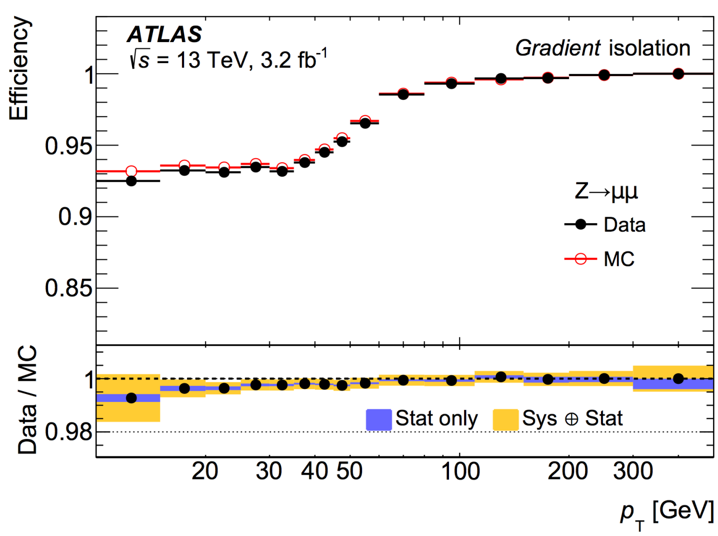

(b)

Figure 3.10: Measured and expected efficiency for isolation requirement for (a) electrons [74] and (b) muons [80], both using the $Z \to ee/\mu\mu$ events. The `FixedCutLoose` working point is shown for the electrons where $E_{\mathrm{T}}^{\mathrm{cone}\ 0.2}/E_{\mathrm{T}} < 0.2$ and $p_{\mathrm{T}}^{\mathrm{cone}\ 0.2}/E_{\mathrm{T}}$¡0.15 is applied.

3.9 Missing Transverse Energy

Missing Transverse Energy ($E_{\mathrm{T}}^{\mathrm{miss}}$) is an extremely important proxy to new physics since it is contains the kinematical information of invisible particle. $E_{\mathrm{T}}^{\mathrm{miss}}$ is calculated by the transverse momentum imbalance of visible particles, using the reconstructed objects as well as isolated tracks that does not associated to any reconstructed objects referred as the soft term. It is contructed by four independent terms as shown in Eq. (3.9):

$$\boldsymbol{E}_{\mathbf{T}}^{\mathbf{miss.}} := -\sum \boldsymbol{\not{E}}_{\mathbf{T}}^{e} - \sum \boldsymbol{\not{E}}_{\mathbf{T}}^{\mu} - \sum \boldsymbol{\not{E}}_{\mathbf{T}}^{\mathrm{jet}} - \boldsymbol{\not{E}}_{\mathbf{T}}^{\mathrm{soft}}. \tag{3.9}$$

Input reconstructed objects for the first three terms in Eq. (3.9) are fully calibrated and the ambiguity between them is resolved by the overlap removal. Jets with $p_{\mathrm{T}} > 20$ GeV are included in the jet term in the MET calculation, otherwise subjected to the soft term with the track momenta. Jets failed in the JVT selection is totally excluded from the MET calculation to prevent the contribution from pile-up.

The track soft term $\boldsymbol{\not{E}}_{\mathbf{T}}^{\mathrm{soft}}$ (TST) [94] accounts for the residual visible momentum mainly from soft jets and unidentified muons. It is constructed by the tracks that are not associated to any jet, and are isolated by $\Delta R > 0.2$ from any reconstructed EM clusters. The momenta of tracks found to associated with reconstructed muons are replaced into that by the combined ID+MS muon tracks. Tracks has its track momentum uncertainties larger than 40%, and high-p_{T} tracks ($p_{\mathrm{T}} > 200$ GeV in $|\eta| < 1.5$ or $p_{\mathrm{T}} > 150$ GeV in $|\eta| > 1.5$) with questionable quality of momemtum measurement satisfying following conditions are removed to prevent potential large error in the calculation:

$$p_{\mathrm{T}}^{\mathrm{cone}\ 0.2}/p_{\mathrm{T}} > 0.1, \quad \text{and} \quad \frac{E_{\mathrm{T}}^{\mathrm{cone}\ 0.2}}{p_{\mathrm{T}} + p_{\mathrm{T}}^{\mathrm{cone}\ 0.2}} < 0.6, \quad \text{and} \quad \frac{p_{\mathrm{T}}^{\mathrm{cone}\ 0.2}}{p_{\mathrm{T}} + p_{\mathrm{T}}^{\mathrm{cone}\ 0.2}} < 0.6 \tag{3.10}$$

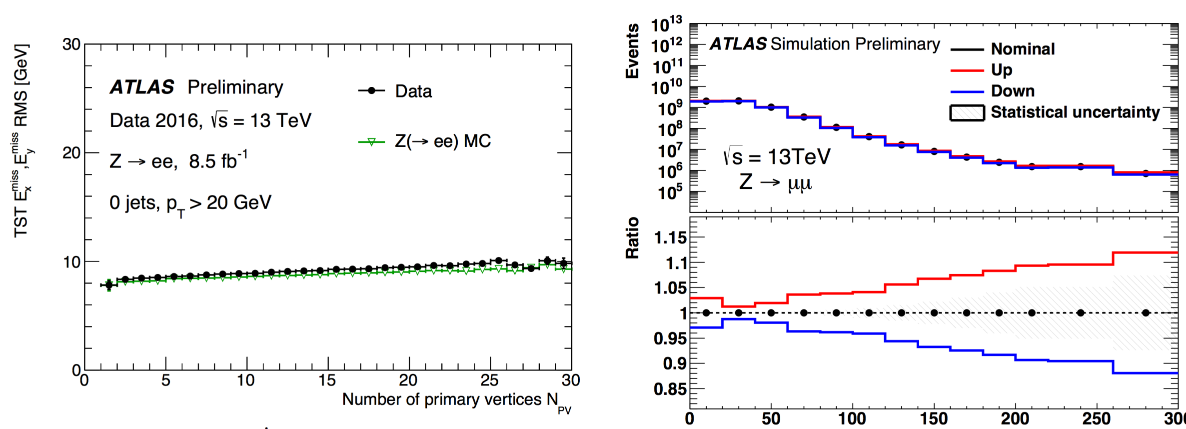

(b) $E_{\mathrm{T}}^{\mathrm{miss}}$ resolution

(a) (b)

Figure 3.11: (a) Pile-up dependency of resolution on the met soft term, and (b) the absolute resolution, simulated or measured using $Z \to \ell\ell$ events in which the soft terms is zero with ideal measurement [95].

3.10 Object Definition in the Analysis

The requirements for objects used in the analysis is summarized in Table 3.2. For electrons and muons, two types of working point are defined; "baseline" is the loose selection criteria oriented to veto extra prompt leptons in the event; "signal" is the tighter working point aiming to reject fake leptons where the impact parameter cut, isolation requirement and tighter identification are imposed in on top of the baseline requirement. Signal regions are defined with exactly one baseline and signal lepton, given that the targeted signal events contain exactly one prompt lepton. Jet used in the analysis is uniquely defined. JVT cut is required to avoid the impact by pile-up on the analysis.

Table 3.2: Summary of all baseline and signal object selection. In addition to the listed criteria, objects are required to pass the reconstruction, identification and overlap removal. The p_{T}-threshold is based on the transverse momentum after calibration.

Electrons	Baseline	Signal
p_T	$p_T > 7$ GeV	$p_T > 10$ GeV
Identification	Loose [3]	Tight [4]
Isolation	-	`GradientLoose`
Impact parameter cuts	-	$z_0 < 0.5$mm, $\lvert d_0 \rvert / \sigma(d_0) < 5$
Muons	Baseline	Signal
p_T	$p_T > 6$ GeV	$p_T > 10$ GeV
Identification	Medium [5]	Medium [6]
Isolation	-	`GradientLoose`
Impact parameter cuts	-	$z_0 < 0.5$mm, $\lvert d_0 \rvert / \sigma(d_0) < 3$
Jets		
Clustering Algorithm	Anti-$k_{\mathrm{T}}(r = 0.4)$	
p_T	$p_T > 30$ GeV	
JVT	JVT> 0.57	
b-tag	MV2c10 77% efficiency working point	

Chapter 4

Monte-Carlo Simulation

Monte-Carlo (MC) simulation is a highly powerful toolkit providing theoretical prediction on event kinematics as well as detector response, which is used extensively from studying signal/background separation, performance evaluation to background estimation.

This chapter mainly discusses the implementation, including the modeling of particle interactions in LHC (widely referred from [96] [97]) in general, as well as the detailed setup of each samples for individual physic processes used in the analysis.

4.1 Phenomenology of a pp-collision

Let's start with seeing what actually happens when protons are collided, and how it is formulated in the theory. At the LHC energy, physics processes involved in a typical interesting pp-collision are schematized in Figure 4.1.

The main process that dominates the entire differential cross-section is the hard scattering where constituent partons in protons interact each other. The cross-section can be constructed by the transition amplitude from an initial state with two partons (a, b) into a certain final state (F):

$$\frac{d\hat{\sigma}_{a,b\to F}}{d\boldsymbol{y}} = \frac{1}{2\hat{s}_{ab}} d\Phi \; |\mathcal{M}_{a,b\to F}|^2 \tag{4.1}$$

where $\boldsymbol{y}$ represents momenta of final state particles; $\mathcal{M}_{a,b\to f}$ the matrix-element (ME); $d\Phi$ the phase space factor; and the flux factor $1/2\hat{s}_{ab}$.

The cross-section Eq. 4.1 is then encapsulated by parton distribution function (PDF) to translate from the parton-level cross-section to that of pp-interaction:

$$\frac{\mathrm{d}\sigma_{pp\to F}}{\mathrm{d}\boldsymbol{y}} = \sum_{a,b\in(q,\bar{q},g)} \int_0^1 \mathrm{d}x_a \int_0^1 \mathrm{d}x_b \; f_i(x_a) f_j(x_b) \; \frac{d\hat{\sigma}_{a,b\to F}}{d\boldsymbol{y}}. \tag{4.2}$$

$x_{a,b}$ denotes the momentum fraction of protons carried by the constituent parton a, b, and $f_i(x)$ is the proton PDF: the probability density that x obeys. a and b are finally added up with possible

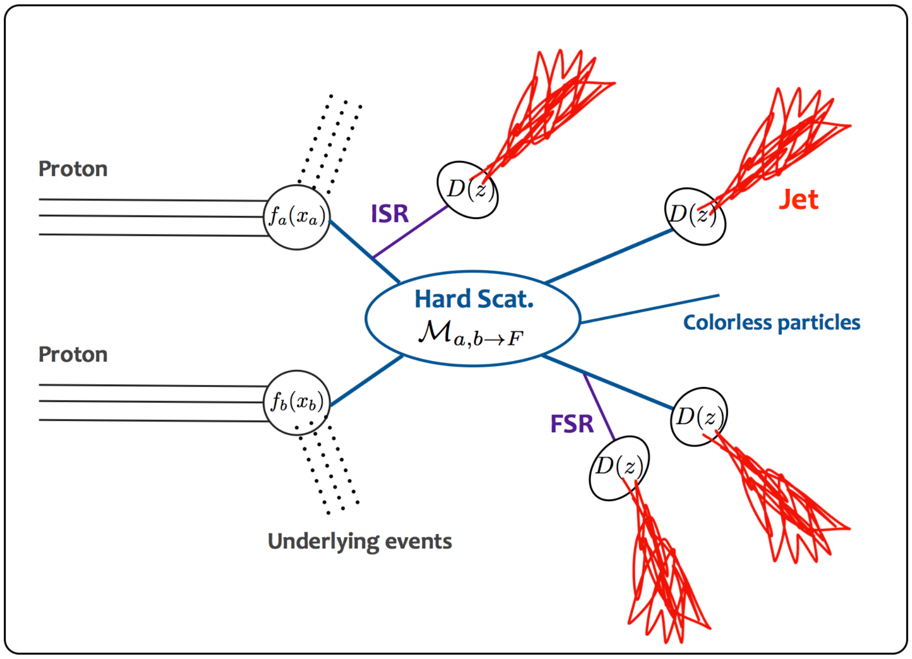

Figure 4.1: Schematic of involved phenomenology in a *pp*-collision.

parton flavors, reflecting our ignorance about the initial parton flavors. Note that this convolution is not in terms of amplitude ($\mathcal{M}$) but rather a statistical addition ignoring the interference between the hard scattering and the dynamics characterized by PDF, which is justified by the factorization theorem.

Resultant quarks and gluons in the final state undergo hadronization, in which they are transformed into a collection of fragmented hadrons ("hadron jet"). This is particular the nature about strong interaction known as "confinement" where the running coupling constant becomes larger for longer distance scattering and eventually diverges at the Laudau pole $Q^2 \sim (200\text{ MeV})^2$. Naively this will lead to infinite cross-section of processes with $Q^2 \sim (200\text{ MeV})^2$, including small angle diffractions and pair production of quark and anti-quark out of vacuum. [1] Those instantaneously generated partons are recombined eventually into hadrons with singlet color quantum number. This hadronization procedure can be understood using the an universal fragmentation function $D(z)$ in the same internal structure with PDF, representing the probability of finding a hadron with momentum fraction of z with respect to that of seed parton.

Additionally, often additional jets accompany from splitting legs of initial and final state partons. They are referred as initial state radiation (ISR) or final state radiation (FSR).

Note that the protons from which the hard scattering partons are kicked out are completely destroyed, no longer keeping the form as protons. The remnants will experience they own hadronization, resulting in a splash of permeating hadrons known as "beam remnant". In addition, multiple

[1] This is picture is incorrect giving the breakdown of perturbation, nevertheless enough to give an idea of the transition toward non-perturbative region.

parton-level hard scatterings (multiple parton interaction; MPI) occasionally take place within a single proton-proton interaction, where usually at least one of them ends up in cheap QCD scattering leaving low-p_{T} jets. These sub-processes resulting in soft remnants as the background of main hard scattering are inclusively referred to "underlying events".

4.2 Implementation of pp-collisions in Simulation

Since it is practically non-calculable with the rigid formulation, what is implemented in the simulation is drastically simplified by employing numerical approach or approximation techniques. The detail for each sub-processes is described in this section.

4.2.1 Parton Distribution Function

Since PDF is purely non-perturbative, numerical input is always used for simulation. [2] This is usually done by a global fit on the experimental data of deep inelastic scatterings (DIS) or hadron-hadron collision. Several collaborations have performed combined fits to the datasets mostly from HERA and Tevatron, with different parameterization and fitting scheme. The following sets recently provide results: PDF4LHC [99], NNPDF [100], CT14 [101], MSTW [102]. The uncertainties mainly results from instrumental uncertainties in the input data, uncertainties on the strong coupling constant and the functional form of parameterization.

4.2.2 Fixed-Order QCD Calculation

The matrix element in Eq. 4.1 is computed based on the QCD and EW theory, with truncated orders of perturbation. While the leading term in the perturbation (lowest order; "LO") dominates over the phase space, the inclusion of high-order terms is significantly important for new physics search. This is because of the much smaller signal cross-section with respect to the SM backgrounds, forcing one to explore the phase space where the bulk SM component is suppressed, to achieve a reasonable S/N. In such regions, typically the LO contribution is more suppressed and the higher-order effects become addressing.

The calculation of higher-order terms are generally challenging giving the skyrocketing increased number of involved diagrams. Currently, the cross-section calculation is available upto next-to-next-to-leading order (NNLO) or NNNLO for typical SM processes happening in LHC, and upto NLO level in event generation. Since the most phenomenologically important higher order effect is the additional parton emission (ISR and FSR), there are also a class of generators dedicated on computing the diagrams with the additional radiations ("multi-leg generators") in the market. Saving the computing resources by omitting the loop diagrams, they can typically afford upto 4-9 additional partons at maximum.

[2] The first principle calculation is strictly speaking doable by lattice QCD. Some results are presented by [98].

4.2.3 Parton Showering

Aside with the straightforward QCD matrix element calculation, the parton shower (PS) technique is another useful approach to describe the dynamics of additional partons emission. The concept is based on following two notions:

- Soft or collinear emission provide dominant contribution to extra parton emission from a parton. In a parton-level process: $ee \to q\bar{q}g$ for a minimal example, the differential cross-section can be expressed:

$$\frac{d\sigma_{q\bar{q}g}}{dx_1 dx_2} = \sigma_{q\bar{q}} \times \frac{\alpha_s}{2\pi}\frac{4}{3}\frac{x_q^2 + x_{\bar{q}}^2}{(1-x_q)(1-x_{\bar{q}})}, \quad x_i := 2E_i/\sqrt{s} \tag{4.3}$$

  with $\sqrt{s}$ being the center-of-mass energy of the ee system. The singularities correspond to the collinear emission of gluon ($x_q \to 1$ or $x_{\bar{q}} \to 1$) or the soft gluon emission ($x_q \to 1$ and $x_{\bar{q}} \to 1$). These collinear and soft singularities are universal to QCD, independent from type of processes.

- In the soft/collinear regime, the cross-section with an additional parton radiation ($\mathrm{d}\sigma_{n+1}$) can be factorized by a product of the original cross-section ($\mathrm{d}\sigma_n$) and the probability of the splitting $P_{i\to jk}$:

$$\mathrm{d}\sigma_{n+1} = \mathrm{d}\sigma_n \left[\sum_{j,k} \frac{\alpha_s}{2\pi}\frac{dq}{q}\frac{dz}{z}P_{i\to jk}(z)\right], \tag{4.4}$$

  where the indices i, j represent respectively the parent parton before and after the splitting, and k the emitted parton. z is the momentum fraction the emitted parton carrying from the parent, and q is the momentum transfer between the parton i and j. $P_{i\to jk}$ is known as the Dokshitzer-Gribov-Lipatov-Altarelli-Parisi (DGLAP) evolution equations [103] [104] [105]:

$$P_{q\to qg} = \frac{4}{3}\frac{1+z^2}{1-z}, \tag{4.5}$$

$$P_{q\to gq} = \frac{4}{3}\frac{1+(1-z)^2}{z}, \tag{4.6}$$

$$P_{q\to gg} = 3\frac{z^4+1+(1-z)^4}{z(1-z)}, \tag{4.7}$$

$$P_{q\to q\bar{q}} = \frac{z^2+(1-z)^2}{2}, \tag{4.8}$$

Within this regime, one can calculate the recursive parton splitting ("parton shower") in a picture of stepwise evolution, in contrast to that in the scattering amplitude approach where either initial and final state must be defined beforehand.

The probability of emitting an extra parton at each step can be then represented analogous to the life time of unstable particle decay, using the Sudakov form factor [106]:

$$S_i(q_1, q_2) = 1 - \exp\left(-\sum_{j,k}\int_{q^2}^{q^2_{\max}} \frac{\mathrm{d}Q^2}{Q^2}\int_{z_{\min}}^{z_{\max}} \frac{\alpha_s}{2\pi}P_{i\to jk}(\hat{z})\mathrm{d}\hat{z}\right), \tag{4.9}$$

where q_1 (q_2) denotes the virtuality of parent parton before (after) the splitting. The FSRs are simulated by the evolution of final state parton legs with the splitting probability Eq. 4.9, with giving an arbitrary initial virtuality Q. The evolution is terminated typically until the virtuality becomes ~ 1 GeV. ISRs are simulated in similar manner but with backward evolution with increasing virtuality q along the evolution. Generated sub-branches during the backward evolution are then evolved forward. The procedure is schematized as Figure 4.2.

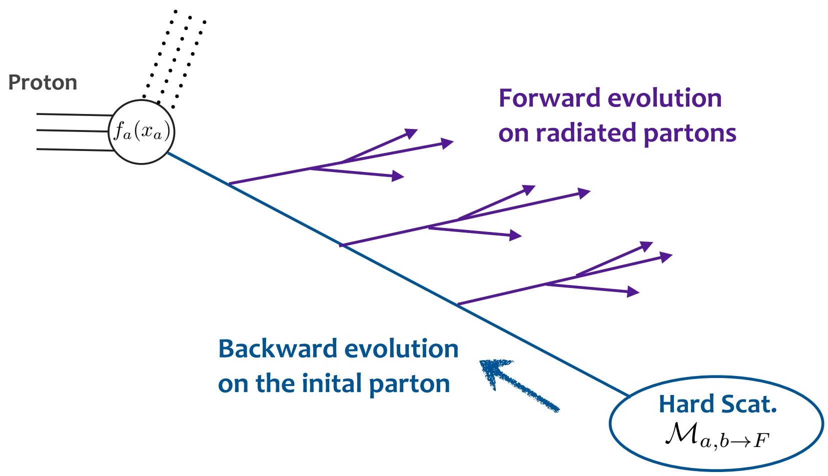

Figure 4.2: Schematic of the backward evolution implemented in ISR simulation. The evolution starts from hard-collided parton with increasing virtuality q along the evolution. Partons split from it are then evolved forward.

Various implementation for the evolution exist, leading to a subtle difference in the final state kinematics. The impact are quoted as theoretical uncertainty in the analysis. The procedure and the assigned uncertainties is summarized in chapter 7.

Note that this shower evolution is fully pertubative though, it still partially includes arbitrarily higher order contribution in the perturbation series (upto n-th order, where n is number of parton branch splitting). However the drawback is that it only takes contribution from collinear and soft singularity into account. This is the main motivation for multi-leg generators that provides hard ME-level additional partons to complement. One issue about this combined approach is the potential double-counting. The correction procedure commonly refers to “matching” or “merging”. There are largely two types of correction; separating the region that each ME and PS is responsible for, in terms of phase space or scale. The most widely used algorithm is the Catani-Krauss-Kuhn-Webber (CKKW) [107] algorithm or Michelangelo-L. Mangano algorithm (MLM) [108]. ; Generating all jets by PS, and correct it by normalizing into the ME differential cross-section (ME correction).

4.2.4 Hadronization

A phenomenological approach is usually preferred for simulating hadronization. The most famous model is the string model [109] where the confinement between partons is represented by a gluonic string. For a quark-antiquark pair, as the partons move apart, the string is stretched leading to an increase in potential energy. When the energy becomes of the order of hadron masses, it becomes energetically favorable for the string to break and create a new quark-antiquark pair. The two segments of string will be repeatedly pulled and break again, until all energy of initial quarks is converted into newly generated fragments.

4.3 Setup of the Simulated Dataset

4.3.1 Event Generation

Events of signal and background processes are generated using preferred generators and setups. Table 4.1 summarizes the configurations for the datasets used in the analysis. Given that the analysis typically explores the phase space with many jets, simulation of physics processes with less jets (e.g. $W/Z+$jets) or only soft jets at tree level (e.g. gluino production with compressed mass spectra) need dedicated modeling of ISR and FSR, for which the multi-leg generators (Sherpa, MadGraph) are preferred in general.

Table 4.1: Setup of simulated SUSY signal and the Standard Model background samples. $n_{\mathrm{ME}}^{\mathrm{a.p.}}$ denotes the number of simulated additional partons in the higher-order QCD processes. The column of "PS/UE" shows the programs in which parton showers and underlying events are generated.

Physics process	Generator	$n_{\mathrm{ME}}^{\mathrm{a.p.}}$	PDF set	PS/UE
SUSY processes	MadGraph 2.3 [a]	2	NNPDF2.3 LO	Pythia 8 [d]
$W/Z+$jets	Sherpa [b]	2(NLO)+2(LO)	NNPDF3.0 NNLO [110]	Sherpa
$t\bar{t}$	Powheg [c]	1	CT10 [111]	Pythia 6 [d']
Single-top (Wt-ch.)	Powheg v2	1	CT10	Pythia 6
Single-top (s-ch.)	Powheg v2	1	CT10	Pythia 6
Single-top (t-ch.)	Powheg v1 [c']	1	CT10f4	Pythia 6
Di-bosons	Sherpa	1-2(NLO)+2-3(LO)	CT10	Sherpa
$t\bar{t}+W$	MadGraph 2.2 [a']	2	NNPDF2.3 LO	Pythia 8
$t\bar{t}+Z$	MadGraph 2.2	1	NNPDF2.3 LO	Pythia 8
$t\bar{t}+WW$	MadGraph 2.2	0	NNPDF2.3 LO	Pythia 8

[a] MadGraph5_aMC@NLO 2.3.3 [112], NLO
[a'] MadGraph5_aMC@NLO 2.2.3, LO
[b] Sherpa 2.2.1 [113], NLO
[c] powheg-box v2 [114], NLO
[c'] powheg-box v1 [114], LO
[d] Pythia 8.186 [115], LO, CKKW matching
[d'] Pythia 6.428 [116], LO, ME correction

The simulated samples are normalized by the total cross-sections that are separately calculated typically with further accuracy such as including higher orders or soft gluon resummation. Table 4.2 shows the summary of the configuration with which the total cross-section is calculated. Further caveats particular to each process are noted in the appendix A.1.

Table 4.2: Cross-section used for the simulated processes. "(N)NLL" denotes the order upto which the soft gluon resummartion is taken into account.

Physics process	Cross-section [pb]	Order	Authors
SUSY processes	See Figure 4.3	NLO+NLL	[117–121]
$W+\text{jets}(\to \ell\nu)$	20079	NNLO	[122]
$Z+\text{jets}(\to \ell\ell)$	1950	NNLO	[122]
$t\bar{t}$	993.8	NNLO+NNLL	[123]
Single-top (Wt-channel)	75.57	NNLO+NNLL	[124]
Single-top (s-channel)	10.32	NLO	[125]
Single-top (t-channel)	216.95	NLO	[125]
Di-bosons	45.42	NLO	[126]
$t\bar{t}+W/Z/WW$	1.36	NLO	[127, 128]

4.3.2 Pileup simulation

All simulated events are generated with a varying number of minimum-bias interactions overlaid on the hard-scattering event to model the multiple proton-proton interactions in the same and the nearby crossing crossings. The minimum-bias interactions are simulated with the soft QCD processes of Pythia 8.186 using the A2 tune [129] and the MSTW2008LO PDF set [102]. Corrections are applied to the samples to account for differences between data and simulation for trigger, identification and reconstruction efficiencies.

4.3.3 Detector Simulation and Emulation

The detector response to generated particles is simulated by a full ATLAS detector simulation model [130] based on Geant4 [131], for the background samples.

The ATLAS fast simulation [48] is used for signal models marked as ✓ in Table 1.5-1.7 in Sec. 1.5.3, as the economical alternative. This is based on a parametrization of the performance of the electromagnetic and hadronic calorimeters measured in the test-beam or on Geant4 elsewhere. The difference between the full simulation is found to be marginal after examining a number of reference signal points. The subsequent procedures are identical to what is processed for the data sample.

For the signal models with no ✓ in Table 1.5-1.7, no detector simulation nor reconstruction is performed. Instead the effect is emulated by smearing the energy of truth-level particles and clustered jets, based on the resolution parameterized using the full simulated samples. The object identification is emulated by randomly accepting the candidates at the rate of the parameterized efficiency. The modeling is extensively tested by comparing the kinematic distributions with the fast simulated samples. The discrepancy is found sufficiently small, staying within 5% in general and never exceed 10%.

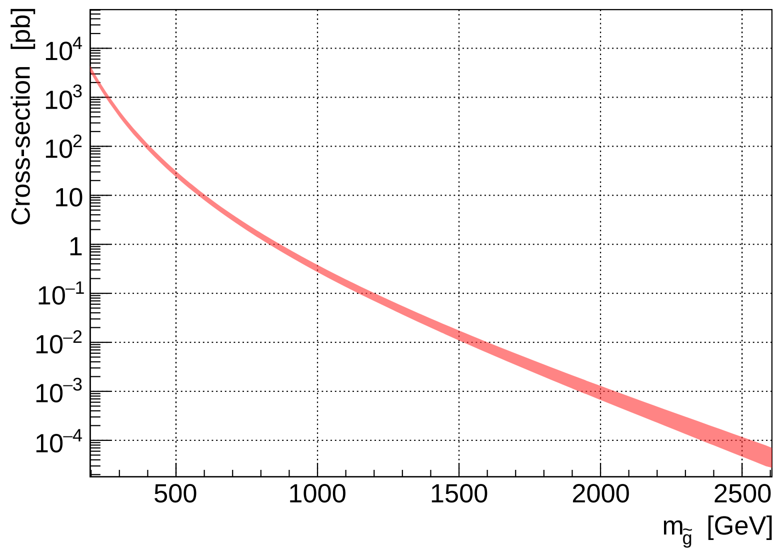

Figure 4.3: Cross-section for gluino pair production. Calculation is performed at NNLO+NNLL accuracy.

4.4 Design of SUSY Signal Grid for Interpretation

Obtained exclusion limits are presented in a form of contours in a 2-dimensional plane, usually in terms of SUSY masses. This is done by generating a set of signal samples with various SUSY masses covering the whole plane with discrete steps, referred as a signal grid. The results of the hypothetical test for the points are interpolated into a continuous limit in the end.

For limits on the direct decay models, $m_{\tilde{g}}$ and $m_{\tilde{\chi}_1^0}$ are chosen as x and y-axis respectively to represent (referred as "`Direct` " grid). The cases with 1-step decay models is a bit tricky, since they involve the third mass; the intermediate EW-gaugino $\tilde{\chi}_1^{\pm}$ or $\tilde{\chi}_2^0$. The full 3-dimensional presentation is not realistic from computational cost of view, due to the enormously increased number of grid points to cover the whole grid. Therefore, a couple of sensible 2D-slices are made that sufficiently capture the essence of the 3D-grid. "`x=1/2` " is the grid with the intermediate EW-gaugino mass is set to midmost between gluino and the LSP, while x is defined as a parameter representing the relative mass splitting:

$$x := \Delta m(\tilde{\chi}_1^{\pm}/\tilde{\chi}_2^0,\, \tilde{\chi}_1^0)/\Delta m(\tilde{g},\, \tilde{\chi}_1^0), \quad x \in [0, 1].$$

The `LSP60` grid is then designed to complement the hole in high or low x, where the LSP mass is fixed to 60 GeV and the gluino mass and the intermediate EW-gaugino mass are set free. There are two additional grids `DM20` and `DM30` in which the intermediate EW-gaugino an the LSP are compressed ($\Delta m(\tilde{\chi}_1^{\pm}/\tilde{\chi}_2^0,\, \tilde{\chi}_1^0) = 20$, 30 GeV respectively), respecting the dark matter relic constraint in discussed in Sec. 1.4.2. Note that these DM grids are not considered in models with $\tilde{\chi}_2^0$ decaying to higgs, since higgs is too far off-shell thus $\tilde{\chi}_2^0$ never almost decays via higgs in the situation.
To summarize, four types of signal grid are designed in the analysis, as shown in Table 4.3.

Table 4.3: List of signal grids used for limit setting. `Direct` is for the direct decay model, and the others are for the 1-step decay models. The latter is four-fold: `x=1/2` , a grid with EW gaugino mass fixed to the middle of gluino and LSP; `LSP60` , in which LSP mass is fixed to 60 GeV; `DM20` and `DM30` are grids with $\Delta m(\tilde{\chi}_1^{\pm}/\tilde{\chi}_2^0,\, \tilde{\chi}_1^0) = 20, 30$ GeV which are considered only in models without $\tilde{\chi}_2^0$ decay into higgs.

Grid name	x-axis	y-axis	Slicing	Note
`Direct`	$m_{\tilde{g}}$	$m_{\tilde{\chi}_1^0}$	-	-
`x=1/2`	$m_{\tilde{g}}$	$m_{\tilde{\chi}_1^0}$	$\Delta m(\tilde{g},\, \tilde{\chi}_1^0)/2 = \Delta m(\tilde{\chi}_1^{\pm}/\tilde{\chi}_2^0,\, \tilde{\chi}_1^0)$	-
`LSP60`	$m_{\tilde{g}}$	$\Delta m(\tilde{\chi}_1^{\pm}/\tilde{\chi}_2^0,\, \tilde{\chi}_1^0)/\Delta m(\tilde{g},\, \tilde{\chi}_1^0)$	$m_{\tilde{\chi}_1^0} = 60$ GeV	-
`DM20` ,`DM30`	$m_{\tilde{g}}$	$m_{\tilde{\chi}_1^0}$	$\Delta m(\tilde{\chi}_1^{\pm}/\tilde{\chi}_2^0,\, \tilde{\chi}_1^0) = 20, 30$ GeV	For models without h-mediated $\tilde{\chi}_2^0$ decays.

Chapter 5

Event Selection

5.1 Trigger Selection

The missing ET trigger (MET trigger) is primarily used throughout the analysis. Since the lowest unprescaled trigger kept evolved according to the increased instantaneous luminosity during the 2016 data taking, a number of different triggers are used in combination. The list of the triggers are shown in Table 5.1,

Table 5.1: Summary of MET triggers used in the analysis along the peak luminosity evolution. Corresponding on-line and off-line threshold are shown altogether.

Period	Peak lumi. [cm^{-2} s^{-1}]	Int. lumi. [fb^{-1}]	L1 (HLT) item	L1/HLT/Off-line thres. [GeV]
2015	0.50×10^{34}	3.19	L1XE50 (xe70_mht)	50 / 70 / 200
2016 A-D1	0.99×10^{34}	6.12	L1XE50 (xe90_mht)	50 / 90 / 200
2016 D1-F1	1.03×10^{34}	6.55	L1XE50 (xe100_mht)	50 / 100 / 200
2016 F2-	1.21×10^{34}	20.2	L1XE50 (xe110_mht)	50 / 110 / 200

The efficiency curve as function of off-line $E_{\mathrm{T}}^{\mathrm{miss}}$ is shown in Figure 5.1 with the example of HLT_xe100_mht. Thanks to the fact that MET is calculated from global information of an event, rather than the feature of a single particular particle, the plateau efficiency amounts almost 100 %. This is a significant advantage over the use of leptonic trigger where efficiency is typically 70% $\sim$ 90%. Generally the downside of MET trigger is on the other hand its slow turn-on in terms of the off-line MET that needs nearly 200 GeV to assure the plateau efficiency despite much lower trigger threshold ($<$ 110 GeV). This is due to the deteriorated resolution of on-line MET which is purely based on calorimeter clusters, with respect to the off-line one which is take into muons and soft tracks into account. The signal acceptance by the trigger requirement is $>$ 95% except when gluino mass and LSP mass are compressed. Nevertheless, given that it is impossible for such signal to be discriminated against background without the MET generated by associated ISRs, the loss in trigger is not problematic.

The single-lepton trigger (SLT) is also used for supplemental purpose, including the efficiency measurement of MET trigger and closure tests of data-driven background estimation. The trigger turn-on is about 28 GeV (26 GeV) for single-electron (muon) in its transverse momentum and 30 GeV (28 GeV) is required as off-line threshold.

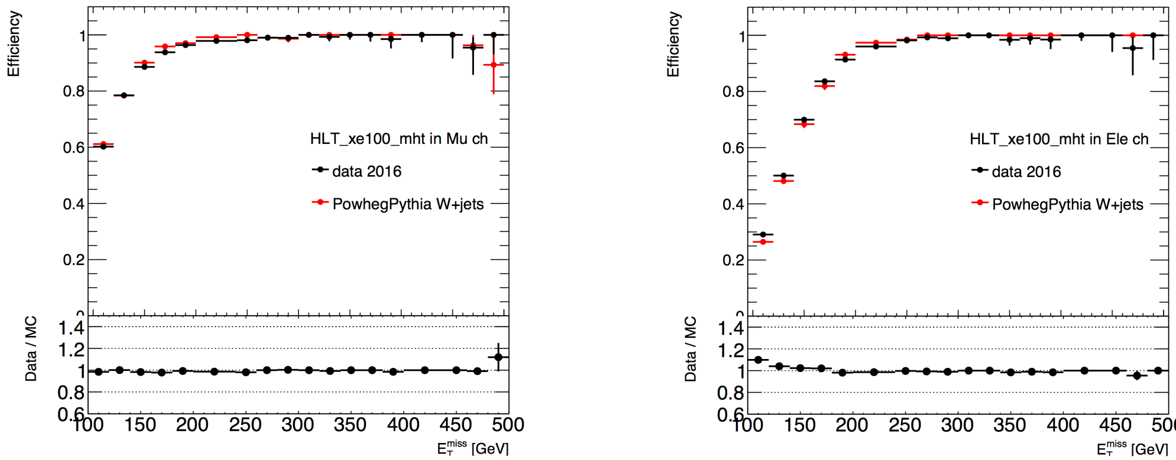

Figure 5.1: Turn-on of MET trigger HLT_xe100_mht simulated or measured using $W+$jets events by performing the tag-and-probe technique. (a) events with exactly one muon, and (b) events with exactly one electron.

5.2 Event Cleaning and the Pre-selection

Event cleaning is applied to get rid of funky data events that are either in bad quality due to inappropriate detector status and badly measured objects, or with objects stemming from somewhere other than the hard collision such as cosmic muons and beam-induced background. As those events could result in extraordinary observables, for instance extremely high jet pt or MET, they are generally critical for search analyses probing the high-end of kinematics where only a few background events in signal regions are in discussion where therefore even a single event of the accidental contamination makes huge impact on the final result. The list of procedure and cut efficiencies are summarized in Table 5.2.

Table 5.2: List of cuts applied as event cleaning. Data and MC shows different efficiencies up-to the top four since MC does not emulates bad data quality and cosmic muons in it.

Cut	Efficiency (Data) [%]	Efficiency (MC, $t\bar{t}$) [%]
Veto bad lumi-clocks	95.12	100.0
Veto bad DAQ events	99.81	100.0
Veto events with no primary vertex	100.0	100.0
Veto events with cosmic muons	95.83	98.52
Veto events with badly measured jets	99.49	99.65
Veto events with badly measured muons	99.99	98.56

Lumi-blocks with more than 10% of the detector in the bad status are firstly removed. Events affected by noise bursts in LAr and SCT, corrupted data transmission in LAr and the Tile calorimeter are then vetoed subsequently. Cosmic muon are vetoed by requiring the muon track passing reasonably close-by the primary vertex i.e.

$$|z_0| < 1\,\text{mm}, \;\; d_0 < 0.2\,\text{mm}.$$

The beam induced backgrounds are events with muons that are generated by the secondary cascades of protons traveling upstream of the interaction point. The energy depositions created by these muons can be reconstructed as jets with energy as high as the beam energy therefore becomes highly signal-like. To reject the fake jets, event with jets flagged as "BadLoose" described in [132] are vetoed.

High energy muons with poor momentum measurement quality are also a source of fake high MET ranging upto a few TeV. Those muons are selected as ones with $\sigma(q/p)/(q/p) > 0.2$ where q is muon charge, p the momentum and $\sigma(q/p)$ is the fitting error. The entire events will be vetoed if containing at least one bad muon. Figure 5.2 demonstrate the performance of bad muon veto. While bad muon events typically peak in $\Delta\phi(l, E_{\mathrm{T}}^{\mathrm{miss}})$ since the fake MET aligns with the muon, it is exclusively resolved by the veto. Also, the role of bad muon veto is shown to be very important in this analysis as the 1-muon high MET phase space generally suffers from severe contamination by bad muon events upto about 20% (90%) with $E_{\mathrm{T}}^{\mathrm{miss}} > 1(2)$ TeV.

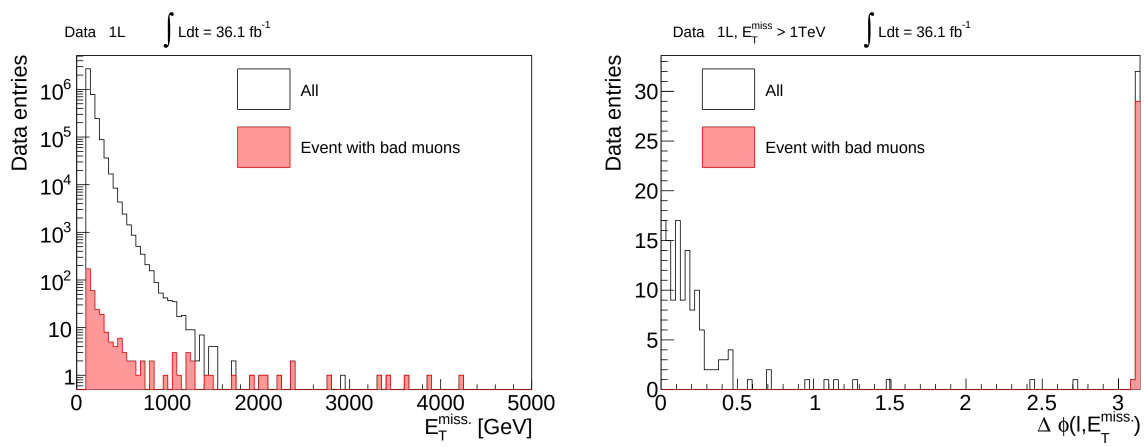

(a) (b)

Figure 5.2: (a) MET distribution after requiring exactly one signal muon and MET trigger, and (b) $\Delta\phi(l, E_{\mathrm{T}}^{\mathrm{miss}})$ distribution with $E_{\mathrm{T}}^{\mathrm{miss}} > 1$ TeV being applied. The pink histogram corresponds to events dropped by the bad muon veto. The veto looks working reasonably considering the apparent spike due to the fake MET: $\Delta\phi \sim \pi$ is cleared.

The pre-selection is the common selection for all the signal regions in the analysis, which is defined as Table 5.3. Figure 5.3 is a validation plot showing transverse mass (m_{T}; invariant mass of lepton p_{T} and MET) of the data and MC, after the pre-selection being applied.

Table 5.3: List of requirements for the 1-lepton pre-selection.

Event cleaning
Pass the MET trigger and $E_{\mathrm{T}}^{\mathrm{miss}} > 250$ GeV
At least one signal electron (muon) with $p_{\mathrm{T}} > 7(6)$ GeV.
At least two jets with $p_{\mathrm{T}} > 30$ GeV.

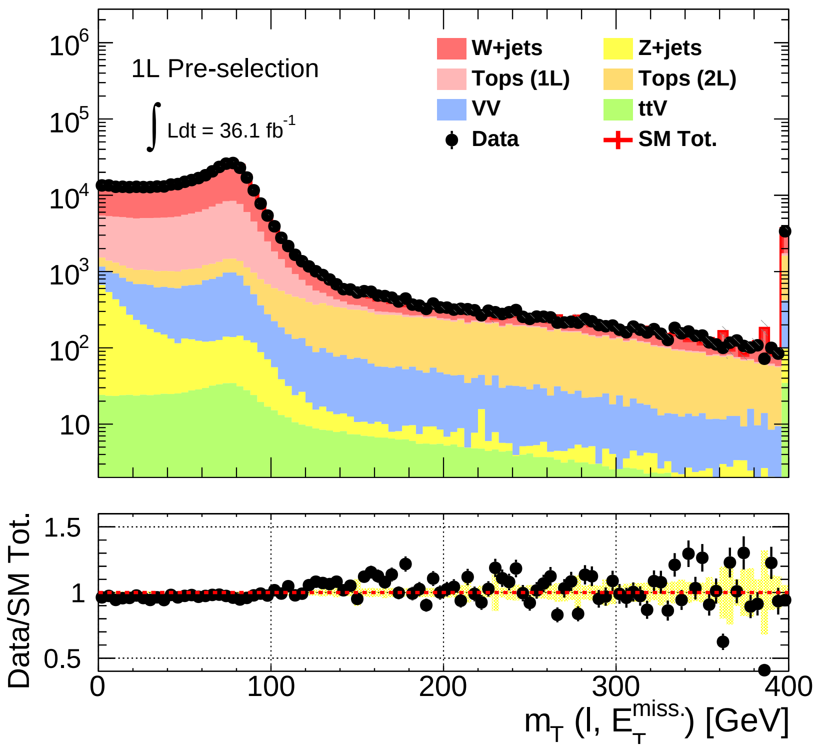

Figure 5.3: Transverse mass (m_{T}; invariant mass of lepton p_{T} and MET) distribution after the pre-selection (Table 5.3). The Jacobian peak and the cut-off structure at $m_{\mathrm{T}} \sim m_W$ are clearly seen.

5.3 Signal Region Definition

5.3.1 Binning Strategy

To inclusively address to all the 45 decay models and all possible mass spectra, a set of tailored multi-bin signal regions (SRs) are employed. Specifically, different decay models are covered by splitting the signal regions in terms of b-jet multiplicity ("categories"), and various scenario of mass spectra in the models are coped with the division in terms of kinematical cuts ("towers"). SR bins are basically designed to be exclusive for each other, aiming at an easy combination afterward so that no signals are lost due to the binning.

The definition of the b-jet based categories: b-vetoed (BV), b-tagged (BT) and 3B follows Table

5.4. The main customers of these categories are respectively the models in Table 1.5, 1.6 and 1.7 in Sec. 1.5.3, which are referred as “BV”, “BT” and “3B” benchmark models from now on. The b-jet multiplicity for the reference signal models versus background at the pre-selection level is shown in Figure 5.4. Note that despite a fraction of signal events falling into other categories than the benchmarked one, they will not be wasted thanks to the combined fit performed in deriving the final result. As the S/N ratio and the background kinematics in BV/BT are found to be more or less similar, further kinematical selections in those categories are set to identical for simplicity. On the other hand, different selection strategy is adopted for the 3B categories since the background level is significantly lower and also the composition is very different.

Table 5.4: The definition of the b-jet based categories and the main backgrounds there.

Category	b-jet multiplicity	Main background
B-vetoed (BV)	0	$W+$jets
B-tagged (BT)	1-2	$t\bar{t}$
3B	≥ 3	$t\bar{t}$, $t\bar{t}+cc/bb$

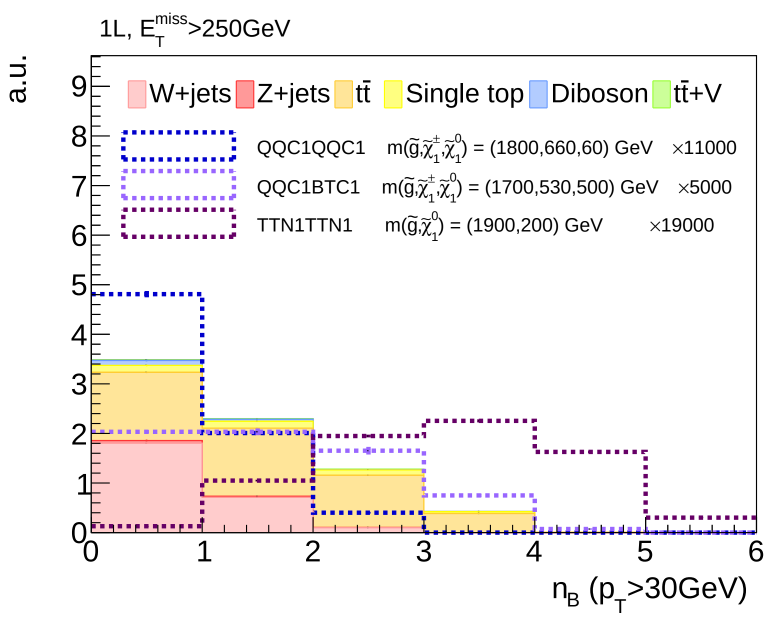

Figure 5.4: B-tagged jet multiplicity for the standard model backgrounds and the reference signals (QQC1QQC1 for the BV, QQC1BTC1 for the BT and TTN1TTN1 for the 3B categories respectively) after the 1-lepton pre-selection.

The BV/BT categories are further divided into 4 “towers”, to tackle the 4 typical configurations of the mass spectra for gluino and the LSP (and the intermediate EW gauginos in case of 1-step decays). The relation is schematized in Figure 5.5, with the benchmark model “QQC1QQC1” being the example. Each of them is further detailed as below:

1. The mass of intermediate EW gaugino is roughly in the middle of those of gluino and the LSP ($x \sim 1/2$). This is the most standard configuration where particles from both gluino and the intermediate EW gaugino decays are hard enough to pass the criteria of hard lepton ($>$ 35 GeV) and jets ($p_{\mathrm{T}} >$ 30 GeV). As the signals targeted by the BV/BT categories typically result in $4-10$ jets at the tree-level, a tower **6J** with $n_{\mathrm{J}} \geq 6$ is defined.

2. Gluino and EW gauginos are all compressed. From either trigger and background separation point of view, hard ISRs are indispensable for probing this type of signatures so that the $\tilde{g}\tilde{g}$ system gets kicked and resulting in large MET. On the other hand, as the kicked gluinos are typically enough heavy to be non-relativistic, the transverse momentum of the boosted $\tilde{g}\tilde{g}$ system is almost solely converted into MET. As a result the particles from gluino decays stay soft. The **2J** tower consisting of a soft lepton, at least two hard jets and large MET is defined for targeting the signature.

3. ,4 The intermediate EW gaugino and either gluino or LSP are compressed ($x \sim 0, 1$). There are also extreme cases where the intermediate EW gaugino mass is degenerate toward either of gluino or LSP and decoupled from the other. Two signal region towers: $High - x$ and $Low - x$ are employed to cover the scenarios.

Similar discussion holds for direct gluino decay models as well i.e. the tower **2J** covers the scenario of compressed mass spectra while the tower **6J** is used for general cases.

In contrast to the BV/BT category, the 3B does not undergo the additional classification in towers since the targeted signal models usually involve top quarks that can result in hard jets, leptons and MET. Therefore the kinematics does not dramatically vary between the mass configurations unless the top-quarks are on-shell. The only exception is when gluino and the intermediate EW gaugino get compressed, and the top-quarks turn to off-shell ending up in only soft particles. However such events are then covered by the BV and BT towers instead, thanks to the dropped ≥ 3 b-jet acceptance according to the decreasing b-quarks' p_{T}.

To summarize, 5 towers (2J/6J/Low-x/High-x/3B) are defined in total out of 3 categories (BV/BT/3B) as in Table 5.5.

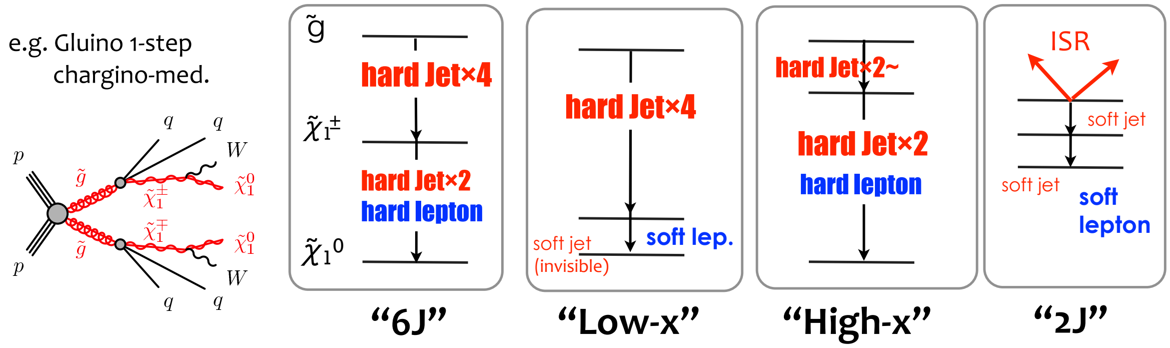

Figure 5.5: The 4 signal region towers for the BT/BV categories, and their targeted mass configuration.

Table 5.5: List of defined towers in each b-category and t kinematical selection required. **2J** and **6J**, **Low-x** and **High-x** are orthogonal to each other. **3B** are orthogonal to all the other towers.

Category	Tower	Electron (muon) p_{T} [GeV]	n_{J} ($p_{\mathrm{T}} > 30$ GeV)
BV/BT	2J	$\in [7(6), 35]$	≥ 2
	6J	> 35	≥ 6
	Low-x	$\in [7(6), 35]$	≥ 4
	High-x	> 35	≥ 4
3B	3B	> 15	≥ 7

Finally, the towers further experience the binning in terms of $m_{\mathrm{eff}} := E_{\mathrm{T}}^{\mathrm{miss}} + \sum_i p_T(j_i)$ to accommodate different absolute scale of mass splitting. The “2J/6J” and “3B” tower are segmented into 3 and 2 bins respectively while “Low-x” and “High-x” are single-binned as their low m_{eff} bins have too much overlap with “2J” and “6J” in phase space which does not provide unique sensitivity. The bin widths of m_{eff} are set to be 400 GeV $-$ 500 GeV driven by the width of m_{eff} distribution for signals that the lower m_{eff} bins typically target ($\Delta m(\tilde{g}, \tilde{\chi}_1^0) = 1$ TeV $\sim$ 1.5 TeV). The “3B” tower enjoys an exceptionally wider bin width with 750 GeV, compromising with limited of statistics in corresponding control regions.

To conclude, the signal regions end up in 5 tower-structured bins as schematized as Figure 5.6, where 3×2 bins in $m_{\mathrm{eff}} \times$ (BV/BT) reside in the tower **”2J”** and **”6J”**, 1×2 bins in **”Low-x”** and **”High-x”**, and 2 m_{eff} bins in **”3B”**. Since all the SRs bins in the towers ”2J/6J/3B” or ”Low-x/High-x/3B” are statistically independent, they can be straightforwardly combined in a simultaneous fit. Figure 5.7-5.8 schematize the mass regions in the signal grids that each signal region tower or bin is supposed to address the sensitivity for the benchmark models.

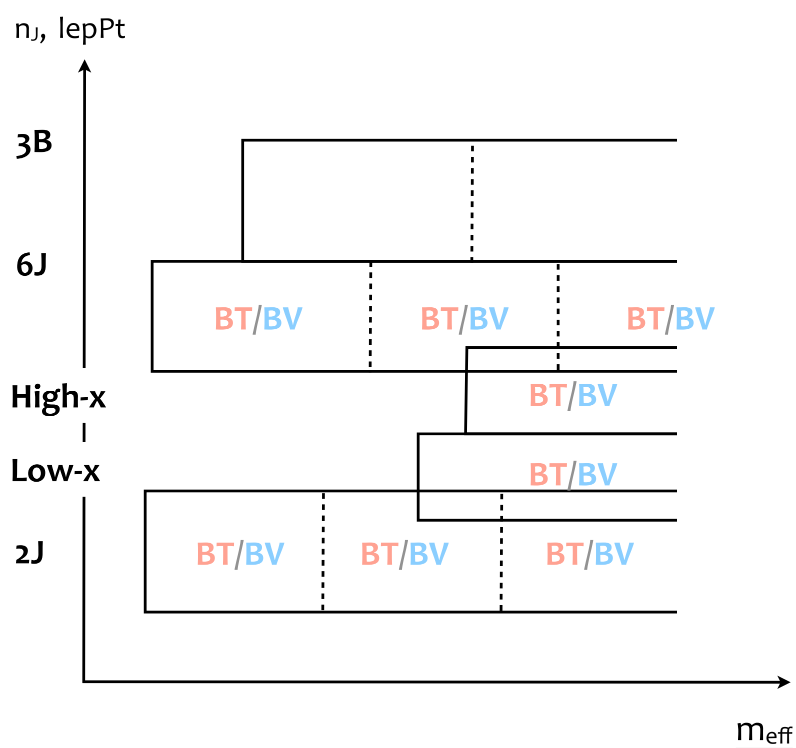

Figure 5.6: Tower structure and the m_{eff} binning of signal regions.

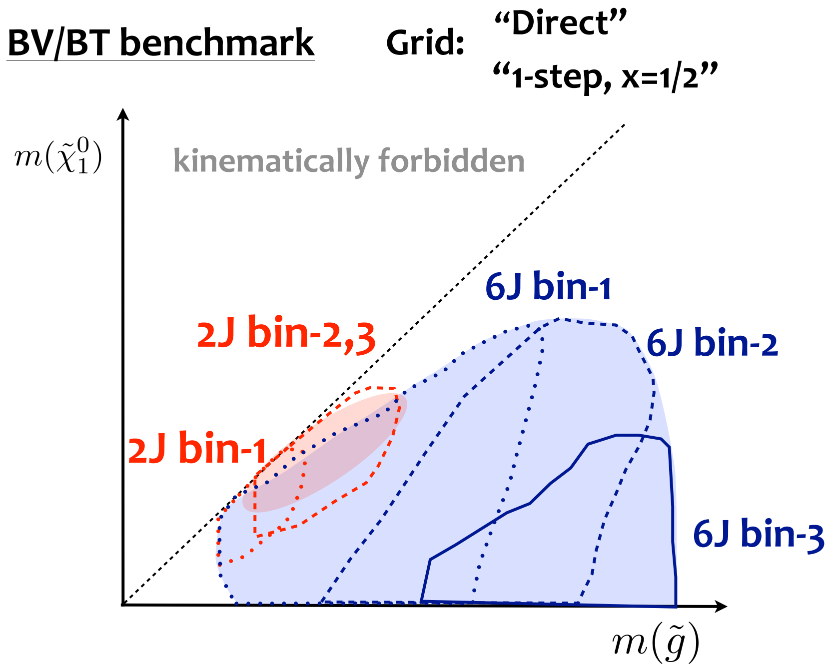

(a)

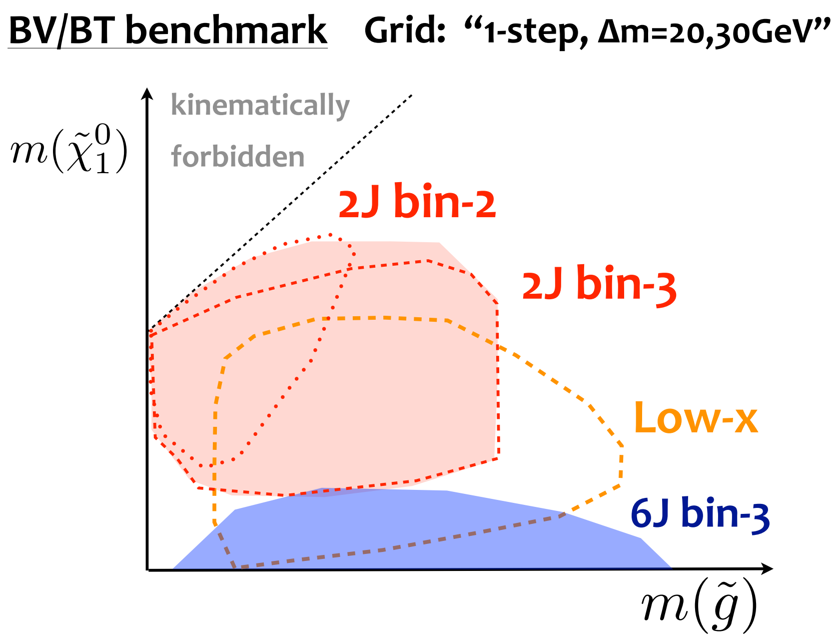

(b)

Figure 5.7: Sensitivity converage by individual signal region towers or m_{eff}-bins in the (a) the `Direct` and `x=1/2` grid, and in (b) the `DM20` , `DM30` grid of the BT/BV benchmark models. Dashed contours and shaded areas schematize the regions that the individual tower or m_{eff}-bin addresses the sensitivity.

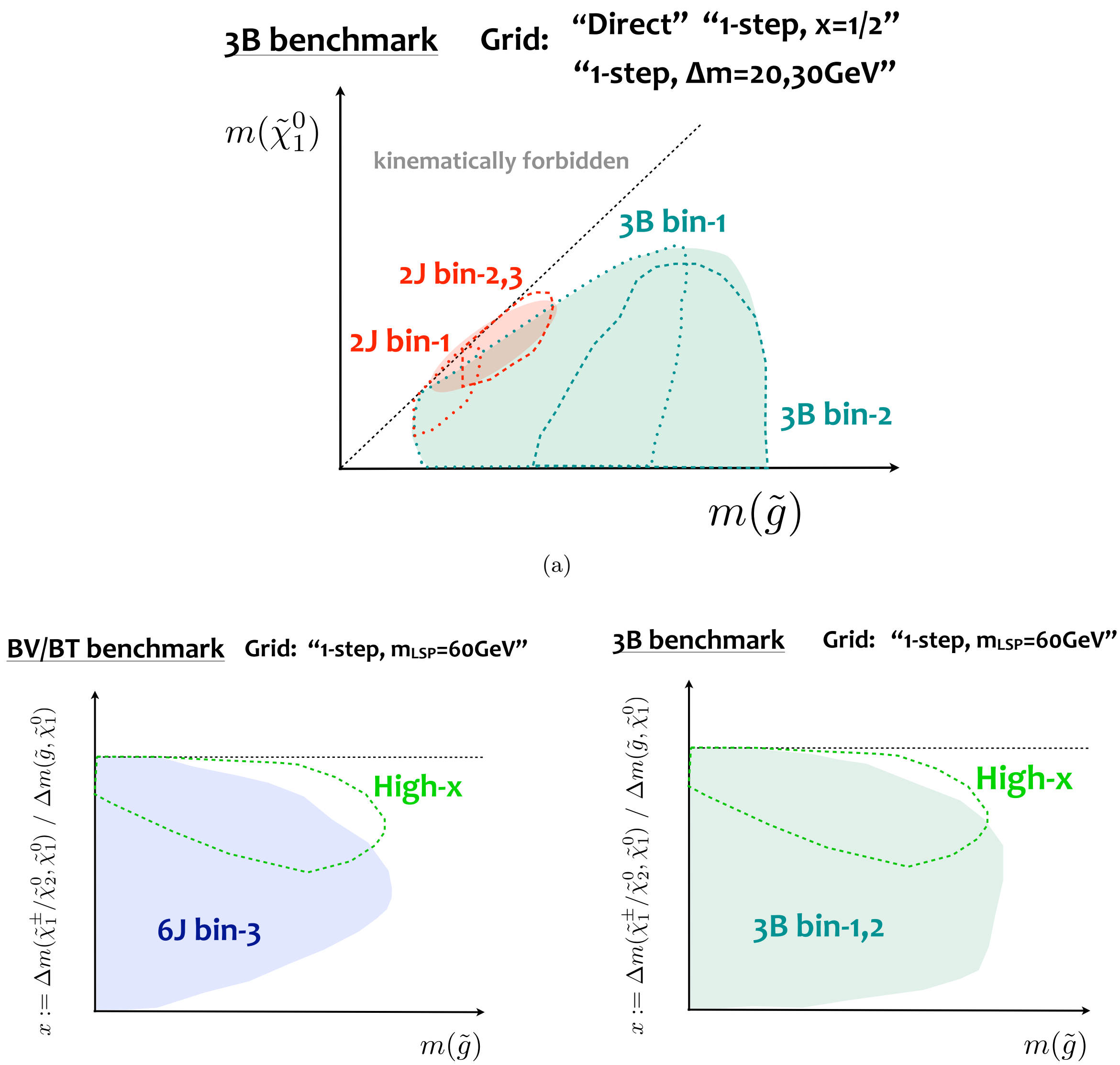

(a)

(b) (c)

Figure 5.8: Sensitivity converage by individual signal region towers or m_{eff}-bins in the (a) `Direct` , `x=1/2` , `DM20` and `DM30` grids of the 3B benchmark models, (b) the `LSP60` grid of the of the BT/BV benchmark models, and in (c) the `LSP60` grid of the 3B benchmark models. Dashed contours and shaded areas schematize the regions that the individual tower or m_{eff}-bin addresses the sensitivity.

5.3.2 Discriminating variables

Kinamtical variables used for background rejection as well as defining control regions are overviewed. The distributions of backgrounds overlaid with benchmark signals at the pre-selection are presented in Figure 5.10 - 5.11. In addition to the pre-selection, a soft lepton ($p_{\mathrm{T}}(\ell) \in [6, 35]$) is required in Figure 5.11 (b), $m_{\mathrm{eff}} > 1500$ GeV in for Figure 5.11 (b), and $n_{\mathrm{B}} \geq 3$ $m_{\mathrm{T}} > 125$ GeV are applied in Figure 5.11 (c) and (d). The definition and the purpose of the variables are as below:

$\mathbf{n}_{\mathrm{J}}$ Jet multiplicity often shows the great discriminating power since the standard model processes suffer a sharp cut-off. However one should mind that the optimum cut is significantly dependent on the gluino decay mode, and also that the aggressive cut will enhance the contribution from higher order effect, putting the modeling at the risk of large theoretical uncertainty. Therefore, it is kept to a moderated use as means of background rejection.

$\mathbf{E}_{\mathbf{T}}^{\mathbf{miss}}$ Signal events result in large $E_{\mathrm{T}}^{\mathrm{miss}}$ reflecting the presence of hard additional undetected LSP when $\Delta m(\tilde{g},\, \tilde{\chi}_1^0)$ is large. At analysis level, this is also true for the compressed case given that the MET via ISRs is nevertheless required for the trigger sake as described above.

$\mathbf{m}_{\mathrm{eff}}$ m_{eff} is the variable best reflecting the magnitude of absolute mass splitting $\Delta m(\tilde{g},\, \tilde{\chi}_1^0)$, providing the best separation against backgrounds. Meanwhile it is also noticeable that the magnitude of m_{eff} is almost uniquely determined by $\Delta m(\tilde{g},\, \tilde{\chi}_1^0)$, regardless of the relative mass splitting and gluino decays, therefore the optimal cut in m_{eff} is highly universal.

$\mathbf{m}_{\mathrm{T}}(\mathbf{p}_{\mathrm{T}}(\ell), \mathbf{E}_{\mathbf{T}}^{\mathbf{miss}})$ Invariant mass of $E_{\mathrm{T}}^{\mathrm{miss}}$ and the lepton with the z-momentum set to 0. Analogous to ordinary invariant mass peaking at the mass of the parent particle, the end point of m_{T} represents the parent mass when they share the same origin. Since SM 1-lepton process is always with a leptonically decaying W-boson without additional hard missing particles, the bulk component experiences a sharp cut-off in m_{T} around $m_W = 81.4$ GeV, therefore the cut above m_W is tremendously effective.

$\mathbf{E}_{\mathbf{T}}^{\mathbf{miss}}/\mathbf{m}_{\mathrm{eff}}$ $E_{\mathrm{T}}^{\mathrm{miss}}/m_{\mathrm{eff}}$ separates backgrounds and signals targeted by the **2J** and **High-x** where jet activity is relatively low compared with the magnitude of MET required.

Aplanarity Aplanarity [133] is a variable characterizing the 3-dimensionality of an event in terms of the final state particles. It is defined by the thirtial eigenvalue of the normalized momentum tensor S constructed from 3-momenta of jets and leptons:

$$\begin{aligned}
S^{\alpha\beta} &:= \frac{\sum_{i\in j,\ell} p_i^\alpha p_i^\beta}{\sum_i |\boldsymbol{p_i}|^2}, \\
P^{-1}SP &= \begin{pmatrix} \lambda_1 & & \\ & \lambda_2 & \\ & & \lambda_3 \end{pmatrix}, \quad \lambda_1 > \lambda_2 > \lambda_3, \\
\text{Aplanarity} &:= \frac{3}{2} \times \lambda_3,
\end{aligned} \tag{5.1}$$

where P stands for the 3×3 matrix diagonalizing S, λ_i for the eigenvalues of S. It ranges from $0 < A < 1/2$; $A = 0$ corresponds to events with jets distributed in the common plain, and $A = 0.5$ represents the isotropically distributed event topology. Aplanarity is an effective discriminator after requiring tight selection in m_{eff} or $E_{\text{T}}^{\text{miss}}$, where the remnant SM events (particularly $W+$jets) are typically heavily kicked by hard ISR radiations, leading to a highly linear event topology in their center-of-mass frame. These events end up in a planar topology in the lab frame once getting boosted toward the beam direction, as a result populating in low aplanarity region accordingly. On the other hand, the decay of gluino pairs keep relatively spherical thus the aplanarity distributing rather flatly, which reflects the fact the gluinos are too heavy to be boosted.

$\mathbf{n}_{\text{J}}/\mathbf{p}_{\text{T}}(\boldsymbol{\ell_1})$ Since the hardness of lepton and jets are positively correlated in normal processes in SM, it is relatively rare to end up in a soft lepton and hard jet activity simultaneously, while it is the case for the compressed gluino signature. A variable $n_{\text{J}}/p_{\text{T}}(\ell_1)$ helps visualize the different correlations, and used in the **2J** signal region towers to improve the sensitivity of the compressed gluino signatures.

$\min_{\mathbf{i=1-4}} \boldsymbol{\Delta}\phi(\mathbf{j_i}, \mathbf{E_T^{miss}})$ vA variable indended to reject the remnant $t\bar{t}$ events after requiring tight selection of m_{eff} and $E_{\text{T}}^{\text{miss}}$. As such $t\bar{t}$ events typically have hard ISR jets to boost the $t\bar{t}$ system, the jets from $t\bar{t}$ decays and associated soft radiation tend to be collimated each other. Conversely, the jets from the gluino decays almost never get collimated as due to the heavy mass of gluino.

Topness One of the most important background in 1-lepton analysis is di-leptonic $t\bar{t}$ events with a hadronically decaying tau lepton or a lepton that fails the baseline requirement. To reject those events, a χ^2-based di-leptonic $t\bar{t}$ tagger "topness" has been designed in context of scalar-top search since Run1 [134]. The χ^2 function is defined as:

$$
\begin{aligned}
&S(p_{\mathrm{W}}^{x}, p_{\mathrm{W}}^{y}, p_{\mathrm{W}}^{z}, p_{\nu}^{z}) \\
&= \chi^2(m_{t,1}^2) + \chi^2(m_{t,2}^2) + \chi^2(m_{W,1}^2) + \chi^2(\hat{s}(t\bar{t})) \\
&= \frac{\left(m_t^2 - (p_{b,1} + p_\ell + p_\nu)^2\right)^2}{a_t^4} \\
&+ \frac{\left(m_t^2 - (p_{b,2} + p_{\mathrm{W}})^2\right)^2}{a_t^4} \\
&+ \frac{\left(m_{\mathrm{W}}^2 - (p_\ell + p_\nu)^2\right)^2}{a_{\mathrm{W}}^4} \\
&+ \frac{\left(4m_t^2 - (p_\ell + p_\nu + p_{b,1} + p_{b,2} + p_{\mathrm{W}})^2\right)^2}{a_{t\bar{t}}^4},
\end{aligned}
\tag{5.2}
$$

assuming an event topology as shown Figure 5.9 where one of the lepton are totally undetected and the momentum does fully contribute to MET.
It consists of four Gaussian constraints imposing the mass constraint of top-quark and W-boson, and the center-of-mass for the $t\bar{t}$ system being close to its minimum threshold ($2m_t$). The width parameters are set to $(a_t, a_W, a_{t\bar{t}}) = (15, 5, 1000)$ GeV, accounting for the Breit-Wigner widths of top-quark and W-boson as well as the tail of $\hat{s}(t\bar{t})$ distribution. Although there are three missing particles in the topology, the number of unknown degree of freedom can be reduced into 4 by combining the missing lepton (ℓ_2) and the paired neutrino (ν') into a single on-shell W-boson and imposing the vectoral sum of transverse momenta of missing particles being equal to $E_{\mathrm{T}}^{\mathrm{miss}}$. Topness is then defined as the minimum χ^2 when scanning over the four DOFs parameterized by $\boldsymbol{p}_{\mathrm{W}}$ and p_{ν}^{z}:

$$
\mathrm{Topness} := \min_{p_{\mathrm{W}}^{x}, p_{\mathrm{W}}^{y}, p_{\mathrm{W}}^{z}, p_{\nu}^{z}} \ln[S]. \tag{5.3}
$$

Events in the topology assumed are supposed to have solutions $(p_{\mathrm{W}}^{x}, p_{\mathrm{W}}^{y}, p_{\mathrm{W}}^{z}, p_{\nu}^{z})$ that satisfy the four constraints at the same time while scanning, however it is not necessarily the case for the other type of events. Figure 5.9 shows typical separation between di-leptonic $t\bar{t}$ and signals. Although di-leptonic $t\bar{t}$ does have a fraction of unfortunate events on the pile of higher values due to the fact that the energy of missing leptons or tau leptons does not entirely contribute to MET, the majority resides on the left pile while signals typically populate more in the opposite one.

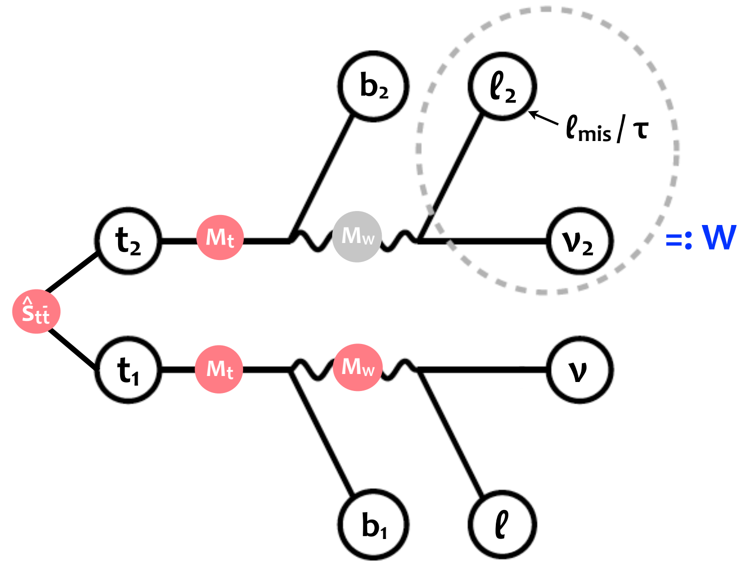

Figure 5.9: Di-leptonic $t\bar{t}$ topology assumed in the topness calculation where one lepton is tagged (ℓ_1) and the other lepton (ℓ_2) is not identified as any objects with its momentum fully contributing to MET. Topness is defined as minimum summed χ^2 of three mass shell constraints for the top, anti-top and the W-boson decaying into ℓ_1, as well as one pseudo-mass constraint in terms of the $t\bar{t}$ systems (labeled as pink circles), while scanning over the momenta space of missing particles. The degrees of freedom by ℓ_2 and the associated neutrino (ν_2) are combined into a 4-momentum p_W with the mass fixed to $m_W = 81.2$ GeV, and the scan is performed in terms of $p^x_{\mathrm{W}}, p^y_{\mathrm{W}}, p^z_{\mathrm{W}}$ and p^z_ν from -4 TeV to 4 TeV respectively.

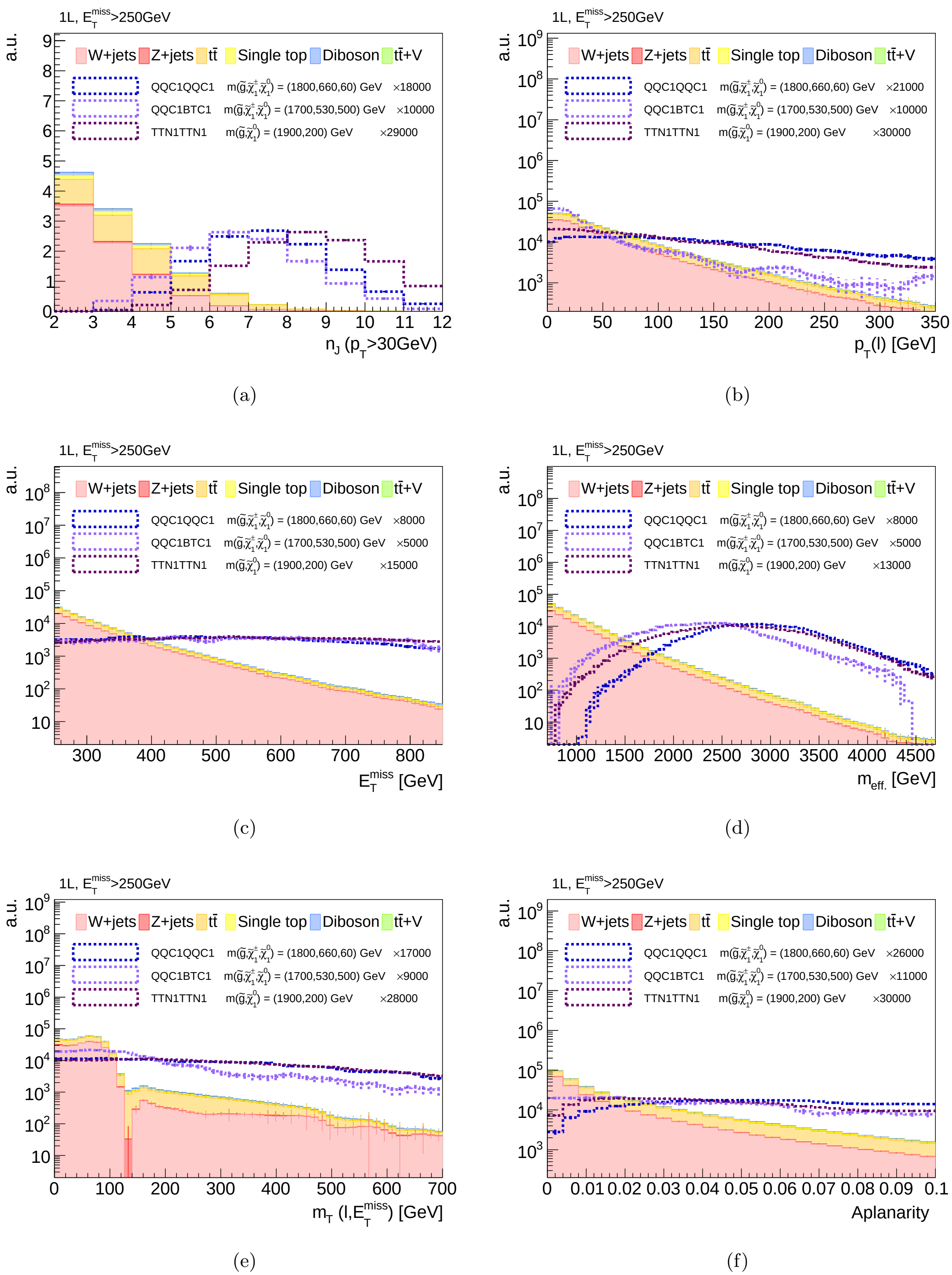

Figure 5.10: Distributions of discriminating variables for reference signal and backgrous, at the pre-selection level. (a) n_J, (b) Lepton p_T, (c) E_T^{miss}, (d) m_{eff}, (e) m_T and (f) aplanarity are respectively shown.

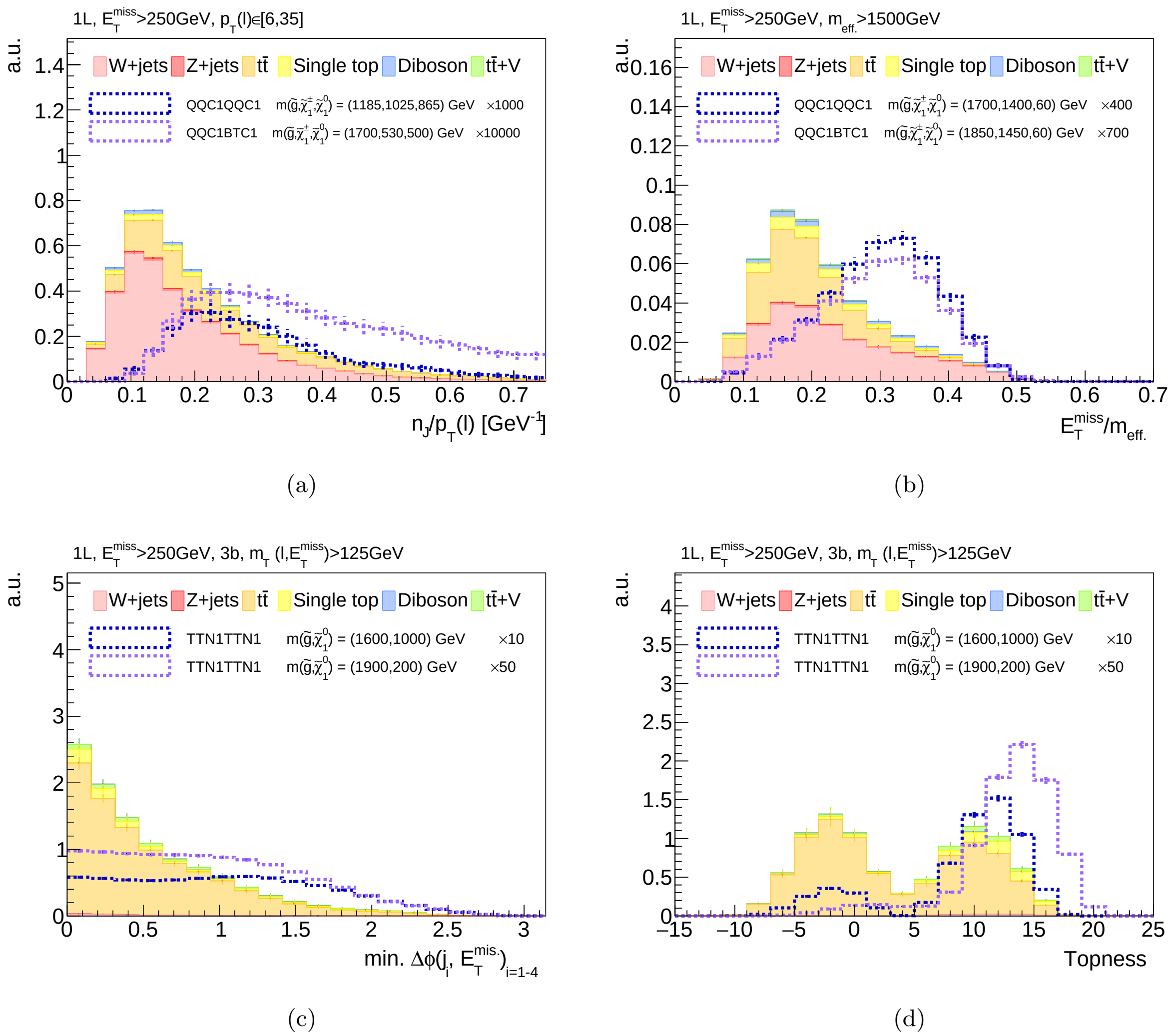

Figure 5.11: Distributions of discriminating variables at the pre-selection level. Soft lepton requirement: $p_{\mathrm{T}}(\ell) \in [6, 35]$ is applied for (b), and $n_{\mathrm{B}} \geq 3$ $m_{\mathrm{T}} > 125$ GeV is applied for (c).

5.3.3 Cut Optimization

The cut values for the kinematic variables listed above are optimized, including the lower m_{eff} cut for the highest m_{eff}-bin. Reference signal points are defined in Table 5.6, to which the sensitivity is optimized. The optimization procedure proceeds as following.

1. The binning of m_{eff} is roughly decided so that the sensitivities for all the reference points in the same tower are maintained.

2. Cuts values in other variables are then optimized by a simultaneous grid scan using machinery. The initial values are chosen based on the target mass regions of each signal region (as depicted by Figure 5.7-Figure 5.8), and the typical kinematics of such signals as shown in Figure B.1.1-B.1.4 in Appendix B.1. The sensitivity as the reference of the optimization is defined by the combined significance of m_{eff} bins such as :

$$
\begin{aligned}
Z_{N,\mathrm{comb.}} &= \sqrt{\sum_i Z_{N,i}^2}, \\
Z_{N,i} &:= S_i / \sqrt{B_i + \alpha^2 B_i^2},
\end{aligned}
\tag{5.4}
$$

   where $Z_{N,i}$ is the significance provided by a single m_{eff} bin, with S_i, B_i being the signal and background yields in the m_{eff} bin. α is relative uncertainty on the background expectation in each m_{eff} bin, which is set to 30% given the typical level systematic uncertainty. The cut between BT and BV bins in the same tower and m_{eff}-bin are always set to common.

3. All the cuts including the m_{eff} binning are re-optimized by pertubating them from the optimum configuration obtained in the previous step simultaneously.

4. Optimum cuts are different between reference points in the same m_{eff} tower. An adjustment is therefore applied for the best compromise, as well as to avoid the over-optimization on specific signal points.

5. Another minor adjustment is done afterwards, required from the context of background estimation. Some of the cuts are loosened to facilitate the control region definition.

Finalized definition of signal regions are shown in Table 5.7-5.11. The m_{eff} distribution in the optimized signal regions are displayed in Figure 5.12-5.16 for backgrounds with the reference signal points overlaid. The segmentation of m_{eff}-bin is found to successfully address the sensitivity in different mass region in the signal grid.

The optimized selection is also validated by a set looking at the kinematic distributions in which the one of the cuts is removed from the optimized signal regions ("N-1 plots"). The N-1 plots are all shown in Figure B.2.1-B.2.9 in the appendix B.2. The sensitivity is calculated as function of the cut position of the removed cut. The decided cuts are shown by the red arrows, which are more or less at the optimum position for all the reference signals.

Table 5.6: The reference signal points for each signal regions to which the selection is optimized to.

	Model	$(m_{\tilde{g}}, m_{\tilde{\chi}_1^\pm}, m_{\tilde{\chi}_1^0})$,$(m_{\tilde{g}}, m_{\tilde{\chi}_1^0})$ [GeV]
2J BV		
	QQC1QQC1	(1550,580,550)
	QQC1QQC1	(1065,1025,985)
	TTN1TTN1	(1000,915)
2J BT		
	QQC1BTC1	(1400,830,800)
	QQC1BTC1	(1550,780,750)
6J BV		
	QQC1QQC1	(1945,1105,265)
	QQC1QQC1	(1850,1350,850)
	QQC1QQC1	(1700,1300,900)
6J BT		
	QQC1BTC1	(1850,1050,250)
	QQC1BTC1	(1700,1300,900)
Low-x BV		
	QQC1QQC1	(1700,460,60)
	QQC1QQC1	(1600,260,60)
	QQC1QQC1	(1700,530,500)
Low-x BT		
	QQC1BTC1	(1700,730,700)
	QQC1BTC1	(1700,530,500)
High-x BV		
	QQC1QQC1	(1800,1600,60)
	QQC1QQC1	(1800,1460,60)
	QQC1QQC1	(1800,1260,60)
High-x BT		
	QQC1BTC1	(1850,1750,60)
	QQC1BTC1	(1850,1450,60)
3B		
	TTN1TTN1	(2000,0)
	TTN1TTN1	(1900,800)
	TTN1TTN1	(1500,1000)

Table 5.7: Definition of signal/control/validation regions (SRs/CRs/VRs) for tower **"2J"**

	SR (BV/BT)	WR/TR	VR $E_{\mathrm{T}}^{\mathrm{miss}}$	VRb	VR QCD	VR DB
$n_{\ell,\mathrm{base.}}$	1	1	1	1	1	2
$n_{\ell,\mathrm{sig.}}$	1	1	1	1	0	2
$p_{\mathrm{T}}(\ell)$	$[6, 35]$					-
$n_{\mathrm{J}}\,(p_{\mathrm{T}} > 30$ GeV)	≥ 2					≥ 1
$n_{\mathrm{B}}\,(p_{\mathrm{T}} > 30$ GeV)	0/[1,2]	0/[1,2]	-	-	-	0
$E_{\mathrm{T}}^{\mathrm{miss}}$	> 430	$[250, 430]$	$[250, 430]$	> 430	> 430	> 250
m_{eff}	$[1100, 1500]$, $[1500, 1900]$, > 1900					
$m_{\mathrm{T}}(p_{\mathrm{T}}(\ell), E_{\mathrm{T}}^{\mathrm{miss}})$	> 100	$[30, 100]$	> 100	$[30, 100]$	> 100	-
$E_{\mathrm{T}}^{\mathrm{miss}}/m_{\mathrm{eff}}$	> 0.25	> 0.15	> 0.1	> 0.2	> 0.25	-
$n_{\mathrm{J}}/p_{\mathrm{T}}(\ell)$	> 0.2		> 0.15	> 0.2		-
Topness	> 4	-	-	> 4	> 4	

Table 5.8: Definition of signal/control/validation regions (SRs/CRs/VRs) for tower **"6J"**

	SR (BV/BT)	WR/TR	VRa	VRb	VR QCD	VR DB
$n_{\ell,\mathrm{base.}}$	1	1	1	1	1	2
$n_{\ell,\mathrm{sig.}}$	1	1	1	1	0	2
$p_{\mathrm{T}}(\ell)$	> 35					
$n_{\mathrm{J}}\,(p_{\mathrm{T}} > 30$ GeV)	≥ 6					≥ 5
$n_{\mathrm{B}}\,(p_{\mathrm{T}} > 30$ GeV)	0/[1,2]	0/[1,2]	-	-	-	0
$E_{\mathrm{T}}^{\mathrm{miss}}$	> 350	> 300	> 250	> 350	> 350	> 250
m_{eff}	$[1100, 1600]$, $[1600, 2100]$, > 2100					
$m_{\mathrm{T}}(p_{\mathrm{T}}(\ell), E_{\mathrm{T}}^{\mathrm{miss}})$	> 175	$[40, 125]$	$[125, 400]$	$[40, 125]$	> 125	-
Aplanarity	> 0.06	< 0.06	< 0.04	> 0.06	> 0.06	< 0.06
Topness	> 4	-	-	> 4	> 4	

Table 5.9: Definition of signal/control/validation regions (SRs/CRs/VRs) for tower **"Lowx"**

	SR (BV/BT)	WR/TR	VRa	VRb	VR QCD	VR DB
$n_{\ell,\text{base.}}$	1	1	1	1	1	2
$n_{\ell,\text{sig.}}$	1	1	1	1	0	2
$p_{\mathrm{T}}(\ell)$			$[6, 35]$			-
$n_{\mathrm{J}}\,(p_{\mathrm{T}} > 30$ GeV)			≥ 4			≥ 3
$n_{\mathrm{B}}\,(p_{\mathrm{T}} > 30$ GeV)	0/[1,2]	0/[1,2]	-	-	-	0
$p_{\mathrm{T}}(j_4)$			> 80			-
$E_{\mathrm{T}}^{\mathrm{miss}}$	> 350	> 300	> 300	> 350	> 350	> 250
m_{eff}			> 1900			
$m_{\mathrm{T}}(p_{\mathrm{T}}(\ell), E_{\mathrm{T}}^{\mathrm{miss}})$	> 100	$[30, 100]$	$[100, 450]$	$[30, 100]$	> 100	-
Aplanarity	> 0.02	< 0.02	< 0.02	> 0.02	> 0.02	< 0.04
Topness	> 4	-	-	> 4	> 4	

Table 5.10: Definition of signal/control/validation regions (SRs/CRs/VRs) for tower **"Highx"**

	SR (BV/BT)	WR/TR	VRa	VRb	VR QCD	VR DB
$n_{\ell,\text{base.}}$	1	1	1	1	1	2
$n_{\ell,\text{sig.}}$	1	1	1	1	0	2
$p_{\mathrm{T}}(\ell)$			> 35			
$n_{\mathrm{J}}\,(p_{\mathrm{T}} > 30$ GeV)			≥ 4			≥ 3
$n_{\mathrm{B}}\,(p_{\mathrm{T}} > 30$ GeV)	0/[1,2]	0/[1,2]	-	-	-	0
$E_{\mathrm{T}}^{\mathrm{miss}}$	> 300	> 300	> 300	> 300	> 300	> 250
m_{eff}			> 2000			
$m_{\mathrm{T}}(p_{\mathrm{T}}(\ell), E_{\mathrm{T}}^{\mathrm{miss}})$	> 300	$[30, 125]$	$[125, 600]$	$[30, 125]$	> 450	-
$E_{\mathrm{T}}^{\mathrm{miss}}/m_{\mathrm{eff}}$	> 0.25	> 0.2	> 0.15	> 0.25	> 0.25	> 0.2
Aplanarity	> 0.01	< 0.01	< 0.01	> 0.01	> 0.01	< 0.02
Topness	> 4	-	-	> 4	> 4	

Table 5.11: Definition of signal/control/validation regions (SRs/CRs/VRs) for tower **"3B"**

	SR	TR	VR m_{T}	VRb	VR QCD
$n_{\ell,\mathrm{base.}}$	1	1	1	1	1
$n_{\ell,\mathrm{sig.}}$	1	1	1	1	0
$p_{\mathrm{T}}(\ell)$			> 15		
$n_{\mathrm{J}}\,(p_{\mathrm{T}} > 30$ GeV)			≥ 7		
$n_{\mathrm{B}}\,(p_{\mathrm{T}} > 30$ GeV)			≥ 3		
$E_{\mathrm{T}}^{\mathrm{miss}}$	> 300	> 250	> 250	> 250	> 300
m_{eff}			$[1000, 1750]$, > 1750		
$m_{\mathrm{T}}(p_{\mathrm{T}}(\ell), E_{\mathrm{T}}^{\mathrm{miss}})$	> 175	$[30, 125]$	$[125, 450]$	$[30, 125]$	> 175
Aplanarity	> 0.01	-	-	> 0.01	> 0.01
$\min\limits_{i=1-4} \Delta\phi(j_i, E_{\mathrm{T}}^{\mathrm{miss}})$	> 0.45	< 0.45	< 0.45	> 0.3	> 0.45
Topness	> 6	-	-	> 6	> 6

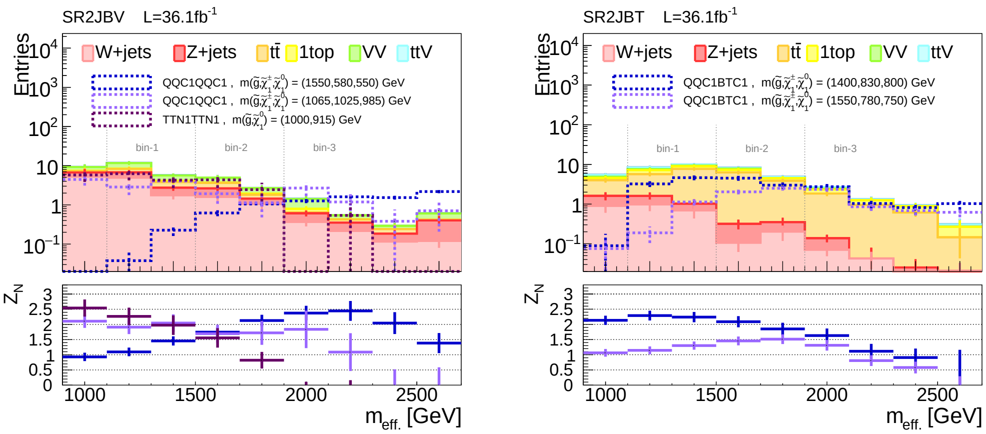

(a) (b)

Figure 5.12: m_{eff} distribution in the (a) b-vetoed (BV) and (b) b-tagged (BT) slices of the optimized **2J** signal region. Bottom row display the sensitivity $Z_N := S/\sqrt{B + \alpha^2 B^2}$ for each reference signals.

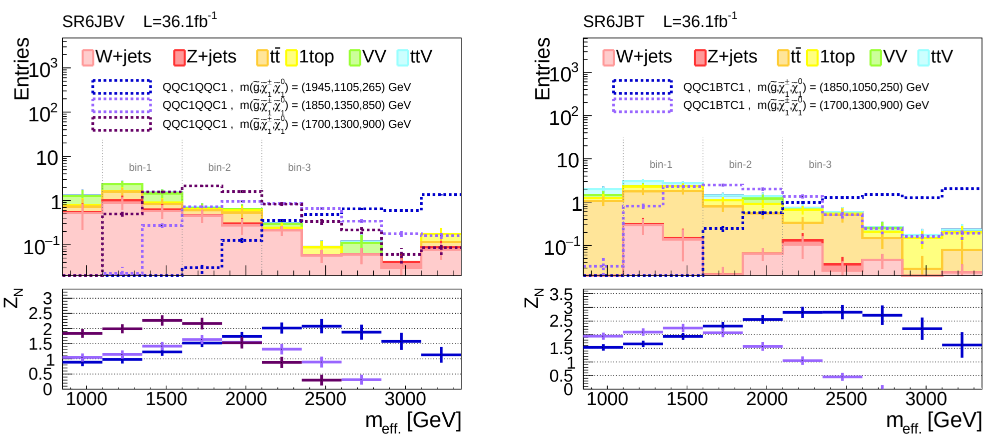

(a) (b)

Figure 5.13: m_{eff} distribution in the (a) b-vetoed (BV) and (b) b-tagged (BT) slices of the optimized **6J** signal region. Bottom row display the sensitivity $Z_N := S/\sqrt{B + \alpha^2 B^2}$ for each reference signals.

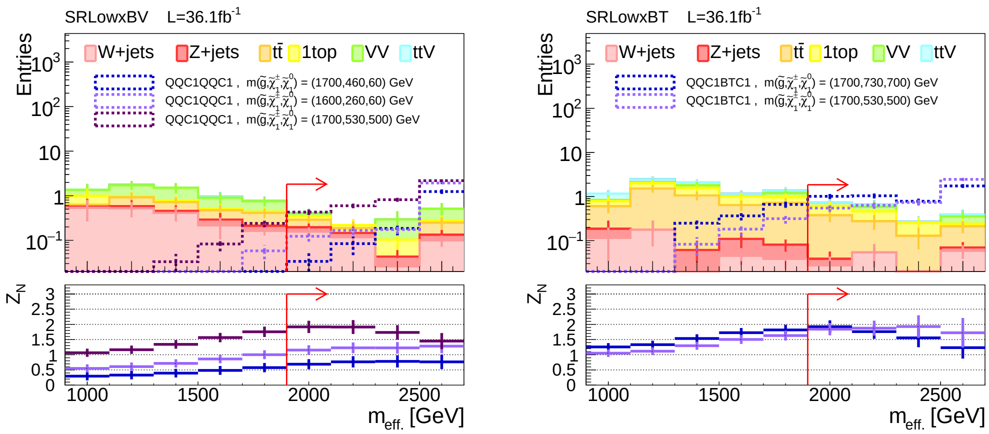

(a) (b)

Figure 5.14: m_{eff} distribution in the (a) b-vetoed (BV) and (b) b-tagged (BT) slices of the optimized **Low-x** signal region. The red arrow indicates the cut position of m_{eff}. Bottom row display the sensitivity $Z_N := S/\sqrt{B + \alpha^2 B^2}$ for each reference signals.

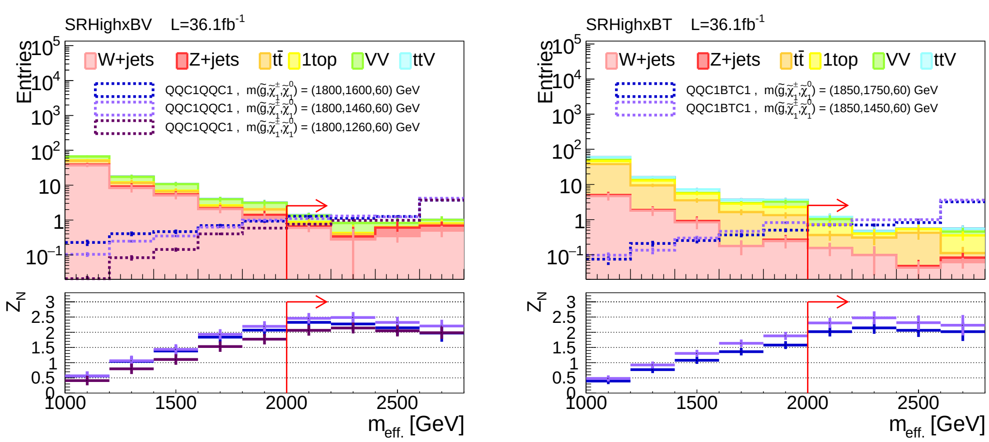

(a) (b)

Figure 5.15: m_{eff} distribution in the (a) b-vetoed (BV) and (b) b-tagged (BT) slices of the optimized **High-x** signal region. The red arrow indicates the cut position of m_{eff}. Bottom row display the sensitivity $Z_N := S/\sqrt{B + \alpha^2 B^2}$ for each reference signals.

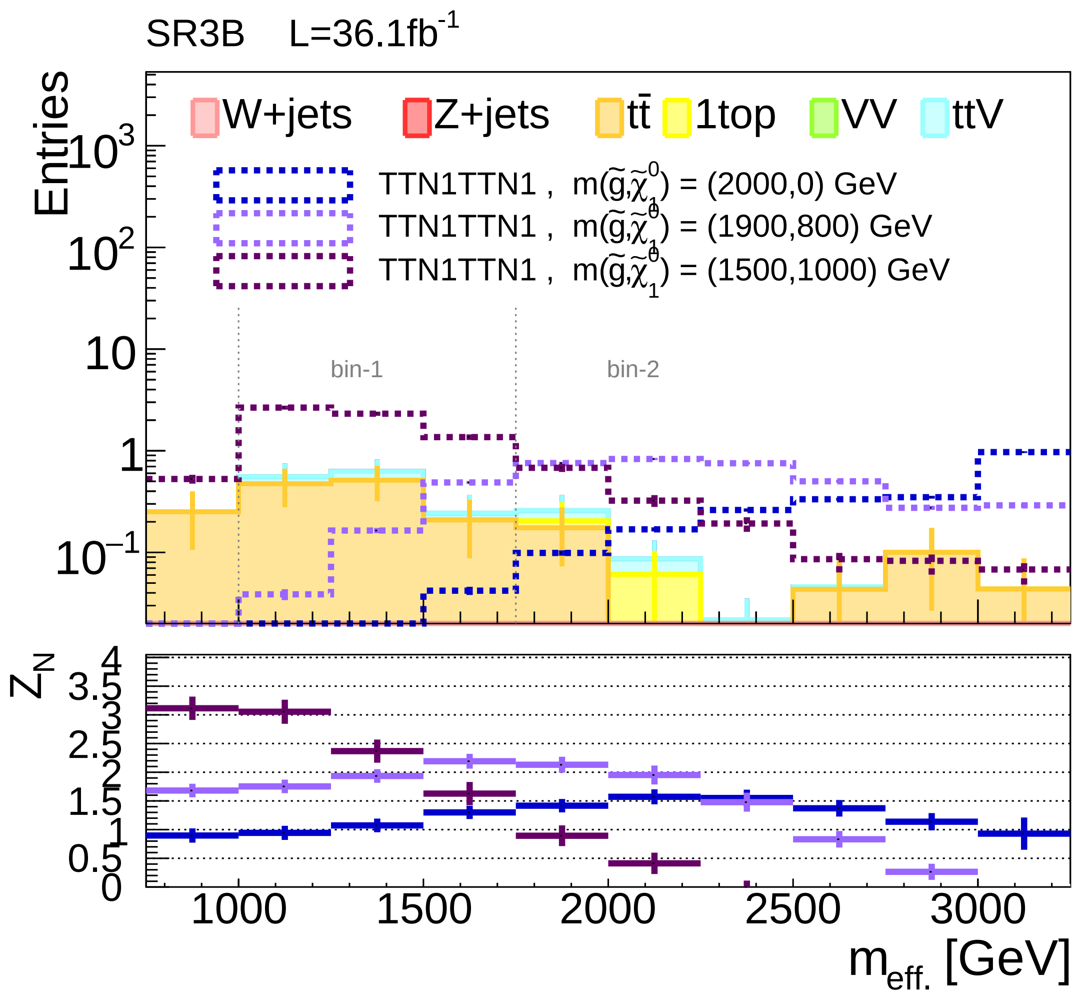

(a)

Figure 5.16: m_{eff} distribution in the (a) b-vetoed (BV) and (b) b-tagged (BT) slices of the optimized **3B** signal region. Bottom row display the sensitivity $Z_N := S/\sqrt{B + \alpha^2 B^2}$ for each reference signals.

5.3.4 Expected Sensitivity

The limits expected by the optimized signal regions are calculated for the grids of reference models. The expected exclusion limit with $L = 36.1\mathrm{fb}^{-1}$ for the TTN1TTN1 `Direct` grid is shown in 5.17. The dashed lines on the left plots indicate the exclusion provided by a single m_{eff} bin, and the solid lines being the limit given by respective signal region towers with combined bins. The ultimately sensitivity provided by the combined towers are shown in the right plots. Since the all five towers are not completely orthogonal (**2J** and **Low-x**, **6J** and **High-x** are partially overlapped), there are four possible way of combining orthogonal towers: {**2J**, **6J**, **3B**}, {**2J**, **High-x**, **3B**}, {**Low-x**, **6J**, **3B**}, and {**Low-x**, **High-x**, **3B**}. The final result will be provided using the combination with best expected sensitivity. The expected sensitivity for QQC1QQC1 and QQC1BTC1 are presented in Figure 5.18 and Figure 5.19. Nice complementarity between the signal region towers are shown. No suspicious structure indicating local over-optimization onto specific mass region is found, ensuring the inclusive sensitivity of the search.

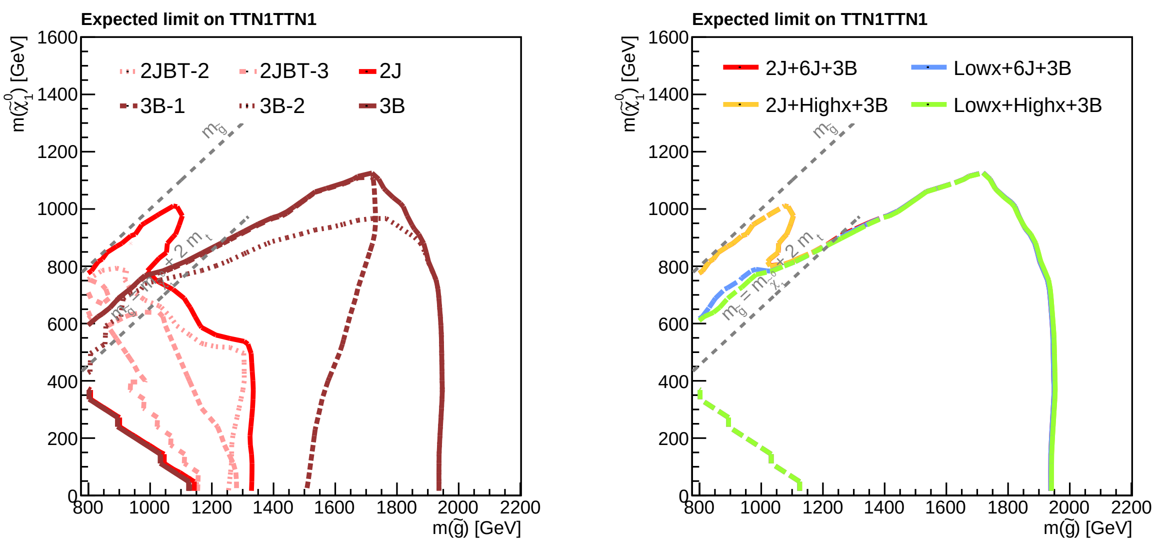

(a)

Figure 5.17: Expected exclusion (95%CL) for the benchmark model TTN1TTN1. The left plot shows the exclusion limit set by individual signal region m_{eff}-bin (dashed) or a tower (solid). The contours in the right plot display the ultimate sensitivity provided by the combined fit. The hypothetical test will be carried out using the best performed combination, in deriving the final result.

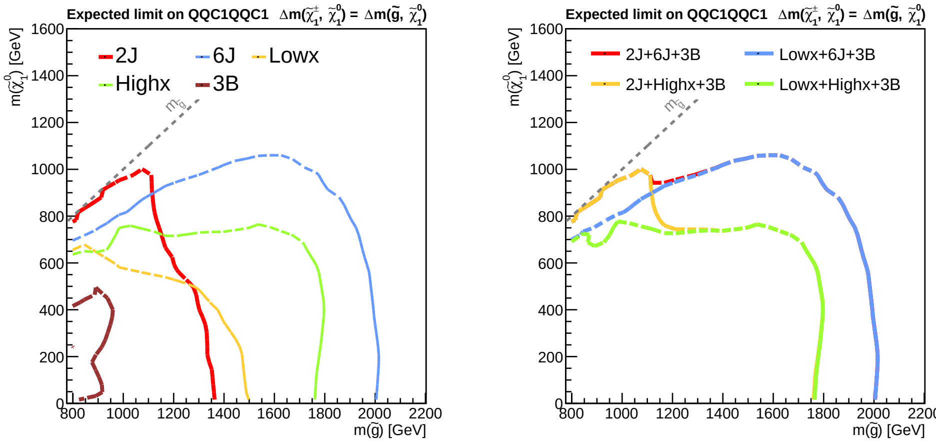

(a)

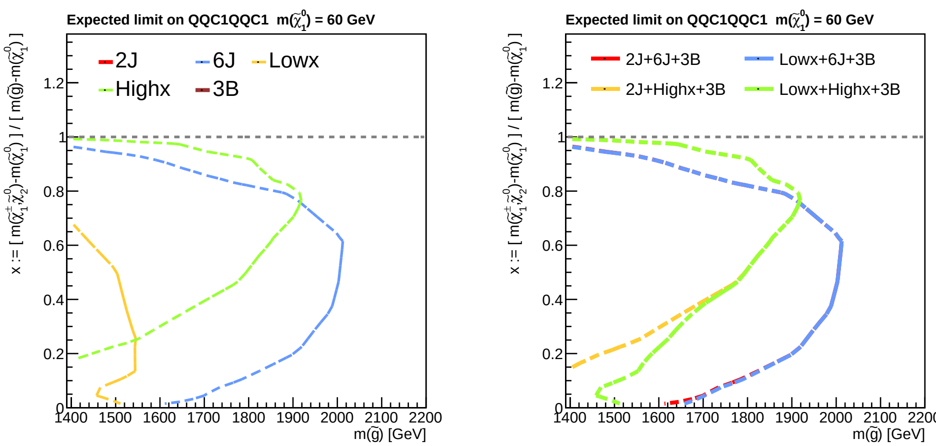

(b)

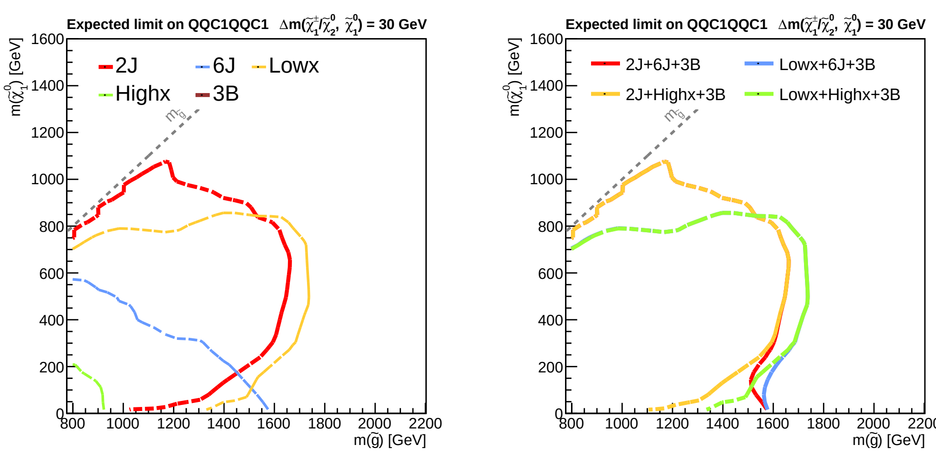

(c)

Figure 5.18: Proejcted expected exclusion (95%CL) for the benchmark model QQC1QQC1 onto the (a)$x = 1/2$ (b)$m_{\tilde{\chi}_1^0} = 60$ GeV (c) $\Delta m(\tilde{\chi}_1^{\pm}, \tilde{\chi}_1^0) = 30$ GeV grid. The contours in the right plot display the ultimate sensitivity provided by the combined fit. The hypothetical test will be carried out using the best performed combination, in deriving the final result.

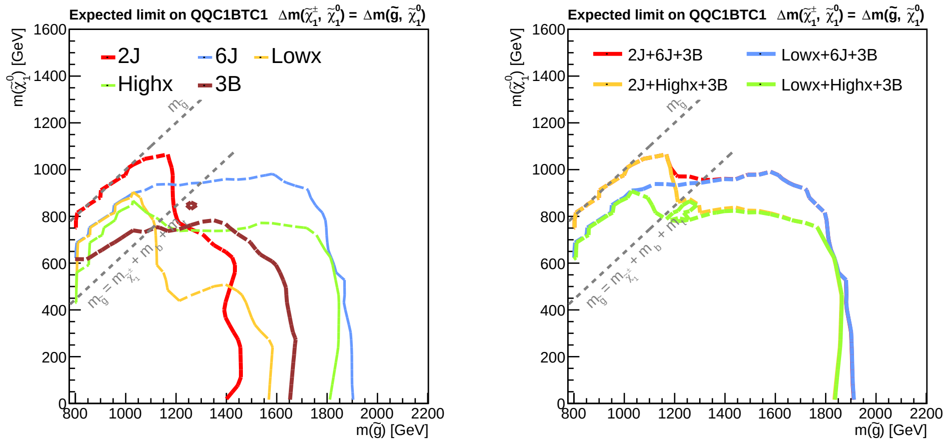

(a)

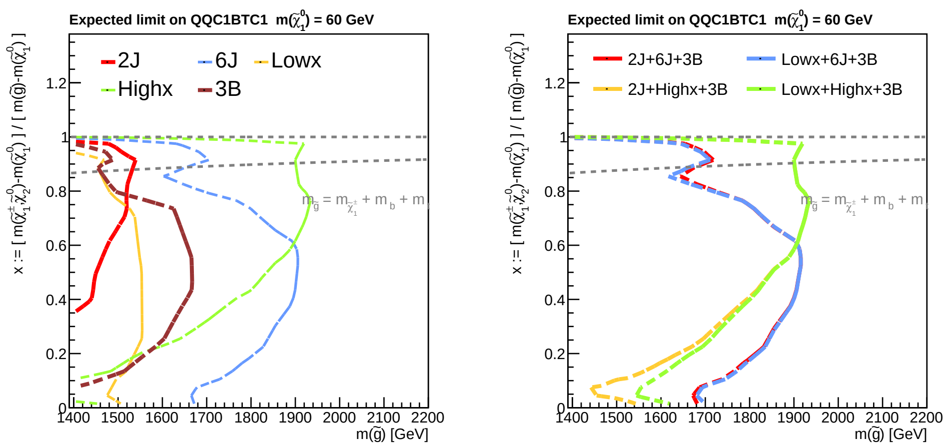

(b)

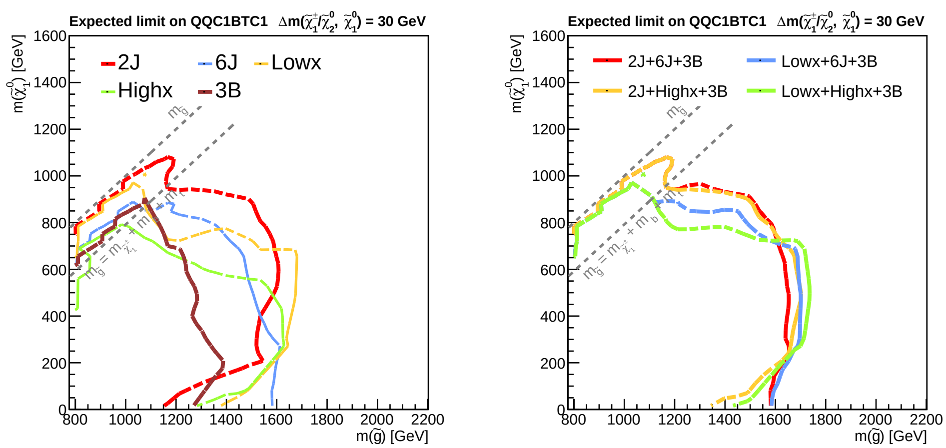

(c)

Figure 5.19: Proejcted expected exclusion (95%CL) for the benchmark model QQC1BTC1 onto the (a)$x = 1/2$ (b)$m_{\tilde{\chi}_1^0} = 60$ GeV (c) $\Delta m(\tilde{\chi}_1^{\pm}, \tilde{\chi}_1^0) = 30$ GeV grid. The contours in the right plot display the ultimate sensitivity provided by the combined fit. The hypothetical test will be carried out using the best performed combination, in deriving the final result.

Chapter 6

Standard Model Background Estimation

Due to the enormously large cross-section of SM processes with respect to the signal, it is the fate for new physics searches to keep exploring the phase space with tight event selections. The consequence is the highly untypical kinematics for the remained SM backgrounds, and the modeling is usually challenging since the standard MC simulation is not necessarily accountable as seen in Sec. 6.2.1.

This is why (semi-)data-driven approach is remarkably motivated in search analyses. The most commonly done practice over the past analyses is to apply an in-situ correction to MC using the data events around the signal region ("control region"). The prediction in signal regions is then given by the corrected MC, assuming the modeling on the phase space between the control region and the signal region is correct. We refer this semi-data driven method as **"kinematical extrapolation method"**. The advantage of the kinematical extrapolation method is that the prediction does not suffer from severe statistical fluctuation, and often leading to relatively smaller total uncertainty. However the drawback is that it has to still rely on MC in the extrapolation from control regions to signal regions, which uncertainty is rather difficult to capture and quantify.

Since statistical error often dominates the uncertainty in the signal regions, it has no point in competing on a few percent precision in the estimation. Instead, it is more sensible to pursue the robustness avoiding risk to introducing unknown systematic effects, even if it will result in larger estimation uncertainty. A nearly fully data-driven method (**"object replacement method"**) is meant to that purpose, estimating particular background components by extrapolating from the 2-lepton control regions. In the study, the object replacement method is utilized as much as possible, while the rest of all is covered by the kinematical extrapolation method.

This section provides a complete description on the background estimation procedures employed in the analysis. After reviewing the breakdown in the signal regions and how they evade the event selection, both estimation methods will be described in detail. Finally, the performance is demonstrated using the data in a certain set of regions.

6.1 Background Breakdown in the Signal Regions

The breakdown of physics processes in the signal regions are shown in Figure 6.1. $W+$jets and top backgrounds ($t\bar{t}+Wt$, mostly $t\bar{t}$) dominate over the b-tagged and b-vetoed regions respectively. The **3B** towers are completely dominated by $t\bar{t}$, where 60 % of them are with heavy flavor jets via radiative gluon splitting ($t\bar{t}+cc/bb$) while the rest are with one light flavor jet or hadronically decaying τ faking into b-tagged jet ($t\bar{t}+b_{\mathrm{fake}}$).

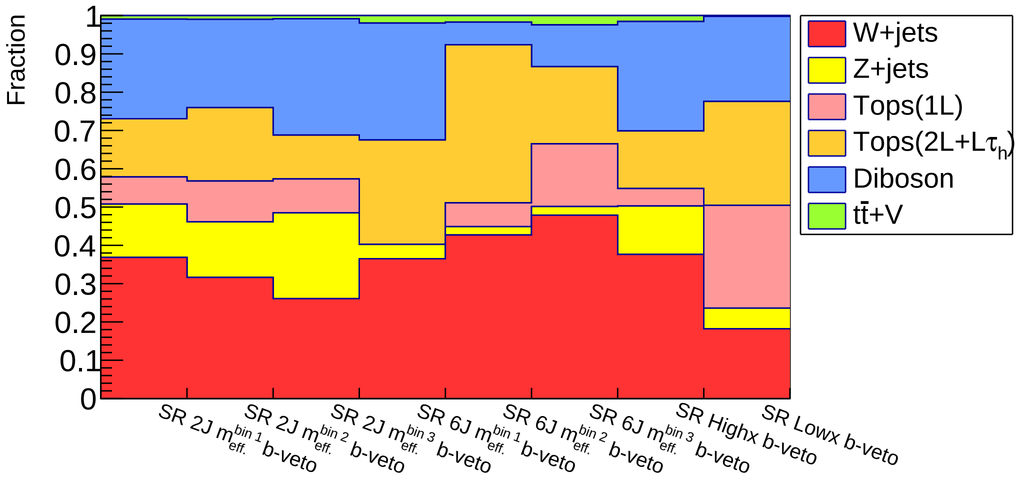

(a)

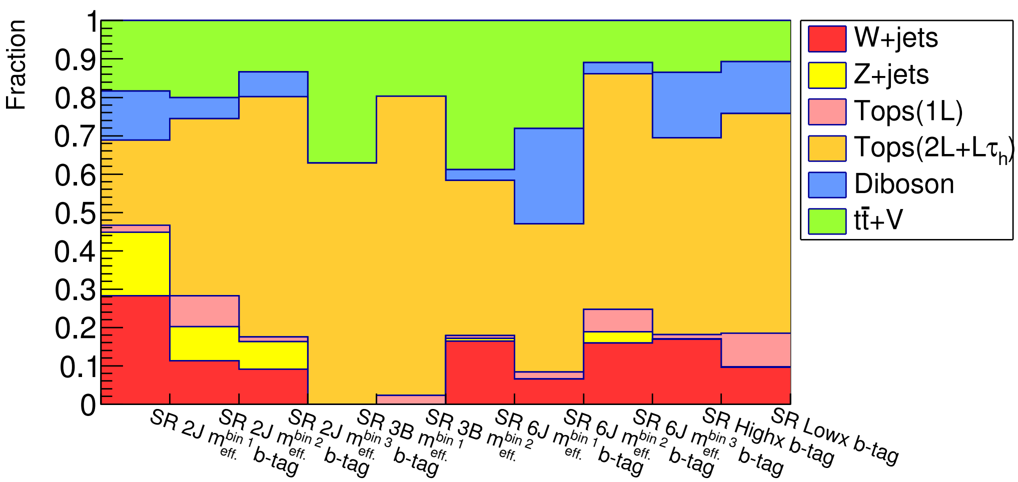

(b)

Figure 6.1: Background composition in terms of physics processes in the (a) BV, and (b) BT/3B signal regions. $t\bar{t}$ and single-top are merged as "Tops", and the semi-leptonic and di-leptonic components are respectively labeled as "1L" and "$2L+L\tau_h$".

Backgrounds are also categorized depending on the mechanism they pass the selection, and different estimation methods are applied based on it. The categorization is shown in Table 6.1.

Table 6.1: Background classification in terms of the origin.

Category		Origin	Main physics process	Estimation method
"Semi-leptonic"		On-shell W with diluted m_{T} / High-mass Drell-Yan	$(W, t\bar{t}, VV) \to \ell\nu$ + jets	Kine. extp. / MC
"Di-leptonic"	$\ell\ell_{\mathrm{mis.}}$	"Out Acc."	$(t\bar{t}, Wt, WW) \to \ell\nu\ell\nu$ + jets	Kine. extp.
		"Mis. Reco."		Obj. rep.
		"Mis. ID"		Obj. rep.
		"Mis. OR"		Kine. extp.
	$\ell\tau_{\mathrm{h}}$	1 real-lepton + τ_h	$t\bar{t}, Wt, WW \to \ell\nu\tau\nu$ + jets	Obj. rep.
"Fake"		0 real-lepton + 1 fake-lepton.	$W \to \tau\nu$, $Z \to \nu\nu$	MC

The **"semi-leptonic"** category is defined by events with exactly one real light flavor lepton (e or μ). In the SM, these are uniquely provided by processes with leptonically decaying W-boson, such as from $W+$jets and $t\bar{t}$. This is by far the dominant component at 1-lepton pre-selection level, however is drastically suppressed after a tight m_{T} cut since the they are largely truncated at m_W. After the m_{T} cut, the remnant events are typically either: 1) Drell-Yan process with virtual heavy intermediate W boson, or 2) events with badly measured MET leading to prolonged tail in m_{T}. The former contribution is typically larger although the latter becomes addressing with increasing jet activity, as shown in Figure 6.2. In this category, the dominant processes $W+$jets and $t\bar{t}+Wt$ are estimated by a semi-data driven approach referred as "kinematical extrapolation method" as detailed in following sub-section, while the other processes are taken from pure MC prediction since they are minor.

The **"di-leptonic"** category consists of processes with real two leptons including τ, mainly from di-leptonic decaying $t\bar{t}$, Wt and WW. The presence becomes highly significant with respect to the "semi-leptonic" after the m_{T} cut, since the source of missing transverse momentum is multiple thus they have no reason to cut-off at m_W. They fall into 1-lepton regions through two channels, namely 1) "$\ell\ell_{\mathrm{mis.}}$" ("missing lepton"): events with two real light flavor leptons and one of them fails the "baseline" requirement (See Sec. 3.10), and "$\ell\tau_{\mathrm{h}}$": events with a real light flavor lepton and a hadronically decaying tau lepton.
The origin of "missing lepton" is further four-fold and symbolized as follow:

"Out Acc."
: Leptons traveling outside the acceptance of "baseline" requirement i.e. $p_{\mathrm{T}} > 7(6)$ GeV, $|\eta| < 2.47(2.5)$ for electrons (muons).

"Mis. Reco"
: Leptons within the (p_{T}, η) acceptance but failing the reconstruction.

"Mis. ID"
: Reconstructed leptons within the (p_{T}, η) acceptance but failing the electron/muon ID.

"Mis. OR"

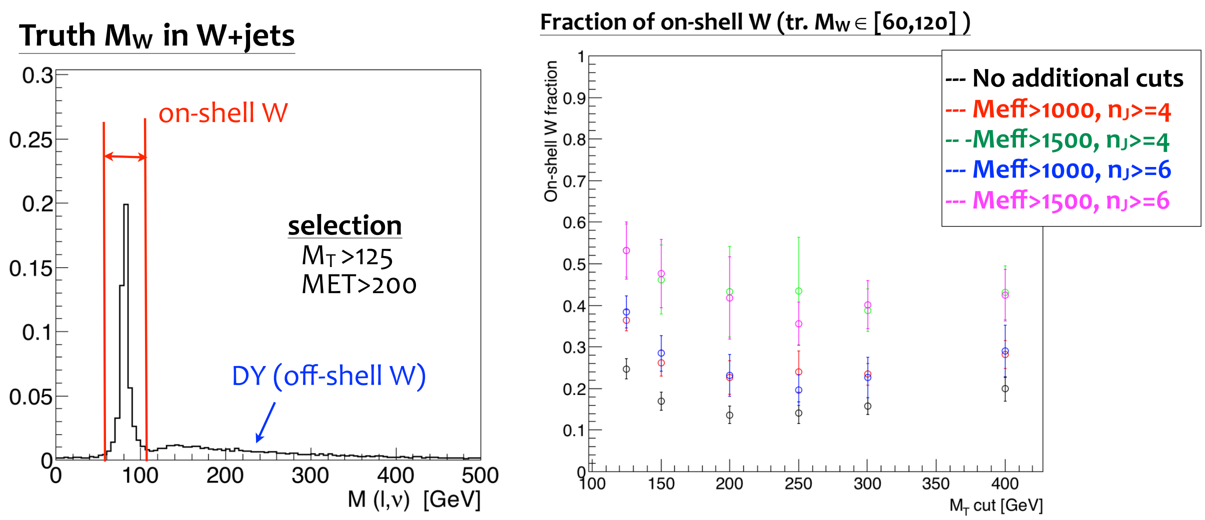

(a) (b)

Figure 6.2: (a) Truth invariance mass $m(\ell, \nu)$ of high-m_{T} W + jets events. Ideally there are only high-mass Drell-Yan type of events, however due to the finite detector resolution, a fraction of on-shell W events with badly measured MET sneak into regions with $m_{\mathrm{T}} > m_W$. (b) The fraction of on-shell events defined by $m(\ell, \nu) \in [60, 125]$, as a function of the m_{T} cut. It is generally below 50 %, however increases with higher jet activity in the event.

Reconstructed leptons within the (p_{T}, η) acceptance passing the ID, but killed in the overlap removal (Sec. 3.7).

One nice thing about this **"di-leptonic"** component is that 2-lepton regions are available for control regions in the estimation. Since no signal regions are set there, exactly the same phase space with respect to SRs can be exploited. The estimation is done by the "object replacement method", however the "Out Acc." and "Mis. OR" events are estimated together with the **"semi-leptonic"** events due to some technical challenges. The third category **"fake"** involves events with a fake lepton, which is not negligible in regions dealing with soft leptons (**"2J"** and **"Low-x"**). The estimation fully relies the MC prediction. Dominant contribution is from $W \to \tau\nu$ and $Z \to \nu\nu$ which accompany a large MET from neutrinos. The contribution from the multi-jets process is supposed to be negligible, it is nevertheless dedicatedly cross-checked since the impact could be hazardous due to the huge cross-section. This is done using a series of validation regions referred as VRs-QCD, shown in Appendix C.3.

The background breakdown based on this categorization is summarized in Figure 6.3 where **"semi-leptonic"** and **"di-leptonic"** (particularly "$\ell\tau_h$") are shown to be overwhelmingly dominant in BV and BT/3B signal regions respectively.

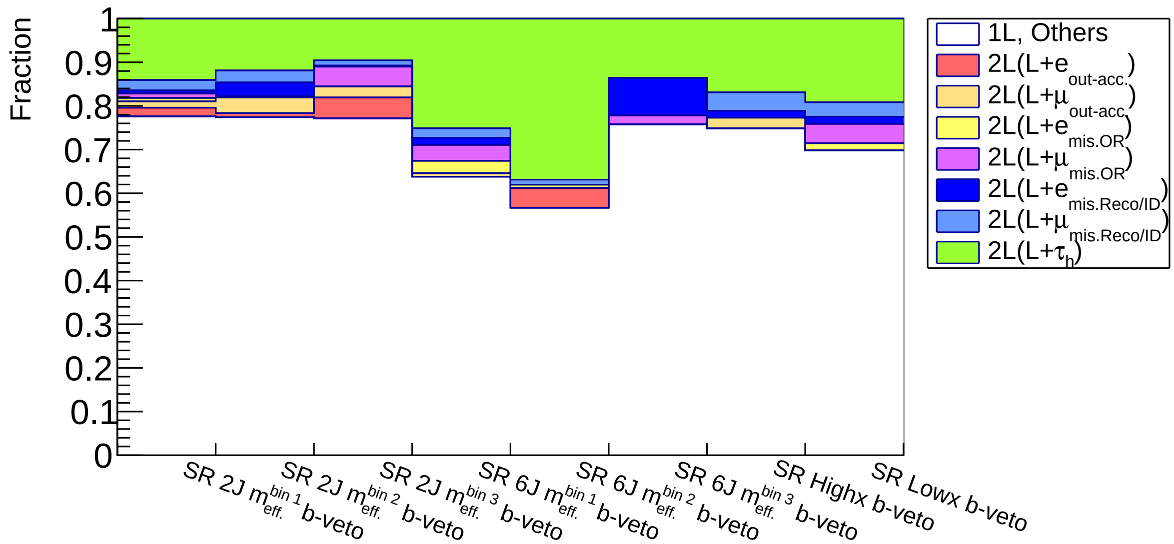

(a)

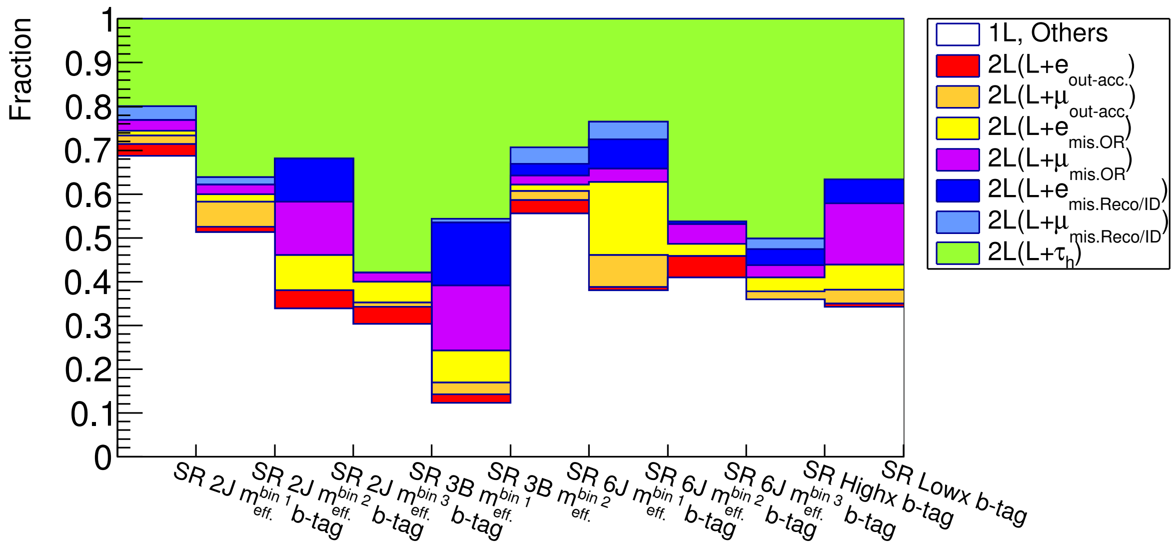

(b)

Figure 6.3: Background breakdown in the (a) BV, and (b) BT/3B signal regions based on the classification in Table 6.1. While the BV signal regions are dominated by the "semi-leptonic" category, BT/3B signal regions are mainly by "di-leptonic", especially the "$\ell\tau_h$" component.

6.2 The Kinematical Extrapolation Method

The main consideration in the kinematical extrapolation method is definition of control regions. It is basically a procedure of 1) specifying kinematical variables that are well-modeled by MC and suitable for the extrapolation from control regions (CRs) to signal regions (Sec. 6.2.1), and 2) deciding the selection of CRs (Sec. 6.2.2). MC is then normalized to data in the CRs. The measured normalization factors and yields in CRs are extensively discussed in Sec 6.2.3.

6.2.1 MC vs Data Comparison and the MC mis-modeling

The MC modeling of dominant background processes ($W+$jets and $t\bar{t}$) is examined in pre-selection regions defined in Table 6.2. Each pre-selection region is intended to be dominated by the process being tested.

Table 6.2: Definition of pre-selection regions and corresponding tested physics processes. MET trigger requirement, event cleaning described Sec. 5.2, $n_{\mathrm{J}} \geq 2$ and $E_{\mathrm{T}}^{\mathrm{miss}} > 250$ are applied as common selection.

Region name	$n_{\ell,\mathrm{base.}}$	$n_{\ell,\mathrm{sig.}}$	$p_{\mathrm{T}}(\ell_1)$ [GeV]	n_{B} ($p_{\mathrm{T}} > 30$ GeV)	Tested processes
1LBV	1	1	> 35	0	$W+$jets
1LBT	1	1	> 35	$[1,2]$	$t\bar{t}/Wt$ ($\rightarrow bqqb\ell\nu$)
2LBT	2	2	-	$[1,2]$	$t\bar{t}/Wt$ ($\rightarrow b\ell\nu b\ell\nu$)
1L3B	1	1	> 15	≥ 3	$t\bar{t}+cc/bb$, $t\bar{t}+b_{\mathrm{fake}}$

W $+$ jets :

Figure 6.4 - 6.5 show the kinematic distributions in the **1LBV** pre-selection region where $W+$jets is enriched. While the bulk phase space is well-described by MC, there is generally a striking overestimation by MC in the tail regions. Discrepancy is mainly observed in distributions related to jet activity, particularly in jet multiplicity when it is above 3. Considering that the jets are all from ISRs or FSRs, and that the jet multiplicity in the event roughly corresponds to the number of QCD-order of the processes, this implies the mis-modeling is due to the truncated higher order contribution beyond NNLO in the simulation. This might not be surprising giving that the MC sample (generated by Sherpa 2.2) does not include loop diagrams beyond NLO and neither diagrams with more than 5 partons in the final state.

Variables that do not scale with transverse momenta of outgoing particles ("non-scaling" variables), such as m_{T} or aplanarity, keep relatively well-modeled up to the tails. Particularly, m_{T} is by construction insensitive to most of the kinematics since the tail is determined by the mass-line of W-boson or MET resolution. aplanarity is also supposed to be robust since it takes a form of ratio of jet momenta. Therefore, these variables are decided to be used for the extrapolation from CRs to SRs. Note that the m_{T} cut-off ($m_{\mathrm{T}} \sim m_W$) is slightly mis-modeled typically when tighter selections are applied, presumably due to the propagated effect from the ISR/FSR mis-modeling mentioned above. The effect becomes visible especially in CRs (e.g. Figure C.4.5) or b-vetoed SRs.

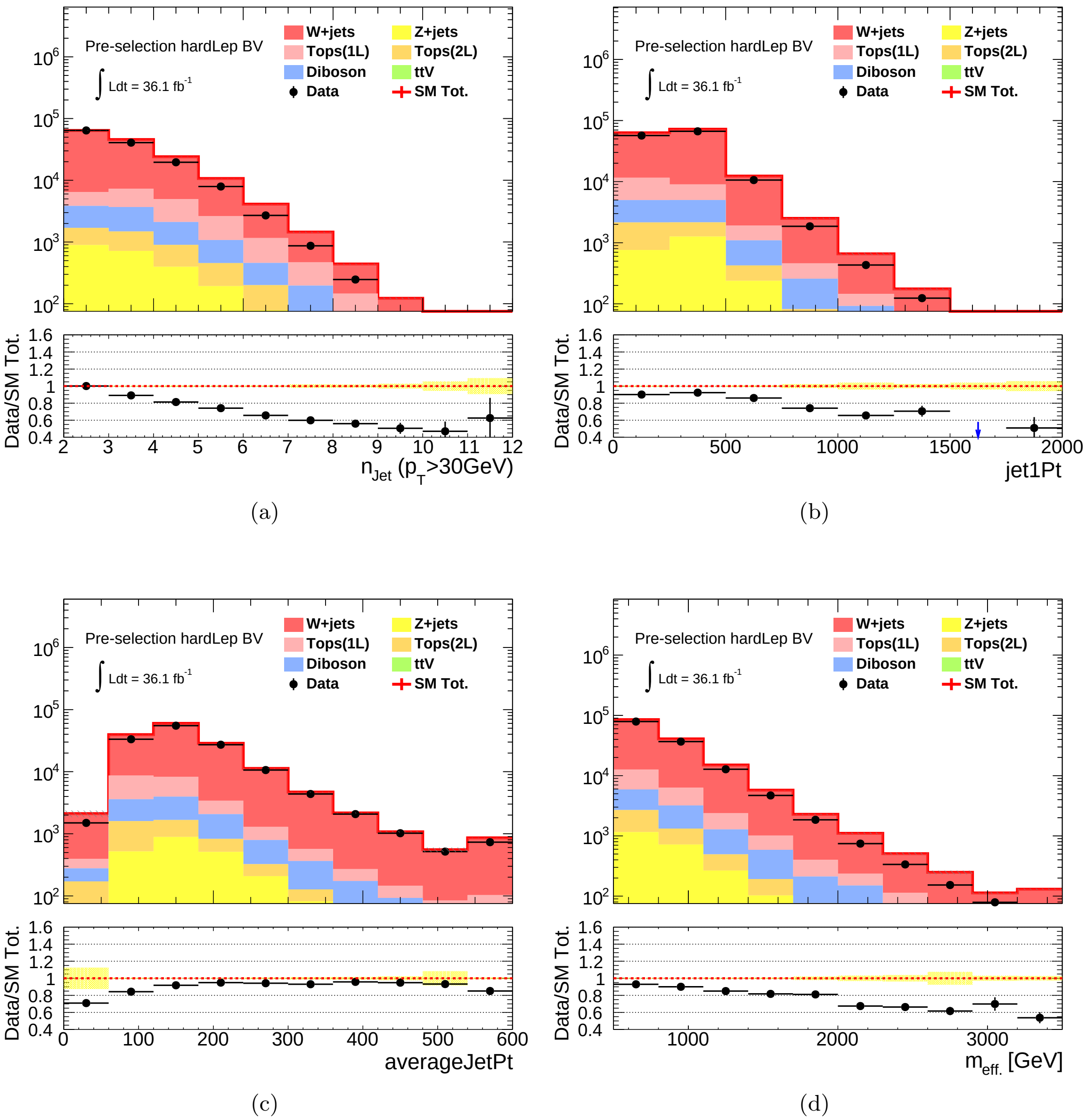

Figure 6.4: Kinematical distribution of (a) Jet multiplicity ($p_T > 30$ GeV) (b) leading-jet pt (c) average jet pt ($p_T > 30$ GeV) (d) $m_{\rm eff}$ in the **1LBV** pre-selection region.

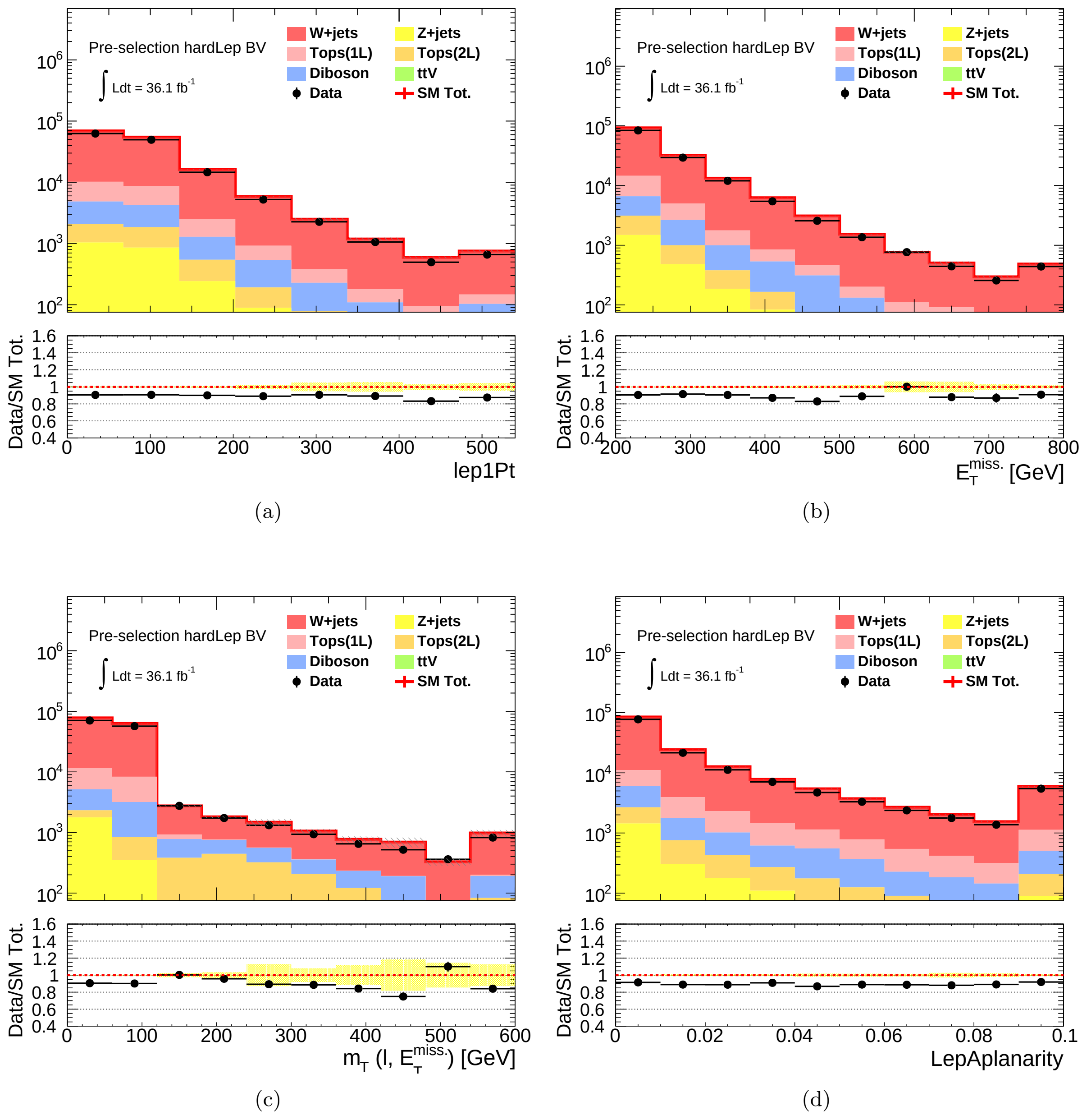

Figure 6.5: Kinematical distribution of (a) leading-lepton pt (b) $E_{\mathrm{T}}^{\mathrm{miss}}$ (c) m_{T} (d) aplanarity in the **1LBV** pre-selection region.

Semi-leptonic $t\bar{t}$:

Figure 6.6 - 6.7 are the kinematic distributions in the **1LBT** pre-selection region dominated by semi-leptonically decaying $t\bar{t}$. It is seen that MC is overshooting the data with increasing transverse momenta of outgoing particles such as jets, lepton and MET.

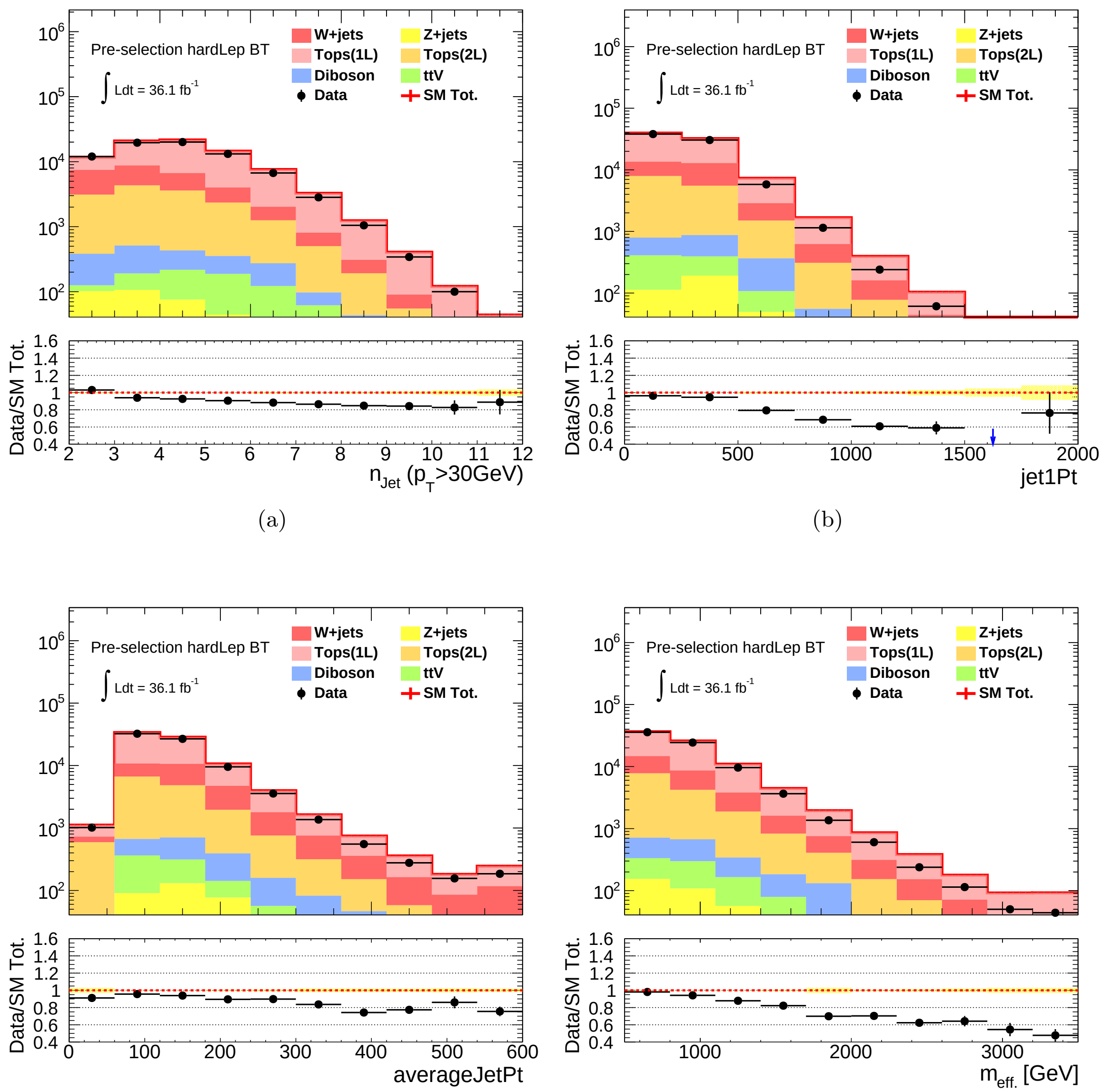

(a) (b) (c) (d)

Figure 6.6: Kinematical distribution of (a) Jet multiplicity ($p_T > 30$ GeV) (b) leading-jet pt (c) average jet pt ($p_T > 30$ GeV) (d) m_{eff} in the **1LBT** pre-selection region.

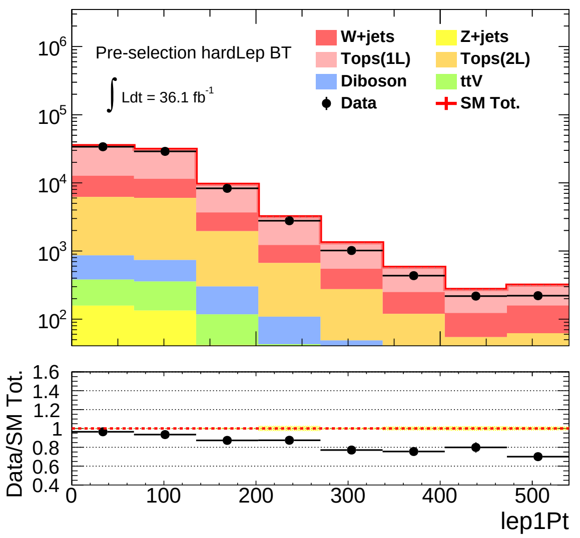

(a)

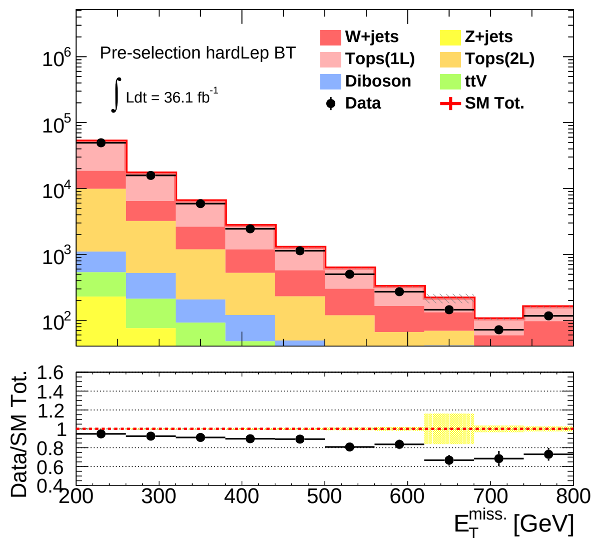

(b)

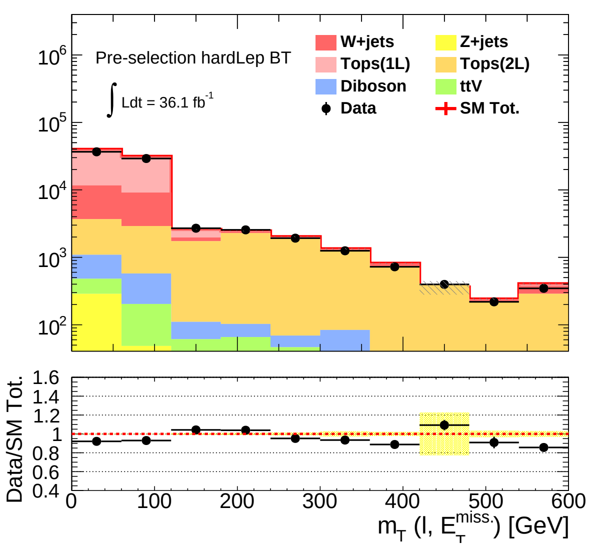

(c)

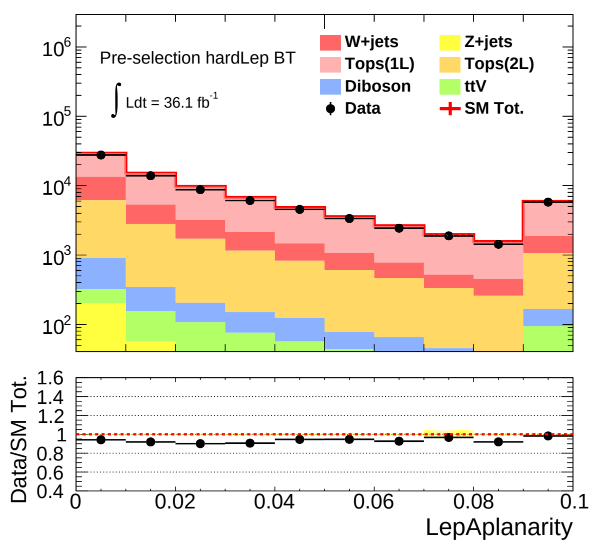

(d)

Figure 6.7: Kinematical distribution of (a) leading-lepton pt (b) $E_{\mathrm{T}}^{\mathrm{miss}}$ (c) m_{T} (d) aplanarity in the **1LBT** pre-selection region.

The mis-modeling in m_{eff} distribution is particularly concerning, given that the signal regions are designed to exploit its shape. The leading source of the mis-modeling is suspected to be in the description of ISR or FSR radiation. This is because hard jets ($p_{\text{T}} > 200$ GeV) become more often non-$t\bar{t}$ origin in the tail of m_{eff}, as demonstrated by Figure 6.8, although $t\bar{t}$ does have 2-4 jets in its tree-level decay.

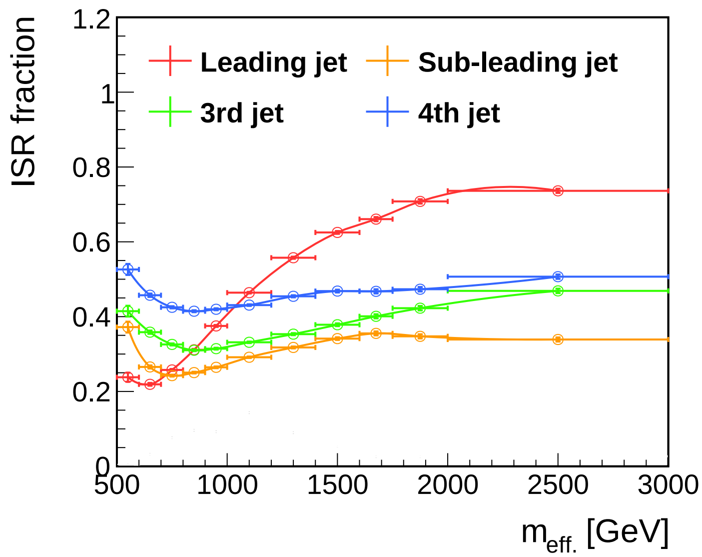

Figure 6.8: Fraction of ISR and FSR jets in the 4 leading jets with the largest transverse momenta, defined by N_{events}(i-th leading that do not match either jets from $t\bar{t}$ decay by $\Delta R < 0.2$)/N_{events}(all i-th leading jets).

This is in fact also supported by a series of MC reweighting studies shown in Figure 6.9 where linear reweighting in various top kinematic variables is attempted to correct the the slope of data/MC in m_{eff}. It turns that $p_T(t\bar{t})$ is the variable most sensitive to the mis-modeling, while reweighting in other variables can only change the normalization but the slope. This strongly indicates that the primary problem is in the radiation recoiling the $t\bar{t}$ rather than in the internal kinematics of the $t\bar{t}$ system. The discrepancies in other variables is also shown to be recovered by the same $p_{\text{T}}(t\bar{t})$ reweighting in Figure C.1.3-C.1.4 in appendix C.1).
In contrast, the "non-scaling" variables such as m_{T} and aplanarity look relatively well-modeled. Therefore, the same estimation strategy is taken as the case of $W+$jets i.e. taking these as the extrapolating variables from CRs to SRs.

It is still acceptable though, note that the modeling of m_{T} is not perfect. For instance in Figure 6.6, there is a small bump-like structure in the ratio plot around $m_{\text{T}} = 100 \sim 200$ GeV corresponding the cut-off of the semi-leptonic $t\bar{t}$. This is suspected to be due to the interference between $t\bar{t} + Wt \to WWbb$ and other $WWbb$ diagrams which is not accounted by the generator, which effect is addressing in regions where bulk $t\bar{t}$ amplitude is suppressed. Corresponding uncertainty is evaluated in Sec. 7.2.1 and assigned as theory systematics.

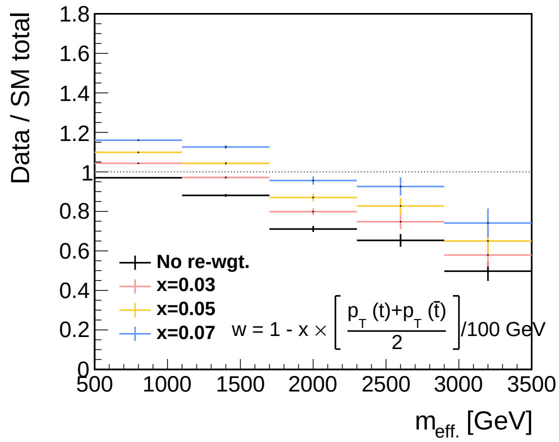

(a)

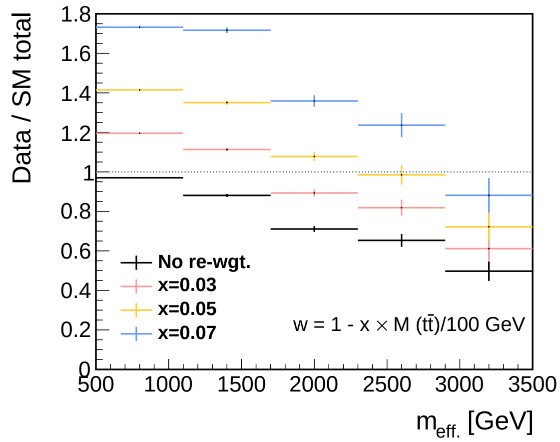

(b)

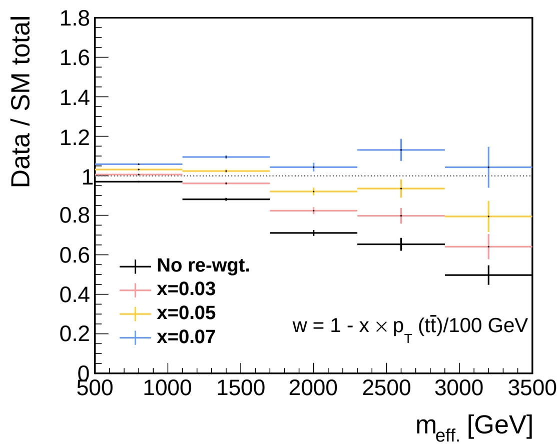

(c)

Figure 6.9: Response of data/MC in m_{eff} against a linear reweighting of $t\bar{t}$ events in terms of (a) average top transverse momentum ($(p_{\text{T}}(t)+p_{\text{T}}(\bar{t}))/2$), (b) invariant mass of $t\bar{t}$ system ($m_{t\bar{t}}$) and (c) transverse momentum of $t\bar{t}$ system ($p_{\text{T}}(t\bar{t})$). $p_{\text{T}}(t\bar{t})$ is found to be sensitive to the slope of m_{eff} and improve the data/MC discrepancy, while the others are only capable of shifting the normalization.

Di-leptonic $t\bar{t}$:

Figure 6.10-6.11 plot the kinematic distributions in the 2-lepton b-tagged pre-selection region (**2LBT**) where di-leptonically decaying $t\bar{t}$ dominates.

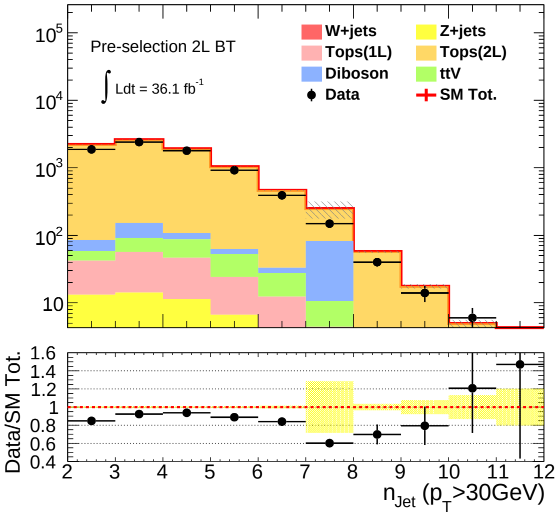

(a)

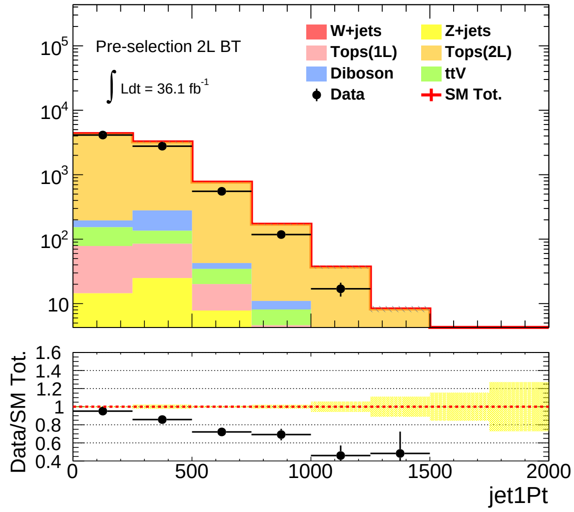

(b)

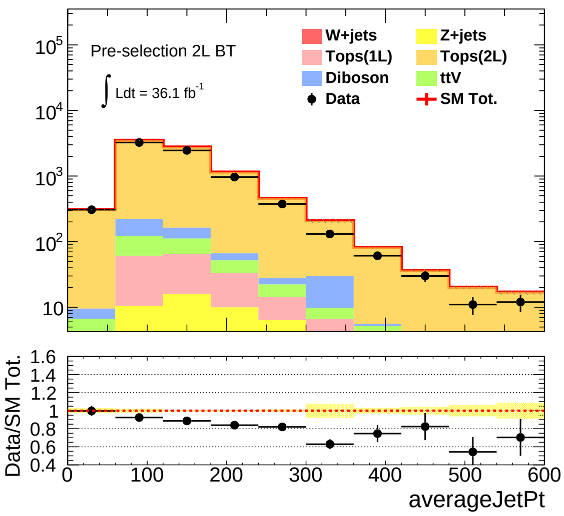

(c)

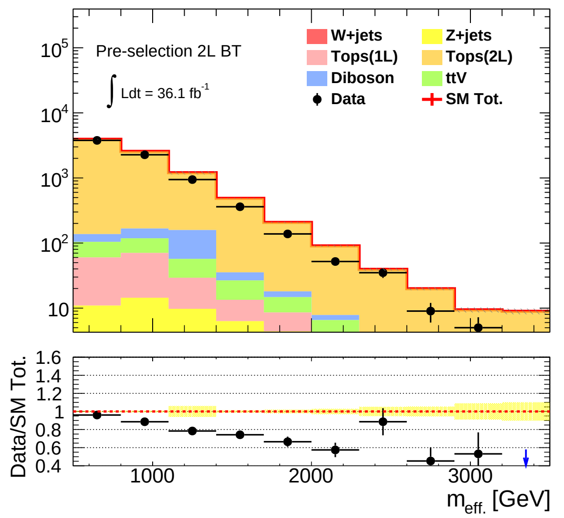

(d)

Figure 6.10: Kinematical distribution of (a) Jet multiplicity ($p_T > 30$ GeV) (b) leading-jet pt (c) average jet pt ($p_T > 30$ GeV) (d) $m_{\rm eff}$ in the **2LBT** pre-selection region.

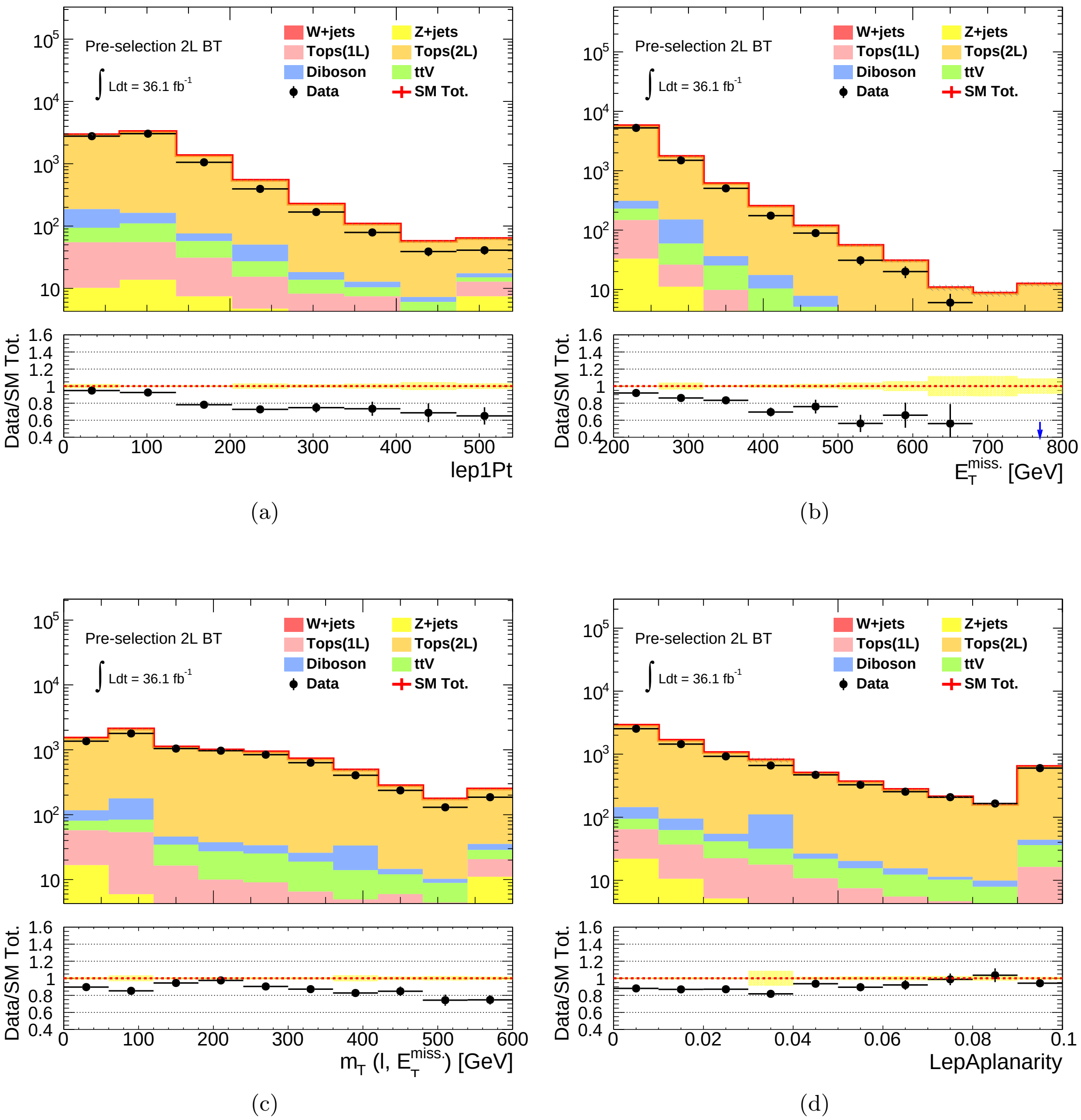

Figure 6.11: Kinematical distribution of (a) leading-lepton pt (b) $E_{\mathrm{T}}^{\mathrm{miss}}$ (c) m_{T} (d) aplanarity in the **2LBT** pre-selection region.

The same trend is observed also in the di-leptonic channel as well; constant slopes in data/MC are seen in variables related to the jet activity (jet transverse momenta, m_{eff} distributions or MET etc.); the other non-scaling variables (mt, aplanarity etc.) are relatively nicely modeled by MC. It might worth noting that the mis-modeling in jet variables can also be corrected by the same $p_{\mathrm{T}}(t\bar{t})$ reweighting as the semi-leptonic case (Figure C.1.5-C.1.6 in appendix C.1). This universality strongly implies that the cause of mis-modeling in $t\bar{t}$ is likely in the kinematics before the W-bosons decay, which is an important underlying assumption for the object replacement method as described later.
The behavior of the "non-scaling" variables is also largely similar to the case of semi-leptonic $t\bar{t}$. The only exception is m_{T} that the m_{T} distribution for di-leptonic $t\bar{t}$ has no reason to cut-off at $m_{\mathrm{T}} \sim m_W$, therefore it simply scales with lepton transverse momentum and MET. As a result, the m_{T} distribution of di-leptonic $t\bar{t}$ is affected by the mis-modeling of jet kinematics. The emerging data/MC discrepancy can be seen in Figure 6.11 (c). To avoid the impact by the mis-modeling in m_{T}, di-leptonic components are designed to be estimated by the other "object replacement" method as much as possible, and only small portion ("Out Acc." and "Mis. OR" in Table 6.1) of them is covered by the kinematical extrapolation.

$t\bar{t}$@3B:
Modeling of $tt + cc/bb$ and $t\bar{t} + b_{\mathrm{fake}}$ are exclusively examined using a preselected region with 3 or more b-jets (**1L3B**). Figure 6.12 - 6.13 displays the data-MC comparison in the region. While the shapes seem to be affected by the same type of mis-modeling as observed in inclusive $t\bar{t}$ selection above, the normalization is also underestimated by about 30% which is thought to be due to the error of $t\bar{t} + cc/bb$ cross-section.

Despite the $t\bar{t}$ components in 3B regions suffer from such even more complex mis-modeling than the bulk, the impact on the final result is not dramatic since the majority of them are di-leptonic components in the SRs, therefore they are largely estimated by the object replacement method.

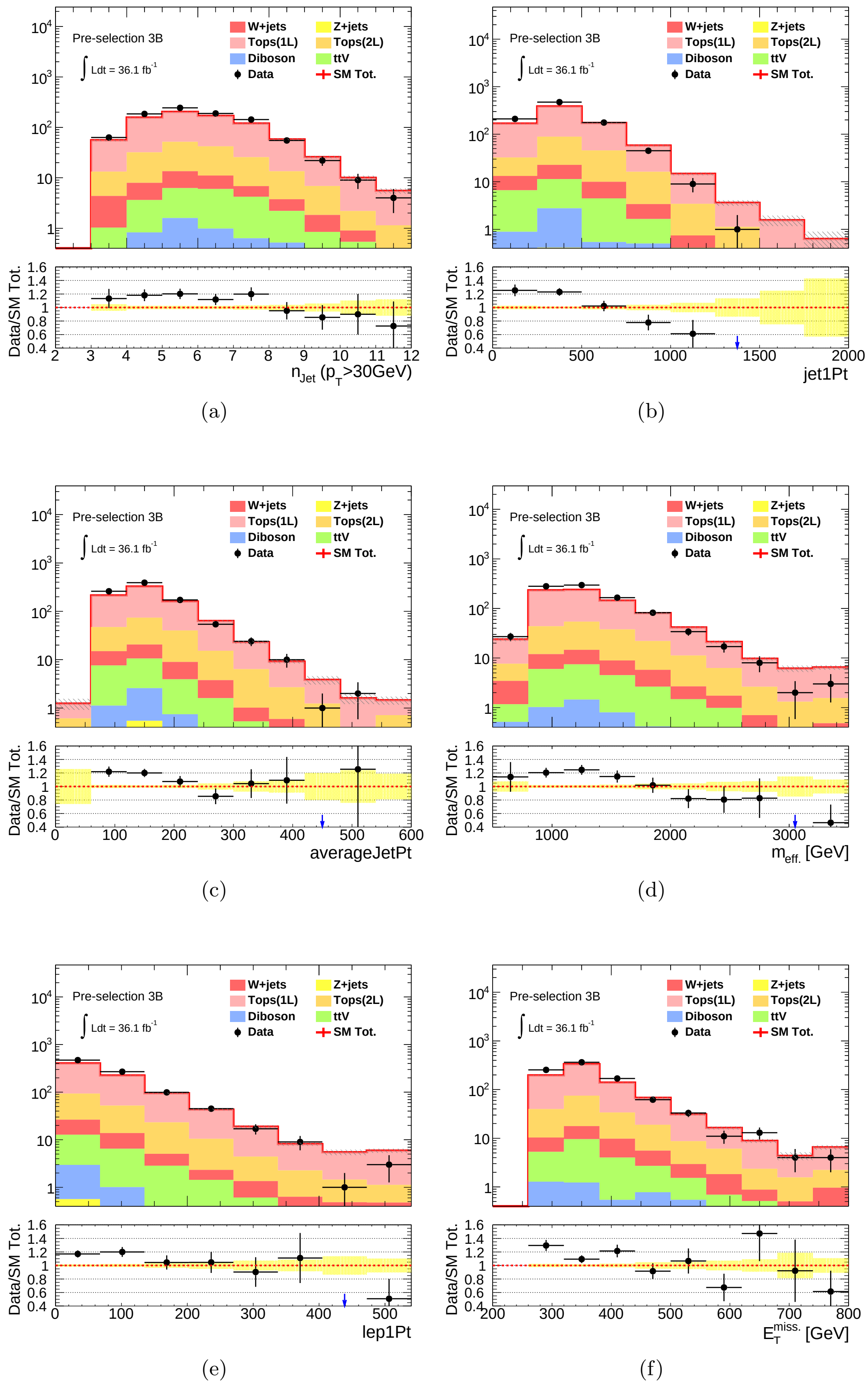

Figure 6.12: Kinematical distribution of (a) Jet multiplicity ($p_T > 30$ GeV) (b) leading-jet pt (c) average jet pt ($p_T > 30$ GeV) (d) m_{eff} (e) leading-lepton pt (f) $E_{\text{T}}^{\text{miss}}$ in the **1L3B** pre-selection region.

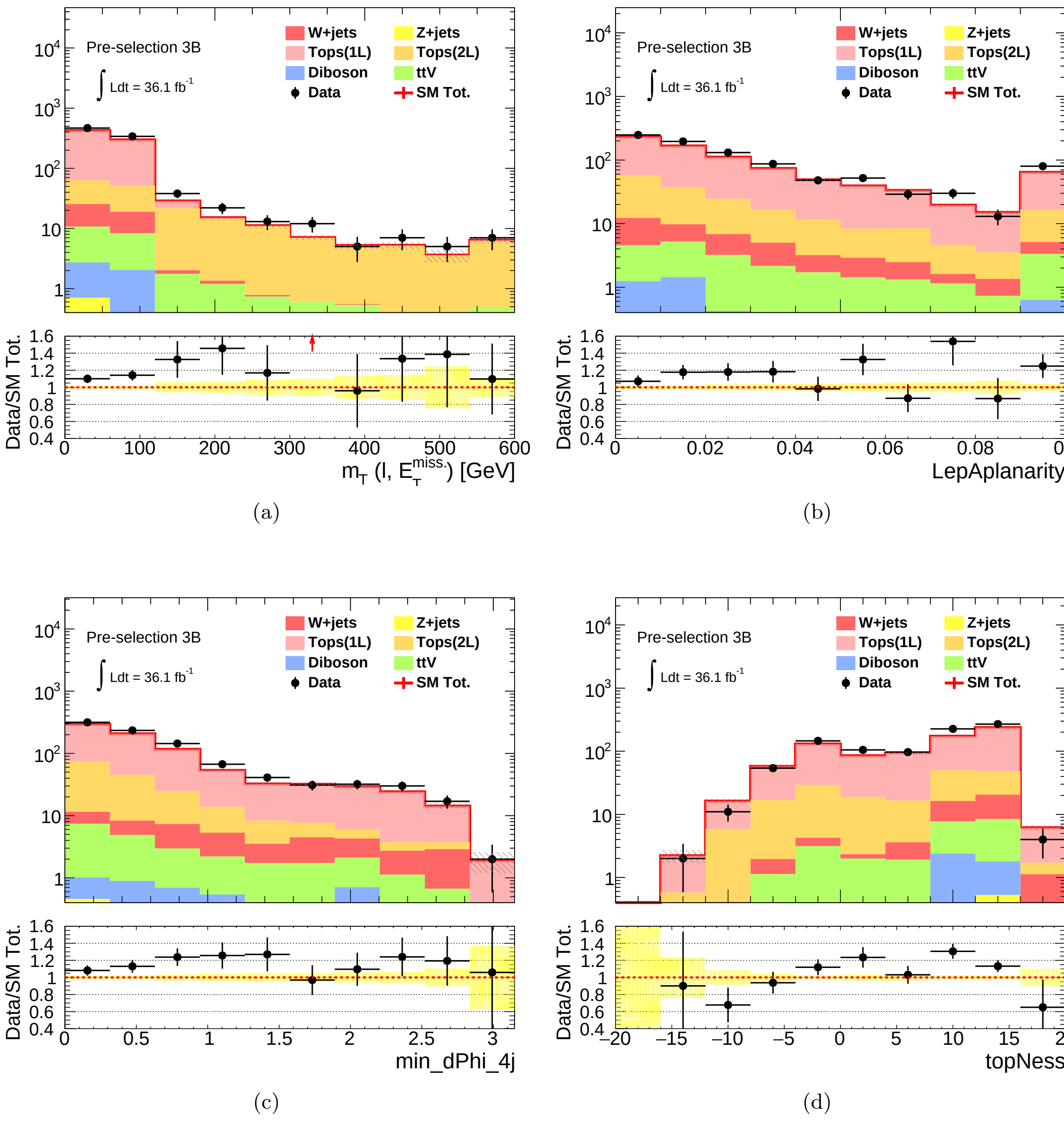

Figure 6.13: Kinematical distribution of (a) m_{T} (b) aplanarity (c) $\min_{i=1-4} \Delta\phi(j_i, E_{\mathrm{T}}^{\mathrm{miss}})$ (d) Topness in the **1L3B** pre-selection region.

6.2.2 Definition of Control Regions and Validation Regions

The key assumption in this method is that the relative modeling of MC between CRs and SRs is correct. In other words, CRs and SRs need to suffer from the same extent of MC mis-modeling, so that the normalization in CRs can be fully compatible for SRs. Therefore, the most important requirement in CR definition is having the similar phase space with respect to the corresponding SR in terms of the mis-modeling.

The easiest realization of CR is to revert the SR cuts in kinematical variables that are well-modeled by MC. In this analysis, m_{T}, aplanarity and topness (and also $\min_{i=1-4} \Delta\phi(j_i, E_{\mathrm{T}}^{\mathrm{miss}})$ for the "3B" tower) are chosen as such variables. A exception is in the"2J" tower where $E_{\mathrm{T}}^{\mathrm{miss}}$ is used instead of aplanarity, since aplanarity is not used in the signal region definition.

A couple of minor modifications follow based on the supplemental requirements below:

- CR statistics have to be sufficient.
  Typically, about 10 times more data statistics in CRs with respect to SRs are desired to make the correction stable particularly in cases where multiple components are corrected simultaneously (in this analysis, $W+\text{jets}$ and $t\bar{t}+Wt$). For this sake, cuts in variables fatally sensitive to the mis-modeling is loosened in some of the CRs, even at some cost of being hit by the mis-modeling. MET is for example always a good candidate to loosen since the gain in statistics increase is large. Although it is affected by the mis-modeling through jet transverse momenta which is known to be the most ill-modeled, the influence is much diluted through the vectoral summation of them, instead of the scalar sum. $E_{\mathrm{T}}^{\mathrm{miss}}/m_{\mathrm{eff}}$ is also loosened in "2J" and "High-x" since it is in a form of ratio which is supposed to be robust against simultaneous variation of the enumerator and the denominator. The impact by the mis-modeling due to these loosened cuts are evaluated in Sec 7.3.1. On the other hand, it is promised that $n_{\mathrm{J}}\,(p_{\mathrm{T}} > 30$ GeV) and m_{eff} are never touched since they are critical to the mis-modeling.

- Lower cut in m_{T} to reduce the contribution from fake leptons.
  Low-m_{T} regions are typically more contaminated by events with fake leptons. As the MC modeling on the fake rate is generally less reliable, $m_{\mathrm{T}} > 30 \sim 40$ GeV is applied in CRs.

CRs are defined for each tower and m_{eff} bins independently, however are shared between b-tagged and b-vetoed SR bins. Normalization is applied only on $W+\text{jets}$, $t\bar{t}$ and single-top while raw MC prediction is quoted for diboson and the other minor backgrounds. $t\bar{t}$ and single-top share the normalization factors as their relative breakdown is similar in CRs and SRs.

There are the third type of regions referred as "validation regions" designed to confirm the validity of the background estimation procedure by comparing with the data. They are typically set in between the CR and SR, with the cut in one of the extrapolation variable is freed with respect to CRs and kept for the other one. VRa and VRb respectively validates the extrapolation in m_{T} and aplanarity ($E_{\mathrm{T}}^{\mathrm{miss}}$ for "2J"). Upper cut on m_{T} is set in some VRa to suppress the signal contamination. VRs-QCD are the regions to examine the contribution from QCD multi-jet processes in SRs which is supposedly negligible. The detail is found in Sec. C.3.

The finalized CRs and VRs are summarized together with the corresponding SRs in Table 5.7 - 5.11, with the graphical schematics being shown in Figure 6.14. While SRs are carefully designed to be orthogonal to CRs and VRs, it is allowed to have overlap between CRs and VRs once the CRs are found to have much larger statistics than that of the VRs so that the overlapped events have no influence to the normalization. For instance, CR and VRa are overlapped in "3B". This is intended to secure the CR statistics, while the number of events in VRa is small enough so that they are still nearly statistically independent.

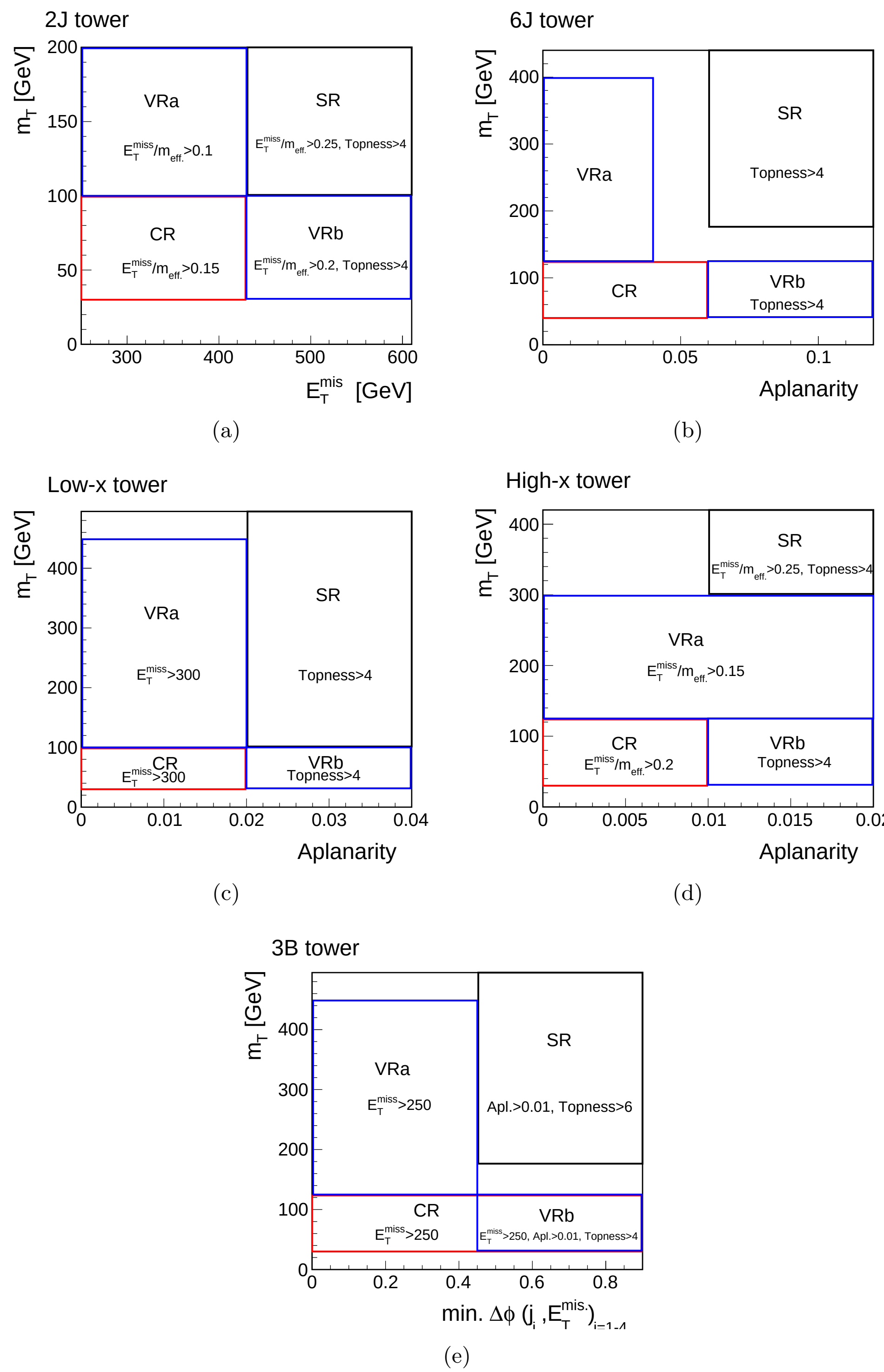

Figure 6.14: Schematics of CR/VR/SR in each signal region tower. Two major extrapolation variables are chosen to illustrate the difference between the regions. Extrapolation in the other variables are explicitly mentioned in the label. Note that the control region in the "3B" tower contains the VRa in it.

6.2.3 Result of the Normalization

The normalization factors are determined by a simultaneous fit on the b-vetoed and b-tagged slice of a CR ("WR" and "TR") in which $W+$jets and $t\bar{t}$ is dominant respectively. During the fit, all the normalization factors and nuisance parameters characterizing theoretical and experimental systematics are allowed to flow. The detail of the statistical procedure is described in Sec. 8.1.

The data yields in control regions are shown in Table 6.3 - 6.7, accompanied with the pre-fit and post-fit prediction by MC. Note that only $W+$jets and top backgrounds ($t\bar{t}$ and single-top) are normalized while the yield of the other processes are kept during the fit. The effect of signal contamination in control regions is neglected.

Fitted normalization factors are summarized in Figure 6.15. Generally small normalization factors are observed in bins with high m_{eff}, reflecting the fact that MC is overpredicting in the tail of m_{eff}.
The normalization factor is about 0.4 in the worst case, corresponding the an error of 150%, while the post-fit uncertainty is typically 20 $\sim$ 40%, displaying a successfully enhancement of robustness of the estimation.

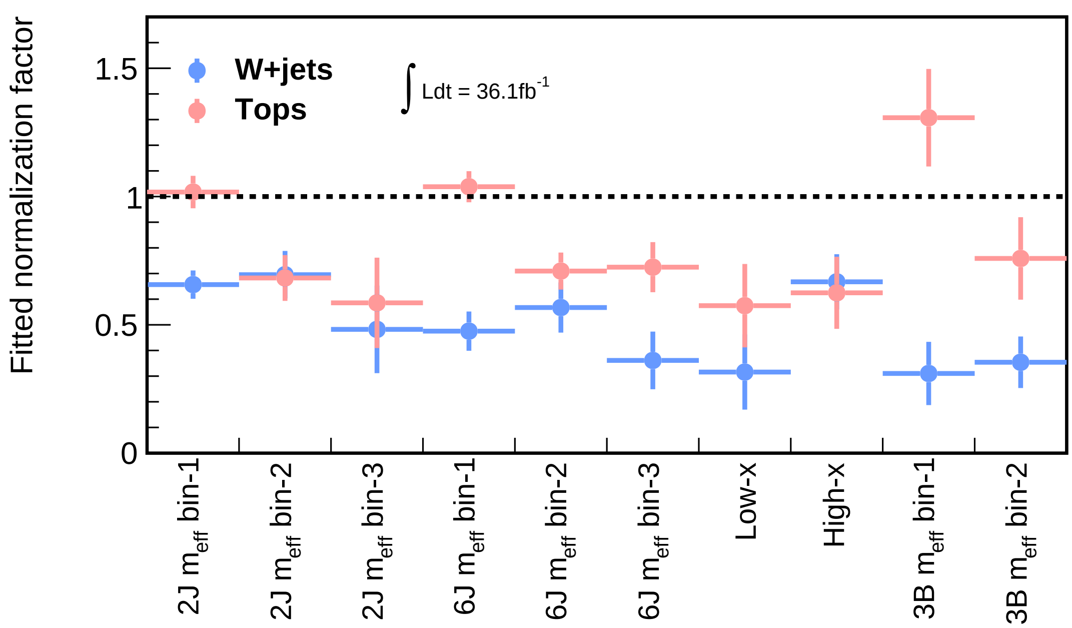

Figure 6.15: Fitted normalization factors for $W+$jets and top backgrounds ($t\bar{t}$ plus single-top). The error bars represent combined systematic and statistical uncertainties.

The post-fit distributions for variables used in the extrapolation in each region are shown in Figure C.4.1-C.4.8 in the appendix.

Table 6.3: Event yields and the background-only fit results in the "2J" control regions. Each column corresponds to a bin in m_{eff}. Uncertainties in the MC estimates combine statistical (in the simulated event yields) and systematic uncertainties discussed in chapter 7. The uncertainties in this table are symmetrised for propagation purposes but truncated at zero to remain within the physical boundaries.

WR 2J	$m_{\mathrm{eff.}} \in$[1100,1500]	$m_{\mathrm{eff.}} \in$[1500,1900]	$m_{\mathrm{eff.}} > 1900$
Observed data	620	127	17
MC total (post-fit)	620.06 ± 24.93	126.89 ± 11.28	17.01 ± 4.14
W+jets	462.0 ± 34.1	99.7 ± 12.6	12.6 ± 4.4
Z+jets	14.3 ± 3.9	2.6 ± 0.7	0.5 ± 0.1
Tops	100.9 ± 17.1	14.9 ± 3.2	2.6 ± 0.9
Di-boson	41.7 ± 13.7	9.3 ± 3.6	1.3 ± 0.4
$t\bar{t} + V$	1.2 ± 0.3	0.3 ± 0.1	0.1 ± 0.0
MC total (pre-fit)	859.70 ± 30.91	177.49 ± 7.33	32.40 ± 1.67
W+jets	703.35 ± 19.15	143.40 ± 4.39	26.19 ± 1.22
Z+jets	14.26 ± 3.92	2.58 ± 0.72	0.45 ± 0.13
Tops	99.27 ± 13.32	21.88 ± 3.16	4.42 ± 0.75
Di-boson	41.63 ± 13.69	9.32 ± 3.55	1.26 ± 0.44
$t\bar{t} + V$	1.18 ± 0.25	0.30 ± 0.07	0.06 ± 0.02
TR 2J	$m_{\mathrm{eff.}} \in$[1100,1500]	$m_{\mathrm{eff.}} \in$[1500,1900]	$m_{\mathrm{eff.}} > 1900$
Observed data	972	150	22
MC total (post-fit)	971.82 ± 31.18	150.01 ± 12.27	22.00 ± 4.71
W+jets	99.5 ± 35.0	23.2 ± 8.4	3.3 ± 1.7
Z+jets	3.9 ± 1.0	0.9 ± 0.2	0.2 ± 0.1
Tops	846.1 ± 48.2	120.2 ± 15.3	17.4 ± 5.2
Di-boson	11.9 ± 4.4	2.7 ± 0.9	0.7 ± 0.3
$t\bar{t} + V$	10.3 ± 1.8	3.1 ± 0.6	0.4 ± 0.1
MC total (pre-fit)	1009.13 ± 52.94	216.02 ± 11.81	37.88 ± 2.67
W+jets	151.50 ± 48.57	33.30 ± 10.57	6.91 ± 2.25
Z+jets	3.86 ± 1.05	0.85 ± 0.23	0.17 ± 0.05
Tops	831.49 ± 14.93	176.11 ± 4.06	29.70 ± 1.15
Di-boson	11.94 ± 4.35	2.67 ± 0.92	0.68 ± 0.27
$t\bar{t} + V$	10.34 ± 1.81	3.08 ± 0.58	0.43 ± 0.11

Table 6.4: Event yields and the background-only fit results in the "6J" control regions. Each column corresponds to a bin in m_{eff}. Uncertainties in the MC estimates combine statistical (in the simulated event yields) and systematic uncertainties discussed in chapter 7. The uncertainties in this table are symmetrised for propagation purposes but truncated at zero to remain within the physical boundaries.

WR 6J	$m_{\text{eff.}} \in$[1100,1600]	$m_{\text{eff.}} \in$[1600,2100]	$m_{\text{eff.}} > 2100$
Observed data	248	120	53
MC total (post-fit)	248.06 ± 15.84	120.02 ± 11.21	52.98 ± 7.30
W+jets	147.5 ± 22.0	83.3 ± 13.9	30.6 ± 9.2
Z+jets	2.5 ± 1.0	1.1 ± 0.5	0.7 ± 0.3
Tops	71.7 ± 11.5	22.9 ± 4.4	14.3 ± 3.1
Di-boson	25.3 ± 7.5	12.1 ± 5.8	7.1 ± 3.8
$t\bar{t} + V$	1.1 ± 0.2	0.6 ± 0.2	0.3 ± 0.1
MC total (pre-fit)	408.20 ± 19.21	192.94 ± 10.30	112.45 ± 7.11
W+jets	310.29 ± 11.30	146.84 ± 5.42	84.62 ± 4.04
Z+jets	2.54 ± 1.03	1.10 ± 0.46	0.72 ± 0.33
Tops	69.12 ± 8.78	32.38 ± 4.37	19.72 ± 2.80
Di-boson	25.19 ± 7.45	12.05 ± 5.78	7.10 ± 3.80
$t\bar{t} + V$	1.06 ± 0.24	0.57 ± 0.17	0.29 ± 0.09
TR 6J	$m_{\text{eff.}} \in$[1100,1600]	$m_{\text{eff.}} \in$[1600,2100]	$m_{\text{eff.}} > 2100$
Observed data	647	232	117
MC total (post-fit)	646.88 ± 25.46	231.79 ± 15.24	116.91 ± 10.85
W+jets	43.2 ± 16.5	25.1 ± 9.7	11.6 ± 5.5
Z+jets	0.9 ± 0.4	0.6 ± 0.2	0.4 ± 0.2
Tops	586.2 ± 31.2	193.1 ± 18.7	98.8 ± 12.8
Di-boson	8.1 ± 2.5	8.2 ± 2.7	3.9 ± 1.7
$t\bar{t} + V$	8.5 ± 1.5	4.7 ± 1.1	2.3 ± 0.6
MC total (pre-fit)	672.53 ± 31.35	329.86 ± 16.23	174.76 ± 11.54
W+jets	90.62 ± 28.71	44.24 ± 14.02	31.99 ± 10.13
Z+jets	0.88 ± 0.36	0.58 ± 0.23	0.41 ± 0.20
Tops	564.43 ± 9.95	272.12 ± 5.74	136.21 ± 3.91
Di-boson	8.11 ± 2.51	8.21 ± 2.69	3.84 ± 1.69
$t\bar{t} + V$	8.48 ± 1.53	4.71 ± 1.14	2.30 ± 0.63

Table 6.5: Event yields and the background-only fit results in the "Low-x" control regions. Each column corresponds to a bin in m_{eff}. Uncertainties in the MC estimates combine statistical (in the simulated event yields) and systematic uncertainties discussed in chapter 7. The uncertainties in this table are symmetrised for propagation purposes but truncated at zero to remain within the physical boundaries.

CR Low-x	WR	TR
Observed data	15	25
MC total (post-fit)	15.02 ± 3.89	24.97 ± 5.03
W+jets	9.3 ± 4.2	2.9 ± 1.8
Z+jets	0.4 ± 0.2	0.2 ± 0.1
Tops	2.7 ± 0.9	20.4 ± 5.7
Di-boson	2.6 ± 0.8	1.0 ± 1.0
$t\bar{t} + V$	0.0 ± 0.0	0.5 ± 0.1
MC total (pre-fit)	37.17 ± 2.56	46.38 ± 3.87
W+jets	29.51 ± 1.84	9.26 ± 3.05
Z+jets	0.38 ± 0.15	0.17 ± 0.07
Tops	4.62 ± 0.75	35.47 ± 1.52
Di-boson	2.61 ± 0.79	0.99 ± 0.98
$t\bar{t} + V$	0.05 ± 0.02	0.48 ± 0.11

Table 6.6: Event yields and the background-only fit results in the "High-x" control regions. Each column corresponds to a bin in m_{eff}. Uncertainties in the MC estimates combine statistical (in the simulated event yields) and systematic uncertainties discussed in chapter 7. The uncertainties in this table are symmetrised for propagation purposes but truncated at zero to remain within the physical boundaries.

CR High-x	WR	TR
Observed data	92	73
MC total (post-fit)	91.91 ± 9.61	72.97 ± 8.57
W+jets	72.4 ± 11.1	17.0 ± 6.5
Z+jets	1.1 ± 0.4	0.3 ± 0.1
Tops	10.2 ± 2.9	52.0 ± 11.3
Di-boson	8.0 ± 3.5	2.7 ± 1.4
$t\bar{t} + V$	0.2 ± 0.1	1.0 ± 0.4
MC total (pre-fit)	134.04 ± 6.41	112.69 ± 9.52
W+jets	108.42 ± 3.88	25.52 ± 8.13
Z+jets	1.13 ± 0.39	0.29 ± 0.13
Tops	16.32 ± 2.19	83.19 ± 3.25
Di-boson	7.99 ± 3.50	2.70 ± 1.35
$t\bar{t} + V$	0.18 ± 0.08	0.99 ± 0.37

Table 6.7: Event yields and the background-only fit results in the "3B" control regions. Each column corresponds to a bin in m_{eff}. Uncertainties in the MC estimates combine statistical (in the simulated event yields) and systematic uncertainties discussed in chapter 7. The uncertainties in this table are symmetrised for propagation purposes but truncated at zero to remain within the physical boundaries.

WR 3B	$m_{\text{eff.}} \in$[1000,1750]	$m_{\text{eff.}} > 1750$
Observed data	368	107
MC total (post-fit)	368.18 ± 19.69	107.05 ± 10.56
W+jets	146.4 ± 59.3	58.3 ± 16.7
Z+jets	5.3 ± 1.5	2.4 ± 0.4
Tops	176.6 ± 52.2	33.1 ± 11.5
Di-boson	37.7 ± 9.9	12.5 ± 3.3
$t\bar{t} + V$	2.2 ± 0.5	0.8 ± 0.2
MC total (pre-fit)	651.86 ± 28.54	223.90 ± 10.02
W+jets	471.51 ± 7.38	164.58 ± 2.94
Z+jets	5.29 ± 1.45	2.39 ± 0.38
Tops	135.10 ± 21.31	43.59 ± 7.33
Di-boson	37.74 ± 9.93	12.53 ± 3.26
$t\bar{t} + V$	2.21 ± 0.52	0.80 ± 0.22
TR 3B	$m_{\text{eff.}} \in$[1000,1750]	$m_{\text{eff.}} > 1750$
Observed data	234	47
MC total (post-fit)	233.97 ± 15.57	46.98 ± 6.95
W+jets	1.4 ± 1.0	0.9 ± 0.5
Z+jets	0.1 ± 0.1	0.1 ± 0.1
Tops	227.5 ± 15.8	44.1 ± 7.1
Di-boson	$0.2^{+0.3}_{-0.2}$	0.2 ± 0.1
$t\bar{t} + V$	4.7 ± 1.2	1.7 ± 0.4
MC total (pre-fit)	183.60 ± 23.01	62.71 ± 8.28
W+jets	4.54 ± 1.87	2.62 ± 1.00
Z+jets	0.12 ± 0.05	0.10 ± 0.06
Tops	174.00 ± 21.42	58.15 ± 7.43
Di-boson	$0.20^{+0.27}_{-0.20}$	0.18 ± 0.08
$t\bar{t} + V$	4.75 ± 1.17	1.66 ± 0.43

6.3 The Object Replacement Method

A potential concern over the kinematical extrapolation method is that it is still fully relies on MC in the extrapolation. In particular, in case of estimating the "di-leptonic" background by extrapolating in m_{T}, this follows that:

- The MC modeling itself is questionable.
  As observed in Figure 6.11 (c), MC tends to be overestimating in the tail of m_{T}, reflecting the fact that in case of di-leptonic channel, m_{T} scales with the lepton transverse momentum and MET in which MC is found to be is-modeling.

- Different particles contribute to observables between the semi-leptonic and di-leptonic processes. For instance, MET is sourced by a single neutrino in the semi-leptonic channel while it is by a vectoral sum of two neutrinos in the di-leptonic one. More seriously, the number of ISR/FRS jets is different under the same jet multiplicity requirement. For example in $t\bar{t}$, the semi-leptonic channel yields 4 jets by its decay while the di-lepnic channel can only yield 2 (or 3 if hadronic decay product from τ is tagged as a jet). The differences are summarized in Table 6.8. Note that these differences also propagate to the other composite variables using jets and MET (e.g. m_{eff} and m_{T} etc.). Therefore, applying the same selection between CRs and SRs no longer guarantee that CRs grasp the same phase space as SRs.

Table 6.8: Comparison of constituents of MET and n_{J} between the semi-leptonic $t\bar{t}$ and di-leptonic $t\bar{t}$ as example. "1LCR" refers to the control regions used in the kinematical extrapolation method, and "2LCR" is its 2-lepton version with the same kinematical selection. Note that the other composite variables using jet and MET (e.g. m_{eff} and m_{T} etc.) are also affected by the difference accordingly.

	SR	1L CR	2LCR
Dominant $t\bar{t}$ component	$t\bar{t} \to b\ell\nu_1 b\tau\nu_2, \tau \to \tau_h\nu_\tau$	$t\bar{t} \to bqqb\ell\nu$	$t\bar{t} \to b\ell\nu_1 b\ell\nu_2$
n_{J}	$\sim 2(3) + n_{\mathrm{ISR/FSR}}$	$\sim 4 + n_{\mathrm{ISR/FSR}}$	$\sim 2 + n_{\mathrm{ISR/FSR}}$
$E_{\mathrm{T}}^{\mathrm{miss}}$	$\lvert \boldsymbol{p}_{\mathrm{T}}(\nu_1) + \boldsymbol{p}_{\mathrm{T}}(\nu_2) + \boldsymbol{p}_{\mathrm{T}}(\nu_\tau) \rvert$	$\lvert \boldsymbol{p}_{\mathrm{T}}(\nu) \rvert$	$\lvert \boldsymbol{p}_{\mathrm{T}}(\nu_1) + \boldsymbol{p}_{\mathrm{T}}(\nu_2) \rvert$

The use of 2-lepton control regions (2LCRs) is then naturally motivated. However, the MC normalization approach does not dramatically improve the situation, since it can not accomodate the behavior of taus or missing leptons that differ event-by-event (see Table 6.8).

Instead, the approach of event-by-event emulation including the object replacement method can cope with the problem. The object replacement method is an integrated method consisting of:

- "missing lepton replacement" to estimate a part of $\ell\ell_{\text{mis.}}$ events ("Mis. Reco." and "Mis. ID"),
- "tau replacement" to estimate $\ell\tau_{\text{h}}$,

where one of the lepton of data events in 2LCR is replaced into a virtual missing lepton or a simulated hadronic tau decay respectively, as outlined in Figure 6.16. The detector responses and behavior in object reconstruction of those replaced objetcs are carefully emulated so that the replaced event can directly mimic the events in the signal regions.

The object replacement method is a nearly full data-driven method where the used of MC is limited in an area of tau decays and modeling of instrumental effects, such as lepton efficiency and jet energy scale. The MC modeling is highly reliable where the data/MC agreement is closely examined and the discrepancies are typically sub-percent level which are also mostly well-understood. The reliance of MC ensures the extrapolation much more robust, compared with the kinematical extrapolation method where the mis-modeling in kinematic tail is always critical.

Note that the whole method relies on the orthogonality between kinematics and object properties:

$$\frac{d\sigma(\ell\ell)}{d\boldsymbol{x}} \propto \frac{d\sigma(\ell\ell_{\text{ID}})}{d\boldsymbol{x}} \propto \frac{d\sigma(\ell\ell_{\text{mis.}})}{d\boldsymbol{x}} \tag{6.1}$$

and the lepton universality:

$$\frac{d\sigma(\ell\ell)}{d\boldsymbol{x}} \propto \frac{d\sigma(\ell\tau)}{d\boldsymbol{x}}, \tag{6.2}$$

where $\ell\ell_{\text{ID}}$ and $\ell\ell_{\text{mis}-\text{ID}}$ represents the seed events and the missing lepton events respectively, and $\boldsymbol{x}$ symbolizes kinematical variables. Particularly, the kinematics-object orthogonality (Eq. 6.1) is of paramount importance, since it allows to extrapolate the object properties measured in a very inclusive phase space into any phase space including extreme cases such as the signal regions in this analysis. As long as the lepton reconstruction and identification is concerned, the statement is more or less true because their result generally obeys the statistical behavior of detector responses such as fluctuating number of hits or energy deposit, which does not depend on global event kinematics, but rather on the nature of the particle itself (usually only on its momentum) as well as the local material configuration in the detector. Therefore, it is usually enough to parameterize the efficiency of reconstruction or identification simply by the momentum $(p_{\text{T}}, \eta, \phi)$ of the particles. This is however not the case when coming to the probability of lepton being beyond the (p_{T}, η) acceptance ("Out-Acc") or being dropped in the overlap removal ("Mis. OR"), since they do depend on the momentum of parent particle or the proximity to the nearest jet. Hence, the class of seed events do not fully represent the kinematics of "Out-Acc" and "Mis. OR". This is the reason why these events can not covered by the object replacement method.

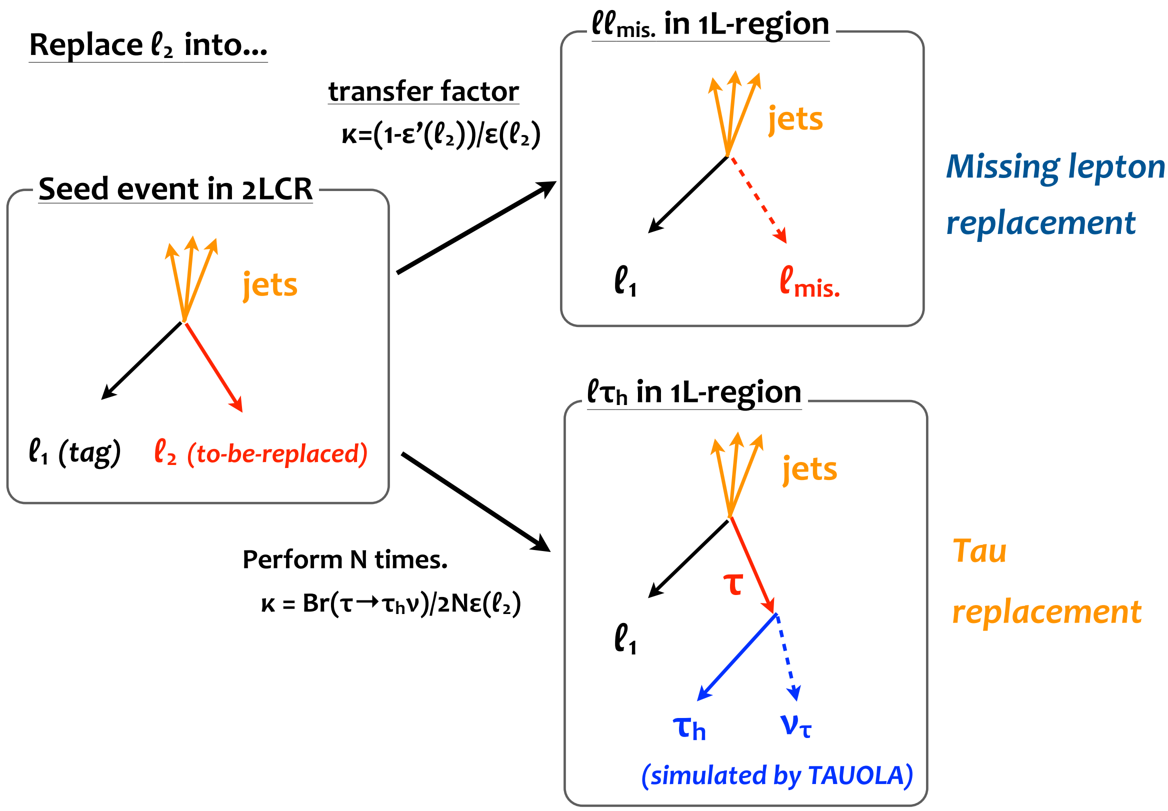

Figure 6.16: Schematic of the object replacement method.

6.3.1 The Replacement Procedure and the Per-event Logic

Figure 6.17 presents the work flow for the replacement procedure in a single seed event, which follows as below:

1. Pick up a 2LCR event ("seed event").
2. Replace a lepton of the seed event into a virtual missing lepton or a simulated hadronic decay of tau lepton, if the two leptons satisfy a certain criteria. This replaced event is called "sub-event".
3. (For tau replacement) Apply the calibration for the hadronic tau.
4. Re-calculate the event-level kinematics such as $E_{\mathrm{T}}^{\mathrm{miss}}$ or m_{eff} etc.
5. Assign a weight κ for each sub-event as the transfer factor from 2LCR to 1L regions.
6. Change the roles (tagged/replaced) between the two leptons and repeat 2-5. Generated sub-events are filled in a single "event-level histogram".
7. (For tau replacement) Repeat the step 2-6 by $N = 50$ times and take the average, in order to fully accommodate the statistical nature of tau decay. Note that the number of iteration N only defines the level of "smoothing" thus has no essential impact on the final result. The average is taken by scaling the κ by 1/N.
8. Apply the analysis level selection (e.g. signal region selection when one wants to estimate the yield in the signal region) and post-selection to reject singal contamination for the generated sub-events.
9. Collect the accepted sub-events and fill them into an event-level histogram. 100% of statistical uncertainty is assigned for each bin of the event-level histogram, accounting for all the sub-events are generated from the common seed event.
10. Loop over all seed event and sum up all the event-level histograms with ordinary statistical treatment where the uncertainty is quadratically summed for each bin of the histogram.

More detail and caveats about each step are as following:

Seed event selection and trigger
For seed event selection, looser kinematical selection is generally preferred, to collect the necessary seed events as completely as possible. In particular, as MET and m_{T} change their values the most during the replacement, those cuts have to be drastically relaxed with respective to signal regions. For instance, Figure 6.18 shows the MET distribution for corresponding seed events of the $\ell\ell_{\mathrm{mis.}}$ and $\ell\tau_h$ events with $E_{\mathrm{T}}^{\mathrm{miss}} > 250$ GeV. About 40% of seeds are with seed MET below 250 GeV, meaning that it will be underestimated by 40% if naively selecting seeds by $E_{\mathrm{T}}^{\mathrm{miss}} > 250$ GeV in 2LCR.

While MET trigger is available for collecting the bulk events above its off-line threshold $E_{\mathrm{T}}^{\mathrm{miss}} > 250$ GeV, the single-lepton trigger (SLT) is introduced to complement the seeds events

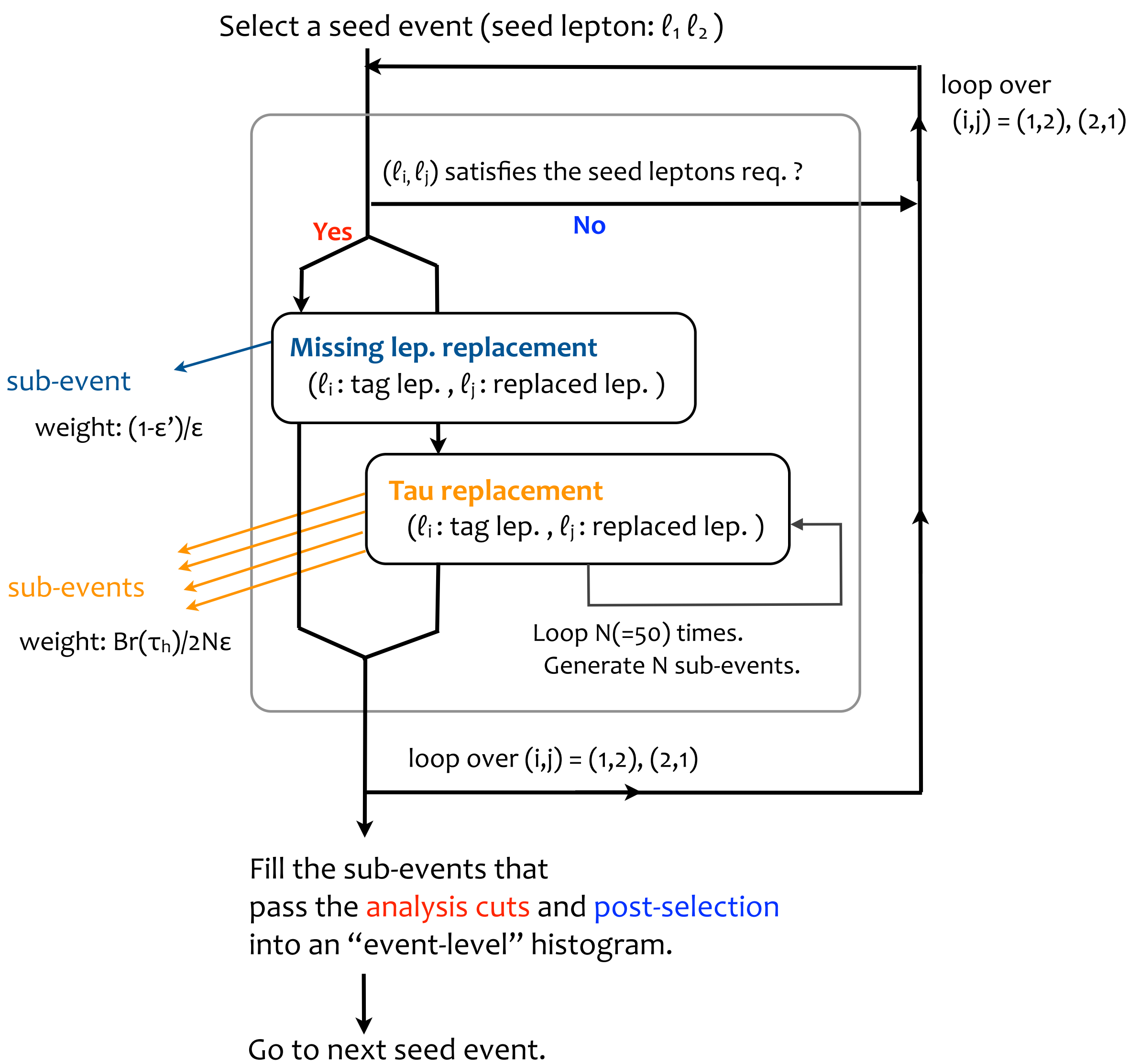

Figure 6.17: Work flow in the replacement procedure for a single seed event.

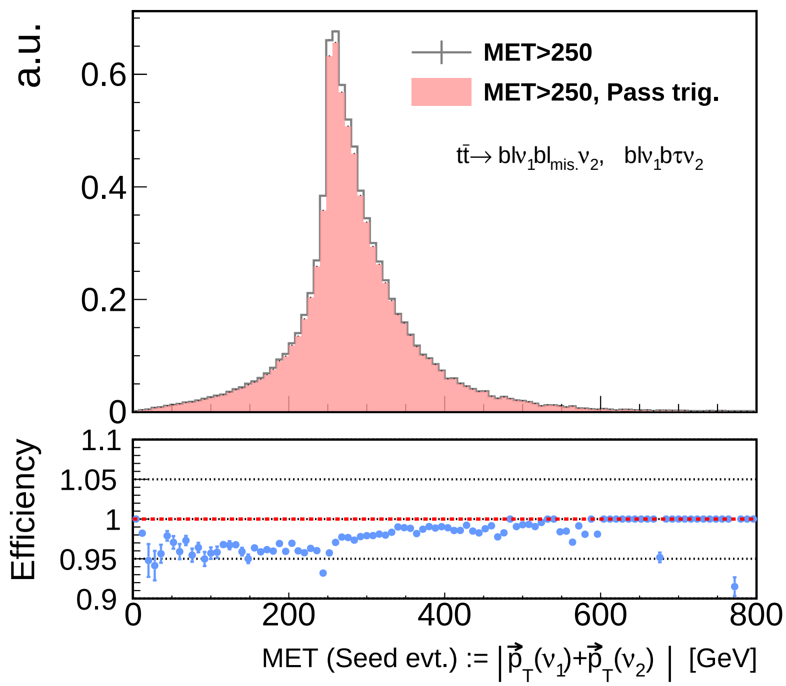

Figure 6.18: Seed MET distribution (gray) for the $\ell\ell_{\text{mis.}}/\ell\tau_h$ events from $t\bar{t}$ resulting in $E_{\mathrm{T}}^{\text{miss}} >$ 250 GeV. The seed MET is defined by the MET component only by neutrinos from top decays: $|\boldsymbol{p}_{\mathrm{T}}(\nu_1) + \boldsymbol{p}_{\mathrm{T}}(\nu_2)|$, which is roughly equivalent to the MET in corresponding seed events ($t\bar{t} \rightarrow b\ell\nu_1\bar{b}\ell\nu_2$). Over 95% of the seed events are shown to be accepted by the combined trigger strategy defined in Table 6.9 (pink).

with $E_{\mathrm{T}}^{\text{miss}} < 250$ GeV. In spite of its relatively low efficiency $70\% - 90\%$ and the off-line threshold of $p_{\mathrm{T}} > 28(26)$ GeV for single-electron (muon), SLT is still fully efficient for the seed events since there are two leptons being the candidate to fire the trigger. Eventually, as shown in Figure 6.18, more than 95% of the overall trigger efficiency can be maintained.

Although the enhanced backgrounds due to the lowered MET selection for 2LCR does not impact as much on the final result since most of them are skimmed out in the analysis-level selection applied after the replacement, the decent cut $E_{\mathrm{T}}^{\text{miss}} > 100$ is required to suppress the bulk background components in 2LCR (Z+jets, 1L+fake lepton etc.) and make sure avoiding the large uncertainty from MC subtraction. The seed event loss due to the selection $E_{\mathrm{T}}^{\text{miss}} > 100$ is negligible when estimating SRs/VRs. Table 6.9 shows the definition of common 2LCR.

Table 6.9: Definition of 2-lepton control region for MC closure test.

$n_{\ell,\text{baseline}} = 2$, $n_{\ell,\text{signal}} \geq 1$
MET trigger, $E_{\mathrm{T}}^{\text{miss}} > 250$ GeV or At least 1 signal lepton with $p_{\mathrm{T}} > 28$ GeV firing the single-lepton trigger, $E_{\mathrm{T}}^{\text{miss}} > 100$ GeV

Requirement on seed leptons for the replacement

A seed event with lepton $\ell_1\ell_2$ have two choices of the replacement namely 1) keeping ℓ_1/replacing ℓ_2 or 2) keeping ℓ_2/replacing ℓ_1. The replacement is proceeded only if the lepton to-be-replaced ("replaced lepton") and the lepton to-be-kept ("tag lepton") satisfy a certain condition as noted below. Note that the replacement can happen twice from the identical seed event if the both combinations (tag,rep.)=($\ell_1\ell_2$), ($\ell_2\ell_1$) are eligible.

As the tag lepton eventually corresponds to the single lepton used in the analysis in 1-lepton regions, it has to undergo the consistent object definition as that used in signal region definition, which is namely in Table 3.2. On the other hand, no such requirement is needed for the replaced lepton, instead, looser definition is preferred from the CR statistics point of view. Therefore, only the baseline lepton requirement when estimating the b-inclusive or b-tagged regions, while the signal lepton requirement is still applied in case of estimating b-vetoed regions since the impact of fake lepton background in 2LCR is relatively large otherwise. The relaiton between and the working point of lepton definition is summarized in Table 6.10.

Table 6.10: Lepton definition used for tag and replaced lepton versus the type of regions to be estimated.

	B-tagged, b-inclusive	b-vetoed
Tag lepton	signal	signal
Replaced lepton	baseline	signal

Treatment of virtual missing lepton

As mentioned in Sec. 3.7, electrons are usually also identified as jets, and the doubly-counted object, either an electron or a jet, is discarded during the overlap removal. Therefore, electrons failing the reconstruction or identification will simply recognized as jets without experiencing the overlap removal. To emulate this effect, in case of replacing an electron in a seed event, the record that the electron is reconstructed as a jet candidate is retrieved, and the 4-vector of electron is replaced into the that of the jet candidate. As the jet candidate is fully calibrated in the hadronic scale, no more correction is needed. In some occasion, electrons do not have corresponding jet candidates typically when the low transverse momentum is too low. In such cases, the electron is replaced into a missing particle with the 4-momentum of original electron.

Muons failing the reconstruction or identification are almost never identified as any other objects. Instead, they are included in the MET track soft term in the MET calculation, and in principle this needs to be emulated in the missing muon replacement. This is technically possible, however the bottleneck is that the muon track quality is totally different between well-identified muons and unidentified ones, and particularly it is difficult to reproduce the resolution of bad muon track from good one with a meaningful correction. As it turns that simply including the 4-momentum replaced muon into the MET soft term even leads to worse performance than not including at all (as demonstrated in Figure 6.34), replaced muons are decided to be simply treated as a virtual missing particle in the same momentum, and added in MET. Although this rough treatment causes a non-zero error in the estimation as one will see in Sec. 6.3.3, fortunately the impact on final estimation is marginal because the rate of missing muon events are generally very low, compared with the other components (missing electron events or $\ell\tau_h$) due to the very high efficiency of muon reconstruction and identification.

Simulation of tau decays and the τ_h-to-jet calibration

Tau decays are simulated by TAUOLA [135] [136] [137] assuming the taus are unpolarized. This assumption is incorrect given the parent W-bosons are left-handed, however the impact on the final result is found to be marginal. This is discussed in Sec. 6.3.3. Branching for leptonic decay is set to zero to reduce the number of loops.

Given that the analysis is without explicit tau selections, hadronic taus within the p_{T}-η acceptance undergo the reconstruction, b-tagging and calibration as an (b-tagged) anti-Kt4 jets, once they pass the JVT cut (Sec. 3.6.4). On the other hand, the output of TAUOLA is merely a 4-vector of truth level hadronic tau. Therefore, following pseudo-calibration is applied for the truth-level τ_h, to emulate the effect either of the detector response, jet calibration, and the b-tagging.

1. Scale the transverse momentum of truth τ_h.
   The scale of a truth τ_h to an anti-Kt4 jets is derived using the $t\bar{t}$ MC samples, by comparing the transverse momenta of truth hadronic taus and that of ΔR-matched reconstructed jet by $\Delta R < 0.2$. It is defined by the mean value of the residual distribution (Figure 6.19) and parameterized in terms of p_{T} and η of truth hadronic taus (Figure 6.20). The scale is always positive and rises significantly in the low-p_{T} limit, due to the fact that the anti-Kt4 jet contains extra underlying tracks inside that become the pedestal. The difference in the calibration between light jets and b-tagged jets are ignored.

2. Smear the p_{T} of hadronic tau.
   After applying the scale above, smearing is subsequently adopted for to account for the detector resolution. The resolution is taken from the Gaussian-fitted RMS of the residual distribution on which the scale above is defined as well (Figure 6.19), and likewise parameterized as function of p_{T} and η of truth hadronic taus (Figure 6.21). The smearing is applied based on the Gaussian profile centered at with RMS being the resolution.

3. Emulation on the JVT cut and b-tagging.
   After the sequence of the p_{T}-scaling and smearing, hadronic taus with $p_{\mathrm{T}} > 30$ GeV, $|\eta| < 2.8$ are selected as the signal jet candidates. Signal jets are then randomly identified from them, based on the efficiency of JVT cut derived from signal jet candidates matched with truth hadronic taus by $\Delta R < 0.2$ in the simulated $t\bar{t}$ sample (Figure 6.22). A random b-tagging is further performed on the signal jets, by assigning a random b-tagging score (MV2c10) following according to the profile obtained from the $t\bar{t}$ MC sample using the same technique (Figure 6.23). While the JVT cut efficiency is mapped as a function of p_{T} and η of signal jet candidates, the b-tagging score profile is measured separately by different tau decay modes (1-prong and 3-prong).

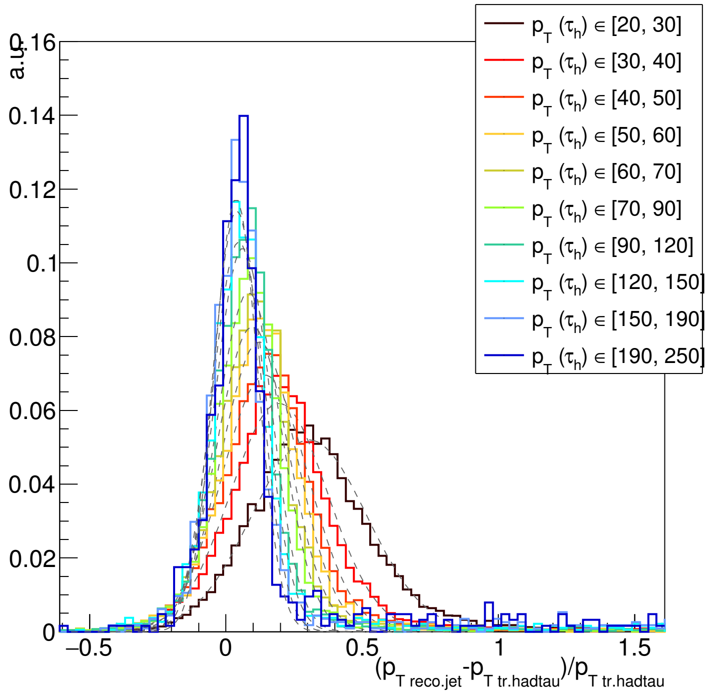

Figure 6.19: The residual of tau momentum measurement: $p_{\mathrm{T}}(\mathrm{reco}.\tau\mathrm{-jet}) - p_{\mathrm{T}}(\mathrm{tr}.\tau_h)/p_{\mathrm{T}}(\mathrm{tr}.\tau_h)$ calculated using the simulated $t\bar{t}$ sample. $p_{\mathrm{T}}(\mathrm{tr}.\tau_h)$ is the transverse momentum of truth-level hadronic tau defined as $|\boldsymbol{p}(\tau) - \boldsymbol{p}(\nu_\tau)|$ and $p_{\mathrm{T}}(\mathrm{reco}.\tau - \mathrm{jet})$ is the corresponding reconstructed anti-Kt4 jet matched by $\Delta R < 0.2$.

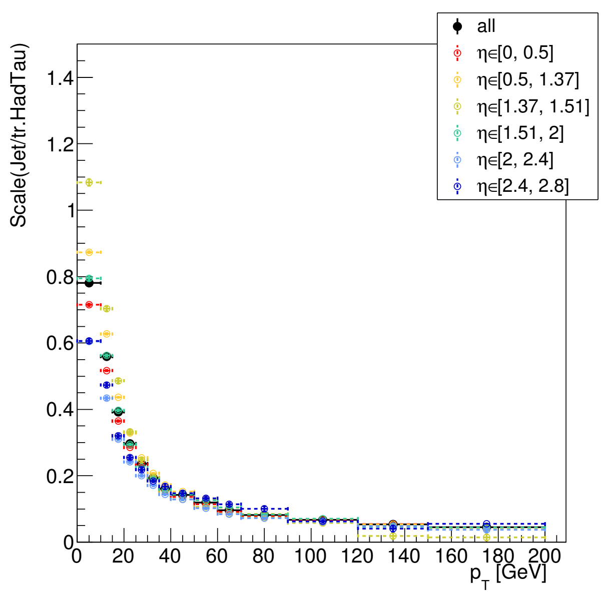

Figure 6.20: Scale of anti-Kt4 jets for truth hadronic taus, defined as the mean of the residual distribution 6.19. Both η-inclusive and η-dependent curves are derived.

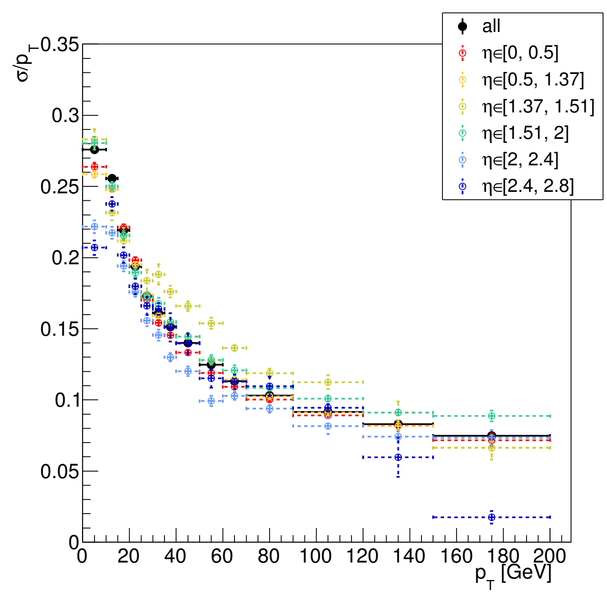

Figure 6.21: Resolution of hadronic tau, defined by the Gaussian-fitted RMS of the residual distribution 6.19. Both η-inclusive and η-dependent curves are derived.

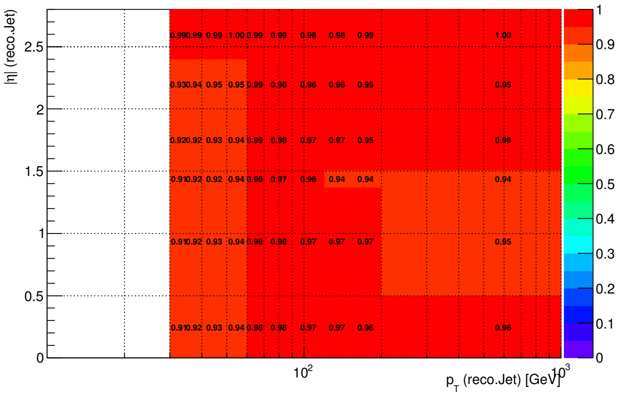

Figure 6.22: The JVT cut efficiency map for a reconstructed hadronic tau jet as function of its p_{T} and η, calculated using the $t\bar{t}$ MC sample. The efficiency is defined by the fraction of signal jet candidates ΔR-matched to the truth hadronic tau by $\Delta R < 0.2$ that pass the signal jet requirement.

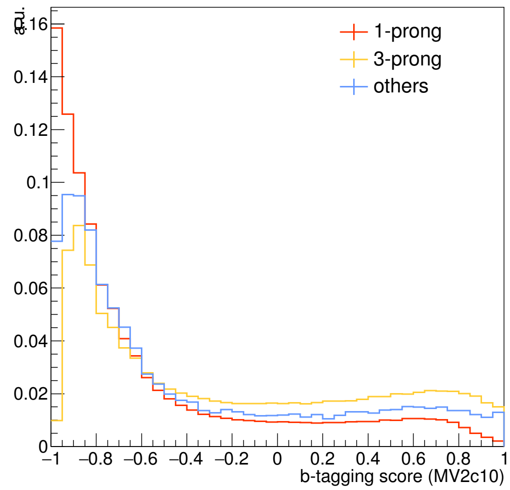

Figure 6.23: Profile of b-tagging score (MV2c10) for signal jets originated from hadronic tau decays. Only the dependency on the decay modes (1-prong or 3-prong) is taken into account. The threshold for the b-tagging is at 0.44. The 3-prong events result in a higher fake rate into b-tagging jets, reflecting the secondary vertex structure more resembling to that of b-hadrons. The simulated $t\bar{t}$ MC sample is used to derive the profiles.

Transfer factor

A weight κ is assigned to each sub-event, to account for the different probability of occurrence between the seed event and the replaced sub-event. For instance, in the missing lepton replacement, this corresponds to the difference between probability of a lepton being identified and being failing the identification. The κ is therefore the inefficiency over the efficiency:

$$\kappa = \frac{1 - \epsilon_{\mathrm{baseline}}(\boldsymbol{p}_{\mathrm{T}}(\ell_{\mathrm{rep.}}))}{\epsilon_{\mathrm{rep.}}(\boldsymbol{p}_{\mathrm{T}}(\ell_{\mathrm{rep.}}))}.$$

Note that the efficiency appearing in the enumerator is for the working point used for the second lepton veto (namely "baseline"), and that in the denominator is for one used for requiring replaced lepton which can be either "baseline" and "signal" depending on cases (see Table 6.10).

As for the tau replacement, the transfer factor is

$$\kappa = \frac{\mathrm{Br}(\tau \to \tau_{\mathrm{h}}\nu)}{2N\epsilon_{\mathrm{rep.}}(\ell_{\mathrm{rep.}})},$$

where N is number of iterations per replacement (set to 50 in this study), and $\epsilon_{\mathrm{rep.}}$ the efficiency for working point used for requiring replaced lepton. The factor 2 originates from the fact that two channels ($e\ell$ and $\mu\ell$) are available as seeds for estimating a single channel $\tau\ell$ (see Table 6.11).

Table 6.11: Correspondence between the seed events and the generated sub-events, in terms of charge and lepton flavor. The sub-events generated by tau replacement need to weighted by 1/2 otherwise will be double-counted.

Seed	Replaced lepton	Sub-evt. by mis. lep. rep.	Sub-evt. by tau rep.
e^+e^-	e^-	$e^+e^-_{\text{mis}}$	$e^+\tau^-$
	e^+	$e^+_{\text{mis}}e^-$	τ^+e^-
$e^+\mu^-$	μ_-	$e^+\mu^-_{\text{mis}}$	$e^+\tau^-$
	e^+	$e^+_{\text{mis}}\mu^-$	$\tau^+\mu^-$
μ^+e^-	e^+	$\mu^+e^-_{\text{mis}}$	$\mu^+\tau^-$
	μ^+	$\mu^+_{\text{mis}}e^-$	τ^+e^-
$\mu^+\mu^-$	μ^-	$\mu^+\mu^-_{\text{mis}}$	$\mu^+\tau^-$
	μ^+	$\mu^+_{\text{mis}}\mu^-$	$\tau^+\mu^-$

By its definition, $\alpha := 1/N_{\text{acc.}}\kappa$ roughly gives the ratio of expected effective statistics in CR with respect to the SR, where $N_{\text{acc.}}$ is average number of accepted sub-events after the kinematical cuts. α is typically $3 \sim 5$ for the missing lepton replacement, and about 1.4 ($\sim 1/\text{Br}(\tau \to \tau_{\text{h}}\nu)$) for the tau replacement at the pre-selection level ($N_{\text{acc.}} \sim 2, 2N$). It is typically enhanced by about factor of 2 when $m_{\text{T}} > m_W$ is required (which is always the case for VRa and SR) for replaced sub-events. This is due to the fact that most of the di-leptonic SM processes follow [1] :

$$\min\left[m_{\text{T}}(\ell_1, E_{\text{T}}^{\text{miss}}), m_{\text{T}}(\ell_2, E_{\text{T}}^{\text{miss}})\right] < m_W, \tag{6.3}$$

in other words, either of the m_{T} must be below m_W, as a result nearly half of the generated sub-events will be discarded ($N_{\text{acc.}} \sim 1, N$). Accordingly, together with the fact that the contribution from the tau replacement is dominant, the effective CR statistics for the object replacement method is constantly about 3 times more than that in SR. This factor of 3 gain in statistics is in fact subtle; given that the expected yields in SRs are typically a few events, it immediately leads to $20\% - 50\%$ statistical uncertainty by itself. Therefore CR statistic is always the biggest source of uncertainty in this method.

Lepton efficiency

The lepton efficiency used in the transfer factor calculation is calculated using $t\bar{t}$ MC sample as well. The efficiency of ID/baseline/signal lepton requirement is respectively defined as the fraction of truth leptons that are ΔR-matched with reconstructed passing the ID / identified / signal lepton requirement by $\Delta R < 0.2$. Leptons overlapped with jets (if the nearest jet closer than $\Delta < 0.4$) are excluded since their efficiency is biased. The efficiencies are parameterized as a function of lepton flavor (e/μ), p_{T} and η of truth leptons. The data/MC scale factor measured by $Z \to ee/\mu\mu$ are applied. The resultant efficiency maps are shown in Figure 6.24.

[1] This holds when the event contains exactly two semi-leptonically W-bosons, and the two leptons and MET are only supplied from them. More detail in [138].

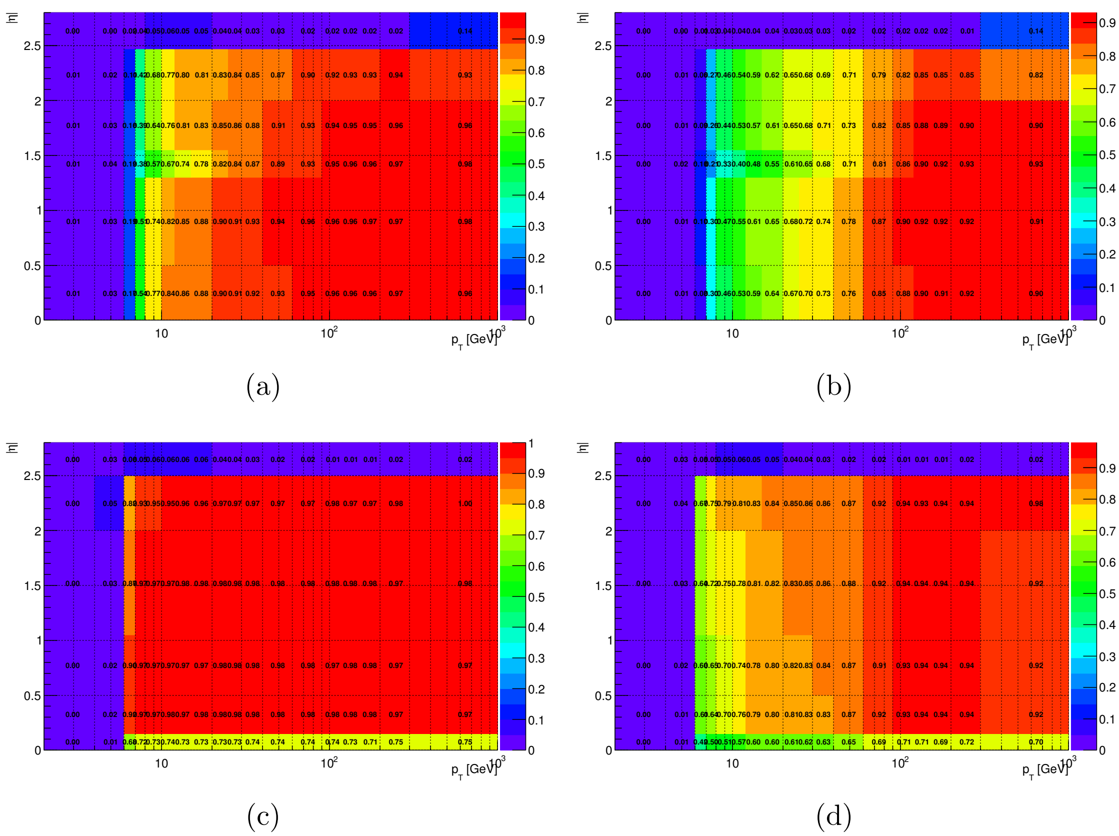

Figure 6.24: Off-line selection efficiency used in transfer factor calulation. (a) Efficiency of electrons passing reconstruction and ID. (b) Efficiency of electrons passing signal lepton requirement. (c) Efficiency of muons passing reconstruction and ID. (d) Efficiency of muons passing signal lepton requirement.

Post selection for rejecting signal contamination

Signal contamination is generally not negligible when estimating SR-like regions in this method, since there are a class of benchmark models that result in $3 \sim 4$ W-bosons giving comparable di-leptonic branching as the semi-leptonic one. The contamination is generally disfavored since it will elevate the expected background level, causing the deterioration of either discover and exclusion sensitivity.

A post selection shown in Table 6.25 is applied for sub-events passing the kinematical selections, to get rid such the signal contamination. The key observation is that only SM processes follow the condition Eq. (), therefore have a sharp cut-off in $m_{\mathrm{T}}(\ell_{\mathrm{rep.}}, E_{\mathrm{T}}^{\mathrm{miss}}) \sim m_W$ when $m_{\mathrm{T}}(\ell_{\mathrm{tag}}, E_{\mathrm{T}}^{\mathrm{miss}}) > m_W$, as shown in Figure 6.25.

The cut is designed to maintain the efficiency greater than 90% in SRs, which will be eventually compensated by MC in deriving the final estimation. On the other hand, signal contamination is largely suppressed typically to $y_{\mathrm{contami.}}/y_{\mathrm{S}} = 0.05 \sim 0.15$ in SRs after the post selection, where $y_{\mathrm{contami.}}$ (y_{S}) is the expected increase of expected background due to the contamination (expected signal yield) in the region.

Table 6.12: Post selection for rejecting signal contamination. Inclusive efficiency of sub-events from SM backgrounds are shown, which is calculated by MC. The inverse is applied to the final result to compensate the loss.

Region	$m_{\mathrm{T}}(\ell_{\mathrm{rep.}}, E_{\mathrm{T}}^{\mathrm{miss}})$ [GeV]	SM efficiency
SR	< 250	$0.9 \sim 0.98$
VRa	< 300	> 0.97
VRb	–	1

Event-level histogram and the statistical treatment

Multiple sub-events are generated by both missing lepton replacement and tau replacement from a single seed event. Those passing the analysis selections are collected and filled into a common histogram, referred as "event-level" (this corresponds to a one-bin histogram when one only wants to estimate the yield in a particular region). To account for their full statistical correlation between the filled sub-events, 100% error is then assigned to each bin of the event-level histogram. The summed event-level histograms over all seed events will be the desired distribution. While the statistical error on each bin is simply the quadratic sum of those over the all event-level histograms, there is generally also the inter-bin correlation since the bins of event-level histograms are not statistically independent between each other. This correlated uncertainty in fact needs to be modeled when performing the combined fit with multiple signal bins, which is examined and summarized in Sec. 7.3.

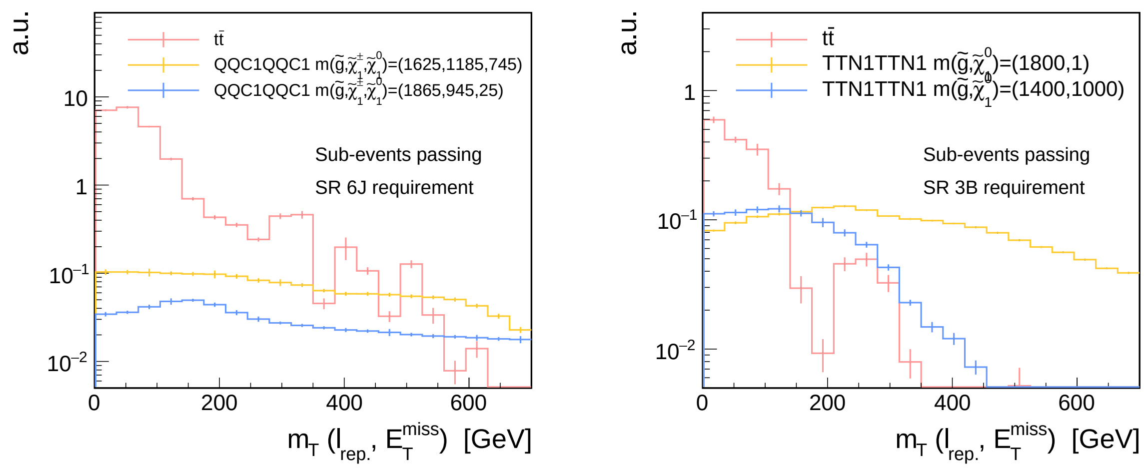

(a) (b)

Figure 6.25: $m_{\mathrm{T}}(\ell_{\mathrm{rep.}}, E_{\mathrm{T}}^{\mathrm{miss}})$ for sub-events passing the (a) SR 6J m_{eff}-inclusive selection, and (b) SR 3B m_{eff}-inclusive selection. Normalization is arbitrary.

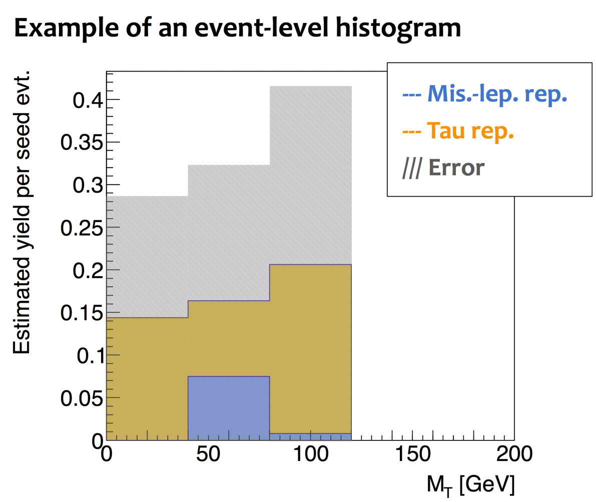

Figure 6.26: An example of event-level histogram. 100% uncertainty is assigned for each bin to account for the fact that all the entries are from the same seed. Final estimation is given by the sum of the event-level histograms over all seed events.

6.3.2 Closure Test using $t\bar{t}$ MC Samples

The methodologies are tested by comparing yields in regions with exactly one baseline lepton, between the estimation using the seed events in 2LCR and the actual $\ell\ell_{\mathrm{mis.}}/\ell\tau_h$ events. The test is referred as "closure test" where the level of disagreement (non-closure) indicates the generic accuracy about this method. The evaluated non-closure is assigned as systematics uncertainty. In the MC closure test, simulated $t\bar{t}$ sample is used in both seed events and the $\ell\ell_{\mathrm{mis.}}/\ell\tau_h$ events. All the other processes are absent thus no subtraction is taken. The common 2LCR selection as defined in Table 6.9 is applied for seed events selection, except that the MET cut is removed in order to boost the statistics.

Figure 6.27 $\sim$ 6.29 show the result with $p_{\mathrm{T}} > 35$ GeV is required for the tag lepton. The test result for the case with a soft lepton ($p_{\mathrm{T}} \in [6, 35]$ GeV) is displayed in the Appendix C.2.
Good closure is seen in overall kinematics. Non-closure generally stay within 10% (5%), and never exceeds 30% (10%) significantly for the missing lepton replacement (the tau replacement). Although the closure of missing lepton replacement is worse than that of tau replacement, it is not worrisome since the contribution of $\ell\ell_{\mathrm{mis.}}$ is typically $5 \sim 10$ times smaller than $\ell\tau_{\mathrm{h}}$.

Closure tests are also performed in phase space close to signal regions. Figure 6.30 $\sim$ 6.31 are the btag/bveto-splitted closure in various regions requiring high MET, m_T, $m_{\mathrm{eff.}}$ etc. The non-closure stay within 30% (10%) for the missing lepton replacement (the tau replacement).

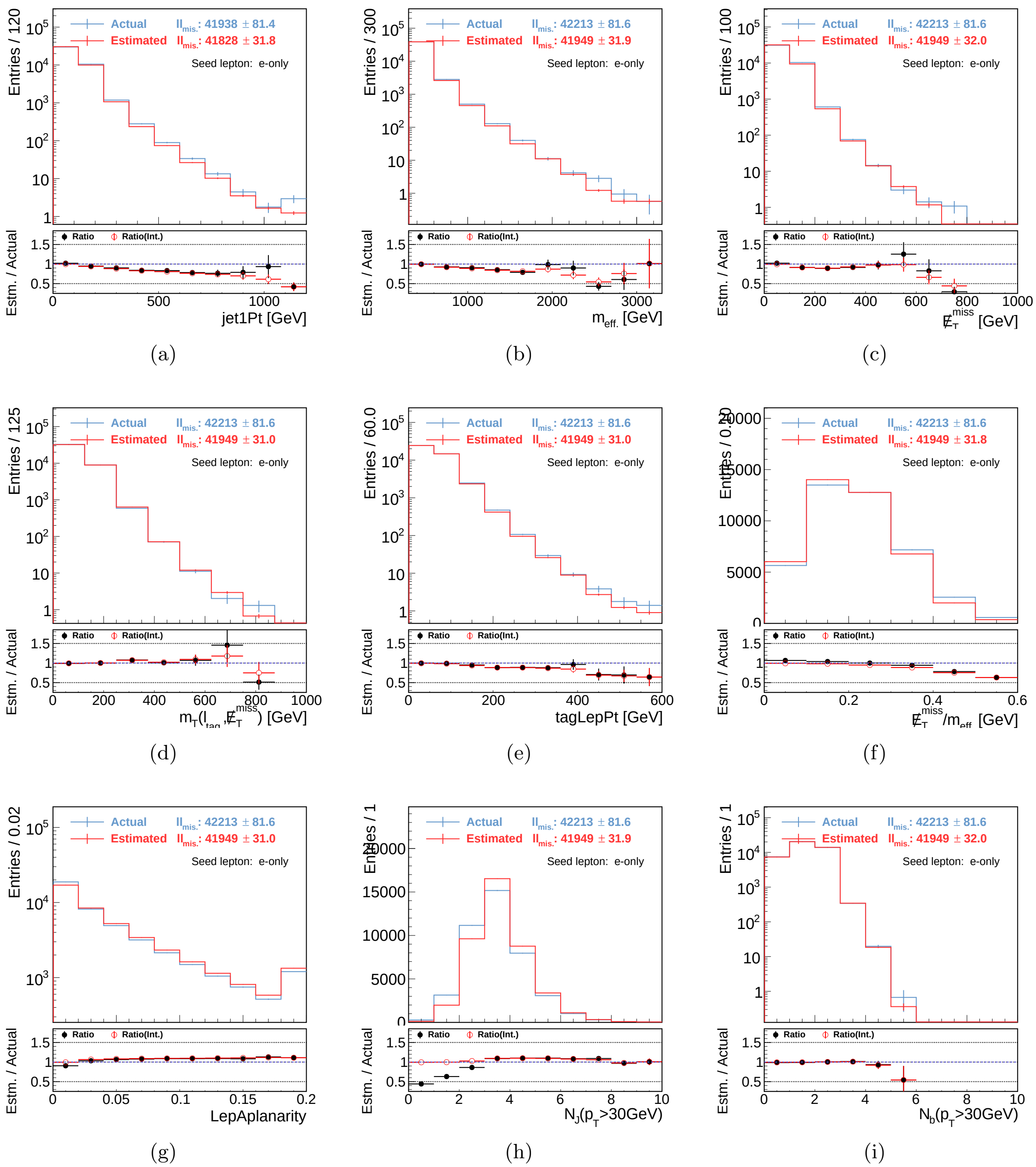

Figure 6.27: MC closure test for **missing lepton replacement** using $t\bar{t}$ MC sample. Seed events are collected by the single-lepton trigger. $p_T > 35$ GeV for the leading lepton is required. **Only electrons in the seed events are replaced**. Red points in the bottom plots show the ratio of integrated yields for the two histograms above the x-position that the point indicates.

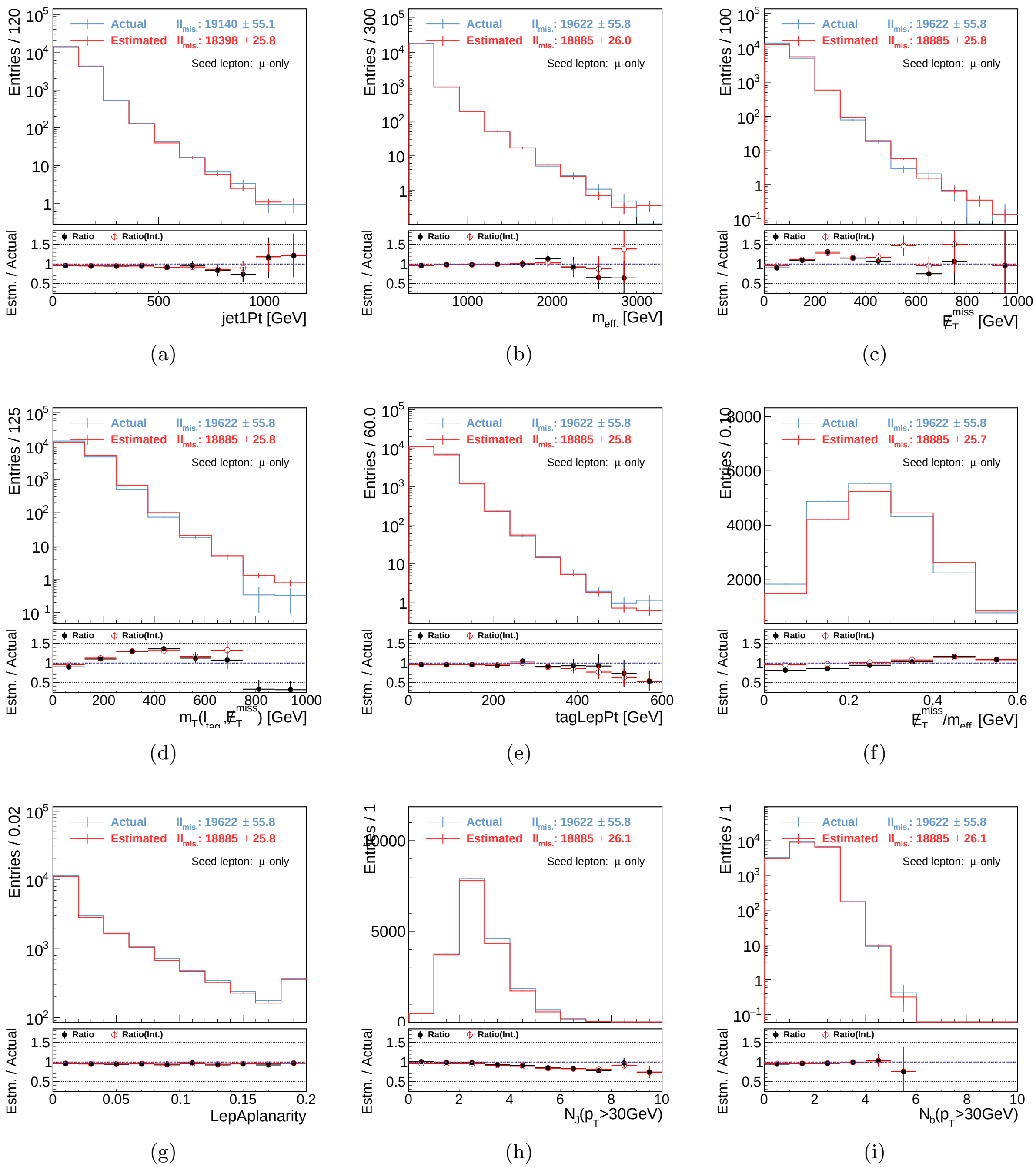

Figure 6.28: MC closure test for **missing lepton replacement** using $t\bar{t}$ MC sample. Seed events are collected by the single-lepton trigger. $p_T > 35$ GeV for the leading lepton is required. **Only muon in the seed events are replaced**. Red points in the bottom plots show the ratio of integrated yields for the two histograms above the x-position that the point indicates.

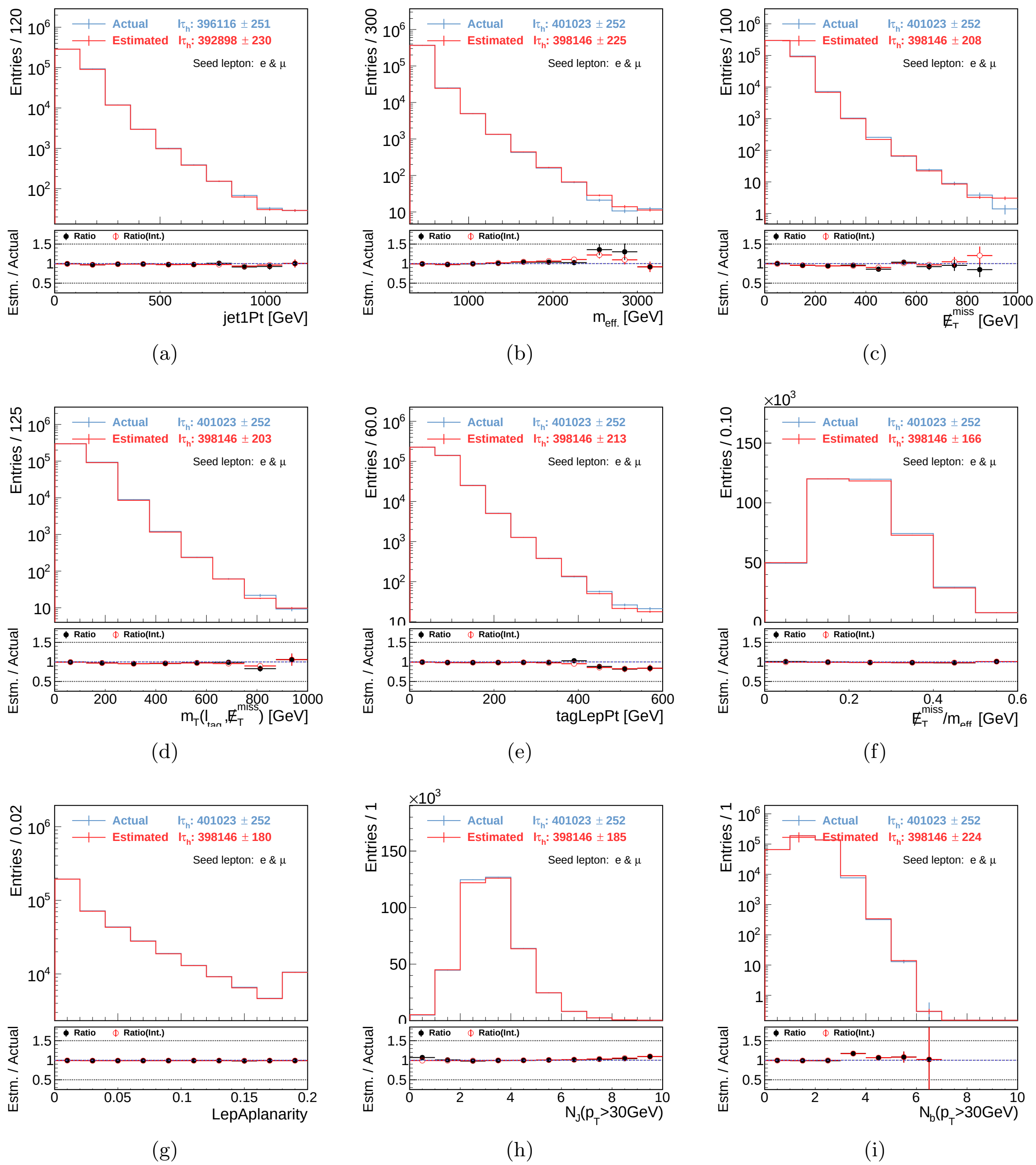

Figure 6.29: MC closure test for **tau replacement** using $t\bar{t}$ MC sample. Seed events are collected by the single-lepton trigger. $p_T > 35$ GeV for the leading lepton is required. **Both electrons and muons in the seed events are replaced**. Red points in the bottom plots show the ratio of integrated yields for the two histograms above the x-position that the point indicates.

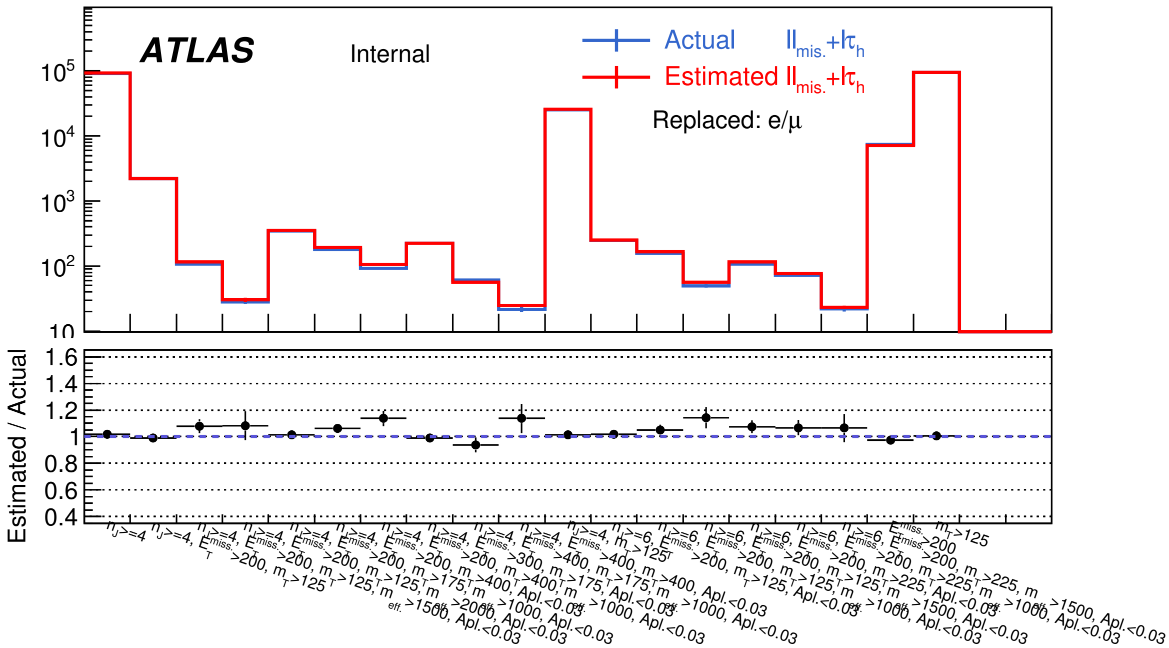

Figure 6.30: MC closure test for **combined estimation of missing-lep. rep. and tau replacement** in SR-like **b-tagged** regions. Pre-selection $p_T(\ell_1) > 35$ GeV is applied on top of the cuts noted by the labels.

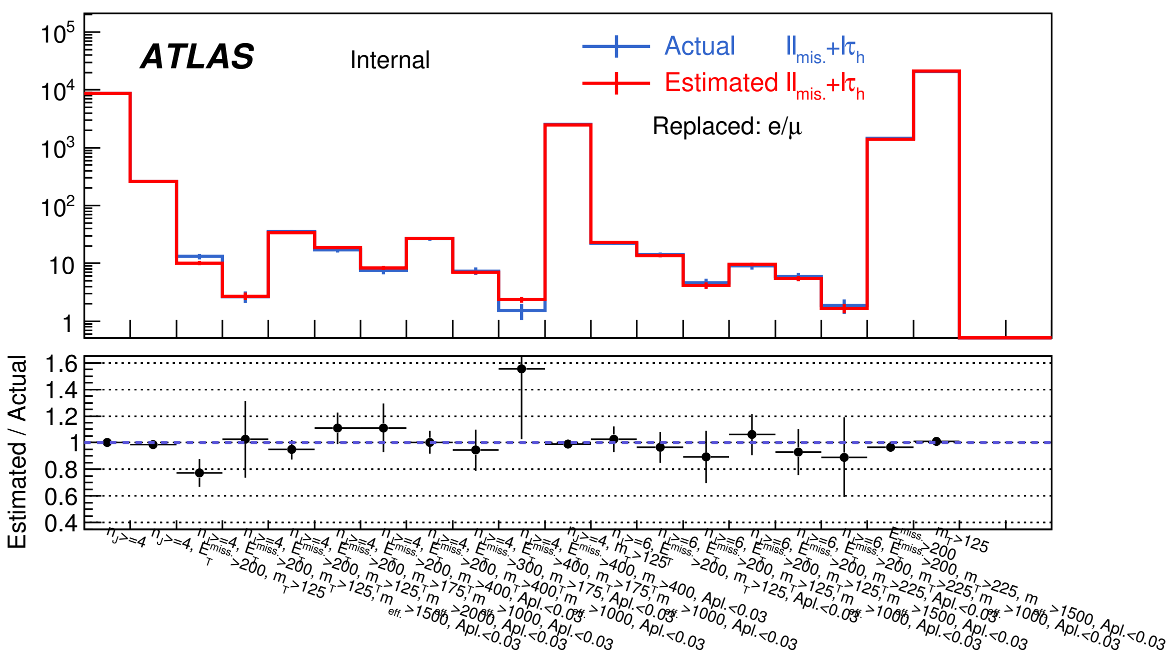

Figure 6.31: MC closure test for **combined estimation of missing-lep. rep. and tau replacement** in SR-like **b-vetoed** regions. Pre-selection $p_T(\ell_1) > 35$ GeV is applied on top of the cuts noted by the labels.

6.3.3 Source of non-closure

Visible non-closures are found in some distributions such as MET and jet transverse momenta, and the cause is nailed down as following:

Kinematical bias triggered by the two lepton requirement in seed event selection (All)

Though the orthogonality between kinematics and object properties (Eq. 6.1) generally hold as a good approximation, there is still some exception. The most notable example is when the parent particles of the two leptons in a seed event are heavily boosted, the leptons get collimated and overlapped each other. This leads to deteriorated reconstruction/ID efficiency, therefore selecting events with exactly two leptons already discard the seed events in such phase space. The estimated spectra is biased and generally become softer. Electrons address more severe effect because the efficiency drop in the boosted environment is more distinct than the case of muons.

Wrong assumption on tau polarization (tau replacement)

For technical simplicity, tau leptons are assumed to be unpolarized during the decay, which is not true given that tau leptons in consideration are mostly generated through weak decays of W-bosons. For example, the case of Figure 6.32 (a) shows the visible tau fraction $x := E(\tau_h)/E(\tau)$, a variable sensitive to tau polarization, for taus in the $t\bar{t}$ process in a blue line, and for the case of unpolarized hypothesis in a red line. This discrepancy is known to eventually propagated to the non-closures in the tail of MET and $m_{\mathrm{T}}(p_{\mathrm{T}}(\ell), E_{\mathrm{T}}^{\mathrm{miss}})$ such as the left plots in Figure 6.32 and fig. 6.33. On the other hand, these non-closure can be cured by a simple reweighting in terms of x, as they are purely caused by the issue of polarization modeling. Obtaining the reweighting function by fitting the non-closure in x with a third polynomial as shown in Figure 6.32 (c), nicely recovered closures in MET and $m_{\mathrm{T}}(p_{\mathrm{T}}(\ell), E_{\mathrm{T}}^{\mathrm{miss}})$ are confirmed as in the right plots in Figure 6.32 and fig. 6.33 respectively.

This x-reweighting is however not brought into practice, because the x-profile varies by the physics processes (e.g. $t\bar{t}$, Wt or WW etc.) and the information of their relative breakdown needs to be provided from MC which uncertainty is not easy to evaluate. Fortunately, since the impact of this non-closure is marginal in estimating VRs and SRs ($< 5\%$), it is decided to be left as it is.

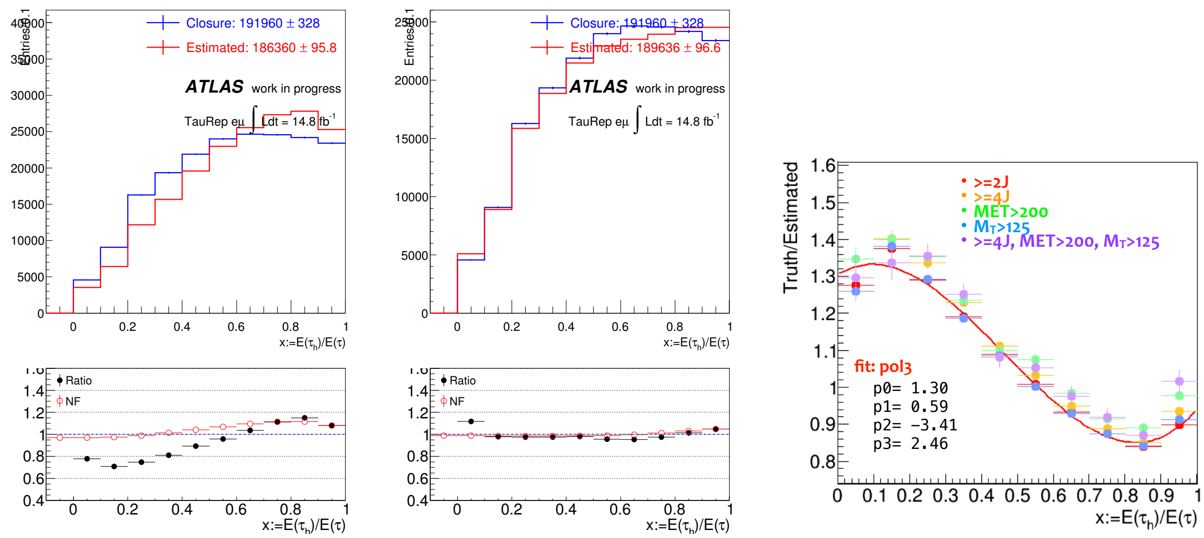

(a) (b) (c)

Figure 6.32: Reweighting in terms of the visible tau fraction $x := E(\tau_h)/E(\tau)$. (a) x distribution before the reweighting , (b) x distribution after the reweighting. (c) An ad hoc fit of the reweighting function by third order polynomial. The reweighting function is almost invariant in terms of phase space.

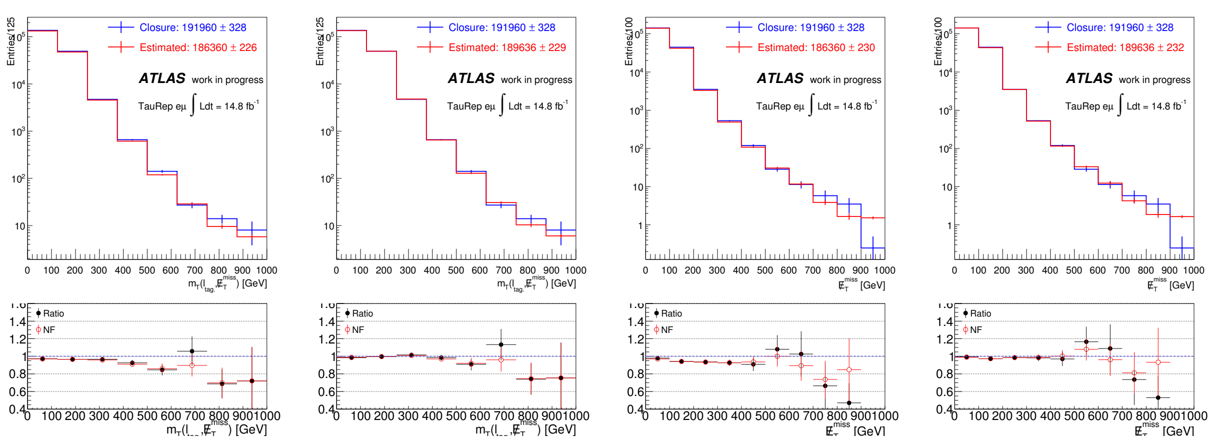

(a) (b) (c) (d)

Figure 6.33: (a) m_{T} and (c) MET distribution before the reweighting in x, and (b)(d) after the reweighting.

Treatment of missing muon

While the emulated missing muons are completely regarded as invisible particles in the replacement algorithm, the momenta of real unidentified muons do contribute to MET since their tracks are often included in the track soft term. This imperfect emulation leads to a non-closure around MET-related variables in the missing muon replacement. Naively thinking, this can be improved by simply stopping adding the missing muons momenta into MET. However, this is unfortunately not the case, as shown in Figure 6.34 where the improvement is limited in bulk region of the MET spectrum and the closure in the tail gets even worse. This is mainly because the poor momentum resolution of high pt unidentified muons is not emulated in the replacement. As the implementation of the full emulation is too costly compared with the small portion of missing muons backgrounds in the estimated regions, it is decided to keep the original treatment. Instead, the 30% of non-closure error is additionally quoted to the estimation of the missing muon background.

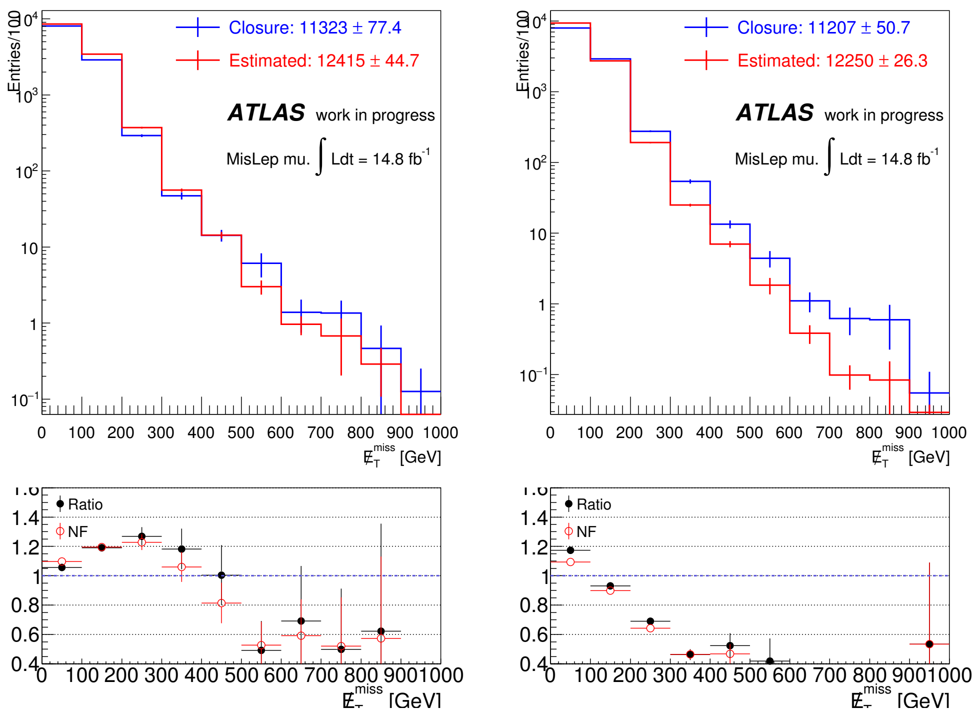

(a) (b)

Figure 6.34: The MC closure of MET distribution for the missing muon sub-events, with (a) the default treatment of missing muons where they are fully counted as invisible particles, and (b) the alternative method where the momenta of missing muons are fully included in the MET soft term and no addition is applied to MET.

6.3.4 Subtraction of Bogus Sub-events

Although the object replacement method is designed to estimate the di-leptonic decays of $t\bar{t} + Wt$ and WW which are the dominant "di-leptonic" backgrounds in b-tagged and b-vetoed regions, it is also applicable to estimate the other minor backgrounds such as $t\bar{t} + W$. Basically any leptons in 2LCR are eligible to be replaced, since the replaced sub-event could exist for most of the case. However, there are couple of exceptions: if the replaced lepton is from Z, sub-events of tau replacement will lead to a bogus topology of $Z \to \tau_h \ell$ $(ell = e, \mu)$ which never happens, thus these sub-events (bogus sub-events) are need to be subtracted.

Likewise, seed leptons from leptonic tau decays $(\tau \to \tau_\ell \nu \bar{\nu})$ have the same issue that tau replacement leads to bogus sub-event where tau decays into tau again. Replacing fake lepton will only end up in bogus sub-events. The summary of legal and illegal replacement is given in Table 6.13 where bogus sub-events are label as "$\times''$. Note that the decision is made on each sub-event level (not seed event level), therefore even $W(\to \ell\nu) + \ell_{\rm fake}$ can be seed events as long as one replaces ℓ rather than $\ell_{\rm fake}$.

Table 6.13: Correspondence between origin of seed lepton and estimated components by the missing lepton replacement or the tau replacement. X represents any arbitrary particles. $''\times''$ indicates that the generated sub-events represent non-existing processes ("bogus sub-events") that requires the subtraction. The subscripts mis. denote missing leptons (leptons categorized in "Mis. Reco" and "Mis. ID" defined in Table 6.1).

Parent of seed lepton	Sub-events of mis. lep. rep.	Sub-events of tau rep.
$W(\to \ell\nu)$	$W + X$, $W \to \ell_{\rm mis.}\nu$	$W + X$, $W \to \tau_{\rm h}\nu$
$Z(\to \ell\ell)$	$Z + X$, $Z \to \ell_{\rm mis.}\ell$	$\times$
$\tau(\to \tau_\ell \nu)$	$\tau_{\ell,\rm mis.} + X$	$\times$
Fake	$\times$	$\times$

While the sub-traction takes place on sub-event basis, if can be only done statistically i.e. evaluate total contribution from bogus sub-events and subtract once. The largest source of bogus sub-events are seed events with τ_ℓ. The contribution is quite large, accounting for $10\% \sim 20\%$ of the estimated yields by the tau replacement. Therefore, a naive MC subtraction could introduce culprits from the MC mis-modeling, for example on $t\bar{t}$ as overviewed in Sec. 6.2.1. Instead, to avoid the impact, the subtraction is done in a form of ratio, such as:

$$y_\ell^{\rm Data} = y_{\ell+\tau_\ell}^{\rm Data} \times \frac{y_\ell^{\rm MC}}{y_\ell^{\rm MC} + y_{\tau_\ell}^{\rm MC}} \tag{6.4}$$

where $y_\ell^{\rm Data}$ $(y_{\ell+\tau_\ell}^{\rm Data})$ denote the total yield estimated by tau replacement using data before (after) the subtraction, and $y_\ell^{\rm MC}$ $(y_{\tau_\ell}^{\rm MC})$ the contribution from legal (bogus) sub-events of tau replcement estimated by MC.
The subtraction of the $\ell\ell_{\rm fake}$ is a little sensitive as MC modeling on fake leptons is less reliable in general. Therefore, relatively more aggressive suppression is applied at the stage of seed selection (Table 6.10) by requiring tighter isolation, in case that it could be addressing.

6.3.5 Closure Test using Data in the Loose Validation Regions.

In order to demonstrate the procedures beyond the ideal MC closure tests done in Sec. 6.3.2 such as the subtraction, another validation study is done using the data events.
Since the nominal VRs (Table 5.7 - 5.11) tends to have too tight selections with small data statistics, a set of high-m_{T} regions "VR-objRep" with relatively loose selections are deliberately defined, in which the object replacement estimation and data is compared. 9 complementary bins are defined as in Table 6.14.

It is populated by $\ell\ell_{\mathrm{mis.}}/\ell\tau_h$ events with the purity of $\sim 50\%$, and the rest of backgrounds that are not covered by the object replacement (namely the "semi-leptonic", "2L-Out. Acc" and "2L-Mis. OR" components) are estimated by a kinematics extrapolation where the MC of $W+\mathrm{jets}$ and $t\bar{t}+Wt$ is normalized in the corresponding control region bins ("CR-objRep") which are only different in m_{T} with respect to VR-objRep, as defined in Table 6.14. An upper cut in aplanarity is set in either the VRs and the CRs so that the signal contamination is subdued. Statistical uncertainty from the control region statistics, and flat 5% non-closure error is assigned for the object replacement estimation in all the VR bins.

The result is presented in Figure 6.35. The agreement with data is found within the uncertainty.

Table 6.14: Definition of VRs(CRs) objRep. MC of $W+\mathrm{jets}$ and $t\bar{t}+Wt$ are normalized in corresponding CR-objRep.

	n_{J} ($p_{\mathrm{T}} > 30$ GeV)	$E_{\mathrm{T}}^{\mathrm{miss}}$ [GeV]	m_{T} [GeV] (CR-objRep)	m_{eff} [GeV]	Aplanarity
bin-1	≥ 4	> 200	> 125 ($\in [60, 125]$)	> 1500	< 0.03
bin-2	≥ 4	> 200	> 125 ($\in [60, 125]$)	> 2000	< 0.03
bin-3	≥ 4	> 200	> 175 ($\in [60, 125]$)	> 1000	< 0.03
bin-4	≥ 4	> 200	> 400 ($\in [60, 125]$)	–	< 0.03
bin-5	≥ 4	> 200	> 400 ($\in [60, 125]$)	> 1000	< 0.03
bin-6	≥ 4	> 300	> 175 ($\in [60, 125]$)	–	< 0.03
bin-7	≥ 4	> 400	> 175 ($\in [60, 125]$)	> 1000	< 0.03
bin-8	≥ 6	> 400	> 400 ($\in [60, 125]$)	–	< 0.03
bin-9	≥ 6	> 200	> 125 ($\in [60, 125]$)	> 1500	< 0.03

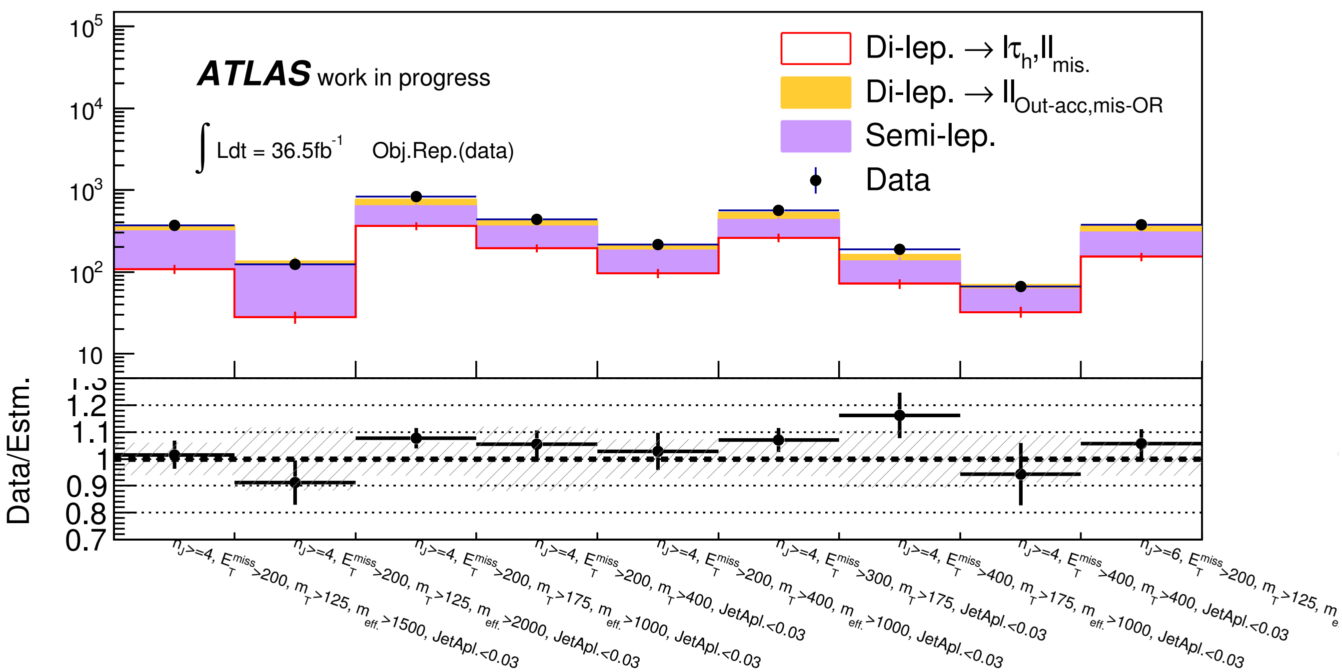

Figure 6.35: Closure test in VRs objRep bins. The white component shows the yield of the $\ell\ell_{\mathrm{mis.}}\ \ell\tau_h$ events that are estimated by the object replacement, while the colored represents the "semi-leptonic" (purple) and "2L-Out. Acc / Mis. OR" components (orange) respectively. The bottom row plots the ratio between the estimated yield and actual number of data. The gray dashed band shows the uncertainty in the estimation which is statistical error due to the CR statistics and flat 5% non-closure for the object replacement.

6.4 Unblinded Validation Regions

The background estimation is inclusively tested in validation regions VRa and VRb defined in Table 5.7 - 5.11, where the phase space are close enough to the signal regions, giving the sensible demonstration of the estimation.

Table 6.15 - 6.19 show the data yields and the expected background together with the breakdowns. The components estimated by the object replacement are merged and denoted as "Di-leptonic" in the tables, while the yields for the other components provided by the kinematical extrapolation are exlusively listed by physic processes. The errors are all post-fit uncertainty with the nuisance parameters profiled (detail found in Sec. 8.1).

The visualized comparison between data and background expectation is illustrated in 6.36, together with the pulls defined by the number of gaussian-equivalent deviation. The tension with respect to data never exceed 2σ, which is still consistent to ascribing to the effects that the systematic uncertainties are paying for. For instance, the trend of underestimating $W+$jets in some of the VRb (in particular 2J) can be understood by the biased extrapolation due to the correlation with the ill-modeled variations, as discussed previously in Sec. 6.2. 15% of uncertainty is in fact assigned for this effect (based on Figure D.1.9, with the the mis-modeling parameter x to be at ~ 0.1). Another source of systematical underestimation is understood by the potential MC mis-modeling in the m_{T} shape as mentioned in Sec. 6.2.1; for $W+$jets, the cut-off at $m_{\mathrm{T}} \sim m_W$ in MC is sharper than that in the data. No theoretical uncertainties are dedicatedly assigned for this effect, however it could still be explained by other theoretical uncertainties given the $\sim 1\sigma$ discrepancy; for $t\bar{t}+Wt$, lack of full description of interference between the non-top $WWbb$ diagrams could be the potential reason for the underestimation for which $5\% \sim 30\%$ of uncertainty is assigned. All in all, underestimation upto 1σ is expected therefore we don't regard this as an issue.

The post-fit kinematical distributions in VRs are presented in Figure C.4.9-C.4.12 in the appendix.

Table 6.15: Event yields and the background-only fit results in the "2J" control regions. Each column corresponds to a bin in m_{eff}. Uncertainties in the MC estimates combine statistical (in the simulated event yields) and systematic uncertainties discussed in chapter 7. The uncertainties in this table are symmetrised for propagation purposes but truncated at zero to remain within the physical boundaries.

VRa 2J	$m_{\text{eff.}} \in$[1100,1500]	$m_{\text{eff.}} \in$[1500,1900]	$m_{\text{eff.}} > 1900$
Observed data	222	46	23
Expected background	209.88 ± 21.80	38.67 ± 5.51	17.28 ± 3.25
Di-leptonic	91.5 ± 11.1	11.7 ± 2.6	5.7 ± 1.6
W+jets	20.9 ± 3.8	8.0 ± 2.6	3.2 ± 1.3
Z+jets	2.6 ± 0.7	0.8 ± 0.2	0.3 ± 0.1
Tops	85.6 ± 18.0	15.6 ± 3.8	6.9 ± 2.8
Di-boson	6.0 ± 2.2	1.5 ± 0.5	0.8 ± 0.3
$t\bar{t} + V$	3.2 ± 0.5	0.9 ± 0.2	0.4 ± 0.1
VRb 2J	$m_{\text{eff.}} \in$[1100,1500]	$m_{\text{eff.}} \in$[1500,1900]	$m_{\text{eff.}} > 1900$
Observed data	390	113	52
Expected background	314.33 ± 36.92	104.33 ± 13.80	41.34 ± 8.95
Di-leptonic	10.5 ± 2.4	3.0 ± 1.1	3.7 ± 1.3
W+jets	219.5 ± 34.9	76.8 ± 13.0	24.9 ± 9.2
Z+jets	5.1 ± 1.3	2.0 ± 0.6	0.8 ± 0.2
Tops	56.7 ± 14.1	15.7 ± 4.5	8.1 ± 3.2
Di-boson	21.3 ± 7.4	6.3 ± 4.5	3.5 ± 1.1
$t\bar{t} + V$	1.2 ± 0.2	0.5 ± 0.1	0.4 ± 0.1

Table 6.16: Event yields and the background-only fit results in the "6J" control regions. Each column corresponds to a bin in m_{eff}. Uncertainties in the MC estimates combine statistical (in the simulated event yields) and systematic uncertainties discussed in chapter 7. The uncertainties in this table are symmetrised for propagation purposes but truncated at zero to remain within the physical boundaries.

VRa 6J	$m_{\text{eff.}} \in$[1100,1600]	$m_{\text{eff.}} \in$[1600,2100]	$m_{\text{eff.}} > 2100$
Observed data	130	60	31
Expected background	134.22 ± 18.17	48.27 ± 7.79	28.71 ± 4.57
Di-leptonic	71.9 ± 15.2	24.7 ± 6.8	11.5 ± 3.5
W+jets	7.6 ± 1.8	4.0 ± 1.0	2.5 ± 0.9
Z+jets	0.6 ± 0.2	0.3 ± 0.1	0.2 ± 0.1
Tops	45.7 ± 9.8	16.0 ± 3.7	12.0 ± 2.9
Di-boson	4.6 ± 1.5	2.1 ± 0.7	1.6 ± 0.7
$t\bar{t} + V$	3.8 ± 0.7	1.2 ± 0.3	0.9 ± 0.2
VRb 6J	$m_{\text{eff.}} \in$[1100,1600]	$m_{\text{eff.}} \in$[1600,2100]	$m_{\text{eff.}} > 2100$
Observed data	99	53	26
Expected background	84.21 ± 10.42	43.22 ± 5.50	25.15 ± 3.89
Di-leptonic	0.9 ± 0.4	1.0 ± 0.8	0.5 ± 0.4
W+jets	32.9 ± 6.5	21.8 ± 4.7	8.6 ± 2.9
Z+jets	0.4 ± 0.2	0.3 ± 0.1	0.2 ± 0.1
Tops	43.1 ± 9.0	16.3 ± 3.8	13.0 ± 3.4
Di-boson	5.6 ± 2.6	2.9 ± 1.8	2.3 ± 1.1
$t\bar{t} + V$	1.3 ± 0.3	0.9 ± 0.2	0.5 ± 0.2

Table 6.17: Event yields and the background-only fit results in the "Low-x" control regions. Each column corresponds to a bin in m_{eff}. Uncertainties in the MC estimates combine statistical (in the simulated event yields) and systematic uncertainties discussed in chapter 7. The uncertainties in this table are symmetrised for propagation purposes but truncated at zero to remain within the physical boundaries.

VR Low-x	VRa	VRb
Observed data	20	23
Expected background	14.91 ± 2.09	15.77 ± 3.31
Di-leptonic	6.5 ± 1.2	0.6 ± 0.3
W+jets	1.5 ± 0.8	6.9 ± 3.3
Z+jets	0.5 ± 0.2	0.5 ± 0.2
Tops	5.0 ± 1.7	6.1 ± 2.1
Di-boson	1.0 ± 0.3	1.4 ± 0.4
$t\bar{t} + V$	0.4 ± 0.1	0.4 ± 0.1

Table 6.18: Event yields and the background-only fit results in the "High-x" control regions. Each column corresponds to a bin in m_{eff}. Uncertainties in the MC estimates combine statistical (in the simulated event yields) and systematic uncertainties discussed in chapter 7. The uncertainties in this table are symmetrised for propagation purposes but truncated at zero to remain within the physical boundaries.

VR High-x	VRa	VRb
Observed data	66	119
Expected background	49.33 ± 8.80	102.12 ± 13.40
Di-leptonic	18.9 ± 5.4	0.0 ± 0.0
W+jets	8.8 ± 1.8	70.6 ± 13.3
Z+jets	0.4 ± 0.1	0.7 ± 0.3
Tops	16.0 ± 6.8	21.5 ± 7.5
Di-boson	4.2 ± 1.6	8.5 ± 3.2
$t\bar{t} + V$	1.1 ± 0.4	0.8 ± 0.3

Table 6.19: Event yields and the background-only fit results in the "3B" control regions. Each column corresponds to a bin in m_{eff}. Uncertainties in the MC estimates combine statistical (in the simulated event yields) and systematic uncertainties discussed in chapter 7. The uncertainties in this table are symmetrised for propagation purposes but truncated at zero to remain within the physical boundaries.

VRa 3B	$m_{\text{eff.}} \in$[1000,1750]	$m_{\text{eff.}} > 1750$
Observed data	11	8
Expected background	12.46 ± 5.81	5.31 ± 1.58
Di-leptonic	7.3 ± 5.5	2.7 ± 1.3
W+jets	$0.0^{+0.0}_{-0.0}$	0.0 ± 0.0
Z+jets	0.0 ± 0.0	0.0 ± 0.0
Tops	4.8 ± 1.7	2.4 ± 0.9
Di-boson	$0.1^{+0.1}_{-0.1}$	0.0 ± 0.0
$t\bar{t} + V$	0.2 ± 0.1	0.2 ± 0.0
VRb 3B	$m_{\text{eff.}} \in$[1000,1750]	$m_{\text{eff.}} > 1750$
Observed data	69	12
Expected background	60.09 ± 15.83	9.55 ± 2.77
Di-leptonic	3.3 ± 1.4	0.8 ± 0.6
W+jets	0.8 ± 0.5	0.4 ± 0.2
Z+jets	0.1 ± 0.0	0.0 ± 0.0
Tops	54.1 ± 15.7	7.8 ± 2.7
Di-boson	0.1 ± 0.1	0.2 ± 0.1
$t\bar{t} + V$	1.7 ± 0.4	0.4 ± 0.1

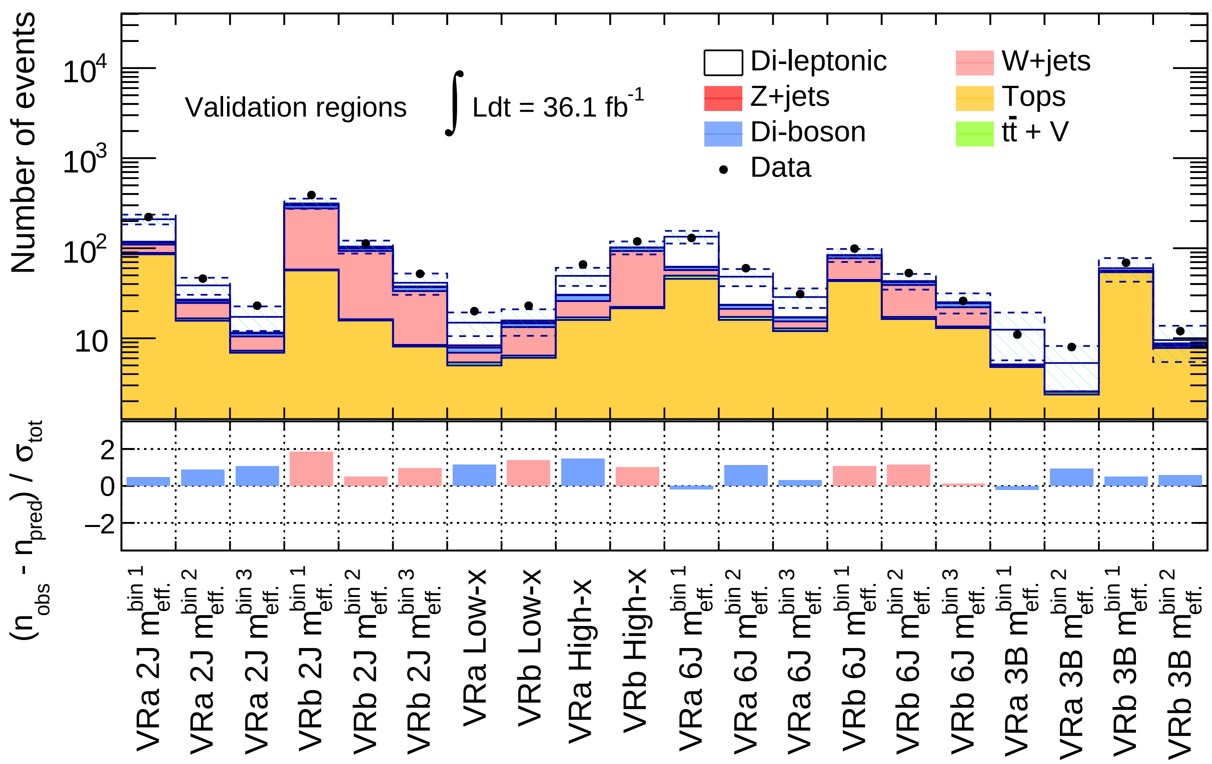

Figure 6.36: (Top) Observed data and the estimated yields in the nominal validation regions (VRa/VRb). The white component is the backgrounds estimated by the object replacement method, while the colored ones are by the kinematical extrapolation method. The dashed band represents the combined statistical and systematic uncertainty on the total estimated backgrounds. (Bottom) Pull between the data and the estimation. Pulls in regions dominated by $W+$jets and tops are painted by pink and blue respectively.

Chapter 7

Systematic Uncertainties

Uncertainties associated with background estimations and the signal modeling is dedicatedly discussed in this section. They are largely three-fold: instrumental uncertainties, theoretical uncertainties and the the generic uncertainties for the background estimation methods.

7.1 Instrumental Uncertainty

Instrumental uncertainties are the systematic uncertainty regarding to the experiment, including the imperfection of calibration and mis-modeling of detector response and so on.

7.1.1 Jets

Despite the dedicated calibration procedures as described in Sec. 3.6, the residual uncertainty on the jet energy scale (JES) is often the largest source of instrumental uncertainty, since a slight shift of JES can drastically change the tail of distribution. 87 independent uncertainties are modeled from each step in the calibration, including the MC uncertainty and observed discrepancy between MC and data. In the analysis, those with similar behavior are statistically combined, reducing into 8 independent nuisance parameters.

The sub-leading jet uncertainty is on the jet energy resolution (JER). JER measurement is done by the same dataset used in the in-situ JES calibration described in Sec. 3.6.2, using the balanced well-measured objects in di-jet or Z/γ^*+jets events [82]. The uncertainty is quoted from the data/MC discrepancy, as well as the magnitude of the noise term reflecting our imperfect understanding of the origin. Figure 7.1 show the measured total uncertainty on JES and JER.

Systematics associated with flavor tagging are also important since the analysis deeply relies on the classification in b-tagged jet multiplicity. The uncertainty on the efficiency of b-jets and wrongly tagged light-flavor jets is separately evaluated by varying input training samples for each sub-algorithm as well as the training configuration of MV2. Resultant uncertainty is typically in a rage of $5\% \sim 10\%$ level.

Other uncertainties are related to the angular position determination (η-calibration uncertainty)

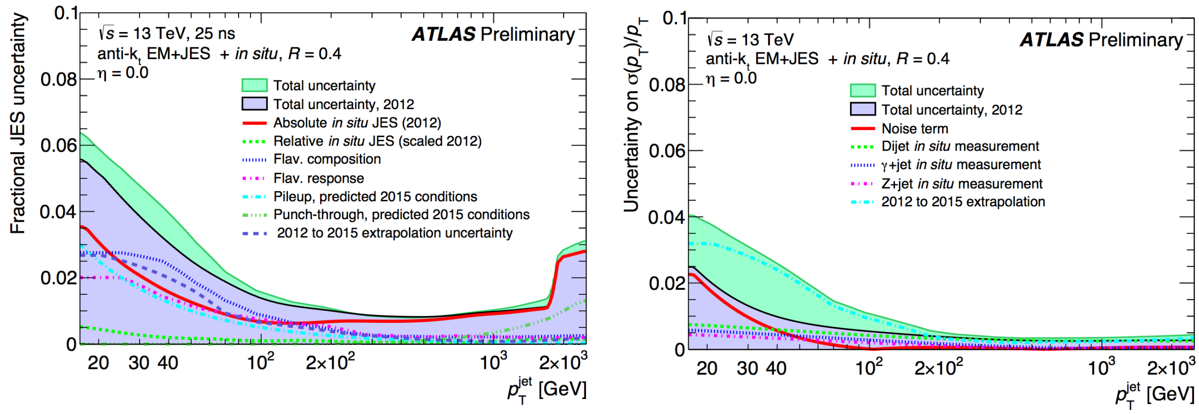

(a) (b)

Figure 7.1: (a) Uncertainty on jet energy scale (JES), and (b) uncertainty on the relative resolution, with the breakdown of each sources being attached [82].

or JVT (Jet Vertex Tagger, Sec. 3.6) modeling uncertainty and so on.

7.1.2 Electrons

Electrons involve three efficiency uncertainties on reconstruction, identification and isolation, as well as the uncertainties on the energy scale and resolution modeling. The efficiencies are measured by exploiting the $Z \to \ell\ell$ process with the tag-probe technique as described in Sec. 3.4, and the uncertainties are derived from the difference between the expected measured efficiencies by MC and the observed ones. The uncertainties on the energy scale and resolution are evaluated based on the discrepancy between simulated and observed response of the EM calorimeter in Run2.

7.1.3 Muons

Four efficiency uncertainties and two separated scale uncertainties are associated to muons. All the uncertainties are derived from the difference between the expectation and observed measurement outcome using $Z \to \mu\mu$ process by the tag-probe technique similarly to the case of electrons. The efficiency uncertainties involve the reconstruction, identification, isolation and TTVA (Tracks-To-Vetex-Association), while the two scale uncertainties corresponds to the statistical and systematic uncertainty in the measurement.

7.1.4 MET

On top of the propagated uncertainties on the scales and resolutions of the reconstructed objects, MET suffers from additional uncertainty regarding to the modeling of the soft term defined in Sec. 3.9. This is measured using the $Z(\to \ell\ell)$ + jets events, by comparing the expected momentum profile of soft terms and the observed ones.

7.2 Theoretical Uncertainty

There are two types of uncertainties subjecting to theoretical uncertainty:

- Cross-section uncertainty affecting the global normalization.
  The primary source contributing to it is the missing higher-order terms in the calculation, such as terms beyond NNLO for the NLO calculation, or the absence of soft gluon resummation. The other typical sources are from PDF, and measurement precision on standard model parameters, particularly in strong coupling constant and quark masses for higher order QCD correction.

- Shape uncertainty affecting the acceptance.
  They are evaluated using the MC samples with specific systematic variations applied. Different recipes for the variation are prepared for each physics process and the generator, and is carefully designed to minimize the double-counting as possible. For the normalized backgrounds (W+jets and $t\bar{t}$), the uncertainties on the extrapolation between CRs to SRs/VRs are considered as the only source of theoretical uncertainty, since the other uncertainties (cross-section uncertainty and the shape uncertainties on CR yields) will be cancelled through the normalization in CRs. On the other hand, the full uncertainties are assigned for the other non-normalized backgrounds ($Z+$ jets, di-bosons and $t\bar{t}+W/Z/WW$) and the SUSY processes, as they are free from any constraints in the analysis. Note that all these theoretical uncertainties are assigned on the post-fit yields without any constraint by the fit.

The impact is only on kinematical extrapolation method and signal modeling. In the kinematical extrapolation, backgrounds normalized to data in CRs ($W+$ jets and tops) are only affected by the shape uncertainty, while the other non-normalized minor backgrounds are hit by both.

7.2.1 Normalized Backgrounds

The shape uncertainties for the normalized backgrounds ($W+$ jets and tops) are essentially the MC modeling uncertainties on the extrapolation variables (mt, aplanarity and topness etc.). They are evaluated by computing the variation in the ratio of MC yields between in a CR and a SR (or VR) when the systematical variations are applied. Some of the cuts are removed to suppress the statistical fluctuation in MC to a sensible level, which is not trivial given that the evaluated variations are often at the level of $5\% - 10\%$. The b-jet requirement is then removed, based on the fact that it is generally orthogonal to kinematics. The m_{eff} cut is also removed in addition to it, based on the concept that the shape variation in terms of the extrapolation variables are tested. Therefore, the evaluated systematics are common to all the bins in the same tower eventually.

The menu of theoretical variations for $W+$ jets are as following:

- Choice of renormalization, factorization and resummation scale for soft gluon.
  The 1σ up/down variations are generated by independently shifting those scales from the default values μ_0 to either $0.5\mu_0$ or $2\mu_0$ respectively.

- Choice of CKKW matching scale.
  The decault matching scale for CKKW is 20 GeV, while it is set to 15 GeV and 30 GeV respectively for variations.

The theoretical variations considered for the top background are as below:

- Choice of renormalization/factorization scale.
  In POWHEG +Box generator, these scales are set to common default values of $\mu_0 = \sqrt{m_t^2 + p_{\mathrm{T},t}^2}$ where m_t and $p_{\mathrm{T},t}$ are the mass and transverse momentum of top quark. The 1σ up/down variations are generated by simultaneously shifting those scales by factor of 2 or 0.5 respectively.

- Parton shower scheme.
  The dependency on parton showering scheme is evaluated by comparing the default scheme (PYTHIA 6.428) with one used in HERWIG. The difference is taken as 1σ variation.

- Interference between top-like $WWbb$ diagrams, and the inclusive $WWbb$ ones.
  The diagrams of $t\bar{t} + Wt$ and the other $WWbb$ diagrams are allowed to interfere each other since they lead to the common final states. This effect is a missed piece in the MC description, however is known to become significant in phase space where the bulk $t\bar{t}$ component is suppressed, for which signal regions are actually designed for. In particular, the topness selection is essentially rejecting the $t\bar{t}$ with the both top quarks being on-shell, in other words, significantly enhancing the contribution from the off-shell tail of top quarks where the interference effect is addressing. The impact is evaluated by comparing two truth-level MadGraph samples: one with the only diagrams of $t\bar{t}+Wt$, and the other with inclusive $WWbb$ diagrams. The difference is taken as 1σ variation.

The evaluated uncertainties are listed in Table 7.1 and 7.2 for W + jets and $t\bar{t}$ respectively. Systematics contributing below 5% or 5 times less than that of the leading uncertainty in the region are ignored.

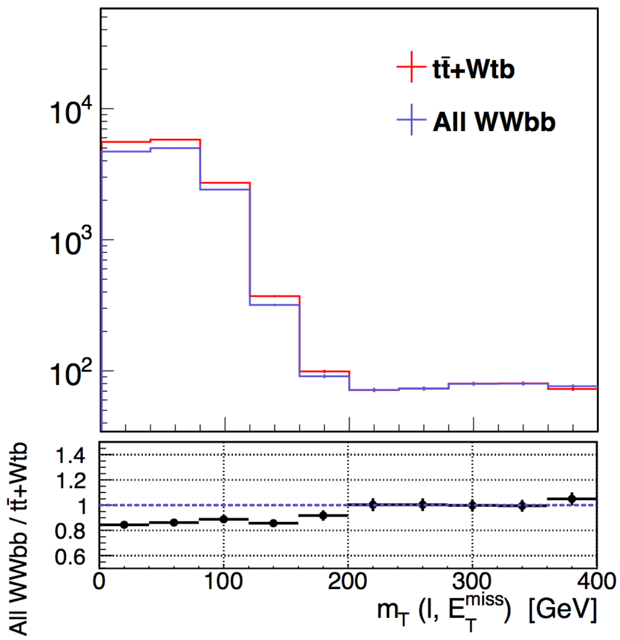

Figure 7.2: Comparison of the m_{T} shape between $t\bar{t} + Wt \to WWbb$ (red) and all $WWbb$ (blue).

Table 7.1: Theory systematics assigned for the post-fit yields for $W+$jets [%]. The numbers are shared by all the m_{eff}-bins in the same SR/VR tower. Systematics contributing below 5% or 5 times less than that of the leading uncertainty in the region are ignored (labeled as ”-”).

	Fact.	Resum.	Renorm.	CKKW
SR 2J	-	7	7	9
SR 6J	9	-	23	-
SR Low-x	-	11	-	6
SR High-x	19	7	-	-
SR 3B	36	15	-	19
VRa 2J	-	8	12	-
VRa 6J	13	11	-	-
VRa Low-x	9	-	8	8
VRa High-x	-	6	-	9
VRa 3B	20	16	7	6
VRb 2J	-	4	3	7
VRb 6J	5	-	5	6
VRb Low-x	-	5	6	5
VRb High-x	5	-	-	5
VRb 3B	-	5	5	5

Table 7.2: Theory systematics assigned for the post-fit yields for $t\bar{t} + Wt$ [%]. The numbers are shared by all the m_{eff}-bins in the same SR/VR tower. Systematics contributing below 5% or 5 times less than that of the leading uncertainty in the region are ignored (labeled as ”-”).

	Renorm./fact. scale	$tt + Wtb$ vs $WWbb$	Parton shower
SR 2J	22	17	8
SR 6J	21	24	25
SR Low-x	15	13	10
SR High-x	15	17	28
SR 3B	27	25	13
VRa 2J	12	5	10
VRa 6J	15	7	9
VRa Low-x	10	12	6
VRa High-x	17	10	-
VRa 3B	13	26	8
VRb 2J	-	21	10
VRb 6J	-	19	5
VRb Low-x	-	18	5
VRb High-x	-	23	8
VRb 3B	-	25	7

7.2.2 Non-normalized Backgrounds

Cross-section uncertainty The cross-section uncertainty for $Z+$ jets, di-bosons and $t\bar{t}+W/Z/WW$ amounts upto level of 5% [139], 6% [140] and 13% [112] respectively.

Shape uncertainty The shape uncertainties for non-normalized background components are dominantly seen in spectra regarding to jet activity, in particular jet-multiplicity and m_{eff}, while the impact on the spectra of other variables are rather limited. Therefore, the shape uncertainties are evaluated in SRs/VRs with the cuts in m_{T}, aplanarity and topness are removed, as well as the b-tagging requirement.

The variations considered for $Z+$jets and di-bosons are the same as those for $W+$jets as described above, but for the CKKW matching variation in diboson. The menu of variations for $t\bar{t}+W/Z/WW$ is minimal since it is the smallest backgrounds:

- Choice of renormalization and factorization scale The 1σ up/down variations are generated by simultaneously shifting these scales from the default value μ_0 to $0.5\mu_0$ and $2\mu_0$.
- Hard process description. As $t\bar{t}+W/Z/WW$ have not dedicatedly measured in precision using data, additional uncertainty is quoted by comparing with the sample generated by the alternative hard process modeling by Sherpa.

The uncertainties derived for each m_{eff}-bin of SR and VR, as in Table 7.3, 7.4 and 7.5 for $Z+$jets, di-bosons and $t\bar{t}$ respectively. Systematics contributing below 5% or 5 times less than that of the leading uncertainty in the region are ignored.

Table 7.3: Theory systematics assigned for the yields of $Z+$jets [%]. The uncertainty is shared by SRs and corresponding VRs. Systematics contributing below 5% or 5 times less than that of the leading uncertainty in the region are ignored (labeled as "-"). The uncertainties in the 3B towers are not evaluated since the $Z+$jets contribution is negligible.

	Fact.	Resum.	Renorm.	CKKW
2J $m_{\mathrm{eff}}^{\mathrm{bin1}}$	-	-	23	7
2J $m_{\mathrm{eff}}^{\mathrm{bin2}}$	-	-	25	-
2J $m_{\mathrm{eff}}^{\mathrm{bin3}}$	-	-	25	-
6J $m_{\mathrm{eff}}^{\mathrm{bin1}}$	-	-	35	-
6J $m_{\mathrm{eff}}^{\mathrm{bin2}}$	10	-	35	-
6J $m_{\mathrm{eff}}^{\mathrm{bin3}}$	-	-	39	15
Low-x	-	-	33	10
High-x	-	-	32	-

Table 7.4: Theory systematics assigned for the yields of Di-boson [%]. The uncertainty is shared by SRs and corresponding VRs. Systematics contributing below 5% or 5 times less than that of the leading uncertainty in the region are ignored (labeled as "-").

	Fact. scale	Resum. scale	Renorm. scale
2J $m_{\text{eff}}^{\text{bin1}}$	-	-	16
2J $m_{\text{eff}}^{\text{bin2}}$	21	-	21
2J $m_{\text{eff}}^{\text{bin3}}$	-	-	23
6J $m_{\text{eff}}^{\text{bin1}}$	8	9	19
6J $m_{\text{eff}}^{\text{bin2}}$	8	7	26
6J $m_{\text{eff}}^{\text{bin3}}$	9	11	37
Low-x	13	-	22
High-x	-	12	34
3B $m_{\text{eff}}^{\text{bin1}}$	-	7	29
3B $m_{\text{eff}}^{\text{bin2}}$	13	-	35

Table 7.5: Theory systematics assigned for the yields of $t\bar{t} + W/Z/WW$ [%]. The uncertainty is shared by SRs and corresponding VRs. Systematics contributing below 5% or 5 times less than that of the leading uncertainty in the region are ignored (labeled as "-").

	Renorm./fact. scale	Hard processes
2J $m_{\text{eff}}^{\text{bin1}}$	-	9
2J $m_{\text{eff}}^{\text{bin2}}$	5	10
2J $m_{\text{eff}}^{\text{bin3}}$	-	16
6J $m_{\text{eff}}^{\text{bin1}}$	-	8
6J $m_{\text{eff}}^{\text{bin2}}$	-	17
6J $m_{\text{eff}}^{\text{bin3}}$	-	22
Low-x	-	16
High-x	-	33
3B $m_{\text{eff}}^{\text{bin1}}$	5	5
3B $m_{\text{eff}}^{\text{bin2}}$	-	13

7.2.3 SUSY Signals

The cross-section uncertainty of gluino pair production amounts up-to 15% $\sim$ 35%, as shown in Figure 4.3 in Sec. A.1.
The shape uncertainty is evaluated by examining following systematic variations:

- Choice of renormalization and factorization scale.
  The variations are generated by independently shifting those scales by factor of 2 or 0.5 respectively.

- Parton shower tuning.
  Five variations are generated by tuning the MadGraph internal parameters dealing with parton shower. The Uncertainties are added in quadrature.

They are evaluated over the signal points in the `x=1/2` grid of the model **QQC1QQC1**, and found to be typically marginal compared with the cross-section uncertainty. This is because the jet activity is predominantly sourced by gluino decays rather than the ISRs and FSRs for most of the cases. The only exception is found in low $m_{\rm eff}$-bins in SR **2J** where the target signals are with highly compressed mass splitting between gluino and LSP ($\Delta m(\tilde{g},\,\tilde{\chi}_1^0) < 50$ GeV) that have to rely on the additional radiation to enter the signal regions. In such case, the acceptance can vary upto by 20% by the theoretical variation. Table 7.6 presents the assigned shape uncertainties, which are common to all the signal models and mass points.

Table 7.6: Shape uncertainties assigned for SUSY signal processes [%]. The uncertainties are common to all the signal models.

	Scale in Fac./Renom.	Parton shower
SR 2J $m_{\rm eff}^{\rm bin1}$	15	20
SR 2J $m_{\rm eff}^{\rm bin2}$	10	10
SR 2J $m_{\rm eff}^{\rm bin3}$	-	5
The other regions	-	-

7.3 Other Uncertainties

7.3.1 Generaic Uncertainty on the BG Estimation Methods

Kinematical extrapolation method

Though all theoretical uncertainties that are already known are assigned for the extrapolation, one has to notice that none of them can explain the mis-modeling observed in the pre-selection region (Sec. 6.2.1). Therefore there obviously exists some unknown theoretical uncertainty, and in principle it can also affect on the extrapolation.

It is seemingly impossible to know the impact of "unknown systematics" though, remember that we can largely cure the mis-modeling by a ad hoc kinematical reweighting:

$$\begin{cases} w &= 1 - 0.1 \times (n_{\mathrm{J}} - 2) \qquad\qquad\qquad (W + \mathrm{jets}) \\ w &= 1.05 \times [1 - 0.061\ \times p_T(t\bar{t})] \qquad\quad (t\bar{t}, \mathrm{@1L,2L}) \\ w &= 1.4 \times [1 - 0.061\ \times p_T(t\bar{t})] \qquad\quad (t\bar{t}, \mathrm{@3B}). \end{cases}$$

Reweighted distributions are shown in appendix C.1. The idea is to emulate the "unknown systematic" by these reweighting, and quote the variation in extrapolation as the systematics. Although this is not trivial how good the reweighting approximation is, this is the current best thing one could do.

Figures in appendix D.1 show the extrapolation error against the magnitude of injected mis-modeling. The mis-modeling is generated by reweighting the MC events with:

$$\begin{aligned} w &= 1 - x \times (n_{\mathrm{J}} - 2), && x \in [0, 0.18] && (W + \mathrm{jets}) \\ w &= 1 - x\ \times p_T(t\bar{t})/100\ \mathrm{GeV}, && x \in [0, 0.09] && (t\bar{t}). \end{aligned} \tag{7.1}$$

The vertical axis on the top panels in the plots show the amount of relative change that CR or SR(VR) experience by the injected MC variation as a function of x. The relative variation in CR (orange) compares to the normalization factor actually obtained via the fit to data, while that in SR (blue) to the ideal normalization factor need to fully correct the SR(VR). The bottom panel display the ratio, namely the resultant extrapolation error. B-tagging requirement is removed to maintain sufficient statistics, assuming the kinematics are invariant with it. For the $t\bar{t}$ process, component estimated by the object replacement method is excluded from the test.

The assigned uncertainty to each SR and VR are decided as Table 7.7, quoting the extrapolation error at $x = 0.1$ and $x = 0.07$ for $W + \mathrm{jets}$ and $t\bar{t}$ respectively.

Table 7.7: Assgined uncertainty for $t\bar{t}$ and $W+$jets for the kinematical extrapolation from CRs to corresponsding VRs and SRs [%].

	$W+$jets	$t\bar{t}$		$W+$jets	$t\bar{t}$		$W+$jets	$t\bar{t}$
SR 2J $m_{\text{eff}}^{\text{bin1}}$	15	5	VRa 2J $m_{\text{eff}}^{\text{bin1}}$	-	10	VRb 2J $m_{\text{eff}}^{\text{bin1}}$	10	5
SR 2J $m_{\text{eff}}^{\text{bin2}}$	15	-	VRa 2J $m_{\text{eff}}^{\text{bin2}}$	5	10	VRb 2J $m_{\text{eff}}^{\text{bin2}}$	5	10
SR 2J $m_{\text{eff}}^{\text{bin3}}$	15	20	VRa 2J $m_{\text{eff}}^{\text{bin3}}$	-	20	VRb 2J $m_{\text{eff}}^{\text{bin3}}$	5	10
SR 6J $m_{\text{eff}}^{\text{bin1}}$	-	5	VRa 6J $m_{\text{eff}}^{\text{bin1}}$	-	5	VRb 6J $m_{\text{eff}}^{\text{bin1}}$	-	-
SR 6J $m_{\text{eff}}^{\text{bin2}}$	-	10	VRa 6J $m_{\text{eff}}^{\text{bin2}}$	-	5	VRb 6J $m_{\text{eff}}^{\text{bin2}}$	5	5
SR 6J $m_{\text{eff}}^{\text{bin3}}$	-	-	VRa 6J $m_{\text{eff}}^{\text{bin3}}$	-	5	VRb 6J $m_{\text{eff}}^{\text{bin3}}$	5	10
SR Low-x	10	-	VRa Low-x	-	5	VRb Low-x	10	5
SR High-x	-	10	VRa High-x	-	30	VRb High-x	5	10
SR 3B $m_{\text{eff}}^{\text{bin1}}$	-	5	VRa 3B $m_{\text{eff}}^{\text{bin1}}$	30	-	VRb 3B $m_{\text{eff}}^{\text{bin1}}$	20	10
SR 3B $m_{\text{eff}}^{\text{bin2}}$	-	10	VRa 3B $m_{\text{eff}}^{\text{bin2}}$	30	5	VRb 3B $m_{\text{eff}}^{\text{bin2}}$	30	15

Object replacement method
For the object replacement method, the observed non-closure error discussed throughout Sec. 6.3.2 - 6.3.3 are included as systematics as listed in Table 7.8.

Table 7.8: Summary of non-closure errors in the object replacement method [%].

	BV/BT	3B
Tau replacement	5	20
Missing electron replacement	15	
Missing muon replacement	30	

7.3.2 Control region statistics

In both of the background estimation methods, reflecting the (semi-)data driven nature, the statistical error in CRs often becomes the primary uncertainty in the estimation. This typically occurs in case of the high m_{eff} bins, for instance the yields in the CRs for the kinematical extrapolation end up in about 15 events, immediately resulting in $20\% - 30\%$ of uncertainty. The tendency is more striking concerning to the object replacement method where the uncertainty is solely dominated by the seed event statistical error that amounts $20\% - 60\%$ in SRs depending on the tightness of selection. Furthermore, one has to mind that the statistical error in the object replacement method is not independent between the regions given that the sub-events from a single seed event can fall into different regions. The correlated statistical error between two signal regions is then evaluated by identifying the fraction of common seed events between their estimation. Table 7.3 shows the correlation coefficient in the estimated yields between SR$_i$ and SR$_j$ defined as:

$$\rho := \frac{\sum_e \sqrt{w_e^i w_e^j}}{\sqrt{\sum_e w_e^i}\sqrt{\sum_e w_e^j}}$$

where e runs over all seed events, and w_e^i denotes the sum of weighted sub-events falling into SR_i generated by the seed event e. Correlation is mainly found in adjacent m_{eff}-bins, high m_{eff} BT/3B bins, and high m_{eff} hard lepton / soft lepton bins. This correlation is taken into accounted in the final fitting. Though large inter-bin correlation can potentially destroy the sensitivity in the shape fit, the impact on the final result to this analysis is limited, since the signal points rarely lay over multiple bins with equal abundance.

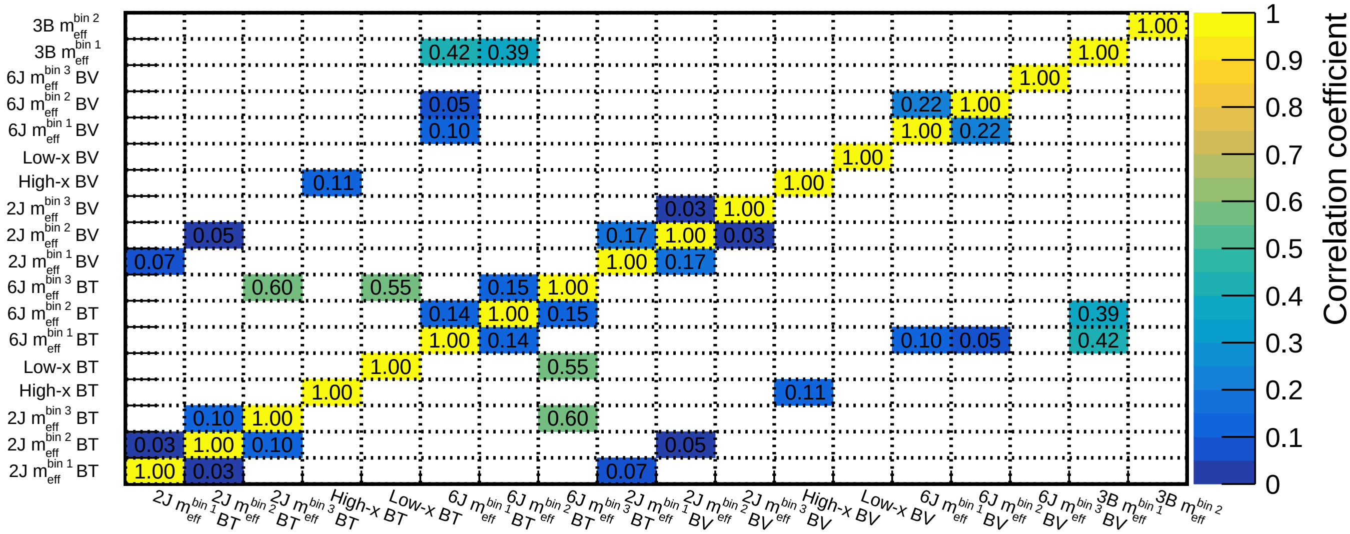

Figure 7.3: The correlation coefficient in the estimated yields between two signal regions, indicating the level of correlated statistical fluctuation.

7.3.3 MC statistics

Limited MC statistics lead to non-negligible uncertainty in signal and background yields in regions with tight selection. The largest impact is found in SR 3B $m_{\mathrm{eff}}^{\mathrm{bin2}}$ amounting upto 15%, which is still minor compared with the other systematics sources. The statistical behavior is carefully taken into account in the fit, as detailed in the Sec. 8.1.

Chapter 8

Result

8.1 Statistical Analysis and Hypothetical Test

The Profile Likelihood and Treatment of Systematics Statistical tests are performed to examine the consistency of observed data with respect to prediction of SM or that with specific signal being overlaid. This is implemented via a likelihood function based on the probability density distribution (PDF) in terms of number of observed events in each signal region bin. The full representation of the likelihood is given by Eq. 8.1:

$$\begin{aligned}\mathcal{L}(\mu;\mu_{\mathrm{W}}^{i},\mu_{\mathrm{Top}}^{i},\boldsymbol{\theta}) &= \mathcal{L}(\boldsymbol{n}^{\mathrm{SR}},\boldsymbol{n}^{\mathrm{WR}},\boldsymbol{n}^{\mathrm{TR}}|\mu,\mu_{\mathrm{W}}^{i},\mu_{\mathrm{Top}}^{i},\boldsymbol{\theta}) \\ &= \mathcal{P}_{\mathrm{SR}}\times\mathcal{P}_{\mathrm{CR}}\times\prod_{k\in\mathrm{syst.}}\rho(\theta_k),\end{aligned}$$

$$\begin{aligned}\mathcal{P}_{\mathrm{SR}} = \prod_{i\notin\mathbf{3B}}&\left[\prod_{b\in\mathrm{BT,BV}}\mathrm{Pois}\left(n_{i,b}^{\mathrm{SR}}|\mu s_{i,b}^{\mathrm{SR}}(\boldsymbol{\theta})+\mu_{\mathrm{W}}^{i}\,w_{i,b}^{\mathrm{SR}}(\boldsymbol{\theta})+\mu_{\mathrm{Top}}^{i}\,t_{i,b}^{\mathrm{SR}}(\boldsymbol{\theta})+b_{i,b}^{\mathrm{SR}}(\boldsymbol{\theta})\right)\right] \\ \times\prod_{i\in\mathbf{3B}}&\mathrm{Pois}\left(n_{i}^{\mathrm{SR}}|\mu s_{i}^{\mathrm{SR}}(\boldsymbol{\theta})+\mu_{\mathrm{W}}^{i}\,w_{i}^{\mathrm{SR}}(\boldsymbol{\theta})+\mu_{\mathrm{Top}}^{i}\,t_{i}^{\mathrm{SR}}(\boldsymbol{\theta})+b_{i}^{\mathrm{SR}}(\boldsymbol{\theta})\right)\end{aligned}$$

$$\begin{aligned}\mathcal{P}_{\mathrm{CR}} = \prod_{i}&\mathrm{Pois}\left(n_{i}^{\mathrm{TR}}|\mu s_{i}^{\mathrm{WR}}(\boldsymbol{\theta})+\mu_{\mathrm{W}}^{i}\,w_{i}^{\mathrm{WR}}(\boldsymbol{\theta})+\mu_{\mathrm{Top}}^{i}\,t_{i}^{\mathrm{WR}}(\boldsymbol{\theta})+b_{i}^{\mathrm{WR}}(\boldsymbol{\theta})\right) \\ &\times\mathrm{Pois}\left(n_{i}^{\mathrm{WR}}|\mu s_{i}^{\mathrm{TR}}(\boldsymbol{\theta})+\mu_{\mathrm{W}}^{i}\,w_{i}^{\mathrm{TR}}(\boldsymbol{\theta})+\mu_{\mathrm{Top}}^{i}\,t_{i}^{\mathrm{TR}}(\boldsymbol{\theta})+b_{i}^{\mathrm{TR}}(\boldsymbol{\theta})\right)\end{aligned} \tag{8.1}$$

where $\boldsymbol{n}^{\mathrm{SR}}$, $\boldsymbol{n}^{\mathrm{WR}}$ and $\boldsymbol{n}^{\mathrm{TR}}$ are respectively the numbers of observed events in SRs, corresponding CRs such as WRs and TRs, with the vector indices running over regions ; s_r is the expected signal yield in region r in the signal model to be tested; w_r and t_r are respectively the expectedyields of $W+\mathrm{jets}$ and $t\bar{t}$ in region r before the normalization, with the components derived by the object replacement method being excluded; b_r are the expectedyields of the other backgrounds in region r; $\boldsymbol{\theta}$ is the vector of nuisance parameters for each systematic uncertainty; μ_{W}^{i} and μ_{Top}^{i} are the normalization factors for $W+\mathrm{jets}$ and $t\bar{t}$ which are allowed to vary between i; and μ is the signal strength, a parameter describing relative normalization with respect to the signal model to be tested i.e. $\mu=0$ corresponds to a background-only hypothesis and $\mu=1$ to a hypothesis with the nominal signal level expected by the signal model. Index i runs along signal region bins joining the combined fit that are orthogonal to each other s.t. :

$$\begin{aligned} i \in \; & \{\; \mathbf{2J}, \mathbf{6J}, \mathbf{3B} \;\} \\ & \text{or } \{\; \mathbf{2J}, \textbf{High-x}, \mathbf{3B} \;\} \\ & \text{or } \{\; \textbf{Low-x}, \mathbf{6J}, \mathbf{3B} \;\} \\ & \text{or } \{\; \textbf{Low-x}, \textbf{High-x}, \mathbf{3B} \;\} \end{aligned} \tag{8.2}$$

where

$$\begin{aligned} \mathbf{2J} &= \{\; \text{2J-}m_{\text{eff}}^{\text{bin1}},\ \text{2J-}m_{\text{eff}}^{\text{bin2}},\ \text{2J-}m_{\text{eff}}^{\text{bin3}} \;\} \\ \mathbf{6J} &= \{\; \text{6J-}m_{\text{eff}}^{\text{bin1}},\ \text{6J-}m_{\text{eff}}^{\text{bin2}},\ \text{6J-}m_{\text{eff}}^{\text{bin3}} \;\} \\ \textbf{Low-x} &= \{\; \text{Low-x} \;\} \\ \textbf{High-x} &= \{\; \text{High-x} \;\} \\ \mathbf{3B} &= \{\; \text{3B-}m_{\text{eff}}^{\text{bin1}},\ \text{3B-}m_{\text{eff}}^{\text{bin2}} \;\} \end{aligned} \tag{8.3}$$

The normalization factors for $W+\text{jets}$ and $t\bar{t}$ backgrounds are simultaneously determined by the fit, in order to correlate the behavior of systematics. Therefore the CRs terms are also placed in the common likelihood with an identical representation as SRs.

The statistical behavior of the PDF is fully characterized by a set of independent Poisson PDF, namely:

$$\text{Pois}\,(n|\nu) := \frac{\nu^n}{n!}e^{-\nu}$$

with ν and n being the expected yield and observed number respectively.

The effect of a systematics (indexed by k) are then incorporated by shifting the Poisson means ν, via a corresponding nuisance parameter θ_k so as:

$$\nu(\theta_k) := f(\theta_k), \tag{8.4}$$

with $f(\theta_k)$ being a continuous function satisfying:

$$\begin{aligned} f(\theta_k = 0) &= \nu(0) \\ f(\theta_k = \pm 1) &= \nu(\pm 1\sigma). \end{aligned} \tag{8.5}$$

$\nu(0)$ is the nominal expectation yields, while $\nu(\pm 1\sigma)$ is given by that with the systematic variation applied by $\pm 1\sigma$ which are evaluated beforehand. $f(\theta_k)$ in the other θ_k is then interpolated or extrapolated using the three points by a polynomial or an exponential function, providing a continuous functional form of $\mathcal{L}$ in terms of $\boldsymbol{\theta}$.
What is here intend to do is to perform a global fit on data, simultaneously determining $\mu, \mu_{\text{W}}^i, \mu_{\text{Top}}^i$ and $\boldsymbol{\theta}$ by minimizing the likelihood $\mathcal{L}$ (Eq. 8.1). While the μ, μ_{W}^i and μ_{Top}^i are allowed to flow based on our total ignorance, the shifts of the nuisance parameters $\boldsymbol{\theta}$ need to be restricted reflecting the level of our confidence. This is implemented by the last terms in the likelihood $\rho(\theta_k)$ known as the "penalty terms" serving as the prior constraints for the likelihood. The form of the penalty terms depends on the statistical nature of each systematics:

- A Gaussian PDF is commonly assumed for most systematic uncertainties:

$$\rho(\theta) = \frac{1}{\sqrt{2\pi}\sigma}\exp\left(-\frac{\theta^2}{2}\right) \tag{8.6}$$

- The Gamma PDF is used to describe uncertainties following according to Poisson distribution, typically associated with the number of data events in control regions, or selected MC events:

$$\rho(a) = \frac{\nu^a}{a!}e^{-\nu} \tag{8.7}$$

  where a is related with θ using the symmetrized uncertainty σ by

$$\theta = \frac{a-\nu}{\sigma} \tag{8.8}$$

A multi-dimensional minimization over the parameter spaces of all the normalization factors, nuisance parameters and signal strength [1] is performed by the Minuit2 algorithm [141] interfaced by a number wrapper packages; `HistFitter` [142], `HistFactory` [143] and `RooFit` [144]. Signal strength and the background normalization factors are allowed to range $0 \sim 5$, while nuisance parameters are to moved by $-5\sigma \sim 5\sigma$ during the fit. Systematics found have tiny enough impact on the yields in the SRs/CRs region bins (evaluated by the Kolmogorov-Smirov test) are excluded from the fit so as to reduce the redundant dimensions of scan ("pruning").

Hypothetical Testing A hypothetical test against a hypothesis H is done by examining the compatibility with observation, via p-value. P-value for testing hypothesis H is commonly defined as the probability to find even rarer outcome than the observation under H. For the simplest one bin counting experiment where signal is manifested as an data excess, the p-value is then:

$$p_\mu := \sum_{n=n_{\mathrm{obs}}}^{\infty} L(n|\mu) \tag{8.9}$$

using the number of observed events $n_{\mathrm{obs.}}$ as the test static. One would claim a discovery against the null hypothesis H_0 if the p_0 is significantly low that the observation can be hardly ascribed to statistical fluctuation out of H_0. In the filed of high energy physics experiment, this is usually set to one corresponding to 5σ gaussian standard deviation ($\sim 10^{-7}$).

On the other hand, one can claim the exclusion of a signal hypothesis H_1 when p_1 is reasonably low. $p_1 < 0.05$ is conventionally used as the threshold, equivalent to an exclusion with 95% confidence level. There are circumstances where observation does not agree with either H_0 and H_1 due to statistical fluctuation or more seriously poor understanding to backgrounds, and result in strong exclusion power typically when data undershoots the expectation. In LHC, in order to prevent such potentially unreasonably strong exclusion, a modified measure CL_s is used:

$$\mathrm{CL}_s := \frac{p_1}{p_0}, \tag{8.10}$$

[1] Remind that we have $8-16$ normalization factors and ~ 150 nuisance parameters in case of combined fit over all SR towers.

and $\mathrm{CL}_s < 0.05$ is accepted as the equivalence of an exclusion at 95% confidence level.

In presence of multiple test statics ($\boldsymbol{n}^{\mathrm{SR}}$) together with bunches of nuisance parameters, it is not obvious how to define the "rareness" on the multi-dimension of space. In such cases, likelihood is often chosen as the test static projecting n-dimension observables into 1 dimension, as well as providing a well-defined measure of "rareness" by definition. In LHC analysis, a normalized likelihood test static λ_μ is widely used:

$$\lambda_\mu = \begin{cases} \dfrac{\mathcal{L}(\mu, \hat{\hat{\boldsymbol{\theta}}}(\mu))}{\mathcal{L}(\hat{\mu}, \hat{\boldsymbol{\theta}})} & (\hat{\mu} > 0) \\ \dfrac{\mathcal{L}(\mu, \hat{\hat{\boldsymbol{\theta}}}(\mu))}{\mathcal{L}(0, \hat{\hat{\boldsymbol{\theta}}}(0))} & (\hat{\mu} < 0) \end{cases} \tag{8.11}$$

where $\hat{\hat{\theta}}(\mu)$ denotes the best-fit nuisance parameters with fixed μ, while $\hat{\mu}$ and $\hat{\theta}$ the best-fit parameters with μ is allowed to float. $\mathcal{L}(\mu, \hat{\hat{\theta}}(\mu))$ presents the conditional likelihood normalized by the μ-agonistic denominator $\mathcal{L}(\hat{\mu}, \hat{\theta})$, forcing the range of λ_μ to $0 < \lambda_\mu < 1$.

The p-value is finally defined as:

$$p_\mu := \int_{q_{\mu,\mathrm{obs.}}}^{\infty} f(q^\mu|\mu) dq_\mu \tag{8.12}$$

where q_μ is:

$$q_\mu = \begin{cases} -2\log\lambda(\mu) & (\hat{\mu} < \mu) \\ 0 & (\hat{\mu} > \mu) \end{cases} . \tag{8.13}$$

$f(q_\mu)$ is the PDF that q_μ obeys, defined by the vaiation of q_μ when suffering from both the statistical fluctuation as well as systematics. Unlike the PDF in the simplest counting experiment Eq. 8.9, $f(q_\mu)$ is in generally unknown neither modeled analytically thus needs a bunch of toy experiments to determine; scanning from $\mu = 0$ upto $\mu = 5 \sim 10$ with a finite step, on each of which a number of the likelihood fits are performed with different fluctuating data statistics and systematic variation applied. This is an incredibly crazy course of computation, and we have to go relying on some analytical approximation after all.
[2]

Fortunately, there are a couple of powerful approximation formula known as Wald's approximation [145]:

$$q_\mu = -2\log\lambda(\mu) = \frac{\mu - \hat{\mu}}{\sigma^2} + O(1/\sqrt{N}) \tag{8.14}$$

and the asymptotic formula based on the Asimov dataset [146]:

$$\begin{aligned} f(q_\mu, \mu) &= \frac{1}{\sqrt{q_\mu}}\frac{1}{\sqrt{2\pi}}\left[\exp\left(-\frac{1}{2}(\sqrt{q_\mu} + \sqrt{R})\right) + \exp\left(-\frac{1}{2}(\sqrt{q_\mu} - \sqrt{R})\right)\right], \\ R &:= \frac{(\mu - \hat{\mu})^2}{\sigma^2}, \end{aligned} \tag{8.15}$$

[2] Each likelihood fit takes approximately 8-15 minutes.

with Wald's approximation 8.14 being applied. σ is the fitting error on $\hat{\mu}$ and N symbolizes the magnitude of number of events in signal regions, with which the PDF $f(q_\mu)$ can be determined by only one fit.

One disclaimer is however about the validity of the approximation where $O(1/\sqrt{N})$ terms are ignored. This may not be the case given that the signal regions typically contains events less than 5. In the thesis, the result for background-only hypothesis (shown in Sec. 8.2) is derived using the rigid toy experiments, however the Asimov's formula (Eq.8.15) is nevertheless used for limit setting due to the unrealistic computing time required for the toy experiments. [3]

8.2 Unblinded Signal Regions with Background-only Hypothesis

The background expectation in signal regions for null signal hypothesis are determined tower-by-tower, by performing a simultaneous fit on the normalization factors (μ_W, μ_{Top}) as well as all the nuisance parameters associated to systematics uncertainties, onto the data in all the relevant bins of control regions and signal regions. The post-fit uncertainties are summarized in Figure 8.1.

For the low m_{eff}-bins, typically the estimation precision is at 20% level where theory systematics is the main source. The signal region bins with tightest selection end up in 40% $\sim$ 60% of total uncertainty, dominated by the control region statistics.

The unblinded yields of observed data together with the expected backgrounds in the signal regions are shown in Table 8.1 - 8.3. Observed data are found to be consistent in general, with no signal regions exhibiting the deviation more than 3σ. The pulls between data and expectation is shown in Figure 8.9.

Figure 8.2-8.8 show the kinematical distributions of either data and prediction in unblinded signal regions. The slight data excess found (SR 2J-$m_{\mathrm{eff}}^{\mathrm{bin1}}$ BV, SR 2J-$m_{\mathrm{eff}}^{\mathrm{bin3}}$ BV and SR High-x BT) are shown to be not highly consistent with the targeted models in the signal regions bins, though the data statistics is too low too conclude.

[3]This is in fact how ATLAS/CMS provides the result. We have to admit the imperfection but this is the best thing we could afford to do.

Table 8.1: Observed yields and backgrounds expectation in the signal region bins in tower **2J** and **6J**. Background component estimated by the object replacement are denoted as "Di-leptonic", while the others are derived from the kinematical extrapolation method. Displayed errors are only systematics uncertainty.

SR 2J b-tag	$m_{\mathrm{eff.}} \in$[1100,1500]	$m_{\mathrm{eff.}} \in$[1500,1900]	$m_{\mathrm{eff.}} > 1900$
Observed data	8	2	1
Expected background	7.20 ± 1.40	2.46 ± 0.60	2.31 ± 0.77
Di-leptonic	2.4 ± 1.0	0.8 ± 0.4	1.7 ± 0.7
W+jets	1.0 ± 0.5	$0.1^{+0.2}_{-0.1}$	0.0 ± 0.0
Z+jets	0.6 ± 0.2	0.2 ± 0.0	0.1 ± 0.0
Tops	2.1 ± 0.7	0.8 ± 0.3	0.4 ± 0.2
Di-boson	0.4 ± 0.1	0.2 ± 0.2	0.1 ± 0.0
$t\bar{t} + V$	0.8 ± 0.2	0.3 ± 0.1	0.1 ± 0.0
SR 2J b-veto	$m_{\mathrm{eff.}} \in$[1100,1500]	$m_{\mathrm{eff.}} \in$[1500,1900]	$m_{\mathrm{eff.}} > 1900$
Observed data	25	8	6
Expected background	13.33 ± 2.59	6.84 ± 1.44	2.53 ± 0.66
Di-leptonic	2.4 ± 1.8	2.3 ± 1.1	0.7 ± 0.6
W+jets	4.2 ± 1.1	1.6 ± 0.4	0.4 ± 0.2
Z+jets	2.3 ± 0.7	1.0 ± 0.3	0.6 ± 0.2
Tops	1.1 ± 0.4	0.3 ± 0.1	0.2 ± 0.1
Di-boson	3.2 ± 1.1	1.6 ± 0.5	0.7 ± 0.2
$t\bar{t} + V$	0.1 ± 0.0	0.1 ± 0.0	0.0 ± 0.0
SR 6J b-tag	$m_{\mathrm{eff.}} \in$[1100,1600]	$m_{\mathrm{eff.}} \in$[1600,2100]	$m_{\mathrm{eff.}} > 2100$
Observed data	7	3	0
Expected background	5.09 ± 1.04	2.14 ± 0.65	2.46 ± 0.89
Di-leptonic	2.6 ± 0.8	1.1 ± 0.6	1.5 ± 0.8
W+jets	0.4 ± 0.2	0.1 ± 0.1	0.1 ± 0.1
Z+jets	$0.0^{+0.0}_{-0.0}$	0.0 ± 0.0	$0.0^{+0.0}_{-0.0}$
Tops	1.0 ± 0.4	0.5 ± 0.2	0.6 ± 0.3
Di-boson	0.2 ± 0.1	0.1 ± 0.1	$0.1^{+0.1}_{-0.1}$
$t\bar{t} + V$	0.8 ± 0.2	0.3 ± 0.1	0.1 ± 0.0
SR 6J b-veto	$m_{\mathrm{eff.}} \in$[1100,1600]	$m_{\mathrm{eff.}} \in$[1600,2100]	$m_{\mathrm{eff.}} > 2100$
Observed data	5	0	1
Expected background	3.93 ± 0.88	1.28 ± 0.36	0.65 ± 0.18
Di-leptonic	1.5 ± 0.6	$0.2^{+0.2}_{-0.2}$	0.0 ± 0.0
W+jets	1.1 ± 0.5	0.6 ± 0.3	0.3 ± 0.1
Z+jets	0.2 ± 0.1	0.0 ± 0.0	0.0 ± 0.0
Tops	0.3 ± 0.1	0.1 ± 0.1	0.1 ± 0.1
Di-boson	0.7 ± 0.2	0.3 ± 0.1	0.2 ± 0.1
$t\bar{t} + V$	0.1 ± 0.0	0.0 ± 0.0	0.0 ± 0.0

Table 8.2: Observed yields and backgrounds expectation in the signal region bins in tower **Low-x** and **High-x**. Background component estimated by the object replacement are denoted as "Di-leptonic", while the others are derived from the kinematical extrapolation method. Displayed errors are only systematics uncertainty.

SR Low-x	b-tag	b-veto
Observed data	0	3
Expected background	2.04 ± 0.70	1.46 ± 0.59
Di-leptonic	1.2 ± 0.7	0.6 ± 0.5
W+jets	0.1 ± 0.0	0.2 ± 0.1
Z+jets	0.0 ± 0.0	0.1 ± 0.0
Tops	0.6 ± 0.2	0.4 ± 0.2
Di-boson	0.1 ± 0.0	0.2 ± 0.1
$t\bar{t}+V$	0.1 ± 0.0	0.0 ± 0.0
SR High-x	b-tag	b-veto
Observed data	6	4
Expected background	2.35 ± 0.59	4.27 ± 0.94
Di-leptonic	0.8 ± 0.5	0.8 ± 0.5
W+jets	0.3 ± 0.1	1.7 ± 0.5
Z+jets	$0.0^{+0.0}_{-0.0}$	0.5 ± 0.2
Tops	0.5 ± 0.2	0.1 ± 0.1
Di-boson	0.4 ± 0.2	1.1 ± 0.5
$t\bar{t}+V$	0.3 ± 0.1	0.1 ± 0.0

Table 8.3: Observed yields and backgrounds expectation in the signal region bins in tower **3B**. Background component estimated by the object replacement are denoted as "Di-leptonic", while the others are derived from the kinematical extrapolation method. Displayed errors are only systematics uncertainty.

SR 3B	$m_{\text{eff.}} \in$[1000,1750]	$m_{\text{eff.}} > 1750$
Observed data	2	1
Expected background	2.06 ± 0.68	1.00 ± 0.52
Di-leptonic	1.3 ± 0.5	0.8 ± 0.5
W+jets	0.0 ± 0.0	0.0 ± 0.0
Z+jets	0.0 ± 0.0	0.0 ± 0.0
Tops	0.6 ± 0.4	0.2 ± 0.1
Di-boson	0.0 ± 0.0	0.0 ± 0.0
$t\bar{t}+V$	0.2 ± 0.1	0.1 ± 0.0

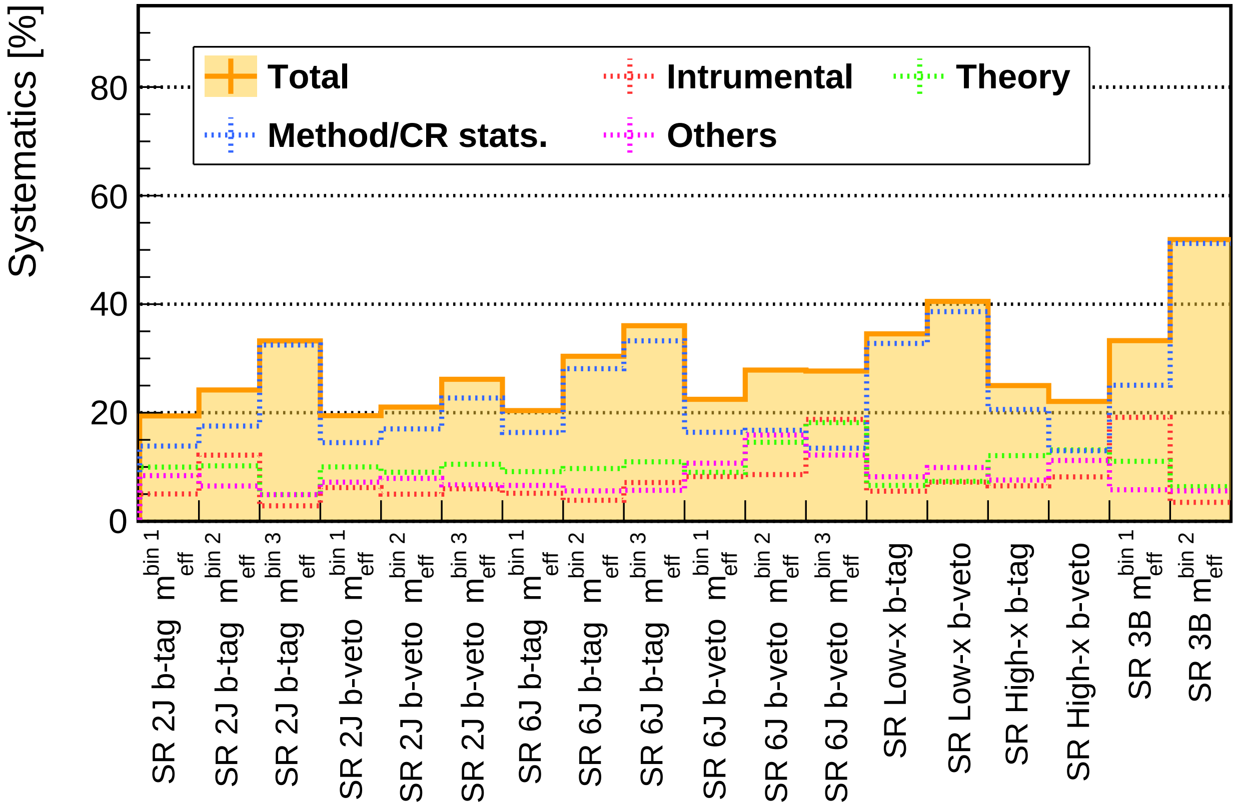

Figure 8.1: Post-fit systematic uncertainty with respective to the expected yield in the signal regions. Total systematics uncertainty is shown by the filled orange histogram, and the breakdowns are by dashed lines. While the systematics in b-tagged bins are purely dominated by control region statistics, it is comparable to the other sources in the b-veto bins. The overall uncertainty ranges between 20% $\sim$ 50%.

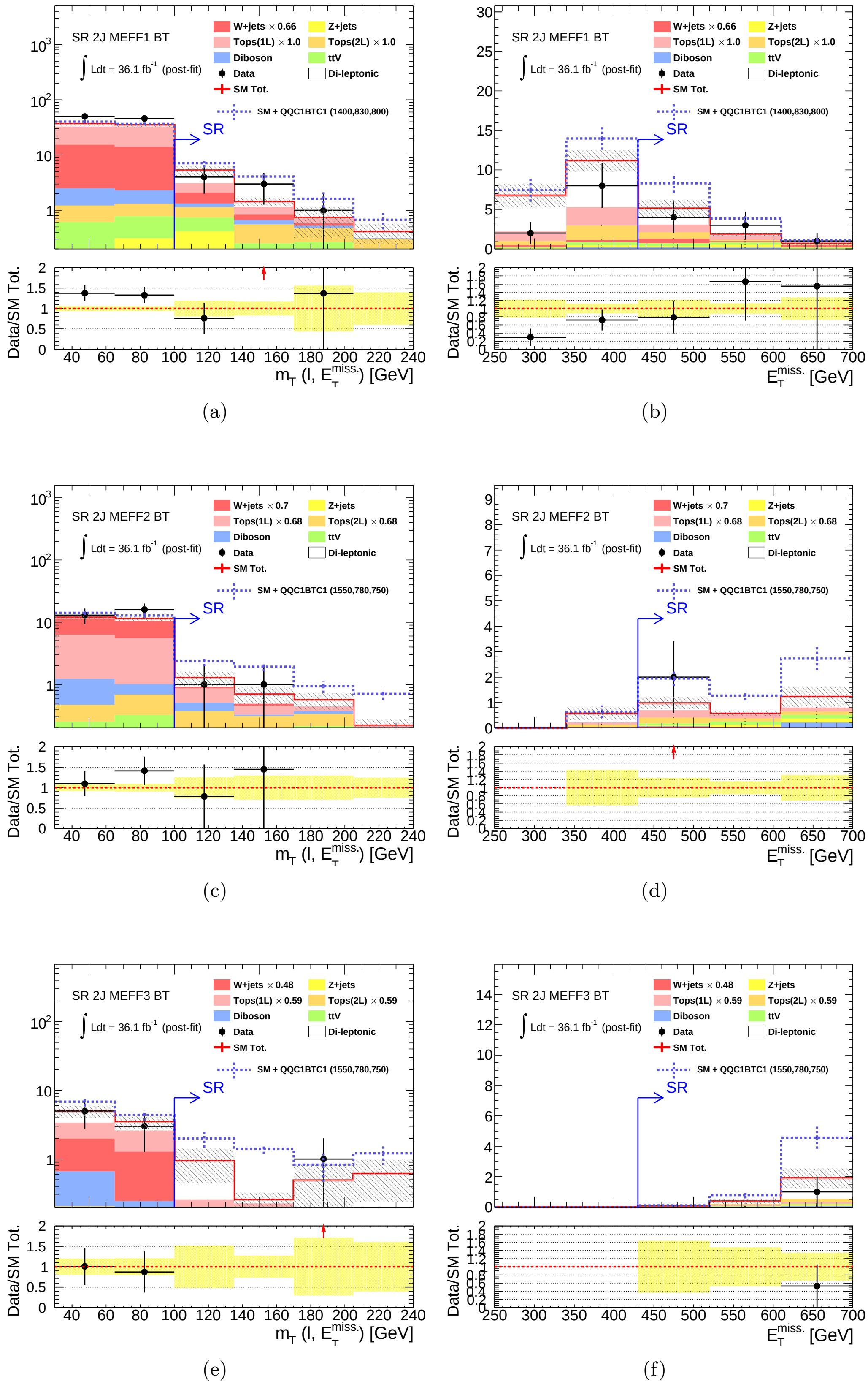

Figure 8.2: Post-fit distruibution of (left) m_{T}, and (right) $E_{\mathrm{T}}^{\mathrm{miss}}$. (a,b) SR 2J-$m_{\mathrm{eff}}^{\mathrm{bin1}}$ BT. (c,d) SR 2J-$m_{\mathrm{eff}}^{\mathrm{bin2}}$ BT. (e,f) SR 2J-$m_{\mathrm{eff}}^{\mathrm{bin3}}$ BT. The yellow band in the bottom panel represents statistical error. The overflow is included in the highest bin. Dashed lines represent the expected distributions of total background plus the typical signal targeted in the signal region bin.

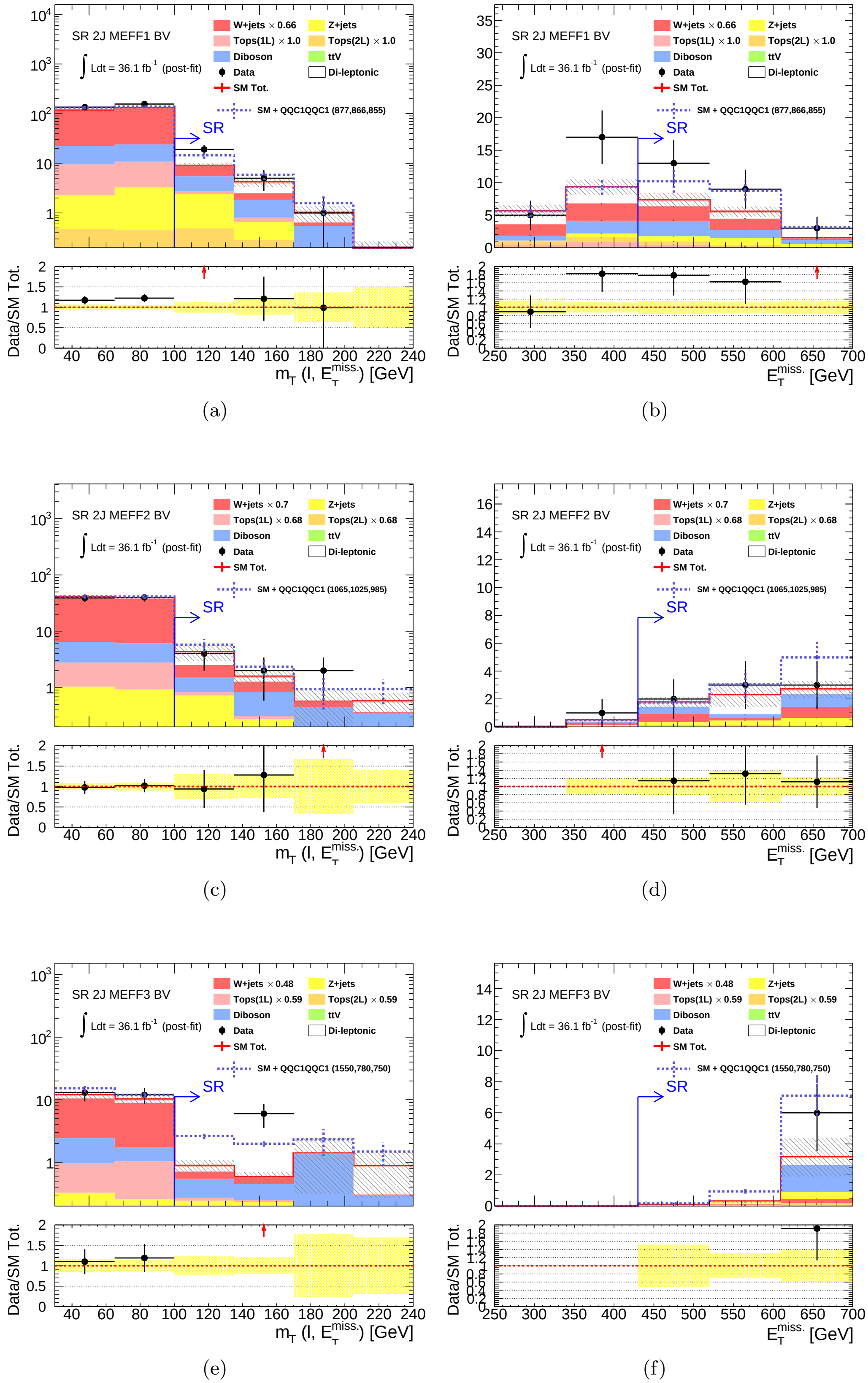

Figure 8.3: Post-fit distruibution of (left) m_{T}, and (right) $E_{\mathrm{T}}^{\mathrm{miss}}$. (a,b) SR 2J-$m_{\mathrm{eff}}^{\mathrm{bin1}}$ BV. (c,d) SR 2J-$m_{\mathrm{eff}}^{\mathrm{bin2}}$ BV. (e,f) SR 2J-$m_{\mathrm{eff}}^{\mathrm{bin3}}$ BV. The yellow band in the bottom panel represents statistical error. The overflow is included in the highest bin. The yellow band in the bottom panel represents statistical error. The overflow is included in the highest bin. Dashed lines represent the expected distributions of total background plus the typical signal targeted in the signal region bin.

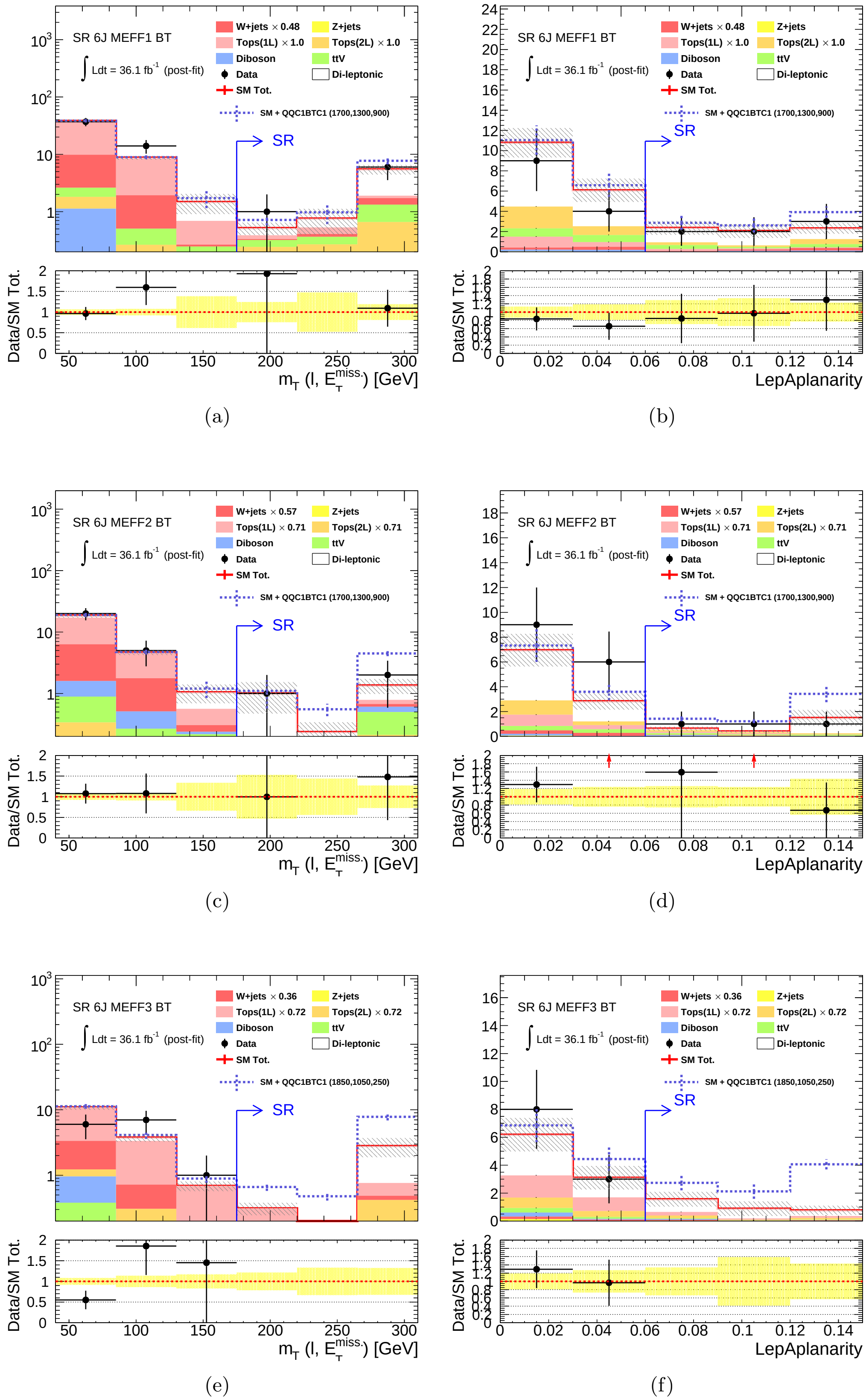

Figure 8.4: Post-fit distruibution of (left) m_{T}, and (right) aplanarity. (a,b) SR 6J-$m_{\mathrm{eff}}^{\mathrm{bin1}}$ BT. (c,d) SR 6J-$m_{\mathrm{eff}}^{\mathrm{bin2}}$ BT. (e,f) SR 6J-$m_{\mathrm{eff}}^{\mathrm{bin3}}$ BT. The yellow band in the bottom panel represents only statistical error. The overflow is included in the highest bin. The yellow band in the bottom panel represents statistical error. The overflow is included in the highest bin. Dashed lines represent the expected distributions of total background plus the typical signal targeted in the signal region bin.

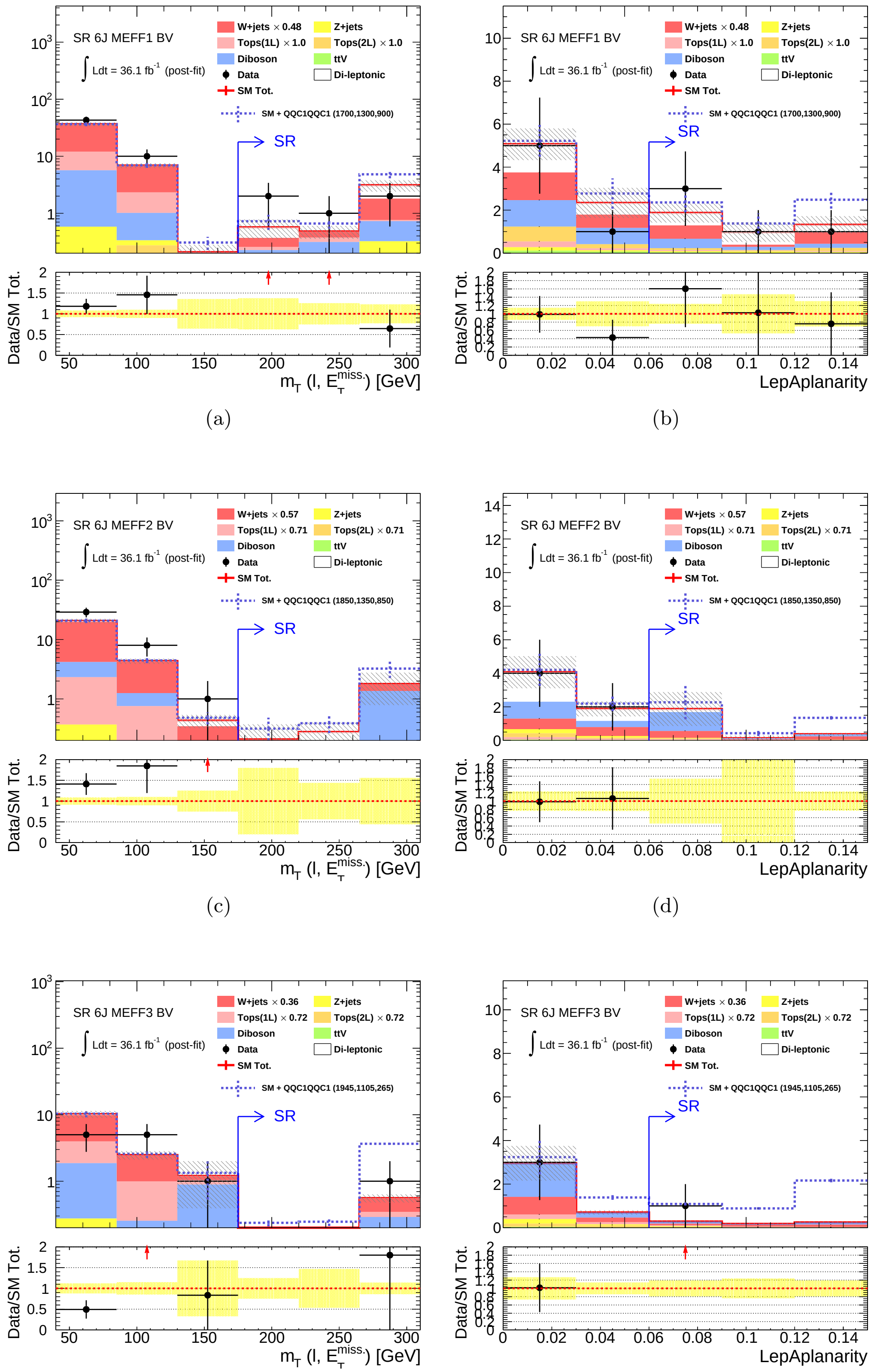

(a) (b)

(c) (d)

(e) (f)

Figure 8.5: Post-fit distruibution of (left) m_{T}, and (right) aplanarity. (a,b) SR 6J-$m_{\mathrm{eff}}^{\mathrm{bin1}}$ BV. (c,d) SR 6J-$m_{\mathrm{eff}}^{\mathrm{bin2}}$ BV. (e,f) SR 6J-$m_{\mathrm{eff}}^{\mathrm{bin3}}$ BV. The yellow band in the bottom panel represents only statistical error. The overflow is included in the highest bin. The yellow band in the bottom panel represents statistical error. The overflow is included in the highest bin. Dashed lines represent the expected distributions of total background plus the typical signal targeted in the signal region bin.

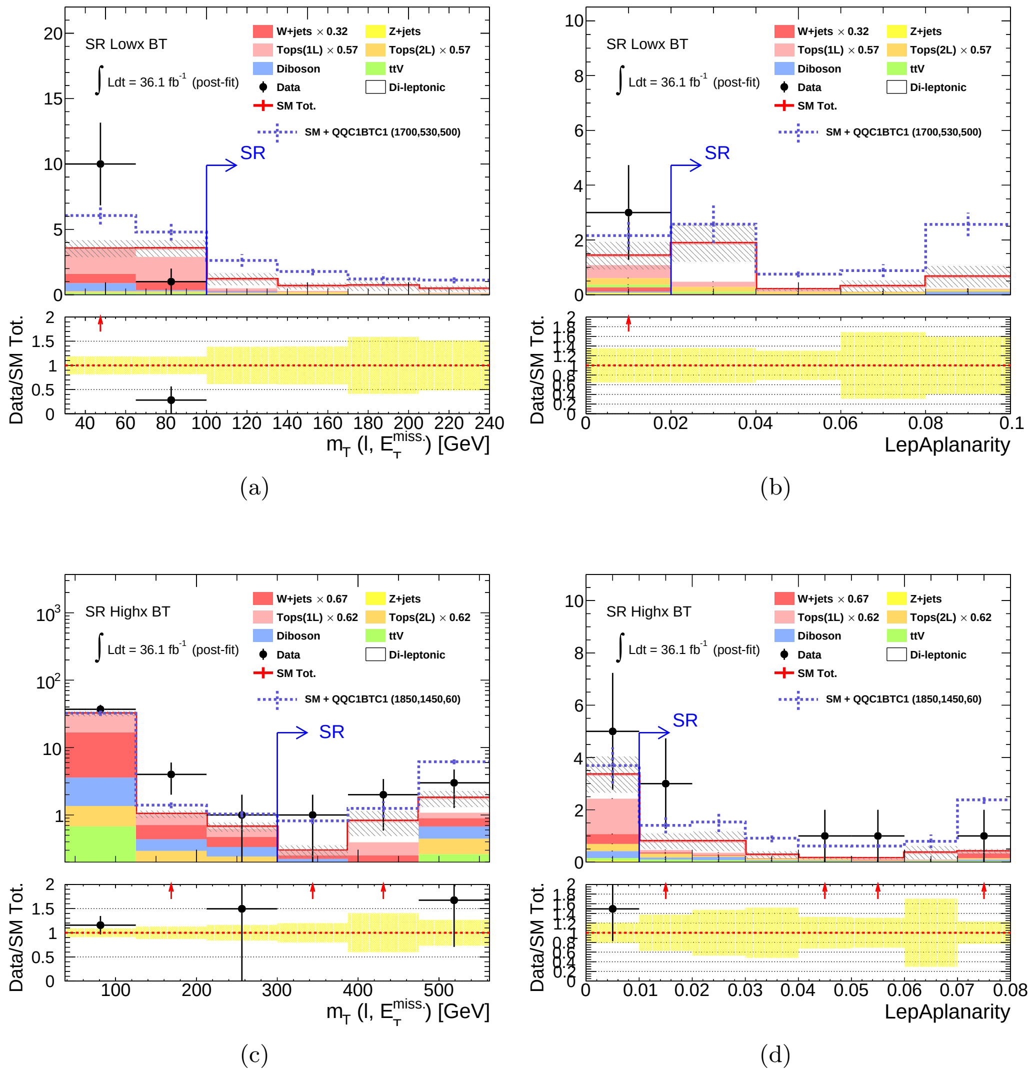

Figure 8.6: Post-fit distruibution of (left) m_{T} and (right) aplanarity. (a,b) SR Low-x BT. (c,d) SR High-x BT. The yellow band in the bottom panel represents only statistical error. The overflow is included in the highest bin. The yellow band in the bottom panel represents statistical error. The overflow is included in the highest bin. Dashed lines represent the expected distributions of total background plus the typical signal targeted in the signal region bin.

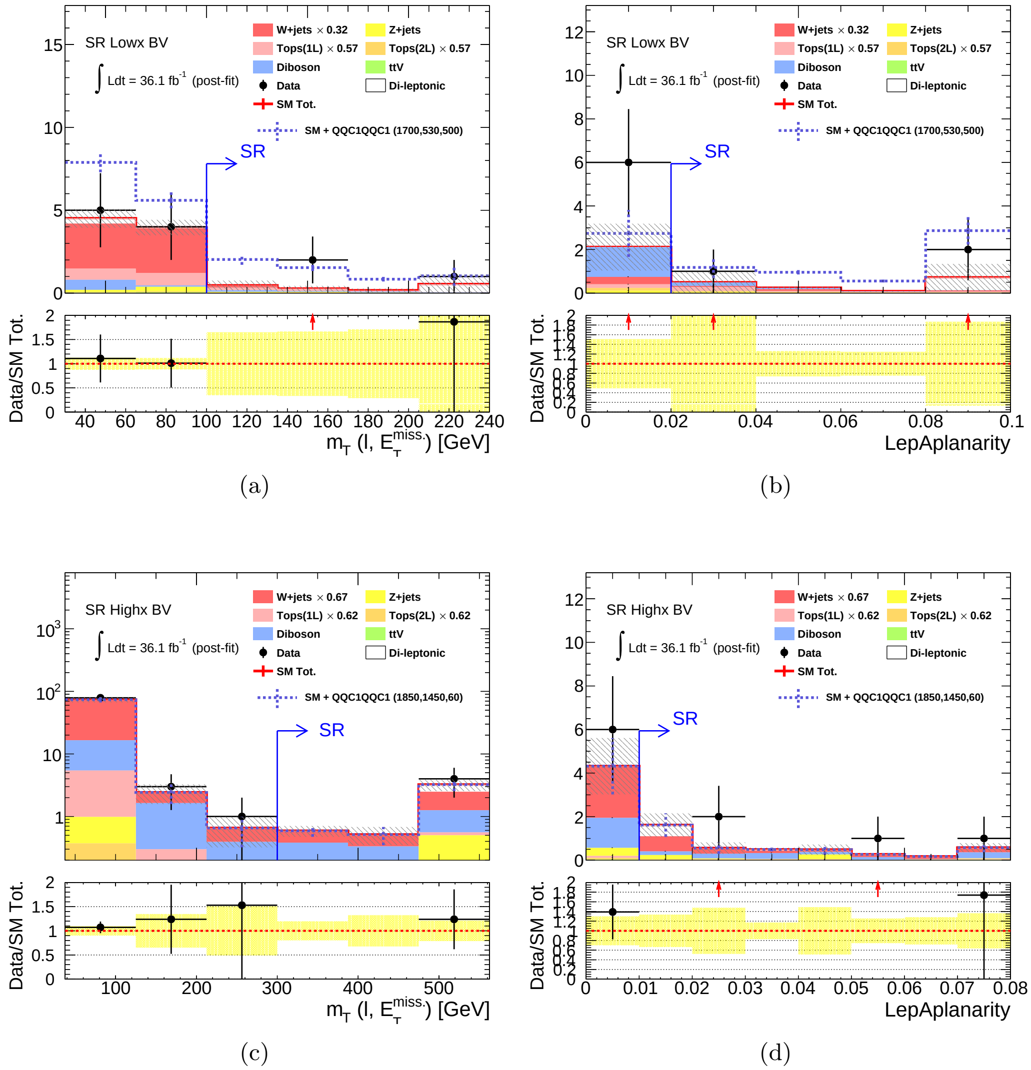

Figure 8.7: Post-fit distruibution of (left) m_{T} and (right) aplanarity. (a,b) SR Low-x BV. (c,d) SR High-x BV. The yellow band in the bottom panel represents only statistical error. The overflow is included in the highest bin. The yellow band in the bottom panel represents statistical error. The overflow is included in the highest bin. Dashed lines represent the expected distributions of total background plus the typical signal targeted in the signal region bin.

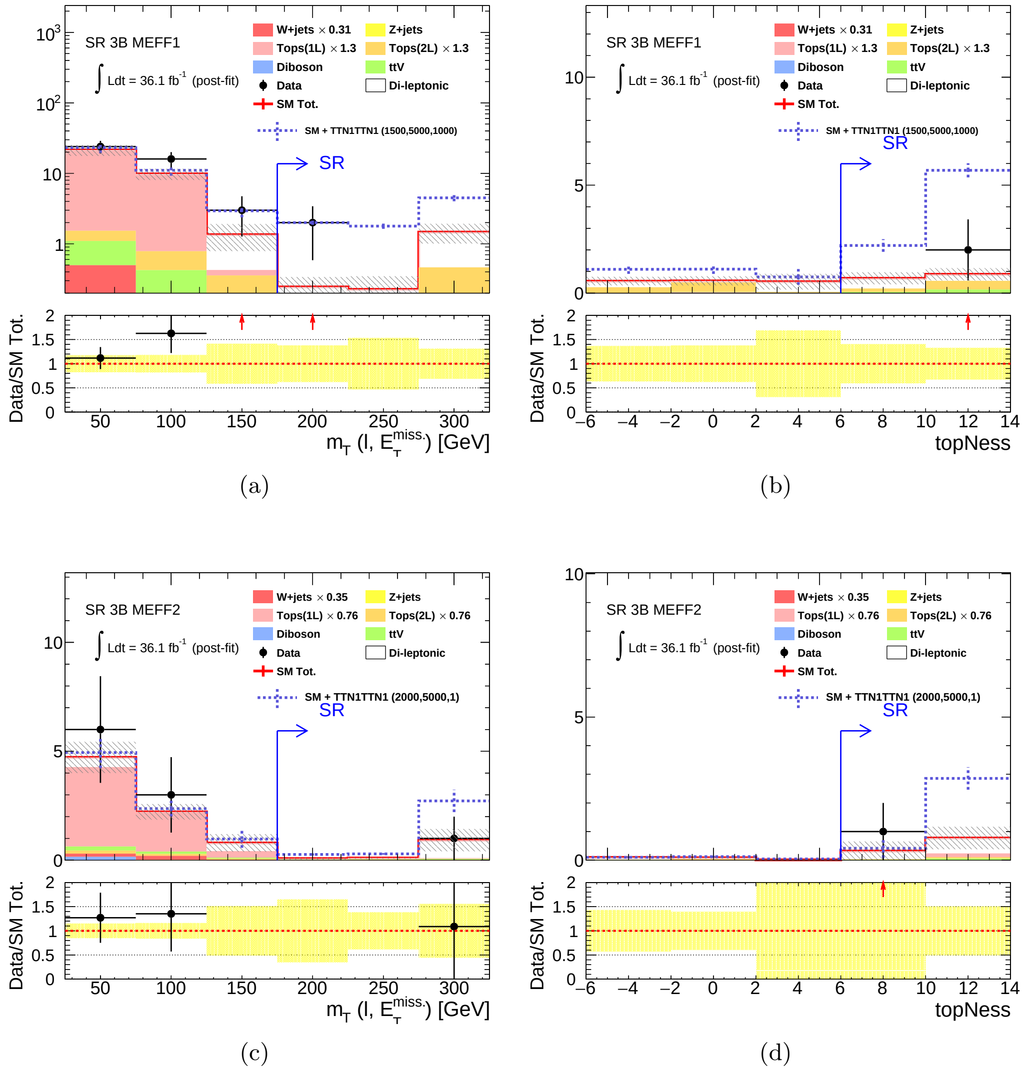

Figure 8.8: Post-fit distruibution of (left) m_{T}, and (right) topness. (a,b) SR 3B-$m_{\mathrm{eff}}^{\mathrm{bin1}}$. (c,d) SR 3B-$m_{\mathrm{eff}}^{\mathrm{bin2}}$. The yellow band in the bottom panel represents only statistical error. The overflow is included in the highest bin. The yellow band in the bottom panel represents statistical error. The overflow is included in the highest bin. Dashed lines represent the expected distributions of total background plus the typical signal targeted in the signal region bin.

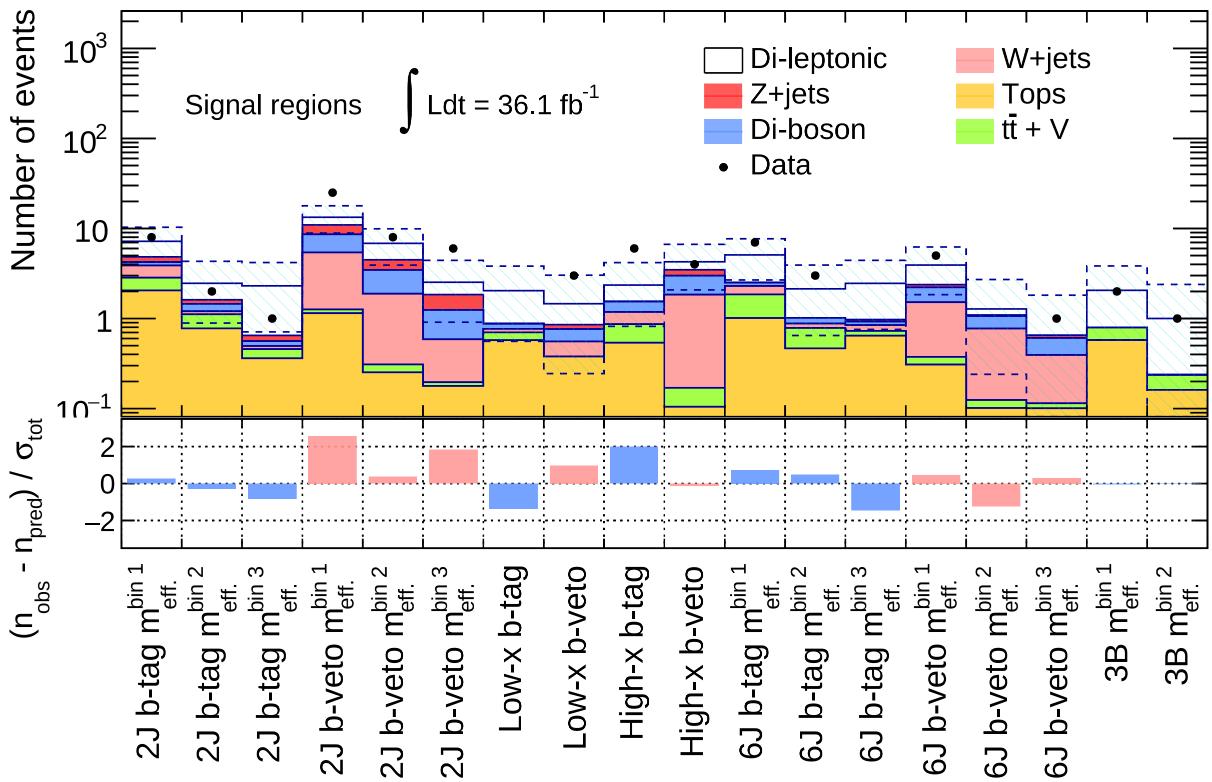

Figure 8.9: (Top) Observed yields and the background expectation in signal regions. The white component is the backgrounds estimated by the object replacement method, while the colored ones are by the kinematical extrapolation method. The dashed band represents the combined statistical and systematic uncertainty on the total estimated backgrounds. (Bottom) Pull between the observed data and the expectation. No significant deviation from expectation exceeding 2σ.

8.3 Constraints on the Benchmark Models

The observed results are then interpreted into constraints on the benchmark models listed in Table 1.5 - 1.7. The obtained limits are also compared with the previous ATLAS results with integrated luminosity of 14.8 fb^{-1}.

QQC1QQC1

Figure 8.10 presents the exclusion limit on **QQC1QQC1**, the reference model for BV benchmarks (Table 1.5). Hypothetical tests are done with each signal point using the combination of signal regions that gives the best expected sensitivity. The excluded region is defined by areas with $CL_s < 0.05$, corresponding to 95% confidence level. The associated expected limit is represented by a blue line surrounded by a yellow band, showing the range of obtained limit if observed data is consistent to the expectation within $\pm 1\sigma$.

Observed limits are typically worse than the expected ones in the mass region where sensitivity is primarily driven by SR **2J** and SR **High-x**, namely the diagonal region in the `x=1/2` grid, and the high-x region in the `LSP60` grid respectively, reflecting the observed excess there which weakens the exclusion power.

Exclusion limits driven by the previous 1-lepton search in ATLAS with $\mathcal{L} = 14.8\mathrm{fb}^{-1}$ [147] are shown by the shaded areas. While the magenta areas are the exclusion limit directly quoted from the reference, the cyan ones indicate the potential exclusion that could have achieved by the previous search, calculated based on the observed yields in the signal regions, since no interpretation has been made with the grids.

For grids `x=1/2` and `LSP60` that has been the main target in previous analyses, the exclusion limits are pushed forward by about 100 GeV $\sim$ 400 GeV in gluino mass with the same mass splitting. The merit of the improved analysis can be clearly acknowledged, given that the cross-section of gluino pair production rapidly falls with respect increased gluino mass by about 1/3 by every 200 GeV (the limit improvement by increased statistics is then $\sim$ 100 GeV). Upto 2 TeV of gluino mass is excluded with the nearly massless LSP scenario, while it also reaches about 1.9 TeV of gluino mass for case with $0 < m_{\tilde{\chi}_1^0} < 1$ TeV.

More radical improvement is seen in the `DM20` and `DM30` grids, since no analysis has been provided dedicatedly sensitivity to the scenario before. The sensitivity improvement is about 200 GeV $\sim$ 450 GeV in gluino mass with the same mass splitting, and the 1.2 TeV $-$ 1.6 TeV is excluded by this study. Though the limit is weaker than the typical signatures in `x=1/2` and `LSP60` , sensitivity is addressed without loopholes.

QQC1BTC1

Figure 8.11 exhibits the limits for model **QQC1BTC1**, the reference model for BT benchmarks (Table 1.5). As the sensitivity is mainly driven by the b-tagged bins for this model, it is relatively more affected by the $\sim 2\sigma$ excess observed in the SR High-x BT, which drastically weakens the limit in part of the `LSP60` grid. Nevertheless, the overall exclusion reach is comparable to the **QQC1QQC1** model, amounting to 1.9 $\sim$ 2 TeV in gluino mass for $m_{\tilde{\chi}_1^0} < 1$ TeV. As the the asymmetric decays of gluino have never been interpreted before, this is the first explicit constrains on such class of models.

Potential exclusion that could have been addressed by the previous 1-lepton search in ATLAS with $\mathcal{L} = 14.8\text{fb}^{-1}$ [147] are shown by the cyan shaded areas. The sensitivity improvement is similar to the case of **QQC1QQC1**, although it is not as drastic in `DM20` and `DM30` grids, since they are relatively more easily without dedicate selection when top decays can emit hard leptons.

TTN1TTN1

The exclusion limit for the model **TTN1TTN1**, the reference model for the 3B benchmarks (Table 1.5) is shown in Figure 8.12. The observed and expected limits agree as the global feature.

The exclusion limit provided by the previous ATLAS analyses (multi-b: [148], same-sign leptons or three leptons: [149]) are displayed by the shade area. The most prominent update is around the diagonal region with the mass splitting $\Delta m(\tilde{g}, \tilde{\chi}_1^0)$ below 400 GeV, where the explicit limit is set for the first time. On the other hand, there is seemingly no improvement in the direction toward high gluino mass despite the increased data, which is because the compared past limit is provided by the combination of both 0-lepton and 1-lepton channel in the analysis, which elevates the sensitivity by $\sim$ 100 GeV in the limit.

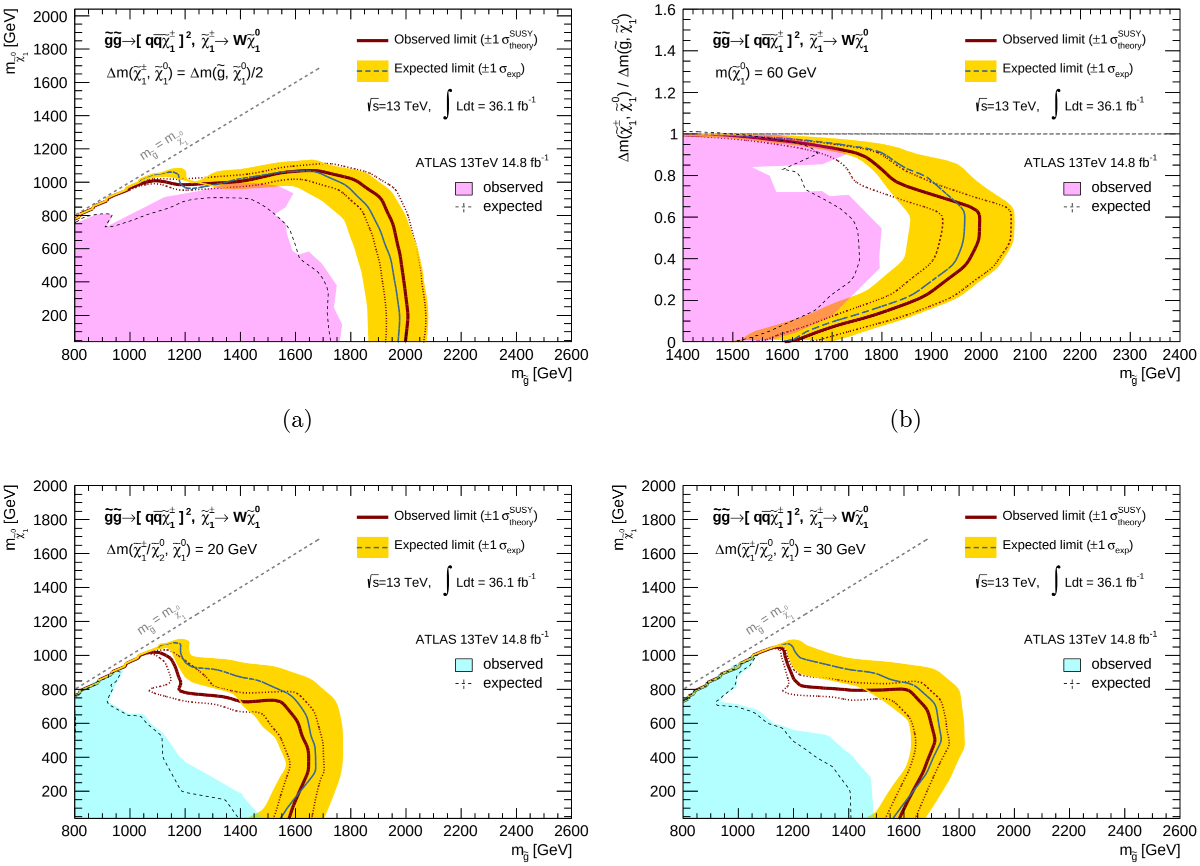

(a) (b) (c) (d)

Figure 8.10: Exlusion limit for the benchmark model **QQC1QQC1** presented in the (a) `x=1/2` (b) `LSP60` (c) `DM20` (d) `DM30` grids. Observed limit is shown by the solid red line, while the expected limit are expressed by the dashed blue line with the yellow band describing the variation due to the deviation within $\pm 1\sigma$. Potential exclusion that could have been addressed by the previous 1-lepton search in ATLAS with $\mathcal{L} = 14.8\text{fb}^{-1}$ [147] are shown by the cyan shaded areas. The previous 1-lepton search result by ATLAS with $\mathcal{L} = 14.8\text{fb}^{-1}$ [147] are overlayed (observed limit: shaded area, expected limit: black dashed line). The magenta areas are the exclusion limit directly quoted from the reference, while the cyan ones are the calculated potential achivable exclusion by the previous search. All limits correspond to 95% CL.

The exclusion limits for all the 45 models and grids are calculated similarly. Observed limits are compared in Figure 8.13-8.17. Models in the same BV/BT/3B type (defined by the different tables in Table 1.5 - 1.7) are overlaid in the same plot. Though the acceptance after the 1-lepton pre-selection are similar between them, the final sensitivity does vary depending on the branching into 1-lepton final state of the model which has relatively a wide variety. This ends up in 300 GeV $\sim$ 400 GeV of difference in gluino mass at the largest. This on the other hand means that the models with less sensitivity can be fully recovered by the combination with 0-lepton final state. Aside such several models with small 1-lepton branches, the variation is typically 100 GeV $\sim$ 200 GeV, which confirms the inclusiveness of the analysis.

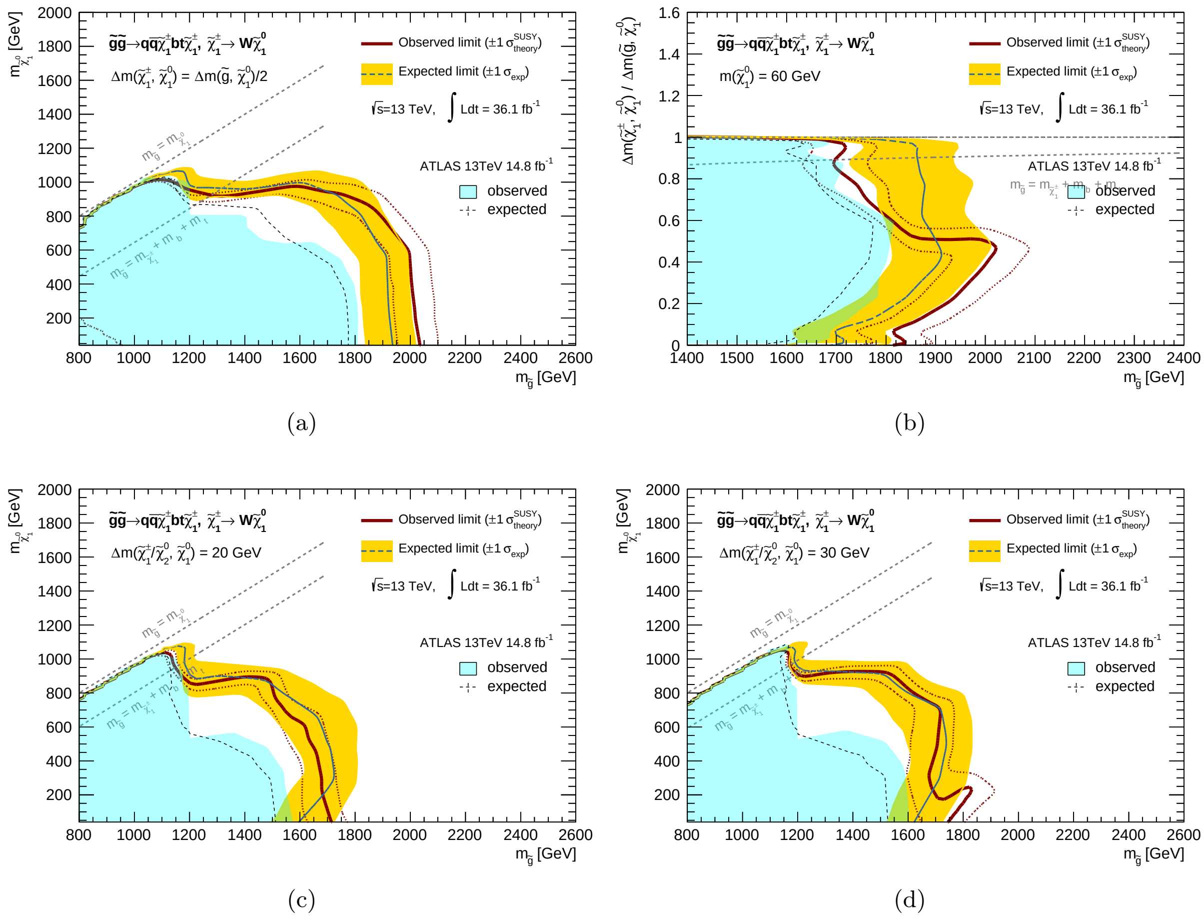

Figure 8.11: Projected exlusion limit (95% CL) for benchmark model **QQC1BTC1** presented in (a) `x=1/2` (b) `LSP60` (c) `DM20` (d) `DM30` . Observed limit is shown by the solid red line, while the expected limit are expressed by the dashed blue line with the yellow band describing the variation due to the deviation within $\pm 1\sigma$. Potential achivable exclusion by the previous 1-lepton search in ATLAS ($\mathcal{L} = 14.8\text{fb}^{-1}$) [147] are shown by the cyan shaded areas. All limits correspond to 95% CL.

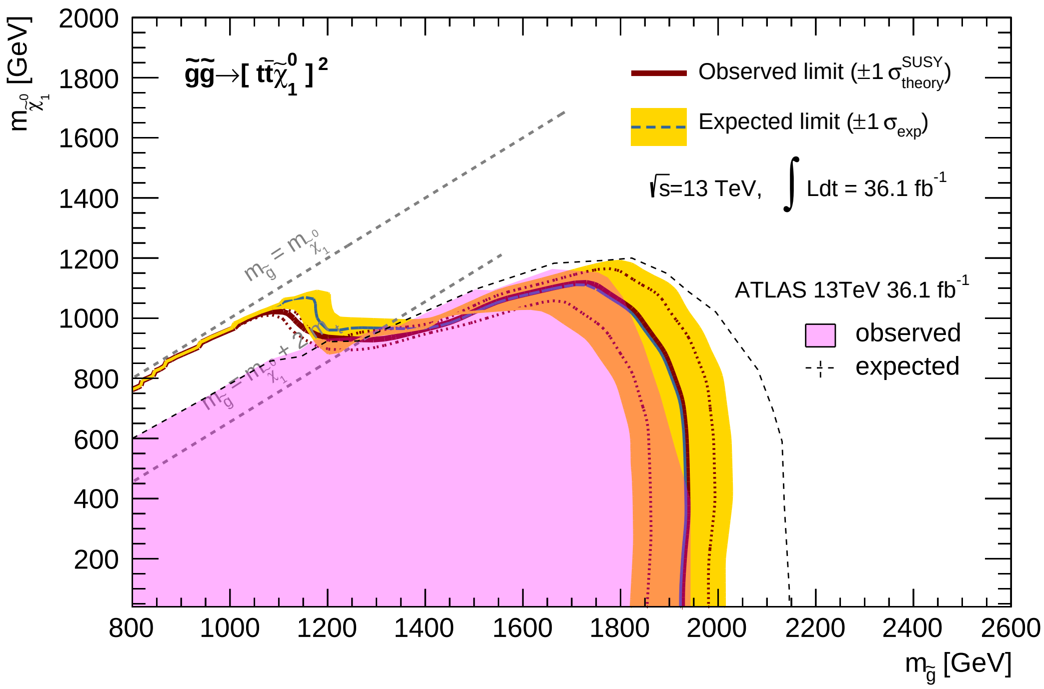

Figure 8.12: Exlusion limit for benchmark model **TTN1TTN1**. Observed limit is shown by the solid red line, while the expected limit are expressed by the dashed blue line with the yellow band describing the variation due to the deviation within $\pm1\sigma$. The past result provided by ATLAS [148] [149] is overlayed (observed limit: magenta shade, expected limit: black dashed line), which is given by the combination of 0-lepton and 1-lepton analyses. All limits correspond to 95% CL.

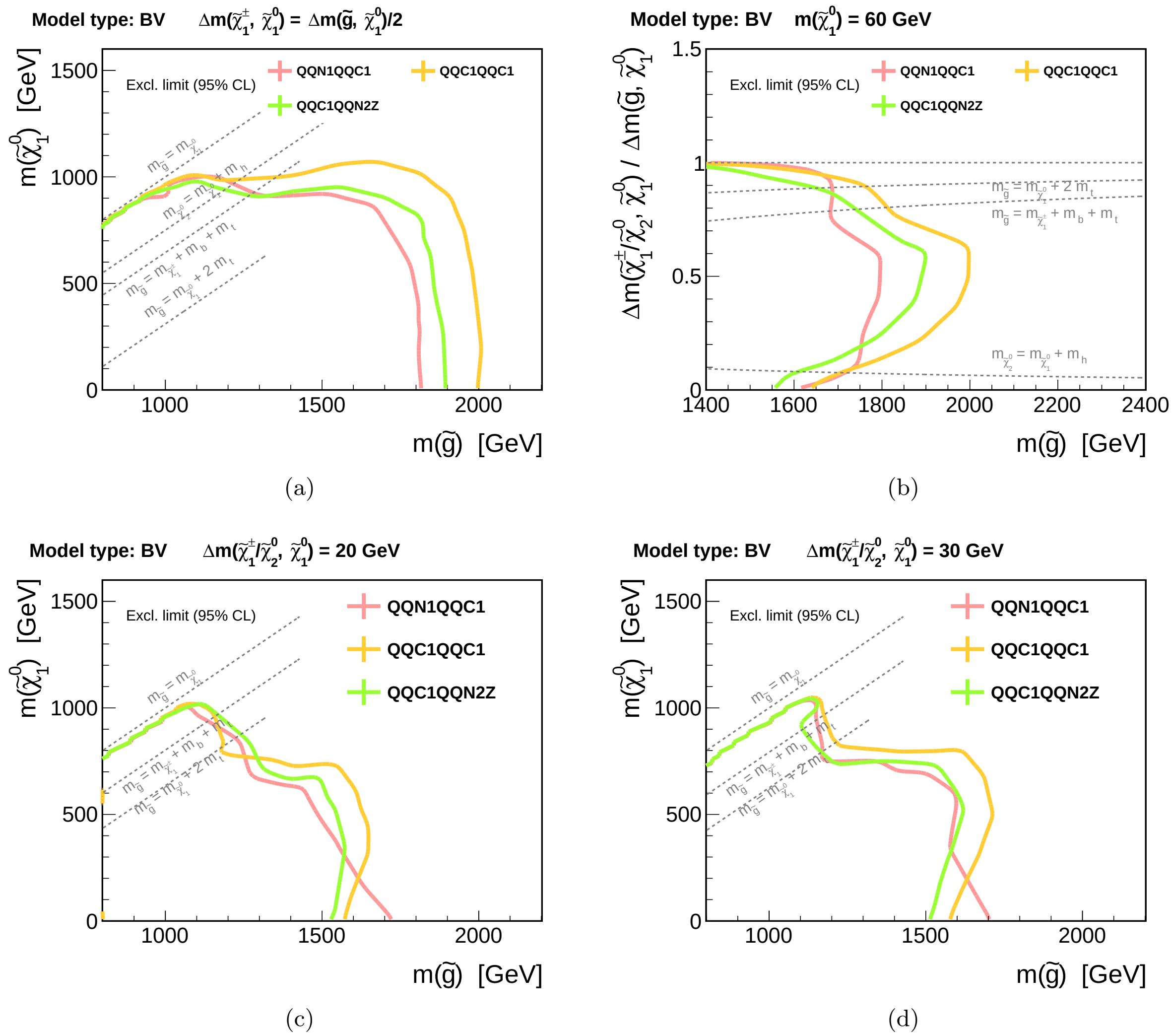

Figure 8.13: Observed limit for benchmark models belonging to "BV"-type in the (a) `x=1/2` (b) `LSP60` (c) `DM20` (d) `DM30` grid.

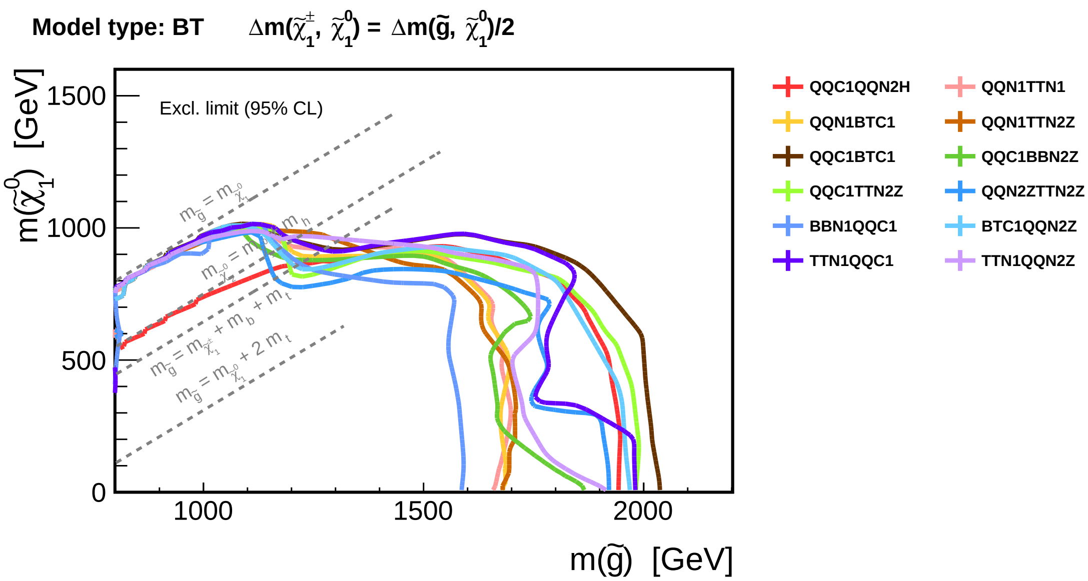

(a)

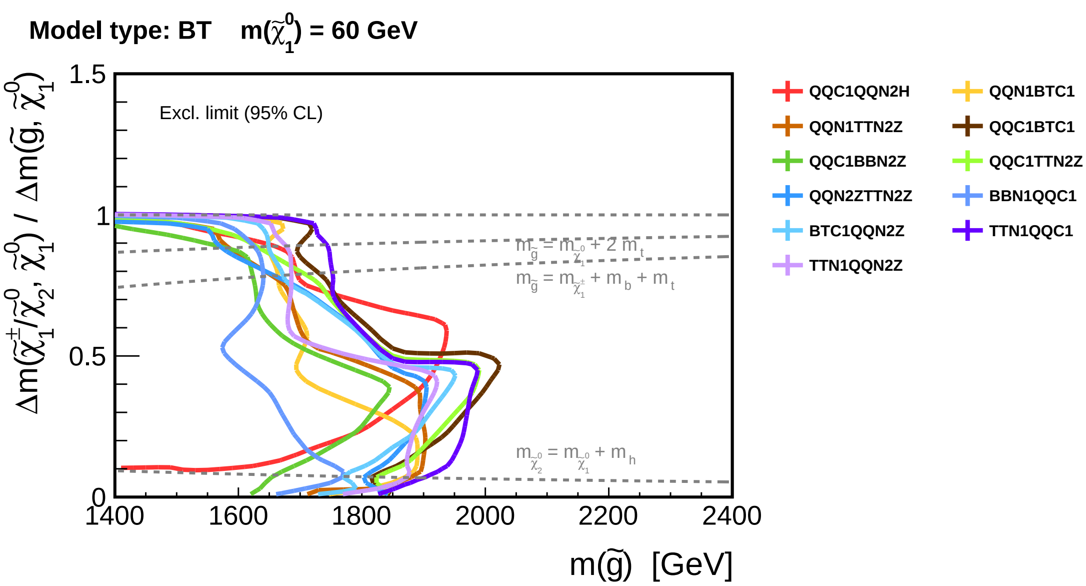

(b)

Figure 8.14: Observed limit for benchmark models belonging to "BT"-type in the (a) `x=1/2` (b) `LSP60` grid.

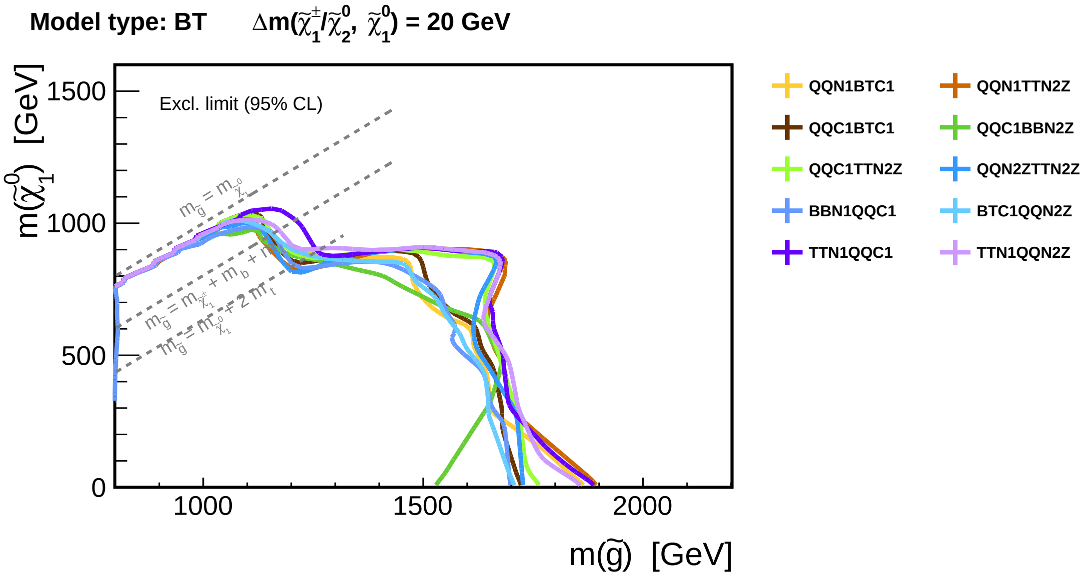

(a)

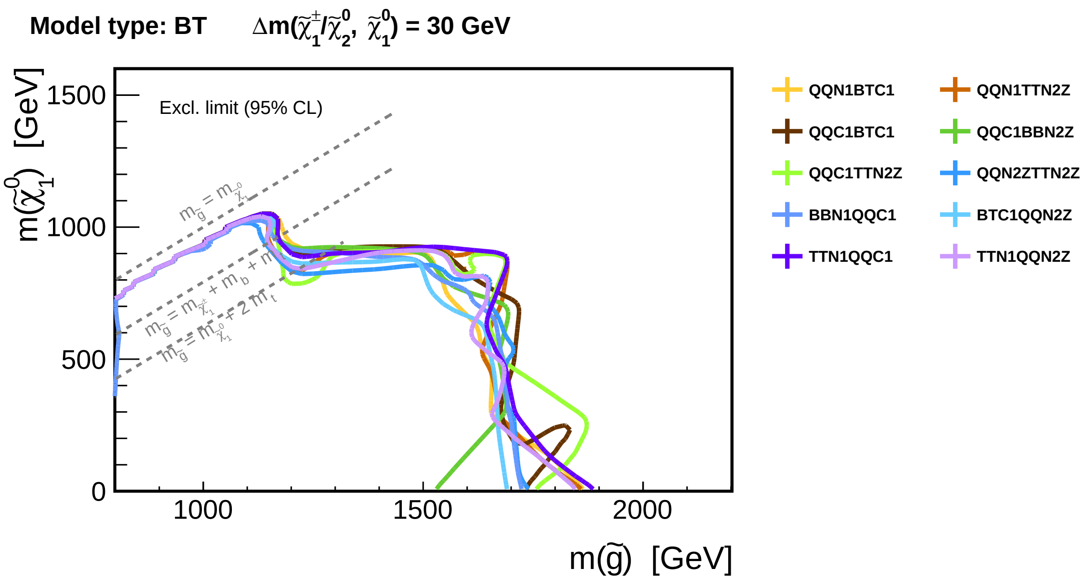

(b)

Figure 8.15: Observed limit for benchmark models belonging to "BT"-type in the (a) `DM20` (b) `DM30` grid.

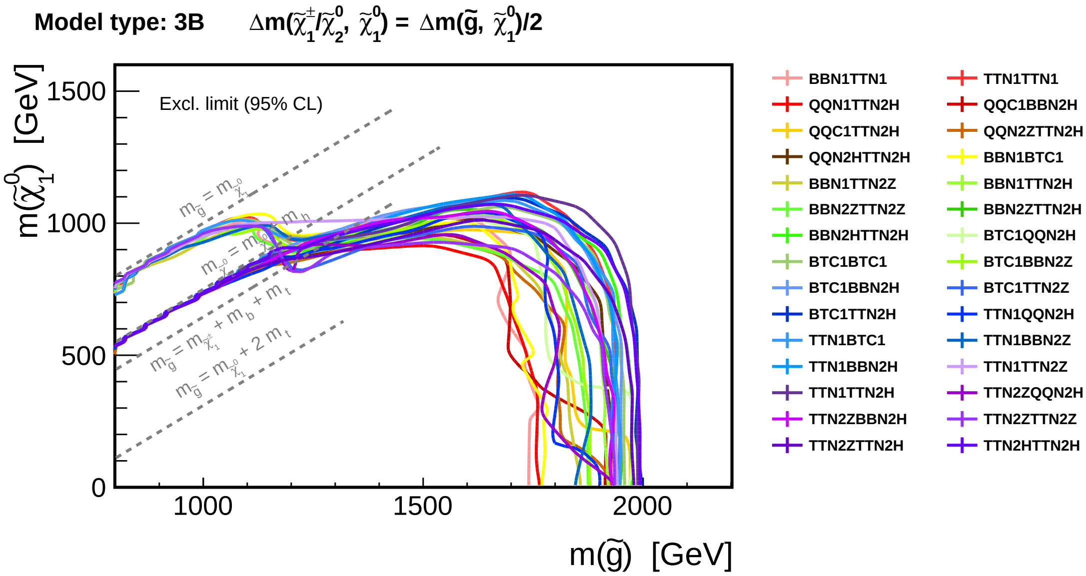

(a)

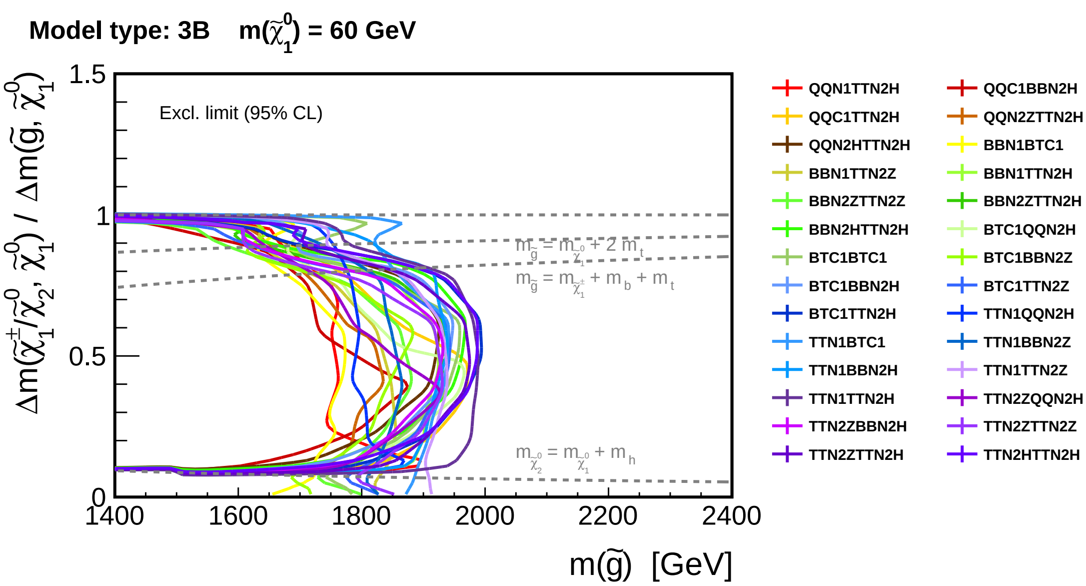

(b)

Figure 8.16: Observed limit for benchmark models belonging to "3B"-type in the (a) `x=1/2` (b) `LSP60` grid.

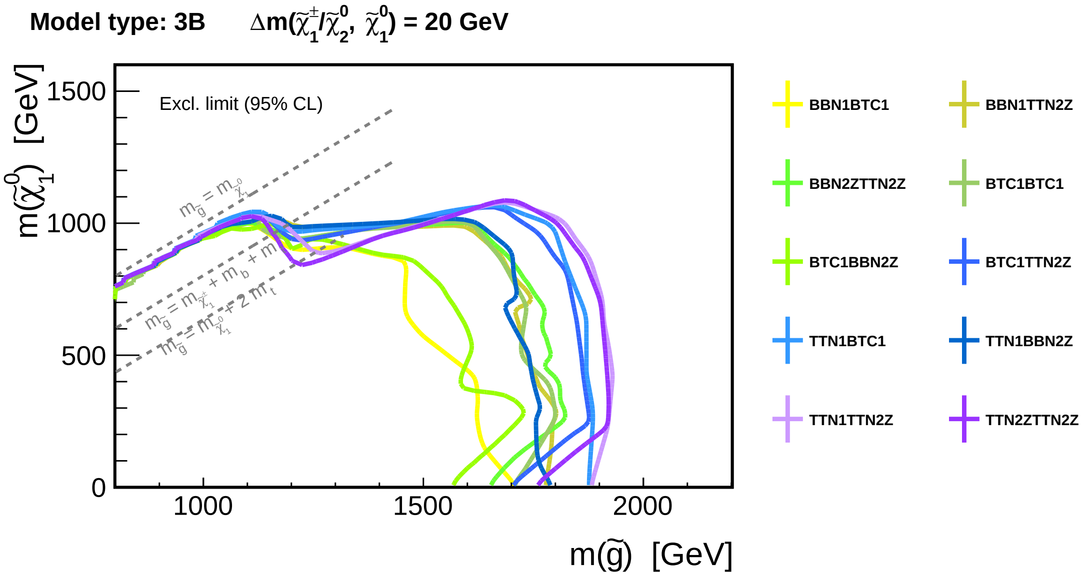

(a)

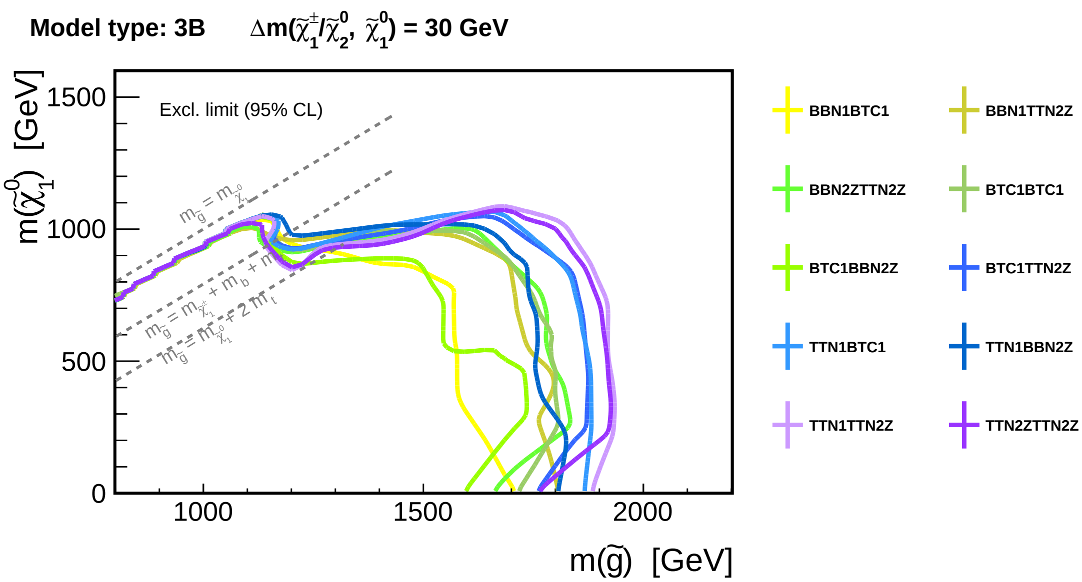

(b)

Figure 8.17: Observed limit for benchmark models belonging to “3B”-type in the (a) `DM20` (b) `DM30` grid.

8.3.1 Obtained Cross-section Upper-limit

$\mathrm{CL_s}$ value is calculated as the function of $\mu_{\mathrm{sig.}}(\in [0, 10])$ in a hypothetical test. Therefore the upper limit on signal strength $\mu_{\mathrm{sig.}}$ can be determined as:

$$\mu_{\mathrm{sig.},95} := \mu_{\mathrm{sig.}}(\mathrm{CL_s} = 0.05). \tag{8.16}$$

This can be straightforwardly interpreted into the upper limit on the excluded cross-section (σ_{95}), and it is a completely model-independent presentation of result once the decay chain and the masses of gluino and EW-gauginos are specified. Figure 8.18-8.20 present the results for the reference models **QQC1QQC1**, **QQC1BTC1** and **TTN1TTN1**.

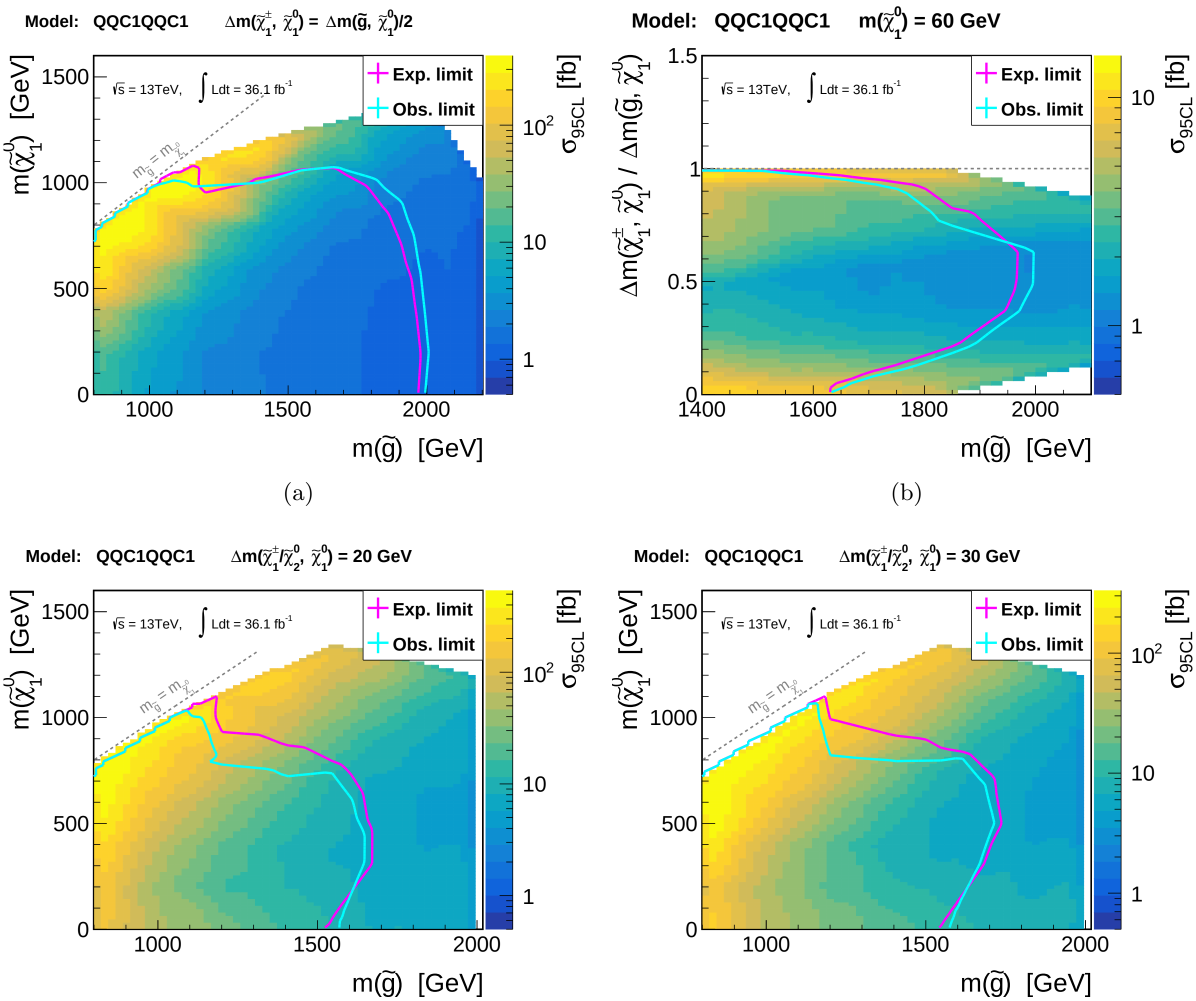

(a) (b)

(c) (d)

Figure 8.18: Upper limit of excluded cross-section (95%CL) as the function of the SUSY masses, for the reference model **QQC1QQC1**, presented in the grids (a) $x = 1/2$ (b) $m_{\tilde{\chi}_1^0} = 60$ GeV (c) $\Delta m(\tilde{\chi}_1^{\pm}, \tilde{\chi}_1^0) = 20$ GeV (d) $\Delta m(\tilde{\chi}_1^{\pm}, \tilde{\chi}_1^0) = 30$ GeV.

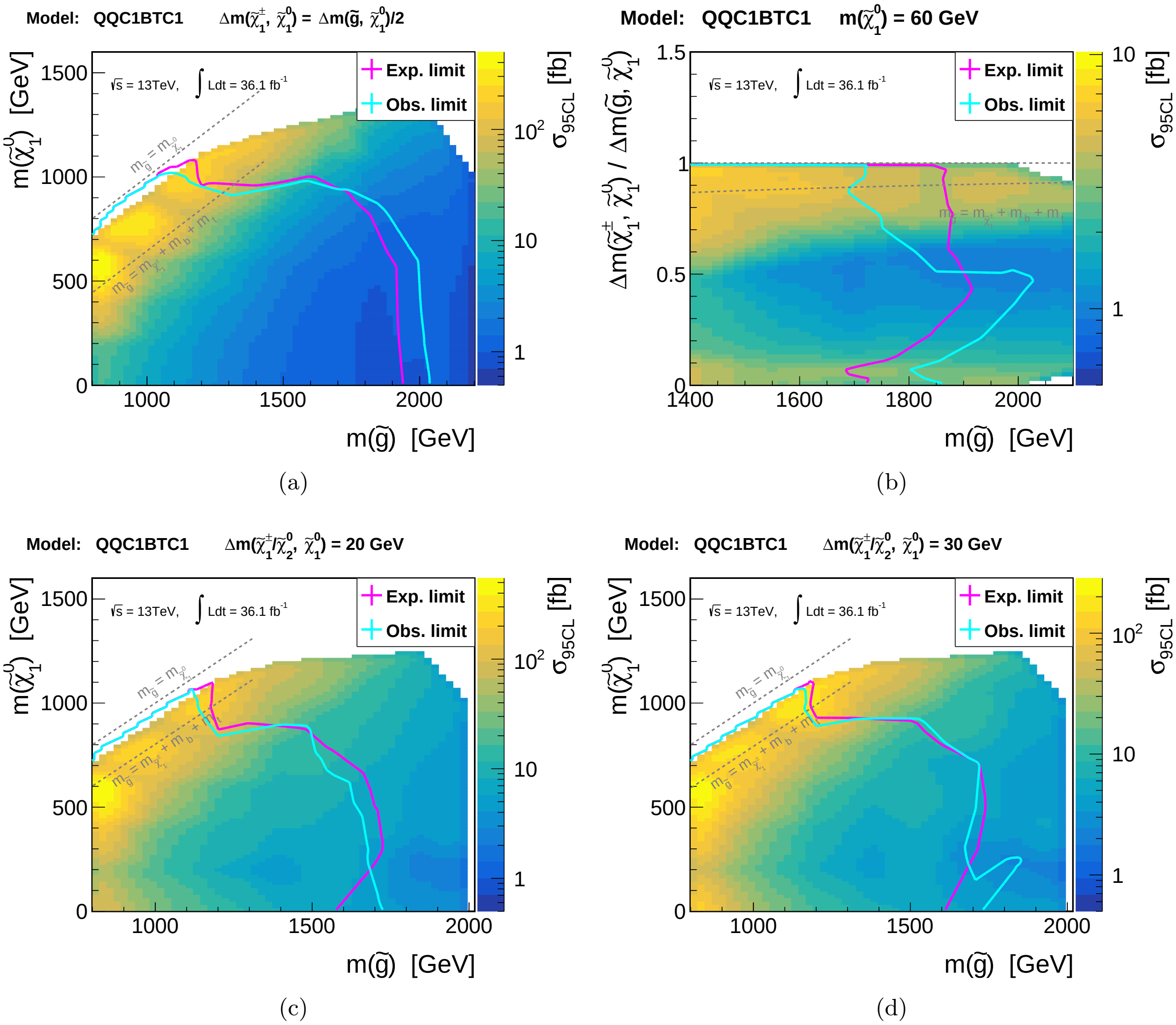

Figure 8.19: Upper limit of excluded cross-section (95%CL) as the function of the SUSY masses, for the reference model **QQC1BTC1**, presented in the grids (a) $x = 1/2$ (b) $m_{\tilde{\chi}_1^0} = 60$ GeV (c) $\Delta m(\tilde{\chi}_1^\pm, \tilde{\chi}_1^0) = 20$ GeV (d) $\Delta m(\tilde{\chi}_1^\pm, \tilde{\chi}_1^0) = 30$ GeV.

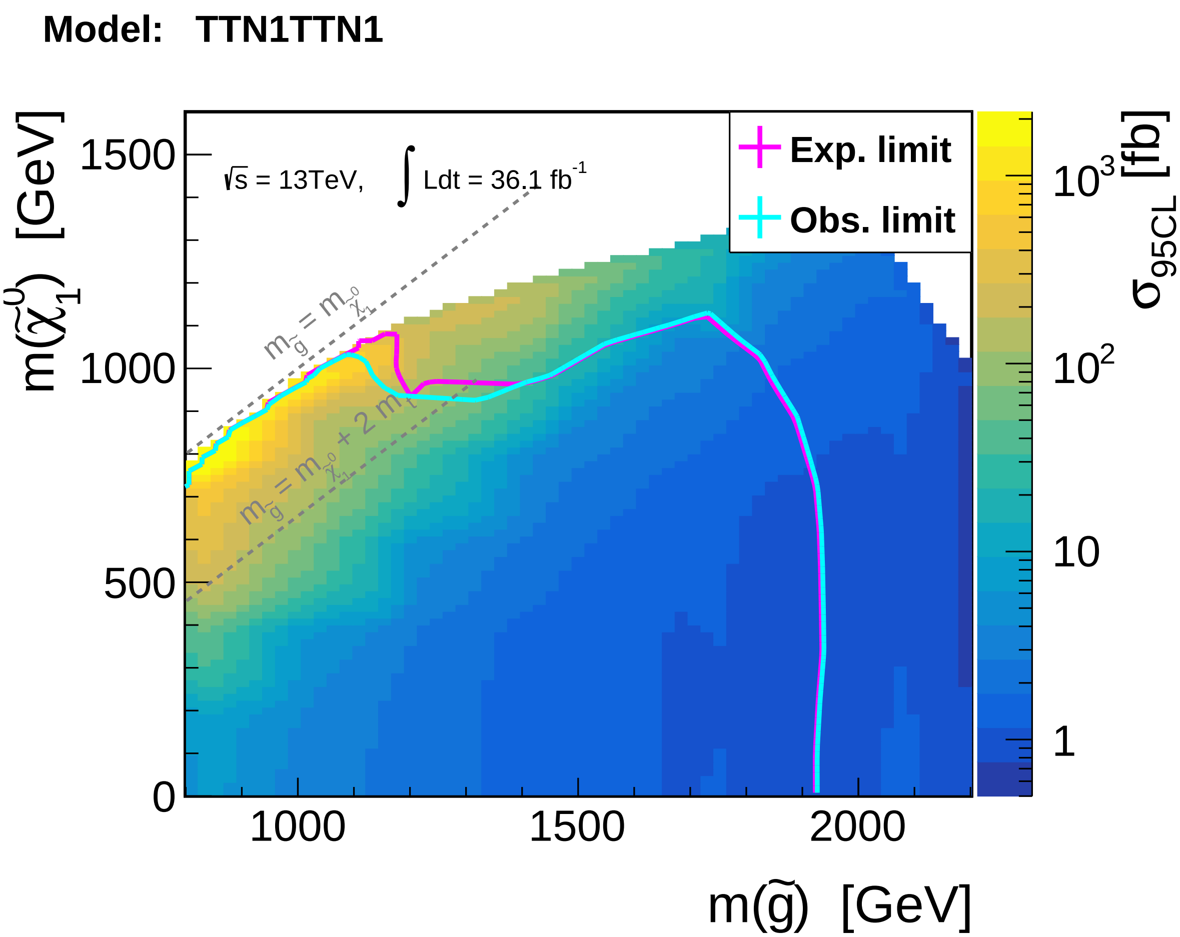

Figure 8.20: Upper limit of excluded cross-section (95%CL) as the function of the SUSY masses, for the reference model **TTN1TTN1**.

Chapter 9

Discussion

In this chapter, the impact and implication of the result provided by the study is further discussed, particularly on the comaprison with the other gluino search analyses using the similar dataset as mentioned in 1.4.3, as well as the unique achivements done by the study. A short remark about the future outlook follows in the end of the chapter.

9.1 Comparison with the Other Up-to-date LHC Searches

Figure 9.1 show the obtained limits on (a) **QQC1QQC1** (`x=1/2` grid) and (b) **TTN1TTN1** which are the conventionally studied gluino decay chains in the 1-lepton final, together with those provided by the other ATLAS/CMS searches appearing in the Figure 1.7-1.8 in chapter 1.4.3.

Sensitivity to decay chain QQC1QQC1 (`x=1/2` grid)
Compared with the ATLAS 0-lepton analysis, the result of this thesis shows the comparable sensitivity in the massless LSP limit, and outperforms for massive LSP scenario as the 1-lepton final state is generally advantageous owing to the additional background rejection power by m_{T}. Quite similar sensitivity is seen between the thesis analysis and the CMS 1-lepton one, except for the region with heavy LSP where the kinematics is not very hard and therefore benefited by the combined multi-bin fit the most. The CMS SUSY analyses do much better job in this front as they often employ an incredibly large number of signal region bins (30-160). Note that the absence of limit in the diagonal region by the CMS analysis is because it only considers the on-shell W-boson emission in the interpretation.

Sensitivity to decay chain TTN1TTN1
The ATLAS multi-b analysis is quite advantageous in sensitivity for high mass gluino scenario, since it exploits the statistical combination between 0-lepton and 1-lepton signal regions as mentioned in previous chapter, though the observed limit is much worse due to the excess found in 0-lepton signal regions. The sensitivity driven by the 1-lepton signal regions are quite comparable between the three cases.

Sensitivity to other decay chains
Although the other gluino decay chains (e.g. asymmetric decaying gluinos) have never been

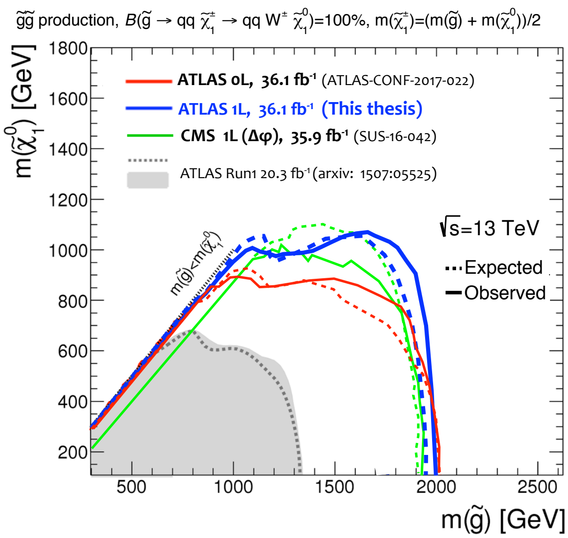

(a)

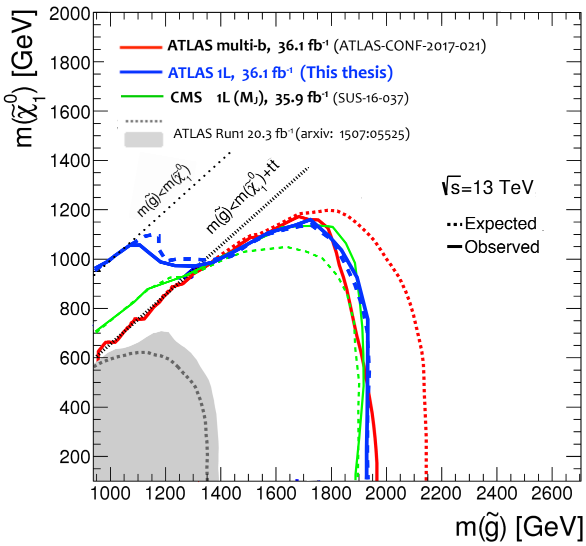

(b)

Figure 9.1: Constraints set by this analysis (blue) and other up-to-date ATLAS/CMS analyses (red/green) on (a) **QQC1QQC1** with the mass being in the middle between gluino and the LSP, and (b) **TTN1TTN1**.

explicitly interpreted into limit before, those signatures could still be captured by the ordinary signal regions. For instance, the CMS analyses are suppose to address reasonable sensitivity to most of the decay chains with typical mass configuration, giving the wide phase space coverage of the signal regions and the large number of signal bins. However, an exception is expected in the case of the DM-oriented scenario where LSP and NLSP EW gauginos are compressed, which requires particular consideration in event selection. One of the nice thing about this thesis is that it provides optimized sensitivity to such scenario as detailed more in the next section.

9.2 What is Unique/Important in This Study

Design of dedicated event selection for the DM oriented scenario.
In the previous ATLAS 1-lepton analyses [150] [147], there has been a signal region indeed targeting scenarios with compressed NLSP and LSP (referred as "Low-x"). However, it was only optimized to the case with massless LSP (low x region in the `LSP60` grid) where the emitted lepton can be hard due to the heavily boosted NLSP, thus the soft lepton selection was not applied. Giving that the massless LSP is no longer realistic for many reasons (see Sec. 1.4.2), the focus is shifted to the massive LSP scenario in this analysis where the soft lepton selection is explicitly applied. Similarly, the CMS analyses do not contain the soft lepton selection in their signal region. This is why the DM-oriented grids have the optimized sensitivity for the first time in this study.

Establishment of a refined background estimation technique.
The most important feat of this study is the establishment of the object replacement method; from the refinement of the previous studies, to the implementation in the analysis together with the conventional kinematical extrapolation method. The dependency on MC is then dramatically reduced as a result, enhancing the confidence in our background estimation by replacing the main systematic uncertainty from theoretical uncertainty (which is in fact often quietionable) to statistical error in CRs. This is a highly important aspect towards claiming the discovery once excesses are found, since the uncertainty can be reduced just by adding data statistics.

In a longer term, the object replacement method is supposed to benefit even more, as heavier gluino will be targeted with tighter selections applied in the future analyses. Since more extreme phase space will be explored where MC is supposed to even more unreliable, it is always sensible to keep the statistical uncertainty as the primary uncertainty.

There is one thing that has to be remarked is that the idea of object replacement itself is not original to the author. The one of the most famous example of such kind of estimation in the past might be the "tau embedding" performed in the Higgs analysis ($h \to \tau\tau$) in ATLAS Run1 [151]. This is to estimate the $Z \to \tau\tau$ background from $Z \to \mu\mu$ data events, by replacing muons into simulated tau decay. Replaced events are re-input in the detector simulation, meant to reduce the instrumental systematics. This is however too computationally costly for search analyses where instrumental systematics has little impact. Therefore, a simplified version has been proposed where detector effect is emulated instead of simulated ("tau replacement") [152]. The author has been working on the refinement and upgrade from the preliminary proposal, including the introduction of "missing-lepton replacement" and establishment of the subtraction method. The first implementation in the published analysis is done by CMS [153] (0-lepton, Run2, $\mathcal{L} = 12.8\ \mathrm{fb}^{-1}$), shortly later it is done for the first time in ATLAS as well by this work. The main difference between the CMS implementation is the use of MC; while it is carefully designed to ensure the object-kinematics orthogonality 6.1 (i.e. lepton efficiency is parameterized by the lepton's p_{T} and η) in this analysis, CMS takes an opposite philosophy where lepton efficiency is parameterized by as many event-level kinematical variables as possible. This might lead to some difference in estimation in highly extreme phase space.

An improvement is also made in the context of the kinematical extrapolation method, with more complete assignment of theoretical uncertainty. Conventionally, it is assigned based only on the known effects, even if an unaccountable mis-modeling is found. Though it has been the best thing one can do, this study makes one more step forward, implementing the approximately effects from "unknown theory systematics" by expressing the unknown mis-modeling by a kinematic reweighting.

First interpretation on a comprehensive classes of the gluino decay chains.
The very low variety of decay chains assumed in ATLAS/CMS SUSY searches has been always an one of the most outstanding concern. As for gluino pair production, only 6 decay scenarios with 100% branching ratio has been considered so far. This is not comprehensive at all, and there is little clue to judge if the provided mass reaches are reasonable or not.

The full-model oriented approach is then gradually attempted recently. The most popular study is done with the phenomenological MSSM (pMSSM) which is a simplified MSSM with most of the parameters are fixed and only 18 important parameters are set free. It is basically a parameter scan in a 18-dimensional space, generating a bunch of points of signal models with inclusive decay patterns (the primary result by ATLAS can be found in [154] [155]). Though much more comprehensive, it suffers from a couple of presentational problems; the limit is hardly expressed by the mass reach hence non-intuitive; the result is so model dependent that it is impossible to re-interpreted to the other models.

On the other hand, the presentation in this study largely addresses all of the problem; this is the first study explicitly testing each direct/1-step gluino decay chain that can be targeted by 1-lepton final state; limits are presented in terms of mass reach; model-independent upper limit on the excluded cross-section is also provided so that any model can be tested based on the result.

9.3 Future Prospect

The future LHC run schedule is schematized in Figure 9.2. After the current Run2 ($\mathcal{L} \sim 150$ fb^{-1}) and following phase-1 upgrade, Run3 is planned to take place upto $\mathcal{L} \sim 300$ fb^{-1}. The HL-LHC project (High-Luminosity LHC) [156] is then planned after Run3, with a large scale upgrade both in the accelerator to boost the luminosity as well as the detectors to cope with more severe radiation environment (phase-2).

The HL-LHC physics runs are planned to be operated with a center-of-mass energy of 14 TeV, accumulating $\mathcal{L} \sim 3000$ fb^{-1} of data in about 10 years. Gluino seach will be still important as it has no experimental or phenomenologically implied upper limit in its mass. The limit can be easily extended by keep applying tighter selection, as the background separation becomes easier with exploring heavier gluinos. The search sensitivity is expected to extend upto 2.5 TeV $\sim$ 3 TeV in gluino mass with $\mathcal{L} \sim 3000$ fb^{-1} (Figure 9.3).

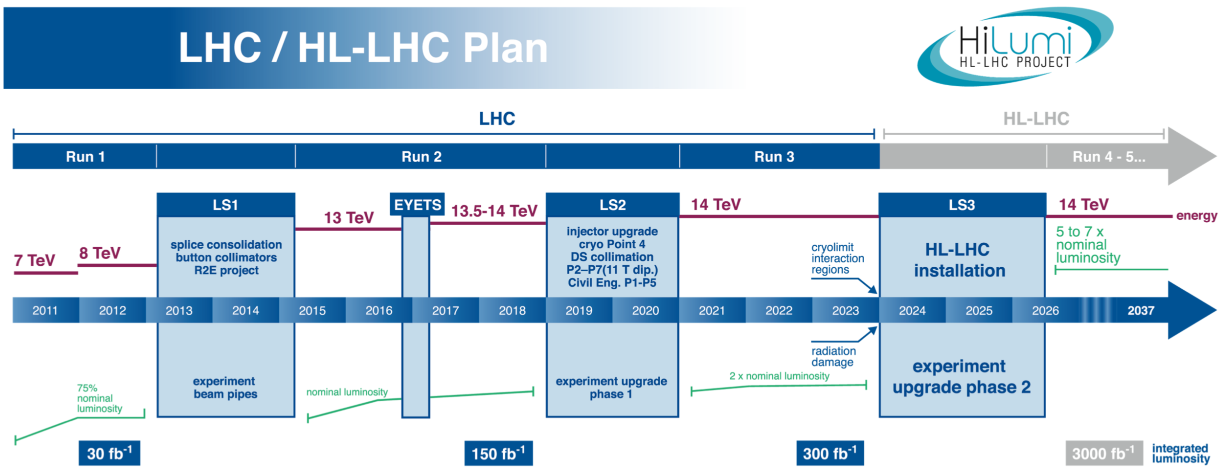

Figure 9.2: The time line of current LHC and foreseen HL-LHC [156].

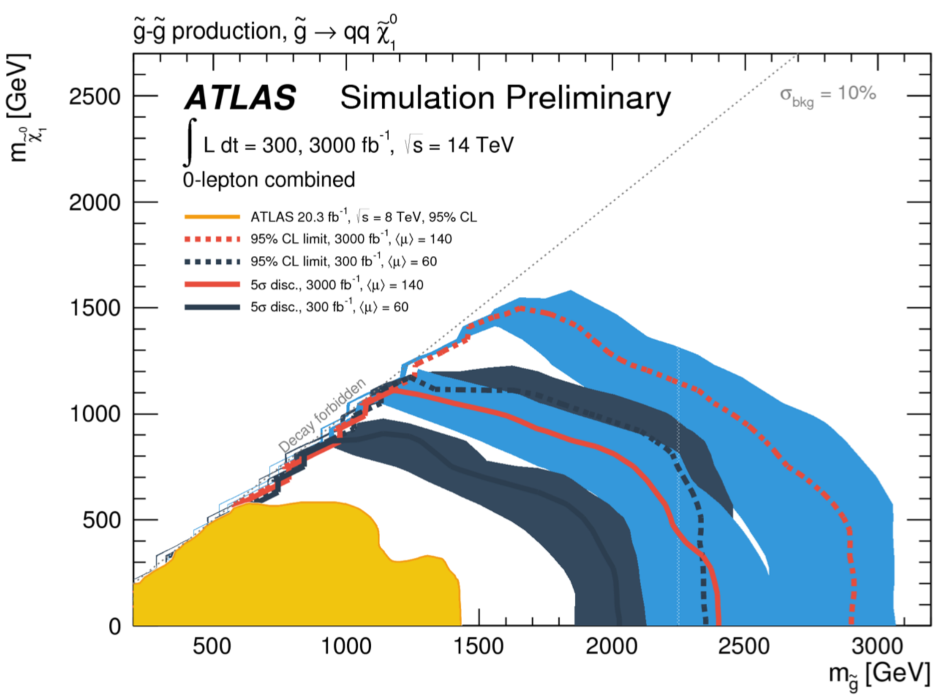

Figure 9.3: Expected discovery reach (5σ) and exclusion limit (95% CL) with whole Run2-3 dataset ($\mathcal{L} \sim 300$ fb^{-1}) and HL-LHC dataset ($\mathcal{L} \sim 3000$ fb^{-1}) [157].

Chapter 10

Conclusion

This thesis presented the search for gluinos using proton-proton collisions in the Large Hadron Collider (LHC) at the center-of-mass energy of $\sqrt{s} = 13$ TeV collected in the ATLAS detector. Focusing on the final state with one leptons, all relevant 45 decay chains for pair produced gluinos are explored, together with various scenarios of the mass spectra, aiming to provide the most general result achievable in principle.

The highlight of the analysis is designing a dedicated data-driven background estimation method, reinforce the confidence on the estimation by reducing the reliance on simulation which typically less performing in an extreme phase space.

Analysis is performed with dataset with 36.1 fb^{-1} of integrated luminosity. In the unblinded signal regions, no significant excess is found. Constraints are set on each of the 45 models of gluino decay chain. Exclusion upto 1.7 TeV $-$ 2.0 TeV in gluino mass, and upto ~ 1 TeV in the lightest neutralino mass is widely confirmed with typical mass spectra of gluino and EW gauginos, while upto 1.5 TeV $-$ 1.9 TeV in gluino mass is excluded in case of compressed EW gaugino masses ($\Delta M \sim 20 - 30$ GeV) which is motivated by dark matter relic observations.

Acknowledgement

The appriciation from the author to people for the contribution of this work is summarized in Table 10.1-10.2.

Table 10.1: List of guys I want to thank.

Name	Relation with the author	The author thanks for ...
Tokyo Group		
Sachio Komamiya	Supervisor	Encouraging the author to jump in the field, reviewing this thesis.
Yoshio Kamiya	Semi-boss	Providing initial how-tos (programing, DAQ, statistics etc.) at the beginning of master
Daniel Jeans	Semi-boss	Teaching physics and software while in master. Proof reading of CV.
Junping Tian	Neighbor desk (Nov. 2016-)	Discussing the prospect of ILC.
Tokyo Computing Team	Host	Maintaing the incrediblely efficient server.
Kono-san	Secretary	Handling numerous paper works for trips, and contact to JPS.
Shiota-san	Secretary	Handling numerous paper works for trips.
Chihiro Kozakai	Colleague	Sharing the tough feeling of Ph.D.
Yusuke Suda	Colleague	Sharing the tough feeling of Ph.D.
Yuya Kano	Colleague	Instruct the author why US people like to say “t’sup” instead of “hello”.

Table 10.2: List of guys I want to thank.

Name	Relation with the author	The author thanks for ...
People in CERN		
Shoji Asai	Local Supervisor in CERN	Suggestion on topics for the Ph.D project.
Junichi Tanaka	Local Supervisor in CERN	Secretly generating samples exerting the priviledge of MC coordinator. Maintaining the server for Tokyo group in CERN.
Takashi Yamanaka	Superving role in the analyis	Answering every technical question from the author, discussing physics in deep, polishing many new/preliminary ideas.
Tomoyuki Saito	Superving role in the analyis	Constant consultant on plans in analysis, codeveloper of the object replacement.
Shimpei Yamamoto	Staff of ICEPP (-2015)	Comprehensive assistance in the initiation of the analysis. Maintaining the server for Tokyo group in CERN.
Yohei Yamaguchi		Teaching the author how to fish.
Yuji Enari	Staff of ICEPP, kebab mate	Providing keen comments to the analysis. Promoting eating kekabs as the desert of a dinner.
Yasu Okumura	Staff of ICEPP	Consultant on post-doc app., proof reading of CV and research proposals.
Keisuke Yoshihara	Foreseen colleague in UPenn	Secure author's life after the Ph. D.
Till Eifert	SUSY convener	Encouraging agreesive ideas. Teaching the author that the life does not end even if SUSY is not found.
Stefano Zambito Moritz Backe Jeanette Lorentz Da Xu	Analysis Contact	Cool coordination.
Nikolai Hartmann Valentina Tudorache	Colleague	Closely working with the most.
Masahiro Morinaga	Room mate	Cooking 10 kg Bolonese per week. Throwing mashrooms from window.
K. Onogi	Room mate	Keep the rooms confortable. Suggesting intersting comics to the author.
Chikuma Kato	Soul mate	Sharing the tough feeling of Ph.D.
Shadachi	Student of Tokyo ICEPP	Exploring Iceland (2016).
Minegishi (Minegy)	Student of Tokyo ICEPP	Exploring Iceland (2016).
Kazuki Motohashi	Buddy	Exploring Iceland (2015).
Dai Kobayashi	Buddy	Exploring Iceland (2015).
T. Nobe	Famous hip-hopper in Japan	Preaching a notion that money is all.
T. Nitta	Famous climber in Japan	Teaching basic movement of climbing.
Others		
Chun Chen / Ying Chen	Parents	Feeding the author for > 25 years.
Maya Okawa	Life-time partnter	Smaggling foods from Japan. Making my life awesome.

Appendix

A Auxiliary Materials for MC Simulation

A.1 Detail Configuration of Event Generation

W/Z+jets

The matrix elements are calculated using the SHERPA 2.2.1 generator [113] up to two partons at NLO and four partons at LO using the Comix [158] and OpenLoops [159] generators. Parton showers are generated by the internal algorithm of SHERPA 2.2.1 [160] and merged based on the ME+PS@NLO prescription [161]. The CKKW scheme is used for ME/PS matching with matching scale set to 30 GeV.

Tops ($t\bar{t}$/single-top)

The h_{damp} parameter controlling the additional radiation is set to the mass of the top-quark [162]. The main effect of this is to regulate the emission of of high p_{T} radiations against the $t\bar{t}$ system recoils. The top-quark mass is set to 172.5 GeV for all the samples. The interference between $t\bar{t}$ and $Wt + b$ is taken into account by the Diagram Removal scheme [163].

Di-bosons: WW/WZ/ZZ

The fully-leptonic processes are simulated with five final states ($\ell\ell\ell\ell$, $\ell\ell\ell\nu$, $\ell\ell\nu\nu$, $\ell\nu\nu\nu$, $\nu\nu\nu\nu$). The intermediated states are not specified therefore the contribution from Drell-Yan-like off-shell diboson and the interference between different diboson processes (e.g. $WW \to \ell\ell\nu\nu$ and $WZ \to \ell\ell\nu\nu$) are taken into account. The semi-leptonic diboson processes are simulated with designated intermediated boson states (W or Z).

$\mathbf{t\bar{t} + W/Z/WW}$

All processes are simulated by MG5_aMC@NLO2.2.3 at LO interfaced to the PYTHIA 8.186 parton shower model, with up to two ($t\bar{t} + W$), one ($t\bar{t} + Z$) or no ($t\bar{t} + WW$) extra partons included in the matrix element.

SUSY signals

Decay of EW gauginos are done in PYTHIA, based on phase space with no consideration of the spin. The CKKW-L matching scheme [164] is applied for the matching of the matrix element and the parton shower, with the corresponding scale parameter set to 1/4 of the gluino mass. The cross-section uncertainty are taken from an envelope of cross-section predictions using different PDF sets and factorization and renormalisation scales, as described in Ref. [165], considering only the four light-flavor left-handed squarks ($\tilde{u}_L$, $\tilde{d}_L$, $\tilde{s}_L$, and $\tilde{c}_L$). Figure 4.3 shows the calculated cross-section and the associated error.

Model parameters irrelevant to SUSY masses are fixed to arbitrary reasonable values, since here we assume they do not change the kinematics as discussed in Sec. 1. The mixing parameters are set so that LSP and NLSP are bino- and wino-like.

B Auxiliary Materials for Event Selection

B.1 Kinematics dependence on Signal Mass Configuration

The trend of the kinematical variables over the mass grids are shown in Figure B.1.1-B.1.4. The color scale (z-axis) indicates the mean of the distribution in the variables, for the signal process in the mass point designated by the xy-coordinate. Three **QQC1QQC1** grids (`x=1/2` , `LSP60` , `DM30`) and one **TTN1TTN1** grid are displayed as the benchmark model for BV/BT signal regions and the 3B signal regions respectively.

One can find that the variables related to transverse momenta of outgoing particles such as m_{eff}, $p_{\mathrm{T}}(\ell)$ and $E_{\mathrm{T}}^{\mathrm{miss}}$ simply scale with the mass splitting, while the other variables such as aplanarity and $E_{\mathrm{T}}^{\mathrm{miss}}/m_{\mathrm{eff}}$ etc. are sensitive to the relative mass spilitting, therefore helpful in defining SR **Low-x/High-x**.

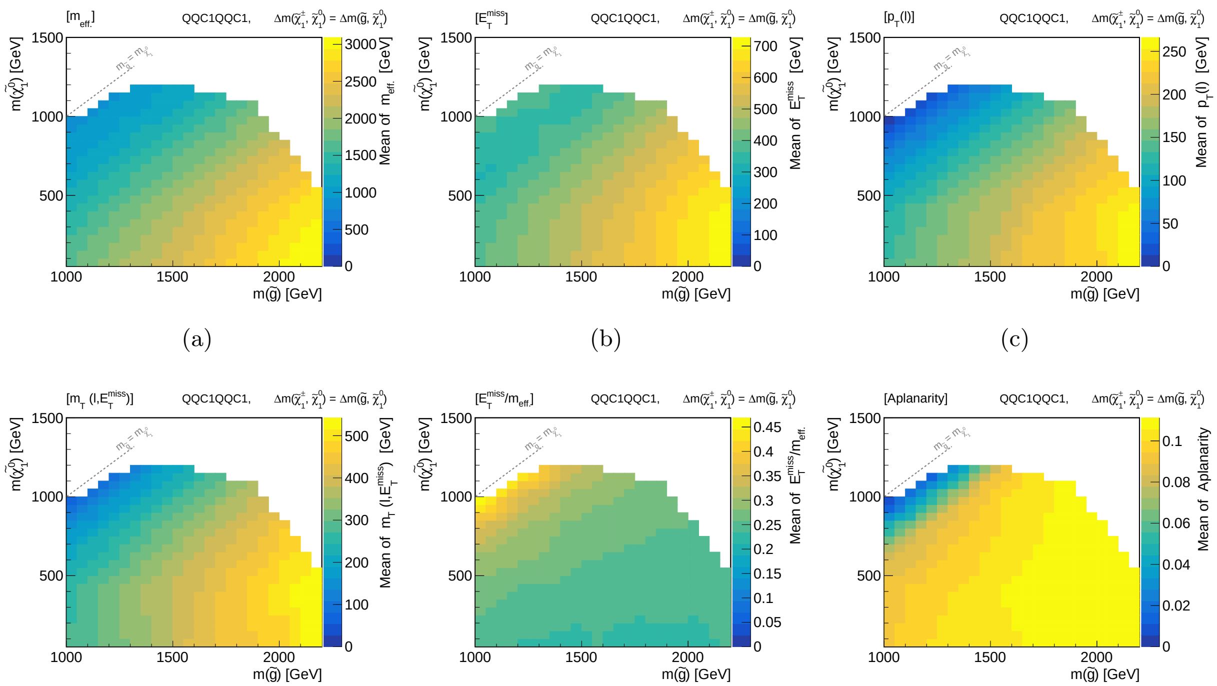

(a) (b) (c)

(d) (e) (f)

Figure B.1.1: Mean of (a) m_{eff} (b) $E_{\mathrm{T}}^{\mathrm{miss}}$ (c) $p_{\mathrm{T}}(\ell)$ (d) m_{T} (e) $E_{\mathrm{T}}^{\mathrm{miss}}/m_{\mathrm{eff}}$ (f) aplanarity, for the **QQC1QQC1** `x=1/2` grid, after the pre-selection.

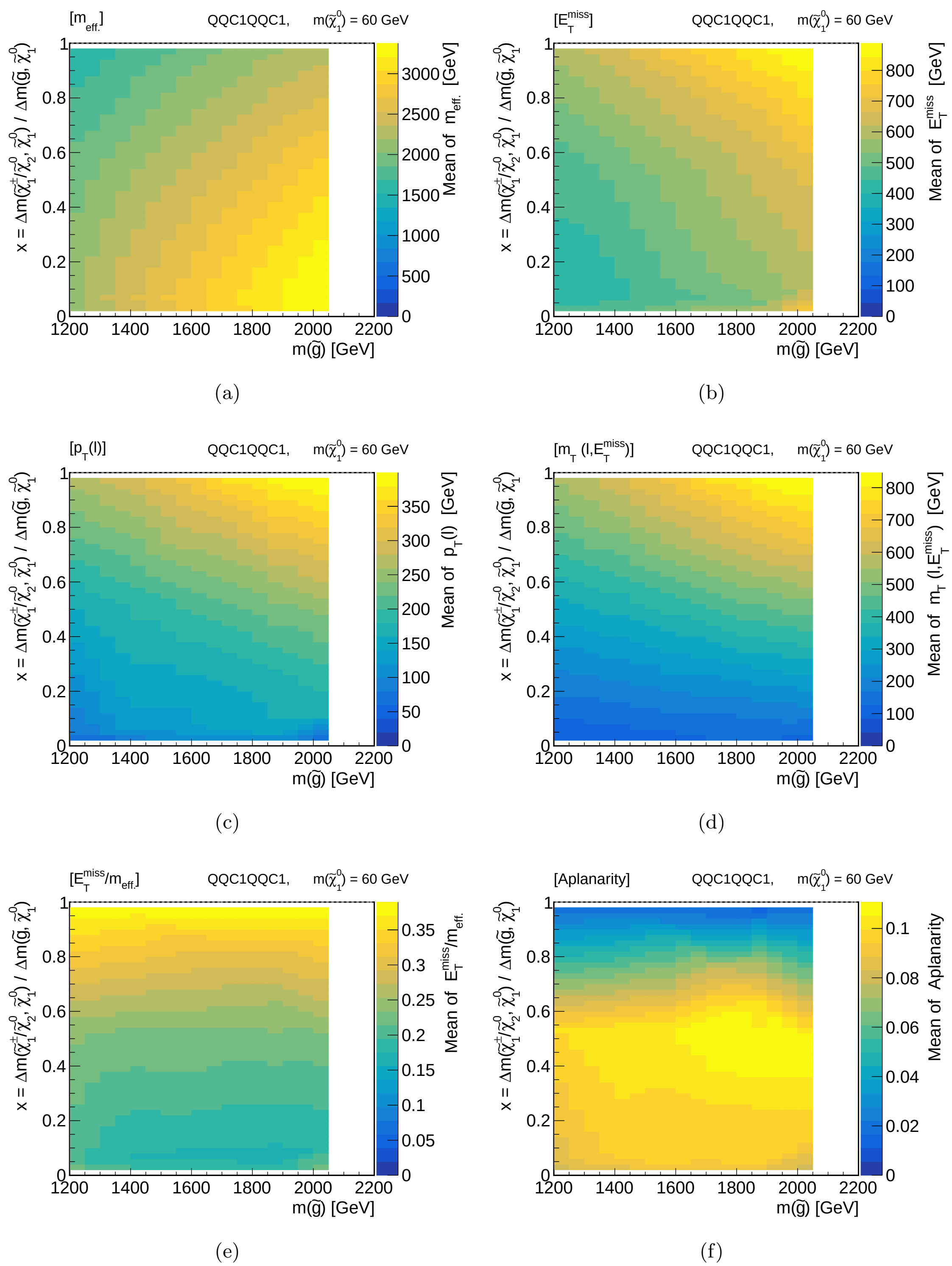

Figure B.1.2: Mean of (a) m_{eff} (b) $E_{\mathrm{T}}^{\mathrm{miss}}$ (c) $p_{\mathrm{T}}(\ell)$ (d) m_{T} (e) $E_{\mathrm{T}}^{\mathrm{miss}}/m_{\mathrm{eff}}$ (f) aplanarity, for the **QQC1QQC1** `LSP60` grid, after the pre-selection.

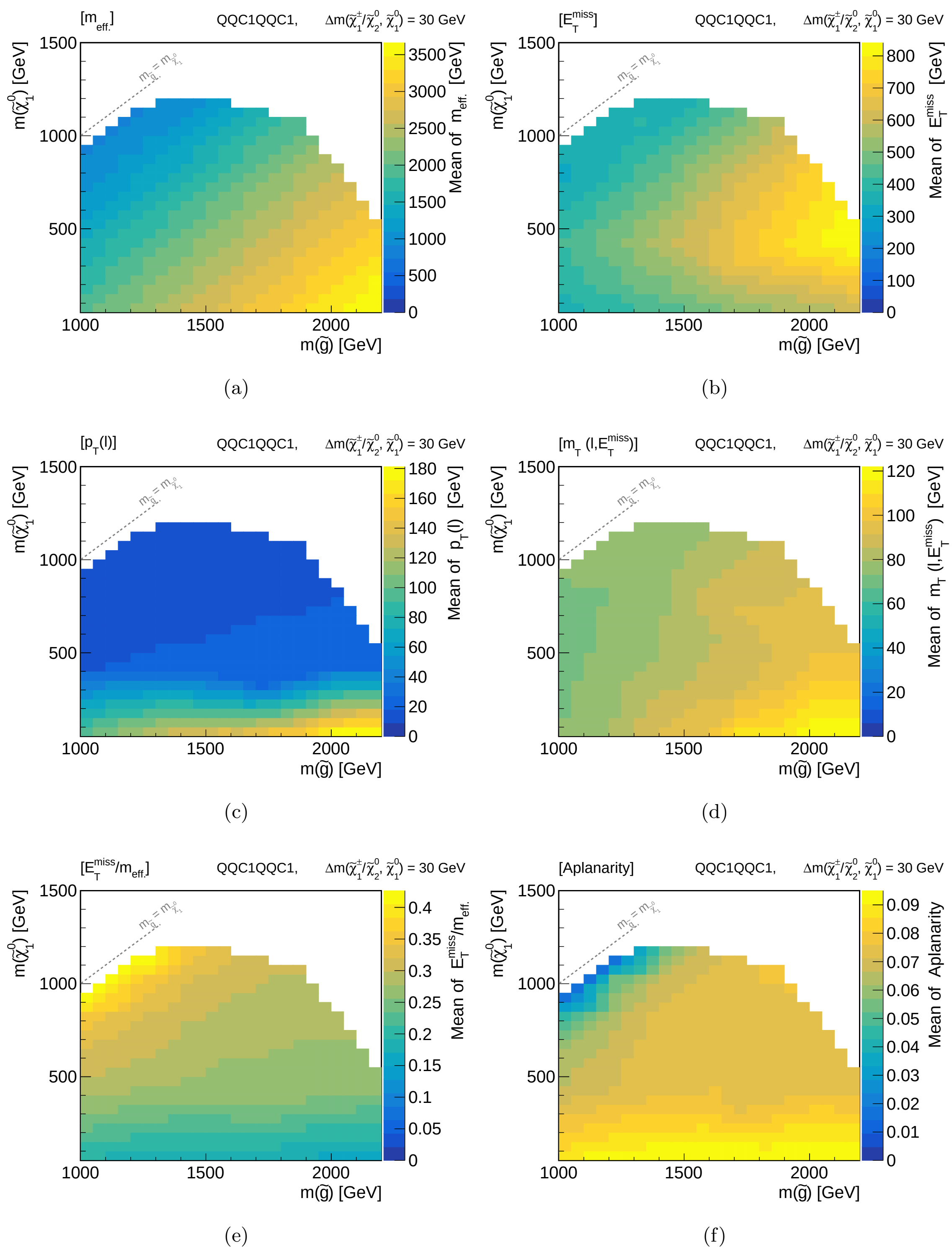

Figure B.1.3: Mean of (a) m_{eff} (b) $E_{\text{T}}^{\text{miss}}$ (c) $p_{\text{T}}(\ell)$ (d) m_{T} (e) $E_{\text{T}}^{\text{miss}}/m_{\text{eff}}$ (f) aplanarity, for the **QQC1QQC1** `DM30` grid, after the pre-selection.

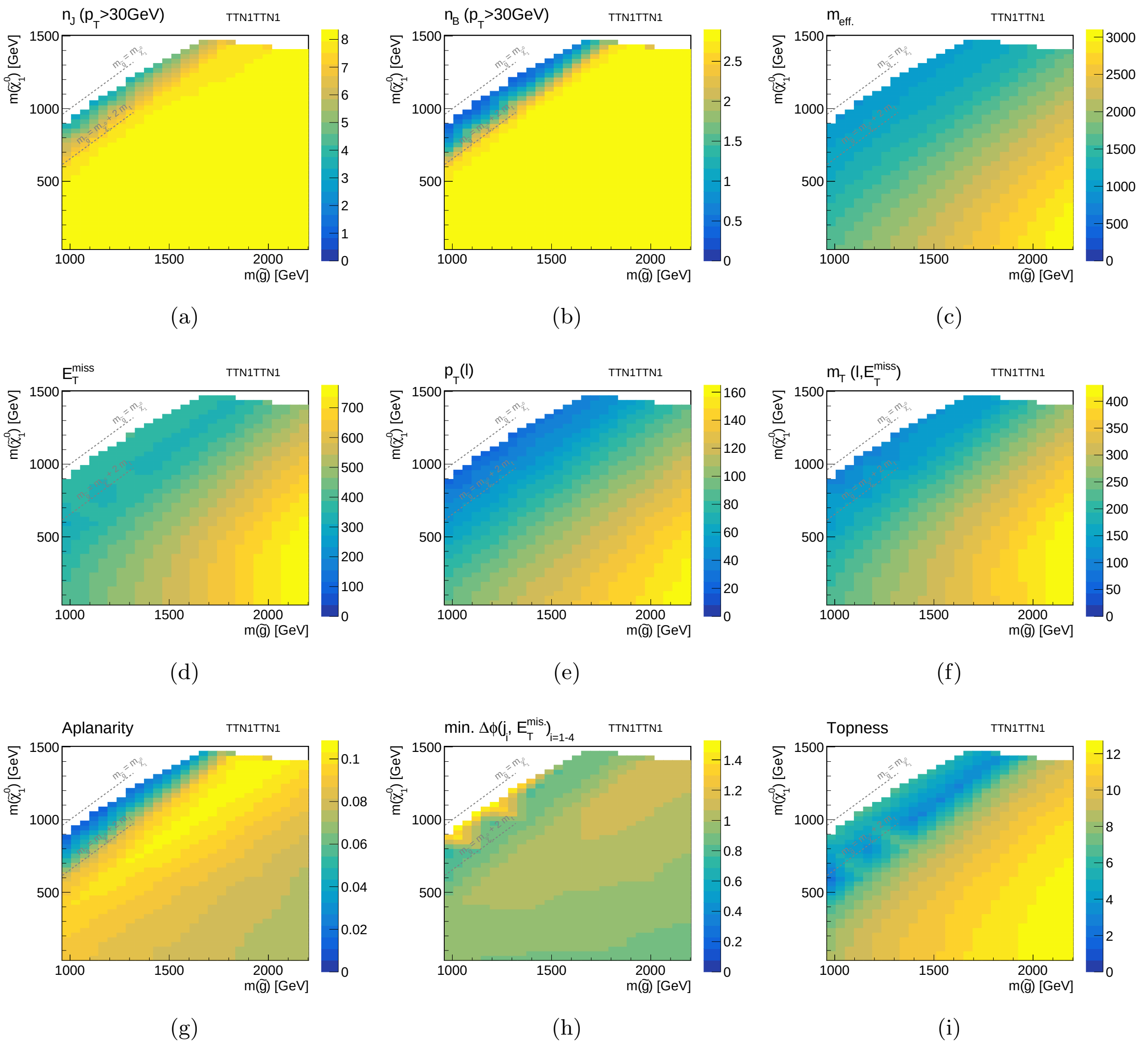

Figure B.1.4: Mean of (a) jet-multiplicity ($p_T > 30$ GeV) (b) bjet-multiplicity ($p_T > 30$ GeV) (c) $m_{\rm eff}$ (d) $E_{\rm T}^{\rm miss}$ (e) $p_{\rm T}(\ell)$ (f) $m_{\rm T}$ (g) aplanarity (h) $\min_{i=1-4} \Delta\phi(j_i, E_{\rm T}^{\rm miss})$ (i) topness, for the **TTN1TTN1** `Direct` grid, after the pre-selection.

B.2 The N-1 Plots in Optimized Signal Regions

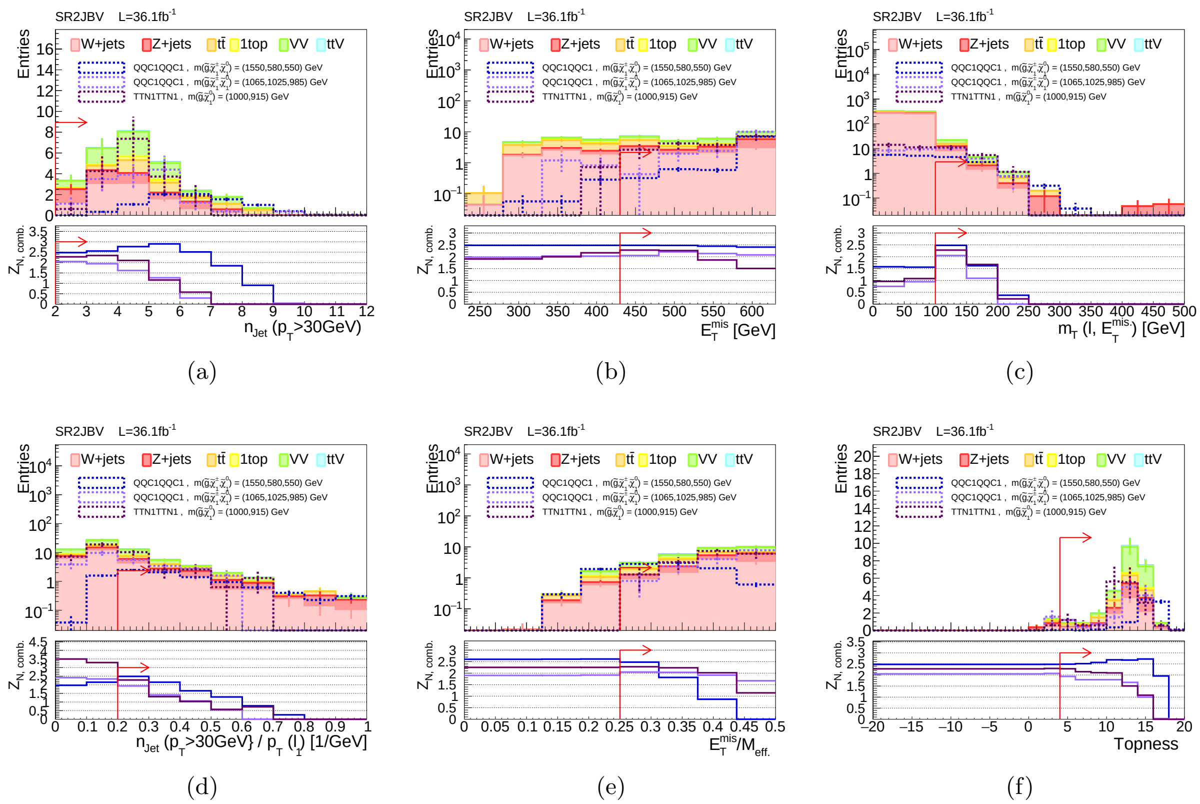

Figure B.2.1: N-1 plots for the b-vetoed (BV) slices of the optimized **2J** signal regions. Bottom row presents the combined significace over the m_{eff} bins defined in Eq. 5.4.

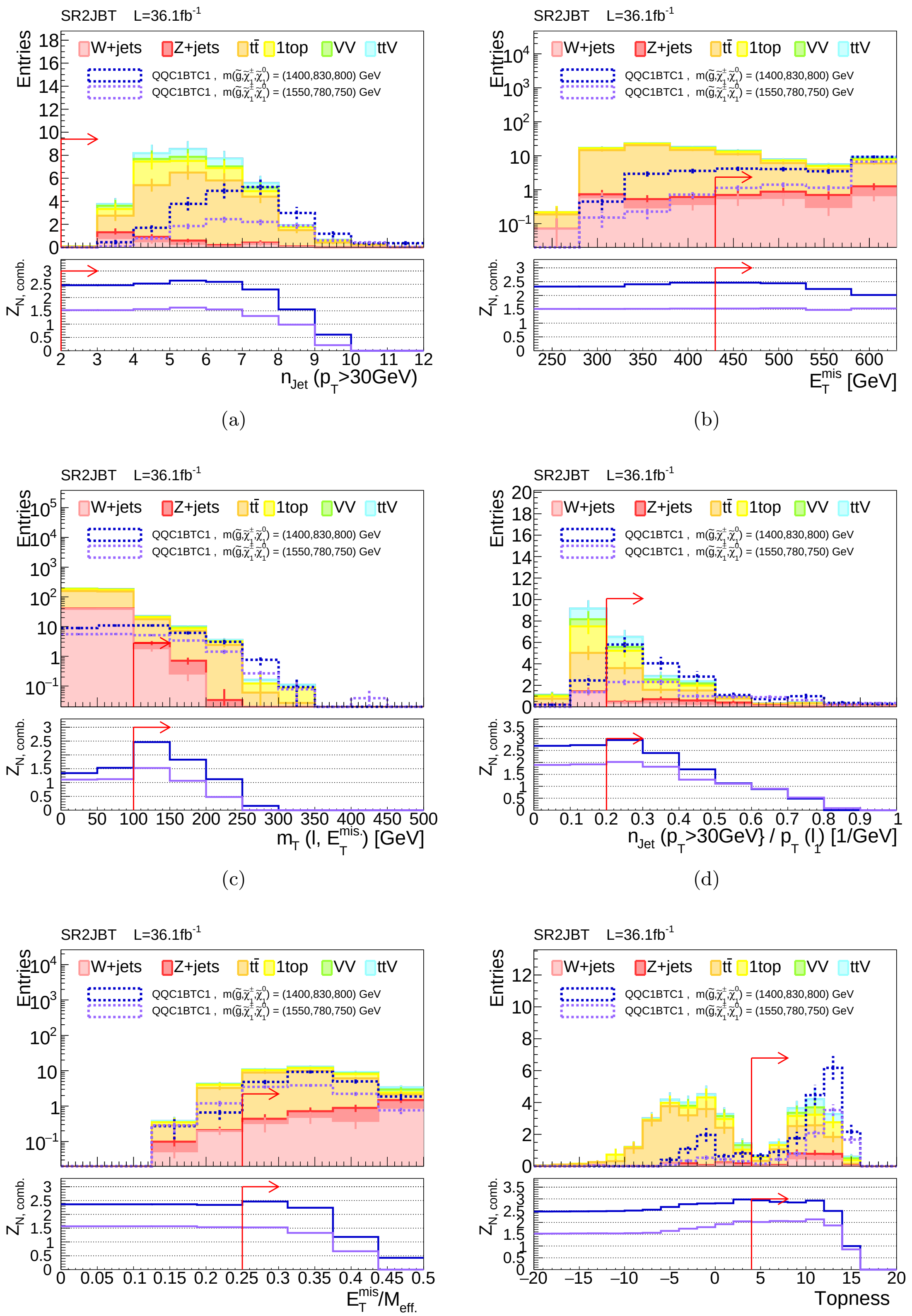

(a) (b) (c) (d) (e) (f)

Figure B.2.2: N-1 plots for the b-tagged (BT) slices of the optimized **2J** signal regions. Bottom row presents the combined significace over the m_{eff} bins defined in Eq. 5.4.

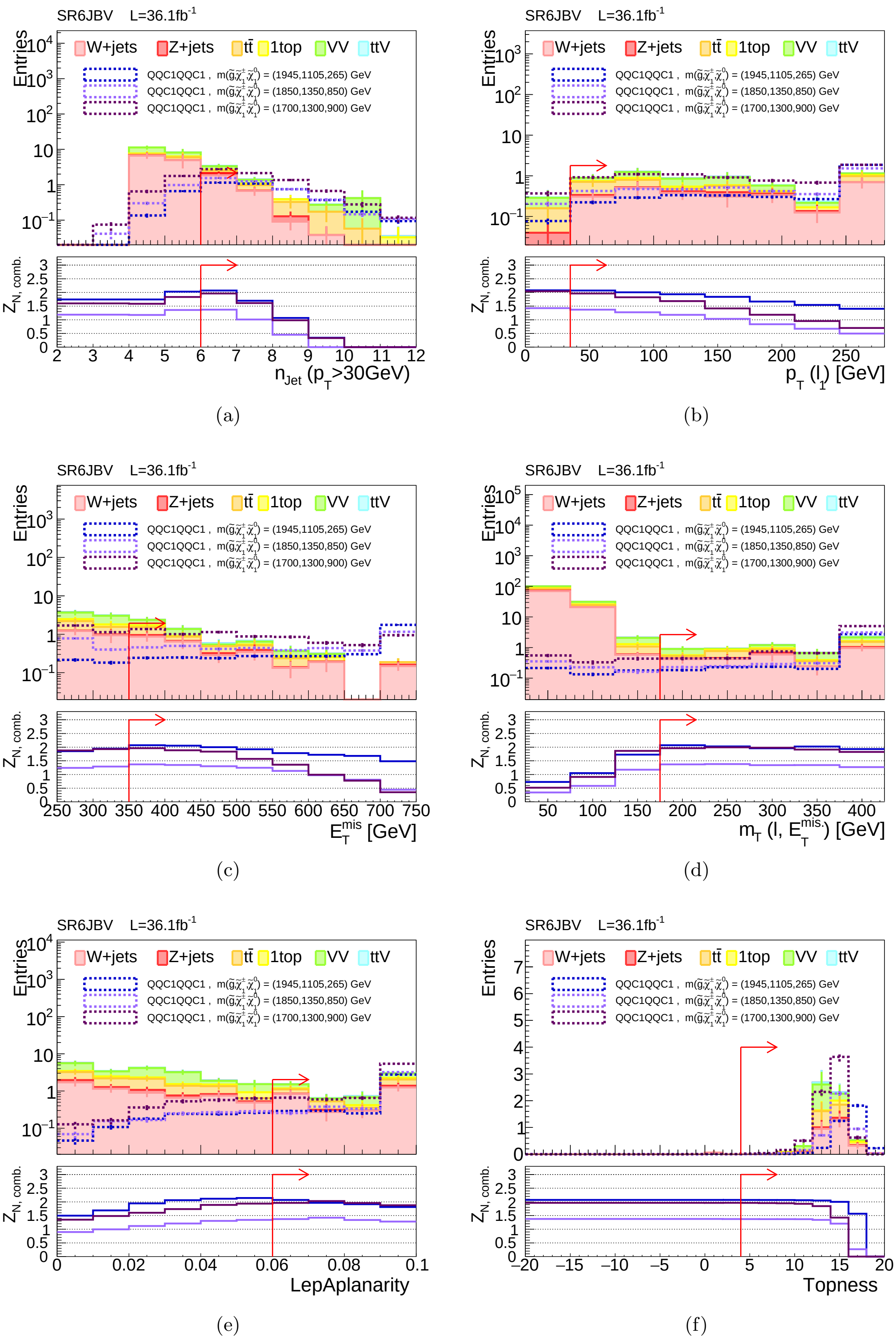

Figure B.2.3: N-1 plots for the b-vetoed (BV) slices of the optimized **6J** signal regions. Bottom row presents the combined significace over the m_{eff} bins defined in Eq. 5.4.

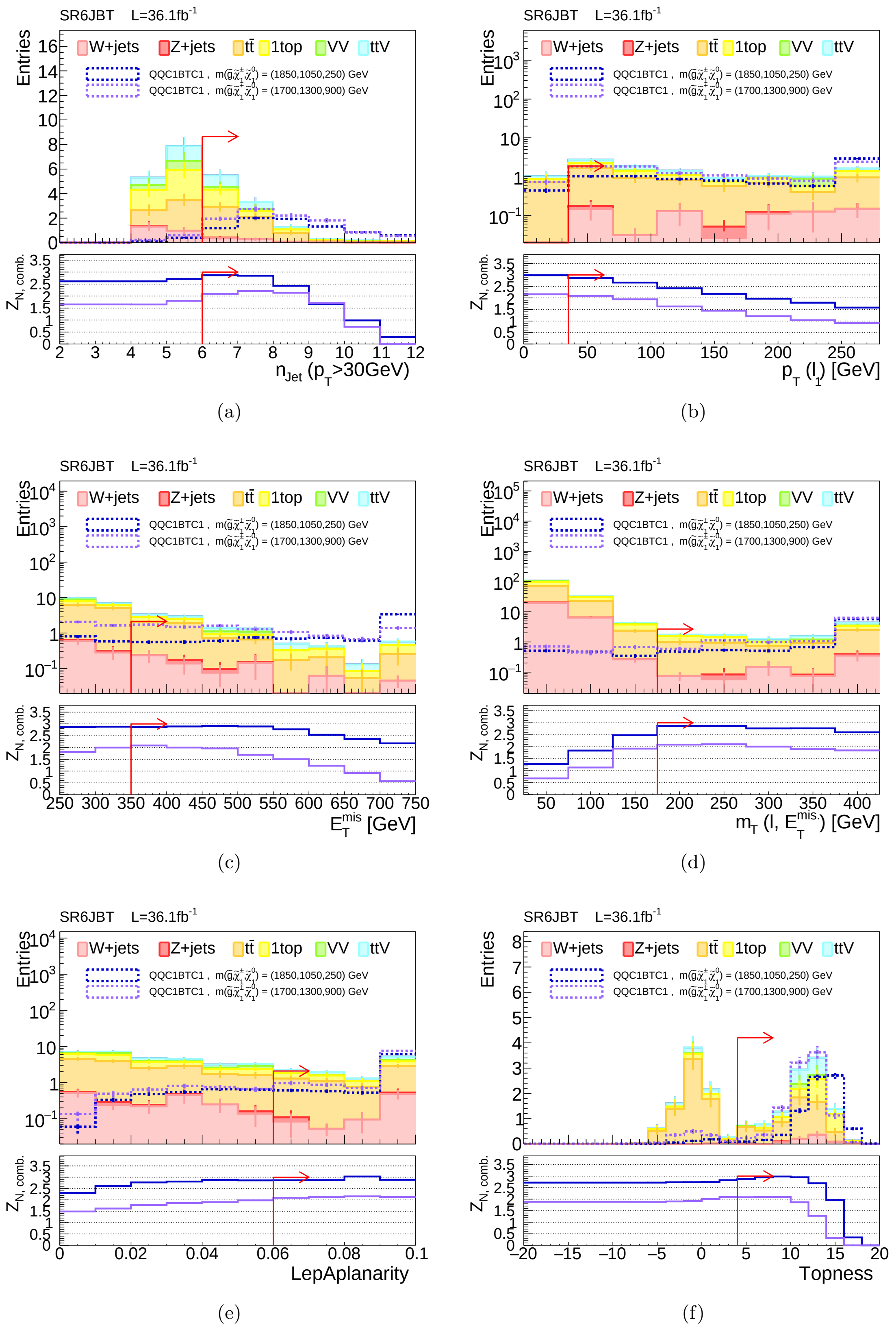

(a) (b) (c) (d) (e) (f)

Figure B.2.4: N-1 plots for the b-tagged (BT) slices of the optimized **6J** signal regions. Bottom row presents the combined significace over the m_{eff} bins defined in Eq. 5.4.

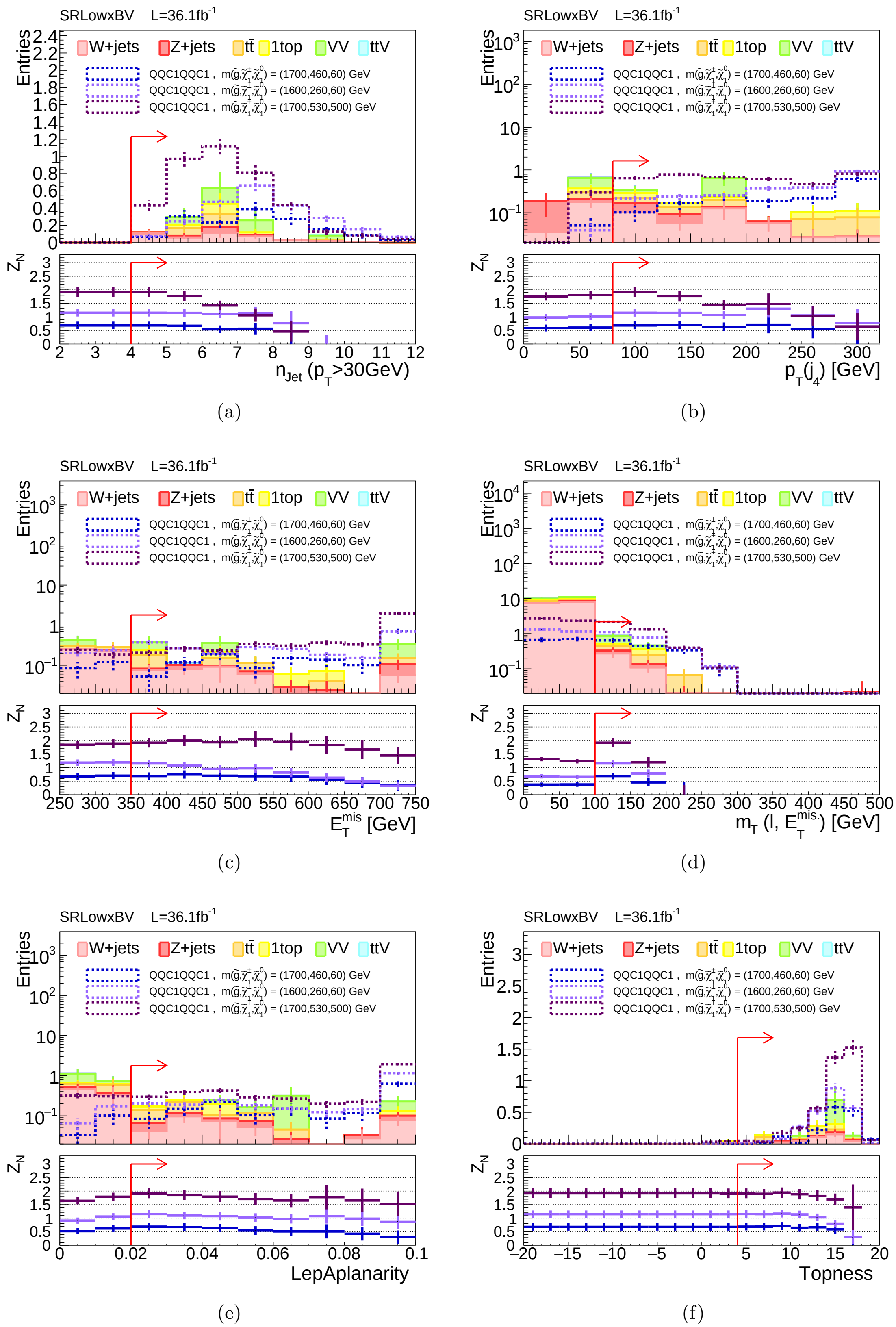

Figure B.2.5: N-1 plots for the b-vetoed (BV) slices of the optimized **Low-x** signal region. Bottom row presents the single m_{eff} bin significace defined in Eq. 5.4.

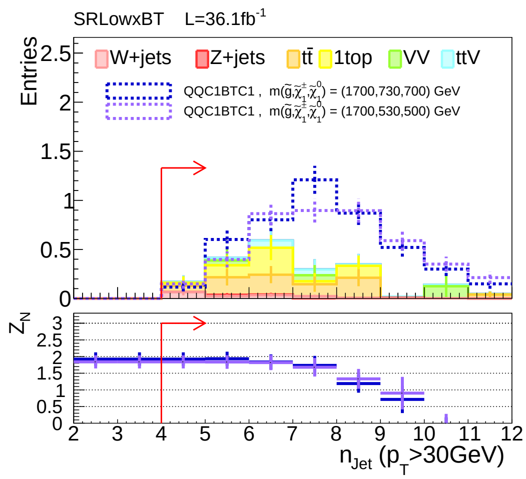

(a)

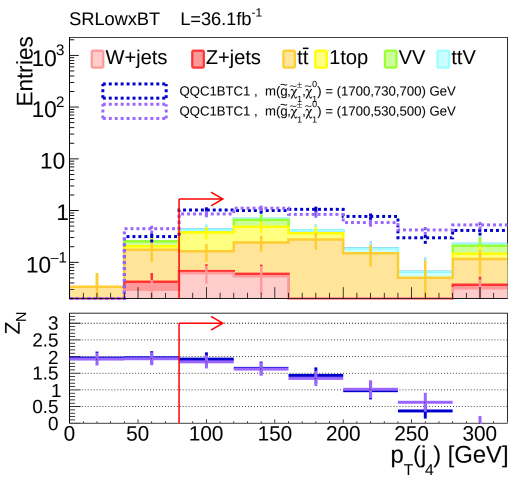

(b)

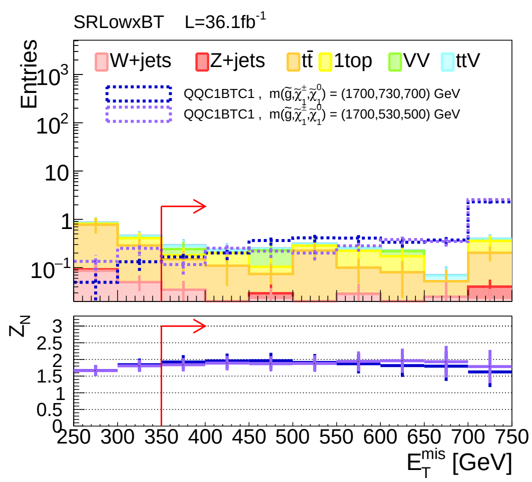

(c)

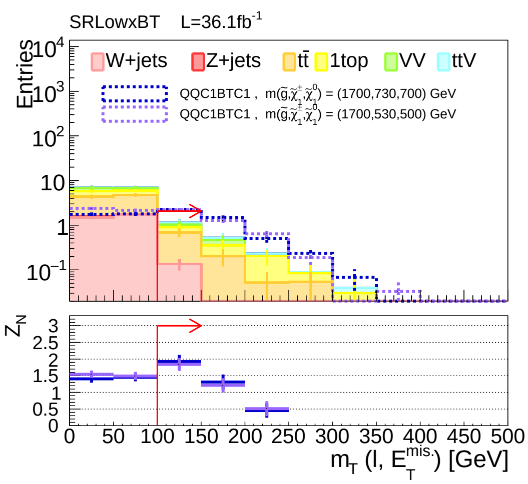

(d)

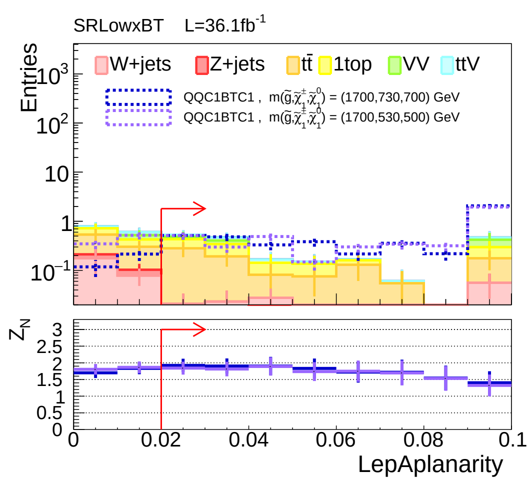

(e)

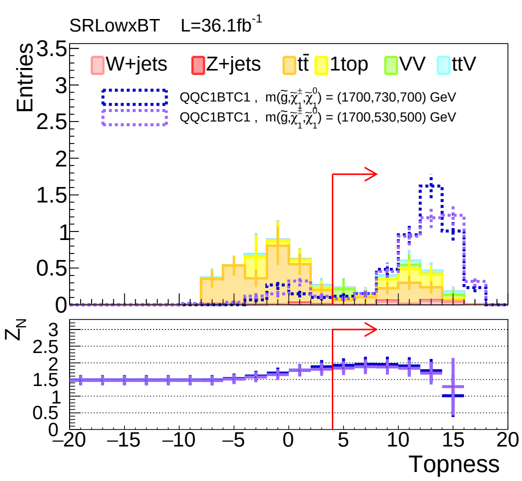

(f)

Figure B.2.6: N-1 plots for the b-tagged (BT) slices of the optimized **Low-x** signal region. Bottom row presents the single m_{eff} bin significace defined in Eq. 5.4.

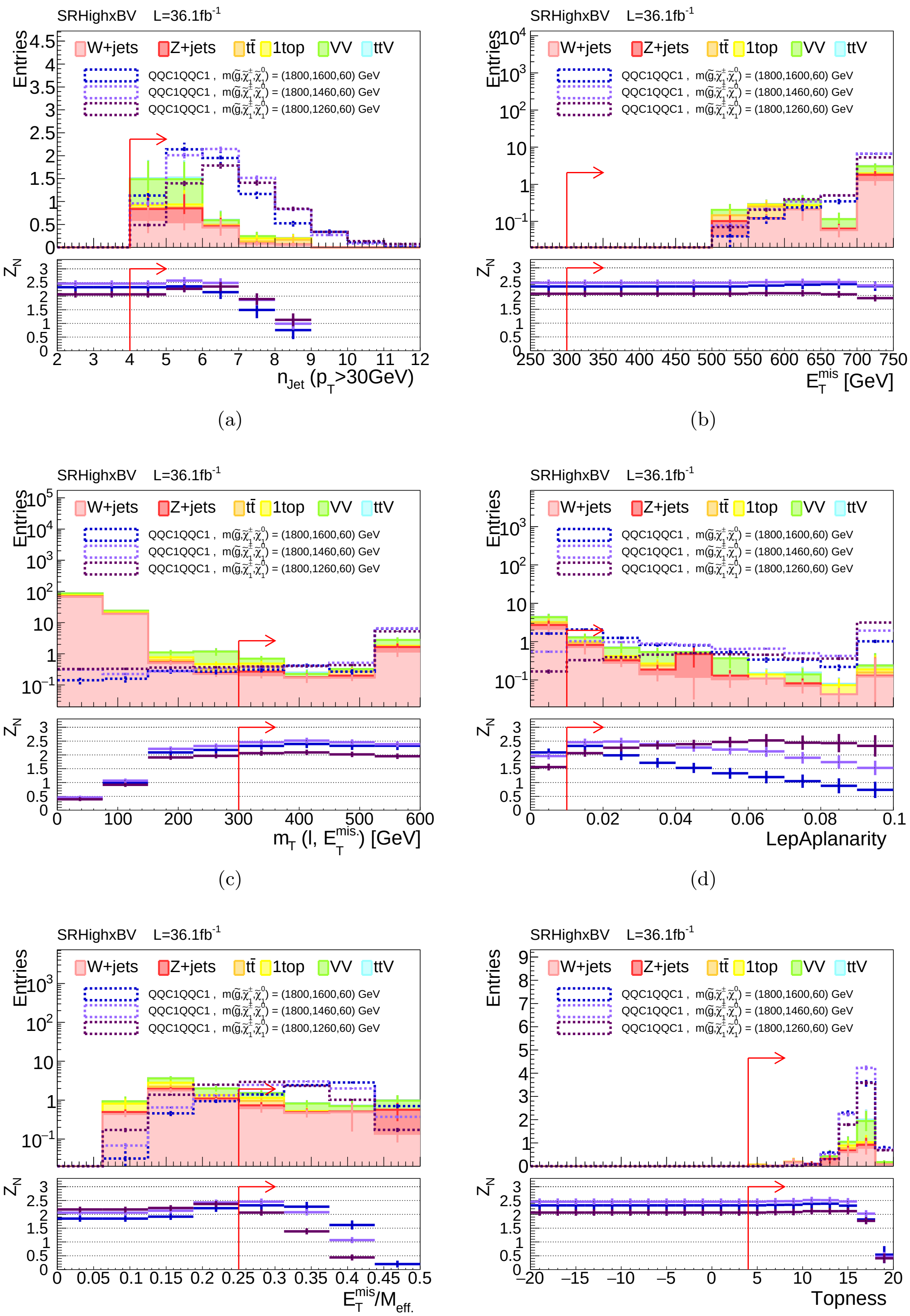

Figure B.2.7: N-1 plots for the b-vetoed (BV) slices of the optimized **High-x** signal region. Bottom row presents the single m_{eff} bin significace defined in Eq. 5.4.

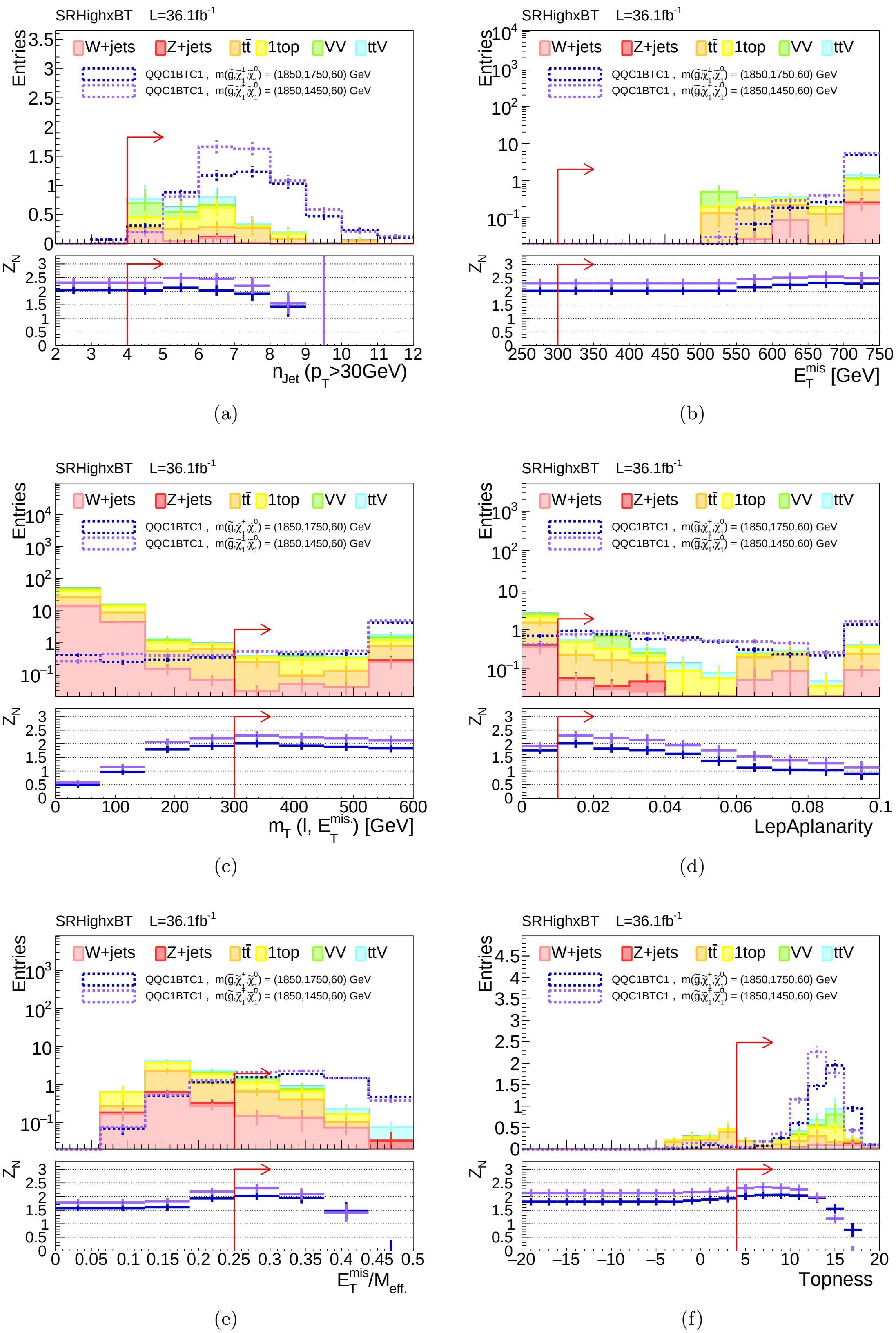

(a) (b)

(c) (d)

(e) (f)

Figure B.2.8: N-1 plots for the b-tagged (BT) slices of the optimized **High-x** signal region. Bottom row presents the single m_{eff} bin significace defined in Eq. 5.4.

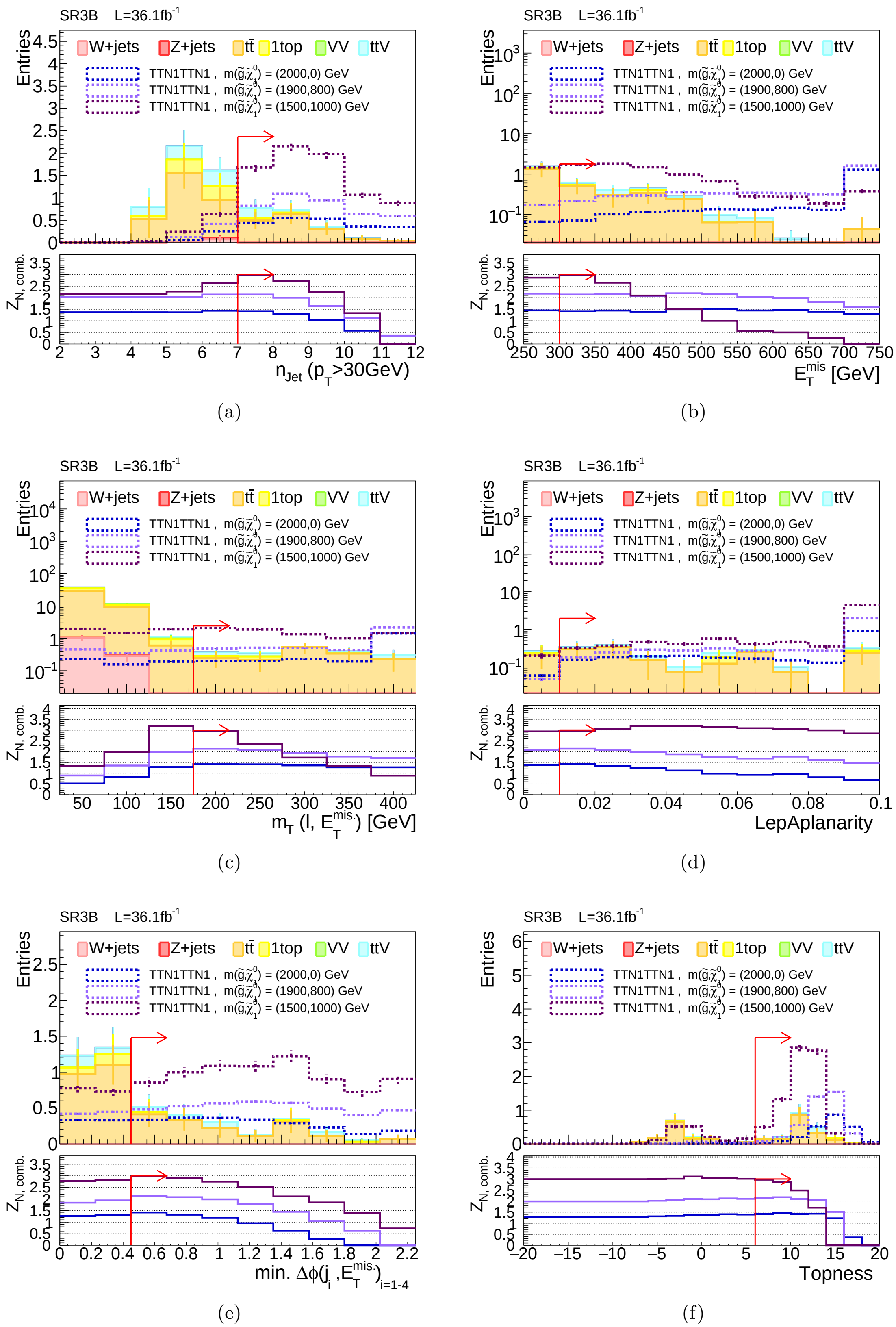

Figure B.2.9: N-1 plots for the optimized **3B** signal regions. Bottom row presents the combined significace over the m_{eff} bins defined in Eq. 5.4.

C Auxiliary Materials for Background Estimation

C.1 Data vs Reweighted MC in Preselection

Following plots are the data/MC in the pre-selection regions that are shown in Sec. 6.2.1, with the MC events of $W+\text{jets}$ and $t\bar{t}$ are reweighted event-by-event by:

$$\begin{cases} w &= 1 - 0.1 \times (n_{\mathrm{J}} - 2) & (W+\text{jets}) \\ w &= 1.05 \times [1 - 0.061\ \times p_T(t\bar{t})] & (t\bar{t}, @1\text{L},2\text{L}) \\ w &= 1.4 \times [1 - 0.061\ \times p_T(t\bar{t})] & (t\bar{t}, @3\text{B}). \end{cases}$$

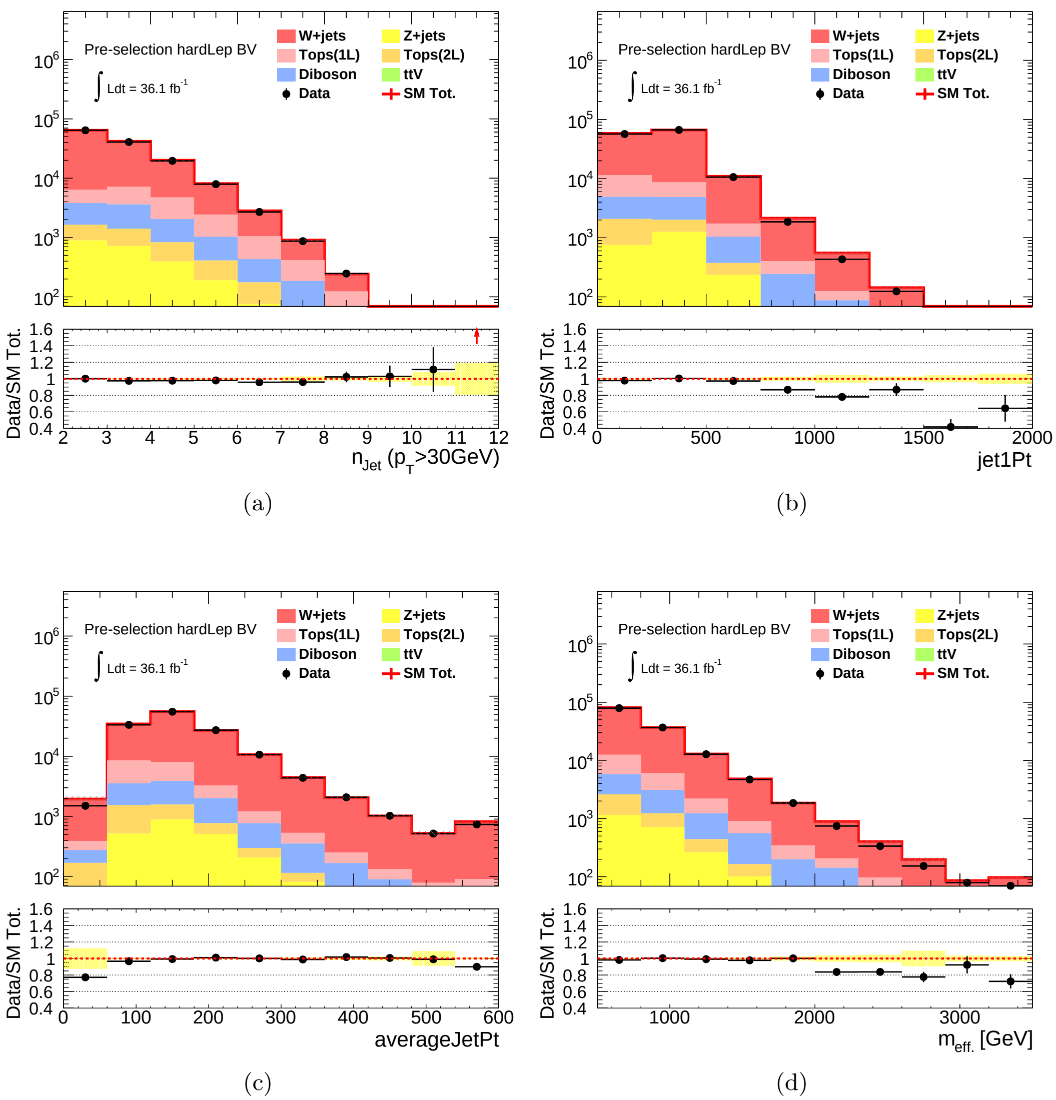

Figure C.1.1: Kinematical distribution of (a) Jet multiplicity ($p_T > 30$ GeV) (b) leading-jet pt (c) average jet pt ($p_T > 30$ GeV) (d) m_{eff} in the hard lepton b-vetoed pre-selection region, with the reweighting $w = 1 - 0.1 \times (n_{\mathrm{J}} - 2)$ being applied for $W+\text{jets}$ MC.

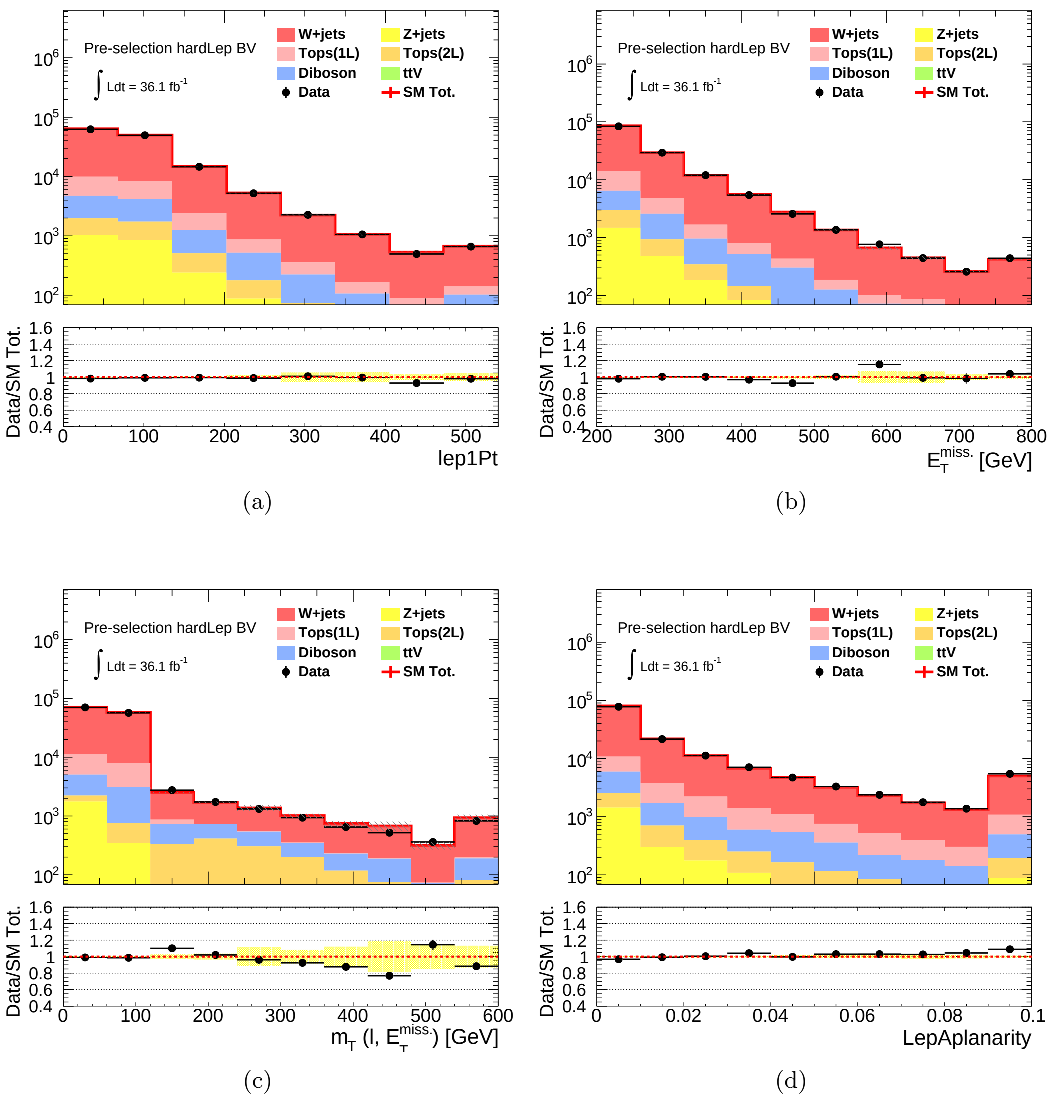

Figure C.1.2: Kinematical distribution of (a) leading-lepton pt (b) $E_{\mathrm{T}}^{\mathrm{miss}}$ (c) m_{T} (d) aplanarity in the **hard lepton b-vetoed** pre-selection region, with the reweighting $w = 1 - 0.1 \times (n_{\mathrm{J}} - 2)$ being applied for $W +$jets MC.

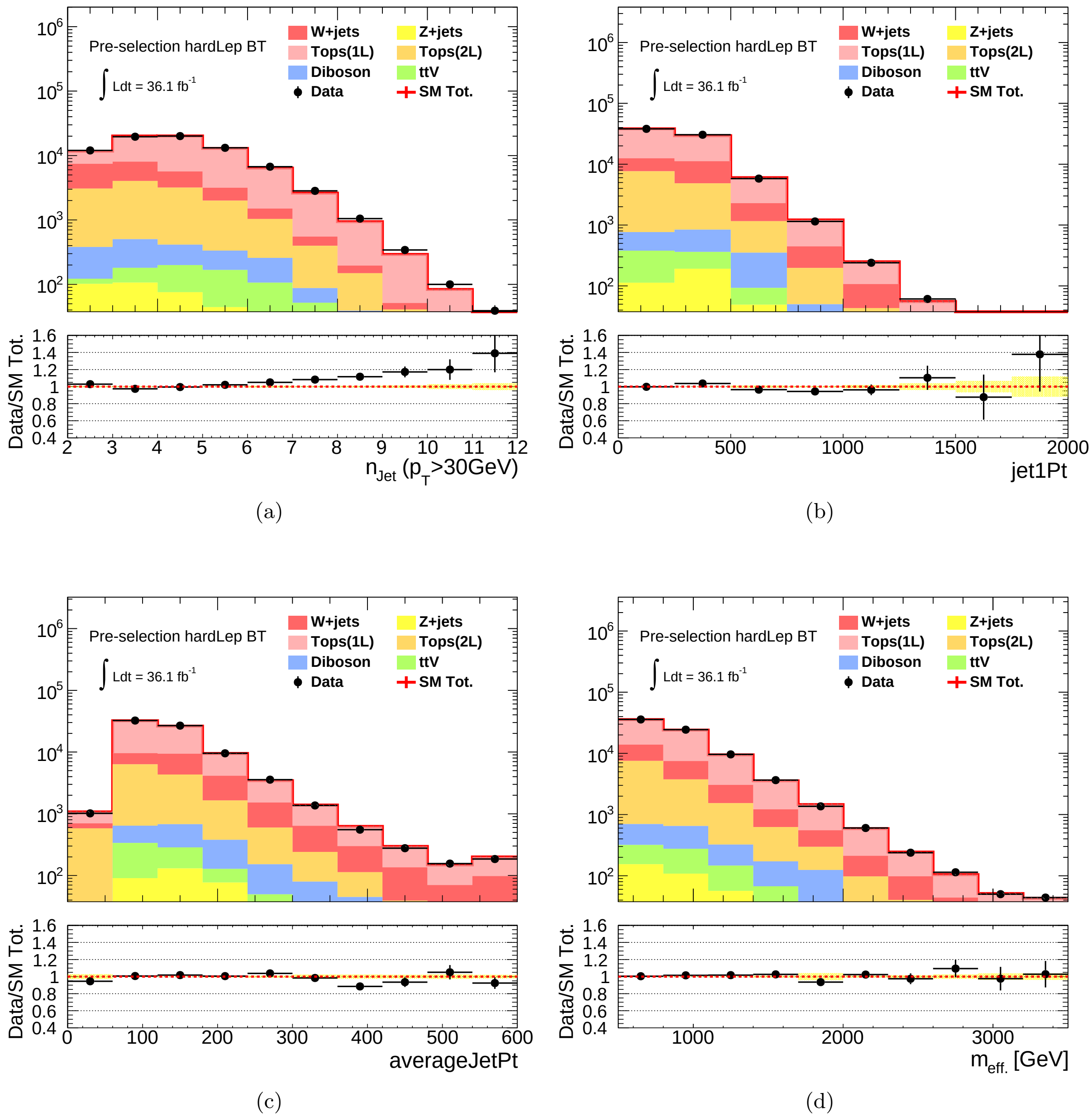

Figure C.1.3: Kinematical distribution of (a) Jet multiplicity ($p_T > 30$ GeV) (b) leading-jet pt (c) average jet pt ($p_T > 30$ GeV) (d) $m_{\rm eff}$ in the hard lepton b-tagged pre-selection region, with the reweighting $w = 1.05 \times [1 - 0.061\ \times p_T(t\bar{t})]$ being applied for $t\bar{t}$ MC.

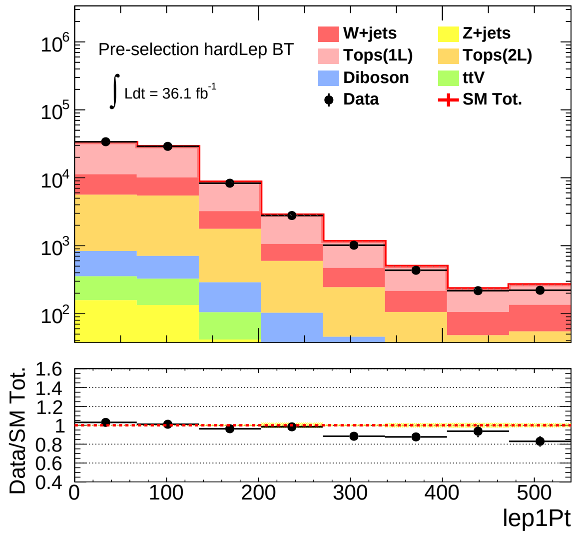

(a)

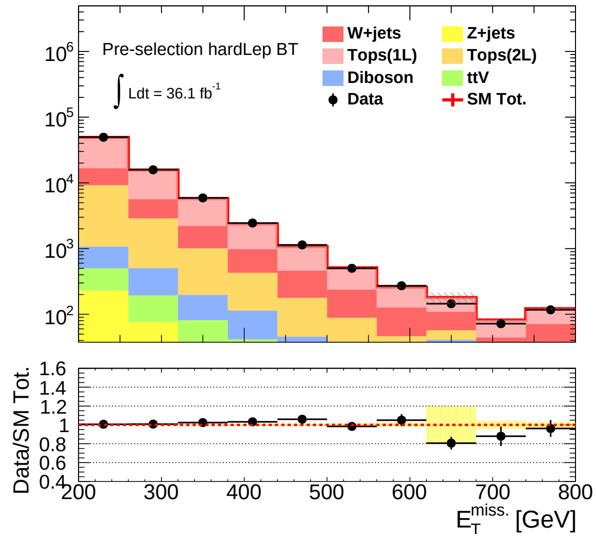

(b)

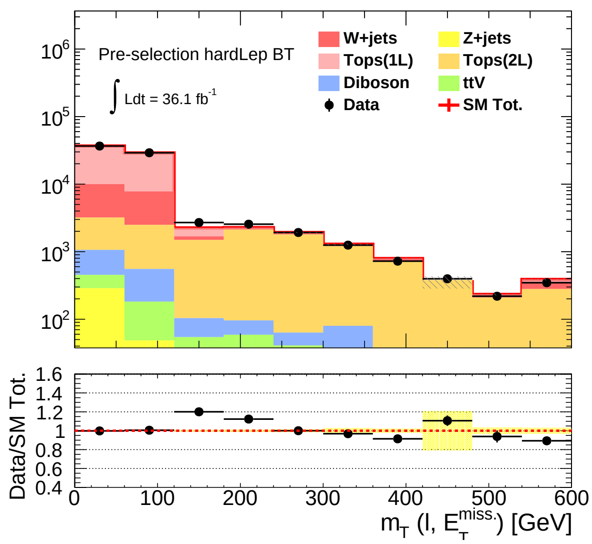

(c)

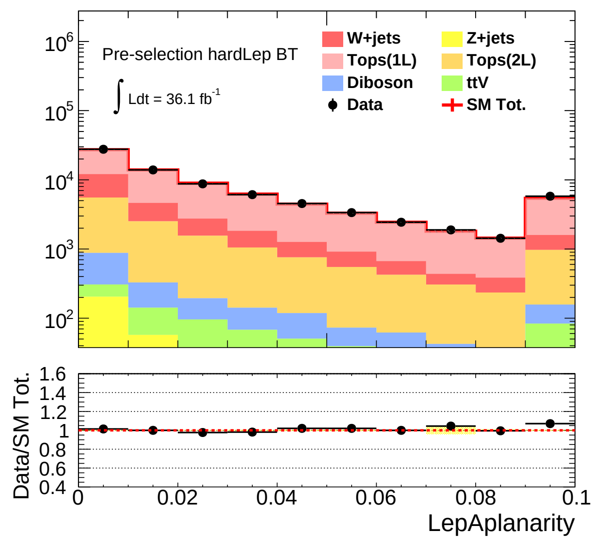

(d)

Figure C.1.4: Kinematical distribution of (a) leading-lepton pt (b) $E_{\mathrm{T}}^{\mathrm{miss}}$ (c) m_{T} (d) aplanarity in the **hard lepton b-vetoed** pre-selection region, with the reweighting $w = 1.05 \times [1 - 0.061 \times p_T(t\bar{t})]$ being applied for $t\bar{t}$ MC.

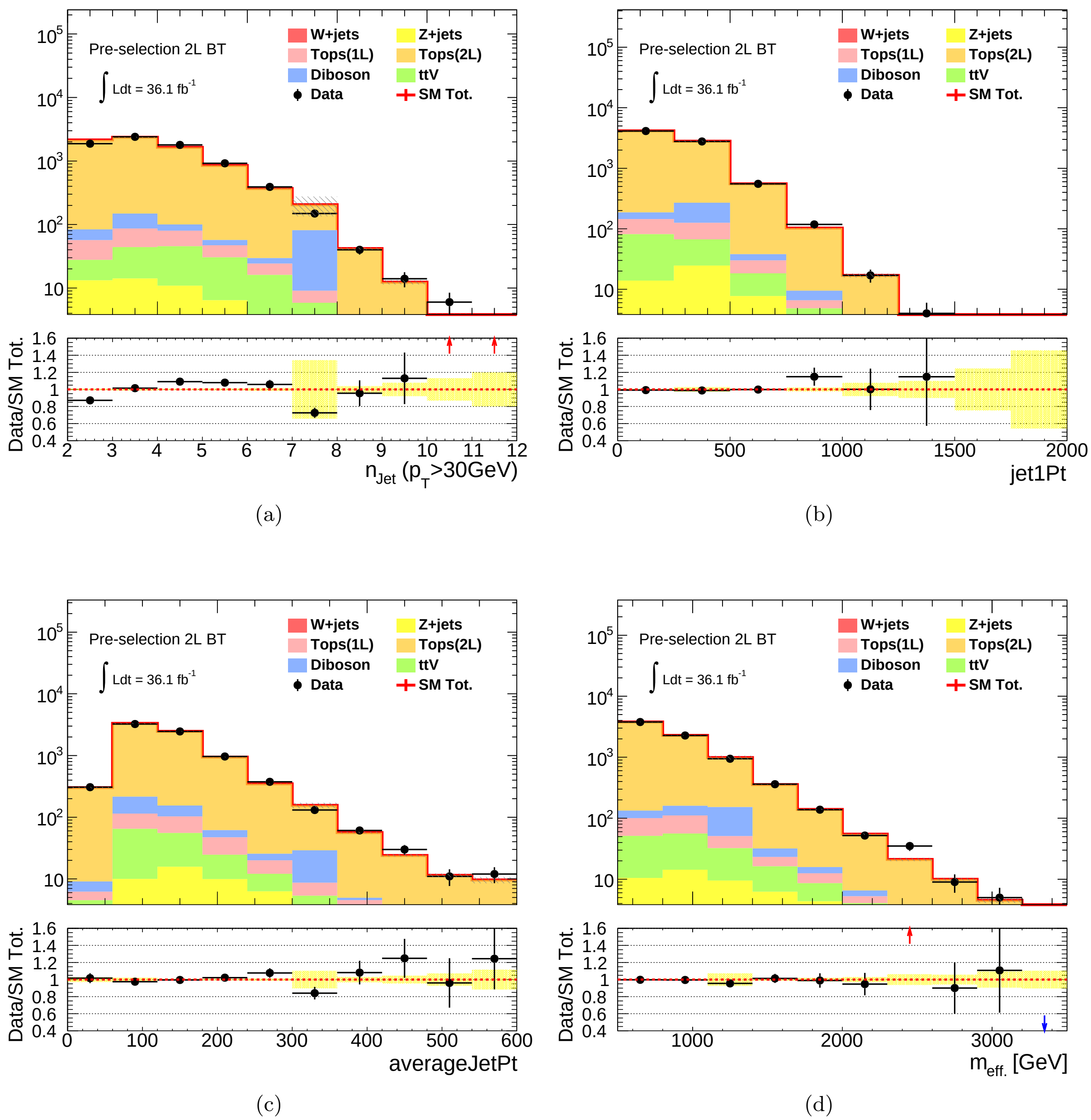

(a) (b) (c) (d)

Figure C.1.5: Kinematical distribution of (a) Jet multiplicity ($p_T > 30$ GeV) (b) leading-jet pt (c) average jet pt ($p_T > 30$ GeV) (d) m_{eff} in the hard lepton b-tagged pre-selection region, with the reweighting: $w = 1.05 \times [1 - 0.061 \times p_T(t\bar{t})]$ being applied for $t\bar{t}$ MC.

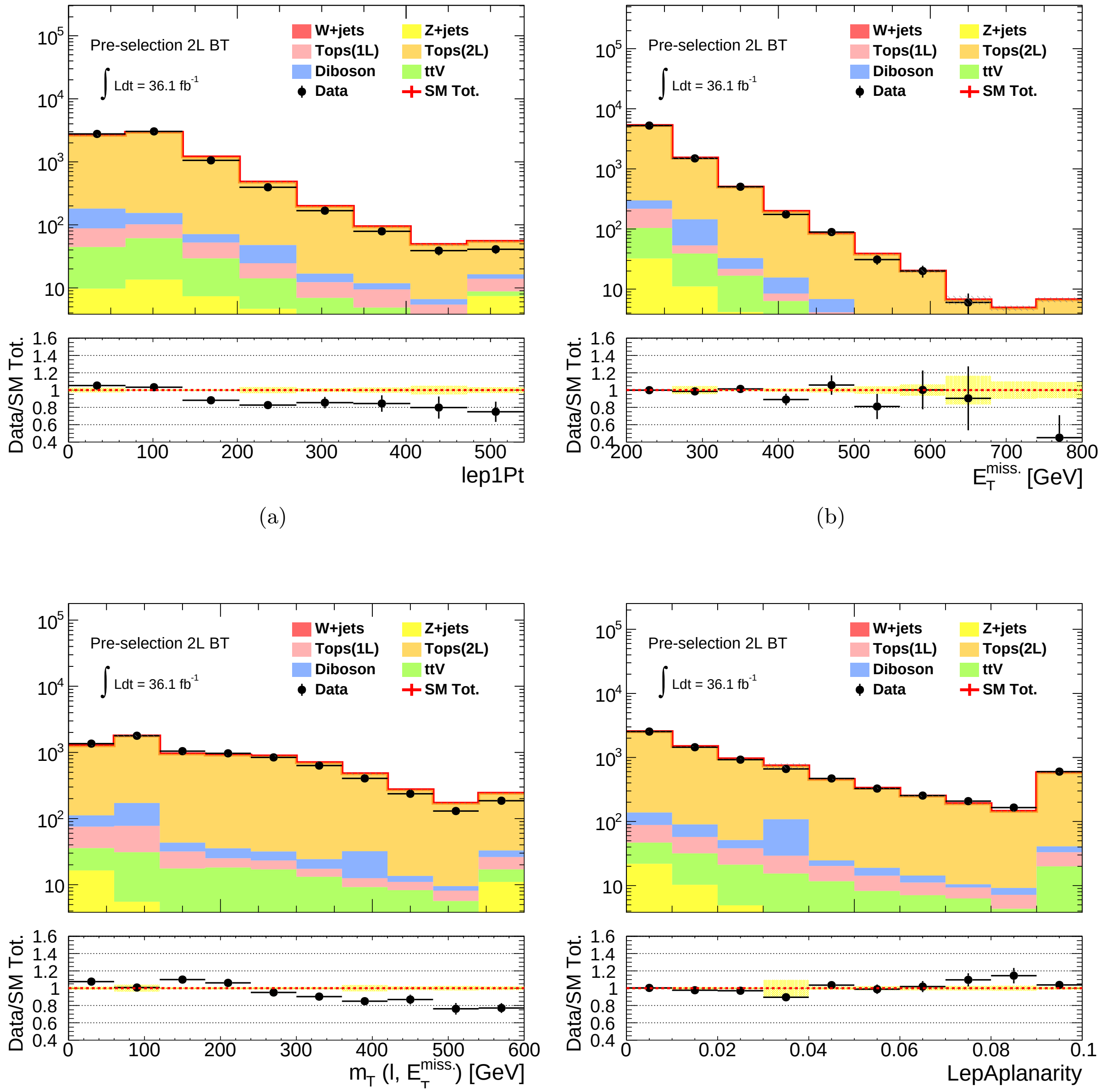

(a) (b) (c) (d)

Figure C.1.6: Kinematical distribution of (a) leading-lepton pt (b) $E_{\mathrm{T}}^{\mathrm{miss}}$ (c) m_{T} (d) aplanarity in the hard lepton b-tagged pre-selection region, with the reweighting: $w = 1.05 \times [1 - 0.061 \ \times p_T(t\bar{t})]$ being applied for $t\bar{t}$ MC.

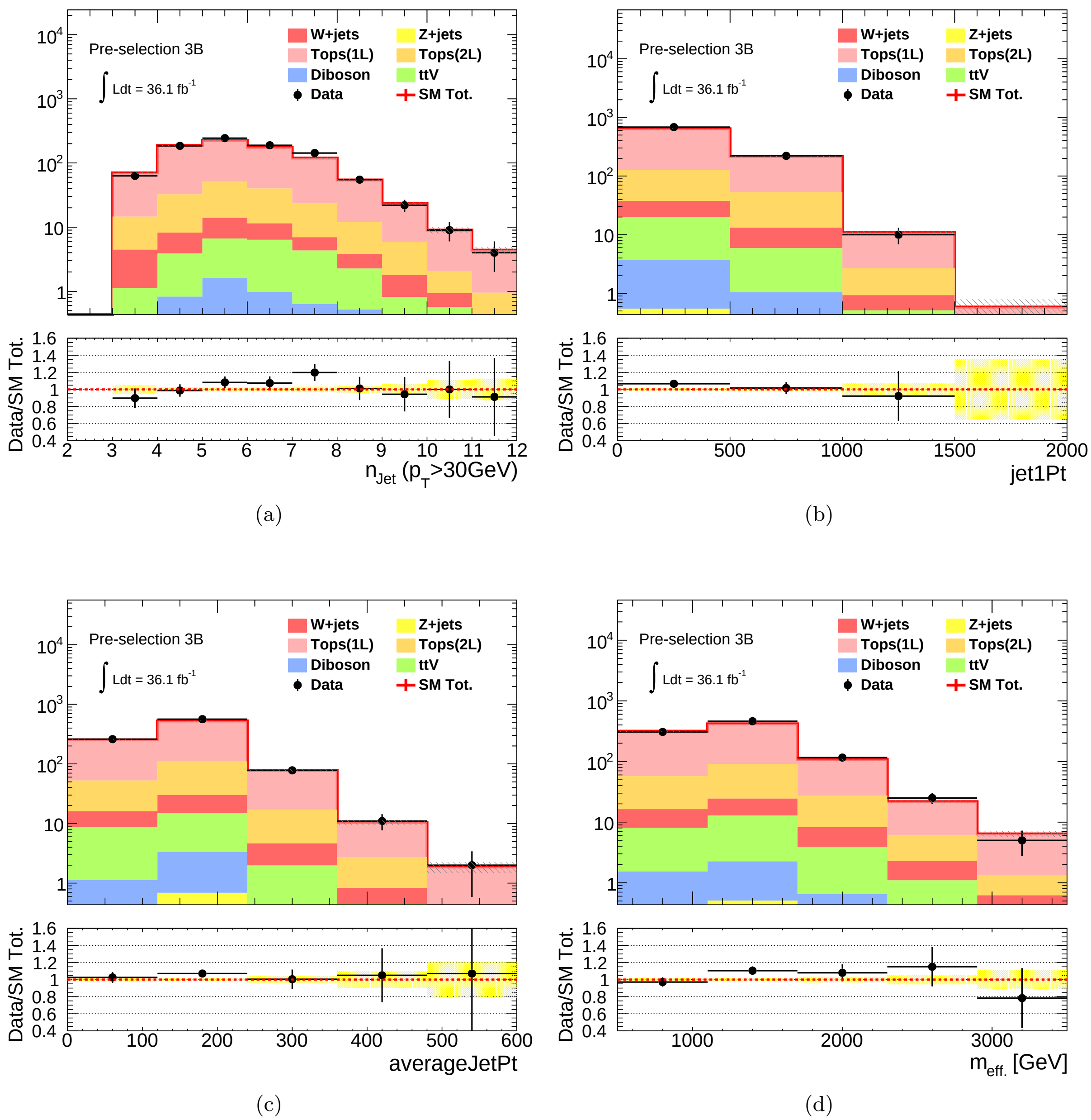

Figure C.1.7: Kinematical distribution of (a) Jet multiplicity ($p_T > 30$ GeV) (b) leading-jet pt (c) average jet pt ($p_T > 30$ GeV) (d) m_{eff} in the **3b-tagged pre-selection region**, with the reweighting $w = 1.4 \times [1 - 0.061 \times p_T(t\bar{t})]$ being applied for $t\bar{t}$ MC.

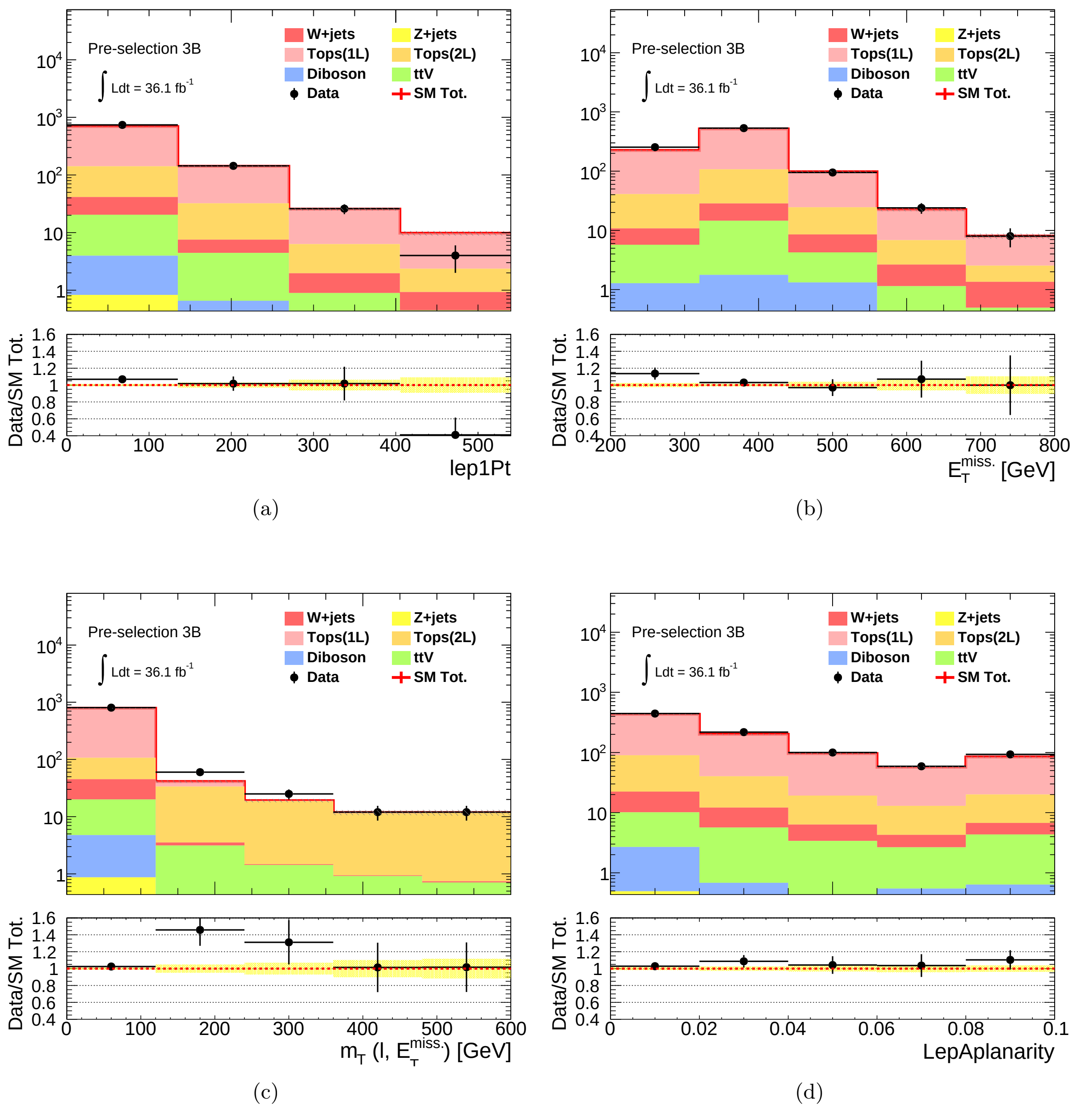

Figure C.1.8: Kinematical distribution of (a) leading-lepton pt (b) $E_{\mathrm{T}}^{\mathrm{miss}}$ (c) m_{T} (d) aplanarity in the **3b-tagged pre-selection region**, with the reweighting: $w = 1.4 \times [1 - 0.061\ \times p_T(t\bar{t})]$ being applied for $t\bar{t}$ MC.

C.2 MC Closure Test for the Object Replacement Method

MC Closure Test with the Soft Lepton Selection Figure C.2.1 ∼ C.2.3 show the closure test estimating a region with a soft lepton ($p_{\mathrm{T}} \in [6, 35]$ GeV).

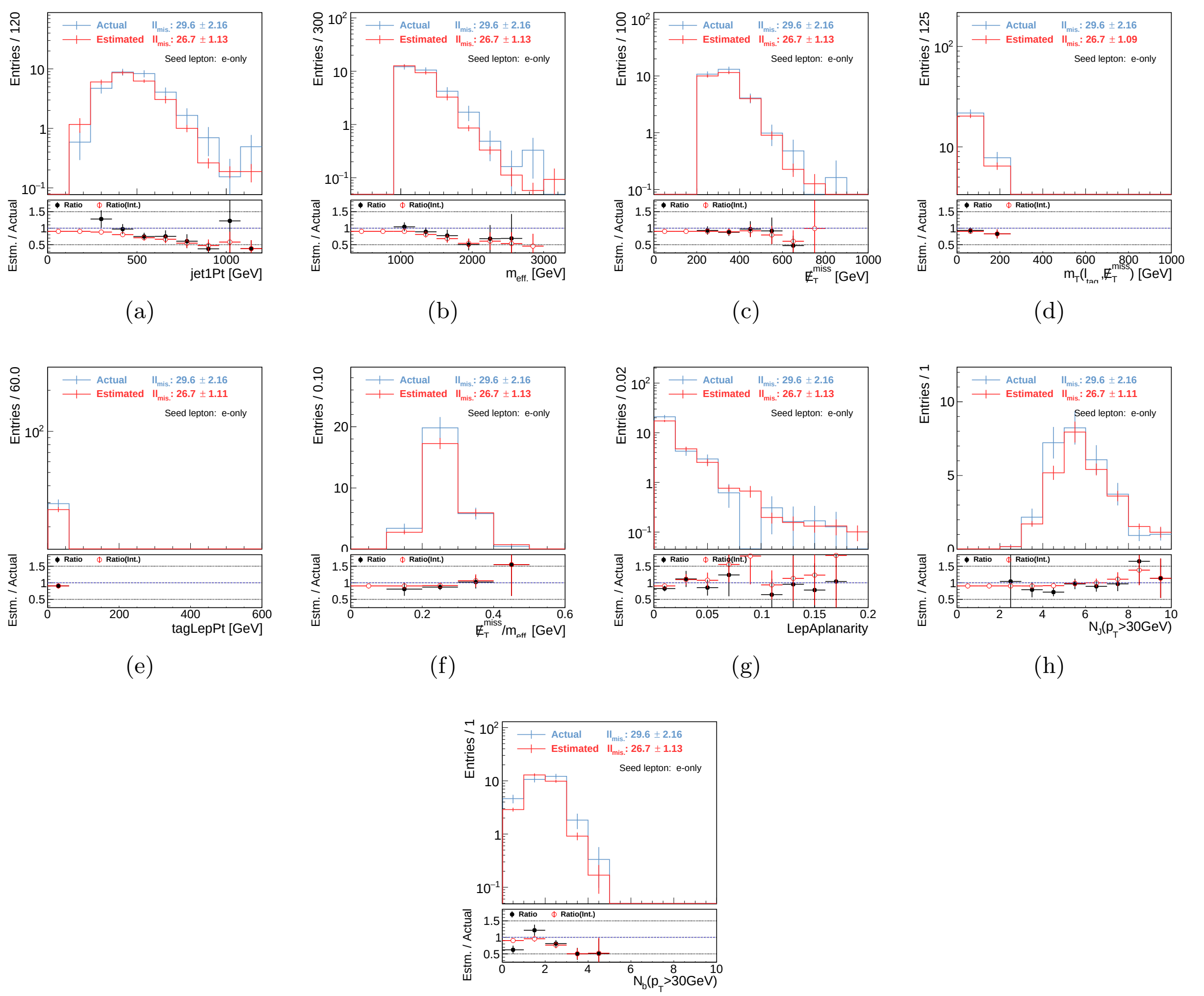

(a) (b) (c) (d)

(e) (f) (g) (h)

(i)

Figure C.2.1: MC closure test for **missing lepton replacement** using $t\bar{t}$ MC sample. Seed events are collected by the use of MET trigger. $p_T < 35$ GeV for the leading lepton is required. **Only electrons in the seed events are replaced**. Red points in the bottom plots show the ratio of integrated yields for the two histograms above the x-position that the point indicates.

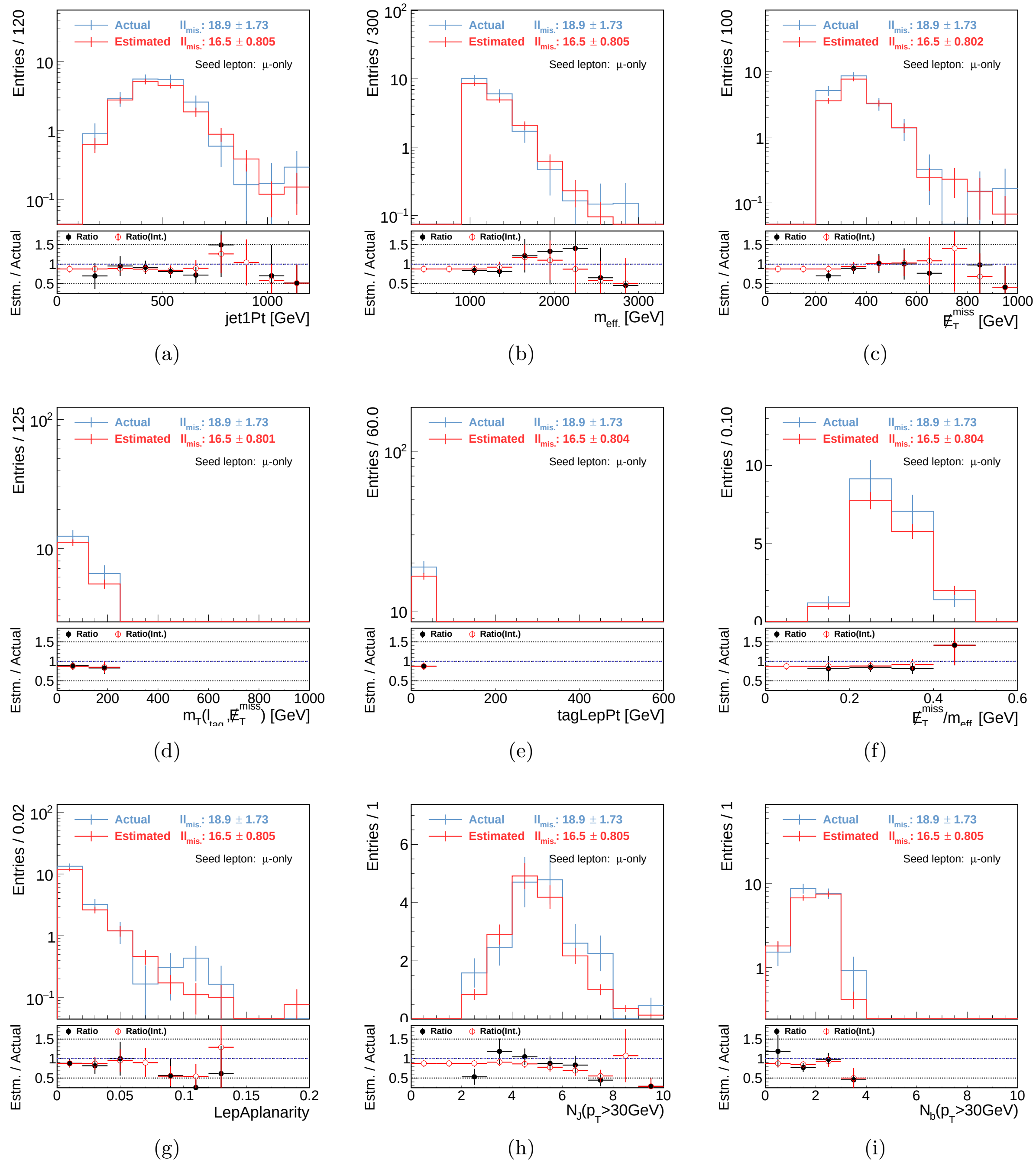

Figure C.2.2: MC closure test for **missing lepton replacement** using $t\bar{t}$ MC sample. Seed events are collected by the use of MET trigger. $p_T < 35$ GeV for the leading lepton is required. **Only muon in the seed events are replaced**. Red points in the bottom plots show the ratio of integrated yields for the two histograms above the x-position that the point indicates.

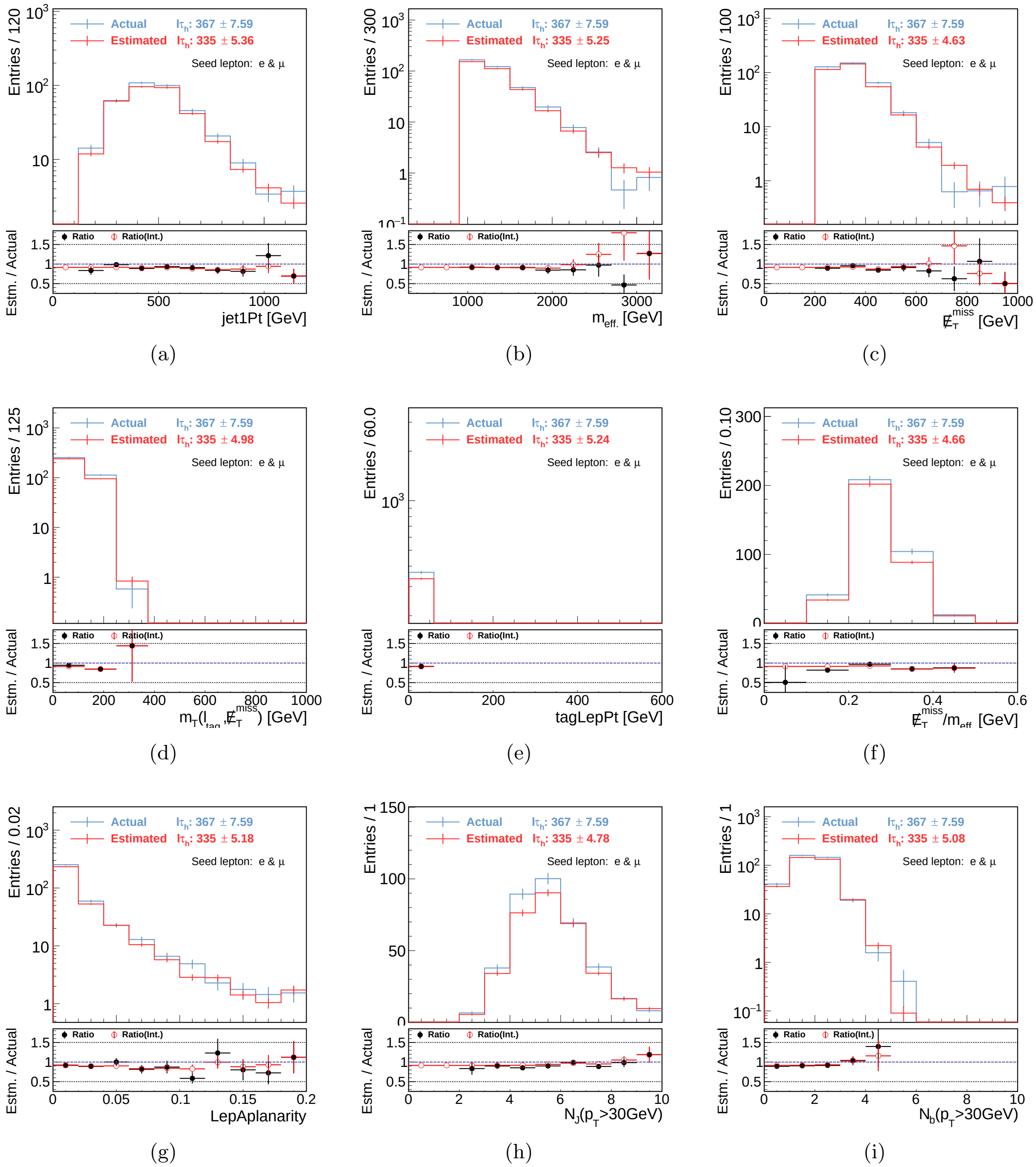

(a) (b) (c)

(d) (e) (f)

(g) (h) (i)

Figure C.2.3: MC closure test for **tau replacement** using $t\bar{t}$ MC sample. Seed events are collected by the use of MET trigger. $p_T < 35$ GeV for the leading lepton is required. **Both electrons and muons in the seed events are replaced**. Red points in the bottom plots show the ratio of integrated yields for the two histograms above the x-position that the point indicates.

Combined Test of Missing Lepton Replacement and Tau Replacement

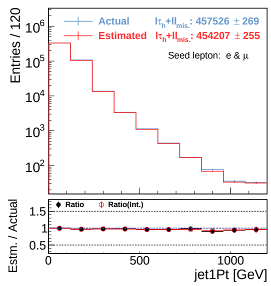

(a)

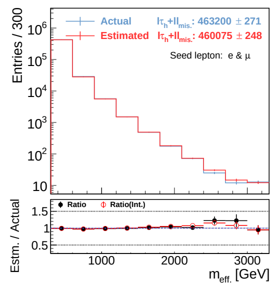

(b)

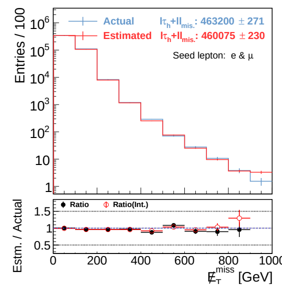

(c)

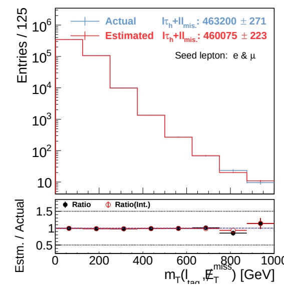

(d)

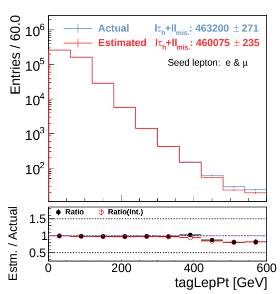

(e)

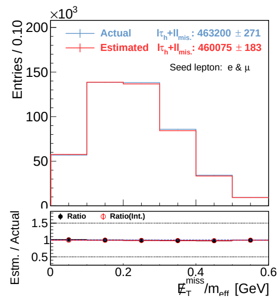

(f)

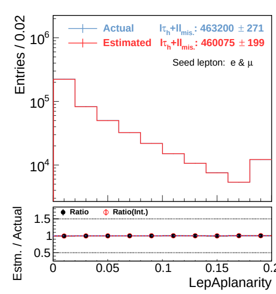

(g)

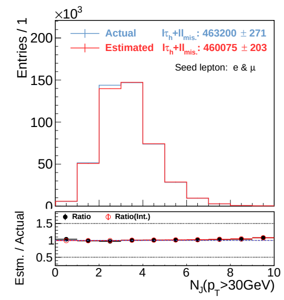

(h)

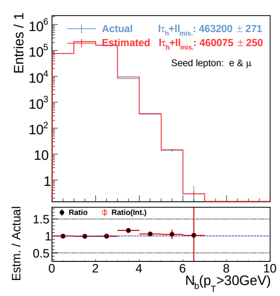

(i)

Figure C.2.4: MC closure test for **combined estimation of missing lepton rep. and tau rep.** using $t\bar{t}$ MC sample. Seed events are collected by the single-lepton trigger. $p_T > 35$ GeV for the leading lepton is required. **Both electrons and muons in the seed events are replaced**. Red points in the bottom plots show the ratio of integrated yields for the two histograms above the x-position that the point indicates.

C.3 Multi-jet Validation using Data

Among the "fake" backgrounds defined in Table 6.1, the multi-jets background including QCD di-jet and full-hadronic decays of $V+$ jets or $t\bar{t}$, is ignored in the estimation since it is supposed to be negligible after requiring one signal lepton and $E_{\mathrm{T}}^{\mathrm{miss}} > 250$ in the events, based on the MC study and the past Run2 ATLAS 1-lepton analyses [150] [147]. However, the cross-check is always worthwhile since the impact could be fatal once it turns to contribute because of its huge cross-section. The other components, dominated by $W \to \tau\nu$ and $Z \to \nu\nu$, are estimated by the kinematical extrapolation method in which the normalization factors in Figure 6.15 are applied for $W+$ jets and top MC. Note that the normalization factors are intended to correct the mis-modeling in the hard process kinematics, but not the modeling on the fake rate of lepton candidates where MC is known to be sometimes unreliable. Therefore, a data-driven validation is performed in a set of specific validation regions (VR-QCD) to check those estimation.

VR-QCDs are defined by inverting the isolation requirement on the final state lepton with respect to the SRs, as shown in Table 5.7 - 5.11. The abundance of "fake" components is enhanced by around factor of 10 with respect to the SRs, due to the high rejection factor of isolation that is typically $10-20$ ($5-10$) for fake electrons (muons).

Figure C.3.1 - C.3.2 are the result for each m_{eff} bin of VRs-QCD. Nice agreement between the estimation and data is seen overall, implying the good MC modeling on fake lepton. Note that the multi-jets process is not included in MC thus the contribution would emerge as excess in data if it is significant, which is fortunately not the case.

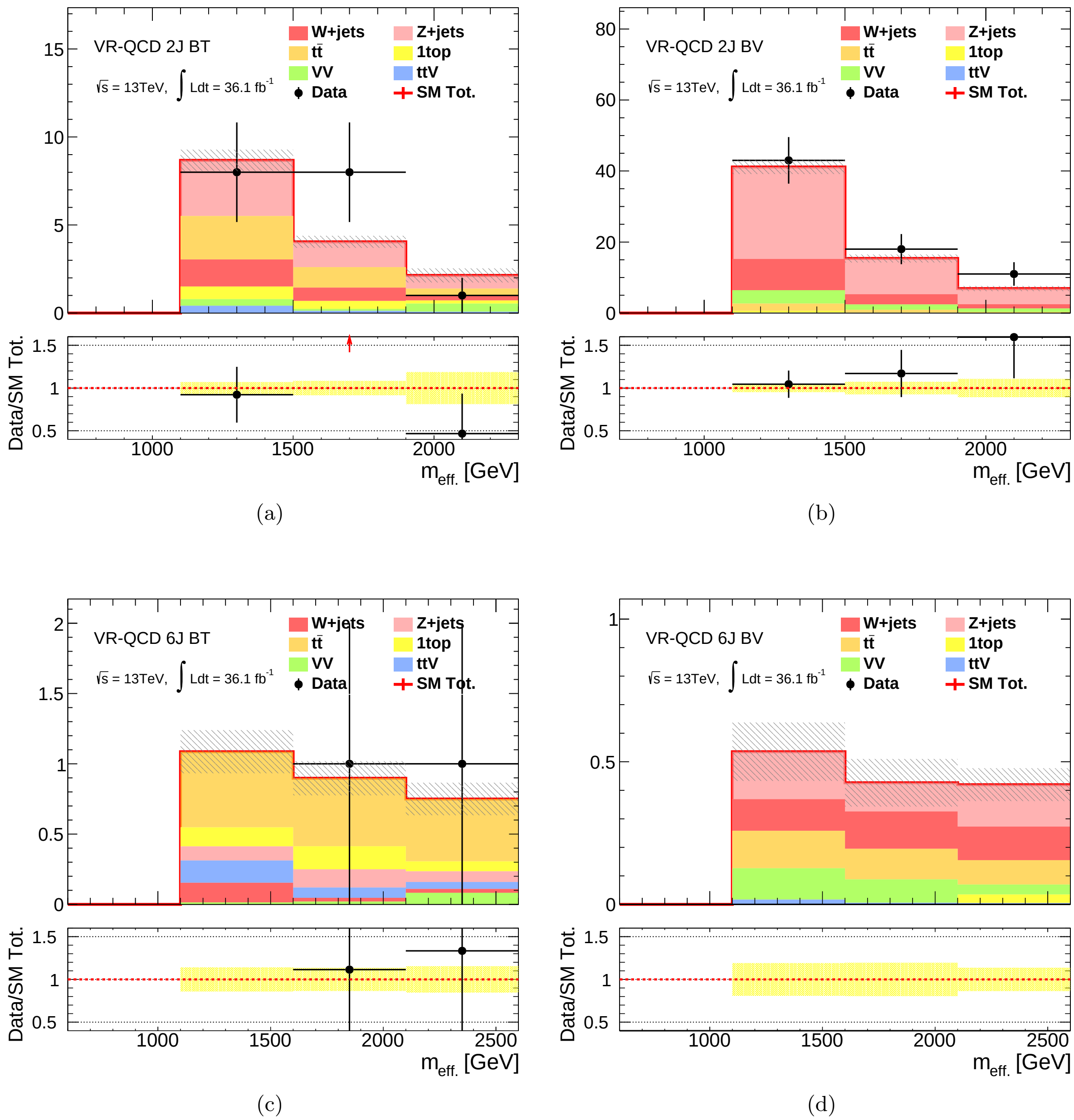

Figure C.3.1: VR-QCD for towers (a) 2JBT (b) 2JBV (c) 6JBT (d) 6JBV.

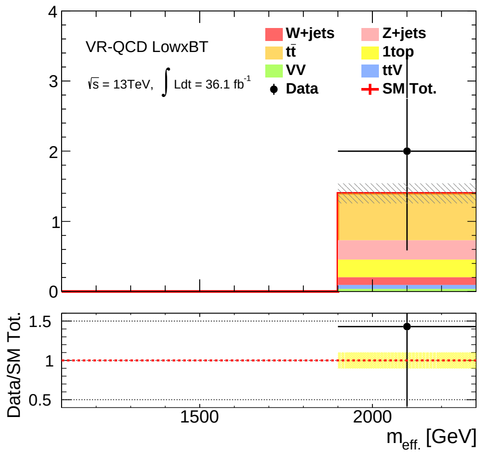

(a)

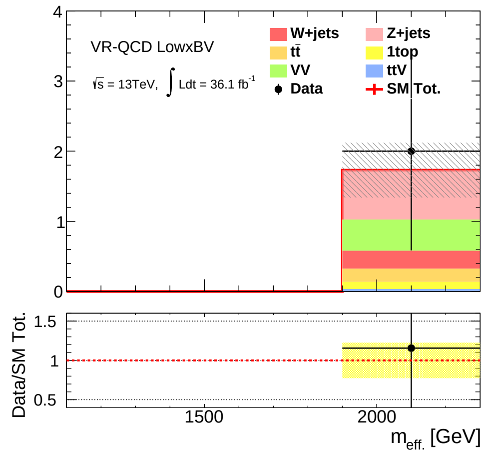

(b)

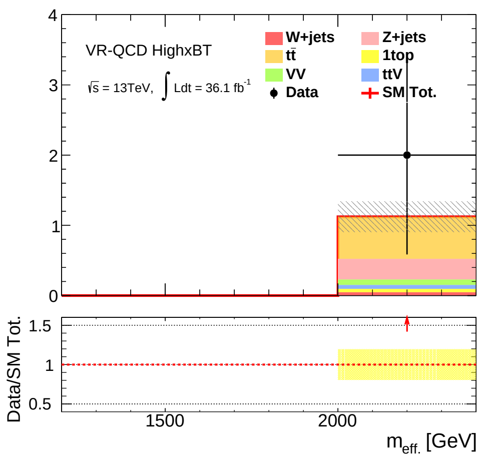

(c)

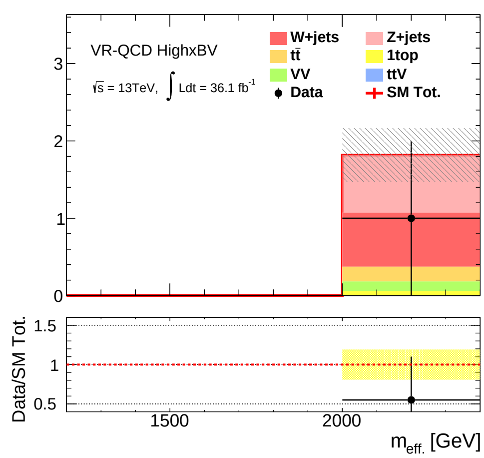

(d)

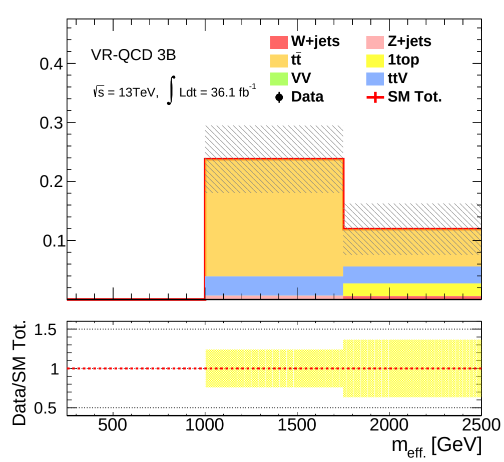

(e)

Figure C.3.2: VR-QCD for towers (a) LowxBT (b) LowxBV (c) HighxBT (d) HighxBV (e) 3B.

C.4 Post-fit distributions in CRs and VRs

Control Regions

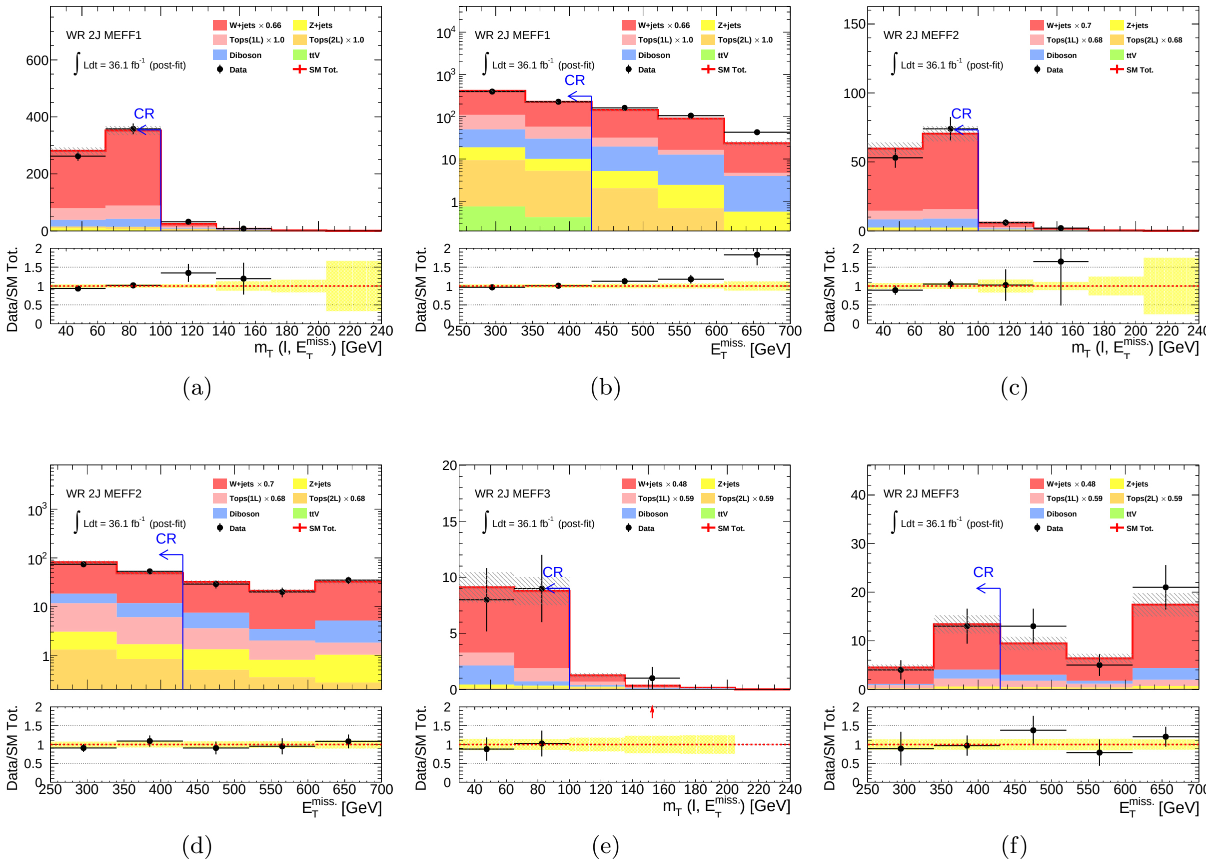

Figure C.4.1: Post-fit distruibution of (left) m_{T} (right) $E_{\mathrm{T}}^{\mathrm{miss}}$. (a,b) WR 2J-$m_{\mathrm{eff}}^{\mathrm{bin1}}$. (c,d) WR 2J-$m_{\mathrm{eff}}^{\mathrm{bin2}}$. (e,f) WR 2J-$m_{\mathrm{eff}}^{\mathrm{bin3}}$. The yellow band in the bottom panel represents only statistical error. The overflow is included in the highest bin.

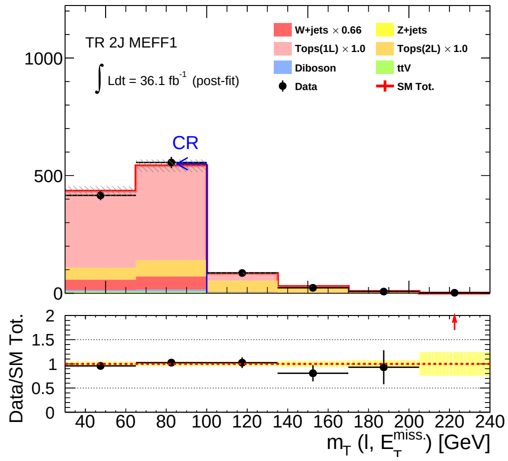

(a)

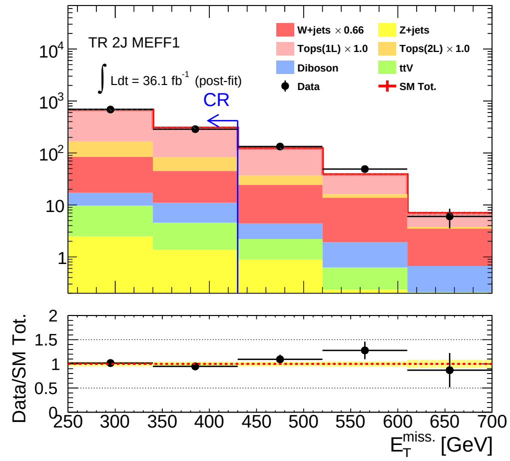

(b)

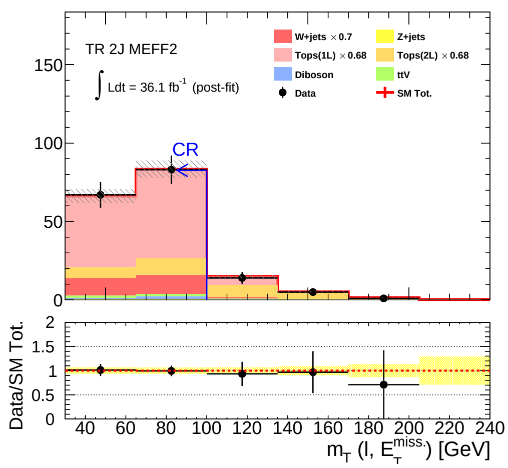

(c)

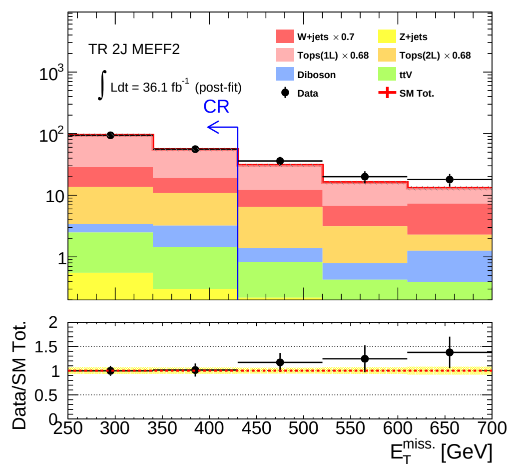

(d)

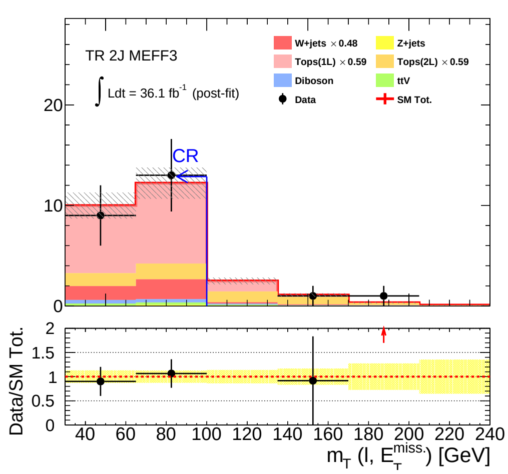

(e)

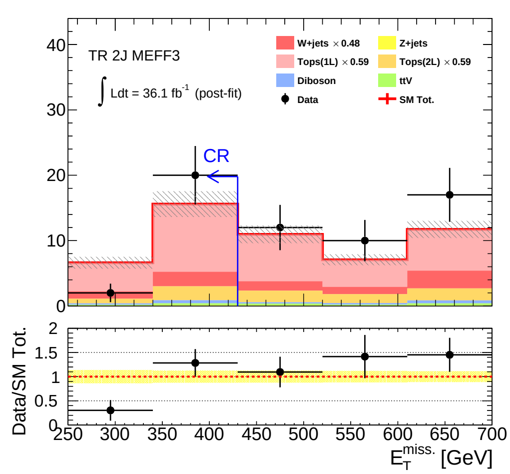

(f)

Figure C.4.2: Post-fit distruibution of (left) m_{T} (right) $E_{\mathrm{T}}^{\mathrm{miss}}$. (a,b) TR 2J-$m_{\mathrm{eff}}^{\mathrm{bin1}}$. (c,d) TR 2J-$m_{\mathrm{eff}}^{\mathrm{bin2}}$. (e,f) TR 2J-$m_{\mathrm{eff}}^{\mathrm{bin3}}$. The yellow band in the bottom panel represents only statistical error. The overflow is included in the highest bin.

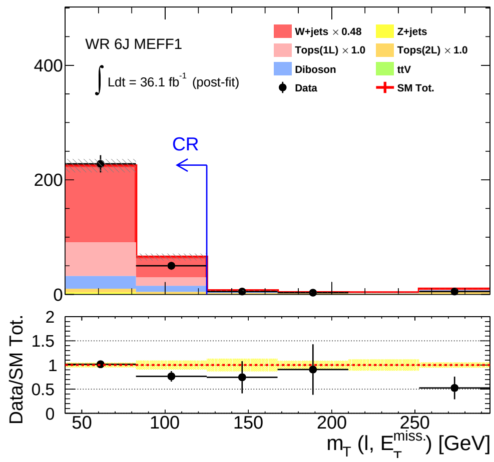

(a)

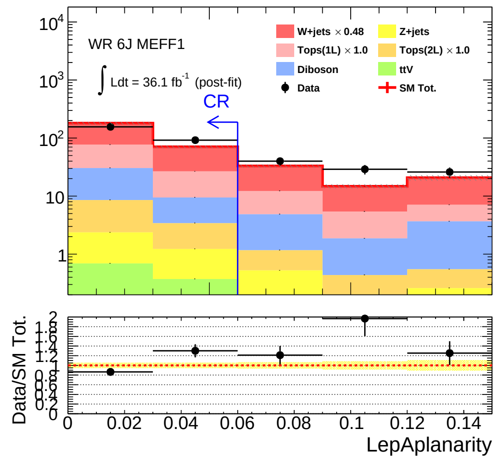

(b)

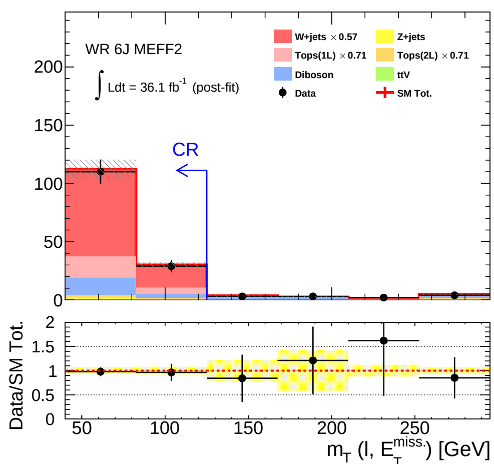

(c)

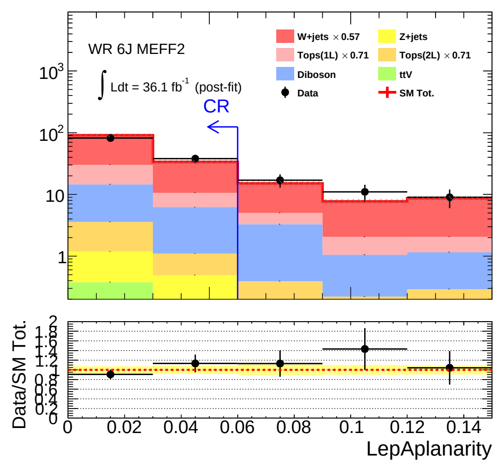

(d)

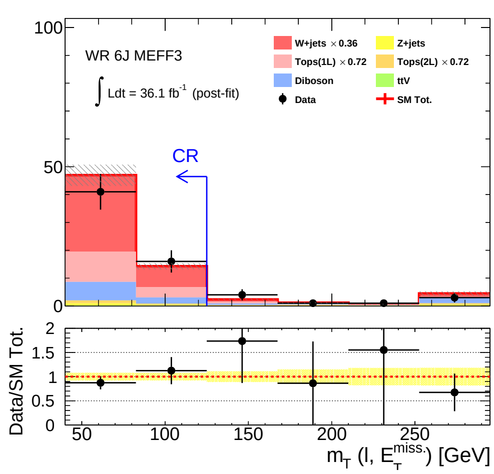

(e)

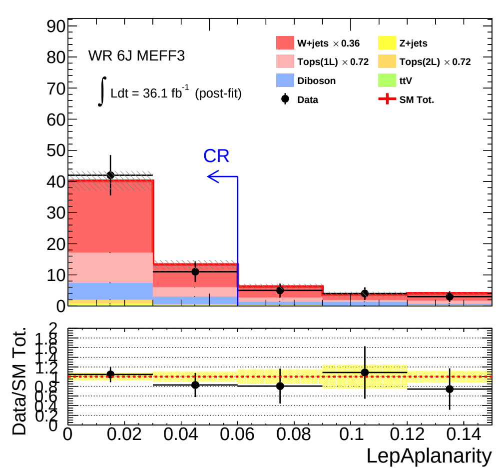

(f)

Figure C.4.3: Post-fit distruibution of (left) m_{T} (right) aplanarity. (a,b) WR 6J-$m_{\mathrm{eff}}^{\mathrm{bin1}}$. (c,d) WR 6J-$m_{\mathrm{eff}}^{\mathrm{bin2}}$. (e,f) WR 6J-$m_{\mathrm{eff}}^{\mathrm{bin3}}$. The yellow band in the bottom panel represents only statistical error. The overflow is included in the highest bin.

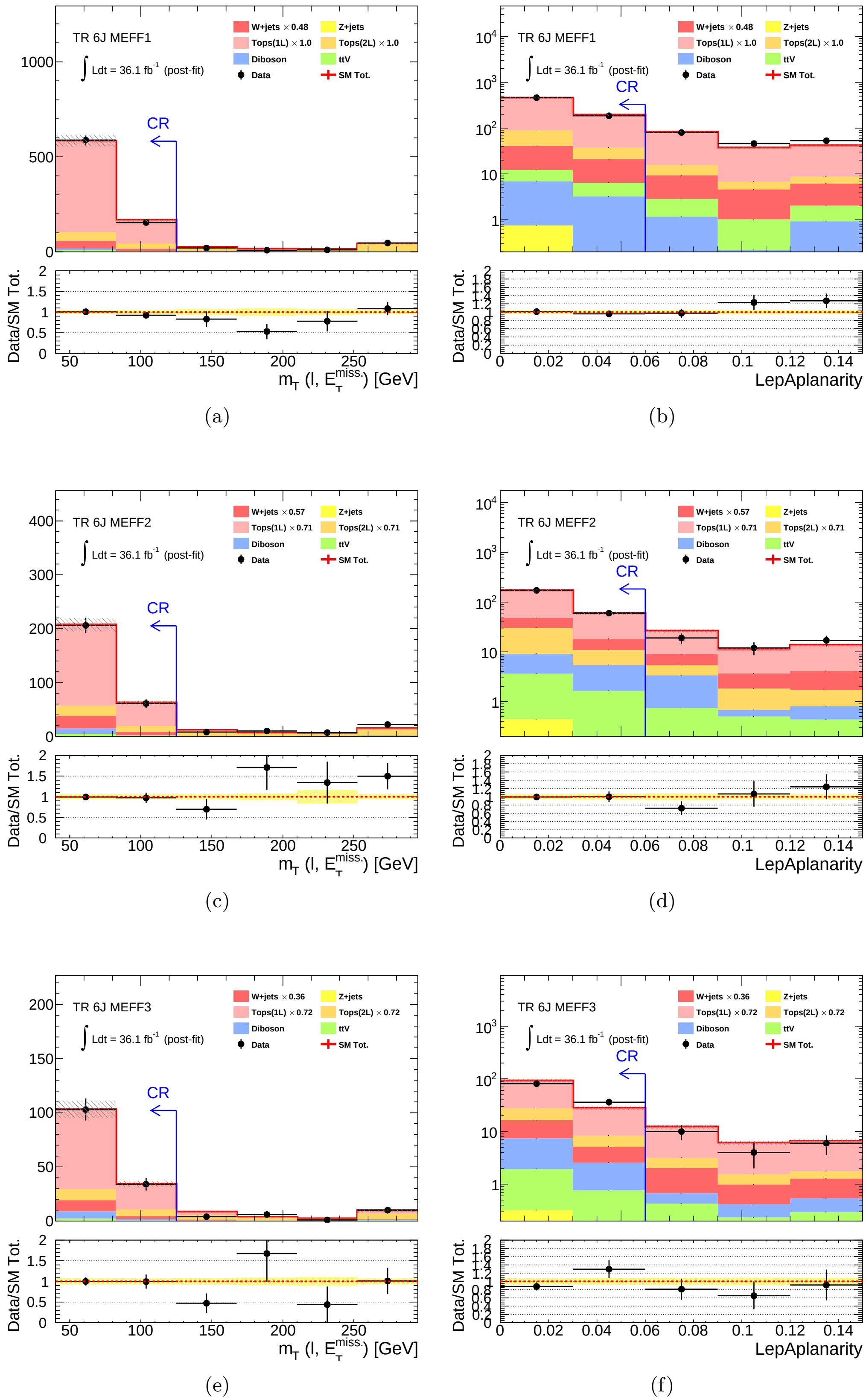

Figure C.4.4: Post-fit distruibution of (left) m_{T} (right) aplanarity. (a,b) TR 6J-$m_{\mathrm{eff}}^{\mathrm{bin1}}$. (c,d) TR 6J-$m_{\mathrm{eff}}^{\mathrm{bin2}}$. (e,f) TR 6J-$m_{\mathrm{eff}}^{\mathrm{bin3}}$. The yellow band in the bottom panel represents only statistical error. The overflow is included in the highest bin.

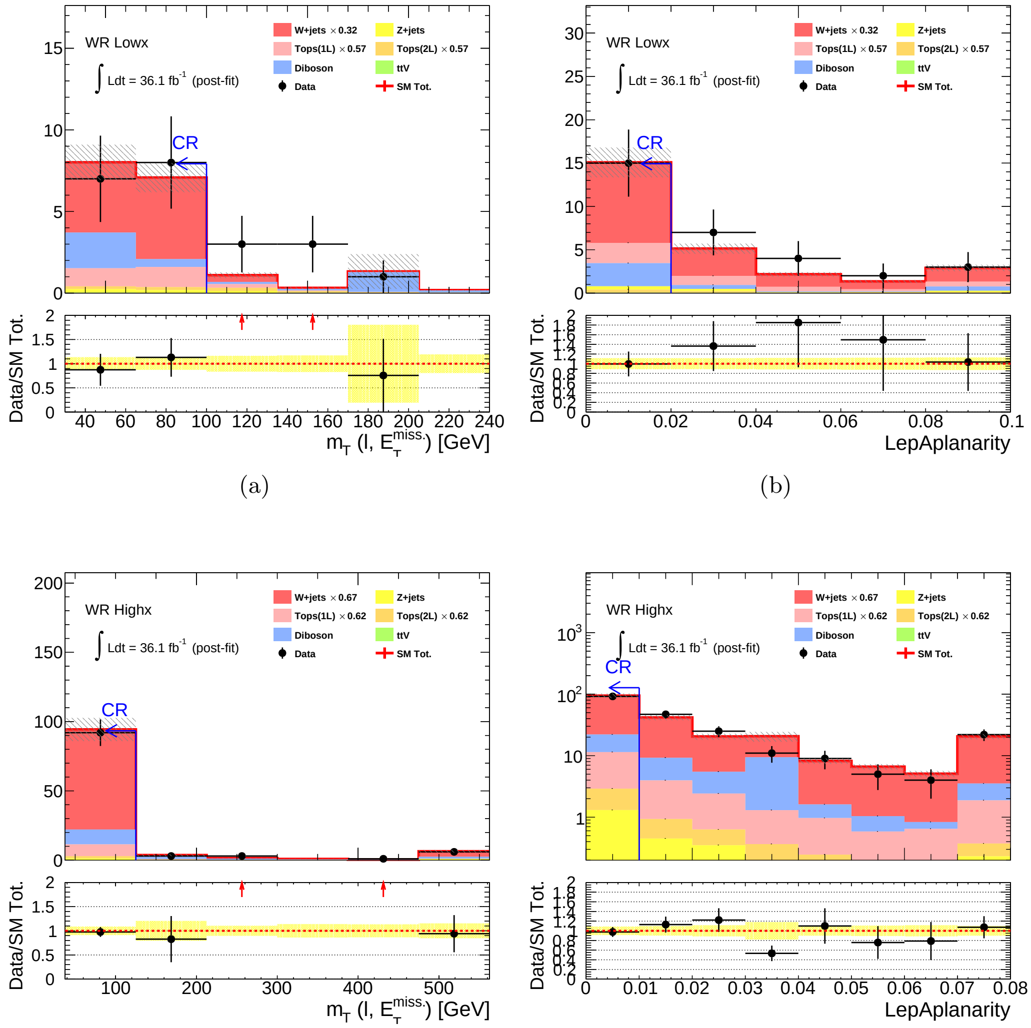

(a) (b)

(c) (d)

Figure C.4.5: Post-fit distruibution of (left) m_{T} (right) aplanarity. (a,b) WR Low-x. (c,d) WR High-x. The yellow band in the bottom panel represents only statistical error. The overflow is included in the highest bin.

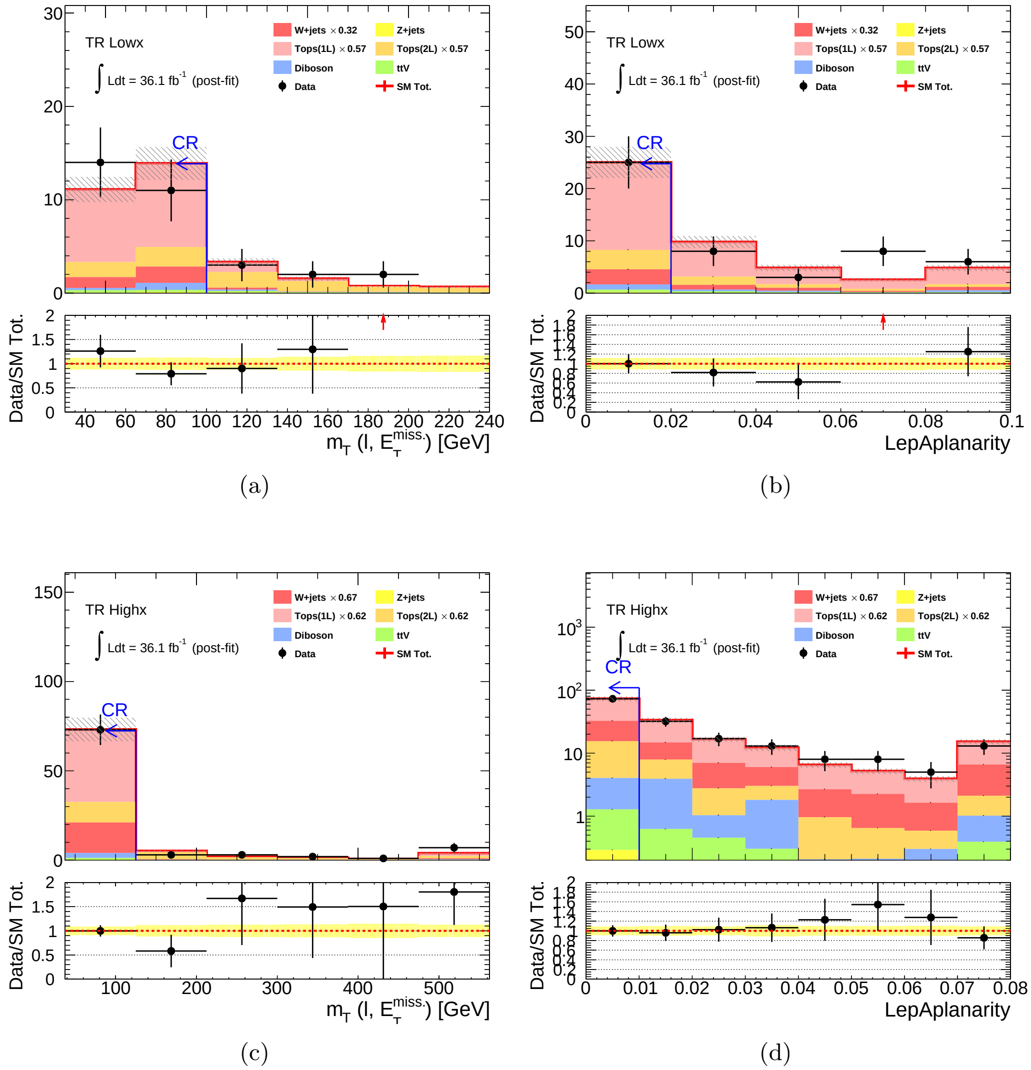

Figure C.4.6: Post-fit distruibution of (left) m_{T} (right) aplanarity. (a,b) TR Low-x. (c,d) TR High-x. The yellow band in the bottom panel represents only statistical error. The overflow is included in the highest bin.

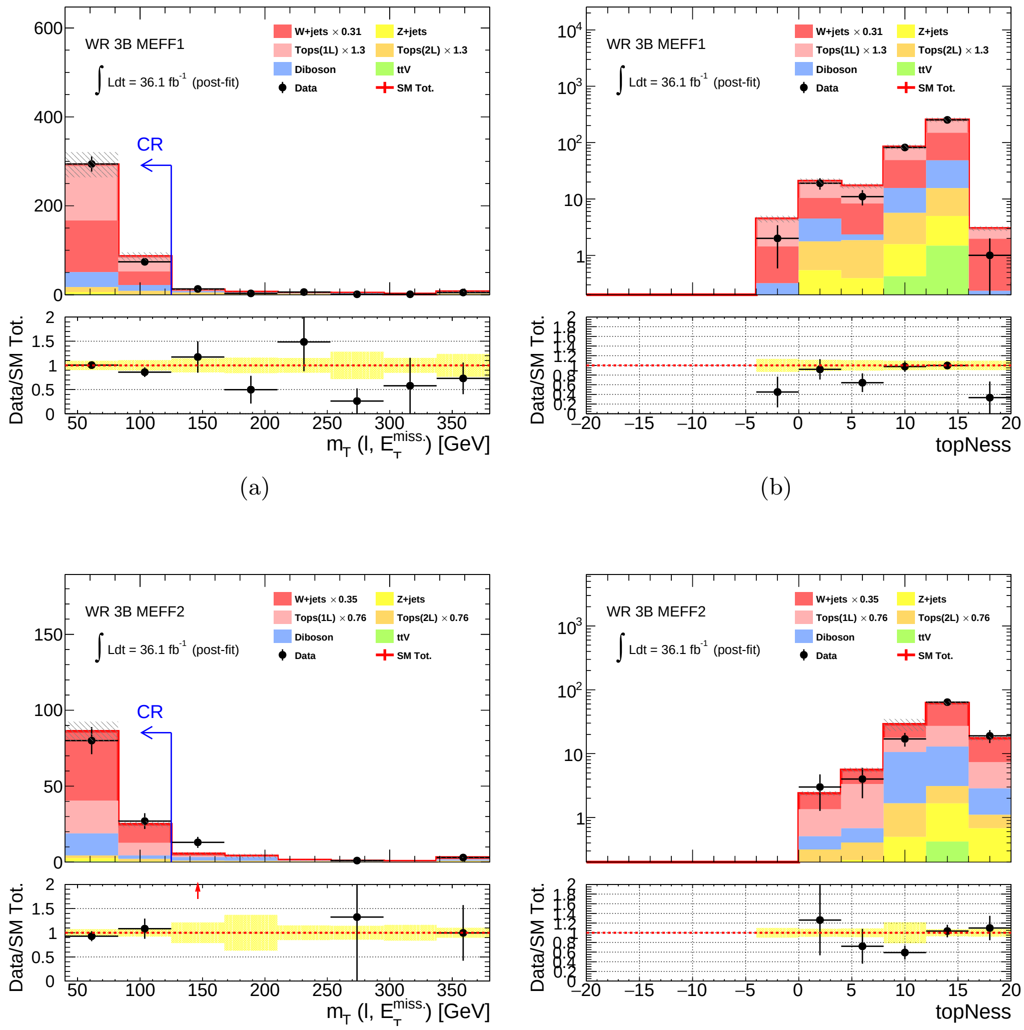

(a) (b)

(c) (d)

Figure C.4.7: Post-fit distruibution of (left) m_{T} (right) topness. (a,b) WR 3B-$m_{\mathrm{eff}}^{\mathrm{bin1}}$. (c,d) WR 3B-$m_{\mathrm{eff}}^{\mathrm{bin2}}$. The yellow band in the bottom panel represents only statistical error. The overflow is included in the highest bin.

Blue arrows indicate the CRs that the MC is normalized.

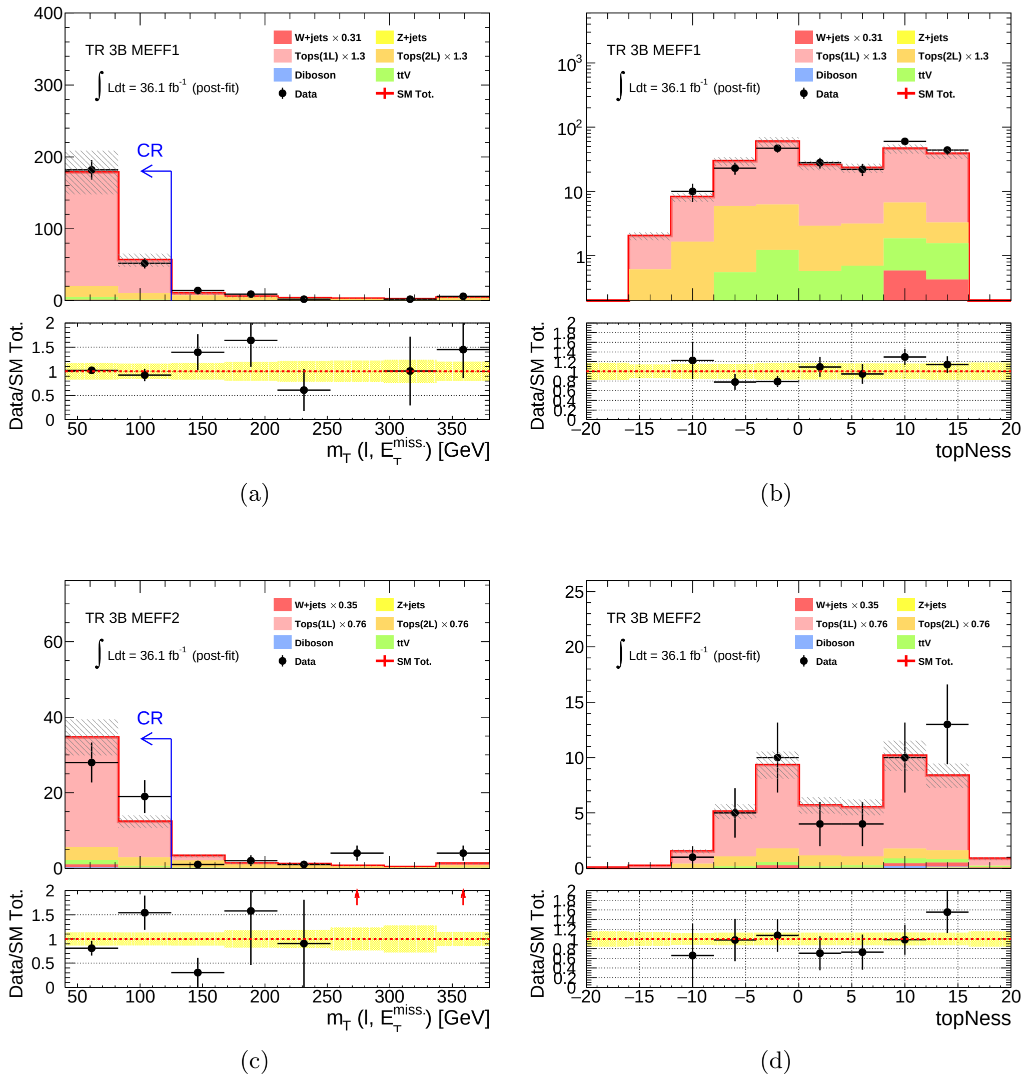

Figure C.4.8: Post-fit distruibution of (left) m_{T} (right) topness. (a,b) TR 3B-$m_{\mathrm{eff}}^{\mathrm{bin1}}$. (c,d) TR 3B-$m_{\mathrm{eff}}^{\mathrm{bin2}}$. The yellow band in the bottom panel represents only statistical error. The overflow is included in the highest bin.

Validation Regions

for variables which VRs are designed to test i.e. m_{T} for VRa and aplanarity/topness etc. for VRb.

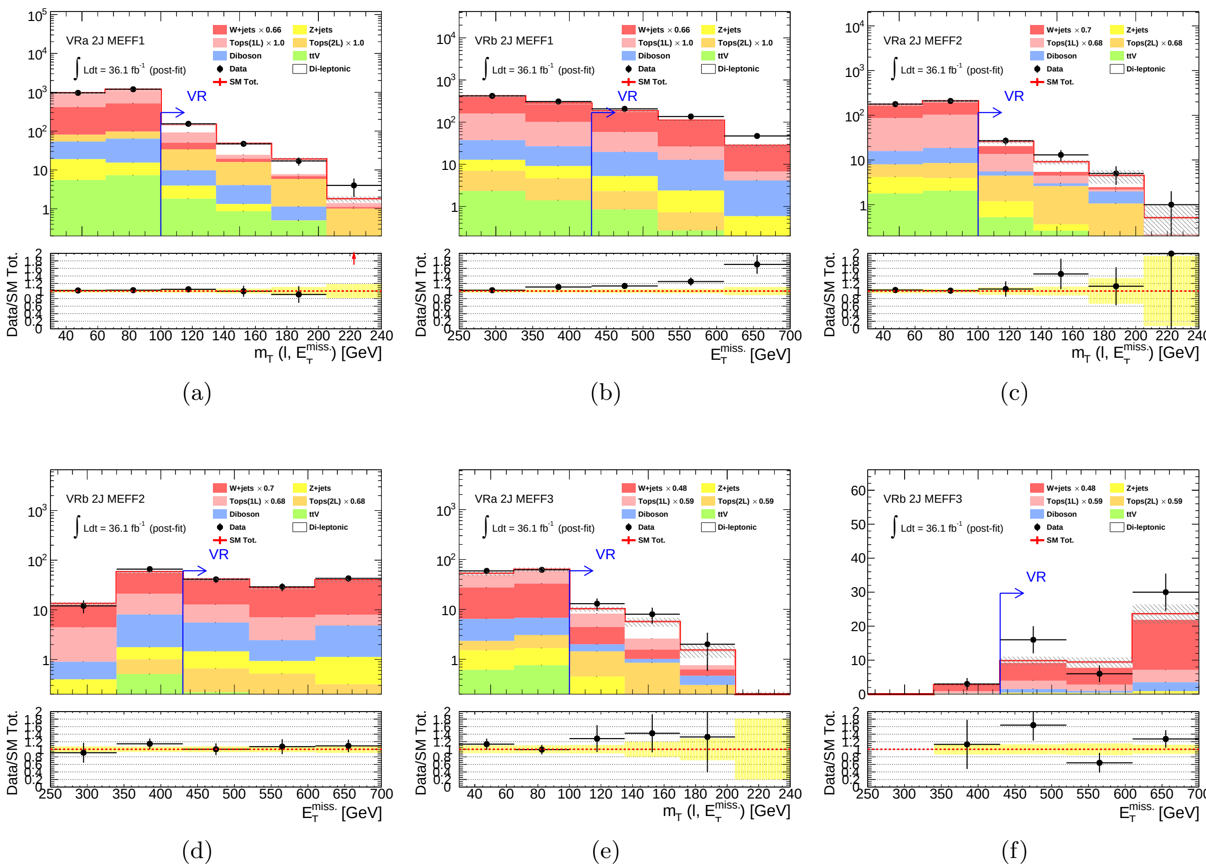

Figure C.4.9: Post-fit distruibution of (left) m_{T} in VRa, and (right) $E_{\mathrm{T}}^{\mathrm{miss}}$ in VRb. (a,b) VR 2J-$m_{\mathrm{eff}}^{\mathrm{bin1}}$. (c,d) VR 2J-$m_{\mathrm{eff}}^{\mathrm{bin2}}$. (e,f) VR 2J-$m_{\mathrm{eff}}^{\mathrm{bin3}}$. The yellow band in the bottom panel represents statistical error. The overflow is included in the highest bin.

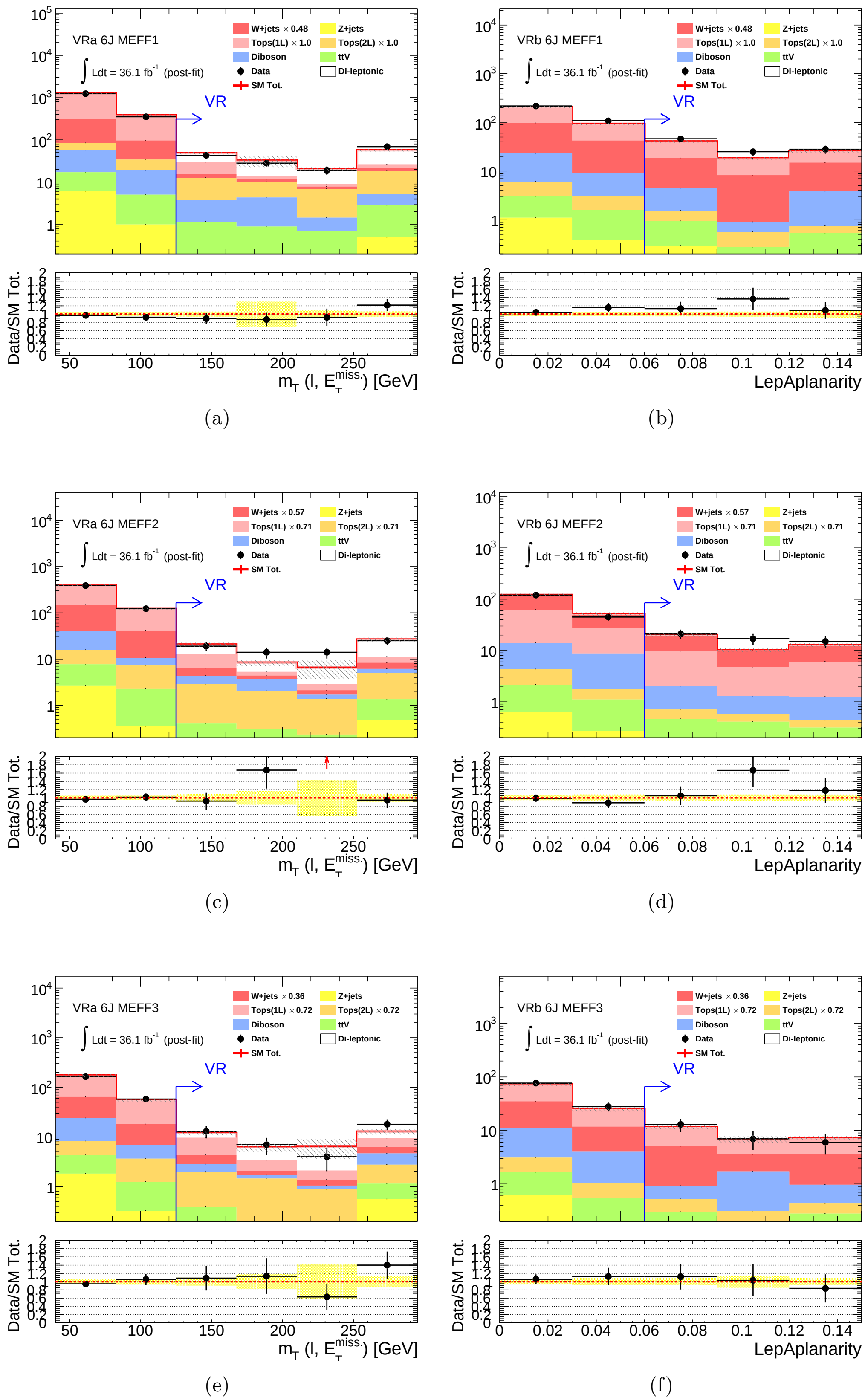

Figure C.4.10: Post-fit distruibution of (left) m_{T} in VRa, and (right) aplanarity in VRb. (a,b) VR 6J-$m_{\mathrm{eff}}^{\mathrm{bin1}}$. (c,d) VR 6J-$m_{\mathrm{eff}}^{\mathrm{bin2}}$. (e,f) VR 6J-$m_{\mathrm{eff}}^{\mathrm{bin3}}$. The yellow band in the bottom panel represents only statistical error. The overflow is included in the highest bin.

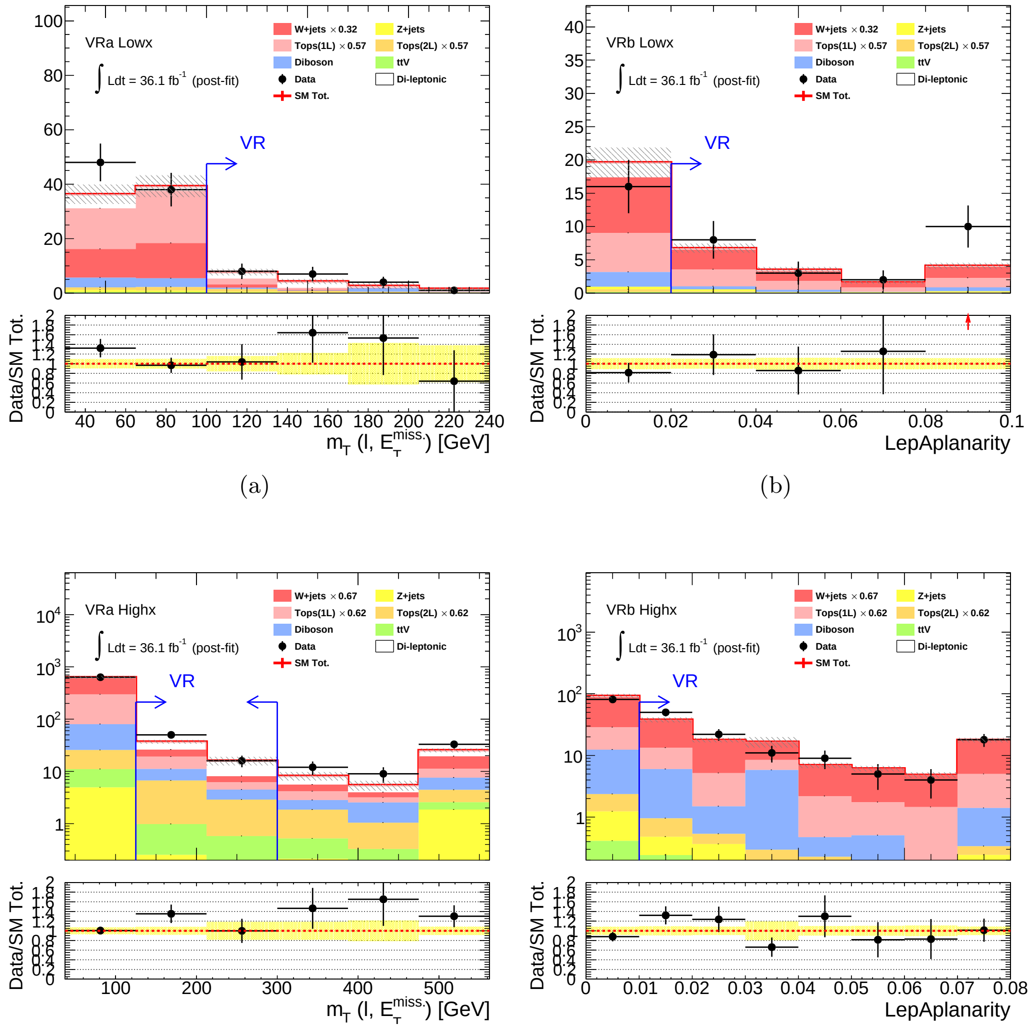

(a) (b) (c) (d)

Figure C.4.11: Post-fit distruibution of (left) m_{T} in VRa, and (right) aplanarity in VRb. (a,b) VR Low-x. (c,d) VR High-x. The yellow band in the bottom panel represents only statistical error. The overflow is included in the highest bin.

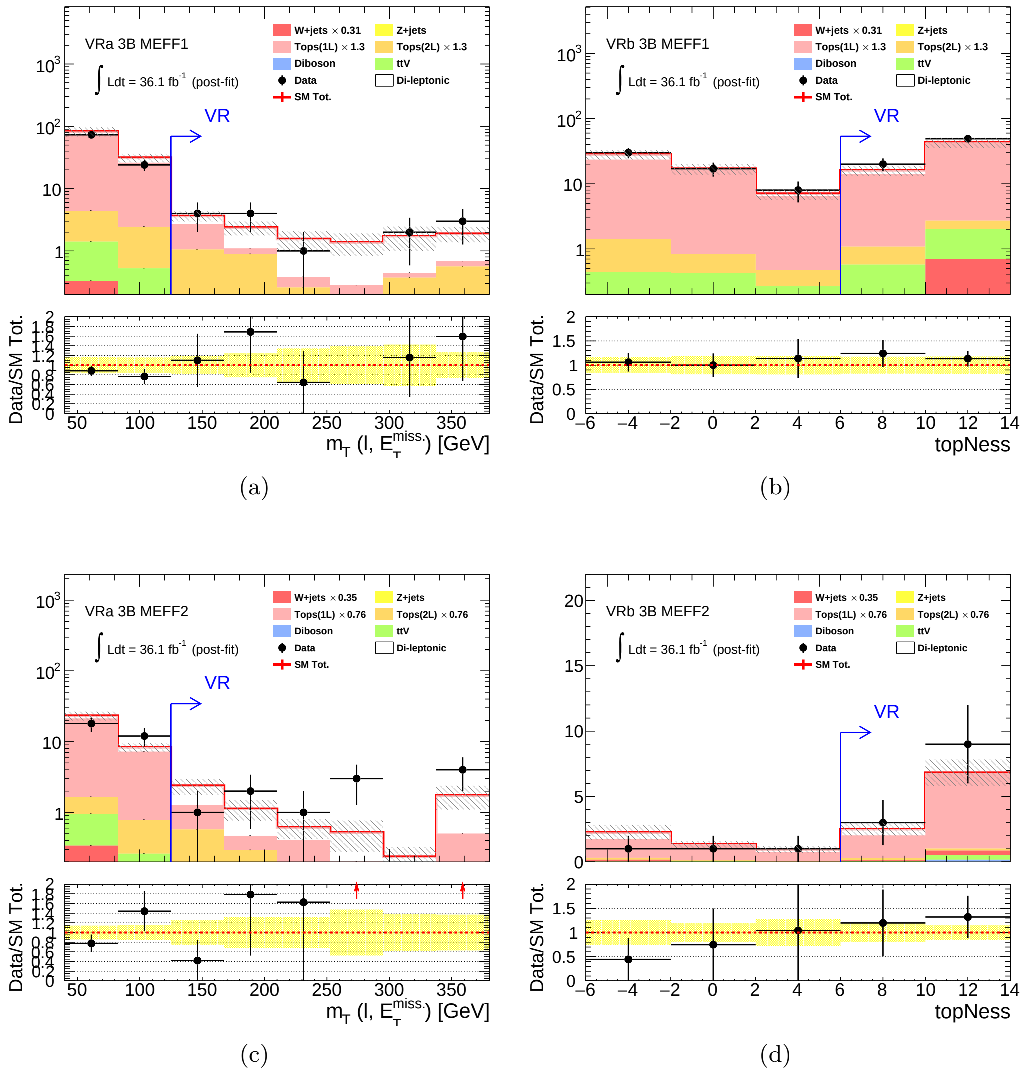

Figure C.4.12: Post-fit distruibution of (left) m_{T} in VRa, and (right) topness in VRb. (a,b) VR 3B-$m_{\mathrm{eff}}^{\mathrm{bin1}}$. (c,d) VR 3B-$m_{\mathrm{eff}}^{\mathrm{bin2}}$. The yellow band in the bottom panel represents only statistical error. The overflow is included in the highest bin.

D Auxiliary Materials for Systematic Uncertainties

D.1 Extrapolation Error vs Artificially Injected MC Mis-modeling

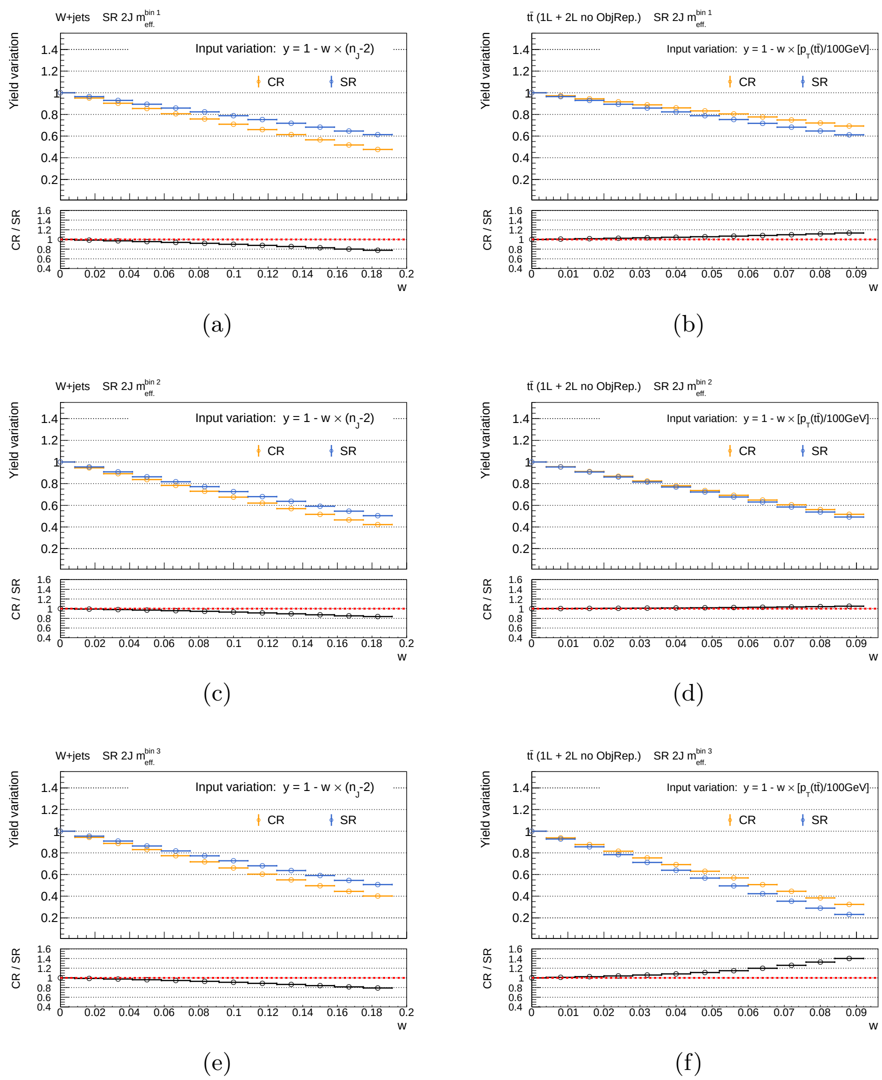

Figure D.1.1: Extrapolation error in SR/CR 2J. B-tagging requirement is removed. Top pannels show the yield variation of (a) $W+$jets and (b) $t\bar{t}$ when injecting the variation by reweighting the MC with Eq. 7.1. Bottom rows are the relative difference in their response against the injected variation, namely the extrapolation errir. For the $t\bar{t}$ process, component estimated by the object replacement method is removed.

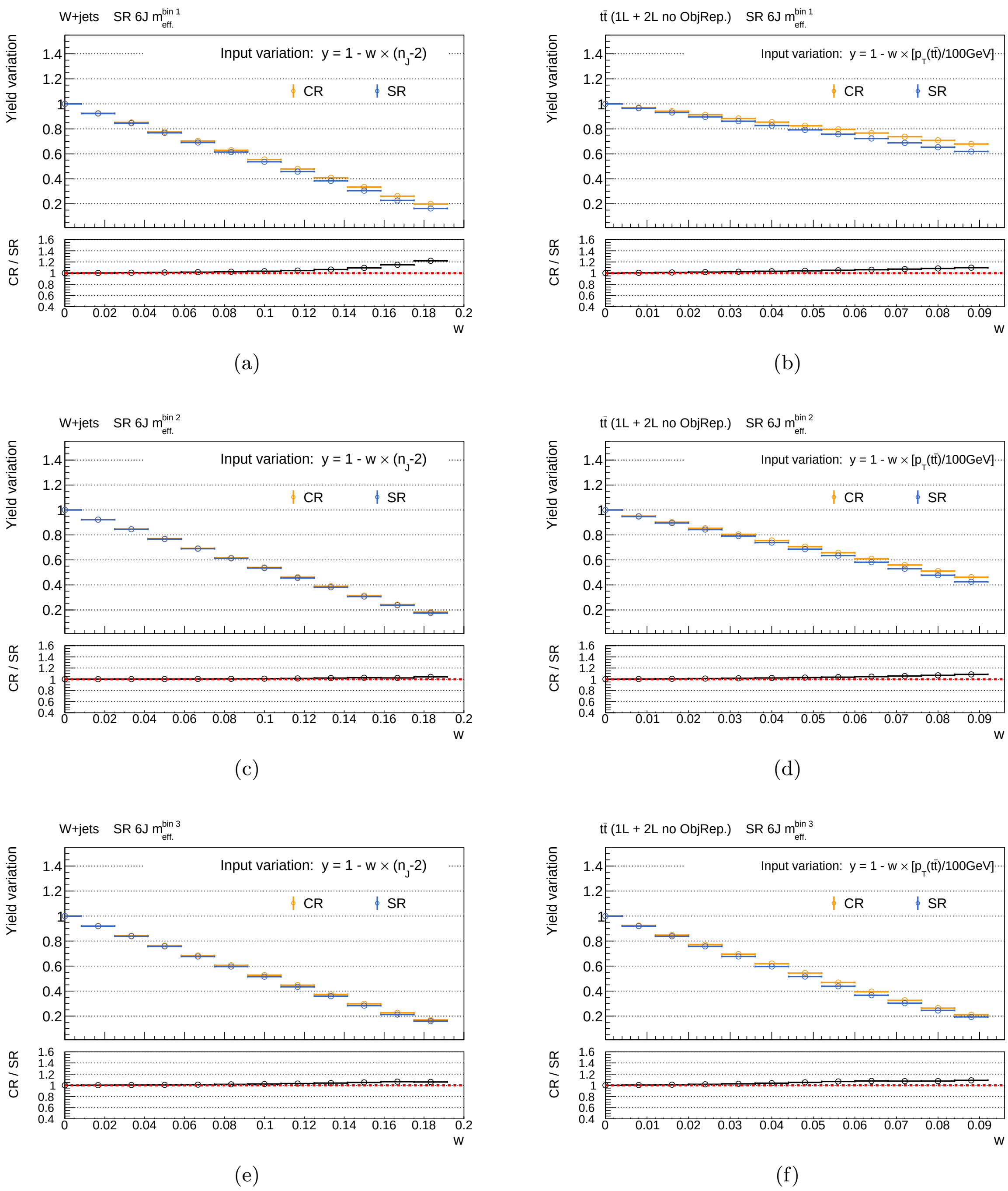

Figure D.1.2: Extrapolation error in SR/CR 6J. B-tagging requirement is removed. Top pannels show the yield variation of (a) $W+$jets and (b) $t\bar{t}$ when injecting the variation by reweighting the MC with Eq. 7.1. Bottom rows are the relative difference in their response against the injected variation, namely the extrapolation errir. For the $t\bar{t}$ process, component estimated by the object replacement method is removed.

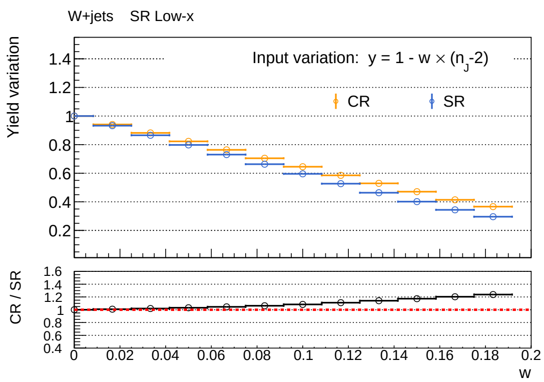

(a)

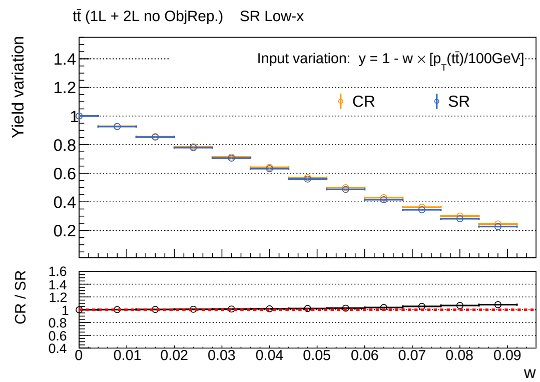

(b)

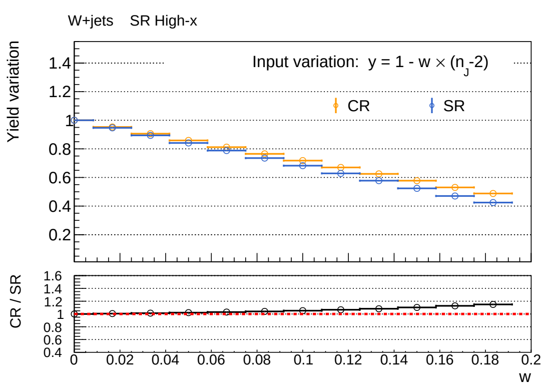

(c)

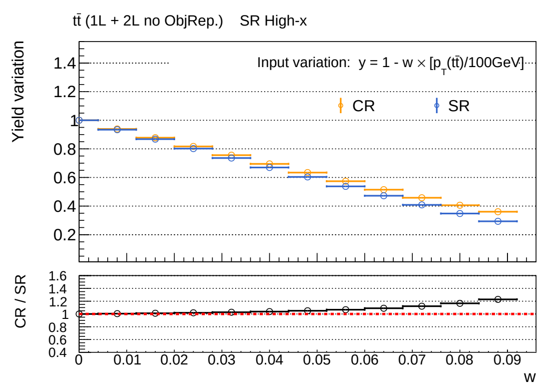

(d)

Figure D.1.3: Extrapolation error in SR/CR (a)(b) Low-x, and (c)(d) High-x. B-tagging requirement is removed. Top pannels show the yield variation of $W+$jets (left) and $t\bar{t}$ (right) when injecting the variation by reweighting the MC with Eq. 7.1. Bottom rows are the relative difference in their response against the injected variation, namely the extrapolation errir. For the $t\bar{t}$ process, component estimated by the object replacement method is removed.

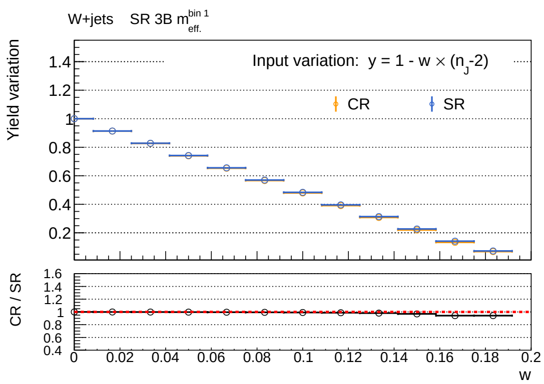

(a)

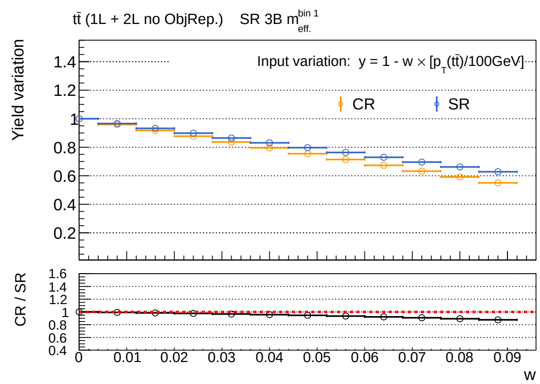

(b)

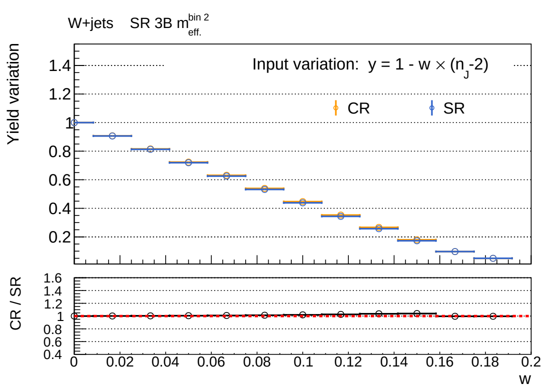

(c)

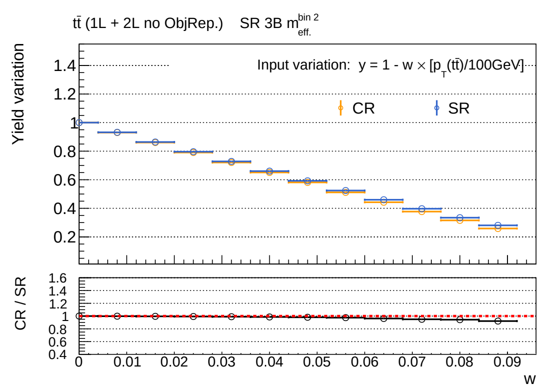

(d)

Figure D.1.4: Extrapolation error in SR/CR 3B. B-tagging requirement is removed for $W+$jets. Top pannels show the yield variation of $W+$jets (left) and $t\bar{t}$ (right) when injecting the variation by reweighting the MC with Eq. 7.1. Bottom rows are the relative difference in their response against the injected variation, namely the extrapolation errir. For the $t\bar{t}$ process, component estimated by the object replacement method is removed.

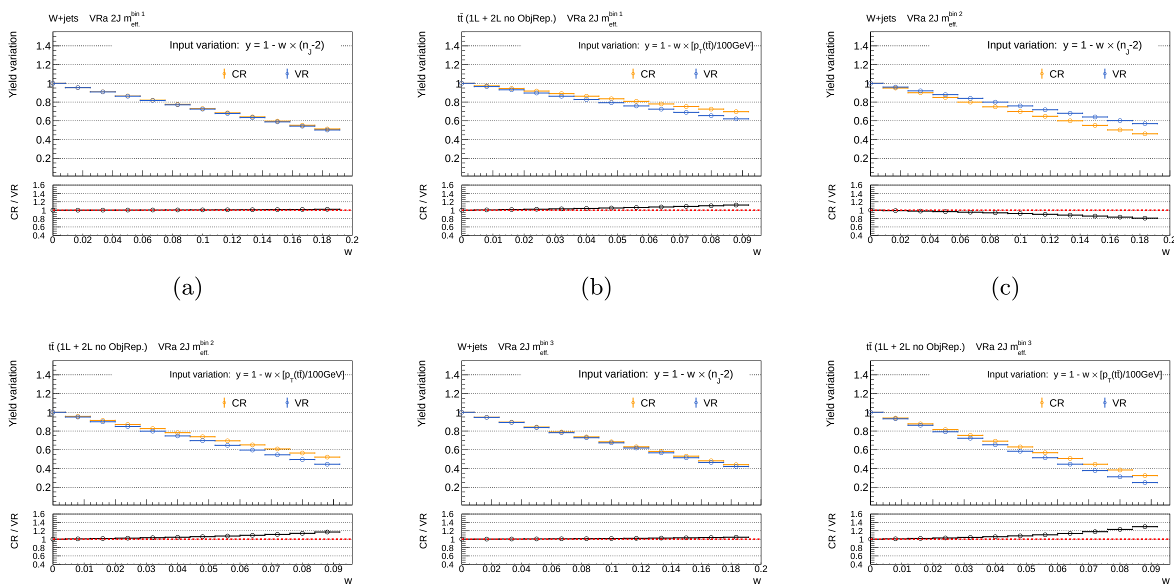

(a) (b) (c)

(d) (e) (f)

Figure D.1.5: Extrapolation error in VRa/CR 2J. B-tagging requirement is removed. Top pannels show the yield variation of (a) $W+\text{jets}$ and (b) $t\bar{t}$ when injecting the variation by reweighting the MC with Eq. 7.1. Bottom rows are the relative difference in their response against the injected variation, namely the extrapolation errir. For the $t\bar{t}$ process, component estimated by the object replacement method is removed.

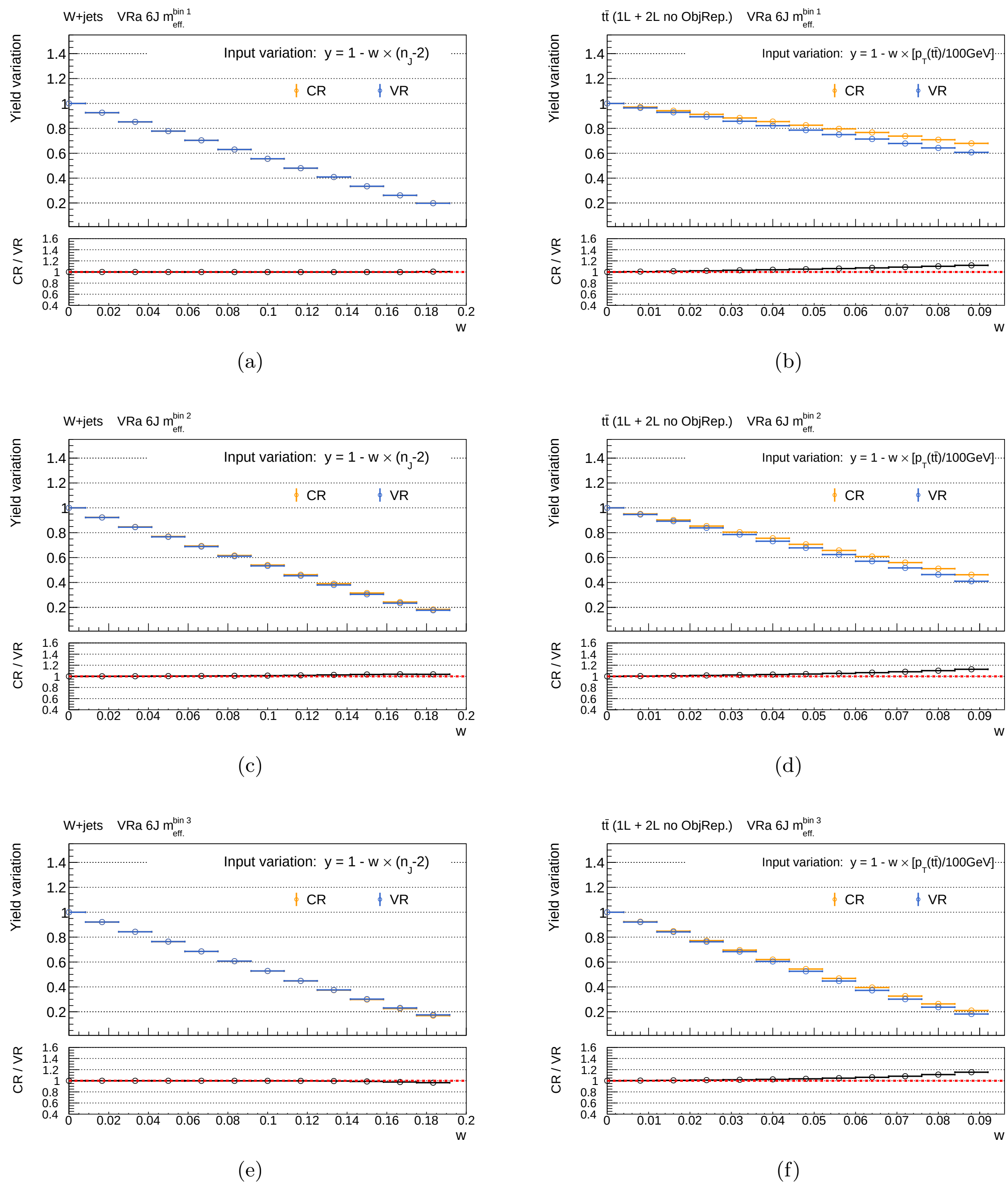

Figure D.1.6: Extrapolation error in VRa/CR 6J. B-tagging requirement is removed. Top pannels show the yield variation of (a) $W+$jets and (b) $t\bar{t}$ when injecting the variation by reweighting the MC with Eq. 7.1. Bottom rows are the relative difference in their response against the injected variation, namely the extrapolation errir. For the $t\bar{t}$ process, component estimated by the object replacement method is removed.

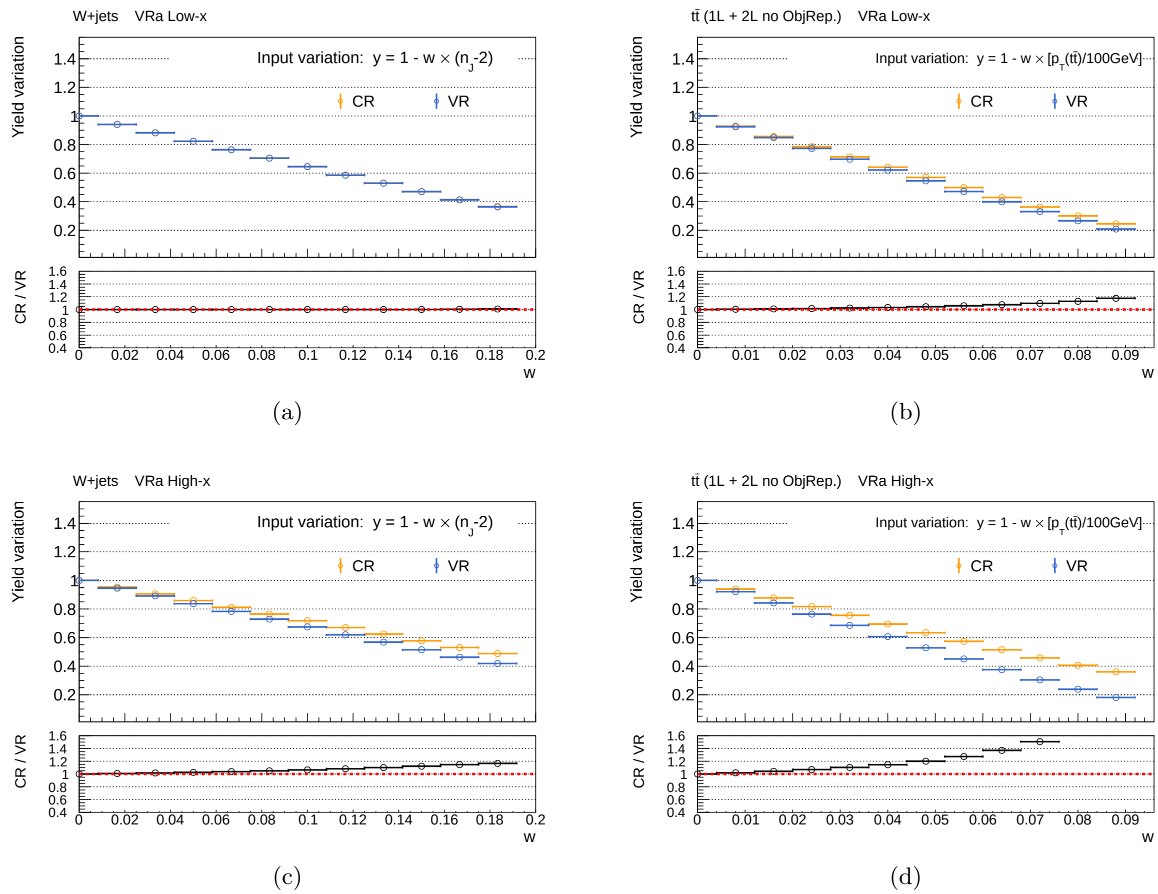

Figure D.1.7: Extrapolation error in VRa/CR (a)(b) Low-x, and (c)(d) High-x. B-tagging requirement is removed. Top pannels show the yield variation of $W+$jets (left) and $t\bar{t}$ (right) when injecting the variation by reweighting the MC with Eq. 7.1. Bottom rows are the relative difference in their response against the injected variation, namely the extrapolation errir. For the $t\bar{t}$ process, component estimated by the object replacement method is removed.

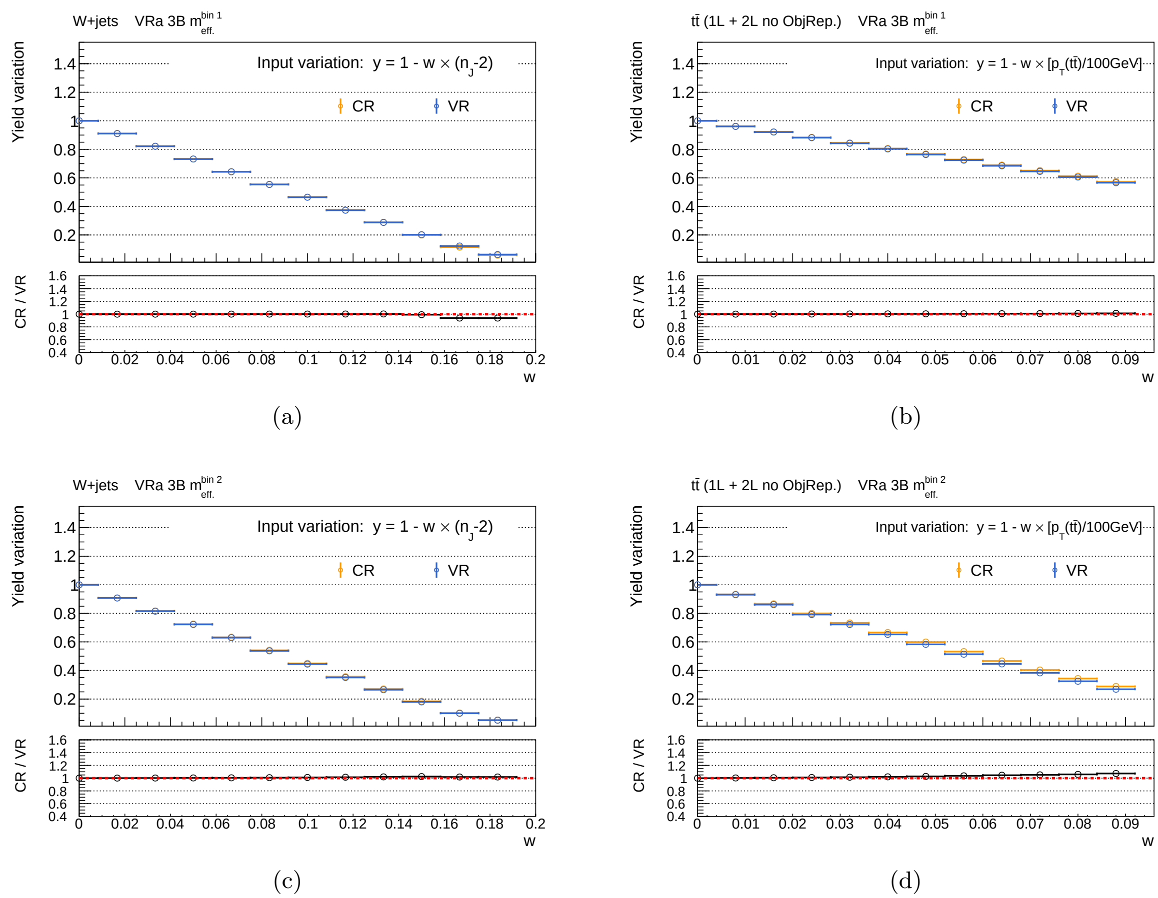

Figure D.1.8: Extrapolation error in VRa/CR 3B. B-tagging requirement is removed for W+jets. Top pannels show the yield variation of W+jets (left) and $t\bar{t}$ (right) when injecting the variation by reweighting the MC with Eq. 7.1. Bottom rows are the relative difference in their response against the injected variation, namely the extrapolation errir. For the $t\bar{t}$ process, component estimated by the object replacement method is removed.

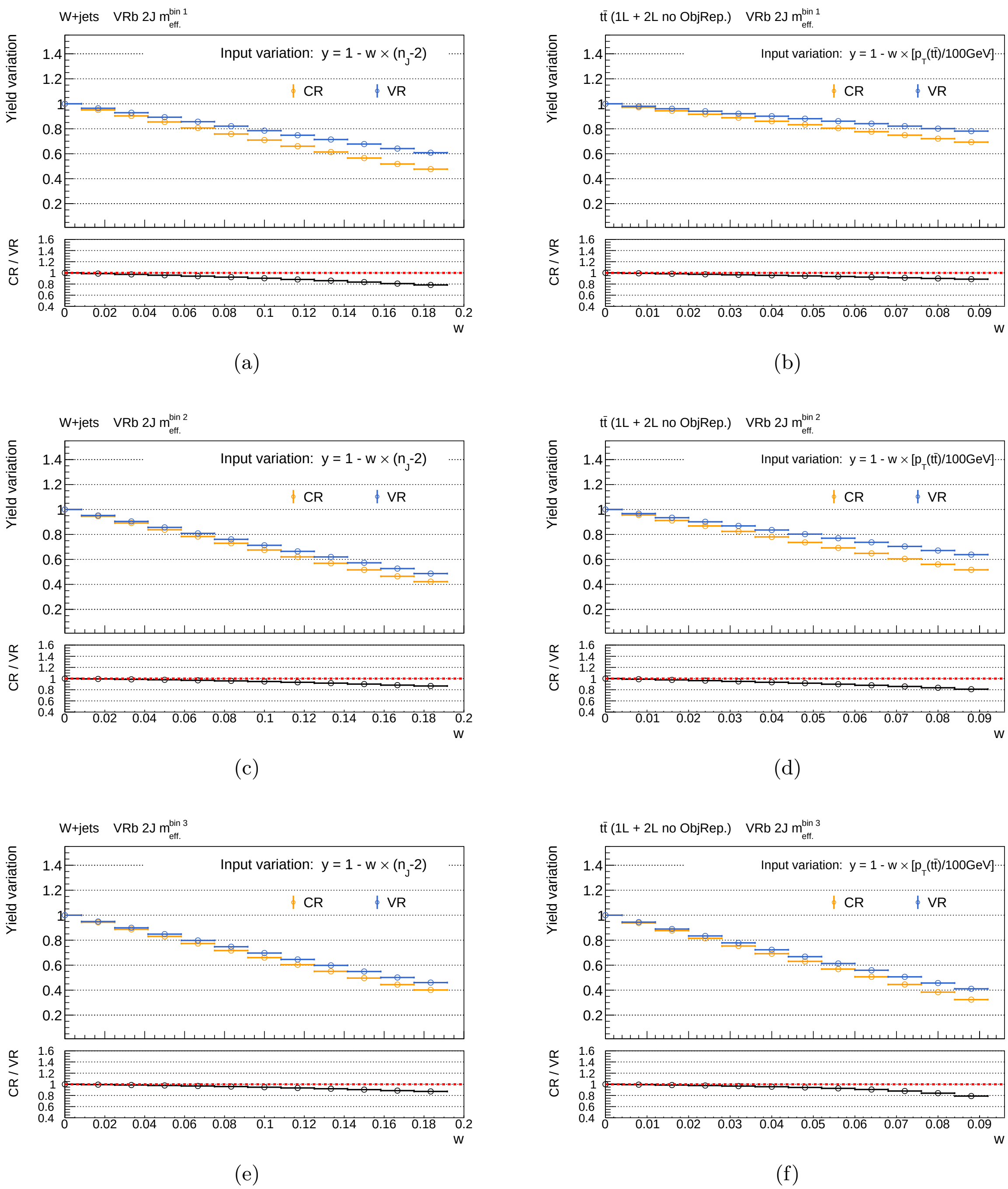

Figure D.1.9: Extrapolation error in VRb/CR 2J. B-tagging requirement is removed. Top pannels show the yield variation of (a) $W+$jets and (b) $t\bar{t}$ when injecting the variation by reweighting the MC with Eq. 7.1. Bottom rows are the relative difference in their response against the injected variation, namely the extrapolation errir. For the $t\bar{t}$ process, component estimated by the object replacement method is removed.

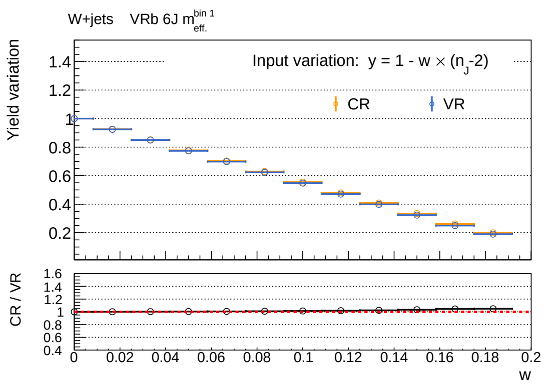

(a)

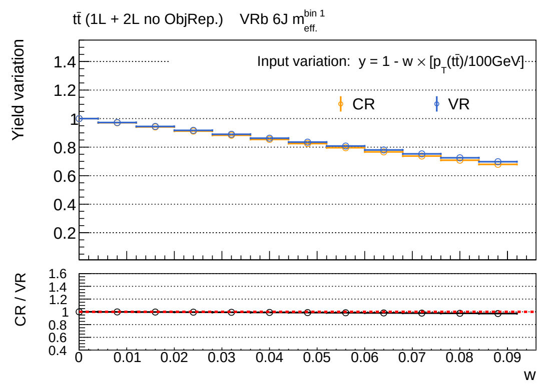

(b)

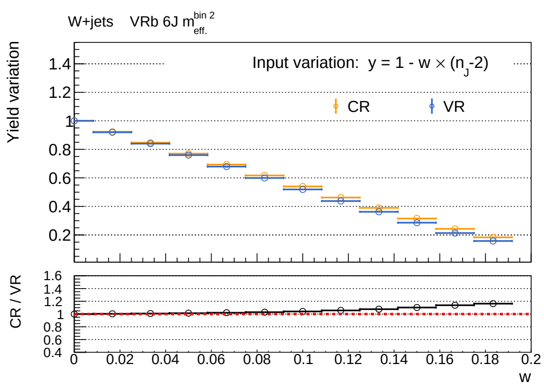

(c)

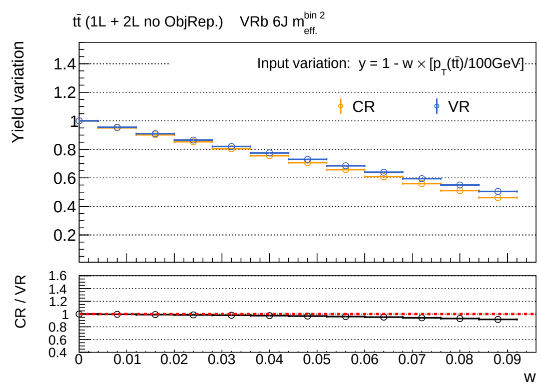

(d)

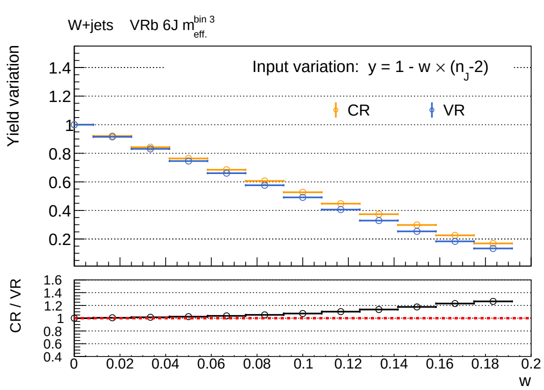

(e)

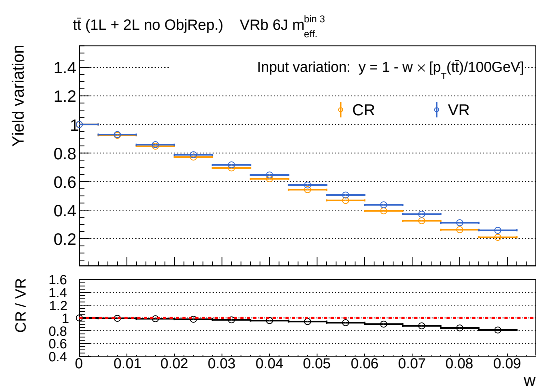

(f)

Figure D.1.10: Extrapolation error in VRb/CR 6J. B-tagging requirement is removed. Top pannels show the yield variation of (a) W+jets and (b) $t\bar{t}$ when injecting the variation by reweighting the MC with Eq. 7.1. Bottom rows are the relative difference in their response against the injected variation, namely the extrapolation errir. For the $t\bar{t}$ process, component estimated by the object replacement method is removed.

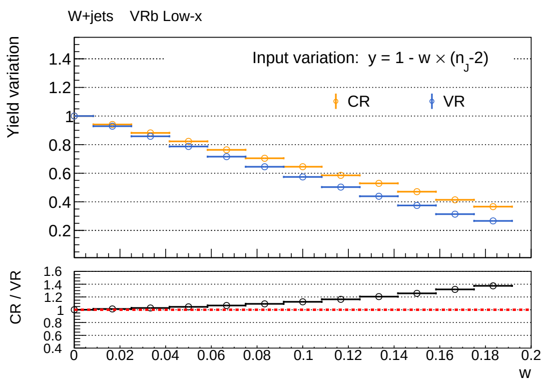

(a)

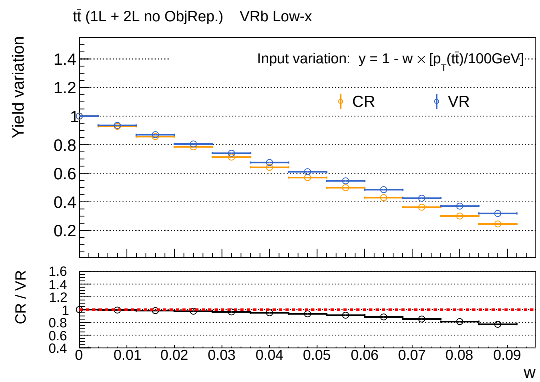

(b)

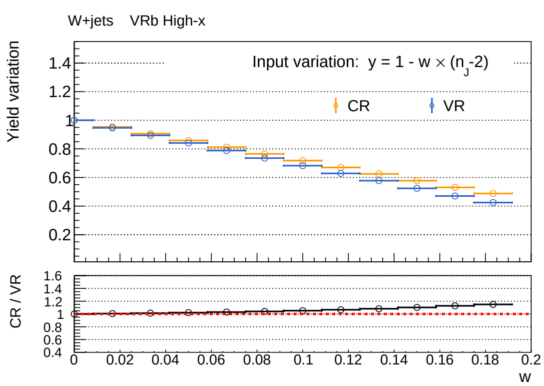

(c)

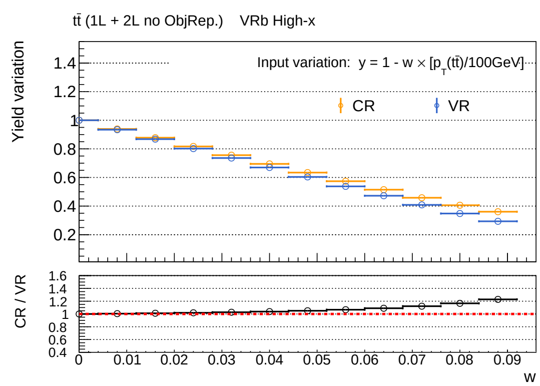

(d)

Figure D.1.11: Extrapolation error in VRb/CR (a)(b) Low-x, and (c)(d) High-x. B-tagging requirement is removed. Top pannels show the yield variation of $W+$jets (left) and $t\bar{t}$ (right) when injecting the variation by reweighting the MC with Eq. 7.1. Bottom rows are the relative difference in their response against the injected variation, namely the extrapolation errir. For the $t\bar{t}$ process, component estimated by the object replacement method is removed.

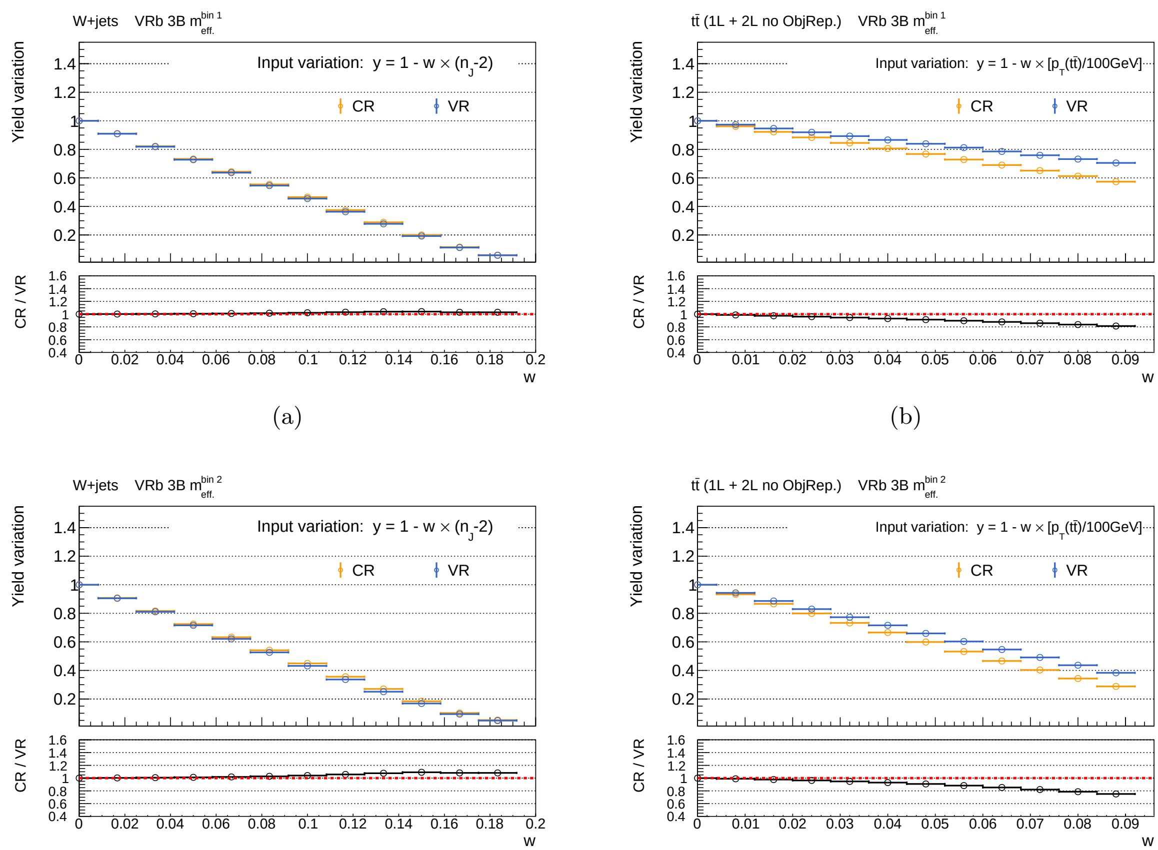

(a) (b) (c) (d)

Figure D.1.12: Extrapolation error in VRb/CR 3B. B-tagging requirement is removed for $W+\text{jets}$. Top pannels show the yield variation of $W+\text{jets}$ (left) and $t\bar{t}$ (right) when injecting the variation by reweighting the MC with Eq. 7.1. Bottom rows are the relative difference in their response against the injected variation, namely the extrapolation errir. For the $t\bar{t}$ process, component estimated by the object replacement method is removed.

E Auxiliary Materials for Result

E.1 Cross-check of Background Estimation by fully using the Kinematical Extrapolation

For cross-check of the background estimation, the SRs/VRs yields fully predicted by the kinematical extrapolation method are presented. The same normalization factors are obtained in Sec. 6.2.3 are used. Figure E.1.1-E.1.2 show the data pull with respect to the estimation in VRs and SRs respectively, and Figure E.1.3 summarized the post-fit uncertainties. For a direct comparison with the object replacement method, the estimated yields of the di-leptonic components ("Mis-Reco", "Mis-ID", "$\ell\tau_h''$") in VRs (SRs) are illustrated in Figure E.1.4 (E.1.5).

The results are fairly consistent with that shown in the main sections derived by a combination of the kinematical extrapolation and object replacement.

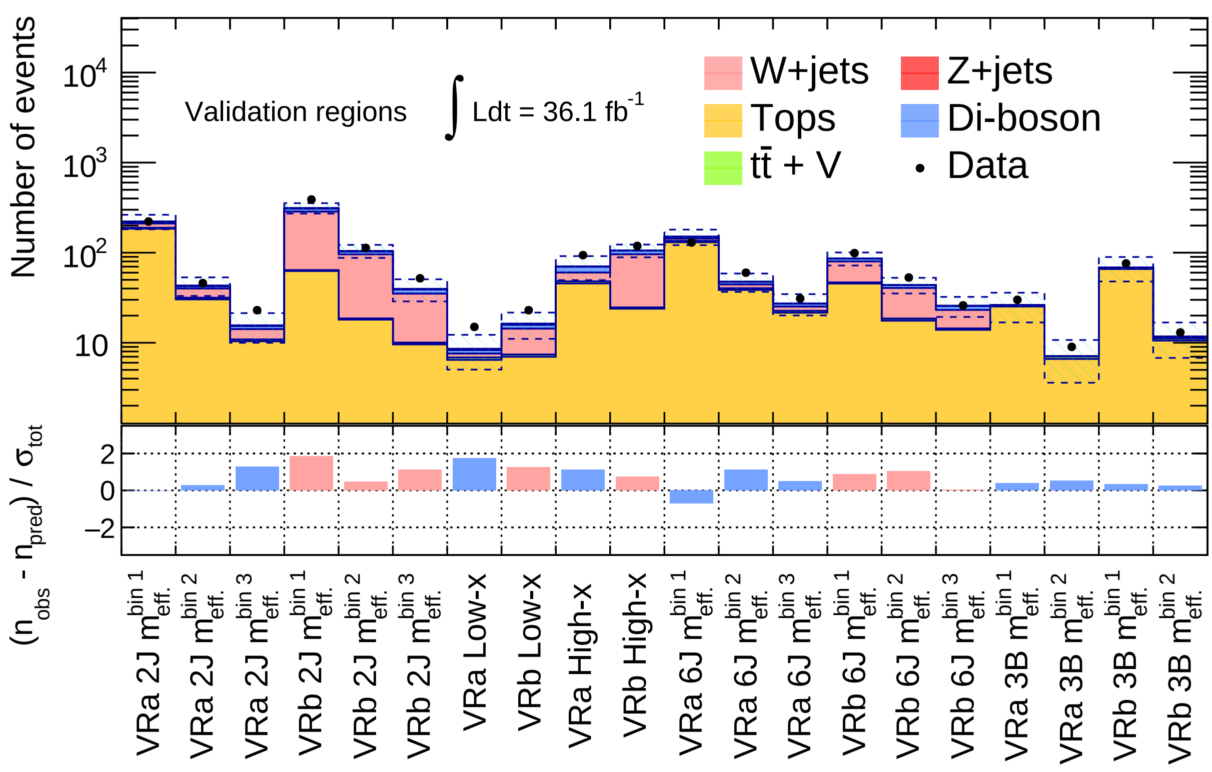

Figure E.1.1: (Top) Observed data and the estimated yields in the nominal validation regions (VRa/VRb). **All backgrounds all estimated by the kinematical extrapolation method.** The dashed band represents the combined statistical and systematic uncertainty on the total estimated backgrounds. (Bottom) Pull between the data and the estimation. Pulls in regions dominated by $W+$jets and tops are painted by pink and blue respectively.

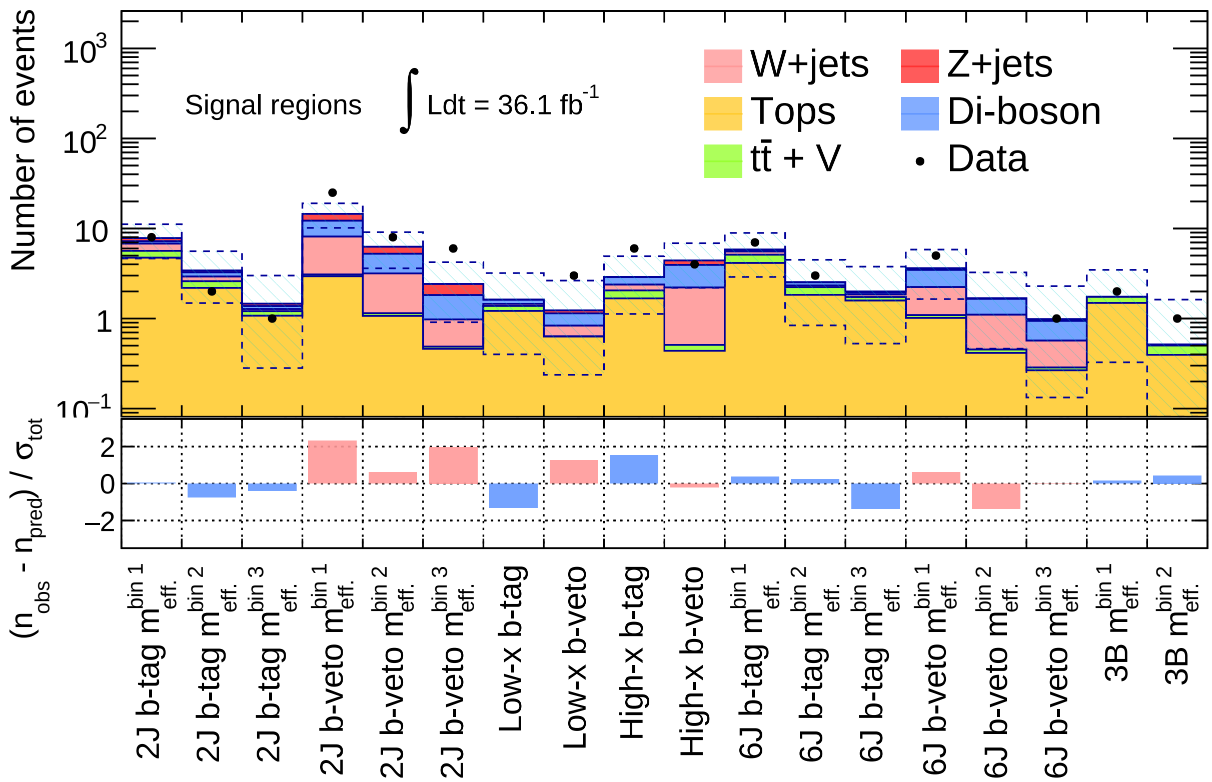

Figure E.1.2: (Top) Observed yields and the background expectation in signal regions. **All backgrounds all estimated by the kinematical extrapolation method.** The dashed band represents the combined statistical and systematic uncertainty on the total estimated backgrounds. (Bottom) Pull between the observed data and the expectation. No significant deviation from expectation exceeding 2σ.

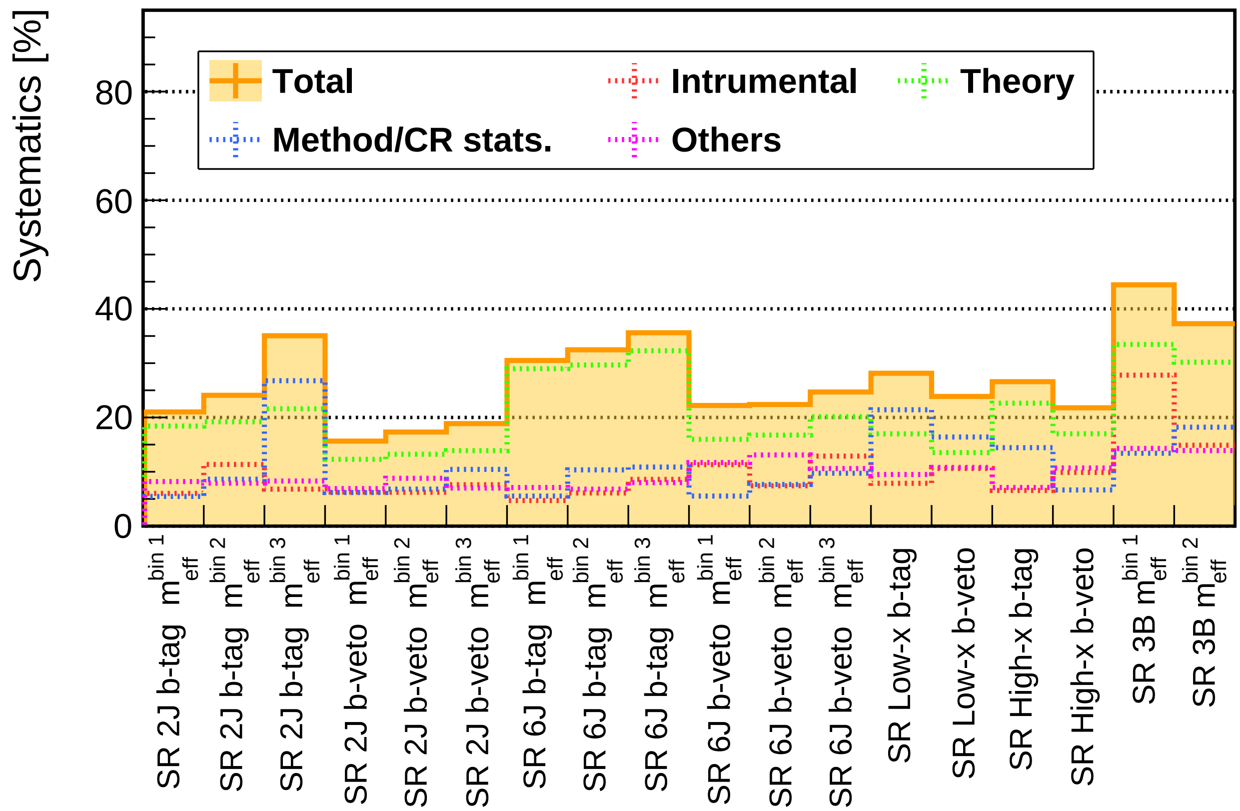

Figure E.1.3: Post-fit systematic uncertainty with respective to the expected yield in the signal regions. Total systematics uncertainty is shown by the filled orange histogram, and the breakdowns are by dashed lines. Total uncertainty is comparable with the case of the nominal estimation, though the leading source of the uncertainty is theory uncertainty here.

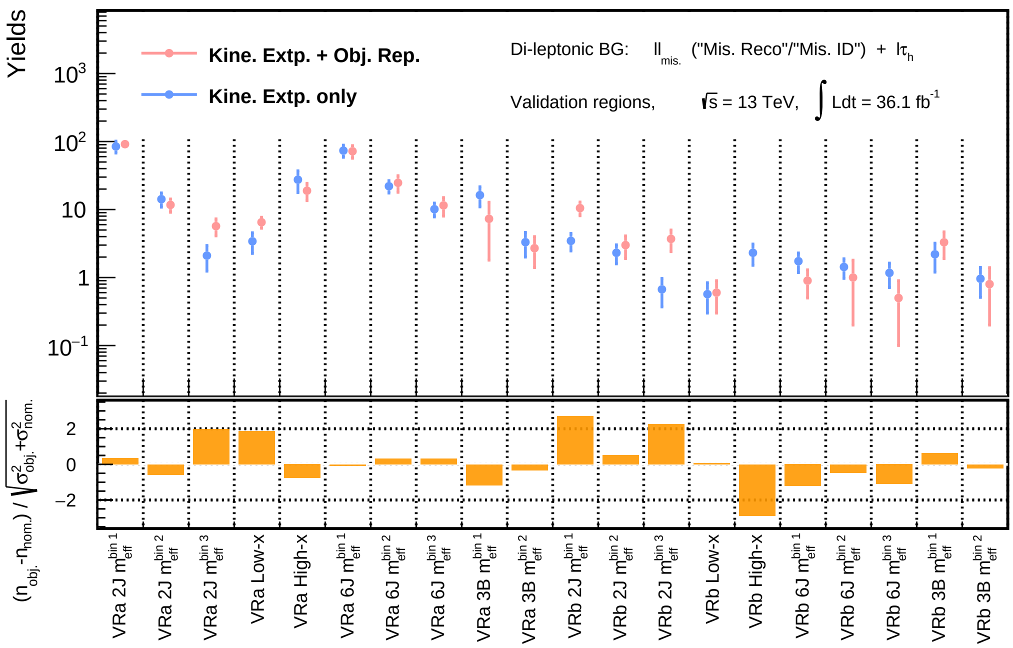

Figure E.1.4: (Top) Estimated yields of the di-leptonic components (“Mis-Reco”, “Mis-ID”, “$\ell\tau_h''$”) in VRs by the nominal method (pink) and the kinematical extrapolation method (blue). Error bars included both statistical and systematic uncertainty. (Bottom) Pull between the two estimations.

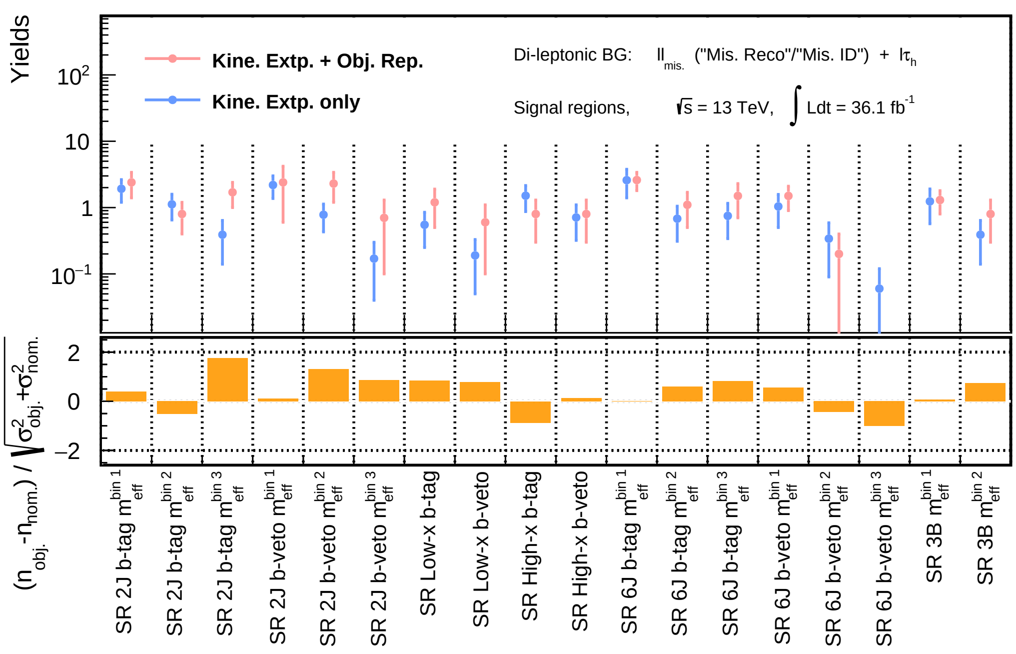

Figure E.1.5: (Top) Estimated yields of the di-leptonic components (“Mis-Reco”, “Mis-ID”, “$\ell\tau_h''$”) in SRs by the nominal method (pink) and the kinematical extrapolation method (blue). Error bars included both statistical and systematic uncertainty. (Bottom) Pull between the two estimations.

Bibliography

[1] Michael Peskin and David V. Schröder. An introduction to Quantum Filed Theory. Westview Press, Boulder, CO, 1995.

[2] Francis Halzen and Alan. D. Martin. Quarks & Leptons: An Introductory Course in Modern Particle Physics. Wiley; 1st edition, 1984.

[3] François Englert and Robert Brout. Broken symmetry and the mass of gauge vector mesons. Physical Review Letters, 13(9):321, 1964.

[4] Peter W Higgs. Broken symmetries, massless particles and gauge fields. Physics Letters, 12(2):132–133, 1964.

[5] J. C. Ward. An Identity in Quantum Electrodynamics. Physical Review, 78(2):182–182, 1950.

[6] Y. Takahashi. On the generalized ward identity. Il Nuovo Cimento, 6(2):371–375, 1957.

[7] G. 'tHooft and M. Veltman. Regulariation and Renormalization of Gauge Fields. Nuclear Physics B, 44:189–213, 1972.

[8] Sheldon L Glashow. Partial-symmetries of weak interactions. Nuclear Physics, 22(4):579–588, 1961.

[9] Steven Weinberg. A model of leptons. Physical review letters, 19(21):1264, 1967.

[10] Abdus Salam and John Clive Ward. Electromagnetic and weak interactions. Physics Letters, 13(2):168–171, 1964.

[11] Tsung-Dao Lee and Chen-Ning Yang. Question of parity conservation in weak interactions. Physical Review, 104(1):254, 1956.

[12] Chien-Shiung Wu, Ernest Ambler, RW Hayward, DD Hoppes, and R Pl Hudson. Experimental test of parity conservation in beta decay. Physical review, 105(4):1413, 1957.

[13] Makoto Kobayashi and Toshihide Maskawa. CP-Violation in the Renormalizable Theory of Weak Interaction. Progress of Theoretical Physics, 49(2):652–657, 1973.

[14] ATLAS Collaboration. Observation of a new particle in the search for the Standard Model Higgs boson with the ATLAS detector at the LHC. Physics Letters, Section B: Nuclear, Elementary Particle and High-Energy Physics, 716(1):1–29, 2012.

[15] CMS Collaboration. Observation of a new boson at a mass of 125 GeV with the CMS experiment at the LHC. Physics Letters, Section B: Nuclear, Elementary Particle and High-Energy Physics, 716(1):30–61, 2012.

[16] Atlas Collaboration et al. Evidence for the spin-0 nature of the higgs boson using atlas data. Physics Letters B, 726(1):120–144, 2013.

[17] Vardan Khachatryan, AM Sirunyan, Armen Tumasyan, Wolfgang Adam, Thomas Bergauer, M Dragicevic, J Erö, M Friedl, R Frühwirth, VM Ghete, et al. Constraints on the spin-parity and anomalous h v v couplings of the higgs boson in proton collisions at 7 and 8 tev. Physical Review D, 92(1):012004, 2015.

[18] ATLAS Collaboration. Measurements of the Higgs boson production and decay rates and coupling strengths using pp collision data at S=7 and 8 TeV in the ATLAS experiment. European Physical Journal C, 76(1):1–51, 2016.

[19] CMS Collaboration. Precise determination of the mass of the Higgs boson and tests of compatibility of its couplings with the standard model predictions using proton collisions at 7 and 8 TeV. European Physical Journal C, 75(5), 2015.

[20] Steven Weinberg. Implications of dynamical symmetry breaking. Physical Review D, 13(4):974, 1976.

[21] Steven Weinberg. Implications of dynamical symmetry breaking: an addendum. Physical Review D, 19(4):1277, 1979.

[22] Eldad Gildener. Gauge-symmetry hierarchies. Physical Review D, 14(6):1667, 1976.

[23] Leonard Susskind. Dynamics of spontaneous symmetry breaking in the weinberg-salam theory. Physical Review D, 20(10):2619, 1979.

[24] Stephen P. Martin. A Supersymmetry Primer. Adv. Ser. Direct. High Energy Phys, 21(515), 1997.

[25] Vera C Rubin and W Kent Ford Jr. Rotation of the andromeda nebula from a spectroscopic survey of emission regions. The Astrophysical Journal, 159:379, 1970.

[26] Vera C Rubin, W Kent Ford Jr, and Norbert Thonnard. Rotational properties of 21 sc galaxies with a large range of luminosities and radii, from ngc 4605/r= 4kpc/to ugc 2885/r= 122 kpc. The Astrophysical Journal, 238:471–487, 1980.

[27] Prateek Agrawal, Francis-Yan Cyr-Racine, Lisa Randall, and Jakub Scholtz. Make dark matter charged again. Journal of Cosmology and Astroparticle Physics, 5(22), 2017.

[28] C. L. Bennett, D. Larson, J. L. Weiland, N. Jarosik, G. Hinshaw, N. Odegard, K. M. Smith, R. S. Hill, B. Gold, M. Halpern, E. Komatsu, M. R. Nolta, L. Page, D. N. Spergel, E. Wollack, J. Dunkley, A. Kogut, M. Limon, S. S. Meyer, G. S. Tucker, and E. L. Wright. Nine-Year Wilkinson Microwave Anisotropy Probe (WMAP) Observations: Final Maps and Results. The Astrophysical Journal Supplement Series, 208(20), 2012.

[29] Planck Collaboration. Astrophysics Special feature Planck 2015 results. Astronomy & Astrophysics, 594(A13), 2016.

[30] GF Giudice and R Rattazzi. Theories with gauge mediated supersymmetry breaking, phys. rept. 322 (1999) 419–499. arXiv preprint hep-ph/9801271, 89.

[31] Gian F Giudice, Riccardo Rattazzi, Markus A Luty, and Hitoshi Murayama. Gaugino mass without singlets. Journal of High Energy Physics, 1998(12):027, 1999.

[32] Lisa Randall and Raman Sundrum. Out of this world supersymmetry breaking. Nuclear Physics B, 557(1-2):79–118, 1999.

[33] Julius Wess and Jonathan Bagger. Supersymmetry and supergravity. Princeton university press, 1992.

[34] H Nishino, S Clark, K Abe, Y Hayato, T Iida, M Ikeda, J Kameda, K Kobayashi, Y Koshio, M Miura, et al. Search for proton decay via $p \to e^+\pi_0$ and $p \to \mu^+\pi_0$ in a large water cherenkov detector. Physical Review Letters, 102(14):141801, 2009.

[35] Lawrence J Hall, David Pinner, and Joshua T Ruderman. A natural susy higgs near 125 gev. Journal of High Energy Physics, 2012(4):131, 2012.

[36] N. Arkani-Hamed, A. Delgado, and G.F. Giudice. The Well-Tempered Neutralino. Nuclear Physics B, 741(1-2):108–130, 2006.

[37] Howard Baer, Tadas Krupovnickas, Azar Mustafayev, Eun-Kyung Park, Stefano Profumo, and Xerxes Tata. Exploring the BWCA (Bino-Wino Co-Annihilation) Scenario for Neutralino Dark Matter. Journal of High Energy Physics, 2005(11), 2005.

[38] Joseph Bramante, Nishita Desai, Patrick Fox, Adam Martin, Bryan Ostdiek, and Tilman Plehn. Towards the final word on neutralino dark matter. Physical Review D, 93(6), 2016.

[39] ATLAS Collaboration. Summary plots from the ATLAS Supersymmetry physics group. https://atlas.web.cern.ch/Atlas/GROUPS/PHYSICS/CombinedSummaryPlots/SUSY/index.html, 2017.

[40] CMS Collaboration. CMS Supersymmetry Physics Results. https://twiki.cern.ch/twiki/bin/view/CMSPublic/PhysicsResultsSUS, 2017.

[41] ATLAS Collaboration. Search for electroweak production of supersymmetric particles in the two and three lepton final state at $\sqrt{s} = 13$ TeV with the ATLAS detector. CONF-SUSY, 2017-039, 2017.

[42] CMS Collaboration. Search for electroweak production of charginos and neutralinos in multilepton final states in pp collision data at $\sqrt{s} = 13$ TeV. CMS PAS SUS, 16-039, 2017.

[43] ATLAS Collaboration. Search for long-lived charginos based on a $\sqrt{s} = 13$ TeV with the ATLAS detector. ATLAS-CONF, 2017-017, 2017.

[44] CMS Collaboration. Search for disappearing tracks in proton-proton collisions at $\sqrt{s} = 8$ TeV. Journal of High Energy Physics, 2015(96), 2015.

[45] LEP2 SUSY Working Group. Combined LEP Chargino Results, up to 208 GeV for low DM. http://lepsusy.web.cern.ch/lepsusy/www/inoslowdmsummer02/charginolowdm_pub.html, 2002.

[46] Wim Beenakker, R Höpker, Michael Spira, and PM Zerwas. Squark and gluino production at hadron colliders. Nuclear Physics B, 492(1-2):51–103, 1997.

[47] C. Patrignani et al. (Particle Data Group). Review of Particle Physics. Chinese Physics C, 40(10):100001, 2016.

[48] ATLAS Collaboration. The simulation principle and performance of the ATLAS fast calorimeter simulation FastCaloSim. ATL-PHYS-PUB-2010-013, 2010.

[49] Lyndon Evans and Philip Bryant. LHC Machine. Journal of Instrumentation, 3(08):S08001, 2008.

[50] ATLAS Collaboration. The ATLAS Experiment at the CERN Large Hadron Collider. J. Instrum., 3:S08003, 2008.

[51] CMS Collaboration. The CMS experiment at the CERN LHC. J. Instrum., 3(S08004):285, 2008.

[52] ALICE Collaboration. The ALICE experiment at the CERN LHC. J. Instrum., 3(S08002), 2008.

[53] ATLAS Collaboration. The LHCb Detector at the LHC. Journal of Instrumentation, 3(08):S08005–S08005, 2008.

[54] CERN. CERN Media Archive Photo. https://mediastream.cern.ch/MediaArchive/Photo/Public/2008/0812015 A4-at-144-dpi.jpg.

[55] ATLAS Collaboration. ATLAS Data Preparation Summary 2016. https://atlas.web.cern.ch/Atlas/GROUPS/DATAPREPARATION/DataSummary/2016/.

[56] ATLAS Collaboration. ATLAS Luminosity Public Results Run2. https://twiki.cern.ch/twiki/bin/view/AtlasPublic/LuminosityPublicResultsRun2.

[57] ATLAS Collaboration. ATLAS detector and physics performance: Technical Design Report, 1. Technical report, CERN, 1999.

[58] ATLAS Collaboration. Studies of the performance of the ATLAS detector using cosmic-ray muons. Eur. Phys. J. C, 71(1593), 2011.

[59] ATLAS Collaboration. ATLAS TRT Public Result. https://twiki.cern.ch/twiki/bin/view/AtlasPublic/TRTPublicResults.

[60] ATLAS Collaboration. Liquid Argon Technical Design Report, CERN-LHCC-96-041. Technical report, CERN, 1996.

[61] ATLAS Collaboration. Tile Calorimeter Technical Design Report, CERNLHCC-96-042. Technical report, CERN, 1996.

[62] Simon van der Meer. Calibration of the Efffective Beam Hight in the ISR. Technical report, CERN, 1968.

[63] ATLAS Collaboration. Improved luminosity determination in pp collisions at $\sqrt{s} = 7$ TeV using the ATLAS detector at the LHC. Eur. Phys. J. C, 73(8):2–39, 2013.

[64] ATLAS Collaboration. Performance of the ATLAS Trigger System in 2015. Eur. Phys. J. C, 77(317), 2017.

[65] ATLAS Collaboration. ATLAS Trigger operation public results. https://twiki.cern.ch/twiki/bin/view/AtlasPublic/TriggerOperationPublicResults.

[66] ATLAS Collaboration. The Optimization of ATLAS Track Reconstruction in Dense Environments. ATL-PHYS-PUB, 2015-006, 2015.

[67] Azriel Osenfeld and John Pfaltz L. Sequential Operations in Digital Picture Processing. Journal of the ACM, 13(4):471–494, 1966.

[68] ATLAS Collaboration. A neural network clustering algorithm for the ATLAS silicon pixel detector. J. Instrum., 9(P09009), 2014.

[69] Giuseppe Cerati, Peter Elmer, and Steven Lantz. Advances in tracking and trigger concepts. In International Conference on Computing in High Enegy and Nuclear Physics, 2008.

[70] ATLAS Collaboration. Performance of primary vertex reconstruction in proton-proton collisions at $\sqrt{s} = 7$ TeV in the ATLAS experiment. ATLAS-CONF, 2010-069, 2010.

[71] ATLAS Collaboration. Performance of the ATLAS Inner Detector Track and Vertex Reconstruction in the High Pile-Up LHC Environment. ATLAS-CONF, 2012-042, 2012.

[72] Wolfgang Waltenberger, Rudolf Frühwirth, and Pascal Vanlaer. Adaptive vertex fitting. J. Phys. G: Nucl. Part. Phys., 34:343–356, 2007.

[73] ATLAS Collaboration. Topological cell clustering in the ATLAS calorimeters and its performance in LHC Run1. CERN-PH-EP, 2015-304, 2016.

[74] ATLAS Collaboration. Electron efficiency measurements with the ATLAS detector using the 2015 LHC proton-proton collision data. ATLAS-CONF, 2016-024, 2016.

[75] ATLAS Collaboration. Improved electron reconstruction in ATLAS using the Gaussian Sum Filter-based model for bremsstrahlung. ATLAS-CONF, 2012-047, 2012.

[76] ATLAS Collaboration. Electron and photon energy calibration with the ATLAS detector using LHC Run 1 data. Eur. Phys. J. C, 74(3071), 2013.

[77] Nencki Neyman and E. S. Pearson. On the Problem of the most Efficient Tests of Statistical Hypotheses. Philosophical Transactions of the Royal Society of London Series A, 231(289), 1933.

[78] ATLAS Collaboration. Electron and photon energy calibration with the ATLAS detector using data collected in 2015 at $\sqrt{s} = 13$ TeV. ATLAS-PHYS-PUB, 2016-015, 2016.

[79] ATLAS Collaboration. Measurement of the muon reconstruction performance of the Measurement of the muon reconstruction performance of the ATLAS detector using 2011 and 2012 LHC proton proton collision data. CERN-PH-EP, 2014-151, 2014.

[80] ATLAS Collaboration. Muon reconstruction performance of the ATLAS detector in proton-proton collision data at $\sqrt{s} = 13$ TeV. Eur. Phys. J. C, 76(292), 2016.

[81] Matteo Cacciari, Gavin P. Salam, and Gregory Soyez. The anti-kt jet clustering algorithm. Journal of High Energy Physics, 2008(63), 2008.

[82] ATLAS Collaboration. Jet energy scale measurements and their systematic uncertainties in protonproton collisions at $\sqrt{s} = 13$ TeV with the ATLAS detector. ATLAS-PHYS-PUB, 2015-015, 2017.

[83] ATLAS Collaboration. Jet energy measurement and its systematic uncertainty in protonproton collisions at $\sqrt{s} = 7$ TeV with the ATLAS detector. Eur. Phys. J. C, 75(17), 2015.

[84] Matteo Cacciari and Gavin P Salam. Pileup subtraction using jet areas. Physics Letters B, 659(1-2):119–126, 2007.

[85] Gavin P Salam. Towards Jetography. Eur. Phys. J. C, 67(3-4):637–686, 2010.

[86] ATLAS Collaboration. Jet energy measurement with the ATLAS detector in proton-proton collisions at $\sqrt{s} = 7$ TeV. Eur. Phys. J. C, 73(2304), 2013.

[87] ATLAS Collaboration. Expected performance of the ATLAS b-tagging algorithms in Run-2. ATL-PHYS-PUB, 2015-022, 2015.

[88] ATLAS Collaboration. Optimisation of the ATLAS b-tagging performance for the 2016 LHC Run. ATL-PHYS-PUB, 2016-012, 2016.

[89] ATLAS Collaboration. Performance of b-jet identification in the ATLAS experiment. Journal of Instrumentation, 11(04):P04008–P04008, 2016.

[90] ATLAS Collaboration. Commissioning of the ATLAS high-performance b-tagging algorithms in the 7 TeV collision data. Europhysics Conference on High Energy Physics, 2011.

[91] Giovanni Pauletta, Franco Simonetto, and Mariusz Witek. A new inclusive secondary vertex algorithm for b-jet tagging in ATLAS. International Conference on Computing in High Enegy and Nuclear Physics, 2008.

[92] ATLAS Collaboration. Tagging and suppression of pileup jets with the ATLAS detector. ATLAS-CONF, 2014-018, 2014.

[93] C. W. Miller, A. Schwartzman, and D. Su. Jet-Vertex Association Algorithm. ATL-COM-PHYS, 2008-008, 2008.

[94] ATLAS Collaboration. Performance of missing transverse momentum reconstruction with the ATLAS detector in the first proton-proton collisions at $\sqrt{s} = 13$ TeV. ATL-PHYS-PUB, 2015-027(July), 2015.

[95] ATLAS Collaboration. Missing Transverse Momentum Distribution and Performance in 2016 data. https://atlas.web.cern.ch/Atlas/GROUPS/PHYSICS/PLOTS/JETM-2016-008/, 2016.

[96] Andy Buckley, Jonathan Butterworth, Stefan Gieseke, David Grellscheid, Stefan Höche, Hendrik Hoeth, Frank Krauss, Leif Lönnblad, Emily Nurse, Peter Richardson, Steffen Schumann, Michael H. Seymour, Sjöstrand Torbjörn, Peter Skands, and Webber Bryan. General-purpose event generators for LHC physics. Physics Reports, 504(5):145–233, 2011.

[97] Peter Skands. QCD for Collider Physics. CERN-TH, 2011-080, 2011.

[98] Constantia Alexandrou. Parton Distribution Functions from Lattice QCD. Few-Body Systems, 57(8):621–626, 2016.

[99] Jon Butterworth, Stefano Carrazza, Amanda Cooper-Sarkar, Albert De Roeck, Joël Feltesse, Stefano Forte, Jun Gao, Sasha Glazov, Joey Huston, Zahari Kassabov, Ronan McNulty, Andreas Morsch, Pavel Nadolsky, Voica Radescu, Juan Rojo, and Robert Thorne. PDF4LHC recommendations for Run II. J. Phys. G: Nucl. Part. Phys., 43(023001), 2016.

[100] Richard D. Ball, Valerio Bertone, Stefano Carrazza, Christopher S. Deans, Luigi Del Debbio, Stefano Forte, Alberto Guffanti, Nathan P. Hartland, José I. Latorre, Juan Rojo, and Maria Ubiali. Parton distributions for the LHC run II. Journal of High Energy Physics, 2015(40), 2015.

[101] Sayipjamal Dulat, Tie Jiun Hou, Jun Gao, Marco Guzzi, Joey Huston, Pavel Nadolsky, Jon Pumplin, Carl Schmidt, Daniel Stump, and C. P. Yuan. New parton distribution functions from a global analysis of quantum chromodynamics. Physical Review D, 93(033006), 2016.

[102] A. D. Martin, W. J. Stirling, R. S. Thorne, and G. Watt. Heavy-quark mass dependence in global PDF analyses and 3- and 4-flavour parton distributions. Eur. Phys. J. C, 70(1):51–72, 2010.

[103] Y. L. Dokshitzer. Calculation of the Structure Functions for Deep Inelastic Scattering and e+ e- Annihilation by Perturbation Theory in Quantum Chromodynamics. Sov. Phys. JETP, 46(641), 1977.

[104] V. N. Gribov Lipatov and L. N. Deep inelastic e-p scattering in perturbation theory. Sov. J. Nucl. Phys., 15(Yad. Fiz.15,781):438, 1972.

[105] G. Altarelli and G. Parisi. Asymptotic freedom in parton language. Nuclear Physics B, 126(2):298–318, 1977.

[106] V. V. Sudakov. Vertex parts at very high-energies in quantum electrodynamics. Sov. Phys. JETP, 3(65), 1965.

[107] S. Catani, F. Krauss, R. Kuhn, and B. R. Webber. QCD Matrix Elements + Parton Showers. Journal of High Energy Physics, 2001(63), 2001.

[108] M.Worek J. Alwall, S. Höche, F. Krauss, N. Lavesson, L. Lönnblad, F.Maltoni, M.L.Mangano, M.Moretti, C.G. Papadopoulos, F. Piccinini, S. Schumann, M. Treccani, J.Winter. Comparative study of various algorithms for the merging of parton showers and matrix elements in hadronic collisions. Eur. Phys. J. C, 53:473–500, 2008.

[109] B. Andersson, G. Gustafson, G. Ingelman, and T. Sjöstrand. Parton fragmentation and string dynamics. Physics Reports, 97(2-3):31–145, 1983.

[110] Richard D. Ball et al. Parton distributions for the LHC Run II. JHEP, 04:040, 2015.

[111] Hung-Liang Lai, Marco Guzzi, Joey Huston, Zhao Li, Pavel M. Nadolsky, Jon Pumplin, and C. P. Yuan. New parton distributions for collider physics. Phys. Rev., D82:074024, 2010.

[112] J. Alwall, R. Frederix, S. Frixione, V. Hirschi, F. Maltoni, O. Mattelaer, H. S. Shao, T. Stelzer, P. Torrielli, and M. Zaro. The automated computation of tree-level and next-to-leading order differential cross sections, and their matching to parton shower simulations. JHEP, 07:079, 2014.

[113] T. Gleisberg, Stefan. Höche, F. Krauss, M. Schönherr, S. Schumann, et al. Event generation with SHERPA 1.1. JHEP, 02:007, 2009.

[114] Simone Alioli, Paolo Nason, Carlo Oleari, and Emanuele Re. A general framework for implementing NLO calculations in shower Monte Carlo programs: the POWHEG BOX. JHEP, 06:043, 2010.

[115] Torbjorn Sjöstrand, Stephen Mrenna, and Peter Z. Skands. A Brief Introduction to PYTHIA 8.1. Comput.Phys.Commun., 178:852–867, 2008.

[116] Torbjorn Sjöstrand, Stephen Mrenna, and Peter Z. Skands. PYTHIA 6.4 Physics and Manual. JHEP, 05:026, 2006.

[117] W. Beenakker, R. Hopker, M. Spira, and P.M. Zerwas. Squark and gluino production at hadron colliders. Nucl. Phys. B, 492:51–103, 1997.

[118] A. Kulesza and L. Motyka. Threshold resummation for squark-antisquark and gluino-pair production at the LHC. Phys. Rev. Lett., 102:111802, 2009.

[119] A. Kulesza and L. Motyka. Soft gluon resummation for the production of gluino-gluino and squark-antisquark pairs at the LHC. Phys. Rev. D, 80:095004, 2009.

[120] Wim Beenakker et al. Soft-gluon resummation for squark and gluino hadroproduction. JHEP, 12:041, 2009.

[121] W. Beenakker et al. Squark and gluino hadroproduction. Int. J. Mod. Phys. A, 26:2637–2664, 2011.

[122] Ryan Gavin, Ye Li, Frank Petriello, and Seth Quackenbush. FEWZ 2.0: A code for hadronic Z production at next-to-next-to-leading order. Comput. Phys. Commun., 182:2388–2403, 2011.

[123] Michal Czakon and Alexander Mitov. Top++: A Program for the Calculation of the Top-Pair Cross-Section at Hadron Colliders. Comput. Phys. Commun., 185:2930, 2014.

[124] Nikolaos Kidonakis. Two-loop soft anomalous dimensions for single top quark associated production with a W- or H-. Phys.Rev. D, 82:054018, 2010.

[125] P. Kant, O. M. Kind, T. Kintscher, T. Lohse, T. Martini, S. Mlbitz, P. Rieck, and P. Uwer. HATHOR for single top-quark production: Updated predictions and uncertainty estimates for single top-quark production in hadronic collisions. Comput. Phys. Commun., 191:74–89, 2015.

[126] ATLAS Collaboration. Multi-Boson Simulation for 13 TeV ATLAS Analyses. ATL-PHYS-PUB-2016-002, 2016.

[127] Achilleas Lazopoulos, Thomas McElmurry, Kirill Melnikov, and Frank Petriello. Next-to-leading order QCD corrections to $t\bar{t}Z$ production at the LHC. Phys. Lett., B666:62–65, 2008.

[128] John M. Campbell and R. Keith Ellis. $t\bar{t}W^{+-}$ production and decay at NLO. JHEP, 07:052, 2012.

[129] ATLAS Collaboration. Summary of ATLAS Pythia 8 tunes. ATL-PHYS-PUB-2012-003, 2012.

[130] ATLAS Collaboration. The ATLAS Simulation Infrastructure. Eur. Phys. J. C, 70:823–874, 2010.

[131] S. Agostinelli et al. GEANT4: A Simulation toolkit. Nucl. Instrum. Meth. A, 506:250–303, 2003.

[132] ATLAS Collaboration. Selection of jets produced in 13 TeV proton-proton collisions with the ATLAS detector. ATLAS-CONF, 2015-029, 2015.

[133] J M Campbell, M A Cullen, and E W N Glover. Four jet event shapes in electron-positron annihilation. Eur. Phys. J. C, 9(2):245–265, 1999.

[134] Michael L. Graesser and Jessie Shelton. Hunting mixed top squark decays. Physical Review Letters, 111(121802), 2013.

[135] Stanisław Jadach, Johann H. Kühn, and Zbigniew Was. TAUOLA - a library of Monte Carlo programs to simulate decays of polarized tau leptons. Computer Physics Communications, 64(2):275–299, 1991.

[136] P. Golonka, B. Kersevan, T. Pierzchała, E. Richter-Was, Z. Was, and M. Worek. The tauola-photos-F environment for the TAUOLA and PHOTOS packages, release II. Computer Physics Communications, 174(10):818–835, 2006.

[137] N. Davidson, G. Nanava, T. Przedziński, E. Richter-Was, and Z. Was. Universal interface of TAUOLA: Technical and physics documentation. Computer Physics Communications, 183(3):821–843, 2012.

[138] C. G. Lester and D. J. Summers. Measuring masses of semi-invisibly decaying particles pair produced at hadron colliders. Physics Letters B, (June):8, 1999.

[139] ATLAS Collaboration. Measurement of the inclusive W and Z/γ^* cross sections in the e and μ decay channels in pp collisions at $\sqrt{s} = 7$ TeV with the ATLAS detector. Physical Review D, 85(7):072004, 2012.

[140] J.M. Butterworth; E. Dobson; U. Klein; B.R. Mellado Garcia; T. Nunnemann; J. Qian; D. Rebuzzi; R.Tanaka;. Single Boson and Diboson Production Cross Sections. ATL-COM-PHYS, 2010-695, 2010.

[141] F James and M Roos. MINUIT A SYSTEM FOR FUNCTION MINIMIZATION AND ANALYSIS LONG WRITE-UP I . Introduction A large class of problems in many different fields of research can be reduced to the problem of finding the smallest value taken on by a function of one or more variable. Computer Physics Communications, 10:343–367, 1975.

[142] M Baak, G J Besjes, D Côté, A Koutsman, J Lorenz, and D Short. HistFitter software framework for statistical data analysis. Eur. Phys. J. C, 75(153), 2015.

[143] K. Cranmer, George Lewis, Lorenzo Moneta, Akira Shibata, and Wouter Verkerke. HistFactory; A tool for creating statistical models for use with RooFit and RooStats. Technical report, 2012.

[144] Wouter Verkerke and David Kirkby. The RooFit toolkit for data modeling. Technical report, 2016.

[145] Abraham Wald. Tests of Statistical Hypotheses Concerning Several Parameters When the Number of Observations is Large. American Mathematical Society,, 54(3):426–482, 2017.

[146] Glen Cowan, Kyle Cranmer, Eilam Gross, and Ofer Vitells. Asymptotic formulae for likelihood-based tests of new physics. Eur. Phys. J. C, 71(1554), 2011.

[147] ATLAS Collaboration. Search for squarks and gluinos in events with an isolated lepton, jets and missing transverse momentum at $\sqrt{s} = 13$ TeV with the ATLAS detector. 38th International Conference On High Energy Physics 2016, ATL-COM-PH, 2016.

[148] ATLAS Collaboration. Search for pair production of gluinos decaying via top or bottom squarks in events with b-jets and large missing transverse momentum in p p collisions at $\sqrt{s} = 13$ TeV with the ATLAS detector. 38th International Conference On High Energy Physics 2016, ATLAS-CONF, 2016.

[149] ATLAS Collaboration. Search for supersymmetry p with two same-sign leptons or three by the ATLAS detector. ATLAS-CONF, (August):1–27, 2016.

[150] ATLAS Collaboration. Search for gluinos in events with an isolated lepton, jets and missing transverse momentum at $\sqrt{s} = 13$ Te V with the ATLAS detector. Eur. Phys. J. C, 76(10), 2016.

[151] ATLAS Collaboration. Modelling Z $\tau\tau$ processes in ATLAS with τ-embedded Z $\mu\mu$ data. Journal of High Energy Physics, 10, 2015.

[152] ATLAS Collaboration. Data-Driven Determination of t\bar{t} Background to Supersymmetry Searches. ATL-PHYS-PUB-2009-083, 2009.

[153] CMS Collaboration. Search for supersymmetry in multijet events with missing transverse momentum in proton-proton collisions at 13 TeV. CMS PAS SUS, 16-033, 2017.

[154] ATLAS Collaboration. Summary of the ATLAS experiment's sensitivity to supersymmetry after LHC Run 1 interpreted in the phenomenological MSSM The. Journal of High Energy Physics, 10(134), 2015.

[155] ATLAS Collaboration. Dark matter interpretations of ATLAS searches for the electroweak production of supersymmetric particles in $\sqrt{s} = 8$ TeV proton-proton collisions. Journal of High Energy Physics, 9(175), 2016.

[156] CERN. The HL-LHC project". http://hilumilhc.web.cern.ch/about/hl-lhc-project.

[157] Altan Cakir and On behalf of the CMS and ATLAS Collaborations. Prospects of New Physics searches using High Lumi - LHC. CMS CR-2014/382, 2014.

[158] Tanju Gleisberg and Stefan Höche. Comix, a new matrix element generator. JHEP, 12:039, 2008.

[159] Fabio Cascioli, Philipp Maierhofer, and Stefano Pozzorini. Scattering Amplitudes with Open Loops. Phys. Rev. Lett., 108:111601, 2012.

[160] Steffen Schumann and Frank Krauss. A Parton shower algorithm based on Catani-Seymour dipole factorisation. JHEP, 03:038, 2008.

[161] Stefan Höche, Frank Krauss, Marek Schönherr, and Frank Siegert. QCD matrix elements + parton showers: The NLO case. JHEP, 04:027, 2013.

[162] ATLAS Collaboration. Comparison of Monte Carlo generator predictions for gap fraction and jet multiplicity observables in ttbar events. ATL-PHYS-PUB, 2014-005, 2010.

[163] Chris D White, Stefano Frixione, Eric Laenen, and Fabio Maltoni. Isolating Wt production at the LHC. Journal of High Energy Physics, 2009(11), 2009.

[164] L. Lönnblad and S. Prestel. Matching Tree-Level Matrix Elements with Interleaved Showers. JHEP, 03:019, 2012.

[165] Christoph Borschensky, Michael Krmer, Anna Kulesza, Michelangelo Mangano, Sanjay Padhi, Tilman Plehn, and Xavier Portell. Squark and gluino production cross sections in pp collisions at $\sqrt{s} = 13$, 14, 33 and 100 TeV. Eur. Phys. J. C, 74:3174, 2014.